

# Transactions of the ASME

Technical Editor  
**ARTHUR J. WENNERSTROM**  
Senior Associate Editor  
**G. K. SEROVY**  
Associate Editors  
Air Pollution Control  
**H. E. HESKETH**  
Diesel and Gas Engine Power  
**G. VanDeMARK**  
Gas Turbine  
**G. OPDYKE**  
Power  
**R. W. PORTER**  
Advanced Energy Systems  
**T. M. BARLOW**  
Fuels  
**H. C. ORENDER**  
Nuclear Engineering  
**J. SUSNIR**

**BOARD ON  
COMMUNICATIONS**  
Chairman and Vice-President  
**K. N. REID, JR.**

Members-at-Large  
**W. BEGELL**  
**W. G. GOTTENBERG**  
**D. KOENIG**  
**M. KUTZ**  
**F. LANDIS**  
**J. T. COKONIS**  
**J. E. ORTLOFF**  
**C. PHILLIPS**  
**H. C. REEDER**  
**R. E. NICKELL**

President, **G. KOTNICK**  
Executive Director,  
**PAUL ALLMENDINGER**  
Treasurer, **ROBERT A. BENNETT**

**PUBLISHING STAFF**  
Mng. Dir., Publ., **J. J. FREY**  
Dep. Mng. Dir., Pub.,  
**JOS. SANSONE**  
Managing Editor,  
**CORNELIA MONAHAN**  
Production Editor,  
**JACK RUMMEL**  
Editorial Prod. Asst.  
**MARISOL ANDINO**

The Journal of Engineering for Gas Turbines and Power (ISSN 0022-0825) is published quarterly for \$100 per year by The American Society of Mechanical Engineers, 345 East 47th Street, New York, NY 10017. Second class postage paid at New York, NY and additional mailing offices. POSTMASTER: Send address change to The Journal of Engineering for Gas Turbines and Power, c/o The AMERICAN SOCIETY OF MECHANICAL ENGINEERS, P.O. Box 3199, Grand Central Station, New York, NY 10163.

CHANGES OF ADDRESS must be received at Society headquarters seven weeks before they are to be effective. Please send old label and new address.

PRICES: To members, \$24.00, annually; to nonmembers, \$90.00.

Add \$6.00 for postage to countries outside the United States and Canada.

STATEMENT from By-Laws. The Society shall not be responsible for statements or opinions advanced in papers or printed in its publications (B 7.1, para. 3).

COPYRIGHT © 1984 by the American Society of Mechanical Engineers. Reprints from this publication may be made on condition that full credit be given the TRANSACTIONS OF THE ASME—JOURNAL OF ENGINEERING FOR POWER, and the author, and date of publication be stated.

INDEXED by the Engineering Index, Inc.

# Journal of Engineering for Gas Turbines and Power

Published Quarterly by The American Society of Mechanical Engineers

Volume 106 • Number 4 • OCTOBER 1984

## TECHNICAL PAPERS

- 716 Nonequilibrium Throughflow Analyses of Low-Pressure, Wet Steam Turbines  
C. C. Yeoh and J. B. Young
- 725 Gas Turbine Cogeneration—Principles and Practice (84-GT-145)  
R. P. Allen and J. M. Kovacic
- 731 The Integrated Approach to a Gas Turbine Topping Cycle Cogeneration System (84-GT-141)  
H. Leibowitz and E. Tabb
- 737 Combined-Cycle System With Novel Bottoming Cycle (84-GT-173)  
A. I. Kalina
- 743 Thermodynamics of an Isothermal Gas Turbine Combined Cycle (84-GT-274)  
M. A. El-Masri and J. H. Magnusson
- 750 A Comparative Study of the Influence of Different Means of Cooling on the Performance of a Combined (Gas and Steam Turbines) Cycle (84-GT-177)  
Chuan shao Wu and J. F. Louis
- 756 Effect of New Blade Cooling System With Minimized Gas Temperature Dilution on Gas Turbines Performance (84-GT-89)  
K. Kawaie, N. Kobayashi, and T. Ikeguchi
- 765 A Numerical Model of Moist Plume Thermodynamics  
B. R. Becker
- 771 Total Absorptivities and Emissivities of Particulate Coal Ash From Spectral Band Emissivity Measurements  
T. F. Wall and H. B. Becker
- 777 A Non-Newtonian Flow Model for Coal-Ash Slag (83-WA/Fu-1)  
E. K. Johnson
- 782 Refuse-Derived Fuel Evaluation in an Industrial Spreader-Stoker Boiler  
K. W. Ragland, R. P. Madding, R. K. Ham, R. J. Vetter, and M. L. Smith
- 789 The Influence of Fuel Hydrogen Content Upon Soot Formation in a Model Gas Turbine Combustor (84-GT-6)  
T. T. Bowden, J. H. Pearson, and R. J. Wetton
- 795 Development of a Dry Low  $\text{NO}_x$  Combustor for a 120-MW Gas Turbine (84-GT-44)  
K. Aoyama and S. Mandai
- 801 Combustion Research Related to Utilization of Coal as a Gas Turbine Fuel (84-GT-285)  
D. M. Davis-Waltermire and R. J. Anderson
- 806 Repowering in Steel Works by Introducing a Blast-Furnace, Gas-Firing Gas Turbine (84-GT-146)  
A. Muyama, H. Hiura, and K. Morimoto
- 812 Crude Oil Burning Experience in MS5001P Gas Turbines (84-GT-293)  
W. J. Bunz, G. N. Ziady, H. vonE. Doering, and R. J. Radice
- 819 The Marine Environment and Its Influence on Inlet System Design (84-GT-137)  
L. V. Shelton and R. S. Carleton
- 825 Evolution of  $\text{NO}_x$  Abatement Techniques Through Combustor Design for Heavy-Duty Gas Turbines (84-GT-48)  
M. B. Hilt and J. Waslo
- 833 An Experimentally Verified  $\text{NO}_x$  Prediction Algorithm Incorporating the Effects of Steam Injection (84-GT-152)  
G. L. Touchton
- 844 Water-Ethanol-Gasoline Blends—Physical Properties, Power, and Pollution Characteristics  
S. Rajan
- 849 Simulation of Fuel Droplet Gasification in SI Engines  
X. Q. Liu, C. H. Wang, and C. K. Law
- 854 Contamination Control in Gas Turbine Oil Systems (84-GT-155)  
F. M. Steele
- 860 Medium-Speed Diesel Engines: Part I—Design Trends and the Use of Residual/Blended Fuels (84-DGP-15)  
F. J. Thomas, J. S. Ahluwalia, and E. Shamah

(Contents Continued)

- 879 **Medium-Speed Diesel Engines: Part II—Lubricants, Their Characteristics and Evaluation**  
(84-DGP-17)  
F. J. Thomas, J. S. Ahluwalia, and E. Shamah
- 895 **Centrifugal Fan Performance With Distorted Inflows** (83-JPGC-GT-5)  
T. Wright, S. Madhavan, and J. DiRe
- 901 **Axial Fan Performance With Blade-Base Clearance** (83-JPGC-GT-6)  
T. Wright
- 906 **Centrifugal Fan Performance With Inlet Clearance** (84-GT-186)  
T. Wright
- 913 **Flow in a Centrifugal Fan Impeller at Off-Design Conditions** (84-GT-182)  
T. Wright, K. T. S. Tzou, and S. Madhavan
- 920 **Prediction of Stiffness and Damping Coefficients for Centrifugal Compressor Labyrinth Seals** (84-GT-86)  
H. R. Wyssmann, T. C. Pham, and R. J. Jenny
- 927 **Analysis for Leakage and Rotodynamic Coefficients of Surface-Roughened Tapered Annular Gas Seals** (84-GT-32)  
C. C. Nelson
- 935 **Development of a Case Vibration Measurement System for the DC-990 Gas Turbine**  
(84-GT-143)  
H. A. Kidd
- 940 **Operational Mode Monitoring of Gas Turbines in an Offshore Gas-Gathering Application**  
(84-GT-77)  
D. F. Toler and R. N. Yorio
- 946 **Lateral Gear Shaft Dynamics Control Torsional Stresses in Turbine-Driven Compressor Train**  
(84-GT-28)  
H. R. Simmons and A. J. Smalley
- 952 **Performance Considerations in Selection and Application of Gas Turbine Drivers for Centrifugal Compressors** (84-GT-45)  
D. L. Blauser and U. Gulati

**DISCUSSION**

- 961 **Discussion of a previously published paper by**  
J. Moore and T. J. Forlini

**ANNOUNCEMENTS**

- 715 **Mandatory excess-page charge notice**  
724 **Change of address form for subscribers**  
919 **Errata on a previously published paper by J. A. Owczarek**  
962 **Information for authors**

# Nonequilibrium Throughflow Analyses of Low-Pressure, Wet Steam Turbines

C. C. Yeoh

G. E. C. Turbine Generators Limited,  
Trafford Park, Manchester,  
England

J. B. Young

Whittle Laboratory, University of Cambridge,  
Cambridge, England

*The paper describes a throughflow computational method that combines wet steam theory with an axisymmetric streamline curvature technique in order to predict nonequilibrium effects in low-pressure steam turbines. The computer program developed is able to deal with both subsonic and fully choked supersonic flows, and steam properties are represented by a truncated virial equation of state. A number of theoretical test cases have been investigated, including the nonequilibrium flow in the primary nucleating stage of a low-pressure turbine and the complete analysis of a six-stage, 320-MW operational turbine. The calculations are the first of their kind in being able to provide information on the spanwise variation of the Wilson point, the average droplet size nucleated, the degree of supercooling throughout the flowfield, the thermodynamic wetness loss, and the nonequilibrium choking mass flow rate in addition to the aerodynamic parameters which are of interest to the designer.*

## Introduction

In 1962, G. Gyarmathy published his thesis, "Bases of a Theory for Wet Steam Turbines" [1]. At the time it appeared likely that, building on these foundations, the turbine designer would soon be in a position not only to predict the formation and movement of water within the machine, but also to tackle the problem of reducing its harmful effects. However, by the early 1970's it had become obvious that the problems were more complex than had previously been suspected and much more work would be required before reliable prediction methods were in the hands of the designers. The turbine manufacturers therefore directed their attention to aerodynamic areas where the returns were more certain, and wet steam theory once more become the province of the academic.

It is instructive to consider the objectives of the steam turbine designer and to speculate why the present wet steam calculation methods are unable to fulfill those objectives. First and foremost, it is necessary to know the magnitude of the departures from equilibrium when the turbine operates below the saturation line and whether the resulting changes in pressure and velocity distribution warrant any alteration in blade design. Secondly, it is desirable to estimate, and hopefully reduce, the loss in efficiency incurred in the wet stages. Thirdly, it is necessary to predict the possibilities of erosion in the machine

Within the broad outlines described above, a knowledge of more detailed aspects of the flow is also required. Departures from thermal equilibrium are characterized by supercooling of the vapor and a knowledge of the distribution of this parameter allows, among their things, the calculation of the

thermodynamic loss. (This is defined as that part of the wetness loss caused by the irreversible, interphase heat and mass transfer). Also of interest is the position of the *Wilson point* (or in the three-dimensional context of a turbomachine, the *Wilson surface*) defined as the point of maximum supercooling. This pinpoints the primary nucleation zone and is the key to the calculation of the resulting fog droplet size, which is the major independent variable controlling the gross effects of wetness. To give just one example, the choking mass flow rate of a low-pressure turbine is a function of droplet size and must be calculated with high accuracy in order to estimate the power output of the machine.

Wet steam theory is now in a position to answer many of these questions for a simple one-dimensional flow, but the flow pattern in a low-pressure turbine stage with high flare and twisted blading is strongly three-dimensional. The simple one-dimensional approach is, therefore, of little value, and in order to provide useful design tools the wet steam researcher must adapt his theory for use with conventional turbomachinery calculation methods. However, in order to make the transition, a number of serious problems must be tackled that do not appear in single-phase calculations. Paramount among these is the necessity of performing the wetness calculations (the nucleation and droplet growth sequences) both efficiently and accurately. One-dimensional procedures deal with single nozzles and usually adopt a marching technique to solve a set of simultaneous ordinary, differential equations. Two-dimensional problems on the other hand invariably require the iterative solution of partial differential equations and may involve the flow in many blade passages in multistage machines. A numerical scheme for integrating the droplet growth equations must therefore be implemented a formidable number of times during the course of a calculation and, even with the capabilities of modern computers, requires

Contributed by the Power Division for publication in the JOURNAL OF ENGINEERING FOR GAS TURBINES AND POWER. Manuscript received by the Power Division February 6, 1984.



phase) and nonequilibrium (two-phase) cases is to be found in the calculation of the wetness fraction  $y$ , which enters the calculations via the density in the continuity equation and the enthalpy in the Euler equation. For equilibrium flow the local values of the mixture enthalpy and entropy completely define the wetness fraction, whereas in the nonequilibrium case the vapor may be supercooled and the wetness fraction depends on the flow history as well as the local conditions.

In order to calculate steam wetness and supercooling in nonequilibrium flow, it is necessary to consider nucleation and droplet growth along the stream surfaces. Because of the often small relaxation times associated with wet steam phenomena, the relevant equations (also to be found in the Appendix of this paper) cannot be applied directly in finite difference form between QO's, and the region must be subdivided into smaller increments for this part of the calculation. An efficient routine for calculating the wetness fraction is described in [3], and it should be noted that the speed with which these computations can be performed determines the overall success, for the routine must be entered very many times before convergence is obtained.

Values of the mixture entropy at each calculation station are also required. In single-phase flow, the increase in entropy along a stream surface is entirely due to viscous effects and is calculated from loss coefficients that can either be specified as input data or computed from empirical correlations at run time. Usual practice is to increment the entropy at blade trailing edges, but in wet steam flows it is preferable to distribute the loss uniformly between the leading and trailing edge in order to avoid numerical, not to mention conceptual, difficulties. In nonequilibrium flows the entropy may also increase due to the irreversible heat and mass transfer between the phases. This *thermodynamic loss* is calculated at run time as part of the procedure for obtaining the wetness fraction and the equations are itemized in the Appendix.

An important aspect of streamline curvature analyses is the specification of the relative tangential component of velocity  $V_\theta$ . In duct regions between blade rows this may be obtained from the conservation of angular momentum

$$rV_\theta = \text{constant} \quad (1)$$

$r$  being the radius measured from the machine axis. Within the blade passages, however, a relative flow angle, defined by

$$\beta = \tan^{-1} \left( \frac{V_\theta}{V_m} \right) \quad (2)$$

must be specified. At the blade trailing edge, if the flow is subsonic, it is sufficiently accurate to assume that

$$\beta = \cos^{-1} \left( \frac{O}{P} \right) \quad (3)$$

where  $O$  is the blade opening and  $P$  is the pitch. If the blade exit flow is supersonic, the expansion around the trailing edge may alter the flow angle significantly and must be allowed for.

Denton's method [4] for calculating this *supersonic deviation* is particularly simple to apply. Essentially, it seeks to satisfy the continuity requirement between the throat and trailing edge of a blade

$$\rho_* V_* t_* O = \rho_{TE} V_{TE} t_{TE} P \cos \beta, \quad (4)$$

where  $t$  is the streamtube height in the meridional plane, subscript  $*$  represents conditions at the throat, and subscript TE conditions at the trailing edge. Because of the proximity of the blade throat to the trailing edge, it may be assumed that the change in streamtube height is negligible and hence

$$\beta = \cos^{-1} \left[ \frac{O \rho_* V_*}{P \rho_{TE} V_{TE}} \right] \quad (5)$$

Expressing equation (5) in terms of the Mach number and

assuming sonic conditions at the throat, it is simple to show that

$$\beta = \cos^{-1} \left\{ \frac{O}{P} \frac{1}{M_{TE}} \left[ \frac{2 + (k-1)M_{TE}^2}{(k+1)} \right]^{\frac{1}{2(n-1)}} \right\} \quad (6)$$

where  $k$  is the isentropic exponent and  $n$  is given by

$$n = \eta k, \quad (7)$$

where  $\eta$  is the local polytropic efficiency and can be calculated from the specified loss coefficient. Equation (6) assumes the fluid to be a perfect gas and equilibrium calculations would normally adopt a value of  $k = 1.12$  to represent low-pressure wet steam properties. This would also be used to calculate to Mach number, i.e.,

$$M_{TE} = \frac{V_{TE}}{\sqrt{1.12p/\rho}} \quad (8)$$

True wet steam, however, is manifestly not a perfect gas, but, at supersonic velocities, when the rate of expansion is high, tends to be characterized by values of the isentropic exponent that are closer to the frozen rather than the equilibrium limiting condition. It was therefore decided to adopt a value of  $k = 1.32$  in equation (6) when calculating the supersonic deviation. The corresponding Mach number was then obtained from

$$M_{TE} = \frac{V_{TE}}{\sqrt{1.32p/\rho_g}} \quad (9)$$

rather than equation (8).

The foregoing procedure, although easy to apply, is open to criticism, and it is probable that a better approximation to the flow in this region could be devised from a consideration of wet steam theory. In any event, it must be emphasized that the isentropic exponent is not required for the general integration procedure along stream surfaces where the interactions between the liquid and vapor phases are represented completely realistically.

Finally, we turn to the problem of convergence of the numerical scheme when the flow in the machine is fully choked. In such cases the boundary conditions are specified by the turbine inlet stagnation conditions, and the back pressure and the mass flow rate is unknown *a priori*. Under such conditions convergence of iteration becomes impossible if an attempt is made to find the correct mass flow rate by small gradual adjustments of this parameter. However, a solution method has been devised by Denton [4] for equilibrium flows that can be applied to nonequilibrium calculations in an identical fashion. In brief, the continuity requirement at the blade trailing edges is abandoned during intermediate iterations and is replaced by a condition to obtain a specified or *target* pressure on the midstream surface at each trailing edge. In this way it is ensured that each blade row is operating at approximately the correct pressure ratio throughout the calculation. For further details, the reader is referred to [4].

### The Primary Nucleating Stage

In a modern, six-stage LP turbine for large-scale power generation, the steam usually crosses the saturation line in the vicinity of stage four. However, nucleation and droplet growth theory (which is well corroborated by experiments in laboratory nozzles) indicate that the steam remains effectively dry until considerable supercooling has developed. The maximum (or Wilson) supercooling is a function of pressure and rate of expansion and typically lies in the range 30–40 K at low pressure [5]. Assuming that similar processes occur in turbines, this would suggest that at least one stage is operating with dry steam, whereas the usual equilibrium analysis would predict significant wetness levels. The *primary nucleating*

stage therefore offers a good starting point for studying the differences between equilibrium wet and dry supercooled operation.

Figure 2 shows the calculation grid for the fourth stage of a low-pressure turbine of a currently operating 500-MW set. The casing boundary streamline has been simplified into a straight line to avoid numerical problems associated with discontinuities in the slope, and an additional QO has been

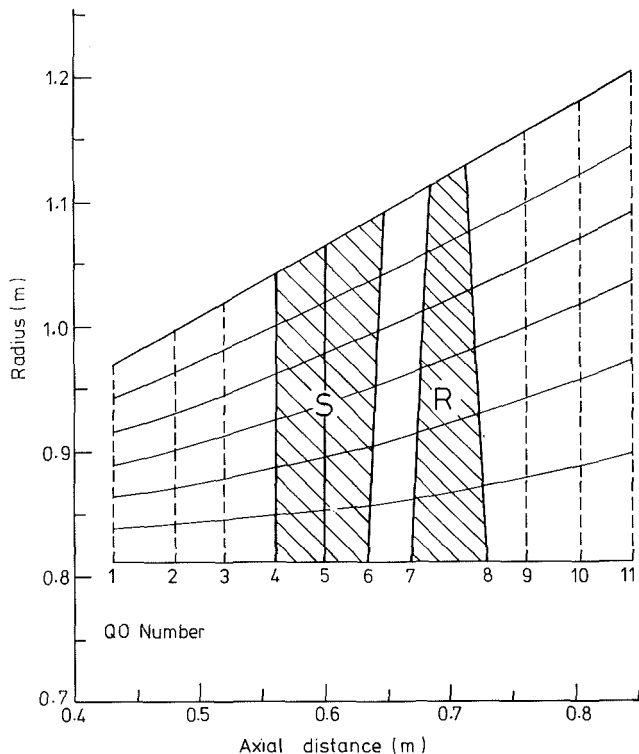


Fig. 2 Computational grid for Stage 4 of a 500-MW, low-pressure turbine

located within the stator row to ensure more even grid spacing. The stream surfaces plotted in Fig. 2 are those obtained from the converged nonequilibrium solution, but they differ only slightly from those calculated assuming equilibrium flow. It is significant, and worth noting that this statement could apply to any of the turbines analyzed to date.

The objective of the exercise was to estimate the likely magnitude of nonequilibrium effects in the stage under consideration. Accordingly, the results are presented as a comparison between equilibrium and nonequilibrium analyses. Unfortunately experimental verification is impossible at the present time, but armed with this type of information, the designer can assess whether the extra complexity of a nonequilibrium calculation is warranted or not.

The differences between an equilibrium and nonequilibrium calculation appear, among other things, as changes in the stage pressure ratio and mass flow rate and depend on the influence exerted by the adjoining stages. For the present calculations, the stage was considered in isolation and in order to demonstrate the salient points, two (slightly artificial) test cases were computed. In the first, equal mass flow rates for both equilibrium and nonequilibrium solutions were specified, while in the second the stage pressure ratio was the parameter specified as constant.

**(i) Specified Inlet Mass Flow Rate.** At inlet to the stage, the steam was assumed to be at the design pressure of 0.7 bars and superheated by 7 K. In both calculations, the prescribed mass flow rate was 45.9 kg/s and aerodynamic loss coefficients were not included in the calculation. A comparison between the equilibrium and nonequilibrium solutions is shown in Fig. 3, where the values of various flow parameters at the blade trailing edges have been plotted.

With reference to Fig. 3, it can be seen that, although the equilibrium wetness at stage outlet is about 2 percent, the nonequilibrium calculation predicts that the steam remains dry and supercooled throughout the stage. The supercooling at the rotor trailing edge is 19 K, and this is not sufficient to promote significant nucleation. However, although the

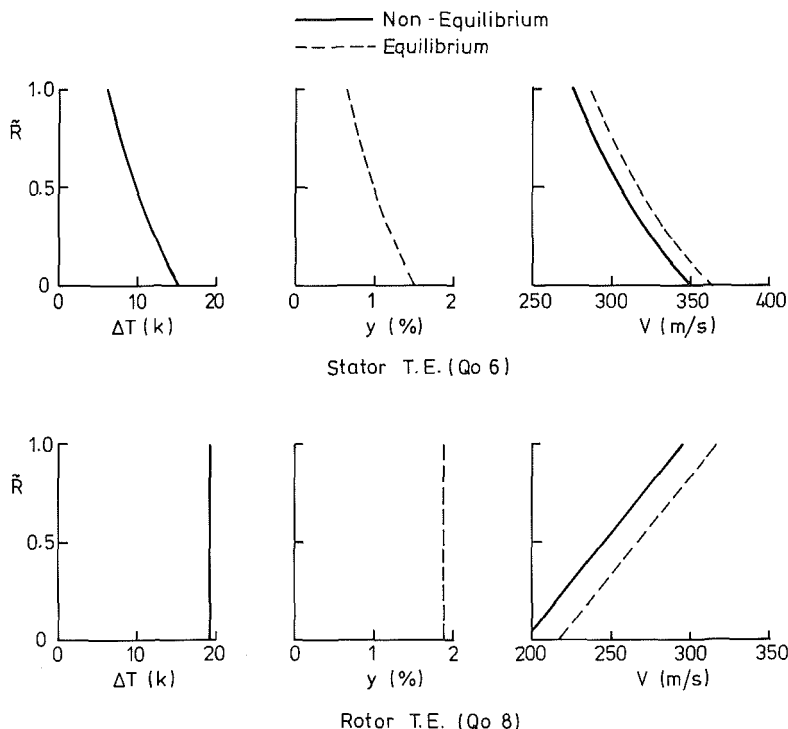


Fig. 3 Variation of flow parameters through the turbine stage of Fig. 2 for a prescribed mass flow rate

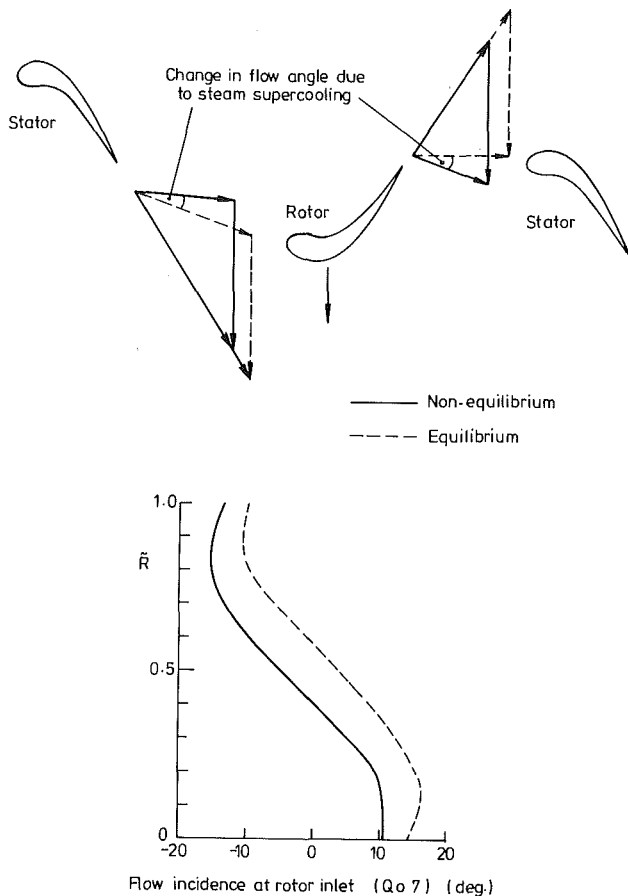


Fig. 4 The effect of steam supercooling on flow incidence angles for a prescribed mass flow rate

magnitude of the supercooling is quite modest, the differences in velocity levels and flow incidence angles as compared with the equilibrium solution are significant. Supercooled steam is denser than equilibrium steam at the same pressure and hence gives rise to lower velocities for the same mass flow rate. The effect of this is to reduce the flow incidence angles onto both stator and rotor blades as shown in Fig. 4. In the present example, the deviation from the equilibrium incidence is between 5 and 10 deg, depending on the spanwise position.

The reduced relative velocities in nonequilibrium flow result in a 14 percent deficit in power output from the stage as compared with the equilibrium solution. The stage pressure ratio also falls slightly, from 1.56 for equilibrium to 1.48 for nonequilibrium flow.

(ii) *Specified Stage Pressure Ratio.* The second test was computed with similar inlet conditions, but the stage pressure ratio was fixed at a value of 2.13. In addition, aerodynamic energy loss coefficients of value  $\xi_A = 0.1$  were specified for both stator and rotor blade rows in order to make the calculations more realistic.

The variation of flow parameters throughout the stage for both equilibrium and nonequilibrium solutions is shown in Fig. 5. The expansion through the stator row displays similar characteristics to the previous test case, with the exception that the equilibrium velocity at the trailing edge is now lower than the nonequilibrium value. This is due to differences in mass flow rate that counteract the effect of increased density due to supercooling and, indeed, the equilibrium analysis predicts a value of 44.9 kg/s, while the nonequilibrium value is 47.0 kg/s, some 4.5 percent higher. This increased mass flow rate for a given pressure ratio is a characteristic of nonequilibrium flows, the magnitude of the increase being

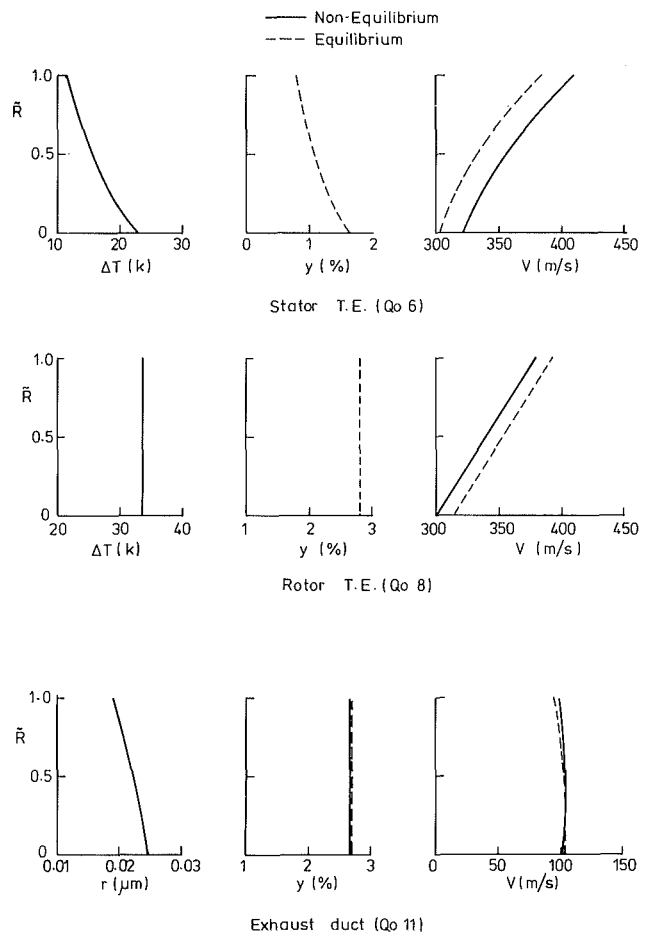


Fig. 5 Variation of flow parameters through the turbine stage of Fig. 2 for a prescribed stage pressure ratio

dependent on, among other things, the departure from equilibrium as measured by the supercooling.

In expanding through the rotor the steam becomes progressively more supercooled, and Fig. 5 shows that the supercooling at the trailing edge is 33 K, a value high enough to induce strong nucleation. Despite this, the nonequilibrium wetness fraction is still negligible because condensation on the droplet nuclei is still minimal. It is interesting to note, however, that the nonequilibrium velocity is now lower than the corresponding equilibrium value because of the increased steam supercooling.

In the duct region immediately following the rotor blade row the droplets grow rapidly as the flow reverts to equilibrium. Figure 5 shows that, at the outflow boundary, QO 11, the droplets are well established with an average radius of  $0.02 \mu\text{m}$  and only a slight variation across the annulus. The supercooling, which has not been plotted, is effectively zero, and the wetness fractions from the two calculations are almost indistinguishable showing that equilibrium has, indeed, been reestablished.

One important consequence of the condensation process is the increase in entropy due to interphase heat and mass transfer resulting in a thermodynamic loss. For the test case under consideration, this amounted to a highly significant  $0.013 \text{ kJ/kg K}$  as compared with an entropy increase of  $0.035 \text{ kJ/kg K}$  due to aerodynamic losses above. Defining a *thermodynamic loss coefficient*  $\xi_T$  by

$$\xi_T = \frac{T_s(p_e) \Delta s_T}{(V_e^2/2)} \quad (10)$$

where subscript *e* represents exit conditions from the blade row, it is found that  $\xi_T \approx 0.07$  for the rotor. Recalling that

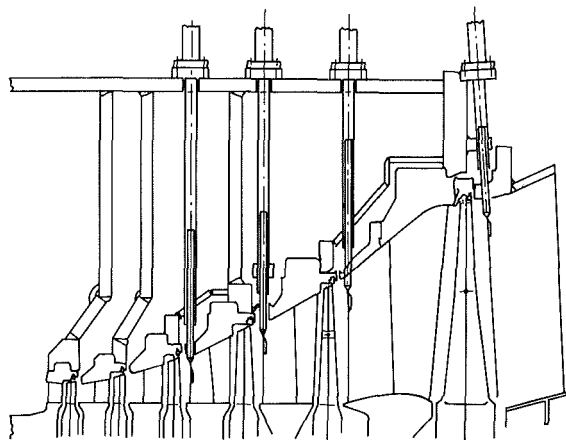


Fig. 6 The 320-MW low-pressure steam turbine

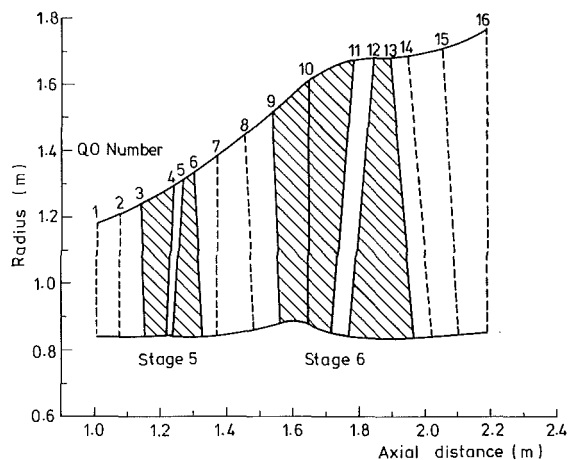


Fig. 7 Computational plane for the last two stages of the 320-MW turbine

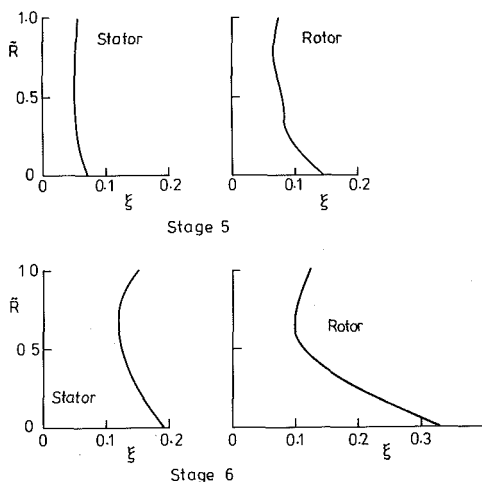


Fig. 8 Input aerodynamic loss coefficients for the 320-MW turbine

the aerodynamic loss coefficient  $\xi_A$  was specified as  $\xi_A = 0.1$ , it appears that, for this particular blade row, thermodynamic losses are of similar magnitude to aerodynamic ones.

The stage power output as calculated by the nonequilibrium analysis is 6.2 percent higher than the equilibrium value due to the increased mass flow rate and a slightly higher stagnation enthalpy drop. This should be contrasted with the reduction

Table 1 Results of calculations for the last two stages of a 320-MW low-pressure turbine

	Equilibrium	Nonequilibrium
$P_{Inlet}$ (bar)	0.753	0.753
$T_{Inlet}$ (K)	370.5	370.5
$P_{Exit}$ (bar)	0.085	0.085
$\dot{m}$ (kg/s)	91.25	94.06
$\Delta s_T$ (kJ/kg K)		0.015
$\Delta s_A$ (kJ/kg K)	0.102	0.102
$\Delta H$ (kJ/kg)	273.5	267.6
Power (MW)	24.95	25.17
$\eta_{TT}$ (%)	89.4	87.5

of 14 percent that was found in the previous test case and demonstrates that nonequilibrium effects can be responsible for comparatively large variations in performance.

### Analysis of a Six-Stage, 320-MW, LP Turbine

The next calculation reported is of the flow in the low-pressure cylinder of a 320-MW turbine designed to operate at 3000 rpm. The turbine geometry, which is shown in Fig. 6, is typical of large, modern LP cylinders, having six stages and a high casing flare towards the exhaust end. Extensive aerodynamic measurements had been made by the manufacturer and the traverse lines are also shown in the diagram. The experimental results have been compared with a number of equilibrium throughflow analyses and reasonably good agreement was achieved.

In order to obtain a full nonequilibrium solution for the machine, it is only necessary to consider the final two stages, as the steam remains superheated during its passage through the first four stages. The computational quasi-orthogonals are shown in Fig. 7, and the aerodynamic loss coefficients in Fig. 8. The latter were obtained from one of the equilibrium analyses and account for the profile, secondary, and tip leakage losses.

During the calculations, it was found necessary to raise the back pressure from the design value of 0.056 bar to 0.085 bar in order to avoid the problem of choking in the exhaust duct. This makes no difference to the flow upstream of the final stage rotor throat and has no effect on the choking mass flow rate. However, the machine work output is underestimated as a result of the reduced pressure ratio across the last stage.

Table 1 shows the overall results for the two stages as a comparison between equilibrium and nonequilibrium solutions. The latter predicts an increase in the mass flow rate of 3.1 percent and a reduction in the stagnation enthalpy drop of 2.2 percent, giving an overall increase in the power output of 0.9 percent. The thermodynamic wetness loss reduces the average total-to-total efficiency for the two stages by 1.5 percent. Other sources of loss due to wetness have not been included in the calculation, however, and may be significant.

The development of the supercooling and the formation and growth of the liquid phase in Stage 5 of the turbine are shown in Fig. 9. During its passage through the stator the steam becomes supercooled, and this is especially pronounced near the hub, where the flow velocities are highest. Nucleation first occurs in this region at the trailing edge of the blade (QO4) and the droplets grow rapidly in the inter row gap. Figure 9 shows that by the following rotor inlet (QO5), equilibrium has been completely reestablished in the hub streamtube, despite the fact that the remainder of the flow is still dry and supercooled. The balance is redressed, however, during the expansion through the rotor, for, by the trailing edge (QO6), the main body of the flow has supercooled sufficiently to induce significant nucleation. It is interesting to note that the steam near the hub deviates only slightly from equilibrium, because the droplets supply sufficient surface area to maintain the required condensation rate. On entering the interstage gap, the expansion rate falls to zero, and by the leading edge of Stage 6 Stator (QO9) reversion is almost



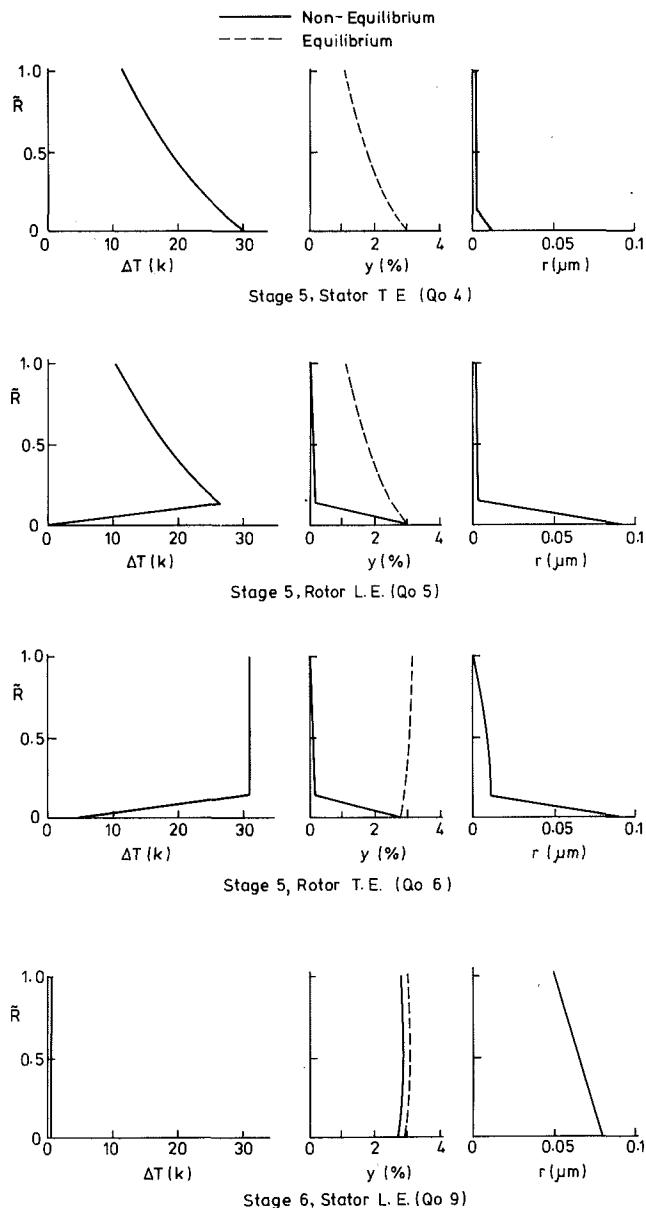


Fig. 9 Development of supercooling and formation of liquid in Stage 5 of the 320-MW turbine

complete. The nonequilibrium wetness fraction agrees closely with that calculated from equilibrium theory, and the supercooling is very low over the whole flow field. Note, however, that there is a considerable variation of droplet radius across the annulus.

The results of the analysis for Stage 6 appear in Fig. 10. Due to the high rate of expansion near the stator hub some supercooling of the vapor develops by the trailing edge (QO11), but this is not sufficient to promote a secondary nucleation. Reversion to equilibrium has occurred by the leading edge of the rotor (QO12) despite the fact that the equilibrium and nonequilibrium wetness fractions are not identical. This is caused by differences in the pressure levels predicted by the two solutions at this station. Somewhat higher values of the supercooling are obtained by the rotor trailing edge (QO13), especially near the tip where the rate of expansion is extremely high. These are still insufficient to induce a secondary nucleation, however, a result attributable firstly to the fine fog droplet size and secondly to the high back pressure used in the calculation. Secondary nucleation would probably occur if an attempt was made to reduce the

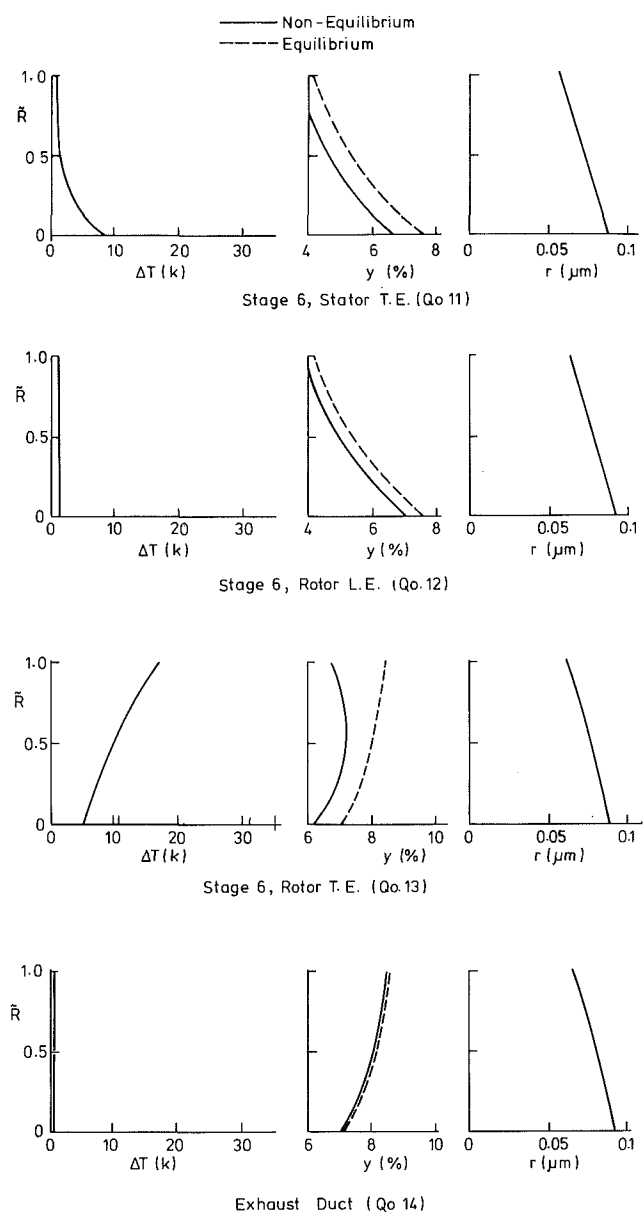


Fig. 10 Development of supercooling and growth of the liquid phase in Stage 6 of the 320-MW turbine

exhaust pressure to the design value. As it is, once the droplets are established they grow slowly to the exhaust (QO14) where their average radius varies from about  $0.09 \mu\text{m}$  at the hub to about  $0.07 \mu\text{m}$  at the casing.

Figures 11 and 12 demonstrate the differences between the equilibrium and nonequilibrium analyses for certain aerodynamic parameters of interest. The spanwise variation of pressure and axial velocity after each blade row is shown, together with the flow incidence angle onto the following blade. Figure 11 deals with Stage 5, and it can be seen that the aerodynamic operation of the stator is only slightly affected by the nonequilibrium phenomena. The axial velocity following the rotor, however, deviates markedly from the equilibrium value, and this gives rise to a significant change in the flow incidence onto the stator of the following stage. Figure 11 shows that the nonequilibrium solution predicts incidence angles some 10 deg more negative than the equilibrium result. The pressure distribution, however, is only slightly affected.

Similar information for Stage 6 can be found in Fig. 12. It should be noted that there is a considerable difference be-

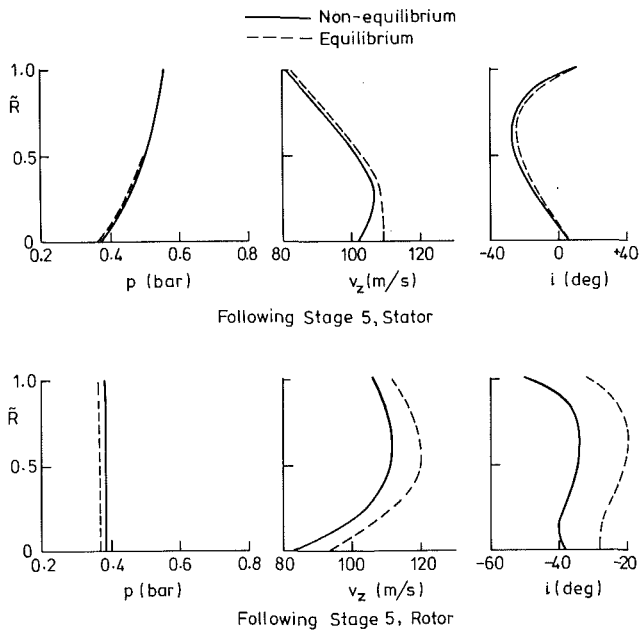


Fig. 11 Variation of pressure, axial velocity and flow incidence angle in Stage 5 of the 320-MW turbine

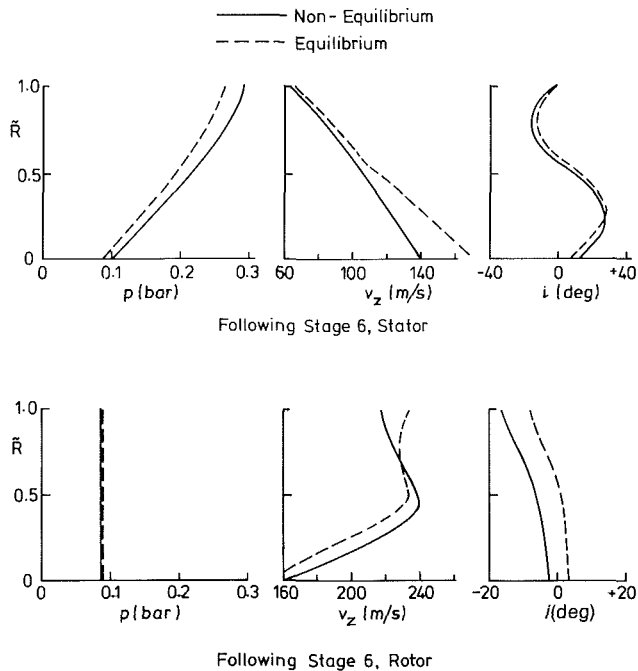


Fig. 12 Variation of pressure, axial velocity and flow incidence angle in Stage 6 of the 320-MW turbine

tween the two pressure distributions following the stator, although the flow incidence onto the rotor is only marginally affected. Following the rotor, the pressures are identical at the prescribed exhaust value of 0.085 bar, and the nonequilibrium solution predicts a slightly greater negative swirl component.

## Discussion and Conclusion

1 Supercooled steam is denser than the corresponding equilibrium mixture, and this has the effect of reducing the velocity levels at various stations in the machine. Reductions of up to 10 percent of the value calculated assuming equilibrium flow can occur depending on the magnitude of the local supercooling.

2 Conversely, departures from thermal equilibrium can manifest themselves by increasing the swallowing capacity of a turbine stage. Typically, the nonequilibrium choking mass flow rate is 3–6 percent higher than the equilibrium value (for the same pressure ratio) and is a strong function of the average droplet size prevailing in the steam flow.

3 The full analysis of a typical low-pressure turbine indicated that the pressure distributions predicted by the equilibrium and nonequilibrium analyses differed only slightly. It is, therefore, unlikely that supercooling of the flow could be detected by measurements of static pressure.

4 In regions of high supercooling, the nonequilibrium calculations predict a change in the relative inlet flow angle onto the blades of up to 10 deg. Generally the effect is to make the flow incidence more negative compared with the equilibrium value. This is one of the most significant results of the analysis from the point of view of blade design. Furthermore, it may be possible to verify the results experimentally by measuring flow yaw and pitch angles at certain stations in the machine.

5 Considerable spanwise variation of droplet size may occur due to the varying locations of the Wilson point on different stream surfaces. This is the most promising area of experimental verification of the theory as measurements of fog droplet size in turbines are now becoming available. Indeed, the probe described in [6] has now been used to traverse the turbine in Fig. 6, and the droplet sizes measured are in close agreement with the theoretical results [7].

6 Secondary nucleations are possible in the last stage of large, low-pressure steam turbines and are controlled by the size of the primary fog. The most likely locations are the hub region of the stator and the tip region of the rotor.

7 The stage thermodynamic wetness loss does not vary linearly with the mean wetness fraction as suggested by the Baumann rule. Typically its contribution can account for a reduction in efficiency of up to 7 percent in the primary nucleating stage. For subsequent stages, its magnitude depends on the prevailing droplet size, fine droplets ( $r < 0.1 \mu\text{m}$ ) being desirable for low losses and low deposition rates. Losses due to the mechanical effects of wetness have not been included in the calculation but may be significant, especially if the fog consists of droplets with radii larger than, say,  $0.5 \mu\text{m}$ .

8 The computational time for a nonequilibrium analysis is generally satisfactory. For example, the CPU time on an IBM 370/165, using a good optimizing compiler for the last two stages of the turbine shown in Fig. 6, was 13 min. Although this was considerably greater than the 30 s taken for the equivalent equilibrium solutions, it is still acceptable for a modern industrial design program. Furthermore, no effort was made to investigate methods for speeding convergence, although it appears likely that considerable scope exists for such improvements.

9 Finally, it should be appreciated that the authors consider the results presented here to be indicative of trends rather than highly accurate numerical values. Many assumptions in the analysis require further detailed investigation (for example, the axisymmetric approximation) and some effects have been totally ignored (for example, the mechanical effects of wetness). Notwithstanding these deficiencies, however, it is hoped that the calculations shed some light on the magnitude of nonequilibrium phenomena occurring in wet steam turbines, and that, by building on this basic foundation, it will be possible eventually to supply the turbine designer with a reliable computational prediction package to deal with the problems of wetness in turbines.

## Acknowledgments

The work described in this paper was supported jointly by N.E.I. Parsons Ltd., the General Electric Company, and the

Central Electricity Generating Board. Thanks are also extended to Dr. J. D. Denton of the Whittle Laboratory, Cambridge for making freely available both his equilibrium throughflow computer program and his expert knowledge.

## References

- 1 G. Gyarmathy, "Bases of a Theory for Wet Steam Turbines," Bull. 6, Inst. for Thermal Turbomachines, Federal Technical University, Zurich, 1962.
- 2 Bakhtar, F., and Tochai, M. T. M., "An Investigation of Two-Dimensional Flows of Nucleating and Wet Steam by the Time-Marching Method," *Int. J. Heat and Fluid Flow*, Vol. 2, 1980, p. 5.
- 3 C. C. Yeoh, and J. B. Young, "Nonequilibrium Streamline Curvature Throughflow Calculations in Wet Steam Turbines," *ASME JOURNAL OF ENGINEERING FOR POWER*, Vol. 104, 1982, pp. 489-496.
- 4 J. D. Denton, "Throughflow Calculations for Transonic Axial Flow Turbines," *ASME JOURNAL OF ENGINEERING FOR POWER*, Vol. 100, 1978, p. 212.
- 5 J. B. Young, "Spontaneous Condensation of Steam in Supersonic Nozzles," *Physico-Chemical Hydrodynamics*, Vol. 3, 1982, p. 57.
- 6 P. T. Walters, and P. C. Skingley, "An Optical Instrument for Measuring the Wetness Fraction and Droplet Size of Wet Steam Flows in L. P. Turbines," Paper C 141/79, Proceedings Steam Turbines for the 1980s, *Inst. Mech. Engrs. Conference*, London, 1979, p. 337.
- 7 M. J. Moore, private communication, Central Electricity Research Laboratories, Leatherhead.

## APPENDIX

### Governing Equations

The derivation of the equations used in the analysis can be found in [3], and they are reproduced below for convenience only. Definition of symbols will be found in the notation and specification of the geometry in Fig. 1.

The momentum equation in the QO-direction,  $q$ , is

$$\begin{aligned} \frac{\partial}{\partial q} \left( \frac{V_m^2}{2} \right) &= \frac{\partial H}{\partial q} - T_g \frac{\partial s}{\partial q} - \frac{1}{2r^2} \frac{\partial}{\partial q} (rV_\theta)^2 \\ &+ \frac{V_m^2}{r_c} \sin(Q - \phi) \\ &+ V_m \frac{\partial V_m}{\partial m} \cos(Q - \phi) + \frac{L\Delta T}{T_s} \frac{\partial y}{\partial q} \end{aligned} \quad (A1)$$

and the mass flow rate crossing a QO from hub-to-tip is

$$\dot{m} = \int_{\text{HUB}}^{\text{TIP}} 2\pi r b \rho V_m \sin(Q - \phi) dq \quad (A2)$$

The Euler turbine equation applied along a stream surface is

$$I = H - r\omega V_\theta = \text{constant} \quad (A3)$$

and the increase in entropy in the meridional direction,  $m$ , is

$$\frac{\partial s}{\partial m} = \frac{\partial s_A}{\partial m} + \frac{\partial s_T}{\partial m} \quad (A4)$$

where

$$\frac{\partial s_T}{\partial m} = \frac{L\Delta T}{T_s T_g} \cdot \frac{\partial y}{\partial m} \quad (A5)$$

Steam properties are represented by a truncated virial equation of state

$$p = \rho_g R T_g (1 + B\rho_g) \quad (A6)$$

where  $B$  is a function of temperature only and is specified empirically.

The rate of nucleation of water droplets in supercooled vapor is assumed to be adequately represented by the classical, Becker-Döring theory and is given by

$$J = \sqrt{\frac{2\sigma}{\pi m^3}} \frac{\rho_g}{\rho_i} \exp\left[-\frac{4\pi r_*^2 \sigma}{3kT_g}\right], \quad (A7)$$

and the droplet growth process is described by Gyarmathy's equation

$$\frac{dr}{dt} = \frac{\lambda_g}{L\rho_L(r + 1.59\bar{l})} \left(1 - \frac{r_*}{r}\right) \Delta T \quad (A8)$$

where  $\bar{l}$  is the mean free path of vapor molecule and is given by kinetic theory as

$$\bar{l} = \frac{1.5\mu_g \sqrt{RT_g}}{p} \quad (A9)$$

# Gas Turbine Cogeneration— Principles and Practice

**R. P. Allen**

General Electric Company,  
Gas Turbine Division,  
Schenectady, N.Y. 12345  
Mem. ASME

**J. M. Kovacik**

General Electric Company,  
Industrial Sales Division,  
Schenectady, N.Y. 12345  
Mem. ASME

*During the decade of the 1960s, industrial users recognized the gas turbine as a reliable prime mover for base load process applications. Gas turbine cogeneration systems were installed in various industries, including chemical, petroleum refining, pulp and paper, and metals. Typically, the size of the cogeneration system considered, and thus the gas turbine size, was governed by the internal heat and power demands of the specific plant. More recently, worldwide concern with regard to the cost and efficient use of energy is providing continuing opportunities for gas turbine cogeneration systems. In some locations, legislation is being enacted to encourage the development of cogeneration to the benefit of the public. This legislation can increase the number of alternative methods in which a cogeneration system can be developed. This paper will briefly review cogeneration principles applicable to the development of gas turbine energy supply systems. The wide range of conditions that can be satisfied using gas turbine cogeneration systems will be introduced. Brief discussions of recent installations are presented, illustrating the actual applications of some of these concepts.*

## Introduction<sup>1</sup>

Even though the price of both fuel and power has increased significantly within the past decade and occasional concerns with regard to the availability of suitable fuels exist, industrial users continue to find gas turbine energy supply systems an economic means of providing their energy needs. One reason for continued emphasis on this prime mover is the many ways that gas turbines can be integrated into the varied energy requirements for industrial plants.

The most common method of integrating a gas turbine into an industrial facility is through use of the exhaust energy for steam generation. Yet, there are other applications where the exhaust energy has been used for drying or process fluid heating, as well as a source of preheated combustion air for process heaters and boilers. The ability to burn additional fuel in the gas turbine exhaust system provides a wide range of power to heat ratios from a gas turbine energy supply system.

The primary factors contributing to favorable economics are excellent thermal performance levels and low incremental investment costs for a gas turbine energy supply system when effectively applied in an industrial facility. This practice of integrating a power generating unit into a system's requirements for heat and power is usually referred to as "cogeneration."

<sup>1</sup> Conversion factors to SI units:

$$\text{kJ} = \text{Btu} \times 1.055$$

$$\text{kg} = \text{lb} \times .4536$$

$$\text{kPa} = (\text{psig} + 14.7) \times 6.895$$

$$^{\circ}\text{C} = (^{\circ}\text{F} - 32) \times 5/9$$

Contributed by the Gas Turbine Division of THE AMERICAN SOCIETY OF MECHANICAL ENGINEERS and presented at the 29th International Gas Turbine Conference and Exhibit, Amsterdam, The Netherlands, June 4-7, 1984. Manuscript received at ASME Headquarters January 7, 1984. Paper No. 84-GT-145.

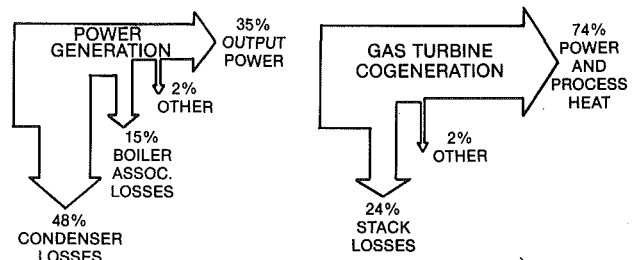
## Cogeneration

Cogeneration is frequently defined as the sequential production of useful thermal energy and shaft power from a single energy source. The shaft power can be used to drive either mechanical loads such as compressors and pumps, or electric generators. For applications generating electricity, the power can either be used internally, or supplied to the utility grid.

The thermal benefit due to cogeneration is illustrated in Fig. 1. The gas turbine cogeneration cycle is arranged to reject a portion of its exhaust energy at the temperature level required in process. The resultant system provides about 75 percent utilization of thermal energy input compared to about 35 percent for a fossil fuel fired steam plant designed to provide power alone. This significant energy savings is one of the prime factors contributing to favorable economics for many gas-turbine-based cogeneration systems.

## Fuel Chargeable to Power – Definition

The fuel chargeable to power generation (FCP) in the in-



**Fig. 1 Fuel utilization effectiveness. Basis: (i) higher heating value; (ii) power generation coal fired and gas turbine cogeneration natural gas fired; (iii) gas turbine cogeneration, unfired heat recovery to 300° F stack temperature.**

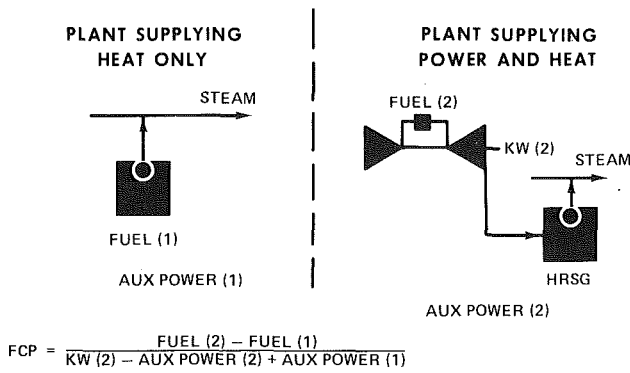


Fig. 2 Fuel chargeable to power

$$FCP = \frac{FUEL (2) - FUEL (1)}{KW (2) - AUX POWER (2) + AUX POWER (1)}$$

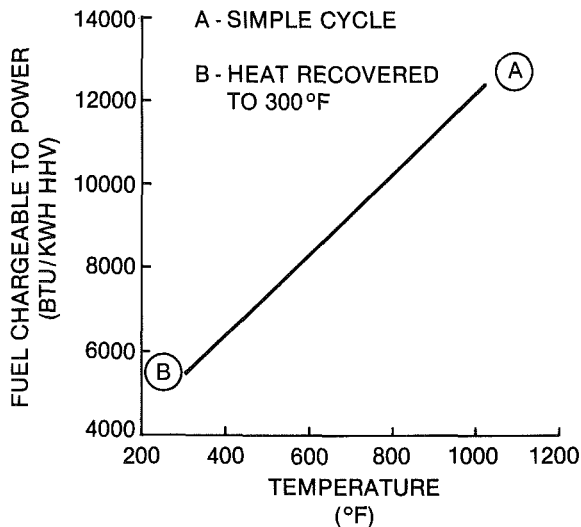


Fig. 3 Gas turbine FCP at various stack temperatures MS6001B. Basis: (i) exhaust heat recovery credited at 84 percent boiler efficiency; (ii) miscellaneous losses are 1½ percent.

industrial plant is the extra increment of fuel for the plant with cogeneration versus the fuel required for the same process heat when all electric power is purchased. For a plant generating electric power only (industrial or utility, the “fuel chargeable to power” and “net plant heat rate” are interchangeable terms. “Net plant heat rate” in Btu/kWh is the more commonly used term for plants generating electric power only.

The FCP concept is illustrated in Fig. 2. Stated in simple terms, the FCP is the total fuel burned in the cogeneration system, minus the fuel which would have been required if all power were purchased (process fuel credit), divided by the gross power generated minus the difference in powerhouse auxiliaries.

### Gas Turbine Cogeneration Systems

Process use of a portion of the thermal energy associated with the hot exhaust of the gas turbine qualifies this prime mover for cogeneration applications. The resulting FCP is primarily a function of the amount of energy recovered from the turbine exhaust for use in process.

The FCP for a natural-gas-fired General Electric Company MS6001B gas turbine/generator, rated at 37,400 kW ISO, whose exhaust energy is used in process, is presented in Fig. 3. This diagram illustrates that the greater the amount of exhaust energy recovered (useful process energy), the lower the stack temperature, and thus the more favorable the FCP.

Assuming that the 300°F stack temperature given in Fig. 3

is a lower limit, the FCP can be improved by adding firing capability to the gas turbine exhaust system. The gain relative to the FCP at 300°F results from added combustion without any increased air (exhaust) supply, a condition required in most fresh-air-fired combustion equipment. For example, if the exhaust of the MS6001B gas turbine in Fig. 3 was fired to 1400°F, and the incremental increase in energy recovered was credited at an 84 percent boiler efficiency and the stack temperature was maintained at 300°F, the FCP would decrease from 5500 to 5310 Btu/kWh HHV, a 3.5 percent improvement. If the gas turbine exhaust were fired to the same excess air as a power boiler, typically 10 percent, the FCP would improve from 5500 to 4200 Btu/kWh HHV, a 23.6 percent improvement.

**Exhaust Heat Recovery Options.** For a specific application, the appropriate heat recovery system is a function of the process heat demand, required temperature levels, process fluid properties, as well as response characteristics to the various process demands. In some applications, the gas turbine exhaust has been used to heat water used in process operations. In other cases, the exhaust energy has been used to heat process fluids or thermal fluids to temperatures as high as 650°F or higher. Other applications have been based on use of the exhaust energy for drying the end products such as in the paper and foods industries. And, there have been cases where the gas turbine exhaust has been used as preheated combustion air for reformers and power boilers. However, the most common use of turbine exhaust energy is for steam production in heat recovery steam generators (HRSG).

The HRSG options available for a given application may include the following designs:

- Unfired
- Supplementary Fired
- Fully Fired

The actual selection is primarily a function of economic evaluations governed by investment and energy cost considerations. For cogeneration applications without any condensing steam turbine power generation, requirements for high power to process heat ratios will usually favor cycle development based on unfired HRSG designs. Addition of firing in the HRSG will decrease the power to process heat ratio.

**Unfired HRSG.** An unfired HRSG is an extended surface convective heat exchanger designed to recover a portion of the sensible heat in the gas turbine exhaust. These units can produce steam at low steam conditions, such as 150 psig, saturated, for direct use in process. Or steam can be generated at elevated steam conditions for expansion in a steam turbine prior to delivery to the process. Some gas turbine units have exhaust temperatures of 1000°F or somewhat higher, temperatures adequate for generation of steam for use at 1500 psig and 925°F, if desired.

The unfired HRSG steam production is a function of the exhaust flow and temperature entering the unit. Thus the unit is a slave of the gas turbine and cannot be easily controlled.

**Supplementary Fired HRSG.** In a supplementary fired application, an auxiliary burner is used to increase the turbine exhaust temperature to 1700°F or less. These units are essentially convective heat exchangers whose construction is similar to unfired designs. The primary difference relative to unfired HRSG’s is in the heat transfer section immediately downstream of the burner where bare tubes and/or tubes with reduced fin pitch and height shield the unit from the radiant energy associated with the burner.

The auxiliary burner permits modulating the steam production capability of the HRSG essentially independent of the gas turbine operating mode.

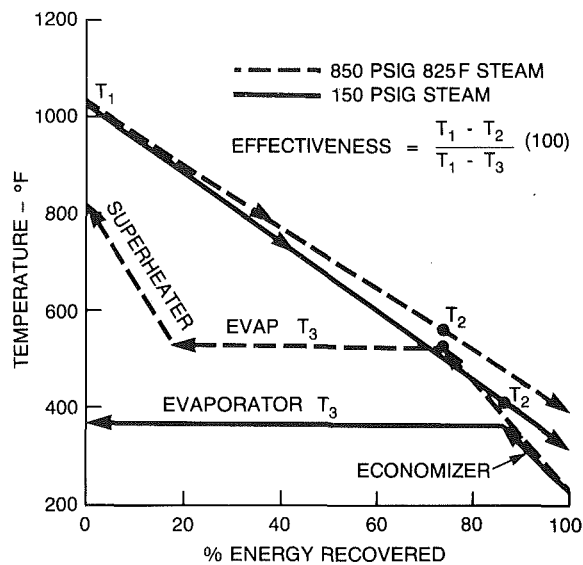


Fig. 4 Temperature relationships: unfired heat recovery boiler

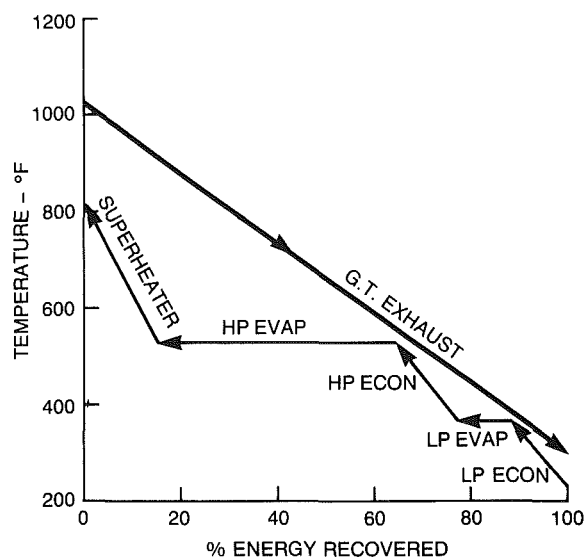


Fig. 5 Temperature relationships: two-pressure level unfired heat recovery boiler

**Fully Fired HRSG.** A fully fired type HRSG is similar in appearance to a power boiler. The design usually admits to its combustion system only the amount of turbine exhaust gas required to generate the desired amount of steam. The balance of the exhaust flow is bypassed and rejoins the gases used for combustion ahead of the heat recovery section.

The maximum amount of steam that can be generated in a fully fired HRSG is usually 6 to 7 times that available from an unfired HRSG. Also, these cycles provide the lowest (best) FCP. Even so, fully fired HRSG's have not been widely used in industrial applications.

**Estimating Steam Production—Unfired and Supplementary Fired HRSG's.** A simplified diagram illustrating the temperature relationships governing unfired HRSG designs is shown in Fig. 4. The temperature difference  $T_2 - T_3$  is frequently referred to as the "pinch point" and is governed by the effectiveness and the degree of subcooling designed into the economizing section. Figure 4 also shows the importance of using a low feedwater temperature in gas turbine HRSG systems, which is in contrast to steam turbine

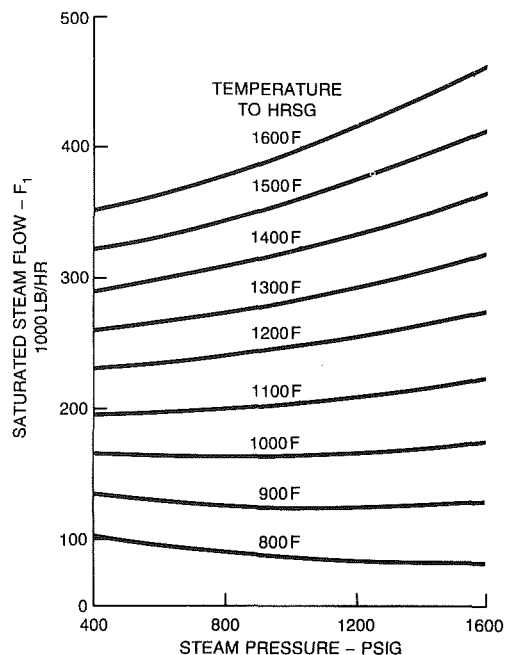


Fig. 6 Saturated steam production in heat recovery steam generators

cogeneration systems where a larger amount of feedwater heating is usually desirable.

The data presented in Fig. 4 also illustrate the lower energy recovery if an HRSG is designed to provide higher steam conditions required to support combined cycles. However, in these instances, opportunities for multiple levels of energy recovery, as shown in Fig. 5, can provide the added benefits of steam turbine cogeneration as well as a lower stack temperature.

The amount of steam that can be generated in single pressure unfired or supplementary fired HRSG's can be estimated using the following relationships:

$$W_{\text{stm}} = \frac{W_{\text{exh}}}{10^6} \cdot F_1 \cdot F_2$$

where:

- $W_{\text{stm}}$  is the steam generated.
- $W_{\text{exh}}$  is the gas turbine exhaust flow in lb/hr.
- $F_1$  is the saturated steam production based on the steam pressure desired and the gas temperature entering the heat transfer surface (see Fig. 6).
- $F_2$  is a factor that adjusts the HRSG production to the desired steam temperature (see Fig. 7).

For units fired to average exhaust gas temperatures of 1700°F or less, the HRSG fuel requirement can be estimated using Fig. 8.

**Selection of Steam Conditions.** The output of a gas turbine cogeneration system can be increased by using suitable steam conditions permitting application of noncondensing steam turbine-generators. These combined cycles provide a higher power to heat ratio and a lower (better) FCP than most cycles providing steam directly for use in process.

The determination of the appropriate initial steam conditions requires an economic analysis that evaluates the benefit of additional power generation relative to the incremental increase in investment cost compared with cycles providing steam directly to process. The contribution of a steam turbine to the cogeneration system output per unit of heat required in process is shown in Fig. 9.

Studies have shown that the higher steam conditions can be more easily economically justified in industrial plants having

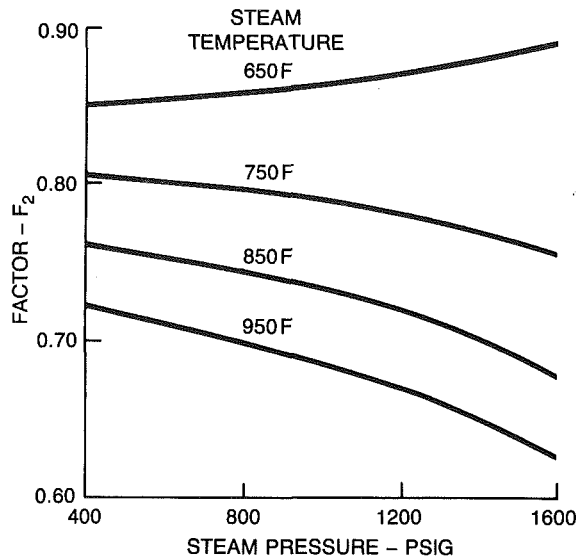


Fig. 7 Superheat adjustment factor

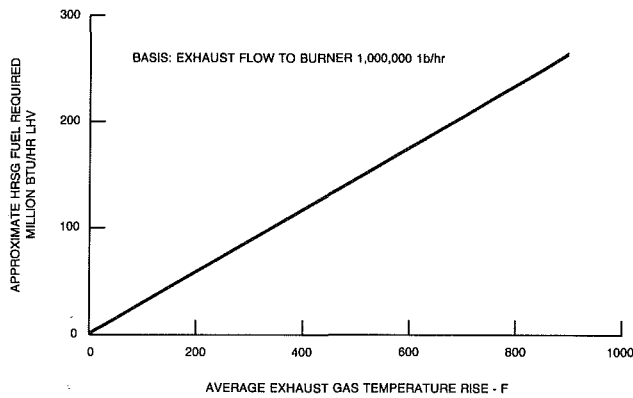


Fig. 8 Estimated HRSG fuel requirements

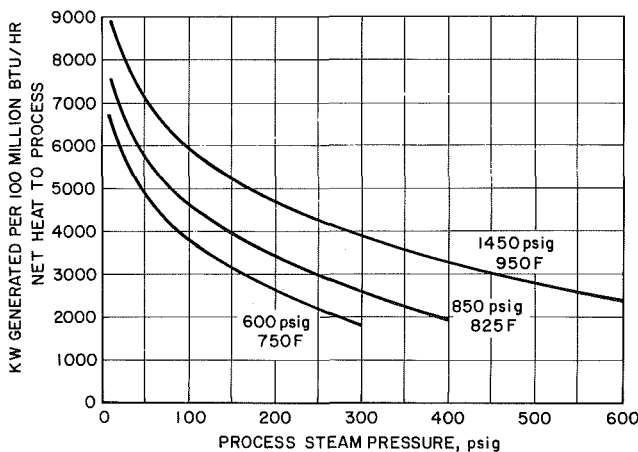


Fig. 9 Effect of inlet steam conditions and process steam pressure on power cogenerated with steam turbines. Basis: (i) 70 percent of process steam flow returned as 200°F condensate and balance as 80°F makeup; (ii) power cycle includes 5 psig deaerating heater; (iii) turbine-generator efficiency is 75 percent.

relatively large process steam demands. Data given in Fig. 10 provide guidance with regard to the initial steam conditions that are normally considered for industrial cogeneration applications. Higher energy costs experienced since the mid-1970s are favoring the upper portion of the bands shown in Fig. 10.

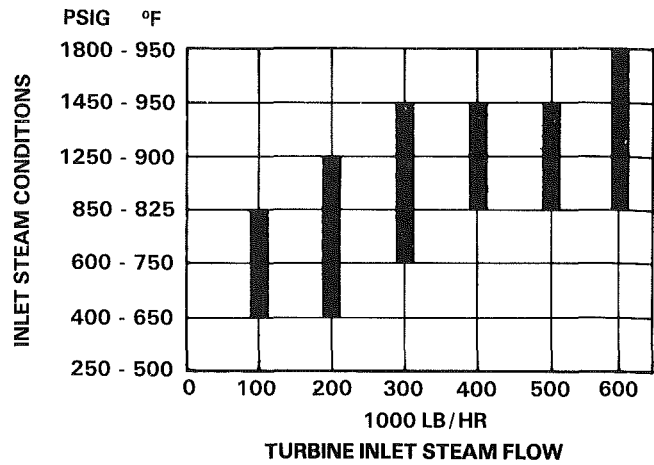


Fig. 10 Range of initial steam conditions normally selected for industrial steam turbines

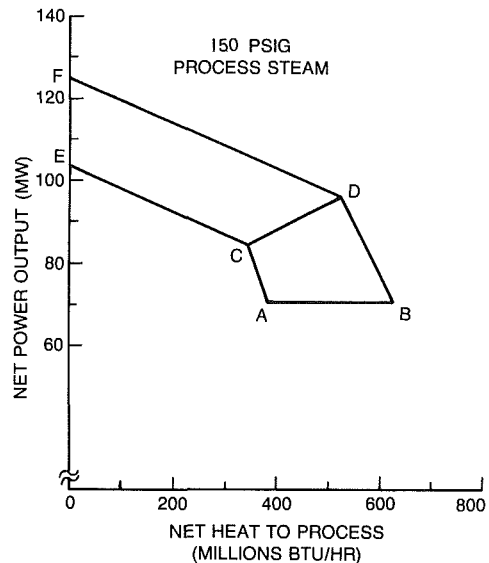


Fig. 11 Performance envelope for various gas turbine cogeneration systems MS7001E gas turbine generator

Basis:

- (i) Sea level site, 80° F ambient, natural gas fuel.
- (ii) Cycle A - Unfired low pressure HRSG
- Cycle B - Supplementary fired (1400°F) HRSG, low pressure process steam
- Cycle C - Combined cycle, unfired, 2-pressure level HRSG, HP at 1450 psig, 950° F, LP at 150 psig sat., non-condensing steam turbine-generator
- Cycle D - Combined cycle, supplementary fired HPSG, steam at 1450 psig, 950° F, noncondensing steam turbine-generator
- Cycle E - Same as Cycle C but with extraction/admission condensing steam turbine-generator
- Cycle F - Same as Cycle D except with straight condensing steam turbine-generator
- (iii) Process returns and makeup enter the 5 psig deaerating heater at a mixed temperature of 180°F.

**Cycle Design Flexibility.** One method of displaying the many options available using a gas turbine in a cogeneration application is shown in Fig. 11. This diagram has been developed for the General Electric Company MS7001E gas turbine/generator (78,400 kW ISO, natural gas fired). A summary of the performance used to develop the performance envelope given in Fig. 11 is presented in Table 1.

Point A represents the 78.4-MW gas turbine generator exhausting into an unfired, low-pressure HRSG. Point C is a combined cycle configuration based on use of a two-pressure level unfired HRSG. The steam turbine in the C cycle is a

**Table 1 Performance of gas turbine cogeneration cycles – MS7001E**

Cycle	A	B	C	D	E	F
Net output – MW	70.4	70.1	84.2	96.4	103.1	124.4
NHP – M Btu/hr	382	627	346	521	0	0
Net fuel – M Btu/hr HHV	396	370	439	496	851	1117
FCP – Btu/kWh HHV	5620	5280	5210	5150	8250	8980
Power per unit heat to process – kW/M Btu/hr	184	112	243	185	NA	NA

Basis: (i) Cycle definition as given in Fig. 11  
(ii) Net output is the total power credited to the cogeneration cycle  
(iii) Net fuel includes credit for the net heat to process (NHP) at an 84 percent process boiler efficiency

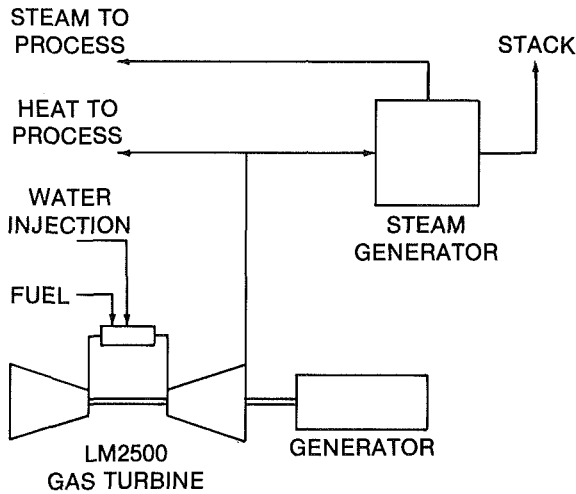


Fig. 12 Cycle diagram for Procter and Gamble cogeneration plant

noncondensing unit expanding the high pressure HRSG steam to the 150 psig process steam header.

Points B and D in Fig. 11 represent operation of the HRSG with supplementary firing to a 1400°F average exhaust gas temperature entering the heat transfer surface. The temperature used for the HRSG firing in Fig. 11 has been arbitrarily limited to 1400°F even though considerably higher firing temperatures and thus steam production rates are possible in the exhaust of this unit.

The “envelope” defined by A, B, C, and D in Fig. 11 represents most effective use of a gas turbine in a cogeneration application. Operation along the line CE, DF, or any intermediate point to the left of line CD represents use of condensing steam turbine power generation, with line EF applicable for combined cycle operation without any heat supplied to process. Thus the cycles along the line EF are combined cycles providing power alone.

The “pure” cogeneration cycles (Cases A–D), cycles without any condensing steam turbine power generation, have a much lower per unit cost of power generation relative to cycles producing large quantities of condensing power. Even so, site-specific fuel and power cost considerations may dictate cycles with considerable condensing power as the appropriate economic choice.

### Recent Gas Turbine Cogeneration Applications

The following sections briefly describe recent General Electric Company cogeneration applications. All are based on the provisions of PURPA (Public Utility Regulatory Policies Act) that permits qualifying facilities to sell excess power generated to the utility grid. Several applications include unique exhaust heat recovery systems compared to conventional HRSG systems.

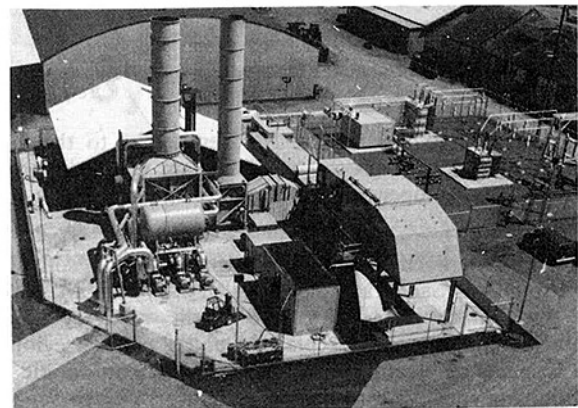


Fig. 13 Pacific Cogeneration facility at Vancouver, Washington

**Procter and Gamble – Oxnard, California.** This was the first GE-packaged LM2500 gas turbine installed for cogeneration. The Procter and Gamble facility manufactures household paper products. As shown in the cycle diagram in Fig. 12, the gas turbine produces a nominal 20 MW of electric power. Approximately half of this energy is used within the plant, with the remainder sold to the neighboring utility, Southern California Edison. On the heat recovery side, the exhaust from the engine is split: about 50 percent goes to an unfired heat recovery steam generator with the remainder used directly in the paper drying process.

The gas turbine passed the 10,000 fired hours mark in May 1983, following a January 1982 startup. This attests to the continuous duty operation required by these plants as well as the high availability that can be achieved. This unit is equipped for dual fuel operation, with water injection to limit NO<sub>x</sub> emissions to the 75 ppmv level.

**Pacific Cogeneration – Vancouver, Washington.** In 1979, Great Western Malting initiated its efforts to establish a cogeneration facility at their plant on the Columbia River. This plant supplies malt to many breweries in the western United States. The malt production process involves an extensive drying phase at the end of the cycle. Prior to the installation of the cogeneration plant, the heat for drying was supplied by natural-gas-fired furnaces.

This heat source was replaced by an LM2500 gas turbine exhausting into a heat recovery, hot water boiler. The hot water is piped to the drying kilns, where the radiant energy from the heat exchanger is used to dry the malt. An aerial photograph of the plant (Fig. 13) shows the LM2500 in the center, the heat recovery equipment on the left, and the electrical system on the right.

The gas turbine generates 20 MW of electrical power, which is sold to the Clark County Public Utility District. Over 80 percent of the fuel input energy to the unit is recovered either as electrical power or hot water. The turbine is equipped with



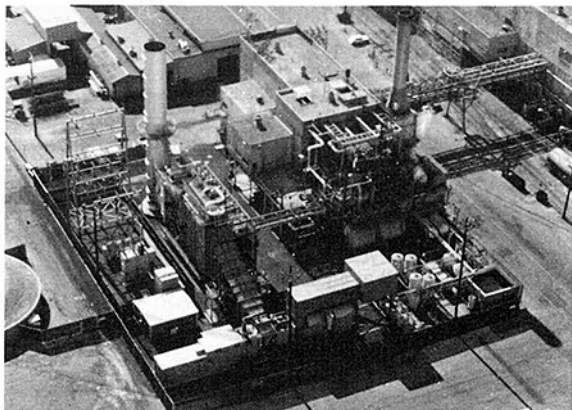


Fig. 14 Crown Zellerbach facility at Antioch, California

water injection to control the  $\text{NO}_x$  emissions to the local environmental code requirements. The plant was dedicated in May 1983 and is operated by Pacific Cogeneration, a subsidiary of Great Western Malting.

**Crown Zellerbach – Antioch, California.** This container board mill near San Francisco installed a 35-MW MS6001B unit with a supplementary fired heat recovery steam generator. This equipment replaces a power boiler previously used to generate steam for an existing single automatic extraction condensing steam turbine-generator used to support process steam demands.

The gas turbine is fueled by natural gas, and the steam generator has dual fuel capability for gas and residual oil. The steam generated goes to a plant header, from which steam for  $\text{NO}_x$  control for the gas turbine is taken. An attemperater is provided to reduce the steam temperature prior to injection into the gas turbine. The steam is injected into the head end of the combustion chambers.

Crown Zellerbach received an award from the American Paper Institute/National Forest Products Association for its excellence in control of nitrogen oxides from the gas turbine. This is a significant achievement, considering the difficulties in siting new generating facilities in California in areas where air quality is a major concern.

This cogeneration plant, pictured in Fig. 14, has been in operation since November 1982. Surplus electric power is sold to Pacific Gas and Electric Co.

**GE Plastics – Bergen Op Zoom, The Netherlands.** This plant, scheduled for startup in mid-1984, will utilize an MS6001 gas turbine and heat recovery steam generator to provide in-plant power and steam for their engineering plastics production. Excess electrical power will be sold to the public utility company.

The heat recovery system includes a hot-oil loop as well as conventional steam generation. The heated oil is used in processes where the presence of water is not acceptable. An overall operating efficiency of 85 percent is anticipated from this plant.

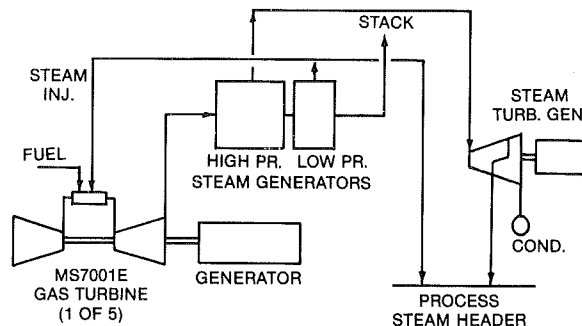


Fig. 15 Cycle diagram for Power Systems Engineering

Further details on this cogeneration plant are presented in the paper entitled, "Cogeneration and Multiple Heat Recovery at a Plastics Manufacturing Facility," by A. P. Van Oostroom of GE Plastics and J. deRuiter of Comprimo. This paper (84-GT-125) was prepared for the 1984 ASME Gas Turbine Conference.

**Power Systems Engineering.** On a much larger scale, this cogeneration plant will generate some 500 MW of power for the local utility and send the steam produced in the heat recovery boilers to a nearby chemical plant. Five MS7001 gas turbine/generators are the heart of this plant, each rated 77 MW. The heat recovery system, shown in Fig. 15, consists of unfired two-pressure level steam generators. Steam for injection into the gas turbine for  $\text{NO}_x$  control is taken from the low-pressure steam section, and the high-pressure steam is expanded through a steam turbine to generate additional power.

This plant, designed by Power Systems Engineering in Houston, Texas, will be located at Channelview, Texas, and is scheduled for operation in 1985.

## Closure

The application of gas turbine cogeneration systems continues to grow as users consider the many ways that gas turbines can be economically used in their plants. In addition to shaft power, these systems can provide process steam, heated process fluids, hot water for process or other plant use, or preheated combustion air to satisfy plant thermal requirements. And there are instances where several different forms of energy recovery have been used from the exhaust of a single gas turbine unit.

This paper has briefly reviewed some of the technical considerations in the application of gas turbine cogeneration technology. The flexibility of these systems in meeting the varied industrial energy demands was discussed.

However, gas turbine cogeneration is not an economic option for all industrials. Site-specific evaluations based on plant thermal demands, available fuels and their costs and the value of power are required to define whether this technology can be justified.

# The Integrated Approach to a Gas Turbine Topping Cycle Cogeneration System

H. Leibowitz

Mechanical Technology Inc.,  
Ballston Spa, N.Y. 12020

E. Tabb

Gas Research Institute,  
Chicago, Ill. 60631

*Under Gas Research Institute (GRI) sponsorship, a new gas turbine cogeneration system was developed by Mechanical Technology, Inc., (MTI) for installation at a General Motors plant in early 1985. Specific emphasis was placed on system integration. A single, prime-reliable drive train and a single control center replace a wide assortment of nonintegrated, free-standing power drives and control centers. On-line availability, installation costs, and overall user acceptance are improved. The cogeneration set produces 3 MW<sub>e</sub> and 8,860 kg/hr (19,500 lb/hr) of 1825 kPa (250 psig) saturated steam using an Allison 501-KH gas turbine and a natural circulation waste heat boiler. The system is designed for multifuel operation using either natural gas or distillate oil. A steam injection feature is employed to increase output to 4 MW<sub>e</sub> when process steam demand diminishes. The system is prepackaged, skid mounted, and delivered in four modules: one each for the machinery, duct burner, waste heat boiler, and controls.*

## Introduction

Although the rules and definitions that govern eligible cogenerators have been in existence since PURPA of 1978, the marketplace has been conspicuously slow in accepting this seemingly better approach to energy utilization. In the entire state of California, where cogeneration has been actively promoted, there are approximately only 35 systems that are operational at this time. Although some point to the poor ratio of electric/fuel prices as the culprit, there is more reason to believe that the major factor causing weak market penetration is poor system integration and the user's perception of the complexity and "unfriendliness" that follows.

An advanced gas turbine topping cycle cogeneration system has been developed by Mechanical Technology, Inc., with support from the Gas Research Institute (GRI). GRI is a gas-utility-financed organization that was established in 1977 to enhance and promote the use of natural gas through externally funded research projects. The major goal of this project was to develop an integrated system with enhanced performance through the implementation of several engineering development tasks, namely:

- Control integration
- Mechanical equipment integration
- Rotary screw gas compressor application
- Steam injection application.

The belief is that well-integrated, efficient, easy-to-operate

systems are "user friendly" and, as such, will gain better marketplace acceptance.

The prototype cogeneration system will be installed at a General Motors plant in early 1985. It consists of an Allison 501-KH steam-injected gas turbine and a supplementary-fired waste heat boiler. Nominally, the system produces 3 MW<sub>e</sub> and 8,860 kg/hr (19,500 lb/hr) of 1825 kPa (250 psig) saturated steam. Supplemental firing increases the steam production to 15,900 kg/hr (35,000 lb/hr). When thermal demand falls off, steam is injected into the gas turbine combustor to increase electrical output and to improve the system's heat rate. At 2.27 kg/s (5 lb/s) of steam injection, the system's output increases to 4 MW<sub>e</sub> and heat rate drops by 20 percent to 11,300 kJ/kWh (10,700 Btu/kWh).

The design strategy, system and component specifications, and estimated system performance levels are the subject of this paper.

## System Design Approach

The system has been specifically designed for industrial cogeneration service, with an emphasis on fitness for duty, modularity, and reliability. This is a major departure from the conventional approach where components, originally specified for other applications, have been specified and arranged in an expedient, suboptimum manner. As a consequence, conventional systems suffer from a redundancy of parts and operations, are more expensive to operate, and suffer in terms of their on-line availability.

The subject system contains components that have been selected or designed for a unique cogeneration function and are integrated as much as possible on a prepackaged skid. System reliability has also been thoroughly addressed.

Contributed by the Gas Turbine Division of THE AMERICAN SOCIETY OF MECHANICAL ENGINEERS and presented at the 29th International Gas Turbine Conference and Exhibit, Amsterdam, The Netherlands, June 4-7, 1984. Manuscript received at ASME Headquarters January 9, 1984. Paper No. 84-GT-141.

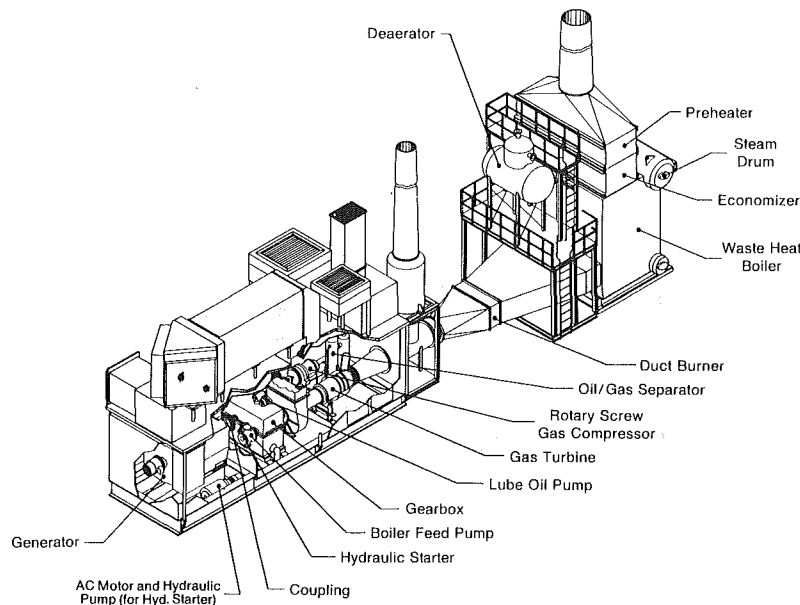


Fig. 1 Cogeneration system—skid arrangement

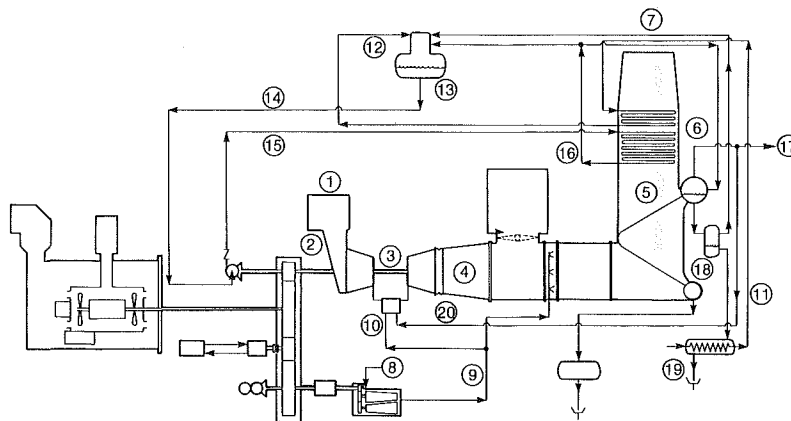


Fig. 2 Cogeneration system energy and mass balance

Cogeneration systems are expected to operate at base load, imposing a greater availability requirement than that for peaking or pump station power systems. Accordingly, the subject system is designed with a single, prime-reliable drive system. All of the major components that transmit or develop power operate within the same drive train. The load gearbox contains six shaft penetrations: one each for the gas turbine, electric generator, fuel gas compressor, lube oil pump, boiler feed pump, and turbine starter (see Fig. 1). The electrical and/or mechanical prime movers and support accessories normally used in conjunction with the gas compressor, boiler feed pump, and lube oil pump, along with their attendant unavailabilities, have been eliminated.

Another feature which enhances integration and system reliability is the gas-turbine-driven fuel gas compressor. Instead of contending with a separate skid-mounted, diesel-engine-driven reciprocating compressor, the compressor selected for the subject system is a compact rotary screw type driven directly by the gearbox and located on the same skid as the gas turbine. Approximately 13.8 m<sup>2</sup> (150 ft<sup>2</sup>) of skid surface is saved by eliminating a redundant cooling system, motor control center, support structure, and piping. The rotary screw compressor is also much smaller and more reliable than its reciprocating counterpart.

The third system feature which addresses the integration issue, and perhaps the most significant feature from an operational consideration, is the overall system control.

Controls that normally accompany each major subsystem (turbine generator, waste heat boiler, duct burner, and gas compressor) as separate panels and displays are now fully merged into a single cabinet and control center. A centrally located motor control center, process controller, annunciator panel, and instrument display console will service the entire cogeneration package. To accommodate a variety of siting requirements, the control skid is prepackaged and may be located adjacent to the machinery skid or at a remote location designated by the user.

### System Specification

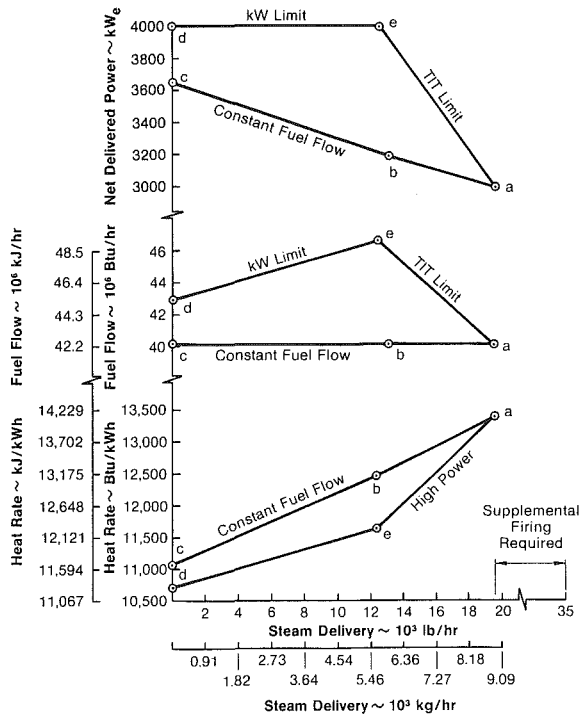
The cogeneration system is shown schematically in a process flow diagram, Fig. 2. The energy and mass balance state points for simple cycle and steam injection operation are presented in Table 1. The addition of 1.82 kg/s (4 lb/s) of steam increases the compressor pressure ratio from 9.3 to 10.3 but decreases the turbine inlet temperature (TIT) to 913°C (1675°F). If an additional 4.4 × 10<sup>6</sup> kJ/hr (4.2 × 10<sup>6</sup> Btu/hr) of fuel had not accompanied the steam injection, the TIT would have been reduced even further to approximately 871°C (1600°F).

### Performance With Variable Steam Demand

The performance maps shown in Fig. 3 illustrate the

**Table 1 Thermodynamic state points energy and mass balance**

Station	Without Steam Injection					With Steam Injection						
	Flow		Pressure		Temperature		Flow		Pressure		Temperature	
	kg/hr	(lb/hr)	kPa	(psia)	°C	(°F)	kg/hr	(lb/hr)	kPa	(psia)	°C	(°F)
1	55,950	(123,100)	101	(14.7)	16	(60)	55,950	(123,100)	101	(14.7)	16	(60)
2	55,950	(123,100)	100	(14.6)	16	(60)	55,950	(123,100)	100	(14.6)	16	(60)
3	56,790	(124,950)	944	(137.0)	982	(1800)	63,420	(139,500)	1033	(149.9)	913	(1675)
4	↓	↓	103	(14.9)	510	(950)	↓	↓	103	(14.9)	456	(852)
5	↓	↓	—	—	222	(431)	↓	↓	—	—	226	(439)
6	↓	↓	—	—	161	(322)	↓	↓	—	—	178	(352)
7	↓	↓	101	(14.7)	136	(277)	↓	↓	101	(14.7)	152	(305)
8	839	(1845)	586	(84.7)	16	(60)	926	(2037)	586	(84.7)	16	(60)
9	839	(1845)	2067	(299.7)	54	(130)	926	(2037)	2067	(299.7)	54	(130)
10	$Q_{GT} = 42.4 \times 10^6$ kJ/hr (40.2 × 10 <sup>6</sup> Btu/hr)					$Q_{GT} = 46.8 \times 10^6$ kJ/hr (44.4 × 10 <sup>6</sup> Btu/hr)						
11	9,180	(20,200)	446	(64.7)	66	(150)	8,909	(19,800)	446	(64.7)	66	(150)
12	↓	↓	446	(64.7)	107	(225)	↓	↓	446	(64.7)	107	(225)
13	↓	↓	205	(29.7)	121	(250)	↓	↓	205	(29.7)	121	(250)
14	↓	↓	136	(19.7)	121	(250)	↓	↓	136	(19.7)	121	(250)
15	↓	↓	2,857	(414.7)	121	(250)	↓	↓	2,857	(414.7)	121	(250)
16	↓	↓	2,857	(414.7)	191	(375)	↓	↓	2,857	(414.7)	191	(375)
17	8,863	(19,500)	1825	(264.7)	208	(406)	2,045	(4,500)	1825	(264.7)	208	(406)
18	318	(700)	205	(29.7)	121	(250)	318	(700)	205	(29.7)	121	(250)
19	318	(700)	101	(14.7)	100	(212)	318	(700)	101	(14.7)	100	(212)
20	No Injection					6,545 (14,400) 1825 (264.7) 208 (406)						
Net Generator Output: 3000 kW <sub>e</sub>						Net Generator Output: 4000 kW <sub>e</sub>						
System Heat Rate (LHV) 14,120 kJ/kWh (13,400 Btu/kWh)						System Heat Rate (LHV) 11,700 kJ/kWh (11,100 Btu/kWh)						



**Fig. 3 Cogeneration system performance—16°C (60°F) day, gas fuel at 583 kPa (70 psig)**

performance of the system as it varies with steam delivered to process. Two possible modes of operation are presented: one at constant fuel flow (points a, b, and c) and the other at the high power setting (points a, e, and d). At constant fuel flow, the injected steam ( $W_s$ ) causes the TIT to drop by approximately 12.6°C/kg/s (50°F/lb/s). Nevertheless, output and heat rate are both improved; the output increases to 3630 kW and the heat rate decreases to 11,700 kJ/kWh (11,100 Btu/kWh) at full injection (no steam to process).

The operator also has the option of maintaining the TIT as steam is injected. This results in the highest power setting. At a steam delivery of 5640 kg/hr (12,400 lb/hr), shown as point e, the slope of the curve changes as the control limit parameter changes from TIT to generator output. Along this mode, the output and heat rate at full injection reach 4 MW<sub>e</sub> and 11,300 kJ/kWh (10,700 Btu/kWh), respectively.

### System Sizing

Although the 501-KH engine has a torque limit corresponding to 6190 kW (8300 hp) (refer to later section on Engine Performance), its maximum rated capacity for this system is 4850 kW (6500 hp). Derating the system to 4000 kW<sub>e</sub> was a result of a conscious decision to optimize user economics instead of output. To the extent that this system deals *primarily* with the cogeneration (electric and thermal output) application, and *secondarily* with the power-only mode of operation, the period of operation at full injection was considered too short to justify increasing the power rating and corresponding cost of the system's major components, e.g., generator, gearbox, fuel gas compressor, starter, etc. Furthermore, operation at levels substantially below capacity increases parasitic losses and, likewise, the system's heat rate; this was another factor which favored the 4 MW<sub>e</sub> power limit.

### General Arrangement

The system is housed on four skids: one each for the machinery, waste heat boiler, duct burner, and one for the controls and electric switchgear. The machinery, duct burner, and waste heat boiler skids are shown in Fig. 4. Together, the skids measure 20.4 m long by 3.25 m wide (67 ft by 10 ft 8 in.).

The integrated drive train featuring the six shaft penetration gearbox and the turbine-driven gas compressor is shown pictorially in Fig. 1. A clutch is installed between the gas compressor and gearbox to uncouple the compressor during start-up and at all other times when operating on distillate oil. The clutch requirement is explained in greater detail in the discussion of the system start-up procedure in a later paragraph.

Due to the close proximity of the gas compressor to the other machinery, a fire wall is installed to separate the generator compartment from the gas turbine and auxiliary machinery. Positive pressure is maintained in the generator compartment with forced draft fans to ensure that no migration of natural gas into the generator compartment can occur. Moreover, an induced draft fan, located behind the gas turbine diffuser, cools the turbine case and evacuates any gas leaks overboard.

The duct burner and waste heat boiler are located directly downstream of the gas turbine diffuser. Provisions have been made in the skid design to accommodate a diverter valve, although this is not shown as a bill of material item. Since the

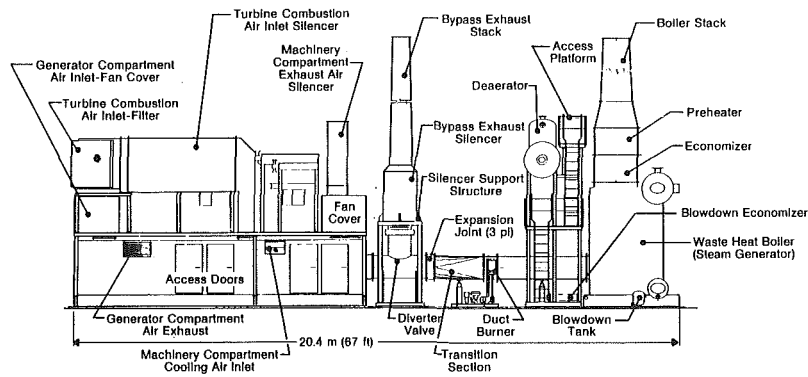


Fig. 4 Cogeneration system—elevation view

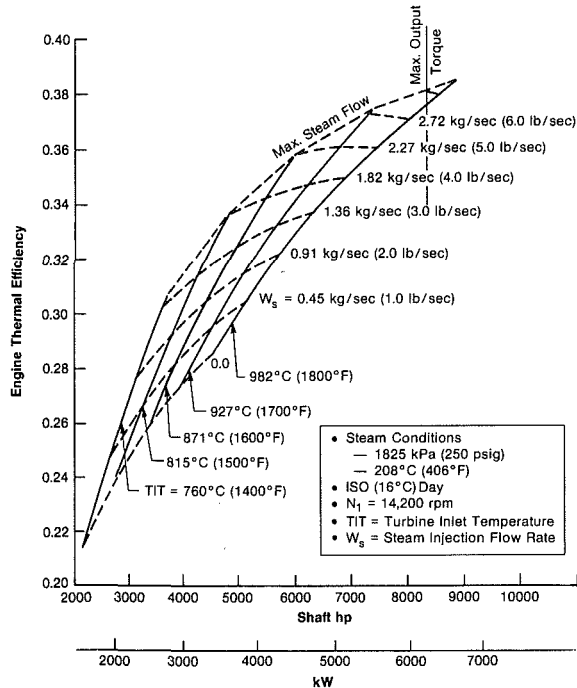


Fig. 5 501-KH engine performance with steam injection

system is expected to generate steam at all times, either for process use or for turbine injection, there is little or no need for a bypass stack. Furthermore, the waste heat boiler specification allows for operation during nonsteaming periods. A level of water will be maintained inside the drum during start-up to minimize tube wall temperatures and weld stresses. Still, if the customer so chooses, a bypass stack can be added without difficulty.

### Steam Injection

Cogeneration systems normally operate on a thermal load following basis (steam demand). Large swings in steam demand, both diurnal and annual, may have significant impact on the economic viability of the installation. An effective way to minimize these "swings" and to keep the gas turbine base loaded is to inject excess steam into the gas turbine when process steam demand is low. Although this particular application is somewhat different, the art and operation of industrial gas turbines with steam injection is not new. Bultzo at Exxon Baytown reported on the performance improvement of the GE MS 3000 with steam injection in 1969 [1], while Kydd and Day (1972) [2] described a system wherein steam generated in an unfired waste heat boiler was injected into a gas turbine.

The subject system contains this feature; the Allison 501-KH is the steam-injected version of the 501-KB. Other than providing steam manifolds on the outer combustor case and strengthening the first-stage compressor disk and output shafts, no other turbine structural modifications were necessary.

The choice of steam injection conditions was made on the basis of performance, cost and end-user familiarity. Market studies showed that 1825 kPa (250 psig), 208°C (406°F) dry saturated steam provided the best market coverage. While injecting with superheated steam improves performance (heat rate) over that with saturated steam by about 6 percent during power-only operation, the selection of the latter over the former results in substantial benefits to the end user. As stated previously, the product addresses the cogeneration duty cycle as its primary application with the power-only mode being less important. That places process requirements first, and hence the bias toward saturated steam. Selecting saturated steam over superheated steam also eliminates the cost of a superheater and a desuperheating station, the attendant superheater unavailability, the additional water treatment requirements, and perhaps most significantly, the end user's lack of familiarity (and corresponding negative perception) with the additional complexity imposed by a superheater. Finally, Allison has completed its shop tests [3] on the 501-KH using 1825 kPa saturated steam. With due consideration given to all of the above, the decision was made to inject dry saturated steam at 1825 kPa.

### Engine Performance

The performance characteristics of the 501-KH, shown in Fig. 5, describe power and efficiency at the output shaft as a function of steam injection flow rate and TIT. The limits of engine operation are denoted by the torque limit line at 6190 kW (8300 hp) and the line of maximum steam flow. At maximum steam flow, the engine is operating at a TIT at which all steam generated in the waste heat boiler (without supplemental firing) is injected into the engine.

At 982°C TIT, 2.3 kg/s, ISO, the engine's output increases by 82 percent, from 3394 kW to 6190 kW (4550 hp to 8300 hp). The corresponding improvement in engine efficiency is 32 percent. Operating in the subject 4 MW<sub>e</sub> system, however, the engine's output is limited to 4850 kW (6500 hp). Maximum engine efficiency drops to 36.0 percent, about 4 percent lower than at the 6190 kW setting, but still 26 percent better than the simple cycle (baseline) case.

The shop tests conducted by Allison in 1982 have confirmed these performance improvements. Saturated steam at 1825 kPa (250 psig) was injected into the combustor of a "workhorse" 501-KB engine at two axial locations: one at the combustor head end and one near the tail end. Agreement between analytical predictions and measured values was quite good. At all levels of injection below 2.3 kg/s, the predicted

Table 2 Waste heat boiler water/steam specification

Component	Temperature		Pressure		Simple Cycle		Steam Injection	
	°C	(°F)	kPa	(psig)	Flow		Flow	
					kg/hr	lb/hr	kg/hr	lb/hr
<b>Preheater</b>								
Inlet Water	65	(150)	274	(25)	9,182	(20,200)	8,136	(17,900)
Outlet Water	107	(225)	205	(15)				
Maximum Allowable Pressure Drop			69	(10)				
<b>Economizer</b>								
Inlet Water	121	(250)	2168	(300)	9,182	(20,200)	8,136	(17,900)
Outlet Water	206	(403)	203	(280)				
Maximum Allowable Pressure Drop			172	(25)				
<b>Vaporizer</b>								
Steam Discharge	212	(413)	1962	(270)	8,863	(19,500)	7,864	(17,300)
Continuous Blowdown (est)					318	(700)	273	(600)
Steam Quality	99.5%							

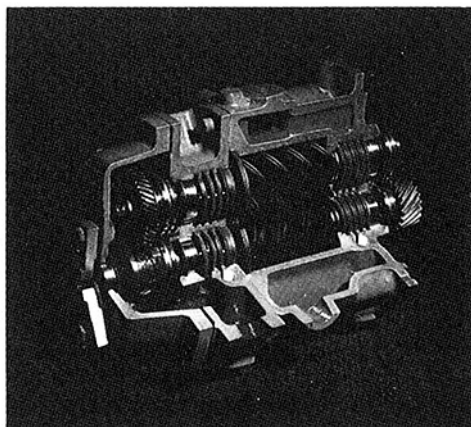


Fig. 6 Rotary screw fuel gas compressor

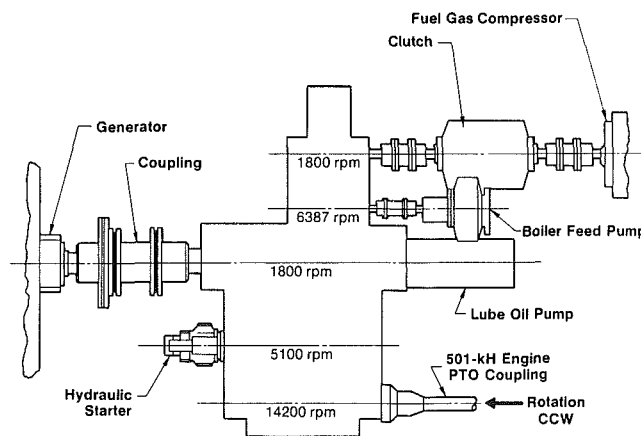


Fig. 7 System gearbox—plan view

and measured values were virtually coincidental with each other. At 2.3 kg/s, the measured power was 1 to 3 percent lower than predicted. No discernible difference was measured due to injection locations, i.e., upstream injection, downstream injection, and a combination of both showed good agreement except at 2.3 kg/s as noted.

A post-mortem examination of the turbine hardware and engine lube oil system showed no adverse effects due to steam injection.

### Major Components

**Gas Turbine.** The Allison 501-KH gas turbine was selected because it is particularly well suited for cogeneration duty with consideration given to size, heat rate, steam generating capacity, reliability/availability, and capital cost. Moreover, with a compressor stall margin in excess of 45 percent, this engine is ideal for steam injection. Injecting steam at a steam/air mass ratio of 0.12 increases the compressor's pressure ratio approximately 20 percent. This would impose a severe restriction on engines with stall margins of only 20 to 25 percent, whose compressors would require extensive redesign for steam injection.

The 501-KH is the steam-injected version of the popular 501-KB. It is the commercial version of the T56-501K turboprop engine of which 14,000 have been built and have logged in excess of 100 million hr of operation. It is a single-shaft engine, utilizing a 14-stage axial flow compressor, 6 combustion chambers within an annular combustor, and a 4-stage turbine with an air-cooled first stage. The compression ratio is approximately 9.3:1 at standard continuous rating. The five main antifriction bearings are pressure lubricated. A dual fuel (gas and distillate oil) version was selected for cogeneration duty.

Two minor hardware changes accompany the transition from the KB to the KH version. Two steam manifolds are welded to the outer case surrounding the combustion liners: one at the combustor head and one downstream in the transition section. Steam entering the case through these manifolds mixes with the compressor discharge air, and the steam/air mixture is metered through the same combustor liner holes used for air-only metering.

The other modification consists of strengthening the first stage compressor disk, extension shaft, and power takeoff (PTO) shaft to accommodate the additional torque.

In addition to these structural changes, the 501-KH is equipped with an incipient stall detection system to prevent stall due to excessive amounts of steam injection.

**Waste Heat Boiler.** A natural circulation waste heat boiler was specified for the subject system. It consists of a vaporizer, economizer, and liquid preheater. Based on a gas turbine exhaust flow of 15.6 kg/s (34.2 lb/s) at 510°C (950°F), the steam generator produces 8,860 kg/hr (19,500 lb/hr) of 1965 kPa (270 psig) saturated steam. The waste heat boiler is also designed to accommodate up to 18.2 kg/s (40.0 lb/s) of flow during periods of steam injection into the turbine. A maximum gas side total pressure drop of 8.2 mm Hg was specified. The specified water and steam conditions are presented on Table 2 for simple cycle and steam injection operation.

Feedwater heating is accomplished by a separate deaerating feedwater heater which withdraws saturated liquid from the outlet of the economizer.

**Supplemental Firing.** A duct burner is employed to increase the steam generation to 15,900 kg/hr (35,000 lb/hr). No refractory material is used. A maximum duct gas temperature of 760°C (1400°F) is specified.

**Fuel Gas Compressor.** As stated previously, the integration of the fuel gas compressor into the main turbine skid represents one of the system's most significant departures from conventional cogeneration packaging practice. Integration within the system required a compact, high-pressure-ratio, low-flow device whose rotational speed was compatible with the other skid machinery. After thoroughly examining several candidate technologies, the selection rapidly converged on a rotary screw compressor (see Fig. 6).

The compressor can deliver 22.2 standard m<sup>3</sup>/hr (783 scfm) of natural gas at 2067 kPa (285 psig), starting with a suction pressure of 138 kPa (5 psig). It provides 49.5 × 10<sup>6</sup> kJ/hr (47 × 10<sup>6</sup> Btu/hr) of fuel to the gas turbine, while consuming approximately 224 kW (300 hp) of shaft power.

The compressor is coupled to a friction-type clutch and driven by a 1800-rpm shaft from the main gearbox. It features two internally driven sets of male/female rotors, each geared to the compressor's 1800-rpm output gear. Lubrication and gas path sealing are achieved via the compressor's lube oil system. No pump is required; the discharge to suction pressure gradient is used for flow metering. The fuel gas and oil mixture leaving the compressor enters a separator tank that removes all but 2 to 5 ppm of oil from the gas. A downstream coalescing filter reduces the oil carry-over to less than 1 ppm.

**Gearbox.** The gearbox was specifically designed to meet the single, prime-reliable drive system objective. Six shaft penetrations are provided which transmit power to and from the skid. In addition to the gas turbine and generator, the gearbox interfaces with the gas compressor, turbine starter, boiler feed pump, and lube oil pump. A plan view of the gearbox is shown in Fig. 7.

The gearbox has a 4850 kW (6500 hp) input rating at a 1.3 service factor. It has a double-reduction gear set between the 14,200-rpm engine power shaft and the 1800-rpm bull gear. A 6400-rpm intermediate gear drives the boiler feed pump while a 5100-rpm intermediate gear is used for the hydraulic starter. The 1800-rpm shaft near the center of the gearbox drives the electric generator and lube oil pump. At an outboard location, another 1800-rpm shaft drives the fuel gas compressor.

**Start-Up and Control.** The integration of the mechanical drives within the load gearbox affects the start-up procedure. The system requires fuel oil for starting because the gas compressor is driven by the load gearbox.

An electric-driven hydraulic pump provides energy through the hydraulic starter to accelerate the engine to ignition speed, approximately 2200 rpm. The acceleration to ignition speed occurs with the gas compressor declutched. After light-off and subsequent declutching of the starter at 8500 rpm, the engine accelerates to its design speed of 14,200 rpm. At this time, the gas compressor's clutch is engaged and the gas compressor begins producing high-pressure gas. At a fuel gas

pressure of approximately 1930 kPa (265 psig), the engine's fuel control is automatically switched from oil to gas. No discernible change in speed or output is expected during fuel switching. The manner in which the system can readily accommodate either natural gas or distillate, both in the gas turbine and duct burner, is a major feature of this system.

During steady-state operation, the engine's firing rate is used to maintain steam pressure at the process header. The control logic responds to pressure changes in the following manner:

- **Steam Pressure Decreases:** Indicative of increased demand, the turbine firing rate (fuel flow) is increased to meet steam demand. If the maximum TIT is exceeded, the supplementary fired duct burner is operated until steam demand is met.

- **Steam Pressure Increases:** This occurs when there is an excess of steam being delivered to process. In conventional systems, this would result in a droop in the turbine's firing rate causing a simultaneous reduction in output and poor heat rate. In this case, however, the reduction in steam header pressure is effected by diverting excess steam into the turbine. Without changing the firing rate, the header pressure falls and generator output increases. However, if the generator output exceeds the new set point or maximum output (4000 kW<sub>e</sub>), the turbine firing rate is then reduced accordingly.

## Closure

A packaged cogeneration system has been specifically developed to overcome the obstacles that have thus far delayed the widespread use of cogeneration in the industrial process sector. The totally integrated concept combined with the steam injection feature results in better performance, reliability, and reduced complexity. The successful demonstration of this system at a General Motors plant in early 1985 will confirm this approach and will set the standard for packaged cogeneration systems.

## Acknowledgments

The cogeneration system development work conducted at Mechanical Technology Inc. was sponsored by the Gas Research Institute under Contract No. 5083-233-0797. In addition, the authors wish to acknowledge the technical contributions made by the staff at Mechanical Technology Inc. in carrying out the objectives of this project.

## References

- 1 Bultzo, C., "Steam Injection, A Source of Incremental Power," ASME Gas Turbine Conference, Mar. 1969.
- 2 Day, W. H., and Kydd, P. H., "Maximum Steam Injection in Gas Turbines," Joint Power Conference, Sept. 1972.
- 3 Messerlie, R. L., and Tischler, A. O., "Test Results of a Steam Injected Gas Turbine to Increase Power and Thermal Efficiency," IECEC, Aug. 1983.

# Combined-Cycle System With Novel Bottoming Cycle

**A. I. Kalina**  
Exergy, Inc.,  
Houston, TX 77027

*A new thermodynamic energy cycle has been developed using a multicomponent working agent. This cycle is designed to replace the currently used Rankine Cycle as a bottoming cycle for a combined-cycle energy system as well as for generating electricity using low-temperature heat sources. Several combined power systems based on this cycle have been designed and cost-estimated. The efficiency of this cycle is from 1.6 to 1.9 times higher than that of the Rankine Cycle system, at the same border conditions. The investment cost per unit of power output for this cycle is lower than that for the Rankine Cycle system in approximately direct proportion to the energy advantage. The application of this cycle as a bottoming cycle in combined-cycle systems involves the use of an energy system which utilizes heat from the exhaust of a gas turbine, resulting in an increase in overall efficiency of up to 20 percent above the efficiency of the combined systems using the Rankine bottoming cycle. As a result, a thermal efficiency in the range of 50-52 percent can be achieved using a conventional gas turbine. The project to build the first experimental installation is now in progress. This installation is to become operational at the end of 1984.*

## Introduction

The well recognized advantages of combined-cycle systems have resulted in an intensive development of such systems worldwide. Several companies offer such systems for energy generation as well as for cogeneration. Significant efforts are being devoted to the improvement of the efficiency of a gas turbine, i.e., the prime mover in combined-cycle systems. For example, six Japanese gas turbine companies are now mutually developing a high-temperature advanced gas turbine designated as AGTJ-100A, aimed at reaching a gas-turbine cycle per se thermal efficiency of 39.4 percent. This pilot plant is expected to achieve a combined-cycle efficiency of 55 percent by increasing the gas-turbine inlet temperature to 1400°C. This will require the development of new materials and cooling techniques, which are currently the subject of research [1].

At the same time, an intensive development of waste heat recovery systems, using variations of the century-old Rankine Cycle technology, has been directed toward improvement of the mechanical components of the system. As a result, very refined, but expensive, components have been developed. Nevertheless, the gain in efficiency of the Rankine Cycle bottoming system has been insignificant, as the Rankine Cycle itself simply does not adequately fit the thermodynamical border conditions typical of waste-heat recovery systems. It seems appropriate to present here an analysis of these typical

conditions, which are also typical for geothermal and other similar types of systems.

## Theoretical Potential and Border Conditions of Heat Sources

Most heat sources available for further conversion into mechanical and electrical energy are sources of a sensible heat, i.e., of variable temperature. At the same time, it is commonly assumed that the variation in temperature of a cooling medium is insignificant, and that a thermal basin can be considered as isothermal. In reality, because only a limited quantity of a cooling medium can be used, the basin temperature is a variable one as well. If the enthalpy of an available heat source is a linear function of the temperature, and the highest temperature of the cooling source is assumed as a basin temperature, then the energy potential, or exergy, of such a heat source is represented by Formula 1:

$$E_x^{(h)} = H \times \left( 1 - T_0 \frac{\ln \frac{T_1}{T_2}}{T_1 - T_2} \right) \quad (1)$$

From this formula it follows that the rejected heat is equal to:

$$H_r = -H \times T_0 \frac{\ln \frac{T_1}{T_2}}{T_1 - T_2} \quad (2)$$

Due to the fact that, in reality, the basin temperature is

Contributed by the Gas Turbine Division of THE AMERICAN SOCIETY OF MECHANICAL ENGINEERS and presented at the 29th International Gas Turbine Conference and Exhibit, Amsterdam, The Netherlands, June 4-7, 1984. Manuscript received at ASME Headquarters, January 12, 1984. Paper No. 84-GT-173.



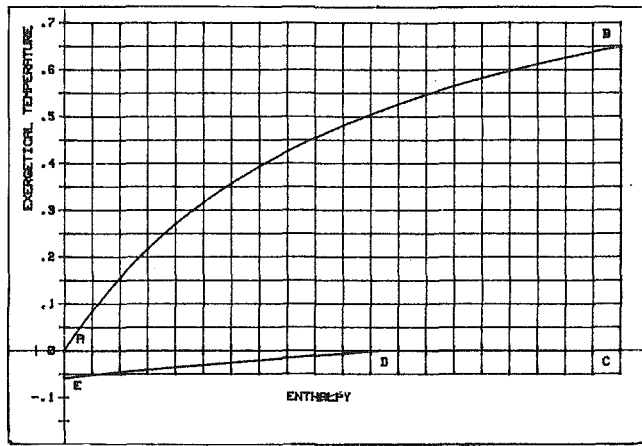


Fig. 1 Exergy of a variable-temperature heat source

variable as well, additional exergy is provided, which is equal to:

$$E_x^{(c)} = -H \times T_0 \frac{\ln \frac{T_1}{T_2}}{T_1 - T_2} \times \left( 1 - T_0 \frac{\ln \frac{T_3}{T_0}}{T_3 - T_0} \right) \quad (3)$$

As a result, the total energy of a source is:

$$E_x = H \times \left[ 1 - T_0 \frac{\ln \frac{T_1}{T_2}}{T_1 - T_2} \times \left( 2 - T_0 \frac{\ln \frac{T_3}{T_0}}{T_3 - T_0} \right) \right] \quad (4)$$

This exergy potential can be properly represented by appropriate areas in coordinates entropy versus temperature or enthalpy versus exergetical temperature, which is:

$$\tau = 1 - \frac{T_0}{T} \quad (5)$$

Such a representation is given in Fig. 1, where the A-B-C-D-E area represents the exergy potential of the flow cooled from B to A. As one can see from this representation, a thermodynamical cycle, in order to achieve high thermodynamical efficiency, must have a triangular shape in coordinates enthalpy versus temperature or entropy versus temperature. It is self-evident that the ideal cycle to convert such heat sources into mechanical and electrical energy is not the Carnot cycle, which has a rectangular shape in the entropy versus temperature coordinates, but the Lorentz cycle, which has in such coordinates the shape of a triangle.

There are two ways usually considered for increasing the efficiency of the Rankine Cycle utilizing variable-temperature heat sources. One is the use of a multipressure boiler, and the other is the implementation of the so-called "supercritical cycle." The use of a multipressure boiler is widely accepted in the industry, but results in only moderate improvement unless

the number of such boiling steps is very large. However, a significant increase in the number of boiling steps is technically and economically unfeasible and, as a result, the number of such steps does not exceed three.

The use of a supercritical cycle, especially with organic and other exotic working fluids, can theoretically achieve a triangular shape of the cycle, and thus high efficiency, but requires extremely high pressure in the boiler, which in turn has an adverse effect on turbine performance. S. L. Milora and J. W. Tester have presented a very complete study of the potential of supercritical cycles [2]. As follows from their data, such a cycle has one more setback, i.e., if the working fluid is heated to a higher temperature on a turbine inlet, the temperature in the turbine outlet is relatively high, and the remaining heat cannot be properly utilized in the cycle.

There is a third alternative, which is the use of a multicomponent mixture as a working fluid, which will certainly provide variable-temperature boiling. However, in a Rankine cycle arrangement such a fluid would have variable-temperature condensation as well and, as a result, improvement in efficiency would be only small. Considering the ultimate requirements for a thermodynamical cycle with high efficiency, one has to come to the conclusion that such a cycle must have the following features:

- (1) A low-boiling working fluid circulating through the evaporator and a turbine that has a variable—within a wide range—boiling temperature.
- (2) Effective utilization of the heat that can be extracted from a turbine-outlet flow before condensation.
- (3) A high-boiling fluid circulating through the condenser that has a constant—or variable within a narrow range—condensation temperature.

It is conventional to estimate the efficiency of a power cycle and power system by a thermal-efficiency number. However, such an estimate, which does not take into account the temperature of a heat source, could be misleading in cases where such a source is waste heat, geothermal heat, or other low-temperature sources. The proper estimation of the effectiveness of a power cycle would be the so-called "thermodynamical" or "exergetical" efficiency, which is a ratio of the power output to the exergy of the heat input. Such a thermodynamical efficiency includes within itself the efficiencies of the turbine, generator, and gearbox. For an estimation of the effectiveness of a cycle per se, the internal thermodynamical efficiency—which is a ratio of thermodynamical efficiency to a product of turbine, generator, and gearbox efficiencies—has to be used. In some cases, not all the available exergy of a source is utilized and transformed in a power system, i.e., exergy input is lower than available exergy. The so-called "exergy utilization efficiency," which is a ratio of the net output to the available exergy, has to be used to estimate the performance of a power system in conjunction with a given heat source.

In 1979 Exergy, Inc. started a research program aimed at the development of a new power cycle with significantly higher internal efficiency and exergy-utilization efficiency than those of a Rankine Cycle [3, 4]. Such a cycle has to be as

## Nomenclature

$E_x^{(h)}$  = Exergy of a heat source with assumption of a basin temperature equal to  $T_0$

$E_x^{(c)}$  = exergy of a cooling source with assumption of a basin temperature equal to  $T_0$

$E_x = E_x^{(h)} + E_x^{(c)}$

$H$  = heat flow of a heat source

$H_r$  = heat rejected to a basin

$T_1$  = initial temperature of a heat source °R or °K

$T_2$  = final temperature of a heat source °R or °K

$T_3$  = initial temperature of a cooling surface °R or °K

$T_0$  = final temperature of a cooling source °R or °K

$\tau = 1 - \frac{T_0}{T}$  — exergetical

temperature (dimensionless)

close a technical approximation as possible to a Lorentz cycle. This goal was achieved by the development of a new thermodynamical cycle. While this cycle can be applied to the utilization of any heat source, it is presented below for a particular use as a bottoming cycle in a combined-cycle power plant comprising a gas turbine and a bottoming cycle utilizing heat from gas-turbine exhaust.

### Bottoming Cycle for Combined-Cycle Systems

A bottoming-cycle system incorporating this newly developed cycle and designed to utilize the exhaust from gas

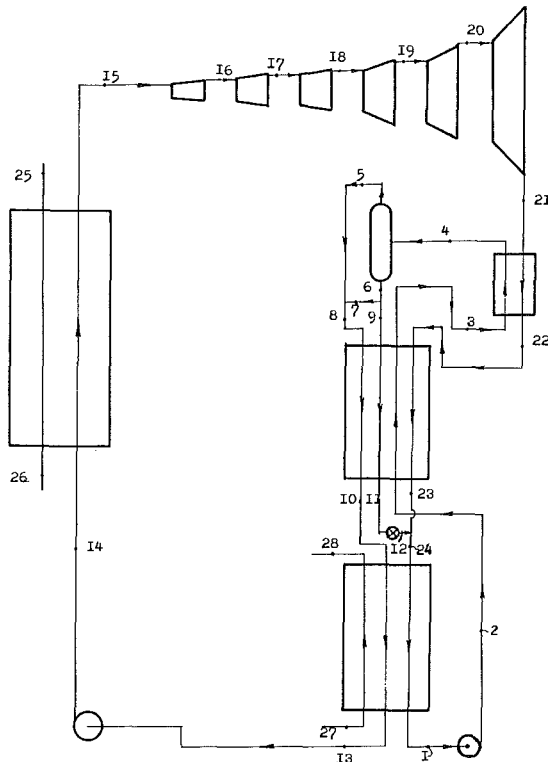


Fig. 2 Presented new cycle schematic flow diagram

turbine 501-KB5 made by the Detroit Allison Gas Turbine Division of General Motors is presented in Fig. 2. This system uses a water-ammonia solution as a working fluid. However, it has to be pointed out that other multicomponent solutions can be used as well. Thermodynamical data for a water-ammonia solution were available up to a pressure of 500 psia. Exergy, Inc. has developed thermodynamical data for a water-ammonia solution up to a pressure of 1200 psia, based on the Peng-Robinson Equation of State and methods of defining thermodynamical properties described in references [4-6]. This subject matter will be covered in a separate publication.

This system works as follows: A completely condensed working fluid of a so-called "basic composition," with parameters as at point 1 (see Table 1 and Fig. 2), after leaving the condenser, is pumped to a first intermediate pressure and attains parameters as at point 2. This flow is heated in a counterflow economizer (process 2-3) and then in a counterflow heater (process 3-4). As a result, the fluid is partially evaporated. The released vapor is significantly enriched by the light component of the mixture, i.e., ammonia. The vapor is separated from the liquid in a flash tank and then mixed with part of the remaining liquid to produce a so-called "working composition" (point 8). This newly created flow, as well as the remaining liquid, is sent to a counterflow economizer to preheat the incoming flow described above and to recuperate heat. After precooling in the economizer (process 8-10), the working solution is completely condensed by the cooling water (process 10-13). Then the working solution is pumped to a high pressure (process 13-14) and sent into the evaporator-boiler, where it is completely evaporated and superheated (process 14-15) in a counterflow heat exchange with the heat source, in this case exhaust gases from a gas turbine. This process is shown in coordinates enthalpy versus temperature in Fig. 3 and in coordinates enthalpy versus exergetical temperature in Fig. 4. The area between the line representing the heat source and the line representing the working fluid corresponds to thermodynamical losses in the process of a heat transfer from the heat source to the working fluid. As one can see from Fig. 4, these losses are minimized by the proper selection of the composition and parameters of the working fluid. It has to be noted that such a selection is

Table 1

Pt. No.	Temperature		Pressure		Enthalpy		Concentration		Weight Flow Rate		Relative Weight Flow Rate
	°F	°C	psia	kPa	Btu/lb	kJ/kg	lb/lb or kg/kg	lb/hr	kg/hr		
1	60.00	15.55	8.5	58.61	-62.57	-145.55	0.2954				5.1670
2	60.00	15.55	33.3	229.60	-62.57	-145.55	0.2954				5.1670
3	130.50	54.44	33.3	229.60	34.78	80.90	0.2954				5.1670
4	142.00	61.11	33.3	229.60	81.78	190.23	0.2954				5.1670
5	142.00	61.11	33.3	229.60	622.01	1446.87	0.9312				0.3704
6	142.00	61.11	33.3	229.60	40.08	93.23	0.2463				4.7966
7	142.00	61.11	33.3	229.60	40.08	93.23	0.2463				0.6296
8	142.00	61.11	33.3	229.60	255.65	594.67	0.5000				1.0000
9	142.00	61.11	33.3	229.60	40.08	93.23	0.2463				4.1670
10	115.10	46.17	33.3	229.60	152.86	355.57	0.5000				1.0000
11	113.75	45.42	33.3	229.60	8.54	19.87	0.2463				4.1670
12	85.13	29.52	8.5	58.61	8.54	19.87	0.2463				4.1670
13	60.00	15.55	33.3	229.60	-79.71	-185.42	0.5000				1.0000
14	60.00	15.55	1200.0	8273.71	-79.71	-185.42	0.5000				1.0000
15	990.00	532.22	1200.0	8273.71	1305.81	3037.47	0.5000	20,195	9160.3		1.0000
16	900.18	482.32	875.0	6032.92	1253.65	2916.14	0.5000				1.0000
17	789.24	420.69	575.0	3964.49	1190.34	2768.88	0.5000				1.0000
18	669.00	353.89	350.0	2482.11	1123.33	2613.00	0.5000				1.0000
19	454.86	234.92	125.0	861.85	1008.93	2346.89	0.5000				1.0000
20	228.74	109.30	32.0	220.63	894.43	2080.55	0.5000				1.0000
21	157.00	69.44	8.5	158.61	813.51	1892.32	0.5000				1.0000
22	142.00	61.11	8.5	58.61	570.61	1327.31	0.5000				1.0000
23	104.20	40.11	8.5	58.61	301.80	702.02	0.5000				1.0000
24	88.93	31.63	8.5	58.61	65.28	151.85	0.2954				5.1670
25	1040.00	560.00	---	---	223.40	519.66	Gas				6.2019
26	150.00	65.55	---	---	0.00	0.00	Gas				6.2019
27	55.00	12.78	---	---	---	---	Water				
28	85.00	29.44	---	---	---	---	Water				

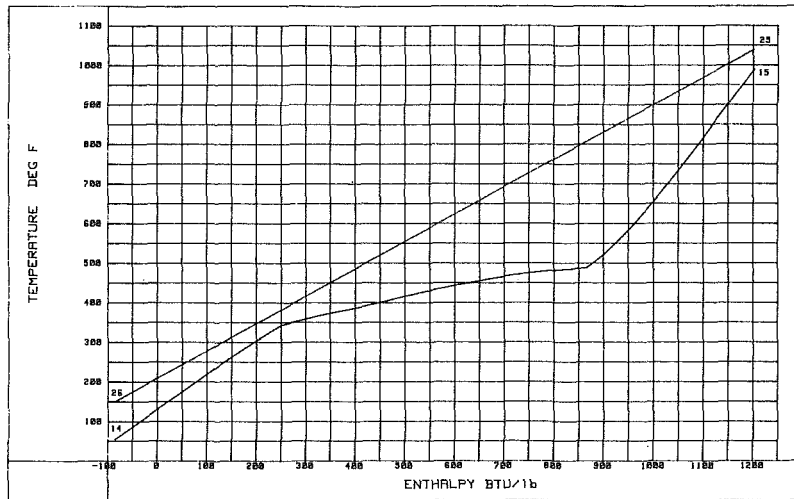


Fig. 3 Heat-exchange process in evaporator

$$t^{\circ}C = (t^{\circ}F - 32) \times \frac{5}{9}$$

$$\frac{kJ}{kg} = 0.4299 \frac{Btu}{lb}$$

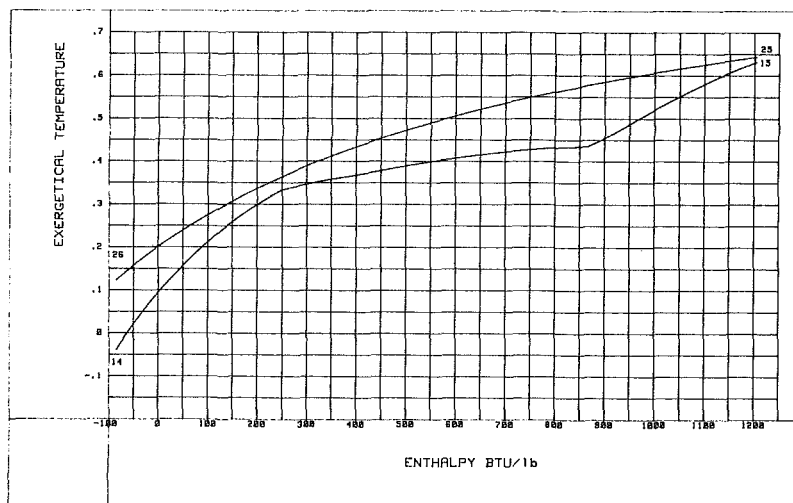


Fig. 4 Heat-exchange process in evaporator exergy losses

$$\frac{kJ}{kg} = 4299 \frac{Btu}{lb}$$

Step No.	Inlet Pressure		Outlet Pressure		Adiabatic Enthalpy Drop Btu/lb	Adiabatic Efficiency	Actual Enthalpy Drop Btu/lb	Shaft Power Output KW		
	psia	kPa	psia	kPa						
1	1200	8273.7	875.0	6032.9	63.06	146.7	0.827	52.16	121.3	308.51
2	875	6032.9	575.0	3964.5	76.13	177.1	0.831	63.31	147.2	374.48
3	575	3964.5	350.0	2413.2	79.85	185.7	0.839	67.01	155.8	396.40
4	350	2413.2	125.0	861.8	134.26	312.3	0.852	114.40	266.1	676.60
5	125	861.8	32.0	220.6	130.76	304.1	0.875	114.50	266.1	677.02
6	32	220.6	8.5	58.6	91.95	213.9	0.880	80.90	188.2	478.53
OVERALL TURBINE EXPANSION					576.01	1339.7	0.854	492.3	1145.0	2853.00

critical for the design of the presented cycle. The vapor of the working solution as at point 15 is sent to six consecutive radial inflow turbines, where it expands, producing mechanical work. Each of such six turbines has its own rpm and uses a separate gearbox and induction-type generator. It is an essential distinguishing feature of this process that the vapor is expanded in the turbine to such a low pressure that it cannot be condensed at the given ambient temperature. As a result of such expansion, a significantly large work output is provided. Hot vapor which exists the turbine is cooled consecutively in the heater (process 21-22) and in the economizer (process 22-23), thus providing the necessary energy for a working-

Table 3

Net thermal efficiency of bottoming cycle	0.3286
Net thermodynamical efficiency of bottoming cycle	0.7003
Internal thermodynamical efficiency of bottoming cycle	0.8200
Exergy utilization efficiency	0.7003
Thermal efficiency of gas turbine (501-KB5)	0.3050
Thermal efficiency of combined system	0.5223
Net thermal efficiency of combined system (electrical)	0.5015
Gas turbine net output	3,770 kWe
Bottoming cycle net output	2,700 kWe
Total output	6,470 kWe
Fuel consumption rate (LHV)	6,808 Btu/kWe
	or 1,716 kcal/kWe
	or 2,909 kJ/kWe

fluid separation. After this, the working solution is combined with the remaining liquid from the flashtank, this liquid having previously been cooled in the economizer (process 9-11) and then throttled to a pressure equal to the pressure of

**Table 4**  
**Performance data for gas turbines combined-cycle systems distillate**  
**oil fuel, ISO conditions**

1. Gas Turbine Type	LM5000	PG6521 (B)	PG7111 (E)	501-D
2. Manufacturer	G E N E R A L	E L E C T R I C		Westinghouse
3. Gas Turbine Output (kWe)	32,670	35,860	75,000	101,410
4. Gas Turbine Fuel Consumption (Million Btu/hr)	315.75*	404.5*	809.25*	1,057.7*
5. Gas Turbine Fuel Consumption Rate (Btu/kWh)	9,650*	11,280*	10,790*	10,430*
6. Exhaust Gas Initial Temperature °F	807	1,020	1,004	970
7. Exhaust Gas Flow lb/hr	984,960**	1,094,400**	2,210,400**	2,909,530**
8. Exergy of Exhaust (kW)	19,867	31,640	62,242	77,320
9. Combined Cycle Systems - Type	N/A	STAG 206B STAG 406P	STAG 107E STAG 407E	PACE 5011
10. Bottoming Rankine Cycle Output per One Gas Turbine (kW)	N/A	12,240	24,400	38,317***
11. Combined System Total Output per One Gas Turbine (kW)	N/A	48,100	99,300	139,727
12. Combined System Fuel Consumption Rate (Btu/kWh)	N/A	8,410*	8,150*	7,570*
13. Presented New Bottoming Cycle Output (kW)	14,678	23,366	45,965	58,570
14. Combined System with Presented New Cycle Output (kW)	47,348	59,226	120,965	159,980
15. Combined System with Presented New Cycle Fuel Consumption Rate (Btu/kWh)	6,668.8*	6,830*	6,690*	6,611*
16. Bottoming Cycle Improvement Ratio	N/A	1.910	1.892	1.529***
17. Combined Cycle Improvement Ratio	N/A	1.231	1.218	1.145***
18. Thermal Efficiency of Combined System with Presented New Cycle	0.512	0.500	0.511	0.517

\*To convert to kJ - multiply by 1.054  
 \*\*To convert to kg - multiply by 0.45359  
 \*\*\*Triple-pressure boiler in Rankine bottoming cycle

the working solution (process 11-12). As a result of such combining, the basic solution is reinstalled at point 24. Then this basic solution is sent to a condenser, where it completely condenses by means of cooling water, obtaining parameters as at point 1. The whole cycle is then repeated.

As one can see from this description, the presented cycle fulfills all the requirements formulated in the previous section:

- The working solution, which passes through the evaporator and turbine, is enriched by a light component and has a variable boiling temperature.
- Heat extracted from a turbine-outlet flow is utilized for a working-fluid preparation.
- Fluid circulating through the condenser is enriched by a high-boiling component and thus provides a higher pressure drop across the turbine.

In summary, the presented cycle, in distinction from the Rankine Cycle, includes a working-fluid preparation sub-system comprising an economizer, heater, and flashtank, and substitutes absorption for condensation of the working fluid following expansion in the turbine. Parameters of all points of a cycle are presented in Table 1.

As follows from the given description, a relatively large pressure drop occurs in the steam turbine and, as a result, special care has to be taken to properly distribute this pressure drop between stages. In small-scale installations, the volumetric flow rate in the first stages is small, which fact has a negative impact on these stages' efficiency. For this reason, it is necessary to distribute the total available enthalpy drop in such a way that it is small in the first stages and larger in the lower stages. A sample of such a distribution of enthalpy drop for the installation described above is given in Table 2. All heat-exchange processes in the designed bottoming cycle include evaporation or condensation of a mixture, either of which occurs at variable temperatures. As a result, a counterflow type of heat exchanger has to be used, and special care has to be taken to avoid pinchpoint problems.

Off-design characteristics of a combined system achieved as a result of the development of a first pilot plant employing this new bottoming cycle are given in Table 3. These data correspond to a conservative assumption of a constant

exhaust-gas specific heat equal to 0.25 Btu/lb/°F (1.0467 kJ/kg × °C). As shown, efficiencies of over 50 percent can be achieved by using conventional gas turbines and the presented bottoming-cycle system, which also incorporates only conventional equipment. It has to be noted that the presented cycle permits cooling of the exhaust gas to a temperature of 150°F (77°C) compared with 300°F (149°C) for the Rankine Cycle. However, this additional heat represents a very small amount of exergy, which can provide an increase in output of a bottoming system only up to 42 kW or about 1.5 percent. It is self-evident that the new bottoming cycle, combined with an advanced, more efficient gas turbine, will provide even higher efficiencies in combined-cycle systems.

It seemed to be of interest to estimate the results which could be achieved by replacing the Rankine cycle bottoming system with this new cycle bottoming system in existing combined systems. Such a comparison is presented in Table 4.

### Summary

The higher thermodynamic reversibility, and consequently higher efficiency, of the presented new cycle system compared with the Rankine Cycle is due to two factors:

- (1) The multicomponent working fluid, having a variable boiling temperature, provides significantly less exergy loss in the evaporator, as the waste-heat source has a variable temperature in the evaporator as well.
- (2) The low-temperature part of the heat available from the turbine outlet is used, not for evaporation, but for distillation, which is thermodynamically more efficient.

The lower specific costs of the presented new cycle system are due to the fact that:

- (1) The working fluid starts to boil almost immediately after entering the evaporator, which increases the efficiency of the heat exchange.
- (2) The quantity of heat rejected in the condenser is significantly smaller than in the Rankine Cycle system, thus reducing the surface and thereby the cost of the condenser, as well as the cost of the cooling tower and auxiliary subsystems.
- (3) Higher efficiency of the presented new cycle system

results in a lower quantity of heat being transferred in the evaporator per unit of power output, and thus in a lower specific cost of the evaporator.

Economic comparison of the presented new cycle system with Rankine Cycle systems, based on a 6¢/KWH sale price of electricity produced, shows that the presented new cycle system provides a payout period of approximately one-and-one-half years versus six-and-one-half years for Rankine Cycle systems. Thus, the presented new cycle system makes cogeneration of electricity using waste-heat recovery economically feasible at current prices of fuel and electricity. Currently, Fayette Manufacturing Corporation, Tracy, California and Exergy, Inc., with the support of the Detroit Allison Gas Turbine Division of General Motors, are developing the first combined-cycle installation. This installation will become operational in the fall of 1984.

### Acknowledgments

The author acknowledges the following people for their help during this project:

Dr. Myron Tribus, Director of the Center for Advanced Engineering Study at M.I.T., for his constant encouragement and advice;

John Eckland, President of Fayette Manufacturing Corporation, who made the whole program possible;

Jim Strother, Manager of the Detroit Allison Gas Turbine Division of General Motors, for his support of the project;

Ivan Rice, Engineering Consultant, for his advice during the preparation of this paper.

### References

- 1 Jeffs, E., "Japan's 124-Mw High-temp pilot plant ready for test," *Gas Turbine World & Cogeneration*, Sept.-Oct. 1983.
- 2 Milora, S. L., and Tester, J. W., *Geothermal Energy as a Source of Electrical Power*, MIT Press, 1977.
- 3 U.S. Patent No. 4,346,561.
- 4 Kalina, A. I., "Combined Cycle and Waste-Heat Recovery Power Systems Based on a Novel Thermodynamic Energy Cycle Utilizing Low-Temperature Heat for Power Generation," ASME Paper 83-JPGC-GT-3.
- 5 Reid, Robert C., Prausnit, John M., Sherwood, Thomas K., *The Properties of Gases and Liquids*, McGraw-Hill, 1977.
- 6 Sandler, Stanley I., *Chemical and Engineering Thermo-Dynamics*, Wiley, 1977.
- 7 Smith, J. M., and Van Ness, H. C., *Introduction to Chemical Engineering Thermodynamics*, McGraw-Hill, 1975.

# Thermodynamics of an Isothermal Gas Turbine Combined Cycle

**M. A. El-Masri**

Associate Professor.

**J. H. Magnusson<sup>1</sup>**

Research Assistant.

Department of Mechanical Engineering,  
Massachusetts Institute of Technology,  
Cambridge, Mass. 02139

*The isothermal (or multiple-reheat) gas turbine performs the combustion/work extraction process at a sustained, elevated temperature. This has distinct thermodynamic advantages in combined cycles for given peak temperature constraints. A thermodynamic model for this cycle is developed. Although based on a simple CO/CO<sub>2</sub>/O<sub>2</sub> chemical system the results are applicable to other reactants and dilutants. Combined cycle efficiency is reported for different gas turbine pressure ratios, peak temperatures, reactant dilution and steam cycle conditions. The range of parameters investigated starts from present-day advanced technologies and examines the potential of higher pressures and temperatures. Balances of thermodynamic availability are used to interpret the results. They show that for a given steam cycle and gas turbine pressure ratio, increasing peak temperature beyond a certain value provides sharply diminishing return. This is because the reduction in combustion irreversibility is offset by increased heat transfer irreversibility. Higher pressure ratios or steam cycle temperatures can raise this optimum peak temperature. In view of the various technological constraints, the authors' conclusion is that an isothermal gas turbine with a peak temperature and pressure-ratio of about 1600K and 100:1, respectively, represents the most promising next step in technology. Coupled with existing advanced steam cycles this should provide efficiencies in the 60 percent range.*

## 1 Introduction

The common method of energy-balance analysis of power cycles is based solely on the first law of thermodynamics. This approach frequently obscures the true sources of losses, and thus, the avenues for improvement. Application of the second law of thermodynamics in the form of availability<sup>2</sup> balances can be revealing. An illustration of this fact is given in Table 1 where energy and availability balances for a simple steam cycle have been calculated and compared side-by-side. It is interesting to note that almost 60 percent of the thermodynamically available work has been lost through the irreversibility of the combustion process and degradation of energy by transferring it to the lower-temperature steam. Both those processes appear as 100 percent efficient when viewed on an energy balance basis. The major energy losses of heat rejection to the condenser and stack represent very minor losses in availability.

The foregoing discussion makes it clear that substantial progress in power cycles can be achieved by reducing the irreversibilities associated with combustion and heat transfer.

Combustion irreversibility can be eliminated if a hypothetical device known as the Van't Hopf equilibrium box were available [3]. This calls for selectively permeable surfaces to allow reactants to be introduced and products exhausted at their partial pressures. Moreover, the Gibb's Free Energy of reactants and products is equalized by having the reaction occurring at the equilibrium temperature. This requires controlled energy extraction for its sustenance. Although this hypothetical device consists of presently unrealistic components, one motivation for the present work was to examine the feasibility of finding a practical approach for reducing the combustion irreversibility. If a gas turbine

**Table 1 Energy and availability balances for a simple steam cycle<sup>(a)</sup>**

Process	Losses as % of Enthalpy of Reaction <sup>(b)</sup>	
	Energy	Availability
Combustion <sup>(c)</sup>	0	38.6
Heat Transfer	0	21.2
Steam Turbine <sup>(d)</sup>	0	4.6
Condenser <sup>(e)</sup>	58.5	2.4
Stack <sup>(f)</sup>	10.8	2.5
<b>Total Losses</b>	<b>69.3</b>	<b>69.3</b>
<b>Useful work</b>	<b>30.7</b>	<b>30.7</b>

<sup>(a)</sup> 1000 psia, 900°F No Reheat or Regeneration

<sup>(b)</sup> C<sub>8</sub>H<sub>18</sub> Availability = 1.0285 × Enthalpy of Reaction

<sup>(c)</sup> With 50 percent Excess Air

<sup>(d)</sup> Isentropic Efficiency 85 percent

<sup>(e)</sup> Condenser Pressure 1 psia

<sup>(f)</sup> Flue Gas Temperature 400°F

<sup>1</sup> Currently with Shell Oil Company, The Netherlands

<sup>2</sup> The concept of available work was first introduced by Gibbs. Although Keenan showed its usefulness for practical engineering analysis [1] its application is infrequent. Some interesting practical applications are given in reference [2].

Contributed by the Gas Turbine Division of THE AMERICAN SOCIETY OF MECHANICAL ENGINEERS and presented at the 29th International Gas Turbine Conference and Exhibit, Amsterdam, The Netherlands, June 4-7, 1984. Manuscript received at ASME Headquarters, January 30, 1984. Paper No. 84-GT-274.

with a highly-effective cooling scheme such as internal liquid cooling [4] or Two-Phase Transpiration [5] were developed, a high temperature simultaneous combustion/work-extraction process could be achieved. Such a turbine, combusting fuel with pure oxygen through its expansion path, and operating at reaction temperatures as close to equilibrium as finite reaction kinetics and component cooling would permit, would provide efficient direct conversion of fuel availability to mechanical work with reduced combustion irreversibility.

The heat transfer irreversibility can be reduced by extracting as much work as possible directly from the working fluid at the highest possible temperature rather than transferring energy to a lower-temperature working fluid. This makes the high-temperature gas turbine an excellent choice.

Two aspects of the foregoing discussion are worth emphasizing. First, the distinction between combustion and heat transfer irreversibilities can be somewhat arbitrary. In a combustor with a diluting fluid it depends on where one draws the hypothetical boundary separating the two processes. For a given dilution, we shall define the combustion irreversibility by considering the increase in availability of the entire gas flow vis-a-vis the availability of fuel consumed. Second, in situations where the entire work extraction process occurs at temperatures significantly below the equilibrium temperature for the reaction, separate consideration for the combustion irreversibility becomes unnecessary. The fuel may be simply regarded as a heat source and the cycle analyzed by just considering the temperature of heat addition to the working fluid. To this end, we may define an efficiency for the heat addition process  $\eta_Q$  as the ratio of increased availability of the working fluid to heat added to that fluid<sup>3</sup>. This increases with increasing heat-addition temperatures.

Since current technology limits the maximum gas temperature in a turbine, maximizing the heat addition at the highest permissible temperature calls for a reheated expansion. Calculations on reheated gas turbine combined cycles by Rice [7, 8] and Jahnig [9] and projections for the efficiency of the "Moonlight Project" under construction in Japan [10] emphasize this fact. The above references considered a moderate pressure ratio gas turbine (about 50) with a single reheat.

The foregoing considerations lead to the next step of considering the potential benefits of multiple gas turbine reheats at a high pressure ratio, or in the limit, a continuous interstage combustion isothermal gas turbine. To glean some insight into the advantages of the isothermal cycle one can compare it to an equivalent Brayton cycle. The latter is defined as having the same efficiency defined in the traditional first law sense, and the same exhaust temperature. Thus with a bottoming steam plant in a combined cycle both would have identical overall performance. The results are plotted for ideal cycles in Fig. 1 as ratio of peak to ambient temperature for the Brayton Cycle  $\theta_B$  vs that for the Isothermal Cycle  $\theta_i$ . The compressor pressure ratio  $r_p$  for each cycle is also indicated. The specific work per unit mass of both cycles is identical under those conditions and is indicated on the right-hand ordinate. Figure 1 also shows the first law efficiency  $\eta_1$ , and a second law efficiency  $e_2$ <sup>10</sup> for those cycles on the top abscissa. The latter is defined as

$$e_2 = (W + \Omega_{ex})/Q$$

and since the calculation was done for reversible cycles it can be shown to be identical to the heat addition efficiency  $\eta_Q$  defined earlier. Moreover, one can show that the heat addition temperature for the isothermal cycle is the same as the

<sup>3</sup>Discussion of the usefulness of those and alternative definitions of process and cycle efficiencies based upon the second law of thermodynamics are given in reference [6].

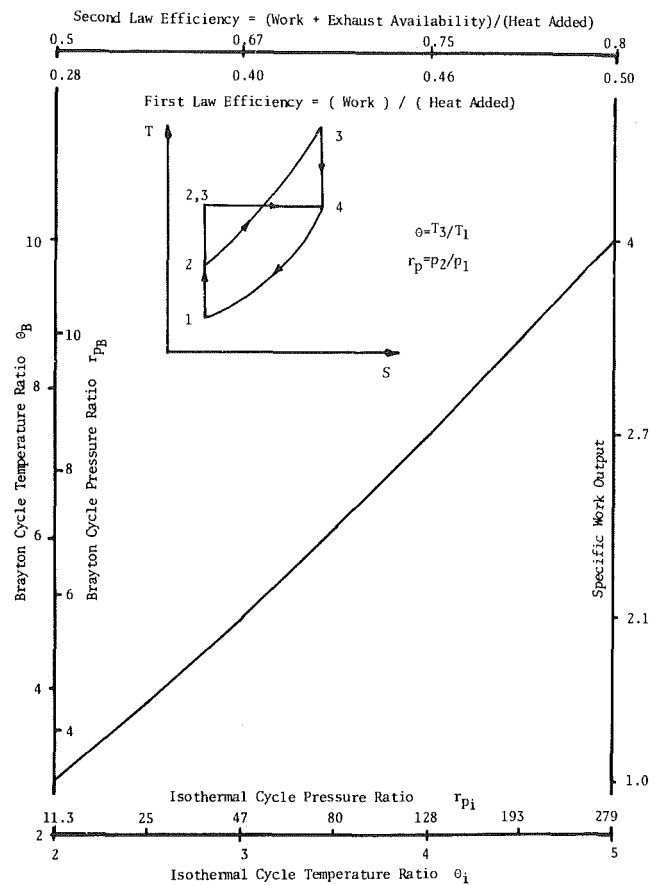


Fig. 1 Comparison between equivalent ideal isothermal and Brayton cycles

logarithmic mean temperature of heat addition for the Brayton cycle under the assumed conditions [6].

Although the results shown in Fig. 1 are based on ideal gas reversible cycles they illustrate an important point. An isothermal cycle of very moderate temperature but high pressure ratio will have equivalent performance in a combined cycle to a Brayton cycle with high temperature and moderate pressure ratio. For example, an isothermal cycle of pressure ratio 128 and temperature ratio of 4 emulates a Brayton cycle having a peak temperature ratio of 7.4 and moderate pressure. For 300K ambient this implies 1200K in the isothermal cycle vis-a-vis 2200K for the Brayton. The former requires little or no blade cooling while the latter is beyond today's technology. Developing a high pressure turbine cycle is believed to be considerably less complicated than going to extreme firing temperatures. Naturally, the results of this simple calculation will be modified by having irreversible compressors and turbines as well as a finite number of reheat stages. To evaluate those effects, a computer program using real gas properties and finite component irreversibilities was used. The computational model and results are described below.

## II Cycle Model

The cycle model, described in greater detail in Magnusson's thesis [11], consists of an interstage combustion gas turbine and a bottoming steam cycle. A system schematic is shown in Fig. 2 and an idealized temperature-entropy diagram is sketched in Fig. 3. Note how the combination approaches a Carnot cycle.

The calculations were performed with CO fuel burnt with pure O<sub>2</sub>. The reasons for this choice are:

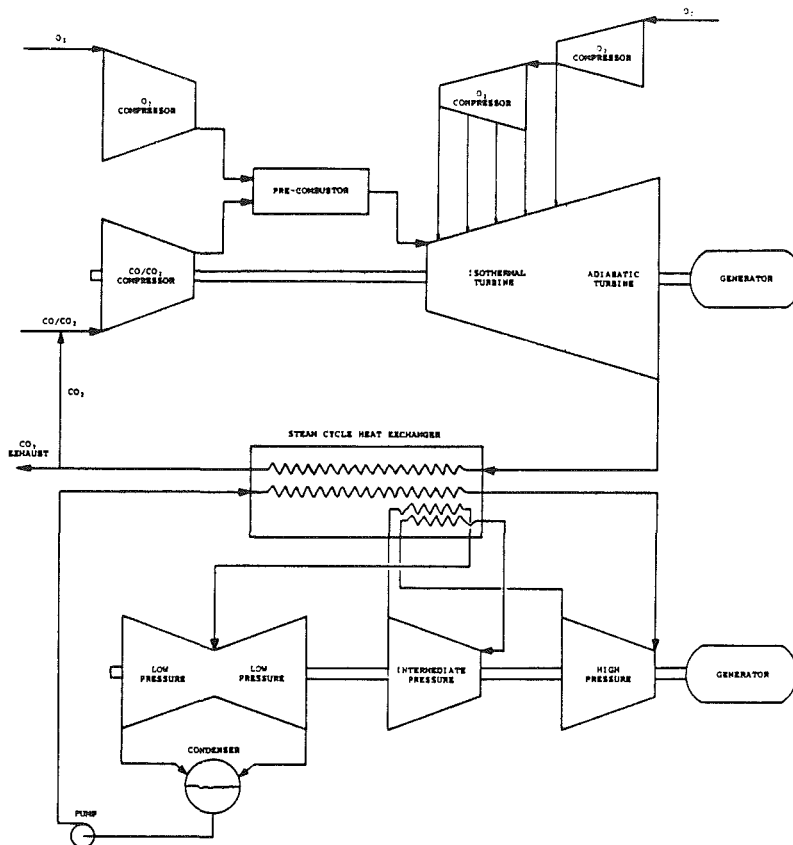


Fig. 2 Schematic of the proposed gas turbine combined cycle with  $O_2$  addition and isothermal expansion and combustion within the gas turbine

1. Simpler calculations for the resulting  $CO/CO_2/O_2$  working fluid.
2. Some proposed coal gasifiers, such as the Texaco  $O_2$ -blown entrained bed process, require an oxygen plant and produce a gaseous fuel that is predominantly  $CO$ .
3. The use of  $O_2$  for combustion accelerates reaction kinetics.
4. The  $CO_2$  produced may have commercial value for enhanced oil recovery applications.
5. No  $NO_x$  is produced.

Since it was found that for the most promising cases the  $CO$  fuel must be diluted with  $CO_2$  by at least 2 moles  $CO_2$ /mole  $CO$ , the overall performance will not change significantly for those cases if the calculations were done with air, which would result in a similar dilution. In the latter event, the kinetics would be slowed to the extent of requiring interstage combustors producing strong mixing and long residence time. Those would impose a pressure drop whose thermodynamic penalty must be included.

The gas turbine model consists of a compressor, a precombustor to raise the temperature to the desired level, followed by an interstage combustion gas turbine. The expansion path was divided into ten segments of equal pressure ratio. In the isothermal section of the expansion path the process in each segment was modeled as an adiabatic expansion at frozen composition, followed by a constant pressure reequilibration then a combustor where sufficient  $O_2$  is added to restore the temperature to that at the stage inlet. When all the fuel was combusted, the remaining turbine segments were treated as adiabatic using the same model except for the  $O_2$  addition. All properties and equilibrium compositions were calculated using ASPEN code [12]. The

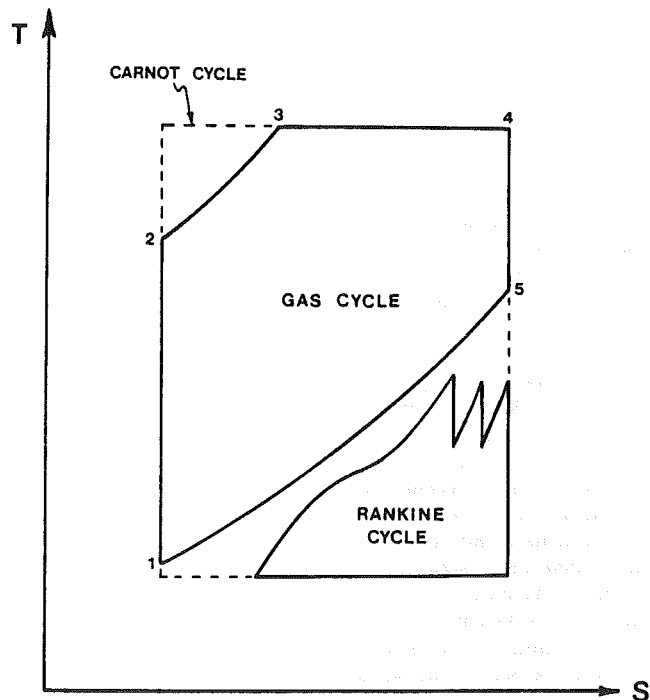


Fig. 3 Temperature-entropy diagram of an idealized gas turbine combined cycle with  $O_2$  addition and isothermal expansion and combustion within the gas turbine

$CO$ ,  $CO_2$ , and  $O_2$  were all assumed to be supplied at 298 K and 1 atm. All compressors and turbines were assumed to have isentropic efficiencies of 88.5 and 92 percent, respectively. A block diagram of the computational model for each turbine segment is shown in Fig. 4.



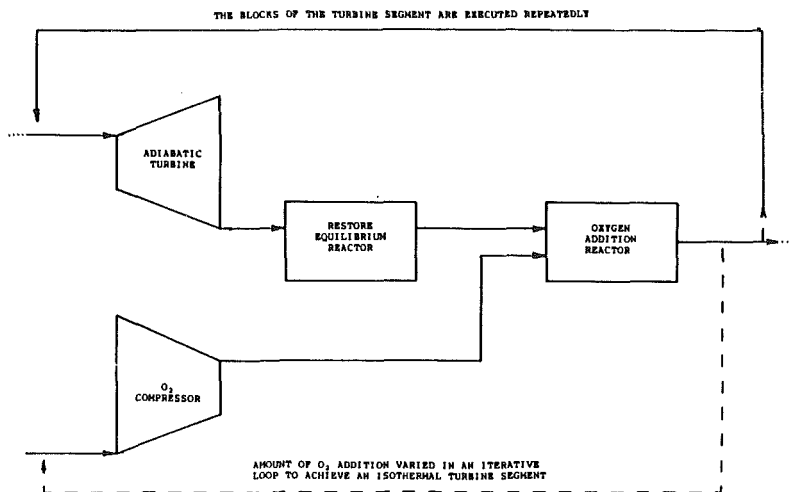


Fig. 4 Outline of the simulation model for the part of the turbine with internal combustion and isothermal expansion

The bottoming steam cycle used was a 340 atm. 922/867/867 K double reheat cycle (5000 psi 1200/1100/1100°F). This is amongst the most advanced steam cycles known to be in practical operation and is described by Nesbit [13]. The condenser pressure was 5 kPa and the gases were assumed to leave the boiler economizer at 125°C. The boiler “pinch point” was set at a minimum of 16°C. Steam turbines were assumed to have an isentropic efficiency of 92 percent and pump work was disregarded.

The one major source of thermodynamic losses not included in the model is that due to turbine cooling. This was purposely omitted since it is a strong function of the type of cooling technology employed. State-of-the-art air cooling technology as applied in today’s aircraft engines has been estimated to penalize the open Brayton cycle by about seven percentage points at turbine inlet temperatures (TIT) of about 1600 K [14]. Most of the loss is due to mixing the cooling air with the turbine gas with resultant losses in both stagnation pressure and temperature. In a combined cycle application some of this would be recuperated from the increased exhaust mass flow. Since a greater proportion of the losses occur in the high temperature portion of a Brayton-cycle expansion, the penalty for a sustained high temperature expansion in an isothermal cycle is expected to be greater. A more detailed analysis of those losses is the subject of a future paper.

Closed-loop internal liquid cooling of the turbine blades and vanes introduces very small losses. Those were estimated at about one percentage point for a Brayton cycle in reference [14] at 1600K TIT. This technology has yet to be developed for an operating machine. Several experimental turbines have been run with internal liquid cooling with various degrees of success [15–17]. Recent research has shown that some of its potential problems may be overcome [18–21]. Various components of an open-loop water-cooled turbine have been developed and tested [4]. This, however, is estimated to introduce thermodynamic losses greater than those with a closed-loop system [22, 23].

In summary, the isothermal turbine combined cycle is expected to suffer an additional penalty of about five percentage points at 1600 K if a gas cooling technology similar to current aircraft engine practice were employed. This penalty would increase drastically at higher isothermal cycle temperatures. Alternative cooling schemes may reduce this penalty and make higher temperatures feasible.

### III Results and Discussion

The cycle model calculation was run for three turbine peak

temperatures: 1600K, 2200K, and 2600K. The first is slightly below today’s aircraft engines whereas the second and third are beyond current technologies and will require more advanced gas turbine cooling schemes, probably liquid cooling. Three pressure ratios were tried for each temperature: 40, 100, and 200. The first is similar to current aero engines in development [24] and below that for the “Moonlight Project” [11]. No gas turbines known to the authors have been operated at the latter pressures but it is believed that the technology may readily be developed for large machines. A low temperature gas turbine has been operated successfully for several years at a pressure of 45 atmospheres as part of a compressed air storage plant [25].

The rationale behind the choice of temperatures and pressures for the calculations was to start at conditions corresponding to state-of-the-art, then examine the influence of increasing temperature and pressure ratios insofar as the potential for overall efficiency improvement.

The results are presented in terms of a First Law efficiency  $\eta_1$  and a Second Law efficiency  $\eta_2$  defined as

$$\eta_1 = W_{\text{net}} / \Delta H_r$$

$$\eta_2 = W_{\text{net}} / \Omega_{\text{fuel}}$$

where  $W_{\text{net}}$  is the net work output of the combined cycle,  $\Delta H_r$  is the enthalpy of reaction at standard conditions, and  $\Omega_{\text{fuel}}$  the fuel availability (difference in Gibb’s Free Energy between reactants and products at standard conditions).

The first task was to determine the optimum dilution of the CO fuel with CO<sub>2</sub> for given cycle pressure and temperature. The results are shown in Fig. 5 as First Law efficiency versus dilution. With too little dilution, the moles of working substance are insufficient to extract all the fuel energy when expanded through the given pressure ratio. Too much dilution decreased the proportion of isothermal to adiabatic turbine expansion. The dashed line on Fig. 5 represents conditions at which there is no isothermal expansion at all. Further dilution would make it impossible to achieve the indicated temperature.

The overall cycle efficiency for each pressure and temperature is presented in Table 2, where the computation was performed at optimum dilution for each condition. The rows marked 922K correspond to the steam cycle described above, whereas those labeled 1273K correspond to a hypothetical 340 atm 1273/1273K single reheat steam cycle. It is interesting to note that for the 922K steam cycle, no benefit derives from increasing TIT from 2200K to 2600K. Moreover, increasing TIT from 1600K to 2200K results in modest efficiency gains

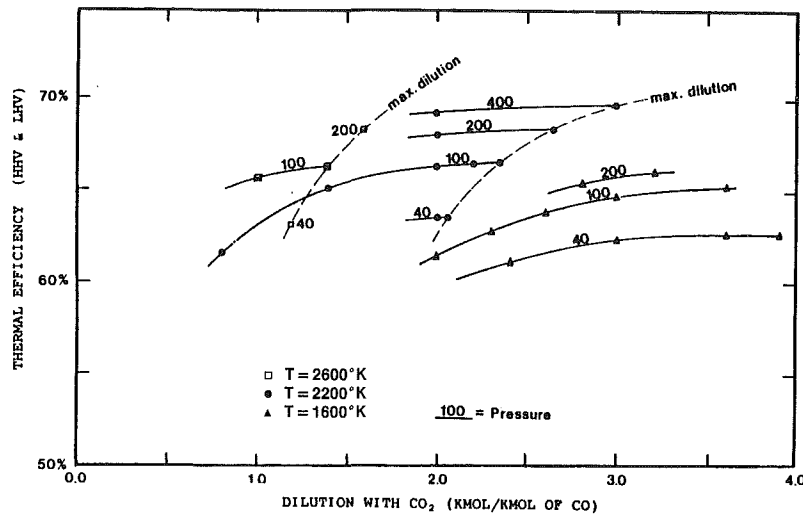


Fig. 5 Efficiencies based on the First Law of Thermodynamics (LHV and HHV) for the proposed gas turbine combined cycle for a range of pressures, temperatures, and fuel compositions

Table 2 Efficiencies based on the First and Second Law of Thermodynamics for three CPR's and TIT's, and two steam cycle peak operating temperatures

TIT (°K)	Steam T CPR (°K)	40	100	200
1600	922	$\eta^1 = 62.7$ $\eta^2 = 69.0$	$\eta^1 = 65.2$ $\eta^2 = 71.8$	$\eta^1 = 66.1$ $\eta^2 = 72.7$
	1273	$\eta^1 = 65.3$ $\eta^2 = 71.8$	$\eta^1 = 66.1$ $\eta^2 = 72.7$	-----
2200	922	$\eta^1 = 63.6$ $\eta^2 = 70.0$	$\eta^1 = 66.6$ $\eta^2 = 73.3$	$\eta^1 = 68.4$ $\eta^2 = 75.3$
	1273	$\eta^1 = 67.5$ $\eta^2 = 74.3$	$\eta^1 = 70.0$ $\eta^2 = 77.7$	$\eta^1 = 71.5$ $\eta^2 = 78.7$
2600	922	$\eta^1 = 63.1$ $\eta^2 = 69.4$	$\eta^1 = 66.3$ $\eta^2 = 73.0$	$\eta^1 = 68.4$ $\eta^2 = 75.2$
	1273	$\eta^1 = 67.2$ $\eta^2 = 74.0$	$\eta^1 = 70.0$ $\eta^2 = 77.1$	$\eta^1 = 71.8$ $\eta^2 = 79.0$

which become more tangible at higher pressures. If, however, the 1273K steam cycle could be built, substantial benefits would derive from raising TIT from 1600K to 2200K, but still no improvement from further raising TIT to 2600K. Since simultaneous development of a 1273K steam cycle and a 2200K Isothermal Turbine would be a monumental and risky technological task, it is the authors' view that the most promising next step is to develop the 1600K, 100 pressure ratio Isothermal Gas Turbine. This with the 922K steam cycle is considered the most promising technology in terms of efficiency improvement and technical feasibility.

To shed further light on the results of Table 2, availability balances for the cycle are presented as a function of TIT at a pressure ratio of 100 in Fig. 6, as a function of pressure ratio for a TIT of 2200K in Fig. 7 and as a function of dilution at 100 pressure ratio, 2200 K in Fig. 8. The 922K steam cycle is used in those figures. The width of each band represents the destruction of thermodynamic availability by the indicated mechanism as a percentage of fuel availability. By subtracting the total availability losses from 100 percent one obtains the Second Law efficiency  $\eta_2$ . As expected, the irreversibilities in the precombustor and due to heat transfer from the gas turbine exhaust to the steam are the largest. Figure 6 shows that raising TIT reduces combustion irreversibility, but that this effect is counterbalanced by the increased heat transfer irreversibility from the higher temperature exhaust to the steam. This explains the diminishing return with higher TIT for the given 922K steam cycle. Figure 7 illustrates the

benefits of high pressure ratio. Combustor irreversibility is reduced due to the higher compressor delivery temperature and smaller precombustor proportion of the total reaction. Moreover, the high expansion ratio reduces exhaust temperature and thereby heat transfer irreversibility. Figure 8 explains the weak dependence on dilution apparent in Fig. 5. Increasing dilution raises combustion irreversibility but decreases the turbine exhaust temperature and thus the heat transfer irreversibility.

Due to the substantial impact of steam cycle peak temperature, the computations were performed for the 100 pressure ratio gas turbine at different TIT's in conjunction with a 164 atm 811/811K single reheat steam cycle (2415 psia 1000°/1000°F). This represents steam conditions in widespread use by U.S. utilities. Figure 9 shows the result. While substantial benefits accrue from the 340 atm 922/867/867K steam cycle, negligible benefits derive from further developments of the steam cycle with the 1600K gas turbine. Further increases in steam temperatures result in substantial gains only with the higher TIT of 2200K. As mentioned previously, the authors' regard those simultaneous increases of both gas and steam conditions technologically impractical in the near term.

One interesting solution to the mismatch between a high-temperature isothermal turbine cycle and a moderate-temperature steam cycle that circumvents the need for a prohibitively high pressure ratio is to use compounded gas turbine cycles as illustrated on T-S coordinates in Fig. 10. The

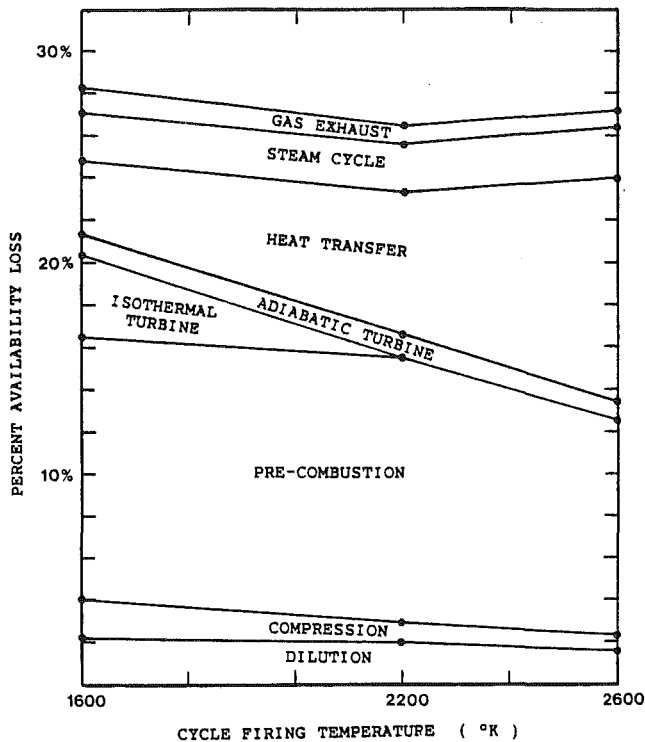


Fig. 6 Percent availability losses in the cycle as a function of the turbine firing temperature

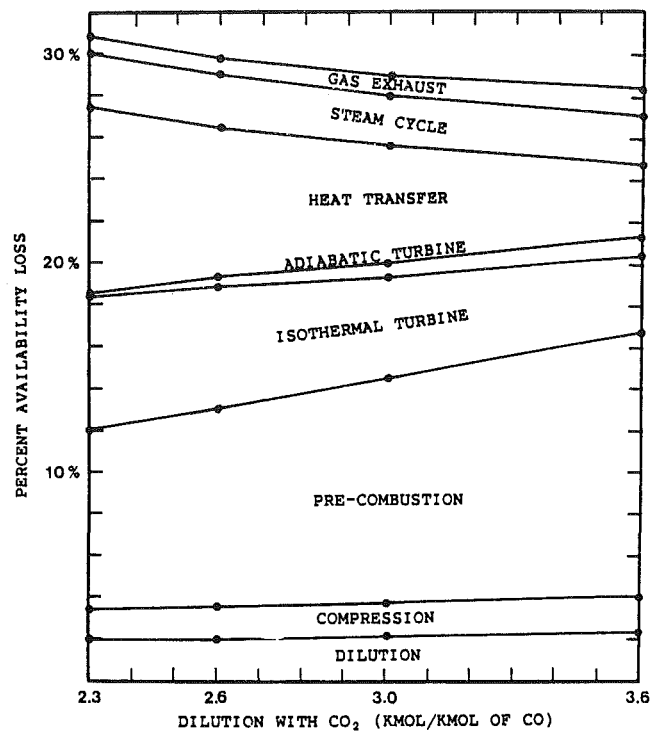


Fig. 8 Percent availability losses in the cycle as a function of the dilution of the CO with CO<sub>2</sub>

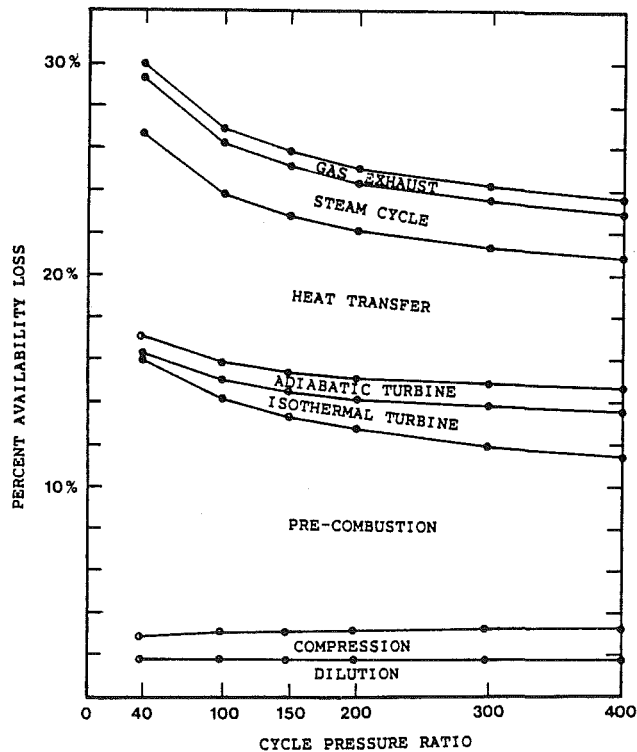


Fig. 7 Percent availability losses as a function of the cycle pressure ratio

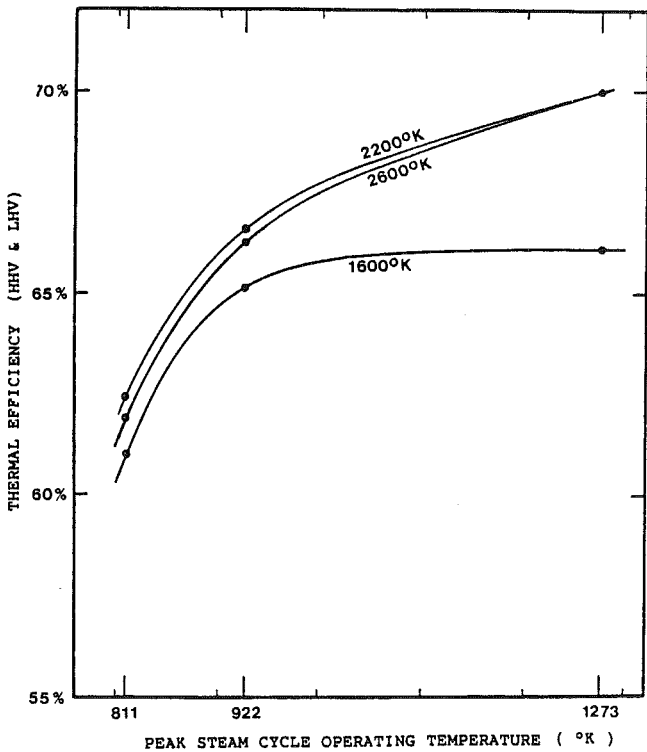


Fig. 9 Thermal efficiency dependency on the steam cycle peak temperature

intermediate Brayton Cycle and steam cycle can consist of existing, well-proven machinery and components. Despite the cost, size and pressure-drop of the gas-to-gas heat exchanger, this concept is believed worthy of further evaluation.

#### IV Conclusions

1. For combined cycle applications, an isothermal (or

multiple re-heat) gas turbine cycle with moderate peak temperature and high pressure can provide the same overall performance as a normal Brayton cycle of moderate pressure and high temperature. In view of the well-known problems associated with raising turbine inlet temperatures, the former is deemed worthy of development.

2. Combustion irreversibility can be reduced by increasing

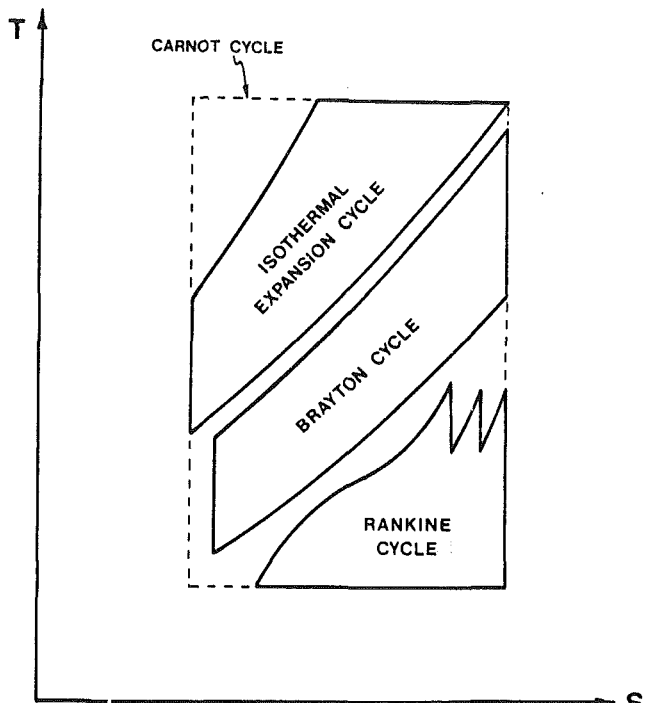


Fig. 10 Temperature-entropy diagram for a combined gas turbine cycle.

isothermal turbine temperature. However, for the range of conditions thought to be practical, this is offset by the increase in heat transfer irreversibility between the gas and steam cycles.

- When combined with existing steam cycle advanced technology, a 1600K, 100:1 pressure ratio multiple reheat gas turbine can yield a first law thermal efficiency of 65 percent before accounting for turbine cooling losses. Those losses are expected to be less than 5 percent for a well-designed system.

### Acknowledgments

This research was funded by the Massachusetts Institute of Technology Energy Laboratory. The authors are indebted to Professor Thomas H. Lee for his support, encouragement and helpful comments. Illuminating discussions with Professor Joseph L. Smith Jr. were quite useful. The authors wish to thank Ms. Kathleen Giordano for her efforts in typing the mats.

### References

- Keenan, J. H., *Thermodynamics*, Wiley, New York, 1941.
- Ahern, J. E., *The Exergy Method of Energy System Analysis*, Wiley, New York, 1980.
- Denbigh, K., "Auxiliary Functions and Conditions of Equilibrium," Chapter 2, *Principles of Chemical Equilibrium*, 3rd Edition, Cambridge University Press, 1971.
- Horner, M. W., and Caruvana, A., "High Temperature Turbine Technology Readiness," ASME Paper No. 82-GT-213.
- El-Masri, M. A., "Two-Phase Transpiration Cooling," ASME JOURNAL OF ENGINEERING FOR POWER, Vol. 105, No. 1, Jan. 1983, pp. 106-113.
- El-Masri, M. A., "On Thermo dynamics of Gas Turbines" Part 1, submitted to the 29th International Gas turbine Conference, The Hague, 1984, Second Law Analysis for Combined Cycles.
- Rice, I. G., "The Reheat Gas Turbine Combined Cycle," *Mechanical Engineering*, Vol. 104, No. 4, Apr. 1982, pp. 46-57.
- Rice, I. G., and Jenkins, P. E., "Comparison of the HTTT Reheat Gas Turbine Combined Cycle With the HTTT Nonreheat Gas Turbine Cycle," ASME Paper No. 81-GT-69.
- Jahnig, C. E., "30% Fuel Saving By Adding Combustion Within Gas Turbine," ASME Paper No. 81-JPGC-GT-4.
- Hori, A., and Takeya, K., "Outline of Plan For Advanced Research Gas Turbine," ASME Paper No. 81-GT-28.
- Magnusson, J. H., "A Gas Turbine Combined Cycle Approaching Minimal Irreversibility," S.M. thesis, Massachusetts Institute of Technology, Department of Mechanical Engineering, Sept. 1982.
- ASPEN-"Advanced System For Process Engineering," Software, Massachusetts Institute of Technology, Department of Chemical Engineering.
- Nesbit, W., "Advancing Pulverized Coal," *EPRI Journal*, Vol. 6, No. 7, Sept. 1981, pp. 17-23.
- El-Masri, M. A., "A Proposed Regenerative Thermosiphon Blade Cooling System For High Efficiency Gas Turbines," *Proc. XIV ICHMT Symposium*, Dubrovnik, 1982, Hemisphere Publishing Co., 1983.
- Schmidt, E., "Heat Transmission by Natural Convection at High Centrifugal Acceleration in Water Cooled Gas Turbine Blades," *Proc. General Discussion on Heat Transfer*, Vol. IV, Inst. Mechanical Engineers, London, 1951, pp. 361-363.
- Friedrich, R., "A Gas Turbine With Cooled Blades For Temperatures Above 1000°C," (in German), *BWK*, Vol. 14, No. 8, Aug. 1962, pp. 368-373.
- Freche, J. C., and Digiula, A. J., "Heat Transfer and Operating Characteristics of Aluminum Forced-Convection and Stainless Steel Natural-Convection Water Cooled Single-Stage Turbines," NACA RM-ESODO3a, June 1950.
- El-Masri, M. A., and Louis, J. F., "Design Considerations For the Closed-Loop Water-Cooled Turbine," ASME Paper No. 79-GT-71.
- Motakef, S., and El-Masri, M. A., "Critical Heat Flux in the Channels of a Closed-Loop Water-Cooled Turbine," ASME Paper No. 81-HT-74.
- Ballentine, P. H., "Stability in the Blade Channels of a Water-Cooled Gas Turbine," S.M. thesis, Massachusetts Institute of Technology, Department of Mechanical Engineering, Feb. 1982.
- El-Masri, M. A., "Fluid Mechanics and Heat Transfer in The Blade Channels of a Water-Cooled Gas Turbine," Ph.D. thesis, Massachusetts Institute of Technology, Department of Aero. & Astro., Sept. 1978.
- El-Masri, M. A., and Louis, J. F., "On the Design of High Temperature Gas Turbine Blade Water-Cooling Channels," ASME JOURNAL OF ENGINEERING FOR POWER, Vol. 100, No. 4, Oct. 1978, pp. 586-591.
- El-Masri, M. A., Kobayashi, Y., and Louis, J. F., "A General Performance Model For The Open Loop Water-Cooled Gas Turbine," ASME Paper No. 82-GT-212.
- Gardner, W. B., Hannah, W., and Gray, D. E., "Interim Review of the Energy Efficient Engine (E<sup>3</sup>) Program," ASME Paper No. 82-GT-271.
- Zaugg, P., and Hoffeins, H., "Brown Boveri Air-Storage Gas Turbines," *Brown Boveri Review*, Vol. 64, Jan. 1977, pp. 34-39.

# A Comparative Study of the Influence of Different Means of Cooling on the Performance of a Combined (Gas and Steam Turbines) Cycle

Chuan shao Wu<sup>1</sup>

J. F. Louis

Professor of Aeronautics and  
Astronautics.

Massachusetts Institute of Technology,  
Cambridge, Mass. 02139

*A comparative study of the influence of different means of cooling on the thermodynamic efficiency and specific power of combined (gas and steam turbines) cycle is presented. The study extends the previously developed methodology evaluating the influence of cooling and coolant requirements on gas turbine performance. In this study, the exhaust gases of the gas turbine are used as the heat source to a steam cycle using single reheat with a specified temperature difference at the pinch point. The sensitivity of the overall cycle efficiency to each key input parameter is reported.*

## Introduction

The successful development of gas turbines has centered on the internal combustion of high grade clean fuels such as oil distillates and natural gas. The high cost of these fuels provides a strong motivation to increase plant efficiencies and to consider the use of cheaper low-grade fuels.

The reduction of fuel consumption can be achieved not only by improvements of component efficiencies but, most importantly, by increasing both turbine inlet temperature and pressure ratio. These improvements require active cooling of the hot turbine components in order to avoid a reduction of operating life due to an unfavorable combination of oxidation, creep, and thermal stresses. However, the coolant mass flow can become so large that the excess compressor power for cooling can offset the power gains associated with an incremental increase in turbine inlet conditions.

Low-grade fuels introduce corrosive agents into the hot stream and the metal temperature of hot components may have to be reduced to levels as low as 800–900 K if corrosion is to be avoided. This reduction in metal temperature results in an increased demand of cooling drawn from the compressor and in a performance penalty. Improvements in air cooling techniques are actively being pursued, particularly for aircraft engines, but other cooling technologies using water and superheated steam are also being considered for ground-based power plants. Both superheated steam or humidified could be

introduced with minimum design changes in air cooled gas turbine technology. Water cooling [1] is still in early development, those with the development of open-loop leading over the use of closed-loop in rotating components. The use of closed-loop water cooling in stationary components is a much more advanced stage of development.

In a previous paper [2], a comparative study of the influence of different means of turbine cooling on the performance of a simple cycle gas turbine was made. The study developed a common methodology and it indicated the advantages derived from the recovery of some of the heat from the turbine exhaust to provide superheated steam for cooling.

The present study considers the use of a combined cycle (gas and steam turbines) to take full advantage of the heat recovered from the gas turbine exhaust to raise steam which can be fully expanded in a steam turbine.

The motivation for this work is the need for a methodology which incorporates the advances in cooling techniques into a realistic simulation of the performance of an industrial combined gas and steam turbine cycle. In its comparison, the study considers the following cooling means:

- 1 Internal cooling by air (forced convection and impingement)
- 2 Internal and film cooling by air
- 3 Internal cooling by steam
- 4 Internal and film cooling by steam
- 5 Closed-loop cooling with water
- 6 Open-loop cooling with water

The model evaluates the mixing losses of coolant with combustion gases, pumping power of coolant, and heat transfer from expanding gases, and calculates combined

<sup>1</sup> Visiting Scholar from Zhuzhou Engine Factory, Zhuzhou, Hunan, P.R.C.

Contributed by the Gas Turbine Division of THE AMERICAN SOCIETY OF MECHANICAL ENGINEERS and presented at the 29th International Gas Turbine Conference and Exhibit, Amsterdam, The Netherlands, June 4–7, 1984. Manuscript received at ASME Headquarters January 12, 1984. Paper No. 84-GT-177.

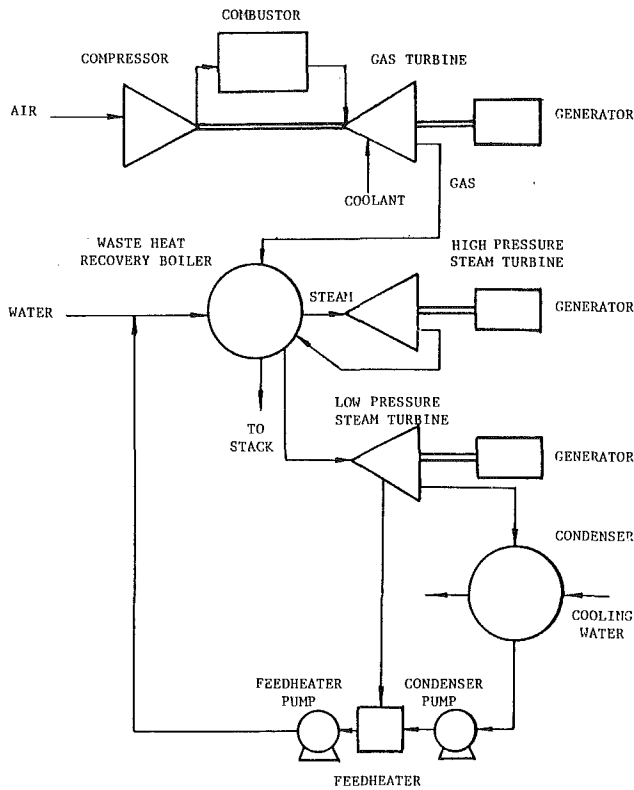


Fig. 1 Combined gas and steam turbines cycle

thermodynamic efficiency and specific power using state of the art knowledge. Design conditions in the combined cycle can be selected to provide optimum design conditions and sensitivity analyses can be conducted around these optimum conditions.

### Combined Cycle

The combined gas and steam turbines cycles have three main components as shown in Fig. 1:

- 1 An open cycle gas turbine
- 2 A waste heat recovery boiler
- 3 A steam cycle

The gas turbine is used as a heat source in a waste heat recovery boiler that produces steam for the steam turbine. There is no supplementary firing in the waste heat recovery boiler. It is the simplest and most efficient of the combined cycles. A T-S (temperature-entropy) diagram, Fig. 2, shows the heat transfer between two cycles.

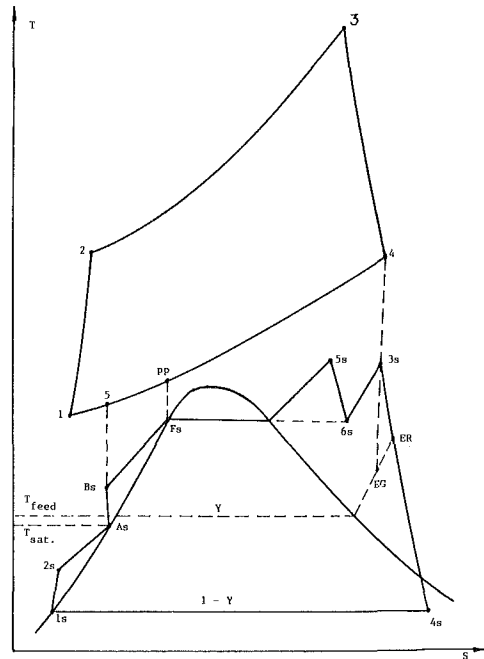


Fig. 2 Temperature-entropy diagram for combined Brayton/Rankine cycle

**Gas Turbine Cycle Efficiency and Specific Power.** The gas turbine cycle efficiency and specific power are defined in the usual way. The thermal efficiency is defined as

$$\eta_{gt} = \frac{W_{net}}{Q}$$

The net work is

$$W_{net} = W_t - W_c$$

The compressor work is

$$W_c = \dot{m}_a (h_{02} - h_{01})$$

The gas turbine work is

$$W_t = (\dot{m}_a + \dot{m}_f) (h_{03} - h_{04}) + \dot{m}_c (h_{0c} - h_{04})$$

where  $h_{0c}$  total enthalpy of coolant

The heat added is

$$Q = (\dot{m}_a + \dot{m}_f) h_{03} - \dot{m}_a h_{02}$$

The equation for efficiency becomes

$$\eta_{gt} = \frac{(\dot{m}_a + \dot{m}_f) (h_{03} - h_{04}) + \dot{m}_c (h_{0c} - h_{04}) - \dot{m}_a (h_{02} - h_{01})}{(\dot{m}_a + \dot{m}_f) h_{03} - \dot{m}_a h_{02}}$$

Substituting coefficients  $a_f$  and  $a_c$  for the fuel to air flow ratio

### Nomenclature

$a$  = mass flow ratio  
 $g$  = specific fuel consumption  
 $h$  = enthalpy per unit mass  
 $\dot{m}$  = mass flow  
 $P$  = specific power  
 PRC = compressor pressure ratio  
 PS = steam turbine inlet pressure  
 $Q$  = heat added to gas turbine cycle  
 $S$  = blade perimeter

TIT = gas turbine inlet temperature  
 $t$  = blade circumferential spacing at pinchline  
 $W$  = work  
 $Y$  = fraction of steam going into feedheater  
 $\eta$  = efficiency  
 $\alpha$  = inlet gas flow angle

### Subscripts

$a$  = air  
 $b$  = blade  
 $c$  = compressor, coolant

$cc$  = combined cycle  
 $f$  = fuel  
 $g$  = gas  
 $o$  = total, stagnation  
 $p$  = pump  
 $pp$  = pinch point  
 $s$  = steam  
 $t$  = turbine  
 1,2,3,4,5,pp = states in gas turbine cycle  
 1s,2s,As,Bs, = states in steam turbine cycle  
 Fs,5s,6s,3s, = states in steam turbine cycle  
 ER,EG,4s

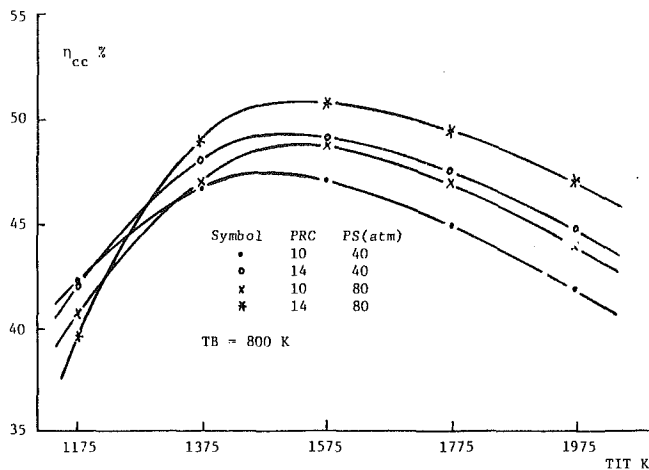


Fig. 3 Combined cycle efficiency of internal steam cooling

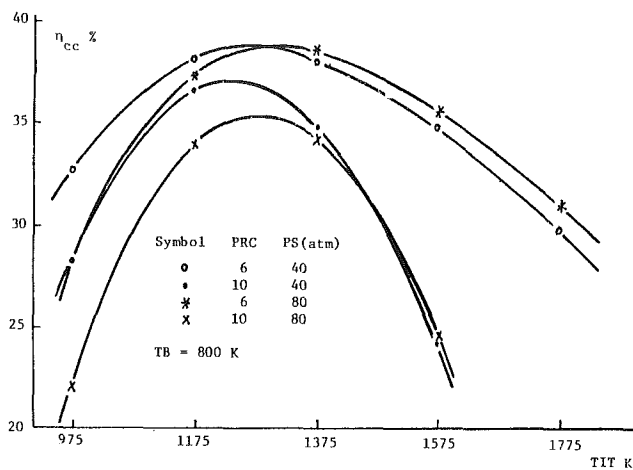


Fig. 5 Combined cycle efficiency of internal air cooling

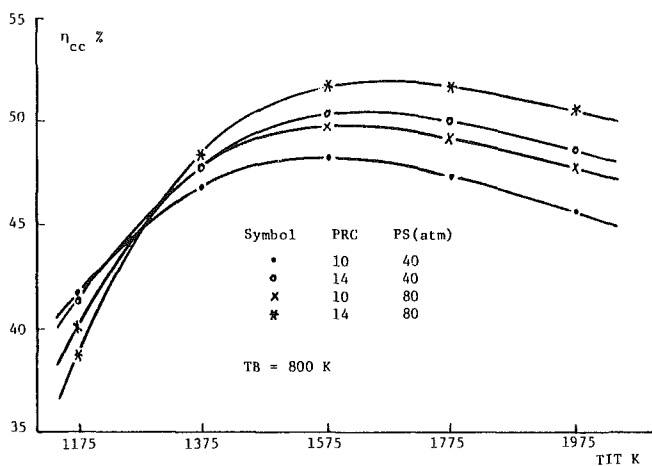


Fig. 4 Combined cycle efficiency of film steam cooling

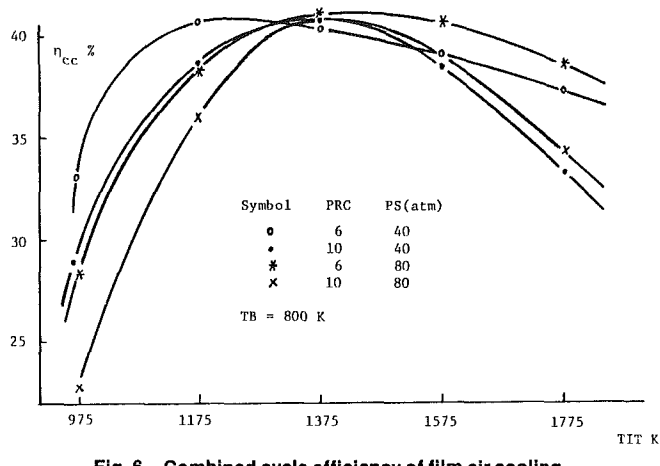


Fig. 6 Combined cycle efficiency of film air cooling

$$\left(a_f = \frac{\dot{m}_f}{\dot{m}_a}\right) \text{ and coolant to gas flow ratio } \left(a_c = \frac{\dot{m}_c}{\dot{m}_g}\right)$$

yields

$$\eta_{gt} = \frac{(1 + a_f)(h_{03} - h_{04}) + a_c(h_{0c} - h_{04}) - (h_{02} - h_{01})}{(1 + a_f)h_{03} - h_{04}}$$

The specific power is defined as

$$P_{gt} = \frac{W_{net}}{\dot{m}_a} = (1 + a_f)(h_{03} - h_{04}) + a_c(h_{0c} - h_{04}) - (h_{02} - h_{01})$$

**Cooled Gas Turbine Model.** In the analysis of the turbine expansion to determine the turbine work done, the following are considered [3]:

1 The thermodynamic state of the working gases is affected by its mixing with the coolant and by the heat transfer to the blades

2 The mass flow of working gases includes the compressor air, the fuel, and the coolant mixed in the upstream stages

Because the required coolant flow and losses associated with a given blade row are dependent on the blade geometry, it is necessary to "design" each blade row or stage in the gas turbine model. In this model, the "design" is simplified by considering only pitchline design (at the blade midspan position), which assumes that the calculations produce the averaged values of flow variables. The mixing and pumping losses are proportional to the coolant flow. Profile and

secondary losses are included. The "profile losses" include all the effects of profile boundary layers and coolant injection. The "secondary losses" include the passage secondary loss, the annulus loss, and the tip clearance loss. The profile loss calculation is based on an analysis by Hertsel [4], and the secondary loss calculation is based on the well-known correlation by Ainley and Mathieson (equation (6) of [5]).

The maximum stage pressure ratio,  $\pi_{tmax}$  is set at 2.0. Thus the required number of turbine stage,  $N_s$  will be determined by

$$N_s = \frac{\ln\left(\frac{P_{03}}{P_{04}}\right)}{\ln \pi_{tmax}}$$

where  $N_s$  is rounded-off to the next highest integer number and maximum  $N_s$  is set at 5. The actual stage pressure ratio is

$$\pi_s = \left(\frac{P_{03}}{P_{04}}\right)^{\frac{1}{N_s}}$$

When the stagnation temperature of the gas entering a given blade row is higher than the allowable blade metal temperature, some types of cooling is required. For a blade row requiring cooling, there will always be internal convection and impingement cooling. If a large amount of coolant is required, some coolant may also be used for film cooling. When the ratio,  $a_c$ , of coolant to the main flow is greater than 0.02, film cooling is introduced in this model. In order to simplify the calculation, blades internally cooled by convection and impingement are treated as heat exchangers operating at constant metal temperature.

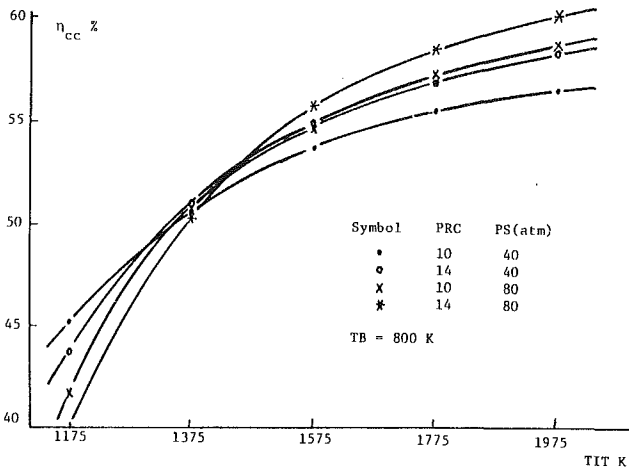


Fig. 7 Combined cycle efficiency of closed loop water cooling

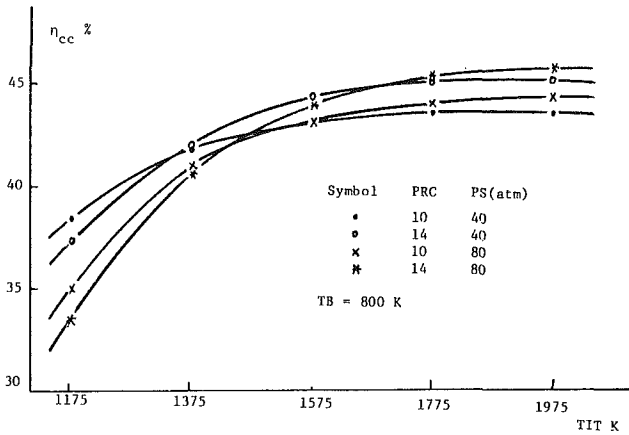


Fig. 8 Combined cycle efficiency of open loop water cooling

The mass ratio of coolant to total gas flow used for internal cooling

$$a_c = \frac{\dot{m}_c}{\dot{m}_g} = \frac{St \cdot S}{\epsilon \cdot t \cdot \cos \alpha} \frac{(h_{og} - h_{ob})}{(h_{ob} - h_{oc})}$$

where

- St = average Stanton number
- S = blade perimeter
- t = blade pitch
- α = inlet gas flow angle
- ε = blade heat exchanger effectiveness

The coolant flow used for film cooling is

$$a_c = (1 - \eta_{iso}) \frac{St \cdot S}{\epsilon \cdot t \cdot \cos \alpha} \frac{(h_{og} - h_{ob})}{(h_{ob} - h_{oc})}$$

where

$\eta_{iso}$  = average isothermal film effectiveness.

**Steam Turbine Cycle.** The gases leaving the gas turbine are taken to a waste heat recovery boiler, which raises steam for the steam cycle. The boiler would have a reheater. The steam cycle performance is calculated for a specified boiler throttle pressure and with a maximum boiler and reheater temperature of 838.7 K (1050°F). With a selected pinch point temperature difference as shown in Fig. 2 (in this model it is equal to 20 K) the mass ratio of steam to exhaust gas flow from gas turbine can be calculated.

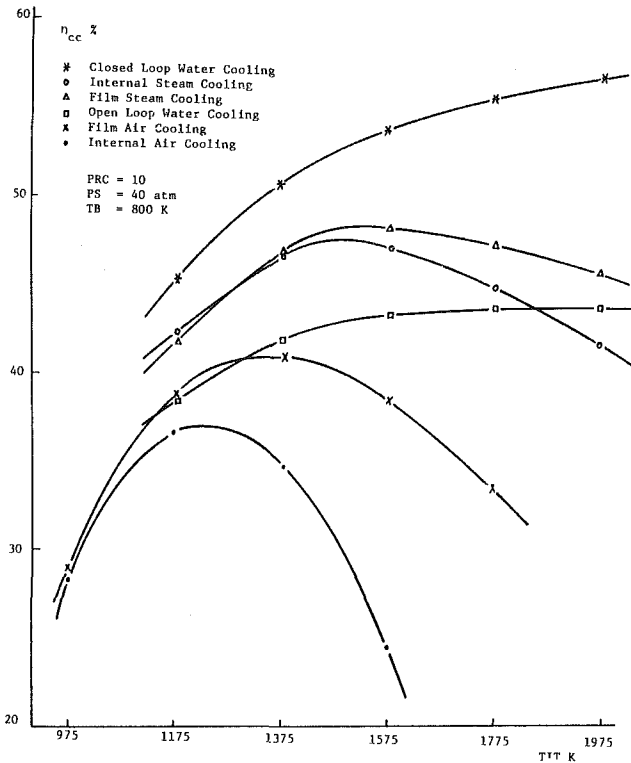


Fig. 9 Combined cycle efficiency of different cooling means

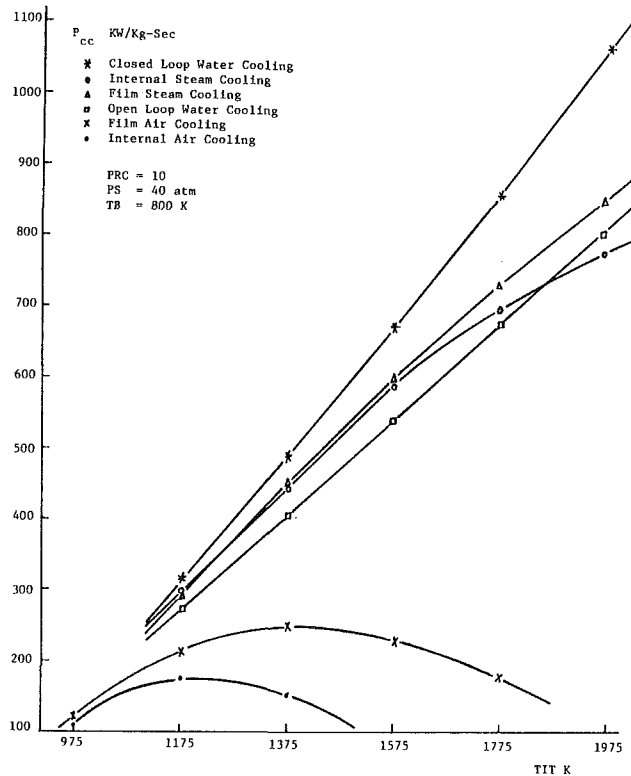


Fig. 10 Combined cycle specific power of different cooling means

$$a_s = \frac{h_{o4} - h_{o5}}{h_{5s} - h_{Bs} + h_{3s} - h_{6s}}$$

The heat exchanger between gas and steam in waste heat recovery boiler is given by

$$\frac{h_{o4} - h_{pp}}{h_{o4} - h_{pp}} = \frac{h_{5s} - h_{Bs} + h_{3s} - h_{6s}}{h_{5s} - h_{Fs} + h_{3s} - h_{6s}}$$



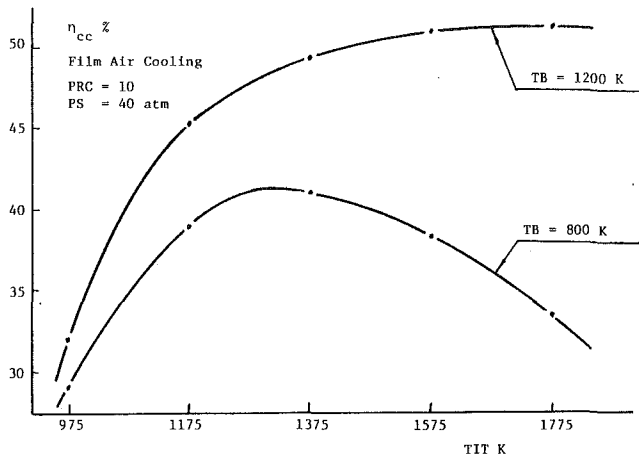


Fig. 11 Combined cycle efficiency with different blade temperature

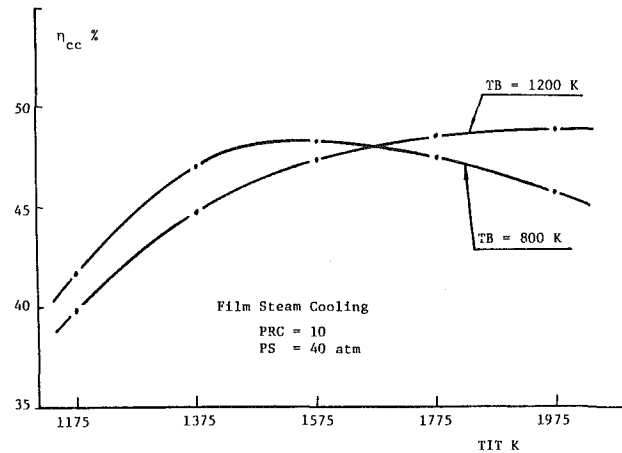


Fig. 12 Combined cycle efficiency with different blade temperature

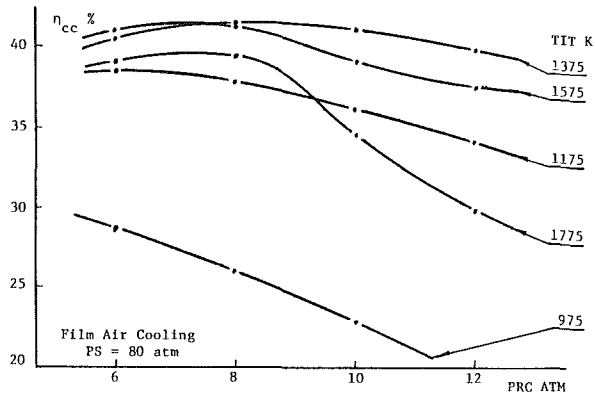


Fig. 13 Combined cycle efficiency versus compressor pressure ratio

The work of the steam turbine is

$$W_{st} = h_{5s} - h_{6s} + h_{3s} - h_{ER} + (1 - Y)(h_{ER} - h_{4s})$$

where  $Y$  is fraction of steam going to the feedheater

$$Y = \frac{h_{A5} - h_{2s}}{h_{ER} - h_{2s}}$$

When steam cooling is used, steam is drawn from the low-pressure steam turbine at the pressure of the feedheater (ref. Fig. 2,  $P_{feed} = P_{ER}$ ). In this model,  $T_{feed} = T_c = 488$  K, and  $P_{feed} = 20.7$  atm. The work of the steam turbine can be written as

$$W_{st} = h_{5s} - h_{6s} + h_{3s} - h_{ER} + (1 - Y - a_c)(h_{ER} - h_{4s})$$

The specific power of the steam cycle referred to the gas turbine mass flow, is

$$P_{st} = a_s (W_{st} - W_{p1} - W_{p2})$$

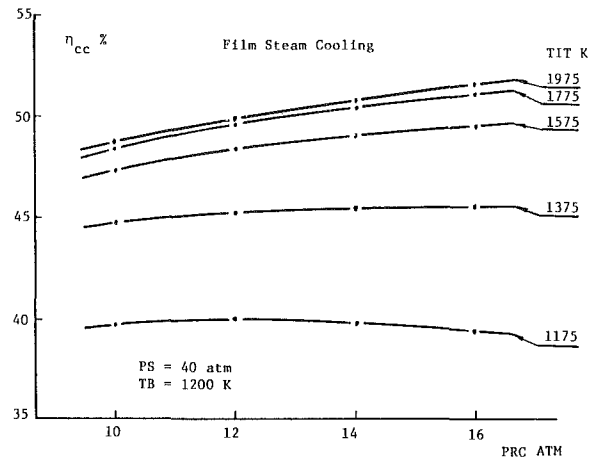


Fig. 14 Combined cycle efficiency versus compressor pressure ratio

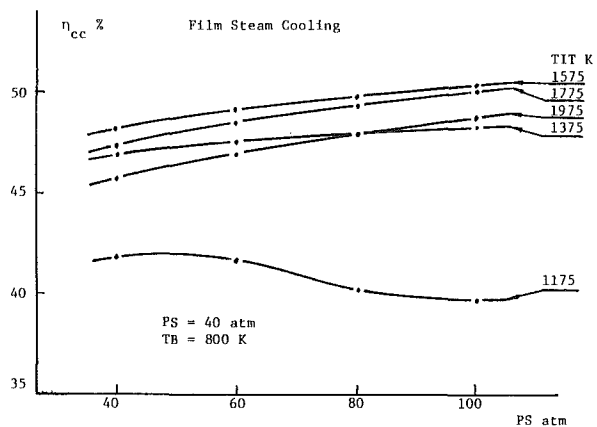


Fig. 15 Combined cycle efficiency versus steam turbine inlet pressure

where

$W_{p1}, W_{p2}$  represent the pumping work.

**Combined Cycle Efficiency and Specific Power.** The total specific power generated by the combined cycle is the sum of the net specific power from the two turbines:  $P_{cc} = P_{gt} + P_{st}$

The overall efficiency is

$$\eta_{cc} = \frac{P_{cc}}{Q}$$

## Results and Discussions

Using this model, combined cycle efficiency and specific power depend on four primary variables and about ten secondary variables. The primary variables are:

- 1 Compressor pressure ratio (PRC)
- 2 Gas turbine inlet temperature (TIT)
- 3 Allowable metal temperature of gas turbine blade (TB)
- 4 Steam turbine inlet pressure (PS)

The base values of the secondary variables are listed in Table 1 and the design parameters are given in Table 2. They define the geometry, aerodynamics, and heat transfer related to the turbine, the combustor and the coolant parameters.

The results to be presented below use the same methodology, the same values of primary and secondary variables, except for those which are characteristic of a given type of cooling. The coolant inlet temperatures are 685 K for air, 488 K for steam, and 298 K for water.

Figures 3-8 show the combined cycle efficiencies as a function of gas turbine inlet temperature for a blade temperature of 800 K, using internal steam cooling, film steam cooling, internal air cooling, film air cooling, closed-loop water cooling, or open-loop water cooling, respectively. The

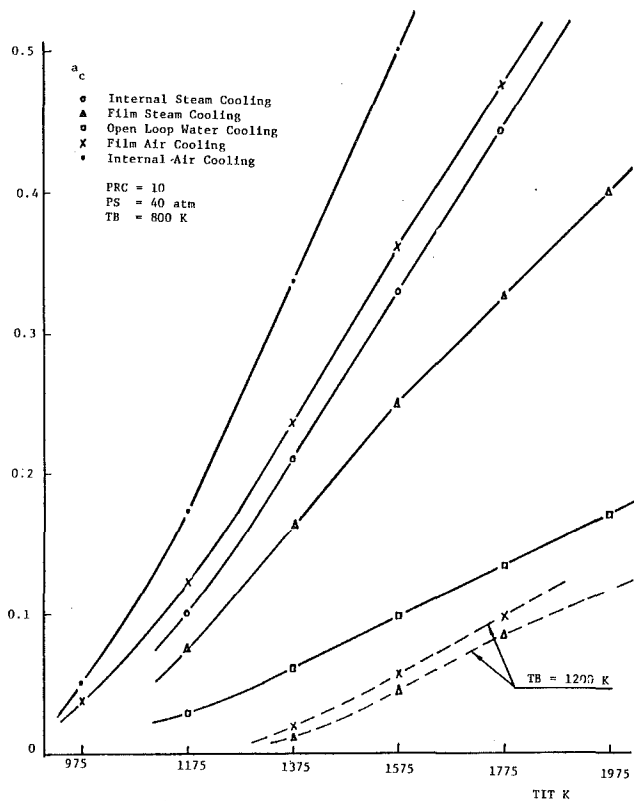


Fig. 16 Coolant flow rate of different cooling means

efficiency of steam-cooled combined cycle is found to optimize at higher values of turbine inlet temperature, gas turbine pressure ratio and steam inlet pressure than the comparable cycles using air cooling.

No optimum turbine inlet temperature is found for closed-loop, water-cooled gas turbines, whereas no increase in overall efficiency is found for turbine inlet temperatures in excess of 1775 K for combined cycles using open loop water-cooled gas turbines.

Figure 9 gives a comparison of combined cycle efficiency to be obtained with different cooling means as a function of turbine inlet temperature for a compressor pressure ratio of 10, blade temperature of 800 K and steam turbine inlet pressure of 40 atm. Closed loop water-cooling performs favorably as it is not penalized by either pumping or mixing losses. Steam cooling also performs favorably as the steam coolant expands with combustion gases. The low blade temperature of 800 K seriously penalizes the air cooling cases. As turbine inlet temperature increases, the coolant flow requirement can become so large that the excess work required for coolant can offset the power gain associated with an incremental increase of turbine inlet temperature. However, a high blade temperature of 1200 K results in a significant improvement of overall efficiency as shown in Fig. 11.

Figure 10 shows the dependence of specific power on gas turbine inlet temperature for the same condition. The specific power is found to vary linearly with turbine inlet temperature in most cases (except for air cooling) because different cooling means require different amount of coolant flows which vary linearly with the heat transfer rate. The specific power with air cooling is found to decrease for turbine inlet temperature in excess of 1375 K when the blade temperature is 800 K.

Figures 11 (air cooling) and 12 (steam cooling) indicate that an increase in blade operating temperature results in higher overall efficiencies because of smaller coolant requirements as shown in Fig. 16.

Figures 13 and 14 indicate the influence of compressor pressure ratio on efficiency with film air cooling and film

steam cooling. An optimum compressor pressure ratio is found for high turbine inlet temperatures with film air cooling. An increase in compressor pressure ratio results in a slight increase of efficiency with film steam cooling.

Figure 15 indicates the influence of steam turbine inlet pressure on efficiency with film steam cooling for a compressor pressure ratio of 10. An increase in steam turbine inlet pressure results in a slight increase of efficiency at high gas turbine inlet temperature and a decrease of efficiency at low turbine inlet temperature.

Figure 16 shows coolant flow rate of different cooling means as a function of turbine inlet temperature for a compressor pressure ratio of 10, a blade temperature of 800 K, and a steam turbine inlet pressure of 40 atm. Coolant flow rate varies linearly with the turbine inlet temperature for different cooling means. Open loop water cooling requires small value of coolant flow rate due to the high heat of vaporization of water. Internal air cooling requires large amount of coolant because of its low specific heat and of the low value of heat exchanger effectiveness. Increases of both turbine inlet temperature and compressor pressure ratio result in large values of  $(T_{03} - T_b)$  and small values of  $(T_b - T_c)$ , which lead to high coolant flow rate. Steam cooling requires less coolant flow rate than air cooling does due to its higher specific heat over that of air. The use of film cooling can significantly reduce the heat transfer to the blades, and subsequently decrease the coolant flow rate. Operation with a blade temperature of 1200 K instead of 800 K dramatically reduces the cooling requirement as shown by the lowest two curves.

## Conclusions

1 A consistent methodology has been developed for evaluation of combined cycle in which different cooling techniques can be used in the high-temperature turbine. Combined cycle efficiency and specific power are found to be sensitive to the type of cooling technique used but higher than the efficiency of the simple open-cycle gas turbine.

2 The combined cycle efficiency has an optimum gas turbine inlet temperature for each cooling means, compressor pressure, and steam turbine inlet pressure.

3 The performance of combined cycle using steam cooled gas turbine, particularly film steam cooling, is very favorable. The advantages derive from the high specific heat of steam, negligible pumping work but most significantly from the fact that the steam is raised using the waste heat from the gas turbine and expands through gas turbine with the combustion gases.

4 The combined cycle efficiency is very sensitive to changes in metal temperature for air cooled blades. The use of high-temperature materials for turbine blades can significantly increase the combined cycle efficiency.

## Acknowledgement

The authors would like to acknowledge the contribution made by their colleagues, Prof. El Masri and Dr. Hiraoka, who developed the computer program found in [2], which was used after modification in this work.

## References

- 1 Van Fassen, G. J., and Stepka, F. S., "Liquid Cooling Technology for Gas Turbines, Review and Status," NASA T.M. 78906-1978.
- 2 Louis, J. F., Hiraoka, K., and El-Masri, M. A., "A Comparative Study of the Influence of Different Means of Turbine Cooling on Gas Turbine Performance," ASME Paper 83-GT-180.
- 3 Janoch, R. E., "Modeling of Film Cooling Gas Turbine Engines," M.S. thesis, Mechanical Engineering, Massachusetts Institute of Technology, Feb. 1977.
- 4 Hartsel, J. E., "Predictions of Effects of Mass Transfer Cooling on the Blade-Row Efficiency of Turbine Airfoils," AIAA Paper 72-11, Jan. 1972.
- 5 Ainley, D. G., and Mathieson, G. C. R., "A Method of Performance Estimation for Axial Flow Turbines," Aeronautical Research Council, R&M 2974, 1957.

# Effect of New Blade Cooling System With Minimized Gas Temperature Dilution on Gas Turbine Performance

K. Kawaike

N. Kobayashi

T. Ikeguchi

Mechanical Engineering Research Laboratory,  
Hitachi, Ltd.,  
Saiwai-cho, Hitachi-shi, Japan

*Recent developments in high-performance and high-reliability gas turbine engines necessitate enforced cooling to maintain the blade temperature at reasonably low levels associated with increased turbine inlet temperature and compressor pressure ratio. However, the gas turbine performance is strongly penalized by the consumption of cooling flow, resulting in temperature dilution of hot mainstream, aerodynamic mixing loss, and pumping power loss. In this paper, a new practical blade cooling system using state-of-the-art engineering, which aims at minimizing the dilution effect, is presented. Trade-off studies between performance and reliability in terms of blade metal temperature are performed to evaluate cooling systems. Analytical comparison of different cooling systems demonstrates that the proposed cooling system provides significant improvements in performance gain and growth potential over conventional air cooling systems.*

## Introduction

Industrial gas turbines offer greater potential for energy efficient base load power generation in a combined cycle power plant operating in continuous duty service. Improvement of gas turbine performance is achieved by increasing the turbine inlet temperature and pressure ratio. In a combined cycle, increased turbine inlet temperature is beneficial for gas turbine performance itself and for bottoming cycle efficiency as well, because it raises the exhaust heat recovery temperature. To meet the more strenuous requirements at the turbine inlet condition, permitting fuel flexibility and durable base load operation, enforced cooling of hot components, particularly the first stage blades, is necessary in order to maintain blade metal temperature lower than in current engines. Emphasis must be placed on both performance and reliability, which determine overall operational costs.

With respect to blade cooling, large cooling effectiveness at a minimized cooling flow is required. Reviewing current air cooling, large amounts of compressor discharge air are supplied to the first stage nozzles and buckets and discharged into the gas path after the blades are cooled. Although the cooling air of the first stage nozzle is returned to the mainstream ahead of the first rotating stage, turbine inlet temperature (defined as the combustor exit average gas tem-

perature) is diluted due to the first stage nozzle cooling, resulting in decreased bucket energy available to do work. Simultaneously, the discharging of cooling air causes total pressure loss by mixing of coolant with the mainstream. As a result, increase of turbine inlet temperature is compensated by large amounts of nozzle cooling air. In evaluating the cooling performance of current industrial engines, the cooling effectiveness of nozzles using impingement cooling seems to reach a considerable level, while that of buckets with simple radial cooling holes is relatively low associated with the current status of turbine inlet temperature level. According to cooling characteristic curves, the rate of gain in cooling effectiveness decreases rapidly as cooling flow continues to increase, resulting in performance penalties. Therefore, the cooling capability of the first stage nozzle is critical in setting limits on attainable turbine inlet temperature, although that of the bucket has growth potential by applying aircraft-derived advanced cooling technologies.

Reducing the cooling air temperature to lower than compressor discharge temperature is an effective and realistic solution to increase the capability of air cooling. But the deficiencies due to mixing still remain. The use of steam or water with a larger specific heat and the boiling heat transfer rate has been investigated for high-temperature gas turbines because of the limitations of air as a cooling medium. Performance advantages for these fluids as a coolant were analytically obtained [1]. Water cooling is seen to be attractive for cooling purpose, but the water-cooled gas turbine is still at a component development stage. Considering the status of these alternatives, a new approach is necessary to break the limitations of air cooling, while the improvement of cooling performance must be pursued.

Contributed by the Gas Turbine Division of THE AMERICAN SOCIETY OF MECHANICAL ENGINEERS and presented at the 29th International Gas Turbine Conference and Exhibit, Amsterdam, The Netherlands, June 4-7, 1984. Manuscript received at ASME Headquarters January 6, 1984. Paper No. 84-GT-89.

In this paper, a new air cooling system is presented, which is aimed at reducing the temperature dilution effect, mixing loss and cooling air consumption.

Trade-off studies of performance versus reliability in terms of blade metal temperature are performed for the proposed cooling systems in comparison to conventional cooling systems to obtain maximum performance with reliability constraints. Analyses evaluate a simple and a combined cycle performance, blade metal temperature, and bucket creep rupture life using the turbine row-by-row aerodynamic design computer code incorporating cooling air mixing effect and preliminary thermal and mechanical analysis. Comparative results giving the effect of cooling system on the gas turbine performance are presented.

## Blade Cooling Systems

A new practical blade cooling system and the conceptual cooling configuration of the first-stage nozzle are described in comparison with a conventional cooling system and a precooled cooling system in Figs. 1 and 2.

In conventional cooling scheme A (Fig. 1 (a)), cooling air is extracted from the compressor exit and supplied to the nozzles through the inner space of the outercasing and routed to the buckets through rotating disks. The cooling air temperature is the same as the compressor exit temperature. In the last interstage, sealing air is extracted from the compressor midstage at the lowest pressure available to reduce the compression work which is common to all the cooling schemes of Fig. 1. The cooling air supplied to the blades is finally discharged into the mainstream through the blade trailing edge slots or bucket tip holes.

Figure 1(b) shows the precooled cooling system, in which the compressor discharge air is extracted from the combustor shell and directed to the cooler to reduce the cooling air temperature. Cooled cooling air is supplied separately to the nozzles, including the first stage ones, and to the buckets and is finally discharged into the mainstream. The first stage nozzle cooling configuration for both cooling schemes A and B basically adopts impingement cooling with pin fin arrays at the trailing edge part and trailing edge ejection slots as shown in Fig. 2(a).

Figure 1(c) illustrates the proposed cooling scheme. The cooling air, extracted from the combustor shell, is directed to the cooler and supplied to the first and the second stage nozzles.

Cooling air, supplied to the first-stage nozzle, passes through the cooling passage inside the airfoil and is extracted from the opposite side of the inlet and then supplied to the buckets routed through the holes in the disk. This allows the air to be utilized again for bucket cooling. It is desirable for the cooling air to be precooled, because the cooling flow into

the bucket is warmed up by the first stage nozzle cooling. Thus an auxiliary cooler is necessary in this system. The first-stage nozzle cooling configuration adopts a so-called multipass design (Fig. 2(b)), composed of internally convective cooling passages with turns, turbulence promoters, and pin fin arrays, which are well proven state-of-the-art cooling technologies.

The intention of the proposed cooling system is to minimize the gas temperature dilution and the pressure loss due to the mixing of cooling air with the mainstream. Additionally, the proposed system has the advantages that the first-stage nozzle can utilize the sum of the cooling flow required for bucket cooling at a reduced temperature and the fresh unwarmed cooling air can be supplied to the trailing edge part.

In cooling schemes B and C, the cooling air temperature can be lowered by either a heat exchanger or water injection and evaporation.

## Analytical Methods

To evaluate effects of cooling schemes, the following analyses are performed. Designing gas turbines is usually an iterative process of aerodynamic, cooling, and mechanical designs for a given set of requirements. It is important, even at an initial aerodynamic design stage where detailed airfoil and cooling configurations are not yet determined, to take these factors into consideration in order to keep the modifications within manageable limits at the detailed design, since interactions between aerodynamic, cooling, and mechanical design are extensive.

The analysis is divided into three sections: mean diameter row-by-row turbine aerodynamic analysis, preliminary thermal analysis of cooling blades and mechanical analysis of bucket and disk stresses, as outlined below.

**Aerodynamic Analysis.** Aerodynamic design determines work splits between stages, gas path geometry, and the radial flow pattern attaining the highest performance by taking cooling air mixing effects into account. Mean diameter velocity triangles are determined by following four parameters for given circumferential speeds. Notations of velocities used are shown in Fig. 3.

$$\text{Velocity ratio: } \sigma_{is} = \frac{U_3}{\sqrt{2\Delta H}} \quad (1)$$

$$\text{Flow coefficient: } \varphi = \frac{C_{a3}}{U} \quad (2)$$

$$\text{Reaction: } \rho = \frac{w_3^2 - w_2^2 + U_2^2 - U_3^2}{2\Delta H} \quad (3)$$

## Nomenclature

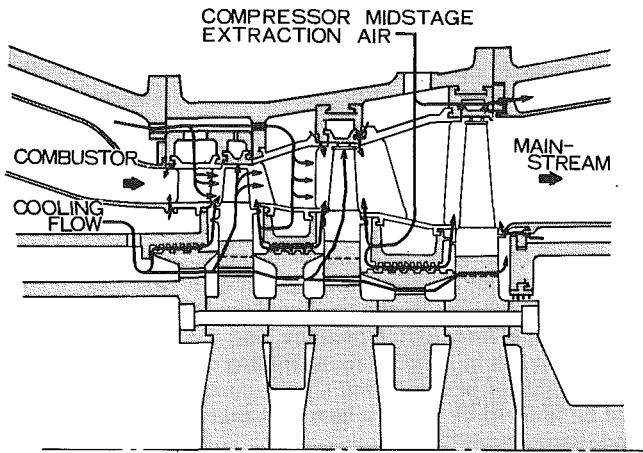
$A$  = section area of blade, area of flow path  
 $C$  = absolute velocity  
 $c_p$  = specific heat  
 $G$  = mass flow rate  
 $H$  = enthalpy per unit mass flow  
 $h$  = heat transfer coefficient  
 $M_{sh}$  = mass of bucket tip shroud  
 $N$  = traverse number  
 $Nu$  = Nusselt number  
 $P$  = pressure  
 $Q$  = heat flux  
 $r$  = radius  
 $Re$  = Reynolds number

$S$  = surface area, stress factor  
 $T$  = temperature  
 $U$  = blade circumferential velocity  
 $V$  = velocity of flow  
 $W$  = relative velocity, work  
 $W_{sp}$  = specific work  
 $x$  = blade percent height  
 $\alpha$  = flow angle, coefficient  
 $\Delta$  = difference  
 $\eta_{th}$  = thermal efficiency (LHV)  
 $\eta_c$  = cooling effectiveness  
 $\rho$  = density, reaction  
 $\sigma$  = stress

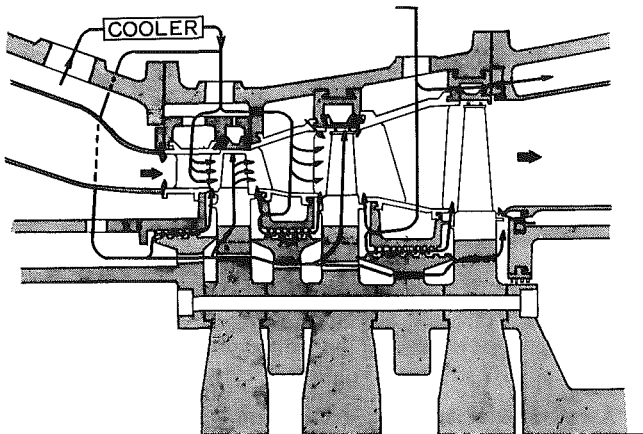
$\sigma_{is}$  = isentropic velocity ratio  
 $\omega$  = angular velocity

### Subscripts

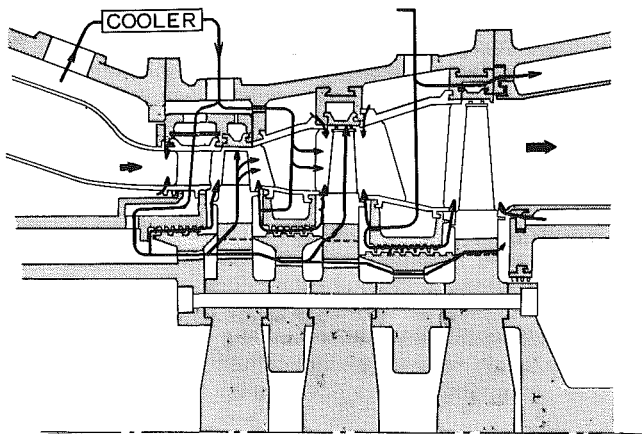
$a$  = axial, airfoil  
 $b$  = blade  
 $B$  = bottoming cycle  
 $c$  = coolant  
 $ct$  = centrifugal stress  
 $comb$  = combined cycle  
 $e$  = end wall  
 $f$  = flow pattern  
 $g$  = mainstream gas  
 $M$  = metal  
 $u$  = circumferential component



(a) Cooling scheme A – conventional cooling system



(b) Cooling scheme B – precooled cooling system



(c) Cooling scheme C – proposed cooling system

Fig. 1 Cooling schemes

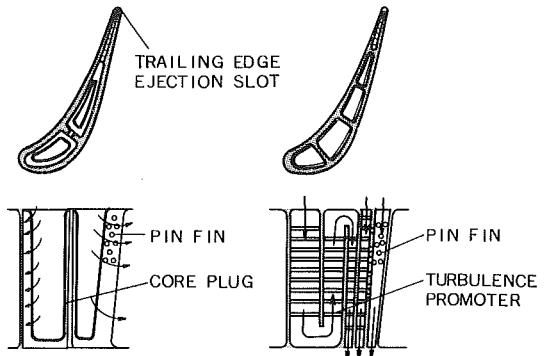
$$\text{Axial velocity ratio: } \beta = \frac{C_{a3}}{C_{a2}} \quad (4)$$

where

$$\Delta H = -U_2 C_2 \sin \alpha_2 - U_3 C_3 \sin \alpha_3 \quad (5)$$

Radial distribution of velocities is obtained by solving the following radial equilibrium equation with no radial velocity component.

$$C_a \frac{dC_a}{dr} + C_u \frac{dC_u}{dr} + \frac{C_u^2}{r} = \frac{dH_t}{dr} \quad (6)$$



(a) IMPINGEMENT COOLING (b) MULTI-PASS COOLING

Fig. 2 Conceptual cooling configuration of the first-stage nozzle

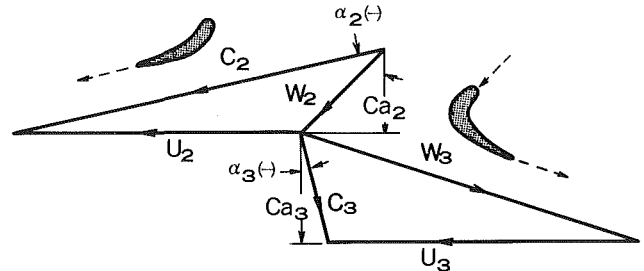


Fig. 3 Notations of velocity triangle

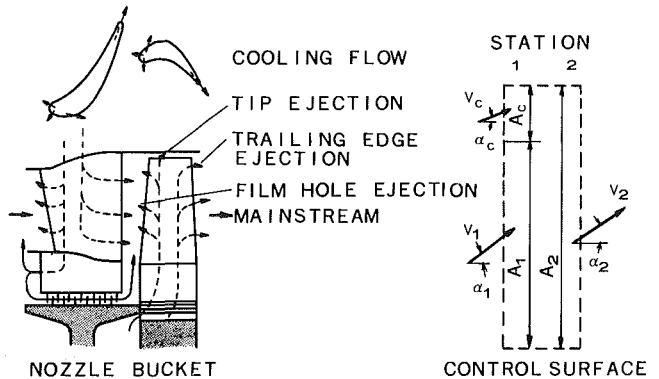


Fig. 4 Types of cooling flow ejection and one-dimensional mixing model

The radial flow pattern is initially a free vortex, and a constant radial work distribution and constant axial velocity are assumed to check the tip and root aerodynamic design criteria, which will be reoptimized in the detailed design stage. The velocity ratio and the reaction, among above velocity triangle parameters, are specified at the root and converted to values at mean diameter location assuming a free vortex in mean diameter design.

Aerodynamic losses of cascades are calculated using a modified Ainley-Mathieson loss prediction method [2]. Additional losses due to mixing of cooling air with mainstream are predicted by an ideal mixing model. Figure 4 shows the types of cooling air ejection and the one-dimensional mixing model [3]. The following one-dimensional equations for conservation of mass, momentum and energy, respectively,

$$G_1 G_c = G_2 \quad (7)$$

$$P_1 A_1 + P_c A_c + G_1 V_1 \cos \alpha_1 + G_c V_c \cos \alpha_c = P_2 A_2 + G_2 V_2 \cos \alpha_2 \quad (8)$$

$$G_1 V_1 \sin \alpha_1 + G_c V_c \sin \alpha_c = G_2 V_2 \sin \alpha_2 \quad (9)$$

$$G_1 H_{t1} + G_c H_{tc} = G_2 H_{t2} \quad (10)$$

where

- $G$  = mass flow
- $P$  = static pressure
- $H_t$  = total enthalpy per unit mass flow
- $A$  = area of flow path
- $\alpha$  = flow angle

The assumptions used for each type of cooling flow ejection are given for:

- Tip ejection:  $A_c = 0, \alpha_c = 90 \text{ deg}$
- Trailing edge ejection:  $\alpha_c = \alpha_1$
- Interstage sealing air:  $A_c = 0, \alpha_c = 90 \text{ deg}$
- Film hole ejection:  $\alpha_2 = \alpha_1, A_c = 0$   
(using equations (7), (8) and (10))

For the trailing edge ejection, the power recovered from the ejection amounts to

$$W = G_c U_3 C_{u,eject} \quad (11)$$

where

- $G_c$  = coolant mass flow
- $C_{u,eject}$  = circumferential component of coolant ejection velocity

The pumping work,  $W$ , done by the blade on the cooling air as it passes radially through the cooling passages, is calculated by equation (12) and is subtracted from turbine work.

$$W = G_c (U_{ex}^2 - U_{in}^2) \quad (12)$$

where

- $U_{ex}$  = blade circumferential speed at coolant exit
- $U_{in}$  = blade circumferential speed at coolant inlet

**Thermal Analysis.** Thermal analysis predicts blade temperatures and heat removed from the first-stage nozzles of the proposed cooling system which result in heat loss. This first requires the information of gas temperature. Nonuniformity of combustor exit temperature directly affects the blade temperature and its associated life. The combustor traverse number gives a measure of the temperature difference between the peak gas temperature and the averaged gas temperature. The peak temperature for the nozzle is given by combustor traverse temperature data.

$$N_T = \frac{T_{max} - T_{ave}}{T_{ave} - T_{comp}} \quad (13)$$

where

- $T_{max}$  = combustor exit maximum gas temperature
- $T_{ave}$  = combustor exit average gas temperature
- $T_{comp}$  = compressor discharge temperature

For the rotating bucket, the circumferential averages are used to give a radial maximum temperature.

$$N_R = \frac{T_{max,r} - T_{ave}}{T_{ave} - T_{comp}} \quad (14)$$

where

- $T_{max,r}$  = maximum of circumferential average temperature

The radial temperature pattern is assumed to be parabolic at the combustor exit and maintained through all stages. From these assumptions, and taking flow pattern effect into account, radial temperature distribution is written in the form

$$T_g = \alpha(x - x_{max})^2 + \bar{T}_g + (T_{ave} - T_{comp})N + \Delta T_f \quad (15)$$

where

- $\alpha$  = coefficient determined by gas averaged temperature condition
- $x$  = blade percent height

$x_{max}$  = location of maximum temperature in blade percent height.

$N$  = traverse number ( $N_T$  or  $N_R$ )

$\Delta T_f$  = temperature difference due to radial flow pattern

$\bar{T}_g$  = average gas temperature

Blade metal temperatures are estimated for given gas temperature and cooling flow rate by assuming the cooling effectiveness curve of cooling blades which depends on internal cooling configuration and external heat load conditions. In addition, the spanwise cooling effectiveness is assumed constant.

$$\eta_c = \frac{T_g - T_b}{T_g - T_c} \quad (16)$$

where

$T_b$  = average blade surface temperature

$T_g$  = mainstream gas temperature

$T_c$  = coolant inlet temperature

From equations (13–16), the blade spanwise temperature distributions can be estimated roughly when combustor traverse numbers are given.

The dilution temperature of mainstream gas after mixing with cooling flow is simply calculated by equation (10). For the first nozzle of the proposed cooling system, the heat loss absorbed through the airfoil and the endwalls is calculated by equation (17), and the dilution of gas temperature, by equation (18).

$$Q = h_a S_a (T_g - T_b) + b_e S_e (T_g - T_b)_{tip} + h_e S_e (T_g - T_b)_{root} \quad (17)$$

$$\Delta T_g = Q / G_g c_{pg} \quad (18)$$

where

$h$  = heat transfer coefficient

$S$  = surface area

and subscripts

$a$  = airfoil

$e$  = endwall

The bucket cooling air temperature rise due to the first stage nozzle cooling amounts to

$$\Delta T_c = Q / G_c c_{pc} \quad (19)$$

Data for mean airfoil heat transfer coefficient  $h_a$  are available from the turbine tests due to Ainly [4] in terms of Nusselt number

$$Nu_g = Nu_g^* \left( \frac{Re}{2 \times 10^5} \right)^x \left( \frac{T_g}{T_b} \right)^y \quad (20)$$

where

$Nu_g^*$  = 400 for the first stage nozzle

$x, y$  = exponents (see [4])

Tip and root endwall heat transfer rates are assumed to be the same as that of airfoil for a lack of available data. For the same reason, the average endwall temperatures are approximated equal to the blade metal temperature at the tip and the root.

**Mechanical Analysis.** Blade and disk stresses impose direct restrictions on stage design. The allowable centrifugal tensile stress and associated creep rupture life limit the annulus area of the gas path. The approximate spanwise centrifugal tensile stress acting on the bucket is given by a one-dimensional analysis as

$$\sigma_{cr} = \frac{\rho_M \omega^2}{A} \int_r^{r_{tip}} A r dr + \frac{M_{sh} r_{tip} \omega^2}{A} \quad (21)$$

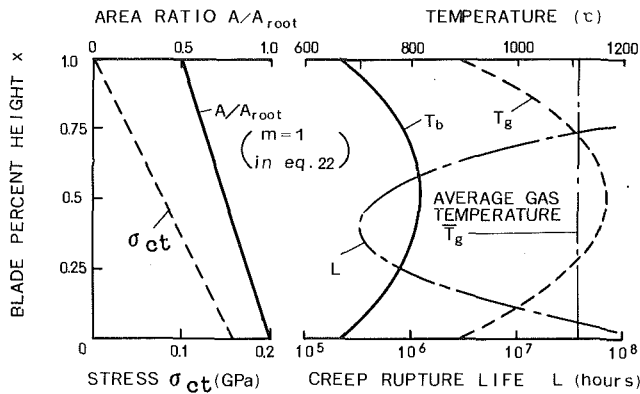


Fig. 5 Example of blade creep rupture life calculation

$$A = A_{\text{root}} \left\{ 1 - x^m \left( 1 - \frac{A_{\text{tip}}}{A_{\text{root}}} \right) \right\} \quad (22)$$

where

- $m$  = exponent of blade area taper
- $x$  = blade percent height
- $A$  = section area of blade
- $M_{sh}$  = mass of tip shroud
- $\rho_M$  = density of metal

Bucket stress-temperature combined creep rupture life for continuous base load operation is calculated using the Larson-Miller curve of superalloys, in this manner

$$T_b(C + \log_{10} t) \times 10^{-3} = f(\sigma_{ct}) \quad (23)$$

where

- $t$  = rupture life (hours)
- $C$  = constant

From the spanwise blade metal temperature and centrifugal stress, the minimum rupture life of the blade can be obtained for the bucket material, as shown by the example plots in Fig. 5.

In practice, the thermal stress and gas bending stress act on the blade. These are difficult to estimate at the initial design stage, where the blade shape is still undetermined. Since actual failure mechanism is complex combination of these stresses, the introduction of a safety factor is recommended in the preliminary analysis.

The mean diameter of the gas path, which determines aerodynamic loading, is restricted by the disk stress. The average tangential stress due to centrifugal force is calculated by [5]

$$\sigma = S \rho_M U^2 \quad (24)$$

where

- $S$  = stress factor depending on disk geometry
- $U$  = circumferential speed at mean diameter

The disk configuration is selected so that the centrifugal stress remains low enough to give a safe margin for thermal stress.

Present turbine aerodynamic design computer code incorporates the foregoing mentioned preliminary thermal, mechanical analysis and has functions of parametric study and plotting of contour lines described later.




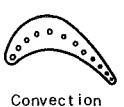
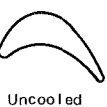
## Results

A practical turbine design is generally the result of compromises between performance, reliability, endurance, manufacturing limitations etc. The blade life is influenced by hot corrosion, creep, and low-cycle fatigue. These failure factors are greatly dependent on blade metal temperature. Accordingly, the blade metal temperature and creep rupture

Table 1 Main component parameters for sample calculations

Component	Conditions at design point
Inlet duct	• Ambient condition=ISO standard condition • Pressure loss $\Delta P/P=0.01$
Compressor	• Pressure ratio=14.5 • Adiabatic efficiency=0.86 • Inlet mass flow =450 kg/s • Pressure ratio of air extracted for turbine last interstage sealing=5
Combustor	• Combustion efficiency=0.999 • Pressure loss $\Delta P/P=0.03$ • Traverse number : $N_T=0.1$ , $N_R=0.06$ • Maximum temperature location $X_{\text{max}}=0.5$
Turbine	• 3000 rpm , others see Table 2
Diffuser	• Pressure recovery factor=0.6
Exhaust duct	• Pressure loss $\Delta P/P=0.05$
Others	• Mechanical efficiency (including generator efficiency)=0.97 • Fuel = Kerosene
Bottoming cycle	• Dual pressure steam cycle

Table 2 Main turbine design parameters for sample calculations

Parameter	1st stage	2nd stage	3rd stage
Velocity triangle			
• Velocity ratio* (at root)	1.0	1.072	1.081
• Flow coefficient	0.475	0.480	0.650
• Reaction (at root)	0.220	0.240	0.340
• Axial velocity ratio	1.335	1.361	1.424
• Mean diameter of gas path (mm)	2300	2350	2400
• Conceptual Cooling Configuration and Cooling air consumption (relative to 1st stage bucket cooling flow)	See Fig.2 Impingement •• for cooling scheme A,B Multi-pass •• for cooling scheme C		
$G_C/G_{C1B}$	1.56	0.67	0.18(for sealing)
• Bucket			
$G_C/G_{C1B}$	1.0	0.56	0
Taper Ratio $A_{\text{tip}}/A_{\text{root}}$	0.5 (unshrouded)	0.35 (shrouded)	0.25 (shrouded)

\* relative to 1st stage

life of the bucket are considered as a measure of reliability. Trade-off studies between the performance and reliability in terms of blade metal temperature and creep rupture life are performed for the different cooling systems already introduced in Fig. 1 to compare the attainable performance with reliability constraints.

As a sample calculation, a large gas turbine with the air flow of 450 kg/s and the pressure ratio of 14.5 is selected. Assumptions of component parameters and conditions at the design point are listed in Tables 1 and 2. A three-stage turbine is considered, as it provides design simplicity and compactness. A high loading design philosophy with relatively low reaction allows that the lowered aerodynamic turbine efficiency to be offset by the reduced cooling flow consumption resulting from higher temperature drop per stage. Velocity ratios defined at the root are adjusted so as to satisfy the exhaust pressure condition. The mean diameters and velocity triangle parameters are chosen by searching the maximum

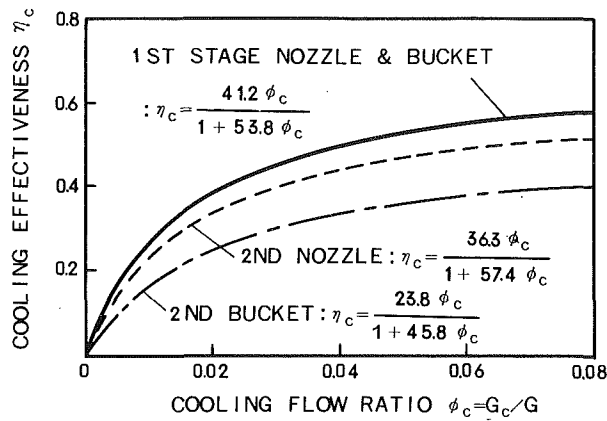


Fig. 6 Assumed cooling effectiveness curves

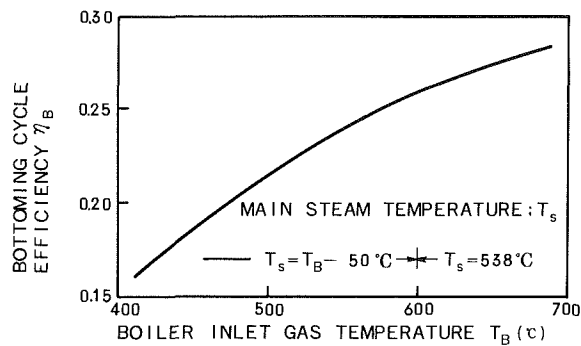


Fig. 7 Overall bottoming cycle efficiency

obtainable efficiency with imposed restriction on aerodynamic and mechanical design. The procedure of selecting these parameters is isolated in this paper.

In the table, the conceptual blade cooling configurations and relative cooling flow distributions are shown. The cooling effectiveness curve for each blade is assumed as shown in Fig. 6. Blade cooling is done by all-internally convective cooling designs to prevent film holes from plugging. The first-stage nozzle cooling configuration was previously shown in Fig. 2. The first-stage bucket cooling adopts multipass design with tip and trailing edge ejection holes. The authors would like to recommend a multipass design in the proposed cooling system in spite of better cooling performance of impingement cooling, as the former can provide structural rigidity and eliminate core plugs. For the second stage bucket, a simple convection cooling configuration with radial holes and tip ejection is considered.

Returning to Fig. 6, for the first stage nozzle and bucket, the cooling effectiveness of  $\eta_c = 0.45, 0.55$  at  $G_c/G = 0.03, 0.06$ , respectively, is assumed. For the second-stage blades, lower cooling effectiveness is assumed. These cooling characteristics, although not general, are based on the accumulated data, both published and our own. These cooling effectiveness curves are assumed common for all cooling systems in Fig. 1, for simplicity in comparison. In order to calculate creep rupture life of buckets, a blade material IN738 is selected as typical of superalloys. Safety factors of 1.5 and 1.3 are used as multipliers for centrifugal stress in equation (23) for cooled and uncooled blades, respectively.

Detailed blading parameters necessary for aerodynamic loss prediction are omitted to be listed.

To evaluate combined cycle performance, the steam turbine bottoming cycle is analyzed. In this paper, and dual pressure steam cycle is assumed to extract a higher heat recovery from gas turbine exhaust gas [6]. The overall bottoming cycle ef-

iciency versus boiler gas inlet temperature used for calculating the combined cycle is shown in Fig. 7.

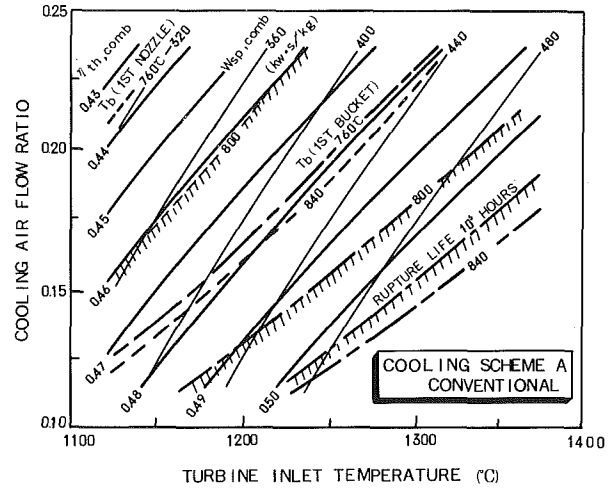
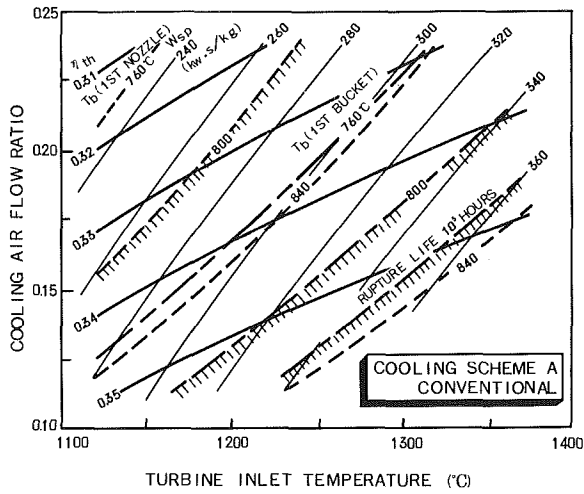
Calculations are conducted according to the analyses described in the previous section and the aforementioned design conditions. The assumptions and design parameters are held constant through the calculations. A systematic operations research technique is used for trade-off studies to find maximum obtainable performance with constraints for each cooling system, thus providing information for comparative studies. Turbine inlet temperature and cooling flow ratio (defined as the ratio of total cooling air flow rate to compressor inlet flow rate) are selected as parameters because of interactions between aerodynamics and cooling.

Calculated results are plotted on a turbine inlet temperature versus cooling flow consumption diagram, presenting performance contours, thermal efficiency, and specific power, together with contours of constraining factors, blade metal temperature, and bucket creep rupture life, as shown in Fig. 8. This presents the trade-off diagrams for each cooling scheme and cycle, which give information for trade-offs between performance and reliability in determining design point turbine inlet temperature. Row-by-row analysis provides reliability parameters for each stage, however only the critical ones are reproduced in the diagrams to avoid confusion. In these diagrams, blade metal temperatures, and bucket creep rupture life, are assumed to be limited by  $800^\circ\text{C}$  and  $10^5$  hr, respectively, as shown by the shaded lines. Accordingly, the left portion of the left shaded line gives the acceptable design region that can be engineered within constraints. The maximum attainable performance with increase of turbine inlet temperature is obtained along the left shaded line. In general, the slopes of thermal efficiency contours  $\eta_{th}$  are smaller than those of metal temperature contour lines  $T_b$  and those of the specific power  $W_{sp}$ , vice versa, in gas turbine cycle. These tendencies imply that the  $\eta_{th}$  decrease with increased turbine inlet temperature.

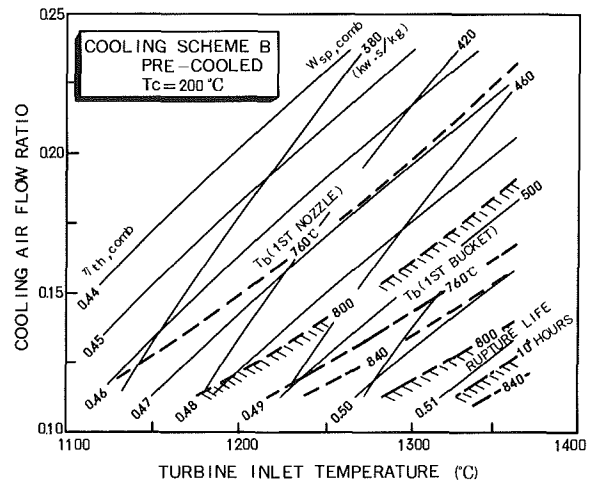
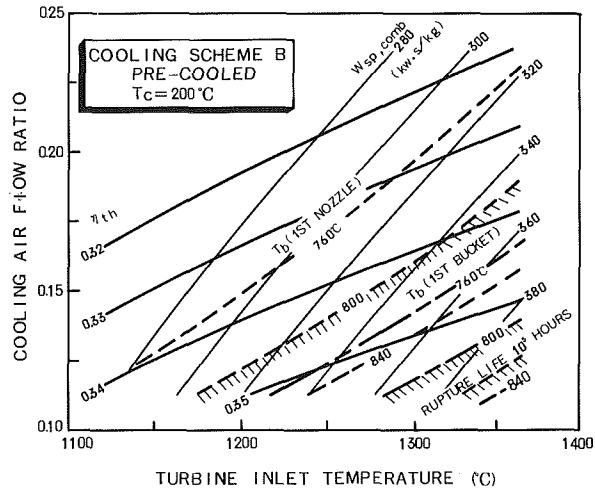
Comparison of the cooling schemes reveals that the proposed and precooled cooling schemes clearly widen the acceptable design region, which suggests the growth potential of air cooling for increased turbine inlet temperature over a conventional cooling system. The attainable performance of the proposed cooling system is limited by the first-stage bucket temperature, whereas that of cooling schemes A and B are limited by the first-stage nozzle metal temperature. This is because the cooling circuit of the proposed cooling system, in which the bucket uses the cooling air, is warmed up by the first-stage nozzle cooling.

Figure 9 plots the attainable performance for the gas turbine and combined cycles with different setting of blade metal temperature constraints. The curves are coincident with the points along the constraining line in Fig. 8. For the gas turbine cycle, the thermal efficiency decreases with increased turbine inlet temperature, while the specific power increases with it. The result is that the turbine inlet temperature is forced to drop in order to increase thermal efficiency maintaining the constant blade metal temperature for the sample conditions and calculation range. For the combined cycle, thermal efficiency tends to increase with increased turbine inlet temperature. However, in the conventional cooling scheme, optimum turbine inlet temperature exists, and in excess of it, increased turbine inlet temperature brings little gain in cycle performance. Specific power of the proposed cooling system varies almost linearly with turbine inlet temperature. These results are mainly due to the gas temperature dilution effect associated with the cooling effectiveness limit, which affects turbine exit temperature for the bottoming cycle. It is seen that the performance gains that can be obtained are strongly dependent on allowable blade metal temperatures. However, the proposed cooling system is less sensitive to allowable blade metal temperature compared

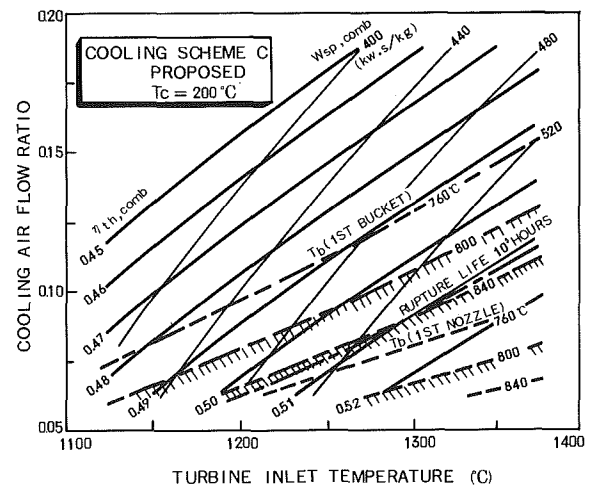
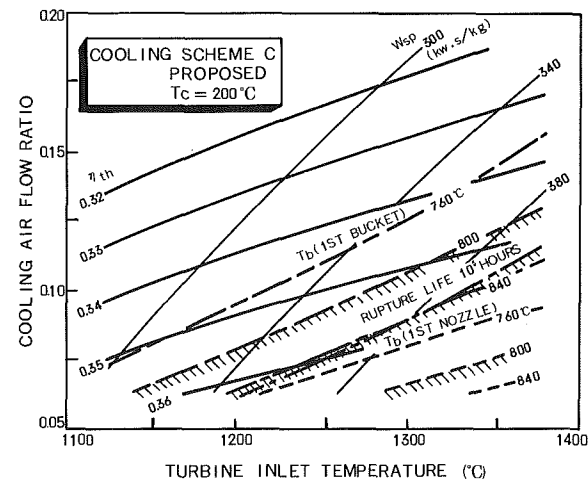




(a) Conventional cooling system



(b) Precooled system



(c) Proposed cooling system

Gas turbine cycle

Combined cycle

Fig. 8 Trade-off diagrams for each cooling system and cycle

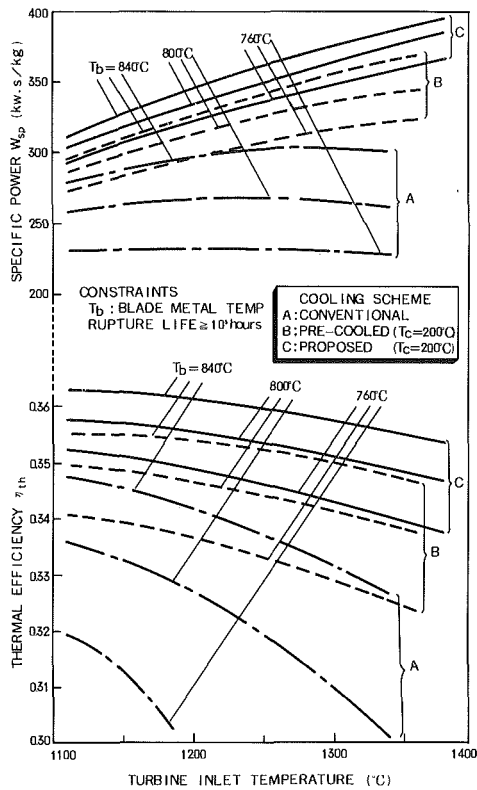


Fig. 9(a) Gas turbine cycle performance versus turbine inlet temperature

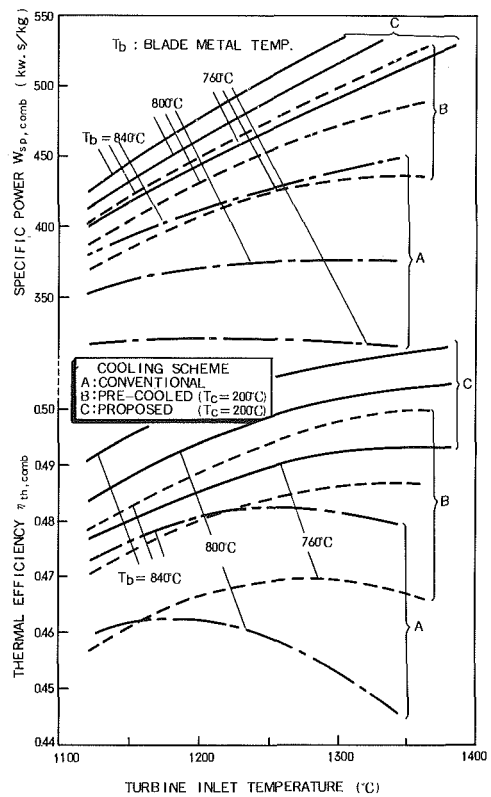


Fig. 9(b) Combined cycle performance versus turbine inlet temperature

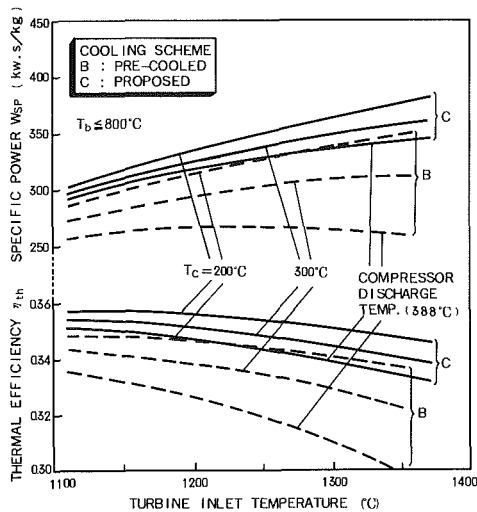


Fig. 10(a) Effect of cooling air temperature on gas turbine cycle performance

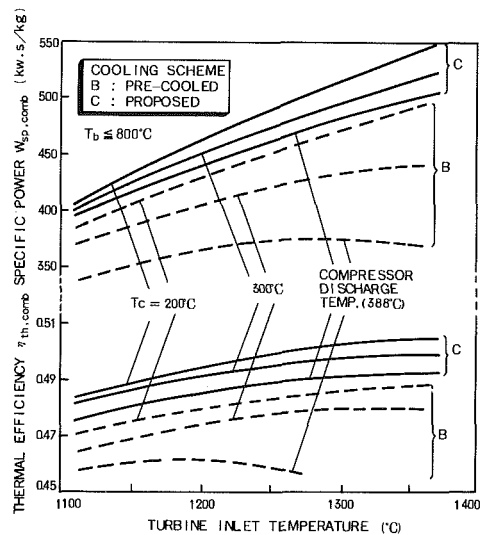


Fig. 10(b) Effect of cooling air temperature on combined cycle performance

to other cooling systems, and the lower setting of allowable blade metal temperature emphasizes the advantage of the proposed cooling system over other cooling systems.

Figure 10 shows the effect of cooling air temperature on performance for precooled and proposed cooling systems. The lower cooling air temperature provides better performance for both gas turbine and combined cycles. This suggests that the heat loss, taken out of the cycle, is recovered by reduced cooling flow consumption. But the proposed cooling system is less sensitive to cooling air temperature than the precooled cooling system.

Figure 11 shows the dilution temperature of mainstream due to the first-stage nozzle cooling. The dilution temperature of the conventional cooling system is so large that the in-

creased turbine inlet temperature is compensated for by the first-stage nozzle cooling, while that of the proposed cooling system is much lower. It is understood that the performance advantages of the proposed system are achieved by minimized dilution effect and associated reduced consumption of cooling air.

## Discussion

The calculation described here demonstrates the feasibilities of the proposed cooling system using existing technologies. Although there may be uncertainties in absolute values of attainable performance due to assumptions made and

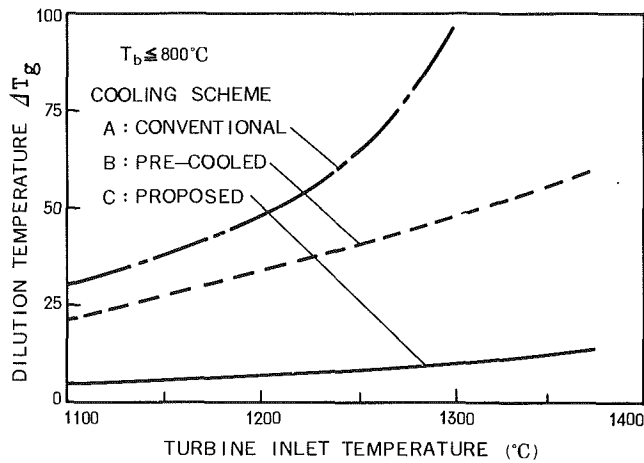


Fig. 11 Gas temperature dilution due to the first-stage nozzle cooling

preliminary analyses, performance advantages of the proposed cooling system relative to other cooling system are of significance, because the results are based on the same methodology and parameters.

With respect to the availability of the proposed cooling system, the sum of pressure losses through the cooling passage composing a flow network must not exceed the pressure difference obtainable between the inlet and the outlet of the cooling circuit in order to supply the required amount of cooling air. Large pressure loss is accompanied by enhanced heat transfer due to roughness elements and the series cooling circuit. Calculated results based on the pressure loss model [7] show that a highly loaded turbine aerodynamic design provides a larger pressure difference than the pressure loss predicted through the proposed cooling circuit.

For reliability considerations, evaluation of thermal stress is necessary, which is not taken into account in this study, since that heat fluxes through the blade are very large due to enforced cooling. To reduce thermal gradients resulting in thermal stress causing low cycle fatigue, the wall thickness of blade is made as thin as possible. The partitioned wall of the

multipass cooling design can give structural rigidity to ballooning and gas bending forces. While the present study has shown the promising potential of the proposed cooling system, detailed reliability analysis is required not only for blades but also for other hot components such as combustor liners and transition pieces to withstand severe conditions.

## Conclusions

Feasibility of the proposed cooling system, aimed at minimizing of coolant mixing effect, is assessed with the constraints of blade metal temperature compared to conventional cooling systems.

The results of the study on the basis of the present assumptions and conditions can be summarized as follows:

1 The proposed cooling system provides significant improvements in performance for both gas turbine and combined cycles as compared to conventional and precooled systems.

2 The proposed cooling system offers growth potential for air cooling and substantially increases turbine inlet temperature due to the minimized dilution effect.

3 The lower cooling air temperature produces improved cycle performance. Performance of the proposed cooling system is less sensitive to allowable blade metal temperature and cooling air temperature as compared to the precooled cooling system.

## References

- 1 Louis, J. F., Hiraoka, K., and El Masri, M. A., "A Comparative Study of the Influence of Different Means of Turbine Cooling on Gas Turbine Performance," ASME Paper No. 83-GT-180.
- 2 Dunham, J., and Came, P. M., "Improvements to the Ainley-Mathieson Method of Turbine Performance Prediction," ASME Paper No. 70-GT-2.
- 3 Hartsel, J. E., "Prediction of Effects of Mass Transfer Cooling on the Blade-Row Efficiency of Turbine Aerofoils," AIAA Paper No. 72-11, 1972.
- 4 Ainley, D. G., "Internal Air-Cooling for Turbine Blades a General Design Survey," R. & M. No. 3013, 1957.
- 5 Balje, O. E., *Turbomachines*, John Wiley & Sons, New York, 1981, pp. 60-61.
- 6 Foster-Pegg, R. W., "Steam Bottoming Plants for Combined Cycles," *Combustion*, Mar. 1978,
- 7 Clark, J. S., Richards, H. T., Poterl, D. J., and Livingood, J. N. B., "Coolant Pressure and Flow Distribution through an Air-cooled Vane for a High Temperature Gas Turbine," NASA TM X-2028.

# A Numerical Model of Moist Plume Thermodynamics<sup>1</sup>

**B. R. Becker**

Martin Marietta Energy Systems, Inc.,  
Oak Ridge, Tenn. 37830

*Evaporative cooling towers and cooling ponds are in ever-increasing use for the dissipation of waste heat. The modeling of moist plumes from these facilities has received considerable attention in recent years. The simulation of plume thermodynamics is a necessary part of the modeling of a moist plume. This paper describes an algorithm which, when supplied with the ambient atmospheric distribution of various thermodynamic properties, performs the necessary psychrometric calculations to simulate the thermodynamics within the moist plume. A unique feature of this algorithm is the modeling of the condensation of "excess" water vapor, which simulates the formation and deposition of water droplets from the moist plume.*

## Introduction

Evaporative cooling towers, both mechanical draft and natural draft as well as cooling ponds, are used for the dissipation of waste heat from industrial sources. As environmental controls become more stringent, such evaporative cooling equipment will become more widely used and the environmental impact of such equipment more closely scrutinized. In particular, it will become necessary to assess the environmental effects of the moist plume emanating from an evaporative cooling device. Numerous models of moist plumes, primarily from evaporative cooling towers, have been developed [1-16]. Several articles have been written which review and compare these models [17-19].

In 1975, the ASME issued a review of the state-of-the-art in moist plume modeling [20]. The reviewers stressed the importance of simulating aerodynamic effects and buoyancy effects due to the thermodynamics of condensation within the plume, as well as accounting for the ambient atmospheric distribution of wind velocity, temperature, and humidity. This ASME review also divided the existing plume models into four general categories; (i) Gaussian plume models, (ii) buoyant plume models, (iii) mathematical models solved in a stepwise fashion, and (iv) models based on the fundamental equations of hydrodynamics.

The Gaussian plume models [1-3] assume that the distribution of the diffusing material is Gaussian in the crosswind and vertical directions with the standard deviation varying as a function of distance from the source. Plume height is calculated separately by an empirical plume rise equation. These models ignore aerodynamic effects as well as atmospheric distributions of wind velocity, temperature, and humidity. Buoyancy is included only as part of the empirical plume rise equation.

The buoyant plume models [4-10] assume that the

distribution of the diffusing material is constant over any plume cross section, with the size of that cross section dictated by an equation involving an empirical entrainment constant. Plume height is given by an empirical plume rise equation. Again aerodynamic effects and wind velocity, temperature, and humidity distributions are ignored, with buoyancy included only through the plume rise equation.

The stepwise models [11-14] include equations that are solved numerically in a stepwise fashion upward from the cooling tower fan. Thus these models can account for vertical gradients in the ambient conditions as well as phase changes within the rising plume. However, aerodynamic effects are again unresolved.

England et al. [15] and Taft [16] report models based on the fundamental equations of hydrodynamics. However, both models assume that the velocity in the downwind direction is constant and undisturbed by the plume or the terrain; and hence, a significant portion of the aerodynamic detail is not included. Also, both of these models utilize the Boussinesq approximation so that the atmosphere is simulated as an incompressible, density-stratified fluid, rather than a truly variable density gas, thus reducing the accuracy of the simulation. Both models ignore local atmospheric distributions of wind velocity, temperature, and humidity.

Therefore, to the author's knowledge, none of the existing plume models are capable of simulating all of the effects deemed necessary by the ASME reviewers. A satisfactory plume model would necessarily include the fundamental equations of hydrodynamics coupled with a detailed numerical model of moist plume thermodynamics.

This paper describes such a thermodynamics model. It is unique in three respects. First, it is designed to be compatible with a complete hydrodynamic flow field model that treats the mass fraction of water vapor as an active, conserved, transported quantity. Second, the effects of the water vapor on the flow field are coupled to the hydrodynamic equations through energy release and variable density. Third, condensation of "excess" water vapor is included that simulates the formation and deposition of water droplets from the moist plume. Given ambient atmospheric distributions of pressure, temperature,

<sup>1</sup>Based on work performed by Martin Marietta Energy Systems, Inc., for the U.S. Department of Energy under U.S. Government Contract W-7405 eng 26.

Contributed by the Air Pollution Control Division for publication in the JOURNAL OF ENGINEERING FOR GAS TURBINES AND POWER. Manuscript received by the Air Pollution Control Division December 6, 1983.

density, and mass fraction of water vapor, this algorithm will determine saturation conditions, condense any "excess" water vapor and increase the wind field temperature by an amount corresponding to the latent heat released by condensation. The model will then update the mass fraction of water vapor, determine the relative humidity, and calculate the moist air density as a function of temperature, pressure, and humidity. Thus this model uniquely captures a considerable portion of the natural phenomena involved in moist plume thermodynamics and, when coupled to a hydrodynamic wind field model, will produce a realistic state-of-the-art plume model.

### Modeling of Moist Plume Thermodynamics

In the modeling of the thermodynamics of a moist plume, the atmosphere is treated as a two-component mixture composed of dry air and water vapor. The dry air and water vapor are both considered to be ideal gases. As discussed below, this assumption greatly reduces the complexity of the moist air thermodynamic (psychrometric) calculations with only a slight decrease in accuracy.

The American Society of Heating, Refrigerating, and Air Conditioning Engineers (ASHRAE) *Handbook of Fundamentals* [21] states that the most complete and exact psychrometric functions were developed at the University of Pennsylvania by Goff and Gratch (1943-46) for a barometric pressure of 29.921 in. of mercury (101.04 kPa) [22-25]. Kusuda (1970) later computerized these complex Goff-Gratch functions and used them to generate psychrometric data for various other barometric pressures [26].

In comparison with these Goff-Gratch-Kusuda formulations, Threlkeld (1970) has shown that in the calculation of humidity ratio, enthalpy, and specific volume, the ideal gas assumption yields errors of less than 0.7 percent for a barometric pressure of 29.921 in. of mercury (101.04 kPa) and a temperature range of  $-60^{\circ}\text{F}$  (222.04 K) to  $120^{\circ}\text{F}$  (322.04 K) [27]. Furthermore, these errors decrease with decreasing pressure [21]. Thus the use of the ideal gas relationships is justified in the modeling of the thermodynamics of a moist plume.

The ASHRAE *Handbook of Fundamentals*, as well as a simplified set of psychrometric functions given by Kusuda [28], calculate the water vapor content of a moist air sample in terms of the humidity ratio  $W$

$$W = (\text{mass of water vapor}) / (\text{mass of dry air}) \quad (1)$$

This type of formulation is not easily used in a numerical hydrodynamic model, where the total mass of the moist air mixture must be conserved and transported from one computational cell to another. For this reason, the current model

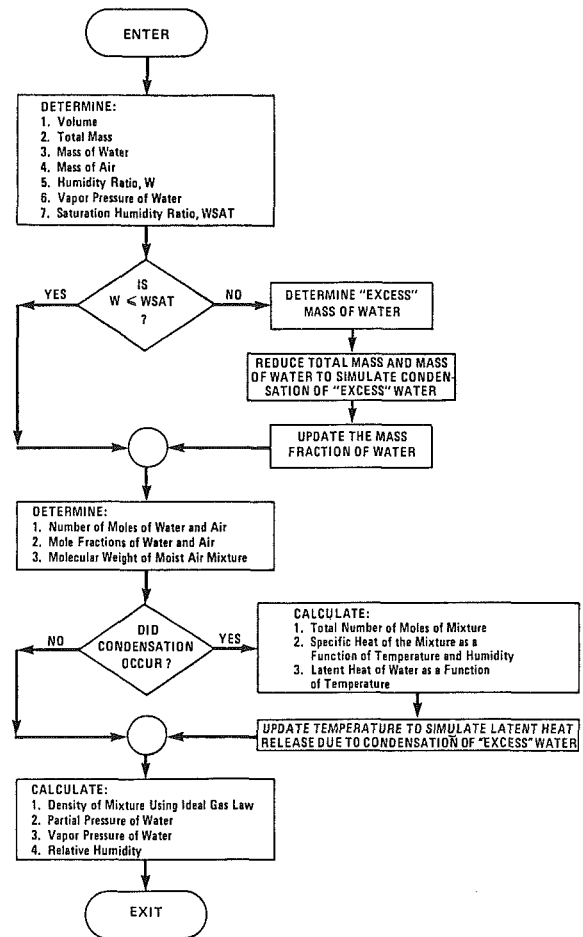


Fig. 1 Flow diagram of moist plume thermodynamics model

calculates water vapor content in terms of the mass fraction of water vapor MFH20

$$\begin{aligned} \text{MFH20} &= (\text{mass of water vapor}) / (\text{total mass of moist air mixture}) \\ &= W / (1 + W) \end{aligned} \quad (2)$$

A flow diagram of the moist plume thermodynamics model is presented in Fig. 1. Given the wind field distribution of pressure, temperature, density, and mass fraction of water vapor, this model first determines the volume per unit depth, VOLUME, associated with each node in the computational

### Nomenclature

CPAIR = constant pressure specific heat of dry air  
 CPH20 = constant pressure specific heat of water vapor  
 CPMIX = constant pressure specific heat of moist air mixture  
 DENSITY = density of the moist air mixture  
 LHEAT = latent heat of water  
 MAIR = apparent molecular weight of dry air  
 MASAIR = mass of dry air  
 MASH20 = mass of water  
 MASTOT = mass of moist air

MIXTURE = mixture contained in the computational cell  
 MASXS = mass of excess water  
 MFAIR = mass fraction of dry air  
 MFH20 = mass fraction of water vapor  
 MH20 = molecular weight of water  
 MMIX = apparent molecular weight of moist air mixture  
 MOLMIX = number of moles of moist air mixture  
 NAIR = number of moles of dry air

NH20 = number of moles of water  
 $P$  = atmospheric pressure  
 PH20 = partial pressure of water vapor  
 PVAP = vapor pressure of water  
 $R$  = universal gas law constant  
 $T$  = temperature  
 VOLUME = volume per unit depth of the computational cell  
 $W$  = humidity ratio  
 WSAT = humidity ratio at saturation  
 XAIR = mole fraction of dry air  
 XH20 = mole fraction of water

grid. The total mass of the moist air mixture, MASTOT, at each node is determined by multiplying the volume of the node times the density at the node

$$\text{MASTOT} = \text{VOLUME} \times \text{DENSITY} \text{ [gm]} \quad (3)$$

The mass of water, MASH20, mass fraction of dry air, MFAIR, mass of dry air, MASAIR, and the humidity ratio  $W$  are found as follows

$$\text{MASH20} = \text{MFH20} \times \text{MASTOT} \text{ [gm]} \quad (4)$$

$$\text{MFAIR} = 1.0 - \text{MFH20} \quad (5)$$

$$\text{MASAIR} = \text{MFAIR} \times \text{MASTOT} \text{ [gm]} \quad (6)$$

$$W = \text{MASH20}/\text{MASAIR} \quad (7)$$

The vapor pressure of water, PVAP, which is a function only of temperature  $T$ , measured in kelvins, is given by an equation taken from the ASHRAE *Handbook of Fundamentals*

$$\text{PVAP}(T) = (1.013260 \times 10^6) \times 10.0^{\text{exp}} \text{ [dynes/cm}^2\text{]}$$

where the exponent, exp, is temperature dependent. That is, for  $T < 273.15$  K

$$\begin{aligned} \text{exp} = & -9.096936 \times (T^* - 1.0) \\ & - 3.56654 \times \log_{10}(T^*) \\ & + 0.876817 \times [1.0 - (1.0/T^*)] \\ & - 2.2195983 \end{aligned}$$

and for  $T > 273.15$  K

$$\begin{aligned} \text{exp} = & 10.79586 \times (1.0 - T^*) \\ & + 5.02808 \times \log_{10}(T^*) \\ & + (1.50474 \times 10^{-4}) \times (1.0 - 10^{-8.29692[(1.0/T^*) - 1.0]}), \\ & + (0.42873 \times 10^{-3}) \times (10^{4.76955(1.0 - T^*)} - 1.0) \\ & - 2.2195983 \end{aligned}$$

where

$$T^* = 273.16/T \quad (8)$$

The humidity ratio at saturation, WSAT, is then determined from the vapor pressure, PVAP, and atmospheric pressure,  $P$ , using another psychrometric relationship from the ASHRAE *Handbook of Fundamentals*

$$\text{WSAT} = 0.62198 \times \text{PVAP}/(P - \text{PVAP}) \quad (9)$$

The humidity ratio  $W$  is then compared to the saturation humidity ratio, WSAT. Any "excess" water (greater than saturation), MASXS, is determined as follows

$$\begin{aligned} \text{MASXS} &= \text{MASH20} - \text{mass of water at saturation} \\ &= \text{MASAIR} \times (\text{MASH20} - \text{mass of water at saturation})/\text{MASAIR} \\ &= \text{MASAIR} \times (W - \text{WSAT}) \text{ [gm]} \end{aligned} \quad (10)$$

The validity of equation (10) is based on the fact that any excess water above saturation would condense out of the moist air sample. In this process, the mass of air in the sample, MASAIR, would remain unchanged. After the "excess" water has been "condensed" from the moist air sample, the mass of water, MASH20, total mass, MASTOT, and mass fraction of water, MFH20, are all updated.

The number of moles of water, NH20, and dry air, NAIR, and the respective mole fractions, XH20 and XAIR, are found as follows

$$\text{NH20} = \text{MASH20}/\text{MH20} \quad (11)$$

$$\text{NAIR} = \text{MASAIR}/\text{MAIR} \quad (12)$$

$$\text{XH20} = \text{NH20}/(\text{NH20} + \text{NAIR}) \quad (13)$$

$$\text{XAIR} = 1.0 - \text{XH20} \quad (14)$$

In equations (11) and (12), MH20 is the molecular weight of water and MAIR is the apparent molecular weight of dry air. Both of these molecular weights are given by the ASHRAE *Brochure on Psychrometry* [29] as follows

$$\text{MH20} = 18.01534 \text{ gm/gm-mole-H20} \quad (15)$$

$$\text{MAIR} = 28.9645 \text{ gm/gm-mole-AIR} \quad (16)$$

The mole fractions, equations (13) and (14), are then used to determine an apparent molecular weight, MMIX, for the moist air mixture [30]

$$\begin{aligned} \text{MMIX} &= (\text{XAIR} \times \text{MAIR}) \\ &+ (\text{XH20} \times \text{MH20}) \text{ [gm/gm-mole-mixture]} \end{aligned} \quad (17)$$

If excess water was condensed, it is necessary to increase the temperature at the node to simulate the latent heat released by the condensation. First, the number of moles of mixture, MOLMIX, is determined

$$\text{MOLMIX} = \text{MASTOT}/\text{MMIX} \quad (18)$$

Then the constant pressure specific heat of the mixture must be found as a function of both temperature and humidity. The latent heat of water must also be found as a function of temperature.

The constant pressure specific heat of dry air, CPAIR, and that of water vapor, CPH20, are determined as functions of temperature,  $T$ , using expressions given by Henley and Bieber [31]:

$$\begin{aligned} \text{CPAIR}(T) &= 6.557 + (1.477 \times 10^{-3}) \times T \\ &- (0.2148 \times 10^{-6}) \\ &\times T^2 \text{ [cal/(gm-mole-AIR K)]} \end{aligned} \quad (19)$$

$$\begin{aligned} \text{CPH20}(T) &= 7.219 + (2.374 \times 10^{-3}) \times T \\ &+ (0.267 \times 10^{-6}) \\ &\times T^2 \text{ [cal/(gm-mole-H20 K)]} \end{aligned} \quad (20)$$

The constant pressure specific heat of the mixture of dry air and water vapor, CPMIX, is then determined as a function of the mole fractions of the components, XAIR and XH20 [30]

$$\begin{aligned} \text{CPMIX}(T, \text{XH20}, \text{XAIR}) &= (\text{XAIR} \times \text{CPAIR}(T)) \\ &+ (\text{XH20} \times \text{CPH20}(T)) \text{ [cal/(gm-mole-mixture K)]} \end{aligned} \quad (21)$$

The latent heat of water, LHEAT, is determined as a function of temperature  $T$  by a linear fit to the data at 64°F (290.7 K) and 122°F (323.0 K), which is given by Keenen and Keyes [32]

$$\text{LHEAT}(T) = (-.56857 \times T) + 752.54570 \text{ [cal/gm - H20]} \quad (22)$$

The condensation process is then completed by adjusting the nodal temperature according to the latent heat release

$$\begin{aligned} T_{\text{new}} &= T_{\text{old}} + (\text{LHEAT}(T_{\text{old}}) \\ &\times \text{MASXS})/(\text{CPMIX}(T_{\text{old}}, \text{XH20}, \text{XAIR}) \\ &\times \text{MOLMIX}) \text{ [K]} \end{aligned} \quad (23)$$

The density of the mixture is now calculated using the ideal gas law

$$\text{DENSITY} = (\text{MMIX} \times P) / (R \times T) \text{ [gm/cm}^3\text{]} \quad (24)$$

In equation (24),  $P$  is the wind field pressure,  $T$  is the wind field temperature (updated for condensation if necessary), and  $R$  is the universal gas law constant given by the ASHRAE *Brochure on Psychrometry* as

$$R = 8.3143 \times 10^7 \text{ [dyne-cm/(gm-mole K)]} \quad (25)$$

The vapor pressure of water, PVAP, is then updated using equation (8). The partial pressure of the water, PH20, and the relative humidity are then calculated using expressions given in the ASHRAE *Handbook of Fundamentals*

**Table 1 Values of the parameters for studies A, B, C, and D**

Study	Temperature (°F)	Pressure (in. Hg)	Humidity (% RH)	
A	80	31.02	50 (nominal)	
		29.92		
		28.86		
		27.86		
B	0 40 80 120	29.92	50 (nominal)	
				1.7
				29.8
				51.1
C	80	29.92	79.6	
			91.6	
			100.0	
			101.0	
D	80	29.92	102.0	
			110.0	
			110.0	

**Table 3 Study B (29.92 in Hg, 50% RH nominal)**

	Saturation vapor pressure (in. Hg)	Actual vapor pressure (in. Hg)	Saturation humidity ratio	Actual humidity ratio
Case 1, 48.9% RH 0°F				
current model	.0376	.0184	.00078	.00038
Kusuda	.0376	.0184	.00079	.00038
Case 2, 53.1% RH 40°F				
current model	.2476	.1315	.00519	.00275
Kusuda	.2477	.1315	.00521	.00276
Case 3, 51.1% RH 80°F				
current model	1.035	.5289	.02229	.01119
Kusuda	1.032	.5277	.02233	.01122
Case 4, 50.0% RH 120°F				
current model	3.457	1.7285	.08126	.03814
Kusuda	3.448	1.7235	.08151	.03822

**Table 2 Study A (80°F, 50% RH nominal)**

	Actual vapor pressure (in. Hg)	Saturation humidity ratio	Actual humidity ratio
Case 1, 50.6% RH, 31.02 in. Hg			
current model	.5239	.02147	.01068
Kusuda	.5225	.02152	.01071
Case 2, 51.1% RH, 29.92 in. Hg			
current model	.5289	.02229	.01119
Kusuda	.5277	.02233	.01122
Case 3, 51.6% RH 28.86 in. Hg			
current model	.5342	.02314	.01173
Kusuda	.5327	.02318	.01175
Case 4, 48.9% RH 27.86 in. Hg			
current model	.5061	.02400	.01151
Kusuda	.5048	.02404	.01153
Case 5, 49.7% RH 20.28 in. Hg			
current model	.5144	.03294	.01595
Kusuda	.5126	.03297	.01594

**Table 4 Study C (29.92 in Hg, 80°F)**

	Actual vapor pressure (in. Hg)	Actual humidity ratio
Case 1, 1.7% RH		
current model	.0176	.00037
Kusuda	.0180	.00038
Case 2, 29.8% RH		
current model	.3086	.00648
Kusuda	.3076	.00649
Case 3, 51.1% RH		
current model	.5289	.01119
Kusuda	.5277	.01122
Case 4, 79.6% RH		
current model	.8238	.01761
Kusuda	.8216	.01764
Case 5, 91.6% RH		
current model	.9482	.02036
Kusuda	.9453	.02039
Case 6, 100.0% RH		
current model	1.035	.02229
Kusuda	1.032	.02233

**Table 5 Study D (29.92 in. Hg, 80°F)**

	Case 1 101% RH	Case 2 102% RH	Case 2 110% RH
Initial conditions			
Temperature (K)	299.8	299.8	299.8
Mass fraction of water vapor	$2.202 \times 10^{-2}$	$2.223 \times 10^{-2}$	$2.393 \times 10^{-2}$
Mixture density (gm/cm <sup>3</sup> )	$1.158 \times 10^{-3}$	$1.158 \times 10^{-3}$	$1.157 \times 10^{-3}$
Condensation criteria			
Mass of water vapor (gm)	$2.550 \times 10^{-5}$	$2.575 \times 10^{-5}$	$2.769 \times 10^{-5}$
Saturation humidity ratio	$2.229 \times 10^{-2}$	$2.229 \times 10^{-2}$	$2.229 \times 10^{-2}$
Actual humidity ratio	$2.251 \times 10^{-2}$	$2.273 \times 10^{-2}$	$2.452 \times 10^{-2}$
"Excess" mass of water vapor (gm)	$2.525 \times 10^{-7}$	$5.049 \times 10^{-7}$	$2.517 \times 10^{-6}$
After condensation			
Temperature (K)	300.3	300.9	305.0
Mass fraction of water vapor	$2.180 \times 10^{-2}$	$2.180 \times 10^{-2}$	$2.180 \times 10^{-2}$
Mixture density (gm/cm <sup>3</sup> )	$1.157 \times 10^{-3}$	$1.155 \times 10^{-3}$	$1.139 \times 10^{-3}$
Relative humidity (%)	97.01	94.12	74.19

$$PH20 = XH20 \times P[\text{dynes/cm}^2] \quad (26)$$

$$\text{RELATIVE HUMIDITY} = (PH20/PVAP) \times 100\% \quad (27)$$

This completes the psychrometric calculations performed by the moist plume thermodynamics model.

### Sample Calculations

The results of four studies performed using the current model are presented in Tables 2, 3, 4, and 5. Table 1 defines the parameter variations used in these studies. The values calculated by the current model in Studies A, B, and C are compared to values given in the literature. Study D involves the simulation of the condensation of "excess" water vapor, a feature which is unique to the current model.

Kusuda gives values of the psychrometric properties he generated using the Goff-Gratch-Kusuda formulations of the psychrometric functions [26]. These values are tabulated as a function of wet-bulb and dry-bulb temperatures. Consequently, the data he provides do not coincide with even intervals of relative humidity. For purposes of comparison in Studies A, B, and C, Kusuda's values of barometric pressure, temperature, and relative humidity were treated as input to the current model. This allows comparison of the saturation vapor pressure, actual vapor pressure, saturation humidity ratio, and actual humidity ratio.

Tables 2, 3, and 4 show that the current model compares very well to the data given by Kusuda. In Study A, the relative error in the calculated values is less than 0.4 percent; in Study B, less than 1.3 percent; and in Study C, less than 2.6 percent. The saturation vapor pressure is a function solely of temperature and hence remained constant throughout Studies A and C. The saturation humidity ratio is a function of the barometric pressure and the saturation vapor pressure and, therefore, also remained constant throughout Study C. Consequently, none of these values are given in Tables 2 and 4. Both saturation vapor pressure and saturation humidity ratio at 80°F (299.82 K) and 29.92 in. of mercury (101.04 KPa) appear in Case 3 of Study B shown in Table 3.

Study D is a demonstration of the capability of the current algorithm as a component of a comprehensive moist plume model. In this study, the barometric pressure was maintained at 29.92 in. of mercury (101.04 KPa) and the temperature fixed at 80°F (299.82 K), while the relative humidity took on three values above 100 percent. Table 5 shows the quantity of water vapor which the current algorithm determined as being in excess of saturation conditions. The algorithm then simulated condensation by reducing the mass of the water vapor by this excess amount. The temperature of the moist air mixture was then increased to simulate the effects of the release of the latent heat due to condensation. The density and relative humidity were also correspondingly adjusted.

Ideally, the relative humidity after condensation would be exactly 100.0 percent. Thus, Table 5 shows that the current model does produce some error in the final value of the relative humidity after condensation and that this error increases as the "excess" water content increases. However, relative error of less than 3.0 percent is certainly acceptable in atmospheric simulations and by concentrating computational cells in areas of high gradients of atmospheric conditions, such small relative error could be maintained.

### Summary and Concluding Remarks

In this paper, a numerical algorithm for the simulation of moist plume thermodynamics has been presented. This algorithm was designed for use in conjunction with a numerical hydrodynamic model of atmospheric flow over a cooling tower, cooling pond, or other source of a moist plume. In this application, the hydrodynamic model would

consist of the momentum equations, the energy equation, and a moisture transport equation written in terms of the mass fraction of water vapor. This hydrodynamic model would pass the wind field distribution of pressure, temperature, density, and mass fraction of water vapor to the plume thermodynamics model.

The plume thermodynamics model would then determine saturation conditions, condense any "excess" water vapor, and increase the wind field temperature corresponding to the latent heat release. The algorithm would then update the mass fraction of water vapor, determine the relative humidity, and calculate the moist air density as a function of temperature, pressure, and humidity. At this point, the thermodynamics model would pass the new wind field distribution of temperature, mass fraction of water vapor, relative humidity, and density to the hydrodynamic model.

Plume rise would be modeled by a decrease in density that would reduce the body force term of the vertical momentum equation for those parcels of air which are included in the plume. These parcels of air would thus become more buoyant relative to their neighbors and rise in the atmosphere. In this way, plume rise would be modeled without the need for an empirical plume rise equation.

Plume dispersion would be simulated in the hydrodynamic model by the moisture transport equation, which would include both convection and diffusion terms, and would calculate the wind field distribution of the mass fraction of water vapor. Droplet formation and the resulting decrease in the mass fraction of water vapor would be simulated by the thermodynamics model, which would also determine the wind field distribution of relative humidity. Contours of relative humidity would define the outline of the moist plume, while contours of temperature would define the outline of the thermal plume. In this way, plume dispersion would be modeled without the need for an empirical dispersion mechanism or an entrainment coefficient.

The sample calculations presented in this paper show excellent agreement with previously published data. These calculations also attest to the applicability of this algorithm to a comprehensive moist plume model.

As outlined above, studies are under way to incorporate this algorithm into an existing cooling tower plume model [33]. This step would allow the prediction of the visible moist plume as well as the thermal plume. Also this step would permit the modeling of the buoyancy effects due to the latent heat released by condensation and due to the lower density of the moist plume as compared to the dryer ambient air. Thus the physical process of plume rise would be realistically represented. It is the author's opinion that the resulting plume model would produce an accurate, state-of-the-art simulation of a moist plume as influenced by the local atmospheric flow field.

### Acknowledgments

The author wishes to acknowledge J. M. Vance and S. H. Park of Martin Marietta Energy Systems, Inc., for their encouragement and support in this work. The author also wishes to express his appreciation to several other members of Energy Systems, Inc., for their technical advice and guidance: R. L. Cox, S. K. Iskander, J. E. Park, and C. A. Sady. Funds for the support of this work were provided by the Process Support Division, Oak Ridge Gaseous Diffusion Plant.

### References

- 1 Wessels, H. R. A., and Wiese, J. A., "A Method for Calculating Sizes of Cooling Tower Plumes," *Atmos. Environ.*, Vol. 5, 1971, pp. 743-750.
- 2 McVehil, G. E., "Evaluation of Cooling Tower Effects at Zion Nuclear Generating Station," Final Report, Sierra Research Corporation, Boulder, Colo., to Commonwealth Edison Company, 1970.



- 3 Altomare, P. M., "The Application of Meteorology in Determining the Environmental Effects of Evaporative Heat Dissipation Systems," Paper No. 71-56, 64th Annual Meeting, Air Pollution Control Assoc., Atlantic City, N.J., 1971.
- 4 Csanady, G. T., "Bent-Over Vapor Plumes," *J. Appl. Meteor.*, Vol. 10, 1977, pp. 36-42.
- 5 Wigley, T. M. L., and Slawson, P. R., "On the Condensation of Buoyant Moist, Bent-Over Plumes," *J. Appl. Meteor.*, Vol. 10, 1971, pp. 253-259.
- 6 Hanna, S. R., "Rise and Condensation of Cooling Tower Plumes," *J. Appl. Meteor.*, Vol. 11, 1972, pp. 793-799.
- 7 Hanna, S. R., "Meteorological Effects of the Mechanical-Draft Cooling Towers of the Oak Ridge Gaseous Diffusion Plant," *Cooling Tower Environment—1974*, ERDA Symposium Series, available as CONF-740302 from the National Technical Information Service, U.S. Department of Commerce, Springfield, Va. 22161, 1975.
- 8 Hanna, S. R., "Cooling Tower Plume Rise and Condensation," Paper No. 53, Air Pollution Turbulence and Diffusion Symposium, Las Cruces, N.M., 1971.
- 9 Slawson, P. R., Coleman, J. H., and Frey, J. W., "Some Observations on Cooling Tower Plume Behavior at the Paradise Steam Plant," *Cooling Tower Environment—1974*, ERDA Symposium Series, available as CONF-740302 from the National Technical Information Service, U.S. Department of Commerce, Springfield, Va. 22161, 1975.
- 10 Meyer, J. H., Eagles, T. W., Kohlenstein, L. C., Kagan, J. A., and Stanbro, W. D., "Mechanical Draft Cooling Tower Visible Plume Behavior: Measurements, Models, Predictions," *Cooling Tower Environment—1974*, ERDA Symposium Series, available as CONF-740302 from the National Technical Information Service, U.S. Department of Commerce, Springfield, Va. 22161, 1975.
- 11 EG&G, Inc., "Potential Environmental Modifications Produced by Large Evaporative Cooling Towers," Series # 16130 DNH, Water Pollution Control Rec., Water Quality Office, Environmental Protection Agency, 1971.
- 12 Stephen, D. W., and Moroz, W. J., "Plume Rise from Wet Cooling Towers in Strong Winds," *Eng. Res. Bull. B-107*, College of Eng., The Pennsylvania State University, University Park, 1972.
- 13 Bogh, P., "Experience with Combined 'Wind Tunnel/Plume Model' Analysis of Cooling Tower Environmental Impact," *Cooling Tower Environment—1974*, ERDA Symposium Series; available as CONF-740302 from the National Technical Information Service, U.S. Department of Commerce, Springfield, Va. 22161, 1975.
- 14 Winiarski, L. D., and Frick, W. F., "Cooling Tower Plume Model," USEPA Corvallis Environmental Research Lab, EPA-600/3-76-100, September 1976.
- 15 England, W. G., Teuscher, L. H., and Taft, J. R., "Cooling Tower Plumes—Defined and Traced by Means of Computer Simulation Models," presented at Cooling Tower Institute Annual Meeting, Jan. 29-31, 1973.
- 16 Taft, J., "Numerical Model for the Investigation of Moist Buoyant Cooling Tower Plumes," *Cooling Tower Environment—1974*, ERDA Symposium Series; available as CONF-740302 from the National Technical Information Service, U.S. Department of Commerce, Springfield, Va. 22161, 1975.
- 17 David, L. R., and Shirazi, M. A., "A Review of Thermal Plume Modeling," presented at the International Heat Transfer Conference, Aug. 1978.
- 18 Dunn, W. E., Cooper, G. K., and Gavin, P. M., "Evaluation of Methods for Predicting Plume Rise from Mechanical-Draft Cooling Towers," University of Illinois at Urbana-Champaign, Urbana, Ill., 1978.
- 19 Carhart, R. A., Policastro, A. J., Ziemer, S., and Kaake, K., "Critical Review of Thirteen Models for Plume Dispersion from Natural Draft Cooling Towers," Division of Environmental Impact Studies, Argonne National Laboratory, Argonne, Ill., 1978.
- 20 ASME Research Committee on Atmospheric Emissions and Plume Behavior from Cooling Towers, "Cooling Tower Plume Modeling and Drift Measurement—A Review of the State of the Art," Library of Congress Catalog Card No. 75-21277, 1975.
- 21 *Handbook of Fundamentals*, ASHRAE, New York, 1977.
- 22 Goff, J. A., Anderson, J. R., and Gratch, S., "Final Values of the Interaction Constant for Moist Air," *ASHVE Transactions*, Vol. 49, 1943, pp. 269.
- 23 Goff, J. A., and Gratch, S., "Thermodynamic Properties of Moist Air," *ASHVE Transactions*, Vol. 51, 1945, pp. 125.
- 24 Goff, J. A., "Standardization of Thermodynamic Properties of Moist Air," *ASHVE Transactions*, Vol. 55, 1949, pp. 455.
- 25 Goff, J. A., and Gratch, S., "Low-Pressure Properties of Water from -160°F to 212°F," *ASHVE Transactions*, Vol. 52, 1946, pp. 95.
- 26 Kusuda, T., "Algorithms for Psychrometric Calculations," NBS Publication BSS21; available as SD Catalog No. C 13.29/2:21 from the Superintendent of Documents, U.S. Government Printing Office, Washington, D.C. 20402, Jan. 1970.
- 27 Threlkeld, J. L., *Thermal Environmental Engineering*, Prentice-Hall, Inc., New York, 1970, pp. 175.
- 28 Kusuda, T., "NBSLD, The Computer Program for Heating and Cooling Loads in Buildings," NBS Publication BSS69; available as SD Catalog No. C13.29/2:69 from the Superintendent of Documents, U. S. Government Printing Office, Washington, D.C. 20402, July 1976.
- 29 *Brochure on Psychrometry*, ASHRAE, New York, 1977.
- 30 Reid, R. C., Prausnitz, J. M., and Sherwood, T. K., *The Properties of Gases and Liquids*, McGraw-Hill, New York, 1977.
- 31 Henley, E. J., and Bieber, H., *Chemical Engineering Calculations*, McGraw-Hill, New York, 1959.
- 32 Keenan, J. H., and Keyes, F. G., *Thermodynamic Properties of Steam*, John Wiley & Sons, New York, 1936.
- 33 Becker, B. R., "Cooling Tower Recirculation as Influenced by the Local Atmospheric Flow Field, A Numerical Study," Union Carbide Corporation, Nuclear Division, Oak Ridge, Tenn.; available as K/CSD-11 from the National Technical Information Service, U.S. Department of Commerce, Springfield, Va. 22161, Apr. 1980.

# Total Absorptivities and Emissivities of Particulate Coal Ash From Spectral Band Emissivity Measurements

T. F. Wall

H. B. Becker<sup>1</sup>

Department of Chemical Engineering,  
University of Newcastle,  
Australia, 2308

*Previous measurements of the spectral emissivity of coal ashes are converted to total absorptivities and emissivities. Below the temperature at which ash sinters, the total absorptivity of an ash layer – which is necessary for the estimation of radiative transfer in furnaces – is shown to depend on both the source (flame) temperature and the ash temperature. Synthetic mixtures of the oxides  $Al_2O_3$ ,  $SiO_2$ , and  $Fe_2O_3$  are shown to give the same trends as those for ashes of the same  $Fe_2O_3$  content.*

## 1 Introduction

The importance of the spectral character of fireside deposits in coal-fired furnace has previously been indicated [1]. Unique results of spectral band emissivities have also been presented [2] for particulate coal ash, together with a review of previous measurements and methods.

The emissivity results indicated that:

- Ashes are highly spectral.
- For the engineering calculation of radiative heat transfer (when surfaces are taken as grey), the surface absorptivity rather than emissivity should be used because the surface absorbs a great deal more energy than it emits.

The present paper considers the conversion of the spectral band emissivity data to the absorptivities necessary for these calculations. Emphasis is given to the difference between the temperature of the incident (flame source) radiation and that of the ash surface.

The observed systematic effect of the iron oxide of the ashes is then reported and investigated.

## 2 Definitions of Radiative Properties of Surfaces

**2.1 Basic Concepts.** It can be shown with the aid of the second law of thermodynamics that there is an upper limit to the amount of radiative energy that can be emitted by surfaces (e.g., see Lee, Sears, and Turcotte [3]). A body that emits or absorbs radiation at the maximum rate is known as a blackbody. The rate of energy emitted into hemispherical space, per unit wavelength interval, from a blackbody is known as the spectral blackbody flux density  $e_b(\lambda, T)$ , given by Planck's law.

Integration of the spectral flux over all wavelengths at a

<sup>1</sup>Present address: Herman Research Laboratories, SECV, Richmond, Australia, 3121

Contributed by the Power Division for publication in the JOURNAL OF ENGINEERING FOR GAS TURBINES AND POWER. Manuscript received by the Power Division November 22, 1983.

fixed temperature yields the total blackbody radiation flux density, or emissive power,  $E_b$

$$E_b(T) = \int_{\lambda=0}^{\infty} e_b(\lambda, T) d\lambda \quad (1)$$

This integral has been evaluated as

$$E_b(T) = \sigma T^4 \quad (2)$$

Integration of  $e_b(\lambda, T)$  over a spectral band of limits  $(\lambda_l, \lambda_u)$  for a given band identified by subscript "j," yields a band emissive power  $\Delta E_{b, \lambda_j}$

$$\Delta E_{b, \lambda_j}(T) = \int_{\lambda_l}^{\lambda_u} e_b(\lambda, T) d\lambda \quad (3)$$

where  $\lambda_j$  is the nominal wavelength position of the band given by

$$\lambda_j = (\lambda_l + \lambda_u) / 2 \quad (4)$$

**2.2 Total Properties.** Radiation properties are designated as total if they refer to the entire spectrum. Total emissivity  $\epsilon_t$  is defined in terms of spectral energy flux density  $e_\lambda(T)$  and emissive power  $E_b(t)$ , as

$$\epsilon_t(T) = \frac{1}{E_b(T)} \int_{\lambda=0}^{\infty} e_\lambda(T) d\lambda \quad (5)$$

Total emissivity can alternatively be defined in terms of spectral emissivity  $\epsilon_\lambda$ , as follows

$$\epsilon_t(T) = \frac{1}{E_b(T)} \int_{\lambda=0}^{\infty} \epsilon_\lambda(T) e_b(\lambda, T) d\lambda \quad (6)$$

Total absorptivity  $\alpha_t$  is defined in terms of spectral absorptivity  $\alpha_\lambda$  and spectral incident flux density  $H_2(T_s)$  as

$$\alpha_t(T_o, T_s) = \int_{\lambda=0}^{\infty} \alpha_\lambda(T_o) \cdot H_2(T_s) d\lambda / \int_{\lambda=0}^{\infty} H_2(T_s) d\lambda \quad (7)$$

Total absorptivity is defined therefore as a function of both surface temperature  $T_o$  and source radiation temperature  $T_s$ . Kirchoff's law states that the total emissivity and total emissivity of a surface in radiative equilibrium with its

surroundings are the same. In this case, there is no net radiative transfer from the surface. The spectral emissivity  $\epsilon_\lambda(T_o)$  and spectral absorptivity  $\alpha_\lambda(T_o)$  are equal, even though there may be net transfer as long as absorptivity is insensitive to a wide variation in the intensity of irradiation [4]. Sparrow and Cess [5] note that, strictly speaking, Kirchoff's law holds for monochromatic radiation in a particular direction and for each component of polarization. The present measurements of normal radiative properties approximate the geometry, which satisfies this directional requirement.

Applying Kirchoff's law, substitution of  $\epsilon_\lambda(T_o)$  for  $\alpha_\lambda(T_o)$  therefore allows calculation of total absorptivity from the spectral emissivity distribution as follows

$$\alpha_t(T_o, T_s) = \int_{\lambda=0}^{\infty} \epsilon_\lambda(T_o) \cdot H(T_s) d\lambda \Big/ \int_{\lambda=0}^{\infty} H_\lambda(T_s) d\lambda \quad (8)$$

Some implications of considerable practical importance for total properties arise from the way spectral properties vary with wavelength. If  $\epsilon_\lambda$  does not vary with wavelength, then it follows that  $\epsilon_t$  does not vary with temperature. The converse is not necessarily true, but in practice invariance of emissivity with temperature usually implies that  $\epsilon_\lambda$  is constant. From Kirchoff's law, it then follows that total absorptivity is equal to total emissivity

$$\alpha_t = \epsilon_t = \text{constant} \quad (9)$$

An absorber or emitter that exhibits this characteristic is known as a grey body. Some real materials approximate this condition (i.e., heavily oxidised metal surfaces), but dielectric materials generally do not [4]. A significant feature of dielectrics – which include ash deposits – is a region of low spectral emissivity at short wavelengths (up to 2 or 3  $\mu\text{m}$ ), followed by a region of high emissivity at longer wavelengths, which is usually strongly banded [5]. The effect of this spectral distribution on total emissivity or absorptivity is to cause  $\epsilon_t$  or  $\alpha_t$  to decrease with increasing temperature. The reason for this is that whilst the emission (or absorption) bands of such materials remain relatively fixed with respect to spectral position as temperature increases, the region of maximum energy of Planck's function moves towards shorter wavelengths. This causes  $\epsilon_t$  or  $\alpha_t$  to be weighted towards the low (short wavelength) spectral emissivities, at high  $T_o$  or  $T_s$ , respectively, from equations (7) and (8).

**2.3 Planck-Weighted Properties.** Consider a partitioning of the wave spectrum at points  $\lambda_1, \lambda_2, \lambda_j, \dots, \lambda_{j+1}, \dots, \lambda_n$ . The incremental band emissive power  $E_{b,\lambda_j}(T)$  at temperature  $T$ , for the  $j$ th band, is

$$\delta\lambda_j = \lambda_{j+1} - \lambda_j \quad (10)$$

and is defined by equation (3) as

$$\Delta E_{b,\lambda_j}(T) = E_b(\lambda_{j+1}, T) - E_b(\lambda_j, T) \quad (11)$$

### Nomenclature

$d$  = ash mean particle diameter,  $\mu\text{m}$   
 $e_b$  = spectral blackbody flux density,  $\text{Wm}^{-2}$   
 $E_b$  = total blackbody flux density,  $\text{Wm}^{-2}$   
 $\Delta E_{b,\lambda_j}(T)$  = incremental band emissive power (equation (11)),  $\text{Wm}^{-2}$   
 $n$  = total number of bands  
 $H$  = incident radiation flux density,  $\text{Wm}^{-2}$   
 $T$  = temperature, K

### Greek Symbols

$\alpha$  = absorptivity  
 $\epsilon$  = emissivity

A (Planck-weighted) band emissivity  $\epsilon_{\lambda_j}$  at an ash temperature  $T_o$  can therefore be defined as

$$\epsilon_{\lambda_j}(T_o) = \int_{\lambda=\lambda_j}^{\lambda_{j+1}} \epsilon_\lambda \cdot e_b(\lambda, T_o) d\lambda \Big/ \Delta E_{b,\lambda_j}(T_o) \quad (12)$$

A (Planck-weighted) total emissivity can be found from the spectral band emissivities of a finite number of adjacent bands as

$$\epsilon_t(T_o) = \frac{\sum_{j=1}^n \epsilon_{\lambda_j}(T_o) \cdot \Delta E_{b,\lambda_j}(T_o)}{\sum_{j=1}^n \Delta E_{b,\lambda_j}(T_o)} \quad (13)$$

which depends on the ash temperature only.

Similarly, a (Planck-weighted) total absorptivity can be determined from band emissivities, using Kirchoff's law, but with incremental band emissive powers evaluated at a radiation source temperature  $T_s$

$$\alpha_t(T_o, T_s) = \frac{\sum_{j=1}^n \epsilon_{\lambda_j}(T_o) \Delta E_{b,\lambda_j}(T_s)}{\sum_{j=1}^n \Delta E_{b,\lambda_j}(T_s)} \quad (14)$$

This total absorptivity therefore depends on both the ash temperature and the source temperature, and assumes the source is a black emitter.

The accuracy that can be obtained for  $\epsilon_t$  or  $\alpha_t$  depends on how accurately a set of discrete band emissivity values can represent the actual (continuous) spectral emissivity distribution. Two obvious factors are the number of bands employed and the fraction of the total energy spectrum covered. If  $\epsilon_\lambda$  does not vary greatly, then good accuracy might be obtained with relatively few bands. Generally speaking, an increase in the number of bands leads to increased accuracy. If  $n$  is sufficiently large, then

$$\sum_{j=1}^n E_{b,\lambda_j}(T) \text{ approaches } E_b(T) \quad (15)$$

and therefore  $E_b(T)$  may be substituted in the denominator of equations (13) and (14) if this is the case.

### 3 Normal Spectral Band Emissivity Measurements on Coal Ashes

Measurements of the emissivity of a number of coal ashes compressed into pellets have been reported elsewhere [2]. The measurements were made with a narrow angle radiometer sighting normal to the surface of the pellets, with bandpass filters to allow measurement of spectral band emissivities  $\epsilon_{\lambda_j}(T_o)$  in the following nominal five bands: 1–2  $\mu\text{m}$ ; 2–3

$\sigma$  = Stefan-Boltzmann constant (= 5.67  $\times 10^{-8}$ ),  $\text{Wm}^{-2} \text{K}^{-4}$   
 $\lambda$  = wavelength,  $\mu\text{m}$  or m

### Subscripts

$b$  = blackbody  
 $\lambda$  = refers to spectral (monochromatic) property  
 $t$  = refers to total property (integrated over wavelength)  
 $j$  = band number  
 $u, l$  = upper and lower wavelength limits of a band  
 $o$  = refers to ash surface  
 $s$  = refers to radiation source

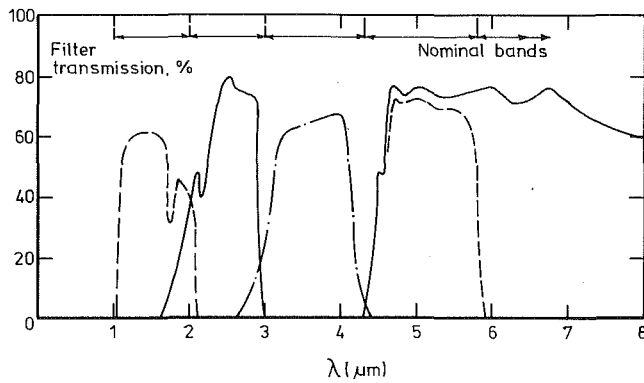


Fig. 1 The spectral transmission characteristics (percent) of the bandpass filters used in the narrow angle radiometer: A, 4.3  $\mu\text{m}$  cut on filter; B, 4.3–5.8  $\mu\text{m}$ ; C, 3.9–4.3  $\mu\text{m}$ ; D, 2.0– $\mu\text{m}$ ; E, 1.0–2.0 $\mu\text{m}$  filter

$\mu\text{m}$ ; 3–4.3  $\mu\text{m}$ ; 4.3–5.8  $\mu\text{m}$ ; and 5.8–35  $\mu\text{m}$ , covering about 99 percent of the effective thermal spectrum. For total emissivity measurement  $\epsilon_t(T_0)$ , no filters are required.

The spectral transmission of the filters used to obtain these band regions are given on Fig. 1. This figure indicates the inevitable problem when using the present technique; the wings of the filters overlap slightly and some spectral regions are not covered adequately by any filter, others of high transmission assume greater significance within the bands. For the analysis of results from equations (13) and (14), we will assume flat transmission characteristics with no overlap or gaps.

The filters, however, do cover the thermal spectrum adequately, the proportion of the blackbody spectrum above a wavelength of 35  $\mu\text{m}$  is negligible; that below 1 $\mu\text{m}$  ranges from less than 0.001 percent at 600 K to 0.78 percent at 1400 K.

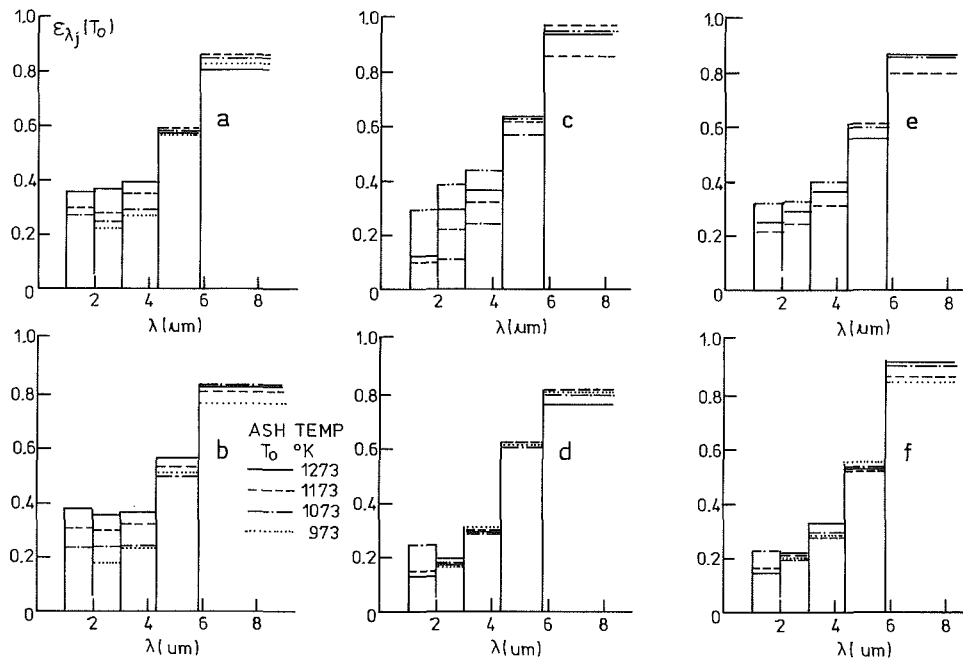


Fig. 2 Band emissivity measurements for the coal ashes: (a) Morwell, (b) Yallourn, (c) Leigh Creek, (d) Tarong, (e) Liddell (f) Swanbank

Table 1 Analysis and mass mean size of the coal ashes (bracketed numbers refer to analysis after heating for emissivity testing; ND means not determined, LOI is loss on ignition)

	Morwell (brown)	Yallourn (brown)	Leigh Creek (hard brown)	Tarong	Liddell (sub-bituminous)	Swanbank
SiO <sub>2</sub>	28.9 (27.2)	9.3 (9.8)	56.2 (56.4)	71.6	51.4 (55.5)	59.1
Al <sub>2</sub> O <sub>3</sub>	11.5 (12.6)	3.3 (4.5)	25.3 (24.6)	25.3	29.3 (29.6)	28.5
Fe <sub>2</sub> O <sub>3</sub>	10.5 (14.2)	18.3 (26.8)	4.3 (4.4)	0.9	6.1 (6.9)	3.5
CaO	23.8 (23.5)	5.6 (6.1)	4.8 (5.8)	1.0	1.4 (2.1)	2.2
MgO	11.2 (11.3)	21.4 (32.5)	1.7 (1.7)	0.3	0.8 (1.0)	1.0
Na <sub>2</sub> O	3.3 (3.0)	5.1 (6.1)	4.0 (3.5)	0.2	0.8 (0.2)	0.8
K <sub>2</sub> O	0.36 (0.1)	0.07 (0.1)	0.8 (0.8)	0.03	0.7 (0.74)	0.6
TiO <sub>2</sub>	0.7 (1.3)	0.06 (0.3)	1.4 (2.2)	0.12	0.9 (1.4)	1.4
SO <sub>3</sub>	5.9 (6.2)	9.8 (10.9)	0.22 (0.1)	—	0.14 (0.1)	0.96
Cl	0.13 (ND)	0.39 (ND)	<0.01 (ND)	<0.01	<0.01 (ND)	<0.01
LOI	1.9 (2.1)	25.4 (1.9)	0.22 (1.0)	0.48	2.6 (1.0)	1.8
Mass mean size, $\mu\text{m}$	22	32	17	9	17	15
Notes:	Dominated by "mixed" oxides of Ca, Mg, Fe		Clays with sodium silicate		Clay dominated, with iron varying	
Reference for Figs.	(a)	(b)	(c)	(d)	(e)	(f)

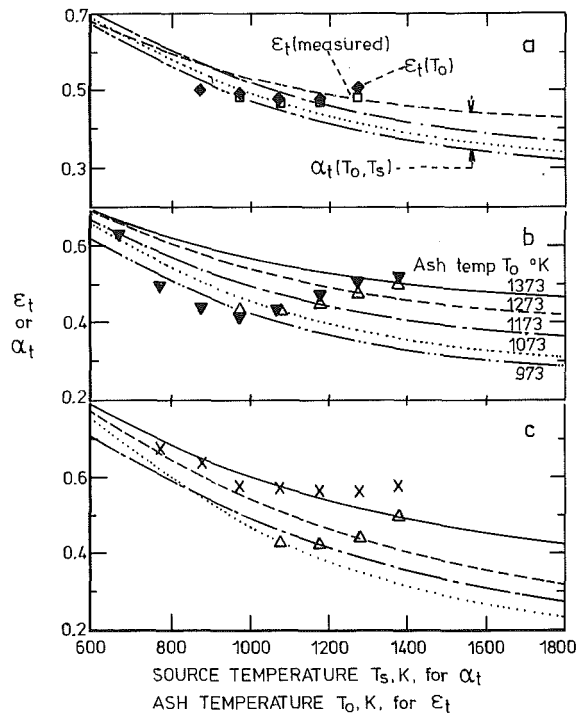


Fig. 3 Estimated total absorptivities (lines), total emissivities (open symbols), and measured total emissivities (full symbols) for the coal ashes: (a) Morwell, (b) Yallourn, (c) Leigh Creek

The results, given on Fig. 2, were obtained on cooling the pellets, after heating to 1300 K. The analysis of the samples are given in Table 1.

#### 4 Calculation of Planck-Weighted Total Emissivities and Total Absorptivities From Measured Band Emissivities for Coal Ashes

**4.1 Band Radiosities,  $\Delta E_{b,\lambda_j}(T_o)$ .** Band radiosities were calculated for the five bands by integration of Planck's law by equation (3).

**4.2 Total Emissivities and Absorptivities,  $\epsilon_t(T_o)$ ,  $\alpha_t(T_o, T_s)$ .** To use equations (13) and (14) when measurements of band emissivities do not cover full spectrum, two approaches are possible:

(i) Obtain  $\epsilon_\lambda(T_o)$  and  $\alpha_\lambda(T_o, T_s)$  over the spectral range covered by the measurements; that is, use equations (13) and (14) as they stand. This is equivalent to the use of a selective radiometer to measure total emissivity, a characteristic of many commercial instruments (for example, those which use arsenic trisulphide as a lens material).

(ii) Assume the band emissivities of the low and high wavelength regions are the same as those of the adjacent bands.

The latter approach was used here for the spectral region below  $1 \mu\text{m}$ .

**Total Absorptivities.** Total absorptivities calculated from Equation 14 and the measured band emissivities of Fig. 2 are presented as the curves on Figs. 3 and 4 at source temperatures of 973 K, 1073 K, 1173 K, 1273 K, and 1373 K for the six ash samples.

Figs 3 and 4 show the total absorptivity is indeed a function of both the ash and the source temperature; the ash temperature increases absorptivity while the source temperature decreases it. The two ashes of lowest iron content (d, f) show the greatest variation with source temperature, and Tarong

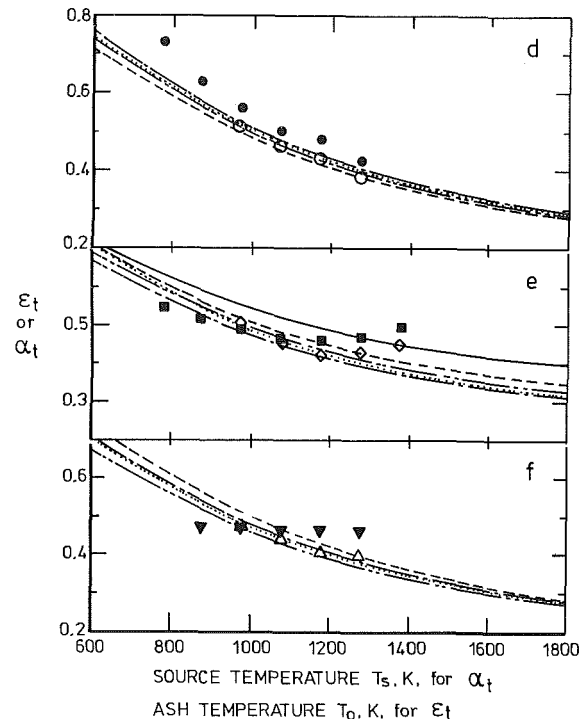


Fig. 4 Estimated and total properties as for Fig. 3: (d) Tarong, (e) Liddell, (f) Swanbank

ash (d), with more than 96 percent of the ash as silica and alumina, is most sensitive to source temperature, while being insensitive to ash temperature changes.

**Total emissivities.** By comparing equations (13) and (14), we can see that when the source temperature  $T_s$  equals the ash temperature  $T_o$ , then the total absorptivity will equal the total emissivity. The total emissivity can therefore be estimated from the total absorptivity curves when the ash temperature is equal to the source temperature. The open symbols of Figs. 3 and 4 give the total emissivities thus estimated (from the spectral measurements), which can be compared with the measured total emissivities (closed symbols) in order to evaluate the adequacy of the Planck-weighting technique.

It should be noted that Figs. 3 and 4 use the abscissa for the total emissivity values as the ash temperature, whereas the abscissa for the total absorptivity is the source temperature. The total emissivity depends on the ash temperature only.

For all but Fig. 3(c) – for Leigh Creek ash – a reasonable agreement is observed between the estimated and measured total emissivities. The Leigh Creek ash was found to undergo the most significant chemical (darkening) and physical (shrinkage) changes on heating. Electron microprobe analysis indicated that iron is lost during this heating, and we believe this results in the lower calculated emissivities when the sample was held at high temperature for the longer period of the spectral experiments.

The difference between the estimated and measured total emissivities for the other samples is probably due to the selective transmission characteristics of the filters.

A systematic trend of absorptivity with increasing iron content can be observed on Figs. 3 and 4. The absorptivity of the high iron ashes (samples a and b,  $\text{Fe}_2\text{O}_3 < 1$  percent) are less dependent on the source temperature than the very low iron ash (sample d;  $\text{Fe}_2\text{O}_3 < 1$  percent), the other ashes generally having a moderate dependence. As the source temperature increases, the effect of ash temperature on the absorptivity of the high iron ashes also becomes more significant.

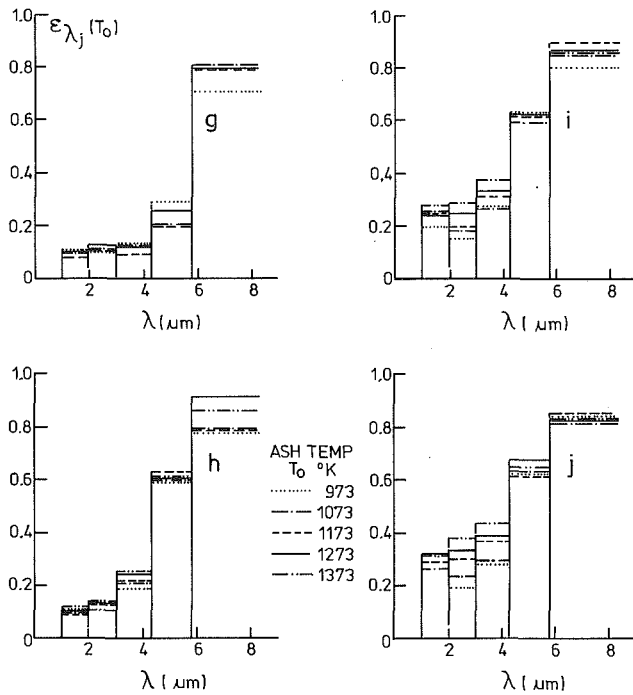


Fig. 5 Spectral emissivity measurements for the synthetic ashes: (g) Al<sub>2</sub>O<sub>3</sub> powder; (h) 67 percent SiO<sub>2</sub>, 33 percent Al<sub>2</sub>O<sub>3</sub>; (i) 60 percent SiO<sub>2</sub>, 30 percent Al<sub>2</sub>O<sub>3</sub>, 10 percent Fe<sub>2</sub>O<sub>3</sub>; (j) 53 percent SiO<sub>2</sub>, 27 percent Al<sub>2</sub>O<sub>3</sub>, 20 percent Fe<sub>2</sub>O<sub>3</sub>

## 5 Investigation of the Effect of Iron Oxide

In order to investigate the effect of iron oxide, four additional samples of synthetic ashes were tested. These were of pure SiO<sub>2</sub> and Al<sub>2</sub>O<sub>3</sub> powders in the mass ratio 2:1 with Fe<sub>2</sub>O<sub>3</sub> added to cover the range commonly found in coal ashes. The synthetic ashes were slightly finer than the coal ashes (mean size <10 μm) with the Fe<sub>2</sub>O<sub>3</sub> powder being very fine (<5 μm). No systematic trend of the radiative properties with size was observed for the present ashes, as has been observed previously [4].

The band emissivity measurements of Fig. 5 show that Fe<sub>2</sub>O<sub>3</sub> influences the spectral region below 4 μm with an increase of the three band emissivities covering this region with Fe<sub>2</sub>O<sub>3</sub> content. By comparison, the Al<sub>2</sub>O<sub>3</sub> sample (g) and the SiO<sub>2</sub>/Al<sub>2</sub>O<sub>3</sub> sample (h) exhibit a smaller change in emissivity in this wavelength region. The total absorptivity curves estimated from these spectral data at a number of ash temperatures, given on Fig. 6, therefore show a greater spread with increasing source temperature for the synthetic ashes containing iron. Ash temperatures therefore have a greater effect on the total absorptivities at the higher ash temperature levels.

For the synthetic ashes, Fig. 6 also gives results for the estimated total emissivities. For the ashes containing Fe<sub>2</sub>O<sub>3</sub>, a minimum in both these values is observed. This minimum is also observed on Fig. 3 for all coal ash samples other than samples (d) and (f) having the lowest Fe<sub>2</sub>O<sub>3</sub> levels.

These observed trends are expected from the physics literature related to Fe<sub>2</sub>O<sub>3</sub> absorption. The absorption spectra of Al<sub>2</sub>O<sub>3</sub> has been found to change little with wavelength in the weak absorption and emission regions at low wavelengths [5], which is consistent with the results of Fig. 5g. In contrast, Fe<sub>2</sub>O<sub>3</sub> absorbs in this weakly absorbing region for Al<sub>2</sub>O<sub>3</sub> with characteristic absorption bands [6], which would result in a minimum of emissivity when plotted against temperature, as shown on Figs. 3 and 6. The spread of the absorption peaks with temperature [6] for Fe<sub>2</sub>O<sub>3</sub> would also result in the ob-

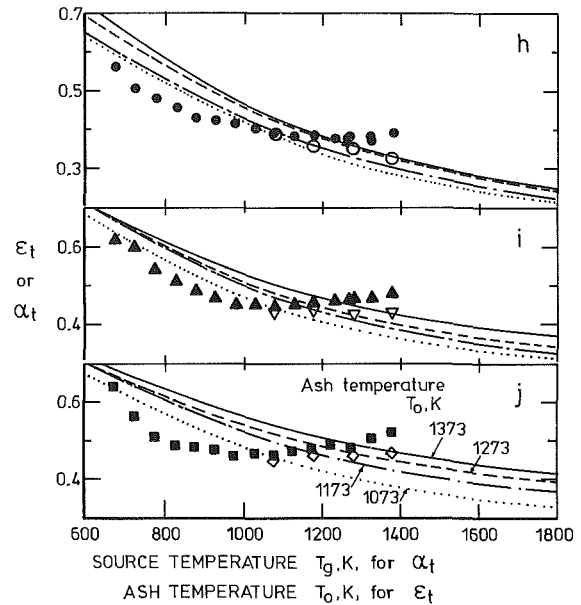


Fig. 6 Estimated total absorptivities (lines) and total emissivities (open symbols), with measured total emissivities (full symbols) for the synthetic ashes of Fig. 5

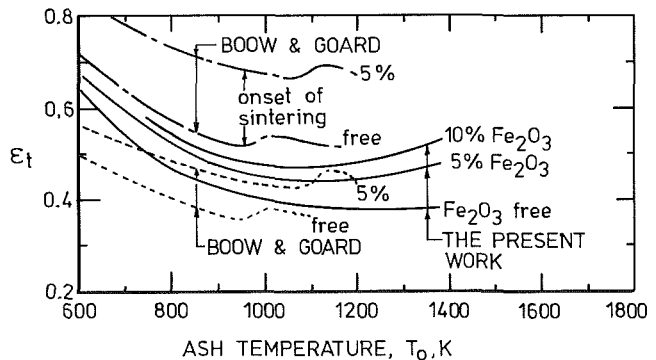


Fig. 7 Comparison of the measured total emissivities with those of Boow and Goard [9] for 53–104 μm synthetic ashes containing 50 percent SiO<sub>2</sub>, 25 percent Al<sub>2</sub>O<sub>3</sub>, 25 percent CaO; and 45 percent SiO<sub>2</sub>, 25 percent Al<sub>2</sub>O<sub>3</sub>, 25 percent CaO, and 5 percent Fe<sub>2</sub>O<sub>3</sub>

served increased emissivity with temperature in the weak emission regions observed on Figs. 2 and 5.

For the pure Al<sub>2</sub>O<sub>3</sub> sample, the total normal emissivity data of Fig. 5(g) can be compared with measurements by Pirani [6] and Brandes, Sully, and Waterhouse [7]. This comparison [8] shows the present results fall between the data from the other sources at temperatures above 900 K. From 600–900 K, the present results fall slightly under the literature data, with a maximum deviation of 0.05.

Few previous measurements allow a direct comparison with the present results for synthetic ashes. Boow and Goard [9] measured the total emissivity of coarse synthetic ashes with a Land hemispherical surface pyrometer. This instrument has been shown to measure total normal emissivity [10].

A comparison of the present results with those of Boow and Goard [9] shown on Fig. 7 for a coarse synthetic ash, having a mean size several times that of the coal ashes, indicates that their emissivity measurements are higher. This appears to be the result of the effect of particle size, which is estimated by Boow and Goard to influence emissivity by the following equations

$$\epsilon_t = 0.25 \log_{10} d + 0.13, \text{ for Fe}_2\text{O}_3 \text{ free ash}$$

and

$$\epsilon_t = 0.30 \log_{10} d + 0.16, \text{ for Fe}_2\text{O}_3 \text{ containing ash}$$

The dotted curves of Fig. 7 show the Boow and Goard emissivity data for their synthetic ash of 53–104  $\mu\text{m}$  (mean 78  $\mu\text{m}$ ) in size corrected to a mean size of 15  $\mu\text{m}$ , using the foregoing equations. A better agreement is seen, but the corrected data now underestimates the results of the present work.

## 6 Conclusions

1 The total absorptivity of coal ash depends on both its own temperature and the temperature of the radiative source. Below the sintering temperature the absorptivity increases with increasing ash temperature, at a rate that has been found to depend on the iron content of the ash, but decreases with increasing source temperature due to the shift of the black-body spectrum of the source to lower, weakly absorbed wavelengths in the radiative spectrum.

2 The total emissivity of coal ash, which depends on the surface temperature only, decreases with temperature at low temperature but may increase before the sintering temperature for high iron ashes.

3 The aforementioned trends have been also observed for synthetic ashes of  $\text{Al}_2\text{O}_3$ ,  $\text{SiO}_2$ , and  $\text{Fe}_2\text{O}_3$ , with measured total emissivities generally agreeing to within 0.05 with that of ash of the same  $\text{Fe}_2\text{O}_3$  content.

4 For temperatures typical of pulverised-coal-fired boilers (source temperature of 1700–1900 K; ash temperature on steam tube surfaces of 700–1000 K) the total absorptivities of flat-ash-covered surfaces can be as low as 0.3 for a low iron ash. At higher ash temperatures and high iron ashes, the absorptivity can increase to 0.5. The roughness of ash

deposits and the curvature of the steam tubes will result in higher “effective” total absorptivities.

## References

- 1 Wall, T. F., Lowe, A., Wibberley, L. J., and Stewart, I. McC., “Mineral Matter in Coal and the Thermal Performance of Large Boilers,” *Prog. Energy Combust. Sci.*, Vol. 5, No. 1, 1979.
- 2 Wall, T. F., and Becker, H. B., “The Total and Spectral Emissivities of Particulate Coal Ashes, Fouling and Slagging from Impurities in Combustion,” edited by R. W. Bryers, Engineering Foundation, N.Y., 1983, pp. 211–224.
- 3 Lee, J. F., Sears, F. W., and Tarcotte, P. L., *Statistical Thermodynamics*, Addison-Wesley, Reading, Mass., 1973.
- 4 Hottel, H. C., and Sarofim, A. F., *Radiative Transfer*, McGraw-Hill, 1967.
- 5 Sparrow, E. M., and Cess, R. O., *Radiation Heat Transfer*, Hemisphere, 1978.
- 6 Pirani, M., “Radiation Properties of Different Substances,” *J. Sci. Instrum.*, Vol. 16, 1939, pp. 372–376.
- 7 Sully, A. H., Brandes, E. A., and Waterhouse, R. B., “Some Measurements of Total Emissivity of Metals and Pure Refractory Oxides and the Variation of Emissivity with Temperature,” *Brit. J. Appl. Phys.*, Vol. 3, 1972, pp. 97–101.
- 8 Becker, H. B., “Spectral Band Emissivities of Ash Deposits and Radiative Transfer in Pulverised-Coal-Fired Furnaces,” Ph.D. thesis, University of Newcastle, 1982.
- 9 Boow, J., and Goard, P. R. C., Fireside Deposits and Their Effect on Heat Transfer in a Pulverised Fuel-Fired Boiler: Part III,” *J. Inst. Fuel*, Vol. 42, 1969, p. 412.
- 10 Becker, H. B., and Wall, T. F., “Effect of Specular Reflection of Hemispherical Pyrometer on Emissivity Measurement,” *J. Phys. E., J. Sci. Instrum.*, Vol. 14, No. 8, 1981, pp. 998–1001.
- 11 Mitsuiski, A., Yoshinagi, H., Fujita, and Suemoto, Y., “Vibrational Spectra of Ruby and Haematite in the Infrared Region,” *Japanese J. of Appl. Physics*, Vol. 1, No. 1, 1962.
- 12 Marusak, LLA., Messier, R., and White, W. B., “Optical Absorption Spectrum of Hematite,  $\alpha\text{Fe}_2\text{O}_3$  Near IR to UV,” *J. Phys. Chem. Solids*, Vol. 41, 1980, p. 981.

# A Non-Newtonian Flow Model for Coal-Ash Slag

E. K. Johnson

Department of Mechanical and  
Aerospace Engineering,  
West Virginia University,  
Morgantown, W.V. 26506

*The performance of high-temperature slagging coal-utilization systems depend on the collection of coal ash on the reactor surfaces and the flow of the slag out of the reactor through a slag-tap hole. In order to develop an analytical model for flow of the slag on a reactor wall, existing data for slag viscosity were reviewed in light of new emerging-process conditions. A Bingham model was selected for viscosity and the flow characteristics along a reactor wall are developed.*

## Introduction

The desire of the United States to become energy independent and to provide a clean, inexpensive fuel from indigenous sources has led to the investigation of many new energy concepts. As much of today's industry is fueled by natural gas and/or oil, it is apparent that any increase in coal consumption will necessitate the development of larger, more efficient, coal-gasification and liquefaction processes. One process that indicates a significant potential for coal gasification is the pressurized, entrained-flow gasification concept.

The entrained-flow gasification process, to be efficient, must operate at high temperatures that produce a molten coal ash that then impinges on the reactor surfaces. The molten ash becomes part of a slag layer on the surface that flows down the reactor wall and out of the reactor through a slag-tap hole. A properly operating entrained-flow process will allow for a minimum of molten ash carryover, which can foul the heat transfer surfaces downstream of the reactor. Thus most of the coal ash entering the reactor must collect on the reactor surfaces and flow unimpeded out through the tap hole.

The molten ash process in entrained-flow reactors is similar to that in the wet-bottom boilers, which were common in the 1930-1960 era. However, there appear to be two significant differences in the two processes. First, the mass of oxidizer per mass of fuel is significantly different in boilers and gasification processes, especially if oxygen is used instead of air. Secondly, boilers normally operate with excess air, thus creating an oxidizing environment, whereas the coal-gasification process occurs in a reducing environment. There is a significant difference in coal-ash chemistry depending on the local environment.

The problem considered in this study is the flow of coal-ash slag down a reactor towards the slag tap. Although a significant effort has been expended on the study of the viscosity of slag, these studies have tended towards the chemistry of coal ash. In addition, these studies have illustrated how complex the problems are in describing or predicting the viscosity of a slag. Thus it is hoped that this

study will illustrate a different approach to slag flow, which will then lead to further, perhaps more appropriate, experimental programs to develop an understanding of the rheology of coal ash [1-5].

## Slag Rheology

The problems of establishing the flow characteristics for coal ash in slagging reactors are numerous. Coal is not a well-defined material and the composition of the mineral matter within coal is a function of prehistoric environments. Also, "dirt" from the coal mine's roof, and partings (or overburden) may intermingle with the mined coal and consequently modify the composition of inherent mineral matter. In addition, the size distribution of the mineral-matter particles in and with the coal as it is injected into a reactor is a difficult, continuously changing, measurement. Thus the quantitative description of the mineral matter entering the reactor, the initial conditions, are difficult to establish.

Ideally, as the mineral matter passes through the high-temperature-reaction zone and impinges on the slag layer, the following sequence of events will occur:

- (a) The mineral matter will rapidly form a homogeneous molten mass.
- (b) The molten coal-ash particle will become attached to the slag layer and will rapidly dissolve into the homogeneous liquid-slag layer.
- (c) The formed slag will flow freely out of the reactor.
- (d) No appreciable slag will be carried out of the reactor by the product gases.

First, the probability of forming a homogeneous molten coal-ash particle is governed by the time required for the formation of a homogeneous molten mass relative to the particle's residence time in the high-temperature-reaction zone. The greater the residence time in a high-temperature zone, the greater the probability of the constituents of the mineral matter melting and dissolving into each other to form a homogeneous molten mass. The composition of the mineral matter in the coal and the environment about the particle have a strong influence on the required residence time in the reaction zone for an ideal homogeneous molten mass.

If the coal-ash particle is not a homogeneous molten mass when it impinges on the slag layer, then the outer slag layer

Contributed by the Fuels Division and presented at the ASME Winter Annual Meeting, Boston, Massachusetts, November 13-18, 1983. Manuscript received by the Fuels Division July 15, 1983. Paper No. 83-WA/Fu-1.



cannot be part of a homogeneous free-flowing slag layer. The coal-ash particle must then continue its melting and dissolution process within the slag layer. Experiments involving dirt on slag in a slow heating process illustrated the following sequence of events [6]:

- (a) Formation of gas bubbles on the surface of dirt, but not on the surface of a pure oxide
- (b) Rounding and reduction in size of particles
- (c) Build-up of crystals in the solvent slag
- (d) Complete solution of the added particles and solvent slag
- (e) Complete solution of the crystals

Although it has not been established how these events occur in a reactor, this sequence of events illustrates the complexity of the problem and that the presence of the final crystals as well as other factors may cause the liquid-slag layer to be a non-Newtonian fluid.

The operating conditions of the reactor must be such that the liquid slag may flow freely towards the slag-tap hole and out of the reactor. As viscosity is the controlling property for the flow of slag, it is appropriate to enumerate the variables which establish the viscosity of slag. These variables are:

- (a) Temperature
- (b) Composition of the slag
- (c) Environment, oxidizing or reducing atmosphere
- (d) History of the slag

At high temperatures, the *homogeneous* slag is a free-flowing Newtonian liquid. As temperatures become lower, crystals begin to form in the slag and the slag starts to exhibit a plastic flow characteristic. The temperature corresponding to the transition from Newtonian to non-Newtonian flow, upon cooling the slag, is designated as the critical viscosity and is denoted as  $T_{cv}$ . The relationship between the slag viscosity and temperature is a function of the composition of the slag and its environment. The composition of the slag, in turn, is a function of the mineral matter in the coal and its history before reaching the slag layer. The thermal history of the mineral matter must also consider the effects of a reducing or oxidizing environment. Several of these characteristics for a homogeneous slag are illustrated in Fig. 1.

Experience has indicated [2, 7] that the limiting slag viscosity for acceptable furnace operation is 250 poise. The temperature-viscosity parameter  $T_{250}$  represents that temperature at which the viscosity of the slag is 250 poise and 20 percent of the iron in the slag is present in the ferric form [7]. This latter condition is typical for furnaces operating with 15–20 percent excess air. The application of the  $T_{250}$  parameter depends on whether the furnace is designed for wet- or dry-bottom operation.

Ideally, the mineral matter entering a gasification system,

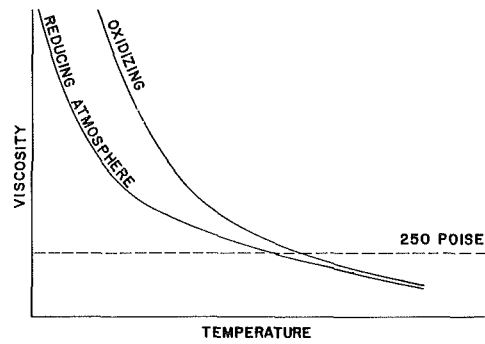


Fig. 1(a) Viscosity-temperature relationship for an Illinois coal [7]

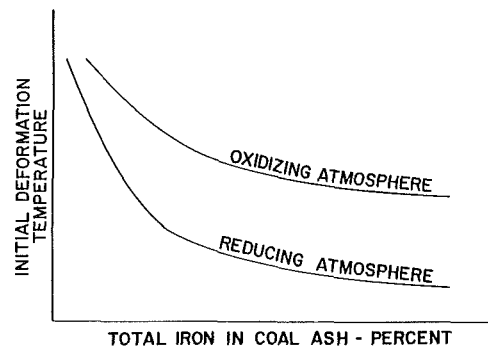


Fig. 1(b) Influence on composition on ash fusion temperature [10]

or wet-bottom boiler, will not become part of the product-gas stream. Thus, for an entrained-flow gasification process, the high solids loading will lead to significant slag flow. In addition, if the process is not operating properly, significant amounts of coal ash will not have formed a homogeneous molten mass before impinging on the slag layer. Also improper design and operation of the gasification process may lead to the precipitation of iron from the slag [8]. Iron is a fluxing agent in the slag. Consequently, if iron precipitates out of the slag [2], the viscosity of the slag may increase significantly and the slag flow may become non-Newtonian.

### Slag Shear Stress Model

An equation for the viscosity of a homogeneous liquid slag has been developed in the form [8, 9]

$$\mu^{1/e} = aT - b \quad (1)$$

where  $e$ ,  $a$ , and  $b$  are constants, depending on the slag composition and environment. This equation may be rearranged to

### Nomenclature

$A = (T_{\infty} - T_w)/(T_g - T_w)$   
 $a, b, e, m$  = empirical constants relating to the viscosity of the slag  
 $F(\xi, A, m)$  = defined by equation (10)  
 $g$  = gravitational constant  
 $G(\xi, A, m)$  = defined by equation (12)  
 $l$  = apparent thickness of refractory wall to produce a linear temperature profile

across the refractory wall and the slag layer  
 $\dot{m}'$  = mass flow rate of slag down the wall, per unit width of wall  
 $\dot{m}'_{CA}$  = mass flux of the impinging coal ash  
 $T$  = temperature  
 $u$  = velocity  
 $x$  = distance along the wall, measured from the top of the wall  
 $y$  = distance measured normal to the wall surface

$\delta$  = thickness of the slag layer  
 $\Delta$  = defined in Figs. 2 and 3  
 $\lambda$  = defined in Figs. 2 and 3  
 $\theta$  = angle between the normal to the wall and the vertical direction  
 $\mu$  = viscosity  
 $\xi$  = dimensionless distance  $(y + 1)/(\delta + 1)$   
 $\xi_{\Delta} = (\Delta + 1)/(\delta + 1)$   
 $\xi_{\lambda} = (\lambda + 1)/(\delta + 1)$   
 $\xi_0 = 1/(\delta + 1)$   
 $\rho$  = density  
 $\tau$  = shear stress  
 $\tau_0$  = internal yield stress

$$\mu = \frac{\eta}{(T - T_{\infty})^m} \quad (2)$$

where  $\eta$ ,  $m$ , and  $T_{\infty}$  are now the constants depending on the composition and environment of the slag. The characteristic temperature  $T_{\infty}$  corresponds to the ratio  $(b/a)$  where the viscosity becomes infinitely large.

The experimental determination of slag viscosity requires significant care and expertise. Mineral matter found in coal, either actual or simulated, is heated for a sufficient length of time to produce a homogeneous molten mass. Data for viscosity is then obtained for several temperature levels, decreasing to a minimum temperature and then returning to the original temperature [3]. This procedure is repeated until acceptable results are obtained. There are a multitude of problems to consider in this effort. The rate of formation of crystals within the liquid, upon cooling, may be (and frequently is) different than the dissolution rate for the crystals during heating. Also the loss of some of the chemical elements due to volatilization and the interaction between the molten slag and crucible material must be considered. In conclusion the data that are represented by equation (1), and other more complex equations in the literature, are data for the viscosity of a homogeneous slag.

Although the measurement of viscosity of a homogeneous liquid slag represents a significant accomplishment, the flow of slag along a reactor surface should include the nonequilibrium, nonhomogeneous effect of the impinging coal-ash particles as a function of its composition and environmental history. With the appreciable time required to establish a homogeneous molten slag for viscosity measurements, it is suggested that the coal-ash particles dissolve slowly in the molten-slag layer in the reactor. Thus the particles interact with the slag layer to form a fluid with the characteristics of a Bingham fluid. The shear stress for the slag may then be written as

$$\tau = \tau_0 + \mu \frac{du}{dy} \quad (3)$$

where  $\tau_0$  is the internal yield stress, and  $\mu$  is the experimentally determined viscosity. It should be noted that equation (3) is frequently employed in viscosity studies for data below the temperature of critical viscosity. However, in this study, equation (3) represents the effect of coal-ash particles on the shear stress for liquid slag, above the temperature of critical viscosity.

Unfortunately, it is extremely difficult to evaluate the internal yield stress due to coal-ash particles. The previous discussion on the life of a coal-ash particle in a reactor illustrates the difficulty in experimentally determining the internal yield stress of the slag. For the moment, it will be considered a parameter to be investigated to determine its significance.

### Flow Model

The slag-flow system for this analysis is shown in Fig. 2. A refractory wall may or may not exist in an entrained-flow, coal-gasification system, but probably does not appear in a wet-bottom boiler. Many gasification systems, and of course wet-bottom boilers, have a water-cooled shell. Thus the water-cooled shell establishes the low-temperature point in the analysis which is to follow. High-temperature-reacting gases sweep over the exposed surface of the liquid-slag layer as the coal-ash particles impinge on the slag layer. It is assumed that the heat and mass transfer are such that the surface of the slag is essentially at the reactor-gas temperature. A linear temperature profile may now be specified across the slag layer and refractory wall by assuming an equivalent refractory wall. In addition, constant values for the thermal conductivity and density for the slag are assumed. Also, perfect thermal

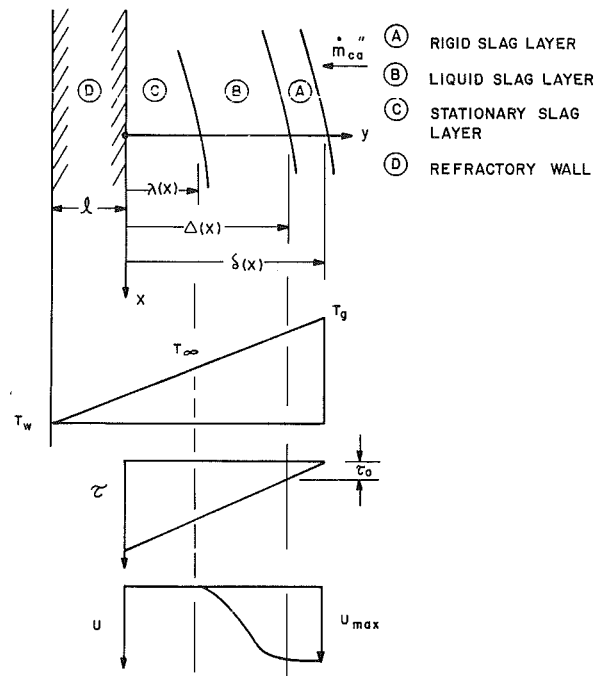


Fig. 2 Sketch of the slag flow system, for case 1 and  $\sin \theta = 1$

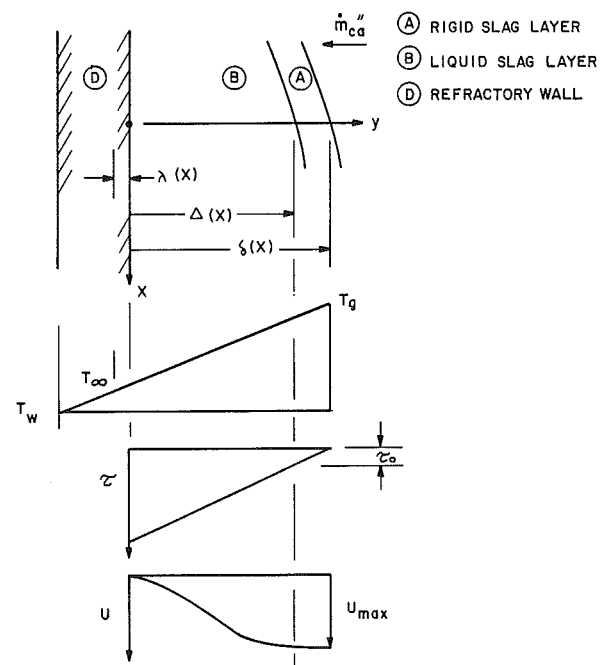


Fig. 3 Sketch of the slag flow system, for case 2 and  $\sin \theta = 1$

contact is assumed between the refractory wall and the water-cooled shell.

The steady-state-force balance for an element of volume in the slag layer may be written as

$$\frac{d\tau}{dy} = -\rho g \sin \theta \quad (3)$$

where  $\theta$  is the angle between the normal to the wall and the vertical direction. The shear stress due to the relative motion between the reacting gases and the slag layer is assumed negligible.

Figure 3 illustrates the variation of shear stress and temperature across the slag layer and their effect on the velocity profile. Thus the boundary conditions for equation (4) are

$$y = \delta; \quad \tau = 0 \quad (4)$$

$$y = \Delta; \quad \frac{du}{dy} = 0, \tau = \tau_0, u = u_{\max} \quad (5)$$

Consequently,

$$\tau_0 = \rho g \sin \theta (\delta - \Delta)$$

thus the rigid portion of the slag layer is of constant thickness.

Introducing the dimensionless distance

$$\xi = \frac{y + 1}{\delta + 1}$$

the temperature profile in Fig. 2 may be written as

$$T - T_{\infty} = (T_g - T_{\infty}) \left[ \xi - \frac{T_{\infty} - T_w}{T_g - T_w} \right]$$

The viscosity expression, equation (2), may not be written as

$$\mu = \frac{\mu_0}{(\xi - A)^m} \quad (6)$$

where

$$A = \frac{T_{\infty} - T_w}{T_g - T_w}$$

and

$$\mu_0 = \frac{\eta}{(T_g - T_w)^m}$$

Note that at  $y = \lambda$  ( $\xi = \xi_{\lambda}$ ),  $T = T_{\infty}$ , and  $\xi_{\lambda} = A$ .

A second boundary condition must be established to completely specify the flow in the slag layer. If  $T_{\infty}$  occurs in the slag layer, then a stationary slag layer will exist. Thus, the boundary condition becomes

$$y = \lambda (\xi = \xi_{\lambda}); \quad u = 0 \quad (7)$$

This situation is illustrated in Fig. 2 and is referred to as case 1. If, however,  $T_{\infty}$  occurs within the refractory wall, then no stationary slag layer will exist and the required boundary condition becomes

$$y = 0 (\xi = \xi_0); \quad u = 0 \quad (8)$$

This situation is illustrated in Fig. 3 and is referred to as case 2. In practice, conditions may be encountered in which a chemical reaction may occur between the slag and the refractory wall. This added complication will not be considered in this study.

**Case 1. For the First Case,  $\lambda > 0$ .** Integrating equation (3), utilizing equation (4), and incorporating the boundary conditions, the velocity distribution in the slag layer may be written as

$$u = 0 \quad (0 \leq y < \lambda)$$

$$u = \frac{\rho g \sin \theta}{\mu_0} (\delta + 1)^2 \left\{ \frac{(\xi - A)^{m+1} (1 - A)}{(m + 1)} - \frac{(\xi - A)^{m+2}}{(m + 2)} - (1 - \xi_{\Delta}) \frac{(\xi - A)^{m+1}}{m + 1} \right\}, \quad (\lambda \leq y \leq \Delta) \quad (9)$$

$$u = u_{\max}, \quad (\Delta < y < \delta)$$

For convenience, let

$$F(\xi, A, m) = \left\{ \frac{(\xi - A)^{m+1} (1 - A)}{(m + 1)} - \frac{(\xi - A)^{m+2}}{(m + 2)} - (1 - \xi_{\Delta}) \frac{(\xi - A)^{m+1}}{m + 1} \right\}$$

The maximum velocity may be written as

$$u_m = \frac{\rho g \sin \theta}{\mu_0} (\delta + 1)^2 F(\xi_{\Delta}, A, m)$$

The mass flow rate of slag at an elevation of the refractory wall, per unit width of surface, is

$$\dot{m}' = \int_{\lambda}^{\Delta} \rho u \, dy + \rho u_m (\delta - \Delta) \quad (11)$$

Substituting equation (9) into equation (11), one obtains

$$\dot{m}' = \frac{\rho^2 g \sin \theta}{\mu_0} (\delta + 1)^3 \left\{ \left[ \frac{(1 - A) (\xi_{\Delta - A})^{m+2}}{(m + 1)(m + 2)} - \frac{(\xi_{\Delta - A})^{m+3}}{(m + 3)} \right] + (1 - \epsilon_{\Delta}) \left[ \frac{-(\xi_{\Delta - A})^{m+2}}{(m + 1)(m + 2)} + \frac{(1 - A) (\xi_{\Delta - A})^{m+1}}{m + 1} - \frac{(\xi_{\Delta - A})^{m+2}}{m + 2} + \frac{(1 - \xi_{\Delta}) (\xi_{\Delta - A})^{m+1}}{m + 1} \right] \right\}$$

or

$$\dot{m}' = \frac{\rho^2 g \sin \theta}{\mu_0} (\delta + 1)^3 G(m, A, \xi_{\Delta}) \quad (12)$$

Equation (12) represents the mass rate of slag at any elevation along the wall. At steady-state conditions, all the coal ash impinging on the slag layer will flow down the wall. Consequently, if the mass flux rate of coal ash arriving at the slag layer is uniform, then

$$\int_0^x \dot{m}''_{CA} \, dx' = \dot{m}''_{CA} x$$

and

$$x = \frac{\rho^2 g \sin \theta}{\mu_0 \dot{m}''_{CA}} (\delta + 1)^3 G(m, \xi_{\Delta}, A)$$

Noting that  $\xi_{\Delta}$  is a function of  $\delta$ , a simple relationship for  $\delta(x)$  apparently cannot be developed.

As a limiting condition for internal yield stress, let  $\tau_0$  approach zero. Then  $\xi_{\Delta} = 1$  and

$$x \propto (\delta + 1)^3$$

for a Newtonian slag flow. The thickness of the stationary layer may now be written as

$$x \propto (\lambda + 1)^3$$

Furthermore, if there is no refractory wall,  $1 = 0$  and

$$x \propto \delta^3$$

which agrees with the results in [8] and [9].

**Case 2. For the Second Case,  $\xi_{\lambda} < \xi_0$ .** Upon employing the condition  $u = 0$  at  $\xi = \xi_0$ , equation (9) becomes

$$u = \frac{\rho g \sin \theta}{\mu_0} (\delta + 1)^2 \{ F(\xi, A, m) - F(\xi_0, A, m) \} \quad (13)$$

The expression for the maximum velocity now becomes

$$u_m = \frac{\rho g \sin \theta}{\mu_0} (\delta + 1)^2 \{ F(\xi_{\Delta}, A, m) - F(\xi_0, A, m) \} \quad (14)$$

Substituting equations (13) and (14) into equation (11), the mass flow rate of slag at any elevation along the refractory wall, per unit width of surface, may be developed as

$$\dot{m}' = \frac{\rho^2 g \sin \theta}{\mu_0} (\delta + 1)^3 \{ [G(\xi_{\Delta}, A, m) - G(\xi_0, A, m)] - (\xi_{\Delta} - \xi_0) F(\xi_0, A, m) \}$$

Similarly, the slag flow characteristics at any location  $x$  for a uniform coal-ash mass flux may be written as

$$x = \frac{\rho^2 g \sin \theta}{\dot{m}''_{CA} \mu_0} (\delta + 1)^3 \{ G(\xi_{\Delta}, A, m) - G(\xi_0, A, m) - (\xi_{\Delta} - \xi_0) F(\xi_0, A, m) \}$$

This result is more complicated than that for Case 1, and limiting conditions do not produce simple expressions.

### Discussion of the Slag-Flow Model

In order to develop a mathematical model for the unusual flow problems involving slag in slagging coal-gasification processes, an internal yield stress was introduced to account for the effect of undissolved coal ash in slags. The proposed slag-flow model also provides a logical approach to analyzing the flow of slag down either a refractory wall or a water-cooled shell surface (boiler tubes), with and without an internal yield stress. Calculations have indicated that an internal yield stress of  $28 \times 10^3$  Newtons/m<sup>2</sup> (4 lb<sub>f</sub>/in.<sup>2</sup>) can have a significant effect on the slag-flow characteristics. The slag-flow model employs an apparent thickness of the refractory wall to determine if a portion of the slag layer will be stationary. Solutions to the slag-flow problems have been established.

An important aspect of the internal yield stress concept is the flow down an inclined surface. The ridged portion of the liquid-slag layer,  $\delta - \Delta$ , increases inversely with  $\sin\theta$ . As the inclined surface is at the bottom of a gasification system, the mass flow rate arriving at the junction between the vertical and inclined surfaces is significant. In order to accommodate this flow on the inclined surface, that portion of the slag layer above  $T_\infty$  (the liquid-slag layer) must increase significantly. This, in turn, implies a corresponding increase in the thickness of the stationary slag layer. In addition, the "corner" between the vertical and inclined surfaces "fills-in" with stationary slag and generates a new surface that minimizes the effect of  $\sin\theta$  on the slag flow.

From inspection of the flow fields in Figs. 2 and 3, it is apparent that, for the same operating conditions, the thickness of a slag layer with an internal yield stress will be greater than that for a free-flowing slag. Consequently, the

heat transfer through the reactor walls will be reduced. However, the average temperature of the non-Newtonian slag layer will then be higher, thus enhancing the rate of formation of a homogeneous slag layer, and thereby reducing the internal yield stress.

The rheology of slag flow may play a significant role in the slag-flow problems encountered in slagging coal-gasification systems. This statement does not lessen the importance of the slag chemistry on these problems. However, the proposed shear stress model for slag is intended to present a new concept for consideration in future experimental studies of slag flow.

### References

- 1 Reid, W. T., and Cohen, P., "The Flow Characteristics of Coal-Ash Slags in the Solidification Range," *ASME Transactions*, Vol. 66, 1944.
- 2 Sage, W. L., and McIlroy, J. B., "Relationship of Coal-Ash Viscosity to Chemical Composition," *ASME JOURNAL OF ENGINEERING FOR POWER*, Vol. 82, 1960, pp. 144-155.
- 3 Watt, J. D., and Fereday, F., "The Flow Properties of Slags Formed from the Ashes of British Coals: Part 1. Viscosity of Homogeneous Liquid Slags in Relation to Slag Composition," *Jour. Inst. Fuel*, Vol. 42, Mar. 1969.
- 4 Watt, J. D., and Fereday, F., "The Flow Properties of Slags Formed from the Ashes of British Coals: Part 2. The Crystallizing Behavior of the Slags," *Jour. Inst. Fuel*, Vol. 42, Apr. 1969.
- 5 Barrick, S. M., and Moore, G. F., "Empirical Correlation of Coal Ash Viscosity With Ash Chemical Composition," *ASME Paper No. 76-WA/FU-3*, Nov. 1976.
- 6 Hoy, H. R., Roberts, A. G., and Wilkins, D. M., "Behavior of Mineral Matter in Slagging Gasification Processes," *Journ. Inst. of Gas Engrs.*, June 1965.
- 7 Winegartner, E. C., ed., "Coal Fouling and Slagging Parameters," *ASME Publication H86*, 1974.
- 8 Reid, W. T., and Cohen, P., "Factors Affecting the Thickness of Coal-Ash Slag on Furnace-Wall Tubes," *ASME Transactions*, Vol. 66, 1944.
- 9 Cohen, P., and Reid, W. T., "The Flow of Coal-Ash Slag on Furnace Walls," *Technical Paper 663*, Bureau of Mines, Gov't Printing Office, Washington, 1944.
- 10 Smith, V. L., "Coal Firing and Industrial Boiler Design—the Modern Approach," *ASME JOURNAL OF ENGINEERING FOR POWER*, Vol. 98, 1976, pp. 297-304.

### **K. W. Ragland**

Professor of Mechanical Engineering.  
Mem. ASME

### **R. P. Madding**

Assistant Professor,  
Engineering Extension.

### **R. K. Ham**

Professor of Civil and  
Environmental Engineering.

University of Wisconsin  
Madison, Wis. 53706

### **R. J. Vetter**

Principal Engineer,  
Department of Public Works,  
City of Madison, Wis.

### **M. L. Smith**

Consulting Engineer,  
M.L. Smith Environmental,  
Oak Brook, Ill.

# **Refuse-Derived Fuel Evaluation in an Industrial Spreader-Stoker Boiler**

*Municipal refuse-derived fuel and coal were cofired in a retrofitted 125,000 lb steam/hr (55,000 kg/hr) spreader-stoker boiler. Results from 19 tests, which include fuel characteristics, boiler performance, particulate and gaseous emissions, and trace element emissions, are reported. System design and economic considerations are also discussed.*

## **Introduction**

A national effort has been under way to improve municipal solid-waste management practices. This effort was prompted by such factors as unacceptable dumping practices, difficulty in siting new landfills, health considerations, and developing resource recovery and energy conservation technologies. The concept of resource recovery developed as a long-term objective for solid-waste disposal. Resource recovery can extend the life of existing landfills and assures long-term stabilization of disposal costs by making fixed capital investment now, and establishing markets for recovered products including an alternate energy source.

Production of refuse-derived fuel (RDF) is one method of resource recovery. RDF has the potential of generating income as a replacement fuel, as will be shown later in the article. The cost of refuse haul and disposal has risen to 15 to 20 dollars per ton at many regional landfills. Therefore, considerable economic incentive exists to consider RDF production as an option for improved municipal solid waste management.

Several North American cities recover energy from municipal solid waste, including Madison, Wisconsin; Ames, Iowa; Saugus, Massachusetts; Chicago, Illinois; Nashville, Tennessee; Hamilton, Ontario; Niagara Falls, New York; Albany, New York; Akron, Ohio; and Pueblo, Colorado.

Spreader-stoker boiler performance when cofiring coal and RDF has been investigated at Ames, Iowa [1, 2]. The Ames

municipal power plant has cofired RDF in a 7.5-MW and a 12.5-MW (electrical) stoker-spreader boiler at up to 50 percent RDF on a heat basis. The information reported in this paper supplements the Ames work and provides an evaluation of design and performance in an industrial setting.

The City of Madison, Wisconsin has developed a resource recovery facility that produces a refuse-derived fuel (RDF) as an energy product [3]. Madison's Resource Recovery Center processes 250 t (227,000 kg) of municipal solid waste daily on a single 50 t/hr (45,000 kg/hr) process line, which consists of a flail type primary shredder, ferrous recovery system, rotary screen separation system, secondary shredder, and pneumatic transport to RDF transfer trailers.

The RDF is hauled by trailer to the City's major fuel customer, Madison Gas and Electric Co., a local privately owned utility [4]. At Madison Gas and Electric the RDF is burned in suspension and replaces 10 percent of the coal in a 50-MW boiler. In addition, the City has been supplying Oscar Mayer Foods Corporation RDF on a test basis since June 1980 under a research grant from the U.S. EPA [5], the results of which are reported here. Oscar Mayer Foods Corporation is a national meat processor whose corporate offices and largest meat packing plant are located in Madison, Wisconsin. The operations include a power plant for cogeneration of process steam and electricity.

The retrofitting of the boiler began in March 1980 and was completed in May of 1980. The construction of the RDF Receiving and Feed Facility and the installation of the RDF feed equipment began in April 1980 and was completed in June 1980. Start-up and shakedown of the RDF system ran

Contributed by the Power Division for publication in the JOURNAL OF ENGINEERING FOR GAS TURBINES AND POWER. Manuscript received by the Power Division July 15, 1983.

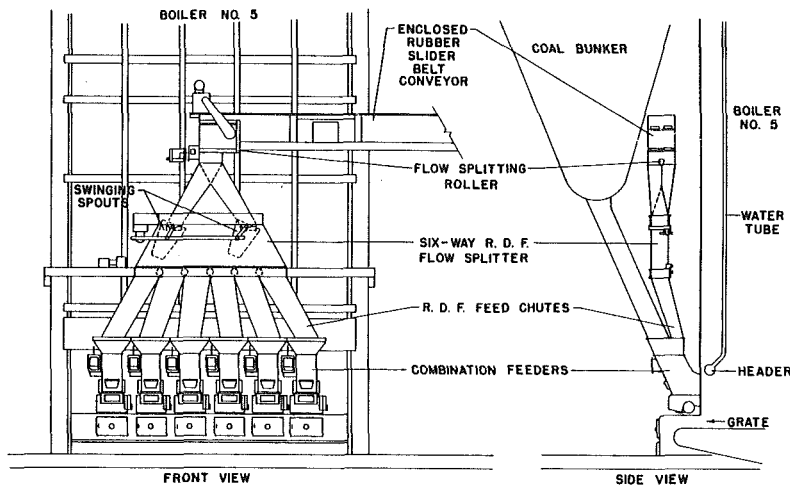


Fig. 1 RDF flow splitting and feed into the boiler

from June to October of 1980. The first cofired RDF and coal test run took place on October 16, 1980. Four cofired test runs were made between October 16, 1980 and November 11, 1980, when testing was suspended because of inclement winter weather. RDF was fired on a daily basis over the winter of 1980-1981 to gain additional operating experience. Formal testing was resumed on March 3 and was completed in May of 1981. RDF test firing has continued and is expected to become operational in 1983.

The project evaluated the operational and emission performance of a coal-fired industrial boiler when cofiring refuse-derived fuel at various boiler loads and RDF feed rates. The results of the test program are presented below. Further details of the project are reported in [5].

### Description of the Retrofitted Boiler and Feed System

The 125,000 lb/hr (56,700 kg/hr) boiler and traveling grate stoker design data are summarized in Table 1. The overfire air system was modified by Detroit Stoker. The original overfire air system consisted of eight jets each on the upper rear, lower rear, and upper front, and no jets on the lower front. Low-pressure air from a 7.5-Hp blower was used to cool the stokers, while a 20-Hp, high-pressure blower supplied the overfire air. These blowers were replaced by a 100-Hp blower. The front arch was rebuilt to accommodate 20 air jets and combination RDF coal feeders. The overfire air was more than doubled.

Emission control equipment consists of a mechanical multicyclone collector. Ash collection occurs at an ash pit below the grate, economizer ash hopper, and cyclone ash hopper. All collected ash is removed by pneumatic conveyor to an ash silo for subsequent disposal to a sanitary landfill. Fly ash reinjection was not used.

RDF is delivered by enclosed transfer trailers to a pilot receiving and storage building. A feed bin contains two augers that transfer the RDF to a slider belt for conveyance into the boiler house. Near the boiler, the RDF is split into two streams and falls into two sloping pant-leg type chutes to discharge into continually swinging spouts as shown in Fig. 1.

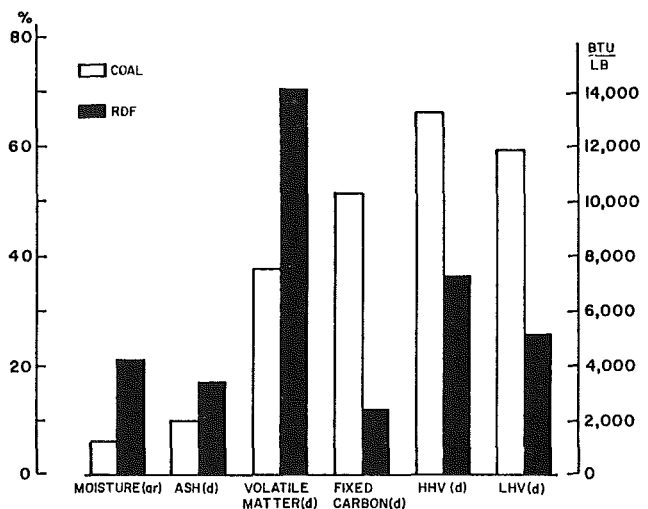


Fig. 2 Average proximate and heating value analysis of coal and RDF (ar = as received, d = dry basis)

Each of the swinging spouts feeds a set of three sloping chutes. The six feed chutes drop the RDF into six combination RDF and coal feeders. RDF falls into the feeder and is swept into the boiler by a rectangular jet of air emitted between the coal and RDF streams. Coal falls on a rotor and is thrown onto the grate.

### Fuel Characterization

Fuel sampling and analysis procedures were done according to ASTM procedures for RDF [6]. A highly volatile Illinois bituminous coal with an as-received higher heating value of  $12,450 \pm 290$  Btu/lbm ( $28,960 \pm 675$  kJ/kg) was used. The actual coal size was 90 percent greater than 2 mm and 10 percent greater than 15 mm. The higher heating value of the as received RDF was  $5780 \pm 760$  Btu/lbm ( $13,440 \pm 1770$  kJ/kg). The actual RDF size was 90 percent greater than 1.5 mm and 10 percent greater than 20 mm. The top size was 50

### Nomenclature

$a$  = decrease in boiler efficiency per increment of RDF  
 $C$  = fuel cost per million Btu output  
 $K$  = increase in capital and operating costs per ton RDF

$HV$  = heating value of fuel, Btu/lb (higher value, as received)  
 $M$  = mass fraction of fuel mixture  
 $N$  = boiler efficiency  
 $P$  = fuel price per ton

### Subscripts

$c$  = coal  
 $r$  = RDF  
 $rc$  = RDF and coal

**Table 1 Boiler design data**

Wickes boiler		
design steaming capacity	125,000 lb/hr	
design pressure	425 psi	
final steam temperature	660 °F	
boiler heating surface	13,865 ft <sup>2</sup>	
waterwall heating surface	2,540 ft <sup>2</sup>	
economizer heating surface	8,100 ft <sup>2</sup>	
furnace volume	8,150 ft <sup>3</sup>	
year built	1949	
Detroit stoker		
number of feeders		6
grate type		continuous front discharge
grate length (shaft to shaft)		18 ft-7 1/2 in.
grate width		17 ft-8 in.
effective grate area		284 ft <sup>2</sup>
recommended coal sizing		1 1/4 in. to 10 mesh
Overfire air		
upper rear:	16 jets 1 in. diam. located 10 ft. above grate, 30 deg below horizontal	
lower rear:	16 jets 1 in. diam. located 18 in. above grate.	
upper front:	16 jets 1 in. diam., 10 ft. above grate, 35 deg below horizontal	
lower front:	20 jets 7/8 in. diam. 1 ft. above grate	
discussion:	The overfire air system is separate from the underfire air system, but 1/2 of overfire goes to RDF feed. Approximately 1/3 of underfire air goes to cool gas burner and is introduced as overfire air	
soot blowing:	removed in 1951	
flyash reinjection:	none	
air preheater:	none	
cyclone collector:	western multicyclone installed in 1949	

**Table 2 Ultimate analysis of coal and RDF (as received)**

	Coal	RDF
Moisture	6.1 ± 1.4 <sup>a</sup>	20.9 ± 4.5 <sup>b</sup>
Carbon	68.4 ± 1.6	33.8 ± 3.7
Hydrogen	4.8 ± 0.2	4.5 ± 0.5
Nitrogen	1.4 ± 0.2	0.42 ± 0.07
Chlorine	0.15 ± 0.04	0.31 ± 0.09
Sulfur	3.3 ± 0.5	0.21 ± 0.03
Ash	9.5 ± 1.2	13.6 ± 2.4
Oxygen	6.2 ± 0.7	26.2 ± 2.2

<sup>a</sup>standard deviation based on 15 samples<sup>b</sup>standard deviation based on 13 samples**Table 3 Mineral analysis of fuel ash (percent by weight)**

Mineral	Coal ash	RDF ash
Silica SiO <sub>2</sub>	45.32	54.30
Alumina, Al <sub>2</sub> O <sub>3</sub>	19.48	14.44
Titania, TiO <sub>2</sub>	0.80	1.94
Ferric oxide, Fe <sub>2</sub> O <sub>3</sub>	23.26	6.54
Lime, CaO	3.70	10.84
Magnesia, MgO	0.85	2.97
Potassium oxide, K <sub>2</sub> O	2.13	1.65
Sodium oxide, Na <sub>2</sub> O	0.55	4.08
Sulfur trioxide, SO <sub>3</sub>	2.98	1.24
Phos. pentoxide, P <sub>2</sub> O <sub>5</sub>	0.19	1.14
Strontium oxide, SrO	0.01	0.00
Barium oxide, BaO	0.06	0.09
Manganese oxide, Mn <sub>3</sub> O <sub>4</sub>	0.05	0.34
Undetermined	0.52	0.43
	100.00	100.00
Alkalies as Na <sub>2</sub> O, dry fuel basis	0.22	0.80
Silica percentage	61.89	72.74
Base: acid ratio	0.47	0.37
ID (reducing) temp. (°F)	1940	2420
FT (reducing) temp. (°F)	2060	2490

mm and the mass mean size was 7.6 mm. The proximate analyses of the fuels are compared in Fig. 2. The RDF is higher in moisture, ash, and volatile matter and lower in fixed carbon and heating value than coal. As seen in Table 2, RDF is considerably lower in carbon and sulfur, slightly lower in

hydrogen, lower in nitrogen, higher in chlorine and much higher in oxygen content than coal.

Results of the mineral analysis of coal and RDF ash are given in Table 3. The main difference is the higher sodium content of RDF ash which indicates possible slagging potential in high temperature zones of the boiler. The ash contains clear, brown, and green glass which has low fusion temperature although the measured softening and fluid temperatures for RDF ash were considerably higher than the coal ash.

### Boiler Performance

Steam loads ranged from 73,000 to 110,000 lb/hr (33,000 to 50,000 kg/hr) during the tests. Maximum rated capacity was 125,000 lb/hr (56,700 kg/hr), however demand did not allow maximum operation. A minimum steam load of 45,000 lb/hr (20,000 kg/hr) on coal was maintained to prevent flame out in the event of RDF interruption. RDF replacement rates varied from 0 to 48 percent on a heat input basis. Twenty-one tests runs were made and a total of 600 tons (544,000 kg) of RDF was burned during the test program.

The boiler operating conditions for the test are summarized in Table 4. For the coal-only runs, overfire air averaged 25 percent of the total inlet air and the excess air averaged 61 percent. For the coal-plus RDF runs, overfire plus RDF feed air averaged 40 percent of the total inlet air, while excess air averaged 83 percent. Stack temperatures were 405–440°F (207–227°C). RDF feed air was usually less than the overfire air. Approximately 30 percent of the underfire air was diverted through gas burners for cooling purposes, as required by the manufacturer when the gas burners are not operating. Therefore, the actual underfire air was only 70 percent of that reported above. Underfire air plenum pressure was typically 0.25 in. water (6 mm water).

Results of the boiler efficiency tests are summarized in Table 5. The ASME PTC 4.1 procedure was followed using the heat loss method, since the fuel feed rates were not measured. The percent RDF on an input heat basis was determined by steadying out the boiler on coal and then

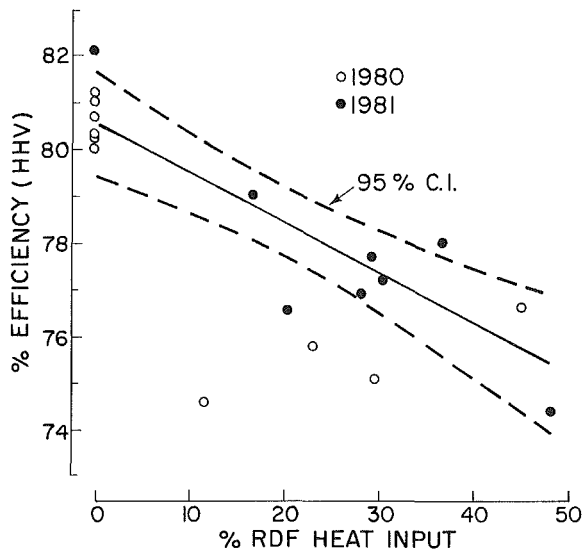
**Table 4 Boiler operating conditions**

Run no.	Steam load lbm steam/hr	% RDF (heat input basis)	Underfire air (SCFM) <sup>a</sup>	Overfire air (SCFM)	RDF feed air (SCFM)	Excess air %	Stack temp. °F
3	110,000	0	27,500	9,800	300	63	415
4	107,700	0	29,900	11,300	300	57	430
5	99,300	0	22,600	8,100	300	58	420
6	98,700	0	24,700	8,500	300	55	425
7	99,100	0	—	—	—	66	425
8	78,200	0	24,500	7,300	300	69	405
9	78,000	23	22,800	6,400	6,700	84	415
10	84,760	12	20,900	6,900	6,600	106	425
11	102,100	30	18,900	9,300	6,400	74	430
12	100,000	45	16,800	7,600	6,800	73	435
13	98,600	37	24,000	9,100	6,000	71	435
14	94,000	48	23,900	6,900	6,200	88	435
15	73,400	30	20,500	6,200	5,700	109	410
16	86,500	48	21,400	7,900	6,400	55	430
17	98,800	29	21,900	7,600	6,500	75	435
18	88,800	27	18,900	8,900	7,900	70	440
19	89,700	16	18,200	7,800	7,000	76	435
20	99,100	0	25,000	8,400	300	61	420
21	87,100	20	23,700	7,300	7,400	115	435

<sup>a</sup>Includes 30 % which is diverted to coal gas burners.

**Table 5 Heat losses and boiler efficiency**

Run no.	% heat loss due to				Boiler efficiency %
	Dry gas	Moisture in fuel	H <sub>2</sub> O from comb. of H	Comb. in ashes	
3	13.24	0.43	4.19	1.43	80.0
4	12.83	0.51	4.16	1.16	80.7
5	13.64	0.49	4.15	0.81	80.2
6	12.48	0.68	4.23	0.74	81.2
7	12.65	0.60	4.17	0.87	81.0
8	13.18	0.47	4.15	1.27	80.3
9	14.83	1.90	5.41	1.34	75.8
10	17.77	1.16	4.86	0.93	74.6
11	14.77	2.86	5.36	1.23	75.1
12	12.71	3.01	6.41	1.13	76.1
13	12.55	1.96	5.81	0.98	78.0
14	13.92	1.80	6.25	0.83	76.5
15	14.28	1.33	5.68	0.84	77.2
16	16.02	1.62	6.46	0.85	74.4
17	13.69	1.38	5.49	1.04	77.7
18	14.10	1.88	5.32	1.10	76.9
19	13.16	1.23	4.94	1.01	79.0
20	11.35	0.86	4.16	0.82	82.1
21	14.66	1.72	5.07	1.39	76.5



**Fig. 3 Effect of RDF heat input on boiler efficiency (based on higher heating value)**

bringing the boiler up to a higher steam load on RDF. The dry gas loss is the largest contributor to boiler inefficiency. Loss due to moisture in the fuel and hydrogen formed water increases with increased RDF. As shown in Fig. 3, the boiler efficiency decreased from 80.6 to 75.3 percent as the RDF percentage increased from 0 to 48 percent on a heat input basis. This represents a 1 percent decrease in boiler efficiency for each 10 percent of the heat load replaced by RDF. The curves exclude the 1980 RDF data since conditions were changing during the tests and steady-state operation was not achieved. The decrease is statistically significant as indicated by the 95 percent confidence interval lines. The linear regression equation is boiler efficiency = 80.6 - 0.109 (percent RDF heat load replacement). If the lower heating value is used the boiler efficiency is 85 percent with 100 percent coal and decreases only 1 percent at 48 percent RDF. Correlations with excess air and steam load were not statistically significant.

Boiler control and response was not compromised by cofiring RDF. The steam load was easily held to within five percent of the desired load. Visual observation indicated that about 1/3 of the RDF burned in suspension above the grate and 2/3 fell onto the grate. Clinker formation was not serious. Furnace wall deposits were relatively light, but oc-



**Table 6 Summary of stack emissions**

Run	PM (lb/10 <sup>6</sup> Btu)	C <sup>a</sup> (%)	O <sub>2</sub> (ppm)	HCT <sup>b</sup> (ppm)	CO <sup>b</sup> (ppm)	NO <sup>b</sup> (ppm)
3	0.64	68	8.6	—	80	—
4	0.76	37	8.0	275	85	—
5	—	—	8.0	—	—	—
6	0.64	—	7.8	—	—	—
7	0.80	61	8.6	—	—	—
8	0.63	69	9.0	175	—	—
9	0.87	40	10.0	275	—	—
10	1.10	29	11.0	—	120	320
11	0.97	26	9.0	400	105	320
12	1.28	—	9.0	250	180	280
13	0.76	23	8.9	—	—	—
14	0.69	18	10.0	—	—	—
15	0.63	25	11.1	506	—	—
16	0.79	13	10.1	250	—	—
17	0.70	—	9.3	200	—	—
18	0.79	29	8.9	250	—	—
19	0.71	43	9.0	—	90	295
20	0.74	51	8.1	—	—	—
21	0.60	31	11.4	230	133	315

<sup>a</sup>Corrected to 3 % O<sub>2</sub><sup>b</sup>Combustibles in fly ash**Table 7 Cascade impactor measurements of fly ash: cumulative percent less than d<sub>50</sub>**

d <sub>50</sub> (microns)	Coal-only (Run 2)	Coal + RDF (Run 17) <sup>a</sup>
5	22	20
2	14	16
1	10	13
0.6	7	11
0.3	5	8

<sup>a</sup>45% RDF by weight or 29% of heat load by RDF

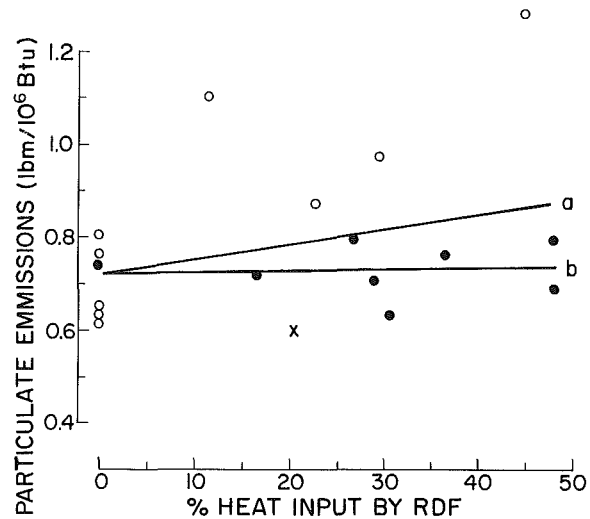
curred on each wall. Deposits were thickest on the back wall around the gas burner openings. Wall deposits were negligible above 15 ft (4.5 m). No deterioration of the furnace grates was observed. The size distribution of the bottom ash did not change significantly [7].

### Stack Emissions

Total particulate emissions were measured according to EPA Method 5 procedures. The sampling point was 13 ft (4 m) above the i.d. fan in the 7.5-ft (2.3-m) stack. It was not possible to sample further up the stack. Two 24-point traverses were made with 2 min at each point for each test run. Six coal-only particulate tests ranged from 0.64 to 0.80 lb/10<sup>6</sup> Btu (0.28 to 0.35 mg/kJ) as shown in Table 6. Twelve coal plus RDF tests ranged from 0.60 to 1.28 lb/10<sup>6</sup> Btu (0.26 to 0.55 mg/kJ). The 1980 coal plus RDF showed higher particulate emissions, probably because of somewhat higher ash content of the RDF and inexperience with RDF by the boiler operators. Also, 1981 testing was started 1 hr after RDF was introduced to provide steadier conditions. Particulate emissions are plotted versus percent RDF in Fig. 4. A linear regression line is plotted using all the data, which shows a slight increase in particulate emissions with percent RDF. If the 1980 RDF data are excluded, the linear regression line has a zero slope indicating no increase of particulate emissions with increasing RDF. The results are not statistically significant. The correlation coefficient is only 0.3.

It is interesting to note that the fly ash averaged 57 percent combustibles in the coal only tests, whereas with RDF the fly ash averaged only 24 percent combustibles (see Table 6). This may be due to increased volatile combustion when burning RDF. This effect helps to explain why the particulate emissions do not increase significantly when burning RDF even though the total ash increased.

The size distribution of the fly ash was measured using a Pollution Control System Corporation cascade impactor. As shown in Table 7, the coal plus RDF test has a slightly greater percentage of submicron particles.



**Fig. 4 Particulate emissions versus heat input from refuse-derived fuel. (Open circles are 1980 data. Closed circles are 1981 data. X represents 4-in. nominal size RDF, Run 21. (a) is linear fit using all data except Run 21. (b) is linear fit excluding 1980 RDF data and Run 21.**

Gaseous emissions were measured in the following way. A modified EPA method 6 [8, 9] was used for HCl. The sample was collected in a sodium hydroxide solution and titrated with mercuric nitrate solution. Oxygen was measured with a Teledyne model 980 fuel cell instrument. Carbon monoxide was measured with a Sensors, Inc. infrared analyzer. Nitric oxide was measured with a Horiba model P-12 infrared analyzer. Sulfur dioxide was measured following EPA method 6; however, the procedure was done incorrectly and the results are not reported.

Hydrogen chloride emissions averaged 225 ppm (corrected to 3 percent O<sub>2</sub>) with coal only, while the coal plus RDF tests ranged from 200–500 ppm (see Table 6). The coal averaged 0.15 percent chlorine as received, while the RDF averaged 0.31 percent chlorine. Analysis of the ash indicated that about 1 percent of the chlorine was removed in the ash [5, 7]. The average emission rate for the coal plus RDF tests was 0.33 lb HCl/10<sup>6</sup> Btu compared to 0.26 lb HCl/10<sup>6</sup> Btu for coal only (0.14 to 0.11 mg/kJ). Carbon monoxide average 95 ppm for the coal only tests and 125 ppm for the coal plus RDF tests. Nitric oxide tests averaged 300 ppm and showed no trend with increasing RDF. Assuming that no thermal NO is formed, this indicates that less than 1/3 of the fuel bound nitrogen was converted to NO. Analysis of the ash [5] indicated that only 1–2 percent of the sulfur was captured by the ash (including

bottom, economizer, cyclone, and fly ash). This implies that essentially all of the sulfur in the fuel is emitted as sulfur oxides.

### Trace Elements

Instrumental Neutron Activation Analysis (and Atomic Absorption Spectrophotometry for lead and cadmium) for 63 elements in the fuel and ash is reported elsewhere [5,7]. Twelve of the elements measured are of possible consideration from either water quality or air emissions points of view [10, 11], and these elements are summarized in Table 8. RDF has higher concentrations of Ba, Cd, Cr, Cu, Hg, Mn, Pb, and Zn, while coal has higher concentrations of As and Se. The data are inconclusive regarding Ag and Sb because of detection limits.

Lead and zinc have the highest levels of trace elements in the fly ash. A mass balance indicates that most of the lead and zinc are contained in the fly ash rather than in the bottom ash, economizer, or cyclone ash, or as gaseous emissions. Lead and zinc emissions were about 1 lb/hr (0.5 kg/hr) when cofiring coal and RDF, which is an increase of 5-10 times over burning coal only. The concentration of Pb and Zn in the fly ash has been noted by other investigations [12]. The other elements are distributed among the bottom, economizer, cyclone, and fly ash. The exception is mercury for which a mass balance indicates that 90 percent was volatilized [5].

### Economic Considerations

Based on the actual construction and modification costs for the test program, capital costs for a permanent installation for a 5 t/hr (4,500 kg/hr) RDF system would cost 690,000 dollars (1981 prices). This includes building contracts, bin-auger assembly, conveyor system, six-way feed splitter system, modification of the existing combination feeders and overflier air system, and other equipment and engineering costs. Annual operating costs for the RDF receiving and feed system based on 5 t/hr, 12 hrs/day, 5 days/week for an annual utilization of 15,000 t are estimated to be 90,000 dollars or 6 dollars/ton.

The price paid for RDF will vary depending on the structure of the agreement between the RDF producer and the fuel user. The value of RDF as a supplemental fuel can be established by comparing costs to the user to produce process steam or power with and without supplemental RDF. The value of RDF may be obtained by assuming equivalent fuel costs per unit heat output less any increased incremental capital and operating costs when using RDF. The heating value of the RDF is typically less than coal. The boiler efficiency is generally reduced when RDF is burned. These factors reduce the dollar value of RDF per ton compared to coal. In the Appendix a general equation is developed relating these factors. The result is

$$P_r = P_c (HV_r / HV_c) (1 - a / N_c) - K \quad (1)$$

For our tests,  $a = 0.1$ ,  $N_c = 0.806$ ,  $HV_r = 5780$  Btu/lb, and  $HV_c = 12450$  Btu/lb. Therefore equation (1) becomes

$$P_r = 0.41 P_c - K \quad (2)$$

The price of the coal was 52 dollars/t. The factor  $K$  consists of operating costs for RDF of 6 dollars/t plus capital costs for the RDF modifications of 690,000 dollars amortized over 10 years at 8 percent interest. Based on 15,000 tons RDF per year the capital costs is 6.90 dollars/ton. For these assumptions, the value of RDF at the boiler site is 21.30 dollars less 12.90 dollars, or 8.40 dollars per ton for 1981 prices.

### Summary and Conclusions

RDF prepared from municipal solid waste can be ef-

Table 8 Elemental analyses of fuels and ash  
(conc. in ppm unless otherwise noted)

Element	Bottom ash		Economizer ash		Cyclone ash		Fly ash	
	Coal only	Coal + RDF	Coal only	Coal + RDF	Coal only	Coal + RDF	Coal only	Coal + RDF
Ag	<0.4	<1.3	<1.0	<0.8	<0.9	≤1.3	≤12	12
As	≤5	≤8	60	80	35	40	345	115
Ba	≤26	660	340	820	420	730	620	1270
Cd	1.2	6	5	7	<3	15	55	360
Cr	12	170	100	185	105	210	345	350
Cu	≤50	≤340	<140	<270	<130	<280	<1230	<2670
Hg	<0.6	<1.4	<1.2	<0.9	<1.1	<1.1	5	29
Mn	26	460	135	1260	170	1780	210	340
Pb	44	100	85	290	260	650	2560	1.89%
Sb	≤2	≤4.5	2.6	≤7	6	≤20	220	800
Se	2	<1.9	<1.2	<0.9	1.3	2.5	10	30
Zn	<16	<130	<15	75	<15	140	2900	1.71%

Note: Coal: average of 10 samples

RDF: average of 11 samples

Ash: coal only; average of runs 6 and 8 for bottom ash, economizer ash, and cyclone ash; run 20 for fly ash coal + RDF; average of runs 9, 11, 12, 16, and 18 for bottom ash, economizer ash, and cyclone ash, with average RDF heat input of 35% and average RDF mass input of 56%; average of runs 15, 16, 18 and 19 for fly ash, with average RDF heat input of 30% and average RDF mass input of 47%.

< all samples below detection limit

≤ at least one sample above detection limit

fectively burned with coal in a retrofitted industrial spreader-stoker boiler rated at 125,000 lb steam/hr (55,000 kg/hr) equipped with a mechanical multicyclone particulate collector. RDF replacements rates up to 48 percent on a heat input basis were tested. For a steam load of 100,000 lb/hr (45,000 kg/h) with 33 percent of the steam load carried by RDF, this represents a coal feed rate of 3.9 t/hr (3,600 kg/hr) and an RDF feed rate of 4.2 t/hr (3,900 kg/hr).

The RDF, as produced for the test program, had an average heating value of 5,780 Btu/lb (13,440 kJ/kg) with 21 percent moisture and 14 percent ash as received. The RDF size was 90 percent greater than 1.5 mm and 10 percent greater than 20 mm. The top size was 50 mm.

Boiler efficiency decreased 1 percent for each 10 percent of heat load replaced by RDF. This decrease in efficiency was due primarily to additional moisture in the RDF and additional moisture from combustion of hydrogen in the RDF.

Particulate emissions ranged from 0.60 to 1.28 lb/million Btu (0.26 to 0.55 kg/kJ). Fall 1980 tests cofiring RDF exhibited some excessive particulate emissions. Spring 1981 tests cofiring RDF showed no increase in particulate emissions as compared to the coal only tests. It is believed that operating experience and lower RDF ash content contributed to the improvement in the later tests. Lead and zinc were each 2 percent of the total particulate emissions. Other trace metals were each 1 to 3 orders of magnitude lower.

When cofiring RDF and Illinois coal at 90,000 lb steam/hr (40,000 kg/hr) with 33 percent of the heat load carried by the RDF, the hydrogen chloride emissions were increased 50 percent to 0.33 lb/million Btu (0.14 mg/kJ), the carbon monoxide emissions were insignificant, and the nitric oxide emissions remained about the same at 0.4 lb/million Btu (0.17 mg/kJ). The sulfur dioxide would theoretically be reduced in half due to the lower sulfur in the RDF.

The RDF receiving and feed system operated dependably, providing a constant flow of RDF to the boiler. The combination feeders distributed the RDF evenly throughout the boiler, maintaining a constant steam load.

The RDF storage and feed system at the Oscar Mayer Plant could be expanded to burn 15,000 t/yr ( $13.6 \times 10^6$  kg/yr) of RDF while operating at 5 t/hr, 12 hr/day, 5 days/week. The projected operating costs to burn 15,000 t of RDF annually in the system described is 6 dollars/t and the capital cost is 6.90 dollars/t. The replacement value of the RDF is estimated to be 8.80 dollars/t (for 1981 prices).

### Acknowledgments

This report was prepared for the Environmental Protection Agency under Grant No. 806328-01-3. Mr. Robert Olexsey, Fuels Technology Branch, Industrial Environmental Research Laboratory, Cincinnati, Ohio, and Mr. Michael Black, Incineration Research Branch, Industrial Environmental Research Laboratory, Cincinnati, Ohio, served as EPA Project Officers. Cooperation of the Oscar Mayer Foods Corporation is gratefully acknowledged, especially Thomas Lisi, John Blandford, Robert Roemer and William Selbo. Graduate student Svein Riibe was a major contributor to the project. University personnel and students Harold Olsen, Philippe Maraval, Carlos Richer, Steven Johnson, Stephen Geisler, Ted Wilinski, Janet Krauze, and Jeff Horning assisted with data collection and analysis. City of Madison personnel who assisted were Kenneth Brunner, Harry Chamberlain, Thaddeus Jagelski, Mark Komurka, and Marsha Peterson. The research grant would not have been

possible without the initial work of Gary L. Boley, formerly of the City of Madison's Engineering Division.

### References

- Hall, J. L., et al., "Operation and Emissions of a Stoker Fired Boiler While Burning Refuse Derived Fuel and Coal Mixtures," ASME Paper 78-WA/APG-2, 1978.
- Hall, J. L., Joensen, A. W., et al., "Evaluation of the Ames Solid Waste Recovery System," Report 600/7-79-222, Parts II and III, U.S. EPA, Cincinnati, Ohio, 1979.
- Boley, G. L., and Smith, M. L., "Development and Implementation of a Resource and Energy Recovery Program for the City of Madison, Wisconsin," *Proceedings Second International Conference and Trade Exhibition Materials and Energy from Refuse*, Berlin, West Germany, Vol. 1, 1979, pp. 195-203.
- Barlow, K. M., Boley, G. L., and Smith, M. L., "Design, Evaluation and Operating Experience of the City of Madison—Madison Gas and Electric Company Energy Recovery Project," *Proceedings ASME National Waste Processing Conference*, Washington, D.C., 1980, pp. 411-425.
- Vetter, R. J., et al., "Test Firing Refuse Derived Fuel in an Industrial Coal-Fired Boiler," U.S. EPA report to be published.
- "Draft Procedures for Analysis of Derived Fuel," American Society for Testing and Materials, 1979.
- Riibe, S. M., "Test Firing Refuse-Derived Fuel in an Industrial Stoker-Fired Boiler," M.S. thesis, Department of Civil and Environmental Engineering, University of Wisconsin, Madison, Wis., July 1981.
- "Methodology for the Determination of HCl Emissions for Stationary Sources," U.S. EPA preliminary report, Research Triangle Park, N.C., 1977.
- Rollins, R., and Homolya, J. B., "Measurement of Gaseous Hydrogen Chloride Emissions from Municipal Refuse Energy Recovery Systems," *Env. Sci. Tech.*, Vol. 13, No. 11, 1979, pp. 1380-1383.
- "Quality Criteria for Water," U.S. Environmental Protection Agency, Washington, D.C., July 1976.
- "Hazardous Waste Management Systems Part III: Identification and Listing of Hazardous Waste," U.S. Environmental Protection Agency, Federal Register, May 1980, pp. 33084-33136.
- Kaakinen, J. W., et al., "Trace Element Behavior in Coal-Fired Power Plant," *Env. Sci. Tech.*, Vol. 9, 1975, pp. 862-869.

## APPENDIX

### Equations for Calculating RDF Value

The fuel cost per million Btu output when burning coal only is

$$C_c = 500 P_c / N_c HV_c \quad (A1)$$

The fuel cost per million Btu output when burning RDF and coal is

$$C_{rc} = (500 / N_{rc}) (M_r P_r / HV_r + M_c P_c / HV_c) \quad (A2)$$

For equivalent pricing (excluding capital costs and operating costs equation (1) and (2) are equated

$$P_c / N_c HV_c = 1 / N_{rc} (M_r P_r / HV_r + M_c P_c / HV_c) \quad (A3)$$

The price of RDF may be obtained from equation (A3) provided two additional relationships are utilized. First, by definition, it follows that

$$M_r + M_c = 1 \quad (A4)$$

Second, assuming that boiler efficiency decreases linearly with increasing percentage of RDF (see Fig. 2),

$$N_r = N_c - a M_r \quad (A5)$$

Substituting equations (A4) and (A5) into (A3) and solving for the price of RDF per ton

$$P_r = P_c (HV_r / HV_c) (1 - a / N_c) \quad (A6)$$

Finally, including an increase in capital and operating costs per ton of RDF, the value of RDF is

$$P_r = P_c (HV_r / HV_c) (1 - a / N_c) - K \quad (A7)$$

Equation (A7) shows that the market value of the RDF depends on the heating value of the RDF and coal.

# The Influence of Fuel Hydrogen Content Upon Soot Formation in a Model Gas Turbine Combustor

T. T. Bowden

J. H. Pearson

R. J. Wetton

Shell Research Limited,  
Thornton Research Centre,  
Chester, England

*The sooting tendencies of various fuel blends containing either single-ring or polycyclic aromatics have been studied in a model gas turbine combustor at a pressure of 1.0 MPa and varying values of air/fuel ratio. Sooting tendencies were determined by flame radiation, exhaust soot, and infra-red absorption measurements. The results of this study have indicated that, even for fuels containing high concentrations of naphthalenes or tetralins (>10 percent v), fuel total hydrogen content correlates well with fuel sooting tendency. The present results are explained by a hypothesis that assumes that the majority of soot is formed in regions of high temperature, low oxygen content, and low fuel concentration, e.g., the recirculation zone.*

## Introduction

Recent work utilizing a number of experimental configurations, including well-stirred reactors [1], model combustors [2, 3, 4], and full-scale combustors [5, 6, 7, 8], has indicated that fuel total hydrogen content provides an effective means of predicting the sooting tendencies of many fuels in gas turbine equipment. However, there have been suggestions that this may not be the case for fuels containing significant concentrations of fused ring polycyclic aromatics, such as naphthalenes and tetralins [9, 2, 3]. As it is possible that some future aviation turbine fuels may contain higher concentrations of polycyclic aromatics than present day fuels, it is important to determine whether a compositional limit exists for these components below which hydrogen content will remain a satisfactory predictor of combustion performance. That such a limit may exist has been suggested by earlier work [3]. However, these studies were performed at a single value of air/fuel ratio and since other results [2] have demonstrated that air/fuel ratio can significantly influence the response of combustion systems to fuel molecular composition, work is continuing on the investigation of the sensitivity of fuel combustion performance to molecular composition over a wider range of air/fuel ratios than previously reported.

In particular, the effect on combustion performance of increasing the concentration of naphthalenes and tetralins in aviation turbine fuels, as compared to fuels containing only single-ring aromatics, has been studied.

## Experimental

The high-pressure aviation combustion facility and

associated instrumentation have been fully described elsewhere [2, 3]. Recently, the range of measurements taken have been extended to include determinations of flame spectral emissivities, and hence soot concentrations, by a scanning infrared emission/absorption technique. This latter system has been incorporated to overcome a shortcoming associated with the correlation of combustion performance with flame total radiation, a technique commonly used in the study of combustor response to fuel composition. The reason for this shortcoming is easily appreciated when the relationships between flame temperature, flame emissivity, and flame soot concentrations are considered.

Making the assumptions that the radiation from the flame is predominantly from soot and that the soot acts as a gray emitter, flame radiation, flame emissivity, and soot concentration are related by equations of the form

$$R_f = \sigma e_f T_f^4 \quad (1)$$

$$e_f = 1 - \exp(-klc) \quad (2)$$

- $R_f$  = flame radiation
- $e_f$  = flame emissivity
- $T_f$  = flame temperature
- $k$  = absorption coefficient
- $l$  = optical path length
- $c$  = soot concentration
- $\sigma$  = Stefan-Boltzmann constant

From the form of equation (2), it can be seen that, as soot concentration increases, so emissivity tends toward 1. Ultimately, therefore, emissivity and hence radiation will become independent of the concentration of soot produced by a fuel during combustion, with the result that measurements of flame radiation will cease to truly measure variation in fuel-sooting tendency. As this situation is most likely to occur at high combustion pressures and/or low values of air/fuel

Contributed by the Gas Turbine Division of THE AMERICAN SOCIETY OF MECHANICAL ENGINEERS for presentation at the 29th International Gas Turbine Conference and Exhibit, Amsterdam, The Netherlands, June 4-7, 1984. Manuscript received at ASME Headquarters December 13, 1983. Paper No. 84-GT-6.

ratio, it is essential that measurements at such conditions include a determination of emissivity.

The position is further complicated when it is realized that neither of the assumptions made earlier regarding flame radiation is truly valid. Soot does not act as a gray emitter, i.e., it shows a marked variation in emissivity with wavelength [10], neither does the soot provide the only source of radiation from a flame, since gases such as water vapor and carbon dioxide can contribute significantly to flame radiation. To overcome these inaccuracies, measurements of emissivity need to be made over narrow wavelength intervals and, if contributions from sources of radiation other than soot are to be avoided, these wavelengths must be ones in which absorption bands of water or carbon dioxide are either absent or very weak.

**Theory and Experimental Method Utilized for Emission/Absorption Measurements.** The orientation of the optical system of the IR emission/absorption spectrometer relative to the combustor is shown in Fig. 1.

The experimental procedure and theory involved in emission/absorption measurements has been described by other workers [11] and only a brief mention will be given here.

For the absorption measurement, a reference source is employed behind the flame tube. The transmitted reference source intensity,  $I(\lambda)$ , at wavelength,  $\lambda$ , is equal to the reference intensity,  $I_o(\lambda)$ , times the fraction of  $I_o(\lambda)$  remaining after absorption in the flame, i.e.,

$$I(\lambda) = I_o(\lambda)(1 - a(\lambda)) \quad (3)$$

where  $a(\lambda)$  is the spectral absorptivity of the gas, which for a gas in local thermal equilibrium (l.t.e.) equals the spectral

emissivity  $\epsilon(\lambda)$  at the same wavelength. Hence,  $\epsilon(\lambda)$  may be calculated once  $I(\lambda)$  and  $I_o(\lambda)$  have been measured.

The next parameter to be determined is the gas spectral emission  $I_g(\lambda)$ . From Kirchoff's radiation law, which applies for gases in l.t.e., the ratio of the gas spectral emission,  $I_g(\lambda)$ , to the gas emissivity,  $\epsilon(\lambda)$ , at the same wavelength is equal to the spectral emission,  $I_b(\lambda)$ , of a black body at the same temperature, i.e.,

$$I_b(\lambda) = I_g(\lambda) / \epsilon(\lambda) \quad (4)$$

where

$$I_b(\lambda) = C_1 \lambda^{-5} \left[ \exp\left(\frac{C_2}{\lambda T_g} - 1\right) \right]^{-1} \quad (5)$$

$C_1$  and  $C_2$  are the first and second radiation constants. The absolute gas temperature  $T_g$  may then be obtained, averaged along the line of sight, as

$$T_g = \frac{C_2/\lambda}{\ln\left[1 + \frac{I_o - I}{AI_g} \exp\left[\frac{C_2}{\lambda T_b} - 1\right]\right]} \quad (6)$$

where  $T_b$  is the black-body furnace temperature.

In the present arrangement, the black-body reference source also provides an absolute calibration once allowances for apertures, window absorption, and inverse square law are made via the constant  $A$  in equation (6). Since  $\epsilon(\lambda)$  and  $I_g(\lambda)$  are both wavelength-dependent, the method has to be monochromatic.

In the present work, the monochromator used was a Spex "Minimate" instrument having a 50 line/mm grating. A Pye Unicam IR-50 Goly cell detector with a thallium-bromiodide window was used and chopped at 15 Hz for optimum signal/noise ratio. Detector signals were amplified before their input to a Bentham Type 223 phase-sensitive detector. Phase reference was provided by variable frequency Bentham 218F optical choppers. Analogue output voltages from the phase-sensitive detector were digitized and stored by a Hewlett-Packard 9845T microcomputer which served to both treat the data and control the monochromator Spex Minidrive 1673 stepping motor. Reference radiation signals  $I_o(\lambda)$  were provided by a Land, Type LCF, furnace operated at 1450°C. The furnace emissivity over the wavelengths of interest was measured, by comparison with an Electro-Optical Industries, Inc., type WS155 black-body standard, to be 0.99. Utilizing the chopper between the flame-tube and the black-body furnace,  $I(\lambda)$  was measured by the Goly cell detector. For the measurement of  $I_g(\lambda)$ , the chopper between the flame and the monochromator was used.

Radiation from both the flame and the reference source was transmitted to the monochromator via a fiber optic light guide, this method was utilized to eliminate misalignment between the flame tube and the monochromator caused by vibration and thermal expansion of the combustor.

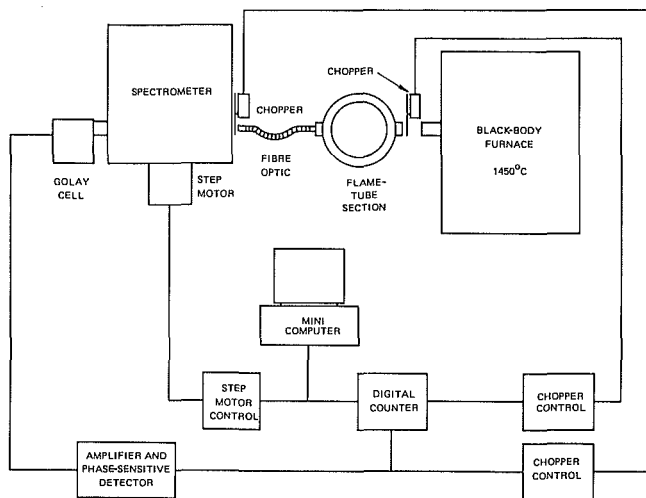


Fig. 1(a) Experimental configuration for emission/absorption determinations

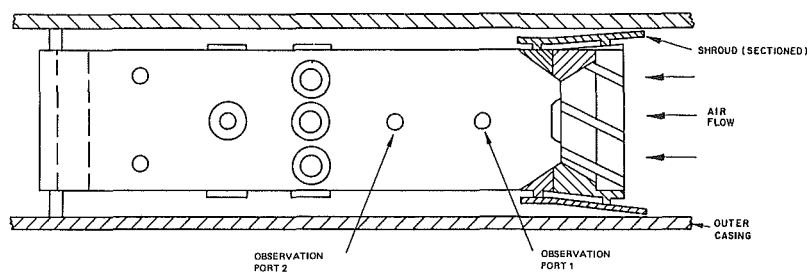


Fig. 1(b) Small-scale flame tube showing observation ports for flame radiation and emission/absorption measurements

**Table 1 Properties of fuel blends**

		Jet A1	Jet A1 + 5% kerex	Jet A1 + 10% kerex	Jet A1 + 15% kerex	Jet A1 + 20% kerex	Jet A1 + 5% tetralin	Jet A1 + 10% tetralin	Jet A1 + 5% 1-methyl-naphthalene	Jet A1 + 10% 1-methyl-naphthalene
[H] content, %w		13.77	13.62	13.56	13.40	13.28	13.53	13.32	13.41	13.06
Aromatics, %v		18.8	22.56	24.18	27.85	32.26	22.26	25.93	22.80	25.61
Smoke point, mm		27	23	21	19	19	22	19	21	17
Naphthalene content, %v		2.64	3.23	3.02	3.1	3.37	2.39	2.63	8.07	13.1
Specific gravity		0.7962	0.8078	0.8101	0.8143	0.8170	0.8105	0.8188	0.8132	0.8255
Vk at 40°C, cSt		1.241	1.264	1.248	1.261	1.242	1.272	1.277	1.280	1.290
ASTM Dist., °C										
IBP		159.5	165.0	164.5	167.0	162.5	158.5	160.0	158.5	163.0
10%		173.5	176.5	176.5	179.0	177.0	174.0	175.0	175.0	178.5
20%		184.5	183.0	182.5	185.0	183.0	182.0	182.0	181.5	186.5
30%		192.0	189.0	188.5	190.0	188.0	187.0	188.5	188.5	193.5
40%		199.0	194.5	193.5	195.0	193.5	193.5	193.5	195.0	200.5
50%		205.0	200.0	199.5	200.0	198.5	199.5	199.0	200.5	207.5
60%		210.5	206.0	205.0	206.0	204.5	205.5	204.5	207.5	213.5
70%		217.0	212.5	211.5	212.5	210.5	212.5	210.5	214.5	220.0
80%		225.0	221.0	219.0	220.0	218.0	220.0	218.5	222.0	227.5
90%		234.0	230.5	229.5	230.0	228.5	231.5	229.9	231.0	236.5
FBP		249.0	249.5	248.0	249.5	249.5	249.5	250.0	249.5	251.5

Soot concentrations within the combustor were calculated from the relationship between spectral absorption coefficient and soot volume fraction [10]

$$k_\lambda = \frac{36\pi nK}{(n^2 - K^2 + 2)^2 + 4n^2K^2} \frac{f_v}{\lambda} \quad (7)$$

where  $f_v$  = volume fraction of soot, and  $n$  and  $K$  are the constants of the complex refractive index of soot ( $m = n - iK$ ). The refractive indices used were calculated from the dispersion equations presented by other workers [12]; these equations provide the most accurate representation of soot optical properties derived to date. The spectral absorption coefficient was obtained from the spectral emissivity using the equation

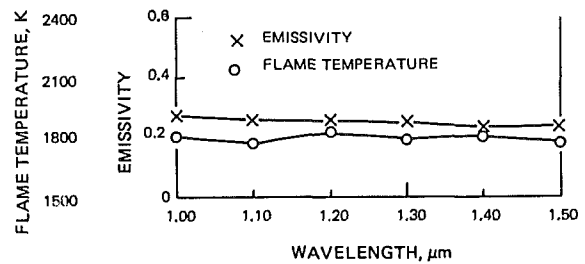
$$\epsilon_\lambda = 1 - \exp(-k_\lambda l) \quad (8)$$

where  $l$  = optical pathlength. Using a density for soot of  $1.86 \times 10^3 \text{ kg m}^{-3}$  [13], a mass concentration of soot can be determined.

In order to minimize signal noise, the experimental procedure adopted was to step the monochromator, automatically, to discrete wavelengths, i.e., 1, 1.1, 1.2, 1.3, 1.4, and 1.5  $\mu\text{m}$ , and signal average over approximately 500 separate readings at each value of wavelength.

A total of nine fuels were utilized in the experimental program, five of the fuels containing varying amounts of single-ring aromatics, obtained by blending a standard Jet A1 with a highly aromatic solvent, the other four fuels contained 5 and 10 percent wt tetralin and 5 and 10 percent wt 1-methylnaphthalene, respectively. Details of the test fuels are given in Table 1. The fuels were burnt at combustion conditions of 1.0 MPa, 400°C inlet air temperature and air/fuel ratios of 50/1, 45/1, and 40/1. In addition to the exhaust soot concentrations, flame radiation, from observation port 1, and flame-tube temperatures were measured at each condition and with each fuel. For all the experiments, the monochromator was aligned with observation port 2 and viewed a region of the combustor which earlier work, utilizing thermocouple scans, had shown to have an essentially flat temperature profile. It is preferable that the monochromator should view through such a region, since large temperature gradients make the interpretation of properties determined by integration across the line of sight very difficult.

In order to compensate for run-to-run variation, test fuels were burnt in groups of two, bracketed by a reference fuel run, i.e.,  $R, T_1, T_2, R$ , and the results for the test fuel blends were nondimensionalized with respect to the reference fuel as follows:



JET A1 AFR 45/1 PRESS 1 MPa AIR TEMP 400°C

WAVELENGTH/ $\mu\text{m}$	EMISSIVITY	TEMP./K	SOOT	Fv
1.0	0.273	1808	2.11E	-06
1.1	0.259	1770	2.05E	-06
1.2	0.254	1820	2.06E	-06
1.3	0.250	1790	2.08E	-06
1.4	0.234	1809	1.98E	-06
1.5	0.240	1777	2.01E	-06
MEAN	0.252	1796	2.05E	-06

**Fig. 2 Trace of emissivity and temperature as derived from emission absorption technique**

$$\text{Normalized flame-tube temperature (NFTT)} = \frac{T_{\text{test}} - T_{\text{ref}}}{T_{\text{ref}} - T_{\text{int}}} \quad (9)$$

where  $T_{\text{test}}$  = flame tube temperature produced by test fuel  
 $T_{\text{ref}}$  = flame tube temperature produced by reference fuel  
 $T_{\text{int}}$  = inlet air temperature

$$\text{Normalized flame radiation temperature (NFR)} = \frac{R_{\text{test}}}{R_{\text{ref}}} \quad (10)$$

where  $R_{\text{test}}$  = radiation produced by test fuel  
 $R_{\text{ref}}$  = radiation produced by reference fuel

$$\text{Normalized exhaust soot concentration (NES)} = \frac{S_{\text{test}}}{S_{\text{ref}}} \quad (11)$$

where  $S_{\text{test}}$  = soot concentration produced by test fuel  
 $S_{\text{ref}}$  = soot concentration produced by reference fuel

$$\text{Normalized flame emissivity (NFE)} = \frac{E_{\text{test}}}{E_{\text{ref}}} \quad (12)$$

where  $E_{\text{test}}$  = emissivity produced by test fuel  
 $E_{\text{ref}}$  = emissivity produced by reference fuel

$$\text{Normalized flame soot (NFS)} = \frac{FS_{\text{test}}}{FS_{\text{ref}}} \quad (13)$$

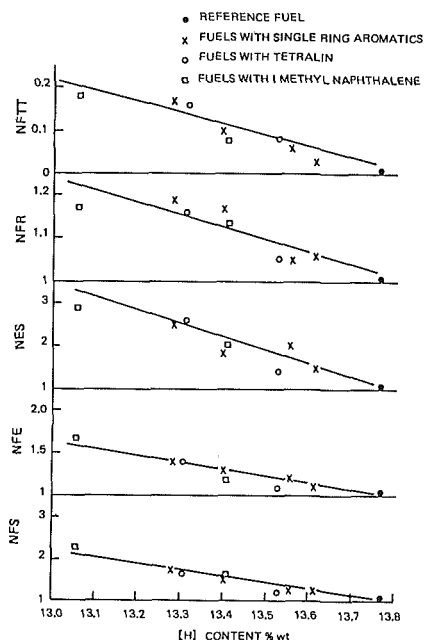
**Table 2 Results of combustion tests on fuel blends**

Fuel	NFTT	NFR	NES	NFE	NFS	Air/fuel ratio
Jet A1 + 5% kerec	0.015	1.04	1.20	1.10	1.25	50/1
Jet A1 + 10% kerec	0.030	1.06	1.30	1.10	1.30	50/1
Jet A1 + 15% kerec	0.022	1.18	1.45	1.35	1.55	50/1
Jet A1 + 20% kerec	0.038	1.17	1.95	1.55	1.62	50/1
Jet A1 + 5% tetralin	0.032	1.05	1.40	1.30	1.30	50/1
Jet A1 + 10% tetralin	0.030	1.07	1.50	1.50	1.50	50/1
Jet A1 + 5% 1 MN <sup>a</sup>	0.020	1.07	1.50	1.35	1.20	50/1
Jet A1 + 10% 1 MN	0.030	1.13	1.70	1.75	1.80	50/1
Jet A1 + 5% kerec	0.020	1.06	1.50	1.10	1.25	45/1
Jet A1 + 10% kerec	0.020	1.05	2.00	1.20	1.25	45/1
Jet A1 + 15% kerec	0.090	1.17	1.70	1.30	1.50	45/1
Jet A1 + 20% kerec	0.110	1.19	2.50	1.35	1.75	45/1
Jet A1 + 5% tetralin	0.050	1.05	1.30	1.10	1.15	45/1
Jet A1 + 10% tetralin	0.100	1.16	2.60	1.40	1.65	45/1
Jet A1 + 5% 1 MN	0.080	1.12	2.00	1.15	1.55	45/1
Jet A1 + 10% 1 MN	0.140	1.17	3.00	1.65	2.20	45/1
Jet A1 + 5% kerec	0.030	1.01	1.41	1.25	1.20	40/1
Jet A1 + 10% kerec	0.060	1.03	1.90	1.15	1.15	40/1
Jet A1 + 15% kerec	0.100	1.05	1.60	1.30	1.45	40/1
Jet A1 + 20% kerec	0.165	1.08	2.60	1.33	1.50	40/1
Jet A1 + 5% tetralin	0.080	1.04	1.90	1.20	1.22	40/1
Jet A1 + 10% tetralin	0.160	1.04	2.60	1.20	1.23	40/1
Jet A1 + 5% 1 MN	0.080	1.06	2.00	1.30	1.40	40/1
Jet A1 + 10% 1 MN	0.160	1.12	2.40	1.30	1.50	40/1

<sup>a</sup>1 MN = 1 - methyl-naphthalene

**Table 3 Absolute values of combustion parameters obtained for reference at each air/fuel ratio**

Air/fuel ratio	Flame-tube temperature	Flame radiation	Exhaust soot concentration	Emissivity	Flame soot concentration
50/1	1144 K	518 kW·m <sup>-2</sup>	2.4 × 10 <sup>-4</sup> mg·liter <sup>-1</sup>	0.175	6.0 × 10 <sup>-4</sup> g·liter <sup>-1</sup>
45/1	1143 K	697 kW·m <sup>-2</sup>	3.1 × 10 <sup>-4</sup> mg·liter <sup>-1</sup>	0.225	7.2 × 10 <sup>-4</sup> g·liter <sup>-1</sup>
40/1	1156 K	792 kW·m <sup>-2</sup>	7.31 × 10 <sup>-4</sup> mg·liter <sup>-1</sup>	0.389	1.3 × 10 <sup>-3</sup> g·liter <sup>-1</sup>



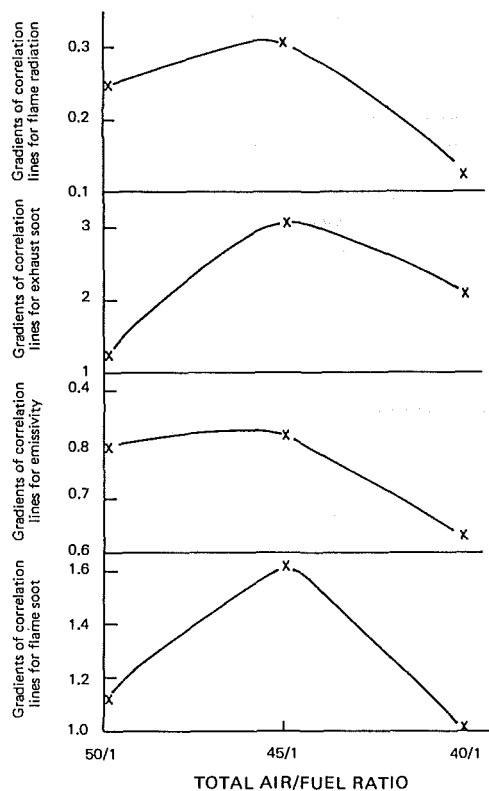
**Fig. 3 Combustion characteristics observed for test fuels at an AFR of 45/1 inlet pressure = 1.0 MPa, inlet air temp. 673 K**

$FS_{test}$  = flame soot produced by test fuel  
 $FS_{ref}$  = flame soot produced by reference fuel

For the purposes of this paper the values of flame soot and flame emissivity reported are those averaged over all the wavelengths utilized.

**Results**

Figure 2 gives a typical trace obtained from the



**Fig. 4 Sensitivity of combustion parameters to variation in hydrogen content at the values of AFR utilized**

emission/absorption spectrometer. As can be seen, the emissivity exhibits a marked decrease with increasing wavelength, a phenomenon that has been suggested in other

work [10] and which further emphasizes the need for measurements of emissivity to be monochromatic. Additionally, it is comforting to note both the good agreement between soot concentrations calculated at each wavelength, a result which provides support for the use of the refractive index values as used herein, and the uniform values of flame temperature calculated at each wavelength, an observation which indicates a flat temperature profile [11] at the observation port utilized.

The results of the combustion tests are given in Table 2, and the mean absolute values of the combustion parameters measured, obtained for the reference fuel runs, are given in Table 3, from which the absolute values for each test fuel may be derived.

The general form of the results obtained during the combustion tests is shown in Fig. 3, which gives the values obtained at an air/fuel ratio of 45/1 versus fuel hydrogen content.

Figure 4 shows the combustor sensitivity to fuel composition, as described by the gradient of the correlation lines for flame radiation, exhaust soot concentration, and flame soot concentration, against hydrogen content, at each of the values of air/fuel ratio utilized.

The results given in Figs. 3 and 4 show a number of interesting features:

1 The fuels containing 1-methylnaphthalene and tetralin exhibit a relationship between hydrogen content and combustion performance, in terms of the parameters measured, equivalent to that of those fuels containing predominantly single-ring aromatics, an observation common to all experimental conditions.

2 The sensitivity of the parameters measured to the fuel hydrogen content rank in the following order; exhaust soot > flame soot > emissivity > flame radiation

3 Flame soot concentration, when corrected to the condition applying for exhaust gas sampling, are approximately 3000 times higher than exhaust soot concentrations.

4 The sensitivity of combustion performance to variation in fuel total hydrogen content appears to peak at an AFR of approximately 45/1.

## Discussion of Results

The results using the model combustor suggest that fuels can tolerate quite high concentrations of naphthalenes or tetralins (>10 percent v) before hydrogen content ceases to adequately correlate with combustion performance, a con-

clusion supported by earlier work [3]. These concentrations are much higher than are found in conventional Jet A1 fuels and the results, if repeated in practice, would cast some doubt on the appropriateness of the present specification requirement for naphthalenes (<3 percent v).

It is encouraging to note that the sensitivities of the parameters measured to fuel hydrogen content are those that would be expected from the arguments presented in section 2, i.e., that owing to the functional relationship between soot concentration and flame radiation, the latter parameter should be a weaker function of fuel hydrogen content than should actual soot concentration. Interestingly, flame radiation, which was measured at port 1, is a less sensitive parameter than is flame emissivity, which was measured at port 2. This phenomenon is probably due to the higher soot concentration that will exist at the port 1 position as compared with that of the port 2 position. Higher soot concentration leads to a more opaque flame, which, from the arguments presented earlier, will exhibit less dependence, in terms of its thermal radiation, upon soot concentrations than will a region of relatively lower soot concentration. That soot concentrations drop dramatically with increasing distance down the flame tube is shown by the large difference between flame soot, measured at port 2, and exhaust soot. This result indicates that although low soot emission can be achieved by increasing soot consumption in the secondary zone of a combustor, design changes to accomplish this will not necessarily lead to lower values of flame soot concentrations and hence lower primary zone radiation. Attempts to decrease soot emission should concentrate on primary zone redesign in order to achieve low soot emission and low flame radiation.

The final observation, that combustor sensitivity to fuel hydrogen content peaks at an AFR of approximately 45/1, is particularly interesting as it provides further clues as to the mechanism of soot formation in gas turbines. In earlier work [2, 3], it was suggested that a major region of soot formation in gas turbines could be the recirculation zone where hot products of combustion are mixed with unburnt fuel, thus providing ideal conditions for pyrolysis and hence the production of soot. It was further suggested that the soot-forming sensitivity of a particular combustor to the molecular composition of a fuel depended on the volume concentration of the fuel in the pyrolysis region. This hypothesis was based on shock tube studies [14], which had shown that, in the temperature range of 1600-1900 K, low hydrocarbon concentration,  $\leq 2 \times 10^{23}$  carbon atoms  $m^{-3}$ , caused very large differences in sooting tendencies between polycyclic

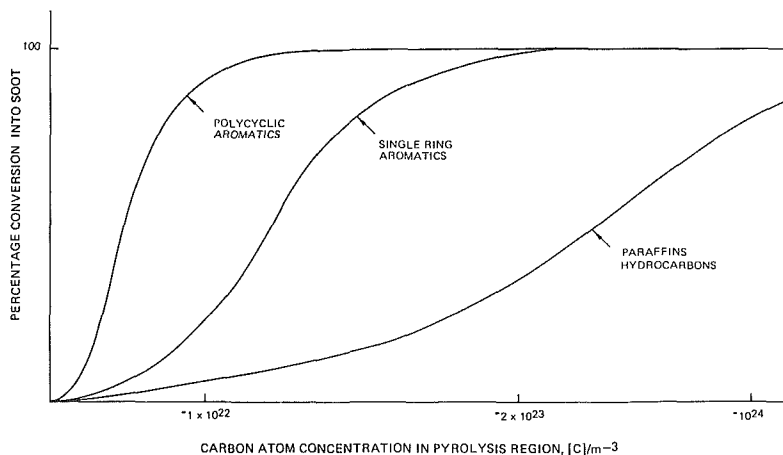


Fig. 5 Schematic representation of sooting tendencies, during pyrolysis, of various hydrocarbon as a function of carbon atom concentration (temperature ~ 1800 K)



aromatics, single-ring aromatics and paraffins, while at higher concentration,  $\sim 10^{24}$  carbon atoms  $m^{-3}$ , the sooting tendencies of most hydrocarbon types became very similar. The general form of the conclusions of this work are summarized in Fig. 5, which shows schematically soot conversion efficiencies versus hydrocarbon concentration for different hydrocarbon types. It can be seen that gradually increasing the concentration of a combination of hydrocarbons during pyrolysis would at first accentuate the differences between the sooting tendencies of the components; however, continued increase in the concentration would ultimately decrease the differences between the soot concentrations produced by the different hydrocarbons. As decreasing the AFR in a combustor will have the effect of increasing the fuel concentration in the recirculation zone, it can be seen that the present results are consistent with the hypothesis that significant quantities of soot are formed, by pyrolysis, in the recirculation zone, as this is one of the few regions in the combustor where high temperatures, low fuel concentration, and low oxidizing environments can exist for significant lengths of time.

It is pertinent to note that recent work using a model combustor [15], covering a wide range of fuel compositions and operating conditions, has shown that long residence times and high inlet air temperatures also decrease the sensitivity of soot formation to fuel molecular composition. As shock tube pyrolysis [14, 16] studies have indicated that high pyrolysis temperatures,  $>2000$  K, and long reaction times,  $>5$  ms, tend to decrease the differences observed between the sooting tendencies of different hydrocarbons, then it can be seen that the foregoing work, from a different source, also supports the present hypothesis.

The foregoing hypothesis could also explain the reason why, in the present work, the fuels containing naphthalene and tetralin showed little difference in their sooting tendencies compared with fuels containing only single-ring aromatics, for, if it is assumed that pyrolysis was occurring at concentrations at which the sooting tendencies of polycyclic and monocyclic aromatics were only slightly different, then very high concentrations of polycyclic aromatics would be required before any variation in soot formation (or concentration) would be observed. Additionally, the latter argument explains the differences between the present work and earlier studies [2] in which the presence of high concentration of naphthalenes and tetralins were seen to significantly affect combustion performance. As this earlier work utilized a much lower combustion pressure, 0.35 MPa, than the present studies, it is probable that fuel concentrations in the pyrolysis zones, were also substantially lower, thus leading to an accentuation of the differences in the sooting tendencies of polycyclic aromatics compared to single-ring aromatics.

If the present hypothesis is correct, then leaner primary zones could lead to engines which could be very sensitive to moderate concentrations of polycyclic aromatics; it is therefore important that work should be performed to accurately identify and eliminate the soot-forming regions within gas turbine equipment in order to prevent such a possibility from occurring.

## Conclusions

The results using the Thornton model combustor indicate that:

(a) Under the experimental conditions adopted, both naphthalene and tetralin concentrations of  $>10$  percent v can be tolerated in jet fuels before hydrogen content ceases to correlate with their combustion performance.

(b) Determination of flame radiation, as a measure of combustor performance, should include a measurement of emissivity.

(c) Sensitivity of soot concentration to fuel hydrogen content is greater than that of flame radiation.

(d) Combustor sensitivity to fuel hydrogen content exhibits a maximum value with variation in AFR.

(e) The results are consistent with a hypothesis that soot is mainly formed in high-temperature pyrolysis regions, such as the recirculation zone.

## Acknowledgments

The authors wish to thank the management of Shell Research Limited for permission to publish the paper and the British Ministry of Defense for their support in this work.

## References

- Blazowski, W. S., "Dependence of Soot Production on Fuel Blend Characteristics and Combustion Conditions," ASME Paper 79-GT-155.
- Bowden, T. T., and Pearson, J. H., "The Effect of Hydrocarbon Structure Upon Fuel Sooting Tendency in a Turbulent Spray Diffusion Flame," ASME Paper 83-GT-90.
- Bowden, T. T., and Pearson, J. H., "The Influence of Fuel Composition Upon Soot Emissions and Flame Radiation in a Model Gas-Turbine Combustor," Paper C70/83, *International Conference on Combustion in Engineering*, Vol. 2, I Mech. E. Conference Publication 1983-3.
- Moses, C. A., and Naegeli, D. W., "Fuel Property Effects on Combustor Performance," ASME Paper 79-GT-178.
- Gleason, C. C., and Bahr, D. W., "Evaluation of Fuel Character Effects on the J79 Engine Combustion System," AFAPL-TR-79-2015, June 1979.
- Gleason, C. C., and Bahr, D. W., "Evaluation of Fuel Character Effects on the F101 Engine Combustion System, final report," AFAPL-TR-79-2018, June 1979.
- Bahr, D. W., "Comparison-Effects of Broadened Property Jet Fuels on Older and Modern J79 Combustors," ASME Paper 83-GT-81.
- Butze, H. F., and Smith, A. L., "Effect of Fuel Properties on Performance of a Single Aircraft Turbojet Combustor and Simulated Idle, Cruise and Takeoff Conditions," NASA TM 73780.
- Naegeli, D. W., and Moses, C. A., "Effect of Fuel Molecular Structure on Soot Formation In Gas Turbine Engines," ASME Paper 80-GT-62, Mar. 1980.
- Dalzell, W. H., and Sarofim, A. F., "Optical Constants of Soot and Their Application to Heat-Flux Calculations," *ASME Journal of Heat Transfer*, Vol. 91, 1969, p. 100.
- Tourin, R. H., *Spectroscopic Gas Temperature Measurement*, Elsevier Publishing Company, 1966.
- Lee, S. C., and Tien, C. L., "Optical Constants of Soot in Hydrocarbon Flames," *Proceedings of the 18th Sym. (Int.) Combustion*, 1981.
- Encyclopaedia of Chemical Technology*, Kirk Othmer Ed., 2d ed., Wiley, New York, Vol. 4, 1964, p. 251.
- Graham, S. C., Homer, J. B., and Rosenfeld, J. L. J., "The Formation and Coagulation of Soot Aerosols Generated by the Pyrolysis of Aromatic Hydrocarbons," *Proc. Roy. Soc.*, A344, 1975.
- Naegeli, D. W., Dodge, L. G., and Moses, C. A., *AFLRL-158*, Dec. 1981.
- Wang, T-S., "Soot Formation from Toluene," Ph.D. thesis, Department of Chemical Engineering, Louisiana State University and Agricultural and Mechanical College, May 1980.

# Development of a Dry Low NO<sub>x</sub> Combustor for a 120-MW Gas Turbine

**K. Aoyama**

Takasago Machinery Works,  
Mitsubishii Heavy Industries, Ltd.,  
Takasago, Hyogo

**S. Mandai**

Takasago Technical Institute,  
Mitsubishi Heavy Industries, Ltd.,  
Takasago, Hyogo

*Two stage premixed combustor with variable geometry has been developed to meet stringent NO<sub>x</sub> goals in Japan without the use of water or steam injection. This combustion system is planned to be applied for 120-MW gas turbine in 1090-MW LNG combined cycle plant. The full-pressure, full-scale combustion tests were conducted over a wide range of operating conditions for this gas turbine. The combustion tests proved that NO<sub>x</sub> levels as well as mechanical characteristics were well within the goals.*

## Introduction

Large capacity LNG combined cycle plants are being built for Japanese utilities for their excellent thermal efficiency. The author's company was awarded the first order of the 1090-MW combined cycle plant, which is scheduled to commence commercial operation at the end of 1984. Following this plant, several units with the capacity of from 500 MW to over 1000 MW are under either construction or consideration in Japan. A hurdle to be cleared in constructing the combined cycle plant in Japan is the NO<sub>x</sub> level. The same NO<sub>x</sub> levels as those of conventional thermal plants are required of a gas turbine. For the 1090 MW combined plant in this location, the NO<sub>x</sub> level of 40 ppm corrected to 5 percent of oxygen is required at the exit of heat recovery boiler. This value corresponds to 15 ppm at 15 percent oxygen that is the normal exhaust gas composition of a gas turbine. To attain this NO<sub>x</sub> level, for instance, "Selective Catalytic Reduction System," SCR, is installed in the heat recovery boiler section to remove 80 percent of NO<sub>x</sub>. By this SCR system, the target value of NO<sub>x</sub> at gas turbine exhaust becomes 75 ppm at 15 percent oxygen. At present, the NO<sub>x</sub> level of 75 ppm with LNG burning is one target value for installing a gas turbine in Japan. This situation becomes more severe for future installations.

The most simple and proven method for reducing thermal NO<sub>x</sub> is water or steam injection into a combustor. But this has the defects of decreases in performance and difficulty in securing water supply. If the quantity of steam injection is 100 percent of the fuel flow rate, the total thermal efficiency of this combined plant will decrease by 1.4 percent. And 3900 tons a day of water will be needed, which are hard to secure in Japan. For the reasons mentioned above, the development of dry low NO<sub>x</sub> combustor is urgently required. The author's

company started the first investigation of a dry low NO<sub>x</sub> combustor in 1980, and developed a hybrid combustor after three years of effort. This hybrid combustor is to be applied for the 120-MW gas turbine for 50 Hz, which is a main component of the 1090-MW combined cycle plant.

The progress of the development of the hybrid combustor and the results of the final combustion test are presented in this paper.

## Program Goals

Program goals for this combustor are shown in Table 1.

## Development Progress

The three years of the development program are shown in Fig. 1. This program was initiated in July, 1980. For the first step of this program, the screening test was carried out to select the most promising configuration for meeting the NO<sub>x</sub> target. The five configurations shown in Fig. 2 were designed and tested in an atmospheric pressure combustion test rig, using LPG fuel.

Configuration 1 is a typical conventional combustor having a primary zone which burns close to stoichiometric conditions to give stable combustion at lower load conditions. Configurations 2 and 3 are the combustors having the lean primary zones. In each the average fuel to air ratio in the

**Table 1 Emissions and performance goals**

Performance goals	
Combustion efficiency	≥ 99.5% (operating range)
Total pressure drop	≤ 4% (base load power)
Pattern factor	≤ 17% (base load power)
Wall temperature	≤ 1033K (operating range)
High cycle fatigue	magnification factor should be greater than 2
Emissions goals	
Oxides of nitrogen (at real O <sub>2</sub> )	≤ 75ppm (operating range)
Carbon monoxide	≤ 50ppm (operating range)

Contributed by the Gas Turbine Division of THE AMERICAN SOCIETY OF MECHANICAL ENGINEERS and presented at the 29th International Gas Turbine Conference and Exhibit, Amsterdam, The Netherlands, June 4-7, 1984. Manuscript received at ASME Headquarters December 27, 1983. Paper No. 84-GT-44.

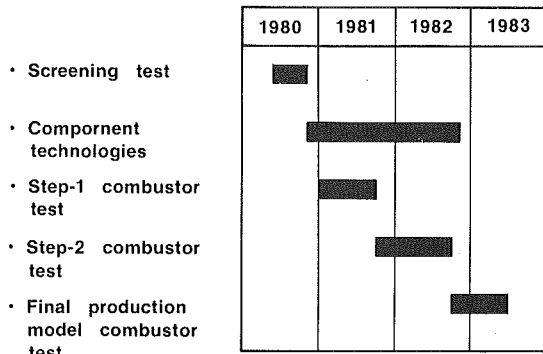


Fig. 1 Program schedule

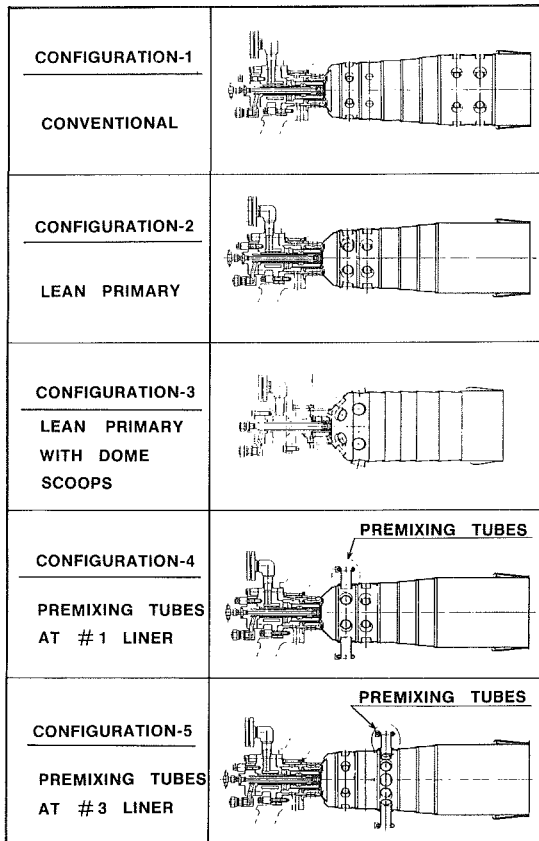


Fig. 2 Combustors for the screening test

primary zone is maintained leaner than stoichiometric values. Configuration 3 has leaner primary zone than configuration 2 and larger diameter at the heat end in anticipation of increase in combustion air volumetric flow in the primary zone. The six scoops at the second liner in Configuration 2 were removed and attached at the dome in Configuration 3 to avoid generation of local rich areas near the fuel injection nozzle. Configurations 4 and 5 utilize the concept of two stage premixed combustor. Fuel is injected not only at the pilot stage in the same way of the conventional combustor of Configuration 1 but also at the premixing tubes, which are projecting radially outwardly from the first and third liner, respectively. Configuration 4 has six premixing tubes and Configuration 5 has twelve, so that fuel to air ratio of mixture in the premixing nozzle of Configuration 4 is 1.3 times richer than that of Configuration 5.

These screening test results are shown in Fig. 3. It is obvious that  $\text{NO}_x$  production is reduced by adopting lean primary or two stage premixed configuration. Among them, the

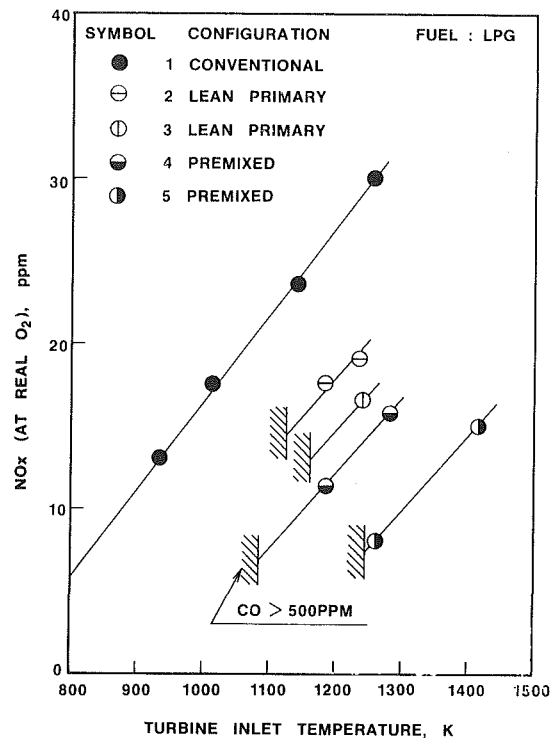


Fig. 3 Screening test results

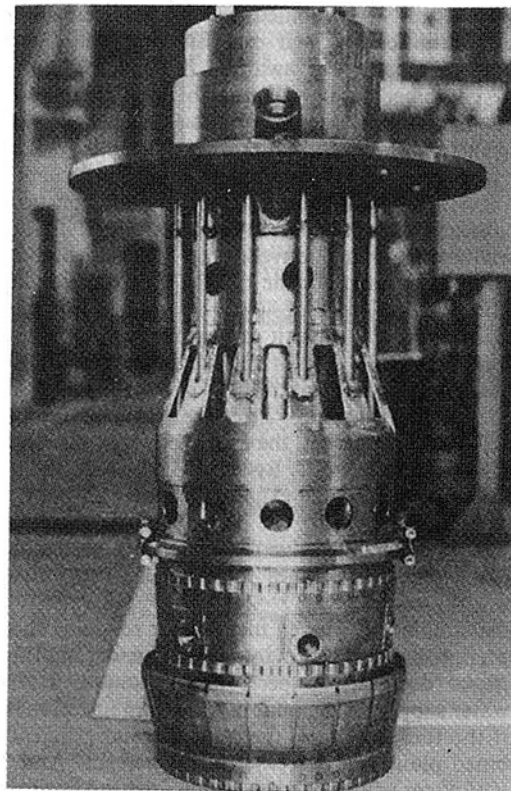


Fig. 4 Step-1 Combustor

premixed type is more promising because of its well-mixed lean mixtures in the primary zone, and only these have a potential for meeting emissions goals of this program. The  $\text{NO}_x$  level of premixed type measured 1/3 of that of conventional diffusion flame combustor of Configuration 1. Based on the results of screening test, the premixed combustor was selected for further development. However, both lean

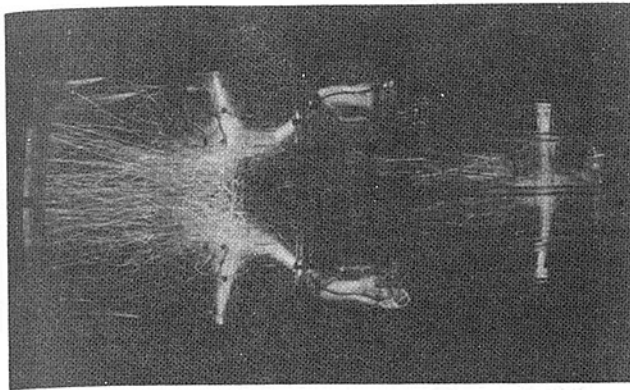


Fig. 5 Cold air flow test

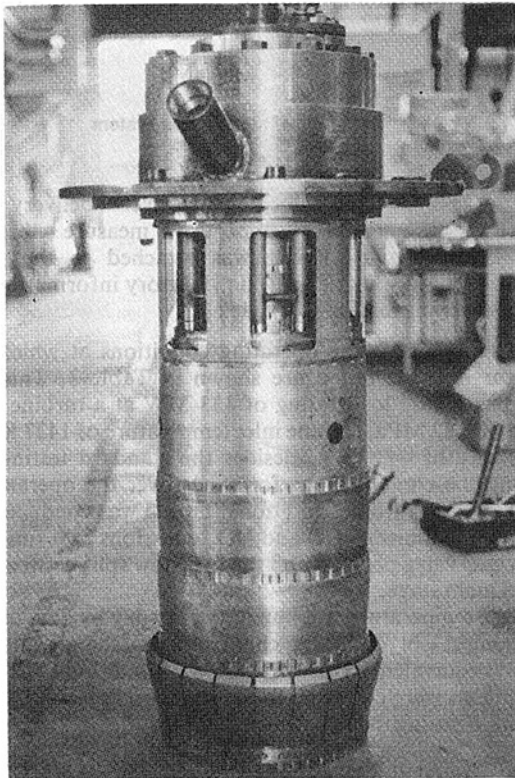


Fig. 6 Step-2 combustor

primary and premixed type showed the limits of inflammability as shown in Fig. 3. This means that it is necessary to put a variable geometry concept to practical use in applying these configurations to gas turbine combustors which have a wide operating range. After the screening test the first prototype, Step-1 combustor shown in Fig. 4, which has twelve premixing tubes, was made. Basic characteristics were measured in the atmospheric combustion test. For the cold air flow test the full-scale model was made of transparent plastic. Ignited charcoal powder was used for tracing the flow pattern in the combustor. The mixing between the pilot flame and premixed gas was visually observed. The typical photograph of this cold air flow test is shown in Fig. 5.

Flashback characteristics of the premixing tube were investigated in a small combustion test rig which can be pressurized up to 0.4 MPa. The test results showed that the minimum velocity in the premixing tube to prevent flashback was about 10 m/s at atmospheric pressure and was increased to more than 20 m/s at 0.4 MPa.

The full-scale, full-pressure tests were conducted at the same conditions as the actual machine. The test results were

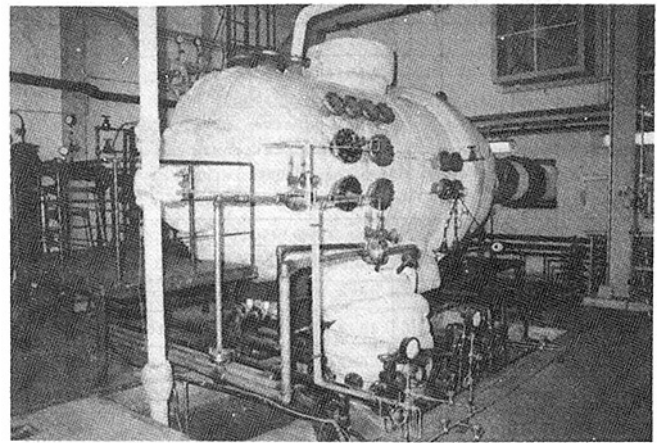


Fig. 7 Combustion test rig

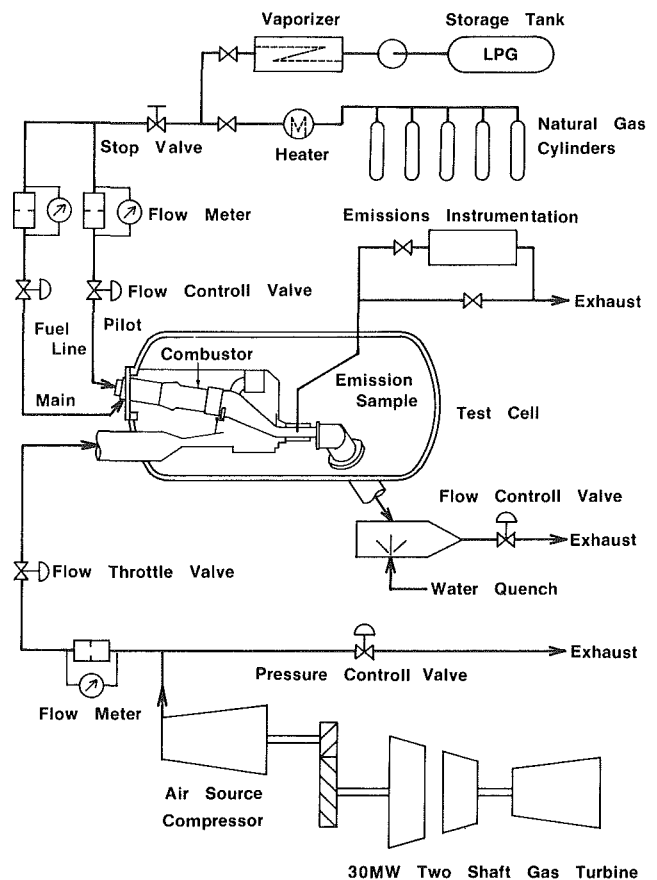


Fig. 8 Schematic of test facility

generally satisfactory. The  $\text{NO}_x$  levels were between 60 and 70 ppm measured at full load conditions. The annular premixing nozzle with swirler vanes in it was also tested in this combustor but burnt out by flashback.

After one year of tests using this configuration, Step-1 combustor was improved and Step-2 combustor shown in Fig. 6 was designed. The noticeable modification of this combustor was the fuel delivery pipes that were provided inside of the combustor to simplify the assembly. Annular premixing nozzle without swirler vanes was adopted. After another year of tests the final production model was designed and manufactured, based on the Step-2 combustor and taking account of easier fabrication. The test results of this final production model are mainly presented later in this paper.

**Table 2 Exhaust gas measurement instruments**

Exhaust gas	Principal of operation
Nitrogen oxides	Chemiluminescence under vacuum
Nitrogen monoxide	Chemiluminescence under vacuum
Carbon monoxide	Nondispersive infrared
Unburned hydrocarbons	Flame ionization detector
Carbon dioxide	Nondispersive infrared
Oxygen	Paramagnetic assembly

**Table 3 Referenced test conditions**

Power level	Idle	25%	50%	75%	Full
Total air flow , kg/s	15.3	15.3	15.3	16.9	20.5
Inlet temperature, K	567	579	589	604	637
Inlet pressure , MPa	0.77	0.83	0.90	1.03	1.27
Exit temperature , K	909	1098	1285	1388	1427

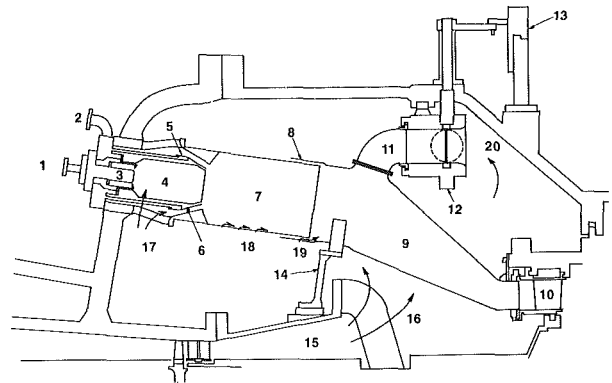
**Table 4 Fuel properties**

	LPG	Natural gas
Specific gravity	0.507	0.558
Gross heat of combustion, MJ/kg	51.5	54.7
Net heat of combustion , MJ/kg	47.4	49.3
Composition		
CH <sub>4</sub> , vol%	-	99.4
C <sub>2</sub> H <sub>6</sub> , vol%	1.0	-
C <sub>3</sub> H <sub>8</sub> , vol%	98.3	-
C <sub>4</sub> H <sub>10</sub> , vol%	0.7	-
N <sub>2</sub> , vol%	-	0.1
CO <sub>2</sub> , vol%	-	0.5

**Facilities and Procedure**

**Test Rig.** The combustion testing was carried out in a high pressure combustion test rig shown in Figs. 7 and 8. The test rig used in this program is capable of operation at rated engine conditions of MW-701D gas turbine. The air source compressor, which is driven by a 30-MW, two-shaft gas turbine, is capable of a air flow rate of 50 kg/s at the pressure ratio up to 16. The pressure and flow ranges are set by operating the pressure control valve, flow throttle valve and flow control valve under the air source compressor while at rated speed. Three types of fuels, distillate oil, natural gas and LPG, can be supplied to the test cell. The natural gas is compressed into the cylinders at the pressure of 15 MPa at a domestic gas well and carried in the facilities. Both fuel and air flow rate are measured by sharp edged orifices conformed to JIS. The fuel delivery system includes lines heated by steam, filters, recirculation circuits and a high pressure steam heater to evaporate LPG.

In the 1900 mm diameter x 4900 mm long explosion proof test cell, a 20 degree sector of the MW-701D engine combustion casing is constructed. And a set of full-scale combustor basket, transition piece and air bypass valve are installed in the sectoral chamber. Downstream of the transition piece, exit instrumentation is provided. That consists of seven equally spaced water cooled thermocouple rakes and four water cooled emission probes. The thermocouple rake has five Platinum-13-percent-Rhodium thermocouples on the centerline. These were used to measure temperature rise and pattern factor. The emission probes are manifolded to a heated sample line leading to the exhaust measurement instruments shown in Table 2. The fuel to air ratio calculated from the measured fuel and air flow rate were checked with those from the compositions of oxygen and carbon dioxide. Combustor liner temperature was monitored through twenty-six embedded chromel-alumel thermocouples. Premixing nozzle wall temperature was also monitored to detect flashback. Strain gauges were installed on five different



- 1 Pilot fuel delivery
- 2 Main fuel delivery
- 3 Pilot fuel nozzle
- 4 Pilot Stage
- 5 Main fuel nozzle
- 6 Premixing nozzle
- 7 Main Stage
- 8 Clam shell
- 9 Transition piece
- 10 Turbine nozzle
- 11 Bypass elbow
- 12 Butterfly valve
- 13 External ring
- 14 Flexible support
- 15 Diffuser
- 16 Compressor discharge air
- 17 Combustion air
- 18 Cooling air
- 19 Dilution air
- 20 Bypassing air

**Fig. 9 Schematic of combustion system**

positions, the main stage, pilot stage, main fuel delivery pipe, flexible support and the U-support, to measure vibratory stress. A pressure transducer was attached to the main combustor wall to provide acoustic vibratory information for detecting the symptoms of flashback [1].

**Test Conditions.** The operating conditions at which the combustor is to be tested are shown in Table 3. This gas turbine has a base load rating of 133 MW at a turbine inlet pressure of 1.32 MPa, turbine inlet temperature of 1427 K and air flow rate of 443 kg/s. Besides the standard testing for evaluating the combustor performance over the operational range of this gas turbine, additional testing was conducted to investigate the limits of CO and NO<sub>x</sub> emissions as a function of air bypass valve position and the fuel flow split between the pilot and main stage.

Since the temperature and humidity vary day by day, the air source compressor discharge characteristics change and are not always equivalent to the standard test conditions. All NO<sub>x</sub> measurements were corrected to the standard combustor inlet conditions by using the following equation:

$$(NO_x)_{corr.} = (NO_x)_{meas.} \left[ \exp\left(\frac{T_1^* - T_1}{250}\right) \right] \text{EXP} \left[ -19(H^* - H) \right] \dots \dots \dots (1)$$

where, T<sub>1</sub> is the inlet temperature in K, H is the weight ratio of water to air commonly known as specific humidity, and the asterisk shows each value at test conditions [2, 3].

**Fuel Properties**

Natural gas and LPG were used for main and supplementary purposes, respectively, during this program. The fuel composition and key properties are listed in Table 4.

**Description of Combustion System**

The dry low NO<sub>x</sub> combustion system comprises a hybrid combustor and air bypass valve, which are illustrated in Fig. 9. The hybrid combustor shown in Fig. 10 is composed of a pilot stage with a conventional diffusion nozzle and a main stage with a premixing nozzle. Main fuel is supplied to the circumferential manifold through four pipes and injected across the air flow from the manifold wall as shown in Fig. 11. The premixing nozzle configuration and length were determined from the test results to prevent flashback. A pilot

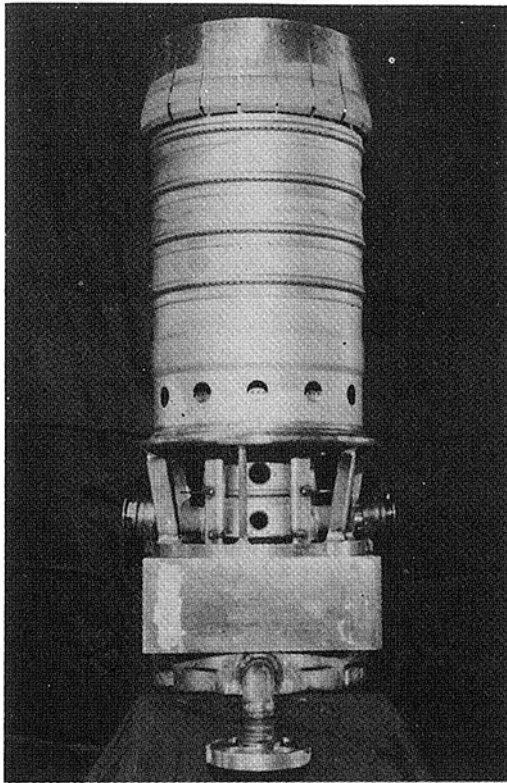


Fig. 10 Test combustor

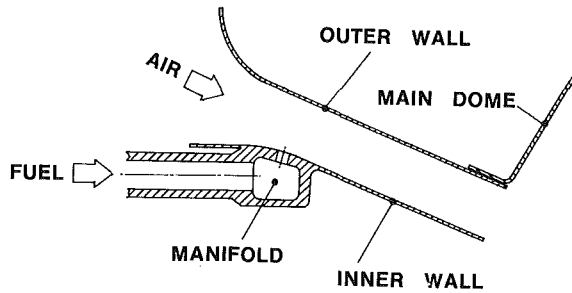


Fig. 11 Premixing nozzle

stage is 165 mm in diameter and 300 mm long, and a main stage is 315 mm in diameter and 490 mm long. Approximately 31 percent of the combustion air is used in the pilot stage, 57 percent in the main stage and remaining 12 percent for dilution. This combustor was constructed of Hastelloy-X and coated on the hot gas side with a thermal barrier coating. The air bypass valve is composed of a butterfly valve, bypass elbow and external ring. The bypass elbow is fixed to a upstream end of a transition piece and the butterfly valve which is moved by external ring is fixed to the combustion casing. The bypass elbow and the butterfly valve are connected by using a spherical sliding seal ring to absorb the difference of thermal expansion in any direction between the bypass elbow and combustion casing.

At low engine power operations and starting, when the total fuel flow rates are low, only the pilot stage is fueled and the air bypass valve is closed. Just before the main stage is fueled at around 38 percent engine power conditions, the bypass valve is fully opened. Then 35 percent of combustion air bypasses the pilot and main stage and flows directly into the upstream end of the transition piece. Above this point, main fuel is injected and controlled in the schedule ratio of main to pilot fuel flow rate. As the engine power increases, the air bypass valve is gradually closed to maintain the fuel to pilot fuel ratio in both the pilot and main stage constant and is almost closed at base load.

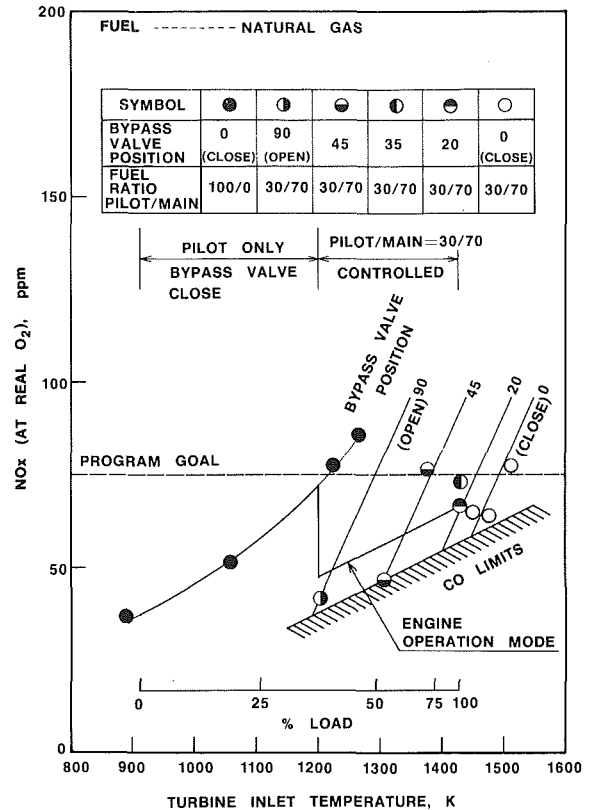


Fig. 12 NO<sub>x</sub> emissions

## Test Results

**Exhaust Emissions.** Exhaust emissions of NO<sub>x</sub> were measured and corrected to specific humidity of 0.008 kg H<sub>2</sub>O/kg dry air and the referenced combustor inlet conditions by using equation (1). A specific humidity of 0.008 was adopted here instead of the ISO convention of 0.0063, adjusting to a wet climate where the first 1090 MW combined cycle plant is planned to be built. Figure 12 shows the NO<sub>x</sub> emissions versus turbine inlet temperature. The NO<sub>x</sub> emissions were lower than the target of 75 ppm. The CO and UHC emissions were approximately 34 ppm and 8 ppm at base load conditions, respectively. When only pilot stage is fueled from 0 to 38 percent load conditions, the NO<sub>x</sub> emissions levels gradually increase as the turbine inlet temperature rises and show the highest value at 38 percent load conditions. However they are well within the program goals. Above 38 percent load conditions, the role of air bypass valve becomes important. When air bypass valve is opened beyond a certain angle, NO<sub>x</sub> emissions increase rapidly. To the contrary, when the bypass valve is closed beyond a certain angle, CO emissions increase abruptly. These points were shown in Figure 12 as CO limits. For example, at the base load conditions, the NO<sub>x</sub> level of 75 ppm is obtained when the angle of air bypass valve is 35 degrees. And the NO<sub>x</sub> level can be decreased to 60 ppm when the air bypass valve closes to the angle of approximately 15 degrees. But if the air bypass valve closes to less than 15 degrees, CO emissions increase higher abruptly. These characteristics of the NO<sub>x</sub> and CO emissions were able to be confirmed complementally in the atmospheric test. The best premixed equivalence ratio was at around 0.7 over the whole operating range while a main stage was fueled. The air bypass valve must be controlled, aiming at this premixed equivalence ratio. The estimated engine operation mode was shown in Fig. 12.

**Liner Temperature.** The measured liner temperature at

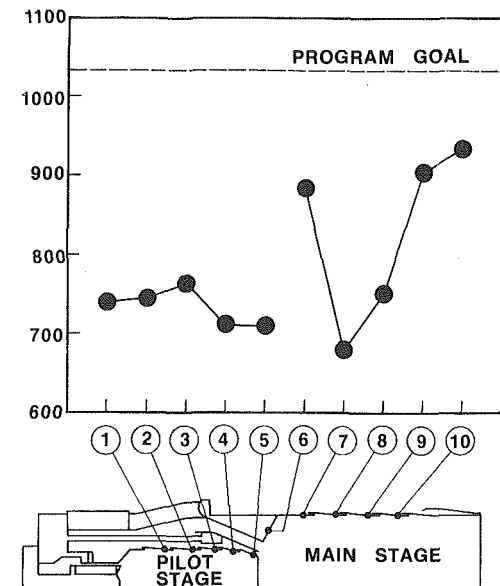


Fig. 13 Linear temperature

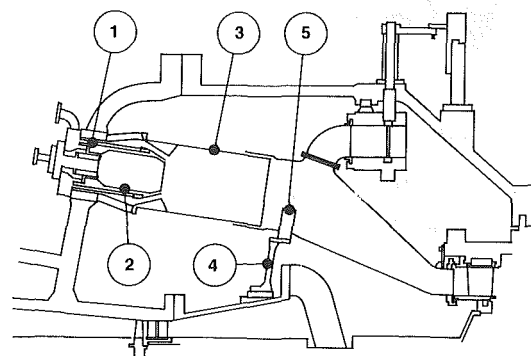
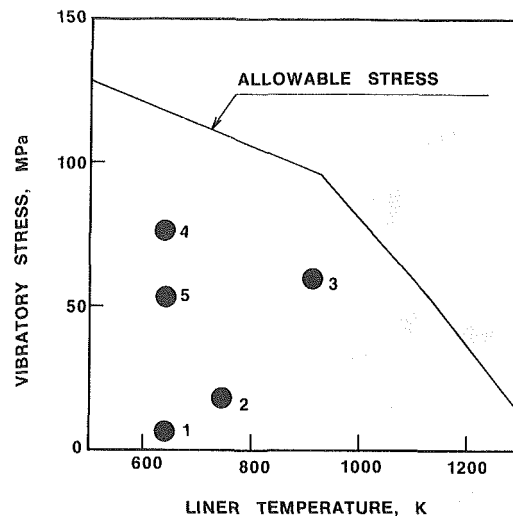
base load conditions is illustrated in Fig. 13. The maximum liner temperature 935 K was measured on the main stage liner. This is well below the target temperature of 1033 K. The maximum liner temperature in the pilot stage is as low as 780 K and well below the target. The lean concept at the pilot stage and premixed concept at the main stage are effective in lowering the liner temperature and contribute to a reduction of cooling air. During lower load conditions, the liner temperature of the pilot stage showed the same level as base load conditions, but the liner temperature of the main stage is by far lower than that at base load conditions.

**Vibratory Stress.** The vibratory stresses of the pilot stage, main stage, main fuel delivery pipe, flexible support and U-support were measured. The directions and locations of strain gauges were decided by investigating natural frequencies, mode shapes and vibratory stresses in shaker test. Stress levels measured were transferred to the maximum stress location by using the calculated results of three-dimensional finite element analysis. Figure 14 shows the vibratory stress versus liner temperature at base load conditions compared with the allowable stress, which is equivalent to a half of the maximum alternating stress that can be imposed in conjunction with the corresponding mean stress. The maximum liner temperature was located in the main stage liner, where the vibratory stress measured was low enough. Vibratory stresses were confirmed to be well within the allowable stress levels.

**Pattern Factor.** Pattern factor is defined as the ratio of the difference of the peak and mean exhaust gas temperature to the mean temperature rise at the combustor. Measured pattern factor at base load conditions was approximately 15 percent and lower than the target of 17 percent. Pattern factor was worse at lower load conditions, but the peak exhaust gas temperature is low enough to have no effect on the durability of turbine nozzles and blades.

## Conclusions

Two stage premixed combustor with a air bypass valve has been designed and tested, which meets  $\text{NO}_x$  emission goals of 75 ppm and has a potential for achieving further ultra-low- $\text{NO}_x$  emissions in future.  $\text{NO}_x$  emissions met program goals over the whole operating range. CO emissions also met



1 Main fuel delivery pipe  
2 Pilot stage liner  
3 Main stage liner  
4 Flexible support  
5 U-support

Fig. 14 Vibratory stress

program goals except at the short transient region where the fuel is changed from pilot to dual stage operation. Metal temperature and exhaust gas temperature profile goals were achieved and durability of combustor was confirmed. The role of air bypass valve is important above 38 percent power at which the main stage is fueled. The air bypass valve should be controlled accurately, aiming at the range between the target of  $\text{NO}_x$  emissions and the limits of CO emissions.

## Acknowledgment

The authors wish to acknowledge the efforts of following personnel who have contributed significantly to this work and thank them for their assistance: T. Sato and the staff of the Takasago Technical Institute who provided support for the rig testing program and evaluation of all data; A. Maekawa who was responsible for the operation of the test rig and the fabrication of the combustor.

## References

- 1 Vaneveld, L., Hom K., and Oppenheim, "Secondary Effect in Combustion Instabilities Leading to Flashback," AIAA Paper No. 82-0037, 20th Aerospace Sciences Meeting, Jan. 1982.
- 2 Lewis, G. D., "Prediction of  $\text{NO}_x$  Emissions," ASME Paper No. 81-GT-119, Mar. 1981.
- 3 Marchiona, N. R., Diehl, L. A., and Trout, A. M., "Effect of Inlet Air Humidity, Temperature, Pressure, and Reference Mach Number on the Formation of Oxides of Nitrogen in a Gas Turbine Combustor," NASA TN D-7396, Oct. 1973.

# Combustion Research Related to Utilization of Coal as a Gas Turbine Fuel

**D. M. Davis-Waltermire**  
Chemical Engineer.

**R. J. Anderson**  
Physicist.

U. S. Department of Energy,  
Morgantown Energy Technology Center,  
Morgantown, West Va. 26505

*A nominal 293 kw (1 MBtu/hr) atmospheric pressure, refractory-lined combustor has been used to investigate the effects of a number of combustor and fuel dependent variables on combustion efficiency and flue gas characteristics for minimally cleaned, coal-derived gas (MCG) and coal water mixtures. The variables which have been evaluated include: percent excess air, air distribution, combustion air preheat temperature, swirl number, fuel feedrate, coal particle size, coal loading in slurry, and slurry viscosity. Characterization of the flue gas included major/minor gas species, alkali levels, and particulate loading, size, and composition. These atmospheric pressure combustion studies accompanied by data from planned pressurized studies on coal-water slurries and hot, minimally cleaned, coal-derived gas will aid in the determination of the potential of these fuels for use in gas turbines.*

## Introduction

The feasibility of using coal-based fuels for the direct firing of open cycle gas turbines is being evaluated by the United States Department of Energy as part of the coal-fueled gas turbine program. This program addresses the perceived need for low cost, short lead time power generating systems which are capable of burning coal in an environmentally acceptable manner.

One of these coal-based fuels is a coal water mixture known as coal water fuel (CWF) which utilizes highly beneficiated domestic coal in a form which can be handled and burned as a liquid. Another potential gas turbine fuel is minimally cleaned, coal-derived gas. In this scheme, coal gasification is used to produce a gaseous fuel. The economics of the combined cycle system become much more attractive when gas cleanup is minimized.

Today's gas turbines are designed to run on relatively clean fuels and to operate with high reliability and low maintenance. Over the past 20 years, the gas turbine technology has been pushing toward higher turbine inlet temperatures to increase cycle efficiency and toward operation on less expensive dirty fuels such as residual oil [1]. More recent efforts have been directed toward the utilization of fuels such as CWF and MCG and dry micronized coal. The advances made in metallurgy and sophisticated cooling have made the possibility of utilizing these fuels more plausible. While gas turbines have become more rugged and tolerant to fuel contaminants, coal beneficiation technology has also advanced. New methods of chemical and/or physical coal

cleaning are being developed which can reduce the ash content of coal to less than 1 percent [2]. Pressurized fluidized-bed combustion experience has indicated that gas turbines have capabilities to tolerate ash levels as great as 0.8 percent providing the particle size is less than 10 microns [3]. An approach to achieve such small ash particles in the products of combustion (POC) of a CWF is to use relatively small coal particles (top size less than 30 microns) in the fuel. An efficient scalping cyclone should insure small particles in the MCG.

The goals of the Morgantown Energy Technology Center in-house combustion studies are to characterize the products of combustion from minimally cleaned, coal-derived gas and coal water fuels and to interpret the potential impact of the POC on turbine operation.

## Facilities Description

The bench-scale atmospheric combustor (BSAC) used in the METC in-house combustion testing of conventional coal water mixture (CWM), CWF, and MCG was configured to provide a high degree of combustion efficiency. The interior of the combustor, shown in Fig. 1, is 1.22 m (4 ft) long, 0.76 m (30 in.) in diameter, and has a 0.46 m (18-in.) long conical region. The walls are made of ceramic material to provide radiant heat to the flame which improved flame stability. Intense recirculation of hot gases, which stabilize the flame for CWM and CWF combustion, is accomplished by the swirl region and the use of swirl air for combustion. The swirl is created by a movable block-type burner fabricated from plans acquired from the International Flame Research Foundation. Transport of the slurry to the combustor is accomplished via pressure feeding from a mix tank. A progressive cavity pump provides a recirculation mechanism

Contributed by the Gas Turbine Division of THE AMERICAN SOCIETY OF MECHANICAL ENGINEERS and presented at the 29th International Gas Turbine Conference and Exhibit, Amsterdam, The Netherlands, June 4-7, 1984. Manuscript received at ASME Headquarters, February 6, 1984. Paper No. 84-GT-285.



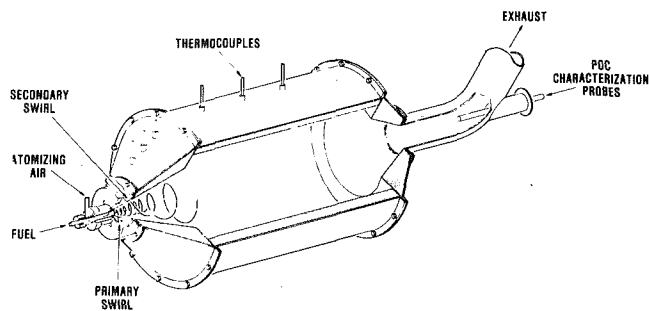


Fig. 1 METC bench scale coal-derived fuel combustor

to keep the slurry characteristics uniform during test operations and storage in the tank.

Atomization is an important parameter in achieving complete combustion of CWF. At present, atomizers suitable for handling CWF are not commercially available. Since CWF are quite abrasive, atomizers must be designed to have minimal erosion. METC has modified a commercially available air assist atomizer which is now capable of producing droplets smaller than 100 microns diameter. A counterbalanced swirl atomizer developed especially for CWF has also been tested in the METC bench-scale rig and been found to produce droplets less than 100 microns. The spray pattern and droplet size distribution produced by atomizers have been evaluated in a separate test stand using a laser-based optical particle monitor. A conventional gas fuel burner block was used for the MCG. This eliminated the high degree of turbulence because swirl air was not required to stabilize the flame when using MCG.

Characterization of the products of combustion included on-line analysis of the major and minor gas species by infrared analyzers and gas chromatography, total alkali species by atomic emission spectroscopy, and particulate samples captured via water-quenched probes. Air-cooled deposition pins were placed in the hot products of combustion, normal to the flow, to provide a gross evaluation of deposition tendencies.

## Fuel Description

Table 1 lists the composition and characteristics of the four slurries tested by METC during 1983. The first two slurries used were the traditional "boiler grade" fuels with 80 percent minus 200 mesh coal particles (median size of ~55 microns) and high ash contents. These two fuels (CWM's I and II) were used to characterize the combustor and evaluate the analytical sampling systems. CWM III was from the same parent coal as CWM II, but contained considerably smaller particle sizes and less ash due to comminution. Because high viscosities (> 2.2 Pa·s) make atomization difficult and, thus, adversely affect combustion efficiency, the first two slurries were diluted with city water to 52 percent coal where they exhibited more manageable viscosities between 0.2 and 0.3 Pa·s. CWM III was fired "as received" with a 60 percent coal loading.

The fourth slurry contained a highly beneficiated bituminous coal cleaned by a fine-grinding, heavy-media flotation process known as the Otisca-T process. CWM IV was received at a coal concentration of 42 percent and was evaporated to a 48 percent coal loading where it exhibited a viscosity of 3 Pa·s. Three-tenths weight percent of a proprietary surfactant manufactured by BASF Wyandotte was added to lower the viscosity to 0.1 Pa·s. The surfactant contained less than 1 weight percent alkali.

CWM IV is highly beneficiated, but still contains about twice as much ash as the ultra-clean coal water mixture proposed for use in gas turbines.

Table 2 lists the composition and characteristics of the MCG used in these combustion tests. The gas was produced

Table 1 Characteristics of CWM's as received

Parameter	CWM I	CWM II	CWM III	CWM IV
Coal Composition				
Moisture (Wt. %) (As Received)	29.61	32.62	39.26	58
Moisture (Wt. %) (As Fired)	48.0	48.0	39.26	52
Volatiles (Wt. %)	34.26	36.68	37.12	41.04
Ash (Wt. %)	2.93	6.63	3.91	1.30
S (Wt. %)	0.77	0.86	0.82	0.76
H (Wt. %) Dry	6.29	5.46	5.63	6.71
C (Wt. %) Basis	81.24	77.87	79.75	81.02
O (Wt. %)	7.28	7.74	8.41	8.27
N (Wt. %)	1.49	1.44	1.48	1.94
Dry Coal Heating Value (kJ/kg) [Btu/lb]	6,960 [14,542]	6,662 [13,922]	6,875 [14,365]	7,000 [14,630]
Slurry Viscosity (Pascal·Second)	2.5	5.2	2.2	1.5
Viscosity As Fired (Pascal·Second)	0.1	0.25	2.2	0.1
Mean Particle Size (Micron)	52	31	9	14
Slurry Heating Value (kJ/kg) [Btu/lb] (As Fired)	4,880 [10,200]	4,489 [9,380]	4,176 [8,725]	3,123 [6,525]

Table 2 Low-Btu gas fuel characteristics

Characteristics of Gas		Characteristics of Particulates in Fuel Gas	
H <sub>2</sub>	15.0 volume percent	C	85.4 weight percent
O <sub>2</sub>	0.7 volume percent	H	4.6 weight percent
N <sub>2</sub>	50.7 volume percent	O	0.0 weight percent
CH <sub>4</sub>	2.2 volume percent	N	1.8 weight percent
CO	22.2 volume percent	S	3.0 weight percent
C <sub>2</sub> H <sub>6</sub>	.44 volume percent	Ash	7.0 weight percent
H <sub>2</sub> S <sup>y</sup>	.43 volume percent	Particulates	1.1 mg/l (32.2 mg/scf)
COS	.03 volume percent		
NH <sub>3</sub>	.015 volume percent		
Alkali			
Na	.01 ppm		
K	.326 ppm	Ash loading in fuel = 0.01 mg/kJ	
Tars	8.8 mg/l (.25 g/scf)	(13 g/MBtu)	
Oils + Water	35.3 mg/l (1.00 g/scf)		
Gas heating value = 5,216-6,334 kJ/m <sup>3</sup> (140 to 170 Btu/scf)		Median particle size of particulates = 12 microns	

by a METC-modified Wellman-Galusha stirred fixed-bed, pilot-scale gasifier using a run-of-mine eastern bituminous coal. The gas exited the gasifier at 811°K (1000°F) and 1136 KPa (165 psia), passed through a cyclone, and traveled through a line which was maintained at 811°K (1000°F). Before entering the BSAC, the pressure was reduced to 136 KPa (20 psia). Cleanup of the gas was limited to a single cyclone; however, additional particle separation from the gas stream occurred during transit through the piping which carried the gas. The estimated efficiency of particulate removal for the cyclone and hot gas pipeline was ~99 percent.

## Combustion Tests

**CWM Combustion Tests.** The run conditions for selected tests representing each slurry are presented in Table 3. Originally designed for 293 kW (1 million Btu/hr), the ideal throughput of the combustor for combustion efficiencies greater than 95 percent was found to be about 117 kW (400,000 Btu/hr). Higher loadings resulted in considerable quantities of unburned coal in the exhaust. For a throughput of 117 kW (400,000 Btu/hr), the residence time in the combustor was about 1 s and the measured combustion efficiency was greater than 99 percent. The maximum swirl value, of 2, produced by the swirl box was utilized during these tests to keep the flame short, bushy, and contained inside the combustor. Initial tests were run at a maximum of 25 percent excess air. The presence of high levels of CO, HC, and un-

**Table 3 Coal-water mixture combustion test parameters and results**

Parameter(s)		CWM I	CWM II	CWM III	CWM IV
Fuel	Slurry Type				
	Slurry Flow (kg/hr) [lb/hr]	34 75	25 55	20 45	45 100
Combustor	Total Air Flow (m <sup>3</sup> ) [scfh]	220 7800	190 6700	198 7000	328 11600
	Excess Air (%)	28	60	90	53
	Preheated Air Temperature (°K)	519	478	483	519
	Swirl Number	2	2	2	2
	Exit Gas Temperature (°K)	1328	1305	1247	1267
	Composition of Products of Combustion	NO (ppm)	550	509	316
	SO <sub>2</sub> (ppm)	480	500	440	220
	O <sub>2</sub> (%)	9.6	11.5	12.0	10.5
	Particulate Loading (g/m <sup>3</sup> )	0.80	0.75	0.99	1.18
	Median Particle Size (Microns)	6.6	5.7	5.4	6.5
	C Content of Water-Quenched Samples (%)	0.5	1.2	5.5	15.9
Calculated POC Characteristics	Ash Passed Through Combustor in POC (%)	13	19	26	69
	Nitrogen Converted to NO (%)	29	33	21	11
Combustion Efficiency (%) <sup>*</sup>		> 99	> 99	> 99	> 99

$$* \text{ Combustion Efficiency} = 1 - \frac{\text{Total mass unburnt C out in POC as solid, CO, or HC}}{\text{Total mass C in fuel fed}}$$

**Table 4 Low-Btu gas combustion test parameters and preliminary results**

Parameters(s)		Cyclonically Cleaned Low-Btu Gas
Fuel	Gas Flow (m <sup>3</sup> /hr)	99 (3,500 scfh)
	Combustor	Total Air Flow (m <sup>3</sup> /hr)
	Excess Air (%)	70
	Preheated Air Temperature (°K)	533 (500°F)
	Exit Gas Temperature (°K)	1,367 (2,000°F)
Composition of Products of Combustion	NO (ppm)	550
	SO <sub>2</sub> (ppm)	1,380
	O <sub>2</sub> (%)	7.8
	Particulate Loading (g/m <sup>3</sup> )	0.78
	Median Particle Size (Microns)	7.3
	C Content of Water-Quenched Samples (%)	14

**Table 5 Turbine manufacturers' tolerances and utility NSPS emission limits**

Technology	SO <sub>2</sub> (4)	NO <sub>x</sub> (5)	Particulates NSPS (5)	Turbine (3)	Alkali K + Na (6)
Stationary Gas Turbines > 10 mmBtu/hr	Limit of 150 ppmv or use fuel with ≤ 0.8 % sulfur by weight	Sliding scale depending on heat rate and fuel nitrogen Range: 150 to 280 ppmv*	None, but likely to be similar to boiler limits of .03 lb/mmBtu	0.26 g/m <sup>3</sup> (210 ppm) if < 2 μm  or	0.8 ppm in fuel 0.024 ppm in POC
Stationary Gas Turbines > 100 mmBtu/hr	Limit of 150 ppmv or use fuel with ≤ 0.8 % sulfur by weight	Sliding scale depending on heat rate and fuel nitrogen Range: 75 to 167 ppmv*	Same as for > 10 mm Btu/hr	0.089 g/m <sup>3</sup> (70 ppm) if < 10 μm	0.8 ppm in fuel

\* Parts per million volume in dry exhaust containing 15 percent oxygen.

burned coal dust in the POC required additional excess air. Excess air levels of 50 percent resulted in optimal combustion efficiency. For these conditions, the average gas temperature at the exit of the combustor was 1,367°K (2,000°F). Combustion efficiencies for all 4 fuels were greater than 99 percent and corresponded to residence times on the order of 1 s in the combustor.

The micronized CWM III was fired "as received" with 60 percent coal and a viscosity of 2.5 Pa·s. Despite the viscosity, the slurry atomized well and combustion efficiencies in excess of 99 percent were observed. Owing to the higher viscosity, it was necessary to double the air flow to the atomizer to achieve good atomization. Isokinetic samples obtained with a water-quenched probe were taken from both the combustion zone and the exhaust gas. Analysis of the sample acquired from the combustion zone (about 1 foot from the nozzle) indicated that approximately 50 percent of the carbon content of the coal had been consumed after a residence time of about 150 milliseconds.

The beneficiated, micronized CWM IV containing 48 percent coal produced a stable flame and had a combustion efficiency greater than 99 percent despite the high water content.

**MCG Combustion Test.** The cyclonically cleaned, coal-derived gas burned with a short stable blue flame which contained a minimal number of yellow streaks due to combustion of entrained coal particles. Table 4 lists the representative run conditions for this test. Combustion efficiencies were well over 99 percent for this fuel.

### POC Composition

**Gases.** Gaseous contaminant levels in the POC, which are of importance to environmental standards as well as the turbine lifetime, are shown in Table 5. The sulfur contents of the fuels tested were close to the 0.8 percent requirements. Another possible sulfur limit would be 70–90 percent removal of total sulfur in the fuel achieved by a combination of coal cleaning and flue gas or hot gas desulfurization devices. This limit is the current standard for new coal-fired power plants [4].

The NO<sub>x</sub> levels produced from the combustion of the four CWM's ranged from 200 to 435 ppmv adjusted to ppmv in dry exhaust containing 15 percent oxygen.

The current gas turbine limit for total alkali in the fuel is 0.8 ppm which translates to 0.016 ppm in the gas entering the turbine.<sup>1</sup> These values assume that all the alkali present in the fuel reacts with sulfur oxides to form the highly corrosive alkali sulfates. The total alkali levels were 100 ppm for the beneficiated fuel, CWM IV, and 0.34 ppm for the MCG. POC from CWM IV, which corresponds to gas entering the turbine, contained between 1 and 2 ppm total alkali. This number includes vapor, liquid, and solid phase alkali.

<sup>1</sup>Numbers corrected from fuel heating value of 8600 kJ/kg to 6460 kJ/kg.

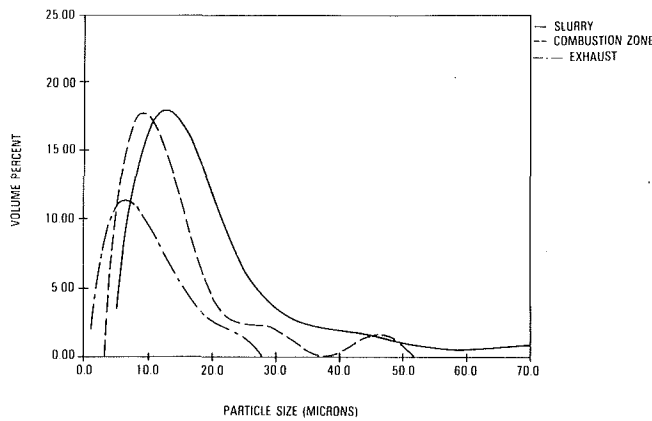


Fig. 2 CWM/POC particle size distributions

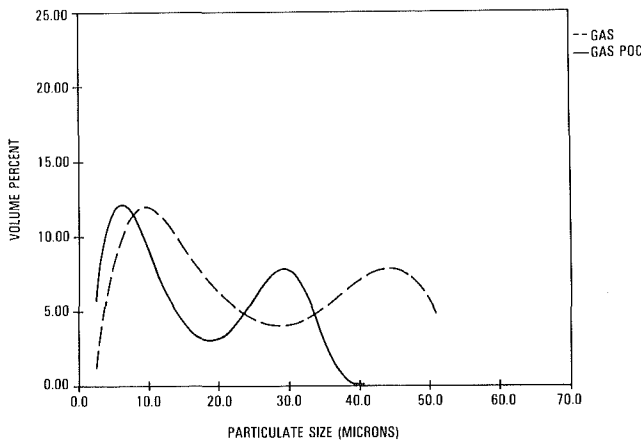


Fig. 3 Comparative particulate sizes low Btu versus low Btu gas POC

Assuming all alkali in the MCG is found in the POC, the total alkali in the POC would be on the order of 0.1 to 0.3 ppm. POC's from both fuels contained more alkali than current gas turbine standards, but the fate of the alkali has yet to be determined. Whether in the more corrosive alkali sulfate will determine actually how much alkali the fuel/POC can contain. Advances in turbine technology, i.e., more aggressive cooling approaches, may also mitigate the effects of alkali.

**Particulates.** Ash balances around the combustor demonstrated the effect of the cyclonic action of the combustor. Due to these cyclonic flow patterns, the larger particles hit the side walls and stuck while the particles < 10 microns followed the stream lines and were carried out by the gas stream. Fifteen to 28 percent of the ash fed into the combustor using CWM I-III stayed in the gas stream and exited the combustor with the remainder being retained inside the combustor or trapped on the deposition probes. CWM IV resulted in considerably more ash being carried through the combustor due to the small particle size of the fuel and the higher throughput of fuel and air as compared to the other slurries.

Although CWM III contained considerably smaller coal particles, the ash deposition pattern for the micronized coal was very similar to that of the other CWM combustion tests. However, the consistency of the ash was distinctly different for the CWM III tests. The deposits from CWM III were much finer and more friable. CWM III ash deposits consisted of spherical particles of ~ 1 micron diameter as compared to CWM II deposits which contained particles greater than 10 microns. In addition, the walls of the plug flow section at the exit of the combustor exhibited little or no deposition for micronized CWM III combustion tests.

Table 6 Characteristics of sampled particles obtained with CWM IV

Sample	Median Particle Size	Residence Time	Combustion Efficiency
Feed Coal	14 Micron	--	--
Water-Quenched Sample 1	13.6 Micron	305 ms	77.0%
Water-Quenched Sample 2	10.2 Micron	610 ms	88.5%
Water-Quenched Sample 3	6.5 Micron	1400 ms	98.3%

Table 7 X-Ray fluorescence analysis of ash from parent coal and combustion deposits from CWM I

	Ash Composition (%)		
	Feed Coal	Front Deposit (A)	Rear Deposit (B)
CaO	1.5	1.5	1.6
K <sub>2</sub> O	1.6	1.4	1.4
P <sub>2</sub> O <sub>5</sub>	0.2	0.1	0.1
SiO <sub>2</sub>	53.3	52.8	51.2
Al <sub>2</sub> O <sub>3</sub>	31.7	31.1	31.7
Fe <sub>2</sub> O <sub>3</sub>	8.6	8.4	8.7
TiO <sub>2</sub>	1.9	1.9	1.9
MgO	1.0	0.7	0.9
SO <sub>3</sub>	0.6	--	--
Na <sub>2</sub> O	0.4	.3	0.8
TOTAL	100.8	99.2	98.3

Figure 2 represents the particle size distribution for CWM III, and water-quenched particulate samples from the combustion zone and the exhaust gas. The sample from the combustion zone contained particles with a median size slightly larger than the feed coal (11 microns versus 9 microns) and a carbon content of 50 percent. The increase in particle size was likely due to swelling caused by volatile release during the early stages of combustion. Particles in the exhaust were about 50 percent smaller than the original coal size.

Water-quenched particulate samples were taken at three different residence times during the combustion of CWM IV. Table 6 shows the median particle size for CWM IV and three water-quenched samples. The particle size for the first two samples, taken at residence times of 305 and 610 ms, were essentially the same in size as the feed coal. Carbon contents of the samples were 76.1 and 45.8, respectively. These carbon levels indicate the same phenomena as seen with CWM III where the coal particle has devolatilized but minimal char burning has occurred. The particulate sample from the exhaust contained particles with a median size of 6.5 micrometers as compared to a feed coal median size of 14.07 micrometers.

Deposits on the combustor walls were found to be highly friable and easily removed by spraying a small amount of water into the combustor. Microscopic observation of the ash collected from the side walls showed evidence of slagging only on the surface of the deposit which was in contact with the ceramic walls for 2 to 4 hrs. The ceramic wall temperatures were within 300K of the gas temperatures. All ash deposits were soft in nature and easily removed from the walls.

A comparison of the chemical compositions of the ash deposits, taken from inside of the combustor, and the feed coal ash is shown in Table 7. Very little difference is noted between the elemental ash composition of the original coal and the deposit compositions taken from the front and rear of the combustor, labeled Points A and B in Fig. 1, respectively. Within the accuracy of X-ray diffraction, there is no evidence of enrichment of any elements in the ash deposits.

The lack of sulfur being observed in either deposit was attributed to vaporization of sulfur compounds.

The size distributions of water-quenched particulate samples collected from the inlet to the combustor and the POC after 610 milliseconds are shown in Fig. 3. After combustion, the particles were reduced in size by ~ 60 percent

and contained less than 15 percent carbon. Owing to the lower ash content of the gaseous fuel, as compared to the CWM, and less turbulent flame, due to the absence of swirl air, minimal deposition of ash was observed inside the combustor.

### Conclusions

Combustion of CWM and CWF containing coal loadings ranging from 48 to 60 percent with good flame stabilities and > 99 percent combustion efficiencies was achieved in the ceramic-lined, bench-scale atmospheric pressure combustor at METC. To achieve these efficiencies in this particular combustor, excess air levels of a minimum of 50 percent, air preheat temperatures ranging from 450-560K (350°-550°F), swirl numbers between 2 and 4, and heat inputs of approximately 87.9 kW ( $0.3 \times 10^6$  Btu/hr) were necessary. The NO<sub>x</sub> levels produced during this series of atmospheric pressure combustion tests for both CWM and low-Btu gas were in excess of the current environmental standards of 75-280 ppmv for gas turbines and boilers.

MCG was combusted with an efficiency in excess of 99 percent. The burnout of particles entrained in the gas was similar to that observed for the coal particles in the CWM's. The significantly lower loading of particles and ash on a per unit energy basis resulted in a much cleaner flame. In addition, the concentration of residual particles and undesirable contaminants in the products of combustion were much lower than those resulting from CWM combustion. However, the particulate loadings in the POC produced by CWM and low-Btu gas were still higher than the currently stated turbine tolerance, because of the number of particles greater than 10 microns.

No evidence of ash particle agglomeration was evident during any of the tests with CWM, CWF, or MCG. This

indicates that, with fine grinding of the coal for slurries and using cyclones to remove particles larger than 10 microns from MCG, the problem of erosion due to large particles in the POC may be controllable.

The types of deposits formed on combustor walls and deposition pins appear to be due to impingement of ash upon surfaces. The deposits were fine, friable and removed from surfaces with relative ease. More research into the composition of deposits and the effect of surface temperature and surface composition is needed.

Further study is needed to determine the impact of combustion at elevated pressures on fuel residence time requirements and NO<sub>x</sub> formation. A NO<sub>x</sub> control system may have to be integrated into the gas turbine power generating system to meet these limits. One alternative may be use of a low-NO<sub>x</sub> combustor design which typically employs a fuel rich combustion region followed by a fuel-lean region. These combustors have been shown to work on various high nitrogen content fuels, such as coal-derived liquids, and may be applicable to coal-water slurries.

### References

- 1 Burton, David, "Combustion Turbines at the Crossroads," *Mechanical Engineering*, Apr. 1982, pp. 79-85.
- 2 Hutton, C., and Gould, R., *Cleaning Up Coal: A Study of Coal Cleaning and the Use of Cleaned Coal*, INFORM, Inc., 1982, pp. 121-135.
- 3 Rubow, L., and Zaharchuck, R., "Hot Gas Cleanup Requirements for PFBC 1982 Perspective," Second Annual Contractor's meeting on Contaminant Control in Hot Coal-Derived Gas Streams, U.S. DOE, Feb. 1982.
- 4 Molberg, John, "A Graphical Representation of the New NSPS for Sulfur Dioxide," *Journal for Air Pollution Control Association*, 1980, p. 172.
- 5 PEDCO, Environmental Inc., "Standards of Performance for New Stationary Sources," EPA 340/1-80-001a, July 1980.
- 6 Doering, H. vonE, Hickey, J. W., and Hilt, M. B., "Fuel Alternatives," Gas Turbine Reference Library, General Electric, 1980.

A. Muyama

H. Hiura

Takasago Machinery Works,  
Mitsubishi Heavy Industries, Ltd.,  
Takasago, Hyogo, Japan

K. Morimoto

Kamaishi Works,  
Nippon Steel Corporation, Ltd.,  
Kamaishi, Iwate, Japan

# Repowering in Steel Works by Introducing a Blast-Furnace, Gas-Firing Gas Turbine

*A 14-MW, high-temperature gas turbine firing extremely low-BTU, blast-furnace gas was developed and installed in a steel works of Japan as a repowering unit. Field tests proved the stable combustion up to 590 Kcal/Nm<sup>3</sup> calorific value and plant efficiency improvement of up to 60 percent on existing steam plant. Design features and two years operational experiences are presented.*

## 1 Introduction

A 14-MW gas turbine firing extremely low-BTU, blast-furnace gas (BFG) was developed and introduced in a Japanese steel works to repower the existing steam power plant in 1982.

The turbine inlet temperature of this gas turbine was designed at slightly higher than 1000°C (1273 K) for the first time as a BFG-firing gas turbine.

The gas turbine and unfired heat recovery boiler compose a combined cycle system with an existing steam power plant. As a result of this repowering, the plant thermal efficiency was improved from 20 to 33 percent, while increasing the plant power output from 14 to 23 MW at the same fuel input.

BFG as a main fuel of the plant is a byproduct in steel works and it has long been a challenge to develop the means for utilizing the BFG more efficiently and economically. The calorific value of BFG is extremely low and fluctuates between 600 Kcal/Nm<sup>3</sup> and 850 Kcal/Nm<sup>3</sup>, and a sufficient amount of BFG to maintain the rated power output cannot always be made available in this steel works. To meet those severe conditions, the gas turbine, which has a specially designed single-can type combustor to accommodate those calorific fluctuations and unstable BFG supply, was developed. During load operation, the supplemental oil fuel can be mixed with any fraction to maintain stable electric power and steam supply.

This gas turbine has the ability to be operated as a normal oil firing gas turbine by introducing the air into the gas compressor that is driven by the gas turbine.

This plant has successfully been operated since March, 1982. This paper describes the design features and the operational experience.

## 2 Plant Details

**Design Conditions.** This plant was designed under the following basic conditions:

Contributed by the Gas Turbine Division of THE AMERICAN SOCIETY OF MECHANICAL ENGINEERS and presented at the 29th International Gas Turbine Conference and Exhibit, Amsterdam, The Netherlands, June 4-7, 1984. Manuscript received at ASME Headquarters January 9, 1984. Paper No. 84-GT-146.

- 1 The BFG with the calorific value from 600 Kcal/Nm<sup>3</sup> to 800 Kcal/Nm<sup>3</sup> has to be burnt.
- 2 The gas turbine has to be started under black-out condition using only oil fuel.
- 3 Fuel changeover from the BFG to oil fuel and vice versa has to be conducted without stopping the gas turbine.
- 4 Capacity of a gas turbine should be matched with the available amount of BFG, 83600 Nm<sup>3</sup>/hr.
- 5 BFG should not be exhausted to the outside of the system even in the case of the emergency gas turbine trip.

**Merit Of Repowering.** The existing steam plant consisted of five BFG and COG (coak oven gas) firing boiler and three steam turbine generators. By introducing the newly developed BFG firing gas turbine (MW 151S) and unfired heat recovery boiler, three of existing boilers stopped operation. The steam from the heat recovery boiler is delivered to the common steam header and used to operate the existing steam turbine. The schematic for repowering is shown in Fig. 1. Energy flows before and after repowering are shown in Fig. 2. BFG supplied for this power plant is mainly consumed by the gas

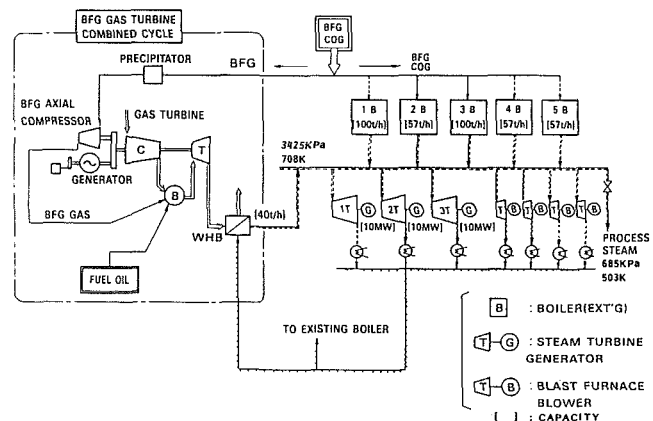


Fig. 1 Total system schematic diagram

turbine and the remainder is consumed by the existing boilers. Figure 2 shows that:

- (i) Plant power output increased from 14 to 23 MW with the same fuel input.
- (ii) Plant thermal efficiency improved from 20 to 33 percent.
- (iii) Electric power bought from the power company was decreased from 35 to 26 MW.

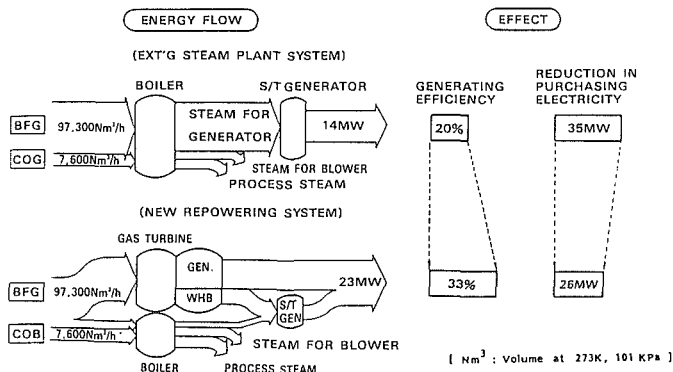


Fig. 2 Effect of repowering

**Details.** The newly installed gas turbine generator and unfired heat recovery boiler consist of a BFG-firing gas turbine, an electrostatic precipitator, a BFG compressor, a gas-decompression device, a heat recovery boiler, and an electric generator.

The generator and the BFG compressor are driven by the gas turbine through the reduction gear. A lubrication oil pump, a turning device, and a starting device—diesel engine, are connected with the generator shaft through the auxiliary gear as shown in Fig. 3.

Four different operational modes can be selected, depending upon the amount of BFG available as shown in Fig. 4. Those are explained as follows:

(i) **BFG Firing Operation Mode.** This is the normal operation mode. BFG is branched from the BFG supply pipeline and is introduced to the wet-type electrostatic precipitator through which the dust in the BFG are removed to the level of 1 mg/Nm<sup>3</sup>.

Then BFG is introduced to the BFG compressor, where it is pressurized and fed into the combustor. In the combustor, BFG is mixed with the compressed air and burnt with the aid of the oil pilot torch. The amount of fuel oil flow to the pilot torch is controlled at 1 L/min, which is equivalent to 1 percent of total heat input.

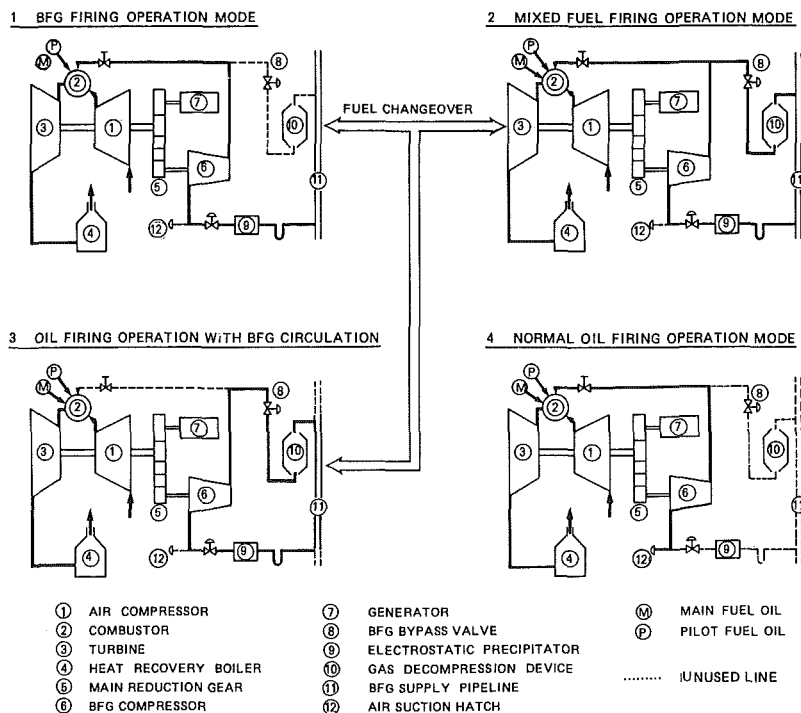
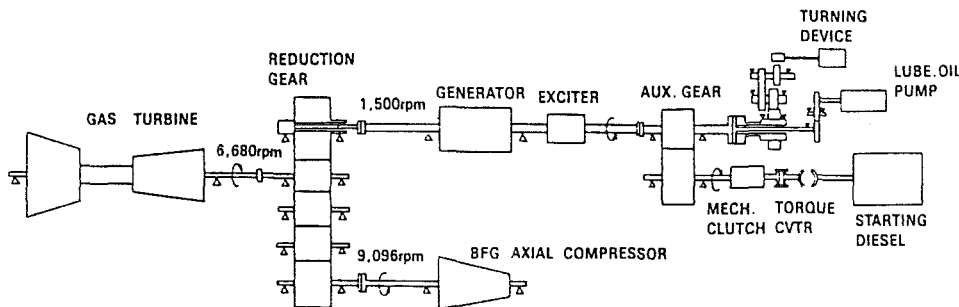


Fig. 4 Operational mode

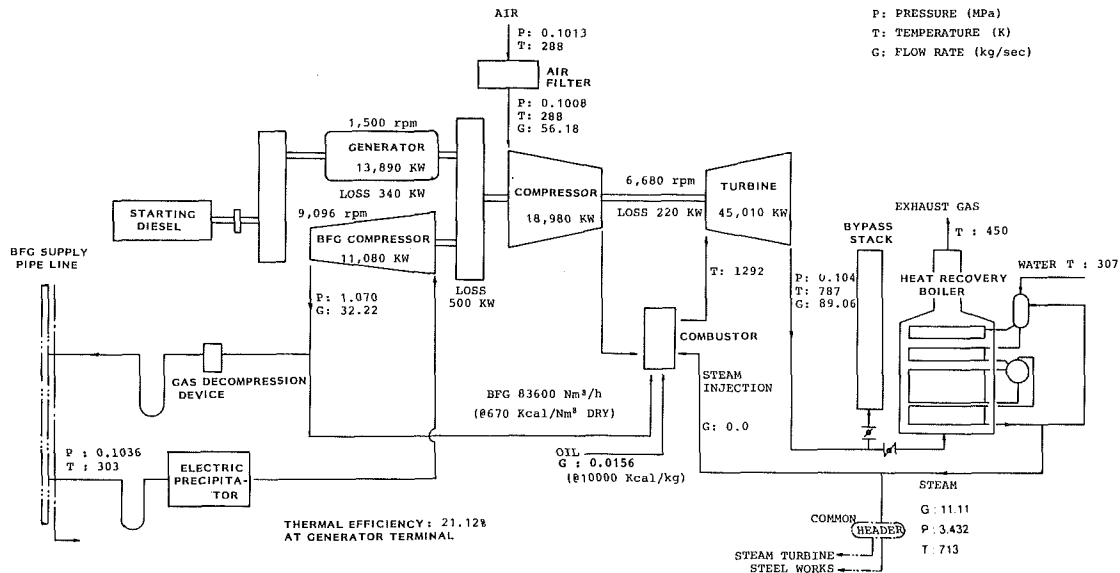


Fig. 5 Heat balance diagram

The exhaust gas is introduced to the unfired heat recovery boiler and is exhausted from the stack.

The gas turbine fuel is controlled by the variable pitch stators equipped on the BFG compressor without bypassing the discharge flow. Under part load operation below 8 MW, the fuel flow is controlled by bypass valves, because the variable pitch stators are fixed at full close position. Surplus BFG is returned to the low-pressure BFG supply pipeline through the BFG decompression device without being exhausted to the outside of the system.

(ii) *BFG and Oil Mixed Fuel Firing Operation Mode.* When the available amount of BFG is not sufficient and the increase of the power is required, additional oil fuel can be injected into the combustor from the main oil fuel nozzles, and BFG and oil fuel can be cofired.

The additive amount of the liquid fuel is adjusted at any amount.

(iii) *Oil Fuel Firing Operation With BFG Circulation.* When the supply of BFG is reduced to zero and continuous minimum power generation of 2,700 kW is required, this operational mode is selected. Changing over to this mode is conducted as follows:

As the BFG fuel flow is decreased by increasing the bypass flow, the fuel oil is increased to compensate the heat input. At the point where almost all the discharge flow from the BFG compressor is bypassed, BFG fuel isolation valve is shut. The steam is injected to produce the additional power, during this fuel changeover.

As the discharged BFG is decreased in pressure and temperature through the gas decompression device, it is circulated in the BFG pipeline. During this operation, the power required to drive the BFG compressor leads to the loss of generated power entirely.

To decrease the load of the BFG compressor and increase the power output at generator terminals, the suction pressure is decreased to 58.84 kPa (0.6 kg/cm<sup>2</sup>) by throttling the suction valve of BFG compressor. At this condition, the power output, over 2,700 kW, is attained even if the steam injection is stopped.

(iv) *Normal Oil-Firing Operation With BFG Compressor Air Breathing.* In this operational mode, the gas turbine is operated as a normal oil-firing machine by introducing the air into the BFG compressor. BFG compressor is isolated from the BFG supply pipelines.

Table 1 Design specification

GAS TURBINE	
* POWER OUTPUT	13890 KW
* THERMAL EFFICIENCY	
(GAS TURBINE)	21.1 %
(COMBINED)	33.2 %
TURBINE INLET GAS TEMPERATURE	1019 °C
EXHAUST GAS TEMPERATURE	514 °C
TURBINE	3 STAGES
COMPRESSOR	18 STAGES AXIAL
BFG COMPRESSOR	16 STAGES AXIAL (SHAFT DRIVEN)
SPEED OF GAS TURBINE	6680 rpm
SPEED OF BFG COMPRESSOR	9096 rpm
FUEL	BFG and OIL

HEAT RECOVERY BOILER	
STEAM GENERATION	40 TON/hr
STEAM PRESSURE	3.432 MPa
STEAM TEMPERATURE	440 °C

\* BASED ON GENERATOR OUTPUT  
ISO CONDITION

BFG CONDITION		AVERAGE	VARIATION	
COMPOSITION	CO	Vol %	20.5	18.0~24.0
	CO <sub>2</sub>	"	20.5	19.0~22.0
	H <sub>2</sub>	"	2.6	1.6~ 3.2
	N <sub>2</sub>	"	56.4	51.0~61.0
** NET CALORIFIC VALUE	Kcal/Nm <sup>3</sup>	670	600~800	
GAS TEMPERATURE	°C	30	25~ 45	
CONTAINED MOISTURE		SATURATED		

\*\* BASED ON DRY COMPOSITION

Under the blackout conditions, the gas turbine is started by this mode because the supply of BFG is interrupted. Change over from BFG firing operation to this operational mode is designed to be carried out within 40 min. This is the longest transfer time and is sufficient to prevent the major equipment in steel works from serious damages under the blackout conditions.

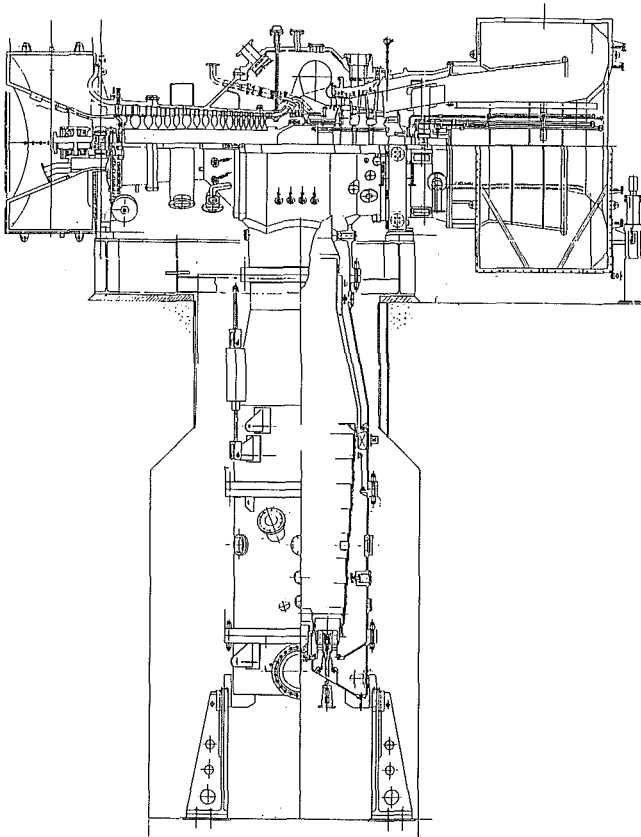


Fig. 6 Mitsubishi MW-151S gas turbine

### 3 Design Features of the Main Components

Specifications of the main components are summarized in Table 1. The heat balance based on the standard condition is shown in Fig. 5.

The features of the main components are described below.

**Gas Turbine (Turbine and Compressor).** In order to assure maximum reliability, the model MW-151S (Fig. 6) was scaled from W-251 gas turbine, which has a long operating history. The scale ratio of 0.76 was determined to match the expected amount of BFG,  $83,600 \text{ Nm}^3/\text{hr}$  at  $670 \text{ Kcal/Nm}^3$  DRY. The turbine inlet temperature of this gas turbine is designed to be  $1019^\circ\text{C}$  ( $1292 \text{ K}$ ) using the advanced air-cooled vanes and blades for the first and the second stage. The cooling air is taken from the compressor discharge and fed to those vanes and blades through the external cooler.

To avoid high-temperature corrosion, those vanes and blades are coated by an advanced coating of Al, Cr and Ni.

The 18 stage axial-flow compressor was modified to decrease the flow capacity by 35 percent by shortening the height of compressor blades to match the increased fuel flow.

The compressor inlet flow is modulated by variable inlet guide vanes to keep the exhaust gas temperature as high as possible at part load condition.

**Combustor.** A single-can-type combustor was designed to burn the extremely low BTU fuel. Previous to designing the combustor, the combustion tests were carried out using the BFG in a steel works to investigate the basic characteristics of BFG burning.

In those tests, the following important conclusions were obtained:

- 1 The excess air ratio in fuel nozzle has to be carefully determined so as not to mismatch the inflammability region of BFG.

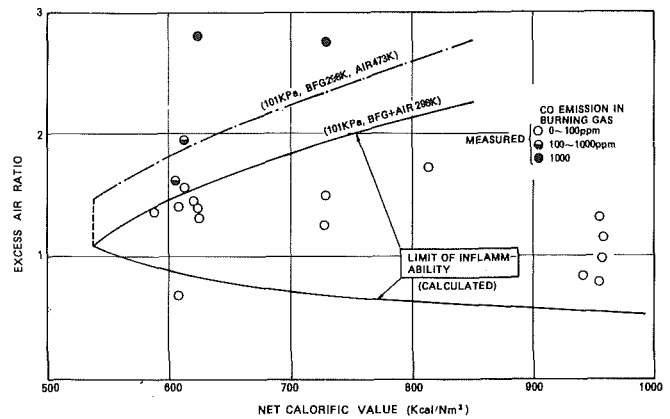


Fig. 7 Inflammability against net calorific value of BFG

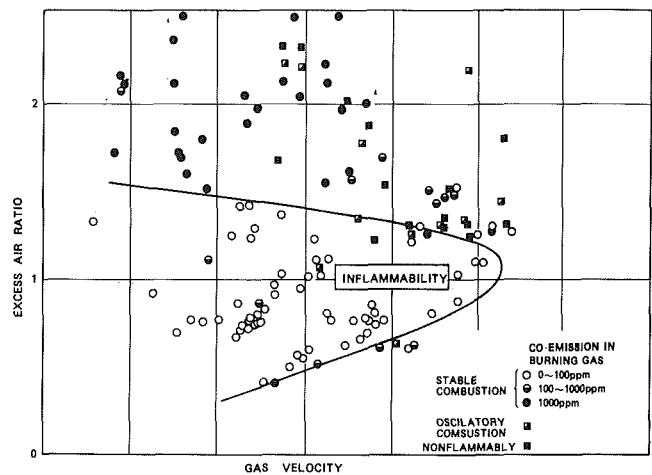


Fig. 8 Inflammability against gas velocity

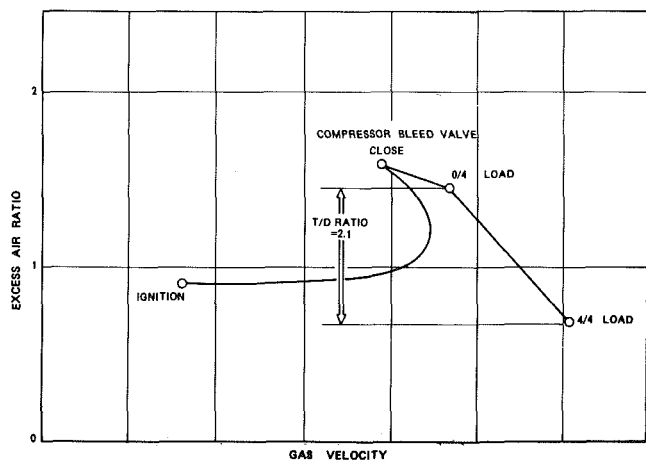


Fig. 9 Excess air ratio variation at starting

Figure 7 shows the relation between inflammability limits and calorific value. The solid lines are the calculated inflammability limits by Le Chatelier's rule.

Plots show measured data in the combustion test using the actual gas turbine nozzle. From this figure, it can be seen that BFG is well combusted within the Le Chatelier's curves and shows insufficient burning at the outside of this region. This means that excess air ratios in the fuel nozzle have to remain within the Le Chatelier's curves at all operating conditions to provide complete combustion. Another conclusion is that the minimum calorific value of gas turbine fuel is about 600



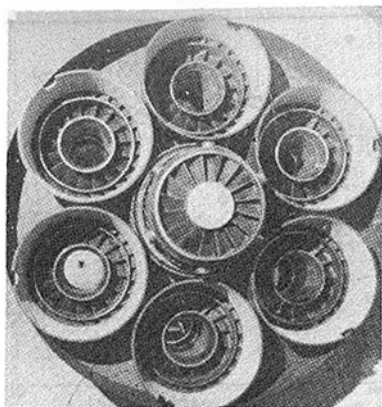


Fig. 10 BFG nozzle

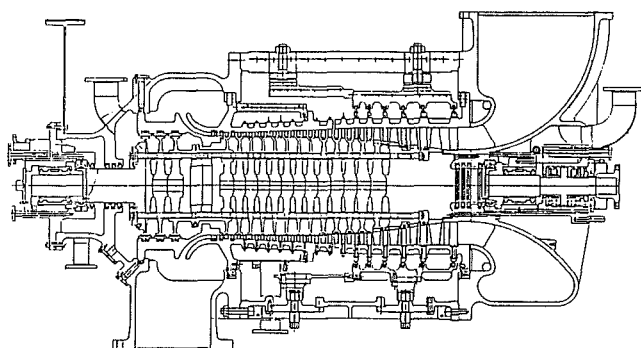


Fig. 11 Blast furnace gas compressor

Kcal/Nm<sup>3</sup> to assure the turndown ratio of 2.1 for normal BFG firing in the gas turbine. This takes into account the effect of preheating of fuel and air flow through the compressors.

2 Reference velocity in the combustor section has to be reduced to burn the BFG.

Figure 8 shows the relations between inflammability and the reference velocity. This shows that the inflammability region is narrowed by increasing the reference velocity. On the other hand, the reference velocity as well as excess air ratio vary in wide ranges in the actual BFG burning gas turbine as shown in Fig. 9.

The fuel nozzle has to be designed to cover the all operating range within both the limits shown in Fig. 7 and limits shown in Fig. 8.

BFG combustor with six fuel nozzles at bottom is suspended under the gas turbine. The combustion gas flows upward and is introduced into the turbine through the scroll.

Each BFG fuel nozzle has an oil fuel nozzle at the center. The photograph of these nozzles is shown in Fig. 10.

One percent of total heat input is fed as a pilot torch through one oil fuel nozzle of the six nozzles assembly during the normal BFG operation. Oil fuel is fed to the all six oil nozzles in oil firing operation. The combustor wall is covered by finned segments to protect the wall from flame radiation during oil firing mode.

**BFG Compressor.** Utilization of a low-BTU BFG fuel requires a great fuel mass flow to maintain the amount of energy available for conversion. Therefore, the adiabatic efficiency and controllability of the flow capacity are important. Considering these points, an axial flow type compressor with 16 stages was selected as BFG compressor (Fig. 11).

The variable pitch stators were adopted in its front stages, by which the discharge flow could be controlled from 70 to 100 percent of the full capacity.

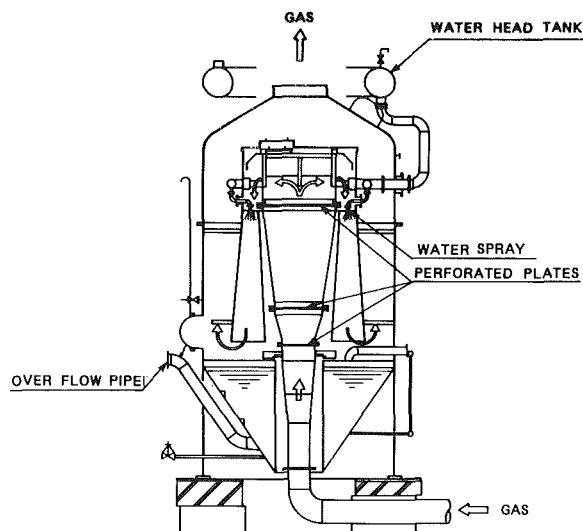


Fig. 12 Gas decompression device

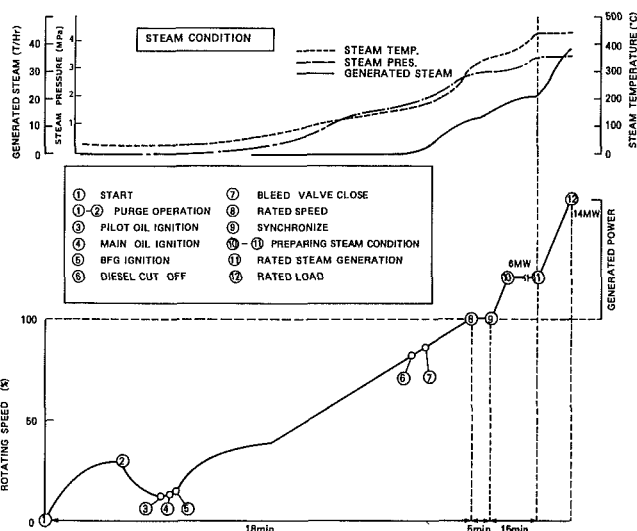


Fig. 13 Starting sequence

**Gas Decompression Device.** As described in the design conditions, the plant was carefully designed not to exhaust the BFG outside of the system in any case. For this purpose, the special designed gas decompression device was installed, which is shown in Fig. 12. The compressed BFG from BFG compressor is expanded through the three stage perforated plates and also cooled by the water spray. Then the surplus BFG is returned to the BFG supply pipeline without giving any dangerous disturbance. This device was designed to absorb the full capacity of BFG flow when the gas turbine trips during full load operation. The noise at this tripping condition is well suppressed by its silencing functions.

#### 4 Two Years Operational Experience

The commercial operation of this plant was begun in March 1982. By the end of August 1983, the unit had logged over 9000 BFG operation hrs.

**Topics During the Trial Operations.** Prior to the commercial operation, trial operations were conducted to confirm its mechanical and electrical functions and performance.

(i) **Starting Sequence.** The starting sequence of this gas turbine with firing BFG is shown in Fig. 13. At first, the

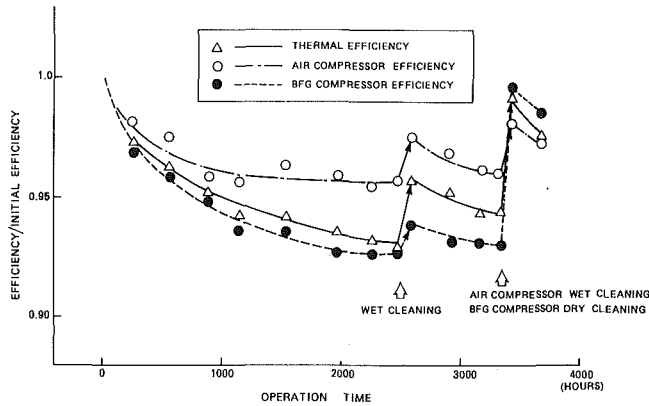


Fig. 14 Efficiency variation depend on time

starting diesel engine accelerates the gas turbine to 30 percent of the rated speed to purge the flow passage of the gas turbine. After 3 min of this purge operation, the gas turbine is decelerated to 13 percent of the rated speed for the ignition. The pilot and the main oil fuel are ignited at first, and these flames ignite the BFG.

To confirm the stable combustion of BFG, which has a dark blue flame, the inside of the combustor is monitored on the color TV from the control panel.

After the stable combustion of BFG is confirmed on this TV, the operator pushes the confirmation button, which permits further acceleration of the gas turbine.

At 80 percent of the rated speed, the diesel engine is cut off. During this acceleration, the BFG fuel is controlled by the bypass valve to regulate the acceleration speed and exhaust gas temperature within the limits. The amount of oil fuel is maintained at the minimum value of 8 L/min which was found to be sufficient to maintain the stable combustion of BFG. It took about 18 min from the start for the turbine to reach the rated speed. When the generator is synchronized, the oil fuel is decreased to 1 L/min.

When the power output is increased slightly over 6,000 kW, the exhaust gas temperature reaches the value high enough to make the required steam condition, and the gas turbine is held at this condition until the steam conditions match that of the existing steam header. It was confirmed that it takes 40 min from start to the generation of required steam.

(ii) *Load Rejection Test.* This was the most challenging problem in the low-BTU fuel firing gas turbine test, because the inflammability range is small and an abrupt change of air-fuel ratio in the combustor has occurred.

The load rejection test was successfully carried out without misfiring under the calorific value of 630 Kcal/Nm<sup>3</sup>. During

this test, the governor functioned well and the maximum speed was 104 percent of the rated speed.

### Topics During Two-Year Operation.

(i) *Compressor Cleaning.* Figure 14 gives the evolutions of the thermal efficiency of the gas turbine unit, air compressor efficiency, and BFG compressor efficiency versus the operational hours. This shows that the thermal efficiency of gas turbine dropped by about 5 percent during the first 1000 hr operation and was due to the fouling of both air and BFG compressors.

To recover this efficiency, both compressors were cleaned by a wet cleaning method. This cleaning method is usually used to remove the deposit on the blade surface such as tar, grease, or oil. A 2 percent solution of a kind of neutral cleanser was poured from the suction of both compressors at about 30 percent of the rated speed. This cleaning was effective on air compressors but not largely effective for BFG compressors.

Hard contaminants were found on the surface of the front stages of BFG compressors and identified as Fe<sub>2</sub>O<sub>3</sub>, CaCO<sub>3</sub>. To remove these contaminants, a dry cleaning method was applied. In this cleaning, shattered shells of nuts were thrown into the suction of the BFG compressor at rated speed operation. As a result of this cleaning, the efficiency of BFG compressors increased by 5 percent and the suction flow increased by 10 percent. The thermal efficiency of the gas turbine recovered to almost initial value.

(ii) *Overhauls of the Gas Turbine.* The first overhaul was conducted in Oct. 1982 after 3200 hr operation. Gas turbine and BFG compressor were disassembled and checked.

Combustor and nozzles were kept in good conditions, and corrosion was not evident on the surface of the turbine vanes and blades.

## 5 Conclusion

The efficient usage of BFG, which is a byproduct in steel works, has been considered with a great interest. The low calorific value and unstable supply of BFG makes the problem more difficult to solve.

By developing the gas turbine which has a specially designed combustor for low-BTU BFG and four operational modes to be selected, depending on the available amount of BFG, the existing steam power plant was repowered with a remarkable improvement of thermal efficiency. Two years of successful operation have been logged by now.

We believe this experience can be an encouraging guide for repowering of existing plants which use byproduct fuel in steel works.

**W. J. Bunz**  
Mechanical Engineer.

**G. N. Ziady**  
Manager, Power System  
Support Services Department

Saudi Consolidated Electric Company,  
Damman, Saudi Arabia

**H. vonE. Doering**  
Manager, Fuels and Corrosion.

**R. J. Radice**  
Engineer, Utility Application Engineering.

Gas Turbine Division,  
General Electric Company,  
Schenectady, N.Y.

# Crude Oil Burning Experience in MS5001P Gas Turbines

*At Qaisumah, Saudi Arabia, there are four GE MS5001P Gas Turbines operated by the Saudi Consolidated Electric Company in the Eastern Province (SCECO East). The Power Plant is not connected to the main SCECO grid and experiences near-capacity peak load demands in the summer months. Its remoteness and proximity to the Trans-Arabian Pipeline (TAPLINE) dictates the burning of Light Saudi Arabian Crude Oil which is desalted by centrifugal purification without the addition of wash water. Eliminating the need for wash water is important because of the scarcity of water at this site. Power loss is controlled and shutdowns minimized during the critical summer months by removing the ash accumulation on the turbine components by on-line nutshell cleaning. This paper describes the first application of this waterless (dry centrifuge) fuel purification system and the impact of various turbine cleaning methods (particularly on-line nutshelling) on turbine performance, availability, and maintenance.*

## Introduction

At Qaisumah, Saudi Arabia, there are four GE MS5001P gas turbines currently being operated by the Saudi Consolidated Electric Company in the Eastern Province (SCECO-East) with a total generating capacity of 62,560 kW (see Table 1). Two of the units were commissioned in 1980 and the balance in 1983. The power plant is not connected to the main SCECO grid and experiences near-capacity peak load demands on the summer months. Summer peak demand for electricity in this region has increased by 37 percent a year. All four units burn primarily Light Saudi Arabian Crude Oil from the Trans-Arabian Pipeline (TAPLINE) that has been desalted by centrifugal purification without the addition of wash water. Eliminating the need for water was important because of the scarcity of water at this site. Power loss is controlled and shutdowns minimized during the critical summer months by removing the ash accumulation on the turbine components by on-line nutshell cleaning. As of July 1983, the four units have in total accumulated 43,160 fired hrs, generating 225,000 MWH.

This paper describes the first application of this waterless (dry centrifuge) fuel purification system and the impact on turbine performance, availability, and maintenance.

## Power Plant

The power plant at Qaisumah serves the load of Wadi Al-Miyah, Hafar Al-Batin, Summan, and other nearby areas.

The plant is located approximately 430 km northwest of Damman and represents a major electrical load center for SCECO.

Because the plant's generation, transmission, and distribution facilities are isolated from the main SCECO grid, generation availability is essential to meet the daily peak demand of the summer months.

In July 1982, the base load capacity of the two MS5001P

**Table 1 Performance ratings**

SITE CONDITIONS: Temperature: 49°C (120°F),  
Pressure: 0.9696 Bar (14.07 psia),  
Elevation: 394 m (1200 ft),  
Pressure Drops, Inlet and Exhaust each:  
10 millibars (4 inch H<sub>2</sub>O)

	Crude Oil		Distillate	
	Base	Peak	Base	Peak
Generator Output (kW)	15640	17280	17280	18700
Heat Rate—LHV KJ/kWh (Btu/kWh)	14640 (13880)	14324 (13580)	14324 (13580)	14082 (13350)
Firing Temperature °C (°F)	900 (1650)	930 (1730)	930 (1730)	985 (1805)
Heat Consumption, KJ/H (Btu/hr × 10 <sup>6</sup> ) LHV	229.0 (217.1)	247.6 (234.7)	247.6 (234.7)	263.4 (249.7)
Exhaust Temperature °C (°F)	473 (884)	503 (938)	504 (940)	531 (988)
Airflow kg/sec (lb/sec)	98.9 (218)	99.3 (219)	99.3 (219)	99.3 (219)

Contributed by the Gas Turbine Division of THE AMERICAN SOCIETY OF MECHANICAL ENGINEERS and presented at the 29th International Gas Turbine Conference and Exhibit, Amsterdam, The Netherlands, June 4-7, 1984. Manuscript received at ASME Headquarters February 10, 1984. Paper No. 84-GT-293.

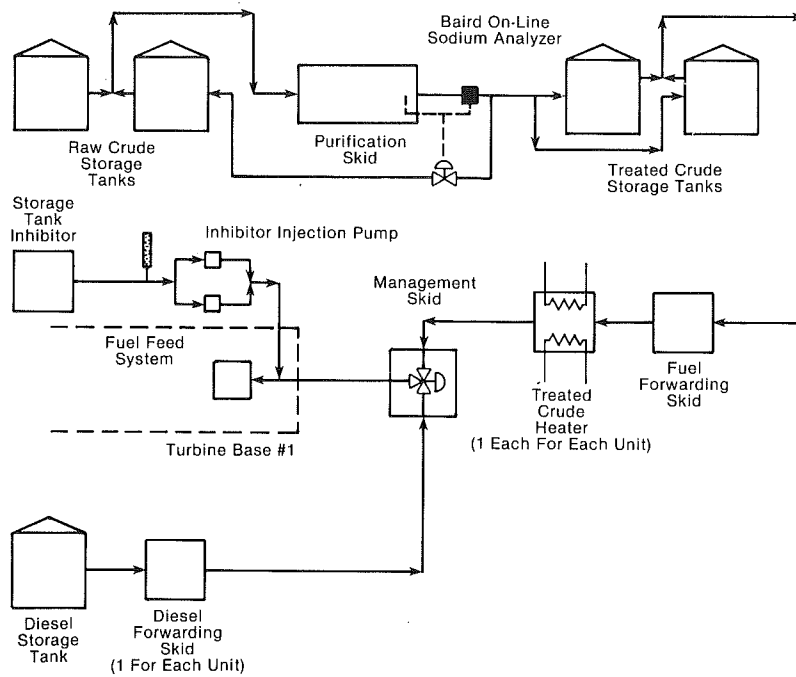


Fig. 1 Fuel treatment system

Table 2 Gas turbine service record

Unit No.	Date Installed	Total Fired Hrs.	Crude Fired Hrs.	Fired Starts	Avail.* %
1	June '80	21,210	20,300	488	97
2	July '80	17,750	16,610	409	98
3	Jan. '83	1,630	1,540	35	44 <sup>A</sup>
4	Jan. '83	2,570	2,410	48	70 <sup>B</sup>

$$* \text{Availability} = \frac{\text{Total Fired Hours} + \text{Standby Hours}}{\text{The Total Number of Hours in the Period}}$$

Standby = The Number of Hours that the Unit Maintained its Ability to Start at a Moment's Notice.

A. Low, due to atomizing air compressor and cooling water system problems and parts availability problems.

B. Low, due to fuel pump clutch problems and parts availability problems.

was less than the system daily peak demand. Mobile generators, installed in 1981, were required to provide backup power and spinning reserve. Availability of the GE units during the critical June/July/August period of 1981 and 1982 was 99.6 and 99.4 percent, respectively. The winter peak is approximately 27 percent of the summer peak. Excess generation capability occurs much of the year. To maximize generation reliability and system response during the off peak period, the load is equally shared by all units. The unit's load utilization factor for the summer and winter months is 0.44 and 0.28, respectively. The history of each unit as of July 1983 is given in Table 2. Ninety-five percent of all fired hours have been with crude oil. The turbines are equipped for dual fuel crude-distillate operation and have black start capability.

The site at Qaisumah has frequent sandstorms which require the turbines to be equipped with automatic self-

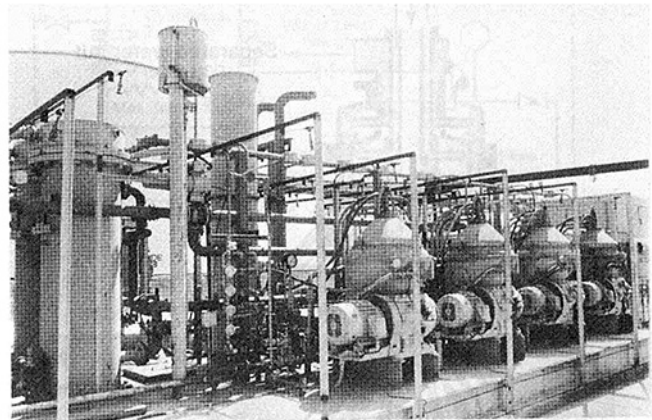


Fig. 2 Purification skid

cleaning inlet air filters. Ambient temperature in the summer can rise above 50°C (120°F) and fall to 0°C (30°F) in the winter.

The fuel system at Qaisumah (Fig. 1) consists of two 3180 m<sup>3</sup> (20,000 BBL) raw storage tanks, one 1200 m<sup>3</sup> (7500 BBL) diesel storage tank, two 1590 m<sup>3</sup> (10,000 BBL) treated crude storage tanks, electric crude oil heater, magnesium injection pumps, a Baird DDS on-line sodium analyzer, and the following skids: purification, crude forwarding, distillate forwarding, and fuel selection.

The fuel purification skid (Fig. 2) consists of a pumping and heating unit followed by four Alfa-Laval MAPX-210 centrifuges operating in parallel with a capacity of 760 l/m (200 gpm) and bottom sediment and water (BS&W) on-line analyzer. The skid, shown schematically in Fig. 3 also includes water washing and demulsifier injection facilities; however, these have not been operated since February 1981 as will be explained in the "Operation and Maintenance" section of this paper.

The Zenith magnesium injection metering pump, a positive displacement gear-type unit, is driven through an adjustable speed gearbox by a constant-speed electric motor. The pump is equipped with a calibration tube to accurately control the amount of oil soluble magnesium compound that is injected

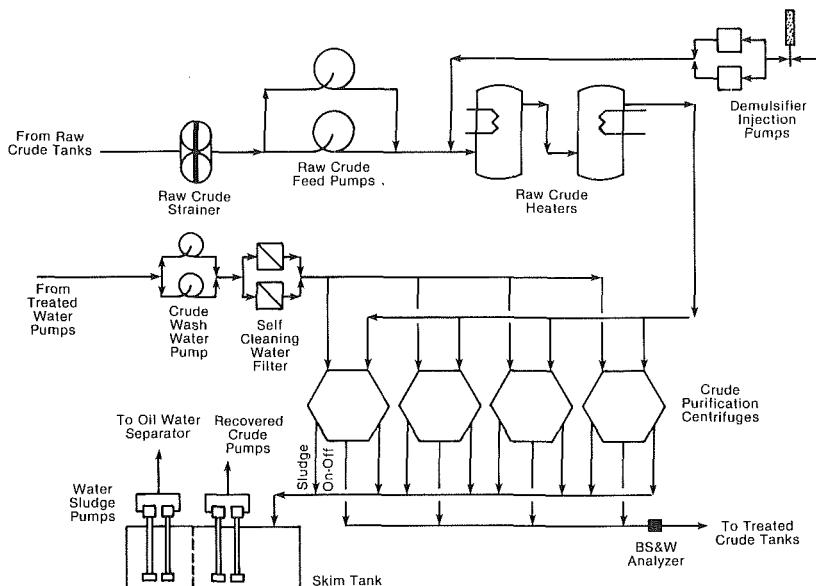


Fig. 3 As-purchased fuel purification skid

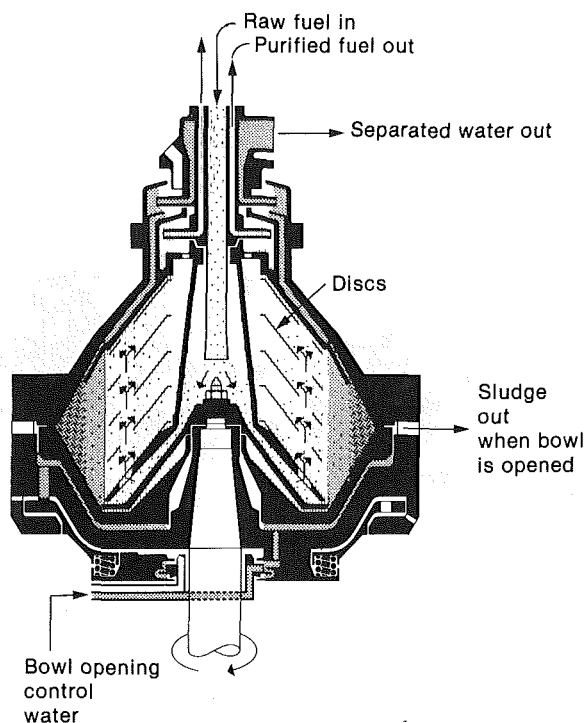


Fig. 4 Typical automatic desludging centrifugal purifier

into the treated crude oil upstream of the on-base, high-pressure fuel pump.

### Fuel Treatment System Operation

In order to utilize crude oil as a gas turbine fuel, the sodium and potassium in the fuel must be reduced to a combined level of one ppmw or less. Other contaminants such as vanadium, lead, calcium, zinc, organics and inorganic particulates are also of concern. Historically, sodium and potassium have been removed by water washing. In this procedure, 5 to 10 percent potable water is mixed with the fuel to contact and dissolve the soluble sodium and potassium salts (NaCl and KCl). A demulsifier is added to enhance the subsequent separation of the wash water by centrifuge or electrostatic precipitation. Considerable quantities of water are required. At Qaisumah, potable water is in short supply and would have

to be produced from brackish water available at the site. Water washing also creates a waste disposal problem due to the quantities of waste water produced.

Work performed in 1979 and 1980 at GE indicated that most crude oils, having low viscosities and specific gravities and up to 15 ppm sodium plus potassium, could have the sodium and potassium levels reduced to less than 1 ppmw by centrifugal purification without adding water to the oil. This approach was first applied to the Qaisumah operation.

Light Saudi Arabian crude oil can be purified to a large extent by simple gravity sedimentation in storage tanks over a long period of time. In a centrifugal purifier, the combination of very high centrifugal force (4000–8000 g) and very short settling distance (about 0.5 mm between disks) results in a highly accelerated purification effect. Short settling distance is achieved through the use of a stack of closely spaced conical disks. A cutaway view of a typical centrifugal purifier is shown in Fig. 4. Raw crude oil enters the axis of the centrifuge and flows down to contact the disk stacks. At this point, the water, particulate matter, and oil are separated. The purified crude oil flows back through a channel just adjacent to the incoming raw crude, and the water and dirt flows to the periphery of the bowl. The water is directed back to the centerline and is discharged through a channel just outside of the purified crude oil channel.

The automatic desludging centrifugal purifier will automatically clean itself of sludge that accumulates at the bowl perimeter while rotating at full speed. Within a fraction of a second, the entire bottom or sleeve of the unit, supported in normal operation by hydraulic force, is dropped downward about 5 mm. The solid particles are discharged through this opening at the bowl perimeter. A small amount of water (about 760 l per day, 200 gallons per day) is used in the operation of the centrifuge to eject the solid particles and seal the centrifuge bowls. For the same size plant, operating as a water wash system with a 5 percent by volume water treatment would consume about 53 m<sup>3</sup> (14,000 gal) of potable water per day.

At Qaisumah, crude oil is pumped from the raw crude storage tanks to the purification skid, Fig. 1. Electric crude oil heaters maintain the temperature of the oil at 52°C (125°F) minimum prior to centrifugal purification to prevent wax from coming out of solution. Purified crude discharges automatically into the treated crude storage tanks after it has been monitored on-line with a Baird DDS sodium analyzer

**Table 3 Crude oil analysis tapline**

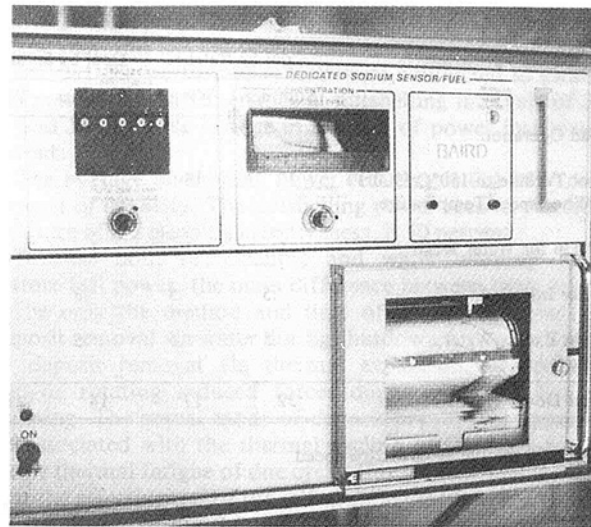
Test	1980-1983 Range	1982-1983 Mean
Density 15°C	0.865 – 0.846	0.858
Gravity, API 60°F	32. – 35.7	33.3
Ash, PPMW	25 – 104	50
Gross Heating Value, kcal/kg (Btu/lb)	10,690 – 10,750 (19,240 – 19,350)	10,690 (19,240)
Pour Point, max °C (°F)	< -29°C (< -20°F)	< -29°C (< -20°F)
Sediment and Water, Vol%	0.05	NIL
Sulfur, Wt%	1.38 – 1.84	1.8
Wax, Holde, Wt%	1.2 – 3.4	1.3
Viscosity, cSt, 20°C (70°F) (SSu, 20°C (70°F))	6.72 – 10.56 (47.9 – 60.8)	9.58 (57.4)
cSt, 40°C (100°F) (SSu, 40°C (100°F))	4.40 – 6.54 (40.5 – 47.3)	5.95 (45.4)
Sodium, PPMW	1 – 8	1.5
Vanadium, PPMW	2 – 18	16
Lead, PPMW	0.5	0.5
Calcium, PPMW	0.1	0.1
Potassium, PPMW	0.5	0.5

(Fig. 5) and BS&W meter. Recirculation to the raw storage tanks will automatically occur on alarm conditions ( $Na > 1$  ppmw). From the treated crude storage tanks, the crude forwarding skid pumps the oil through the crude oil heaters to the fuel selection skid and then to the turbine. The control system automatically selects distillate for start-up and normal shutdown operation. Once pressure and temperature permissives are satisfied, on-line transfer from distillate to crude begins. Crude oil transfer to distillate will also occur automatically whenever permissives are not satisfied. If crude is selected, the oil soluble magnesium inhibitor is injected into the treated crude oil upstream of the on-base high pressure fuel pump to maintain a three to one magnesium to vanadium weight ratio in the crude oil.

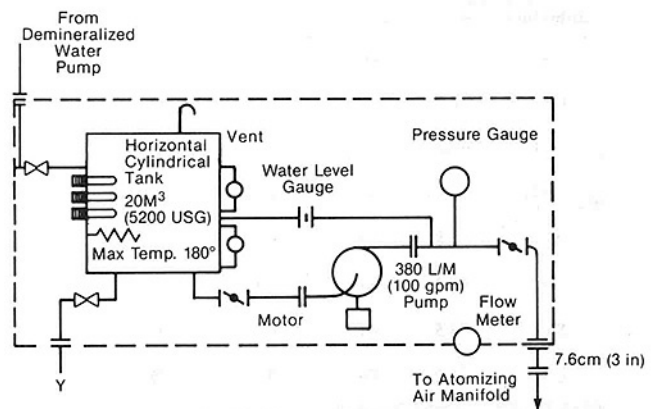
During operation, a Baird FAS analyzer is used to analyze samples taken from the raw and treated crude oil storage tanks, the purification skid crude oil discharge line, and the turbine high-pressure fuel filter after magnesium additive injection.

The analysis of Tapline crude oil (Table 3) shows the minimum-maximum range and mean value for crude oil properties and contaminants. While the mean or time-weighted average of sodium is low, the crude oil has contained, on occasion, upwards of 8 ppmw sodium, high enough to cause severe corrosion. Independent crude oil assays have verified this variation. Current Tapline deliveries originate from Ghawar field, some 560 kkm (350 miles) south of Qaisumah, while prior to mid-1982, the deliveries came from the Abu Hadriya and Fadhili fields.

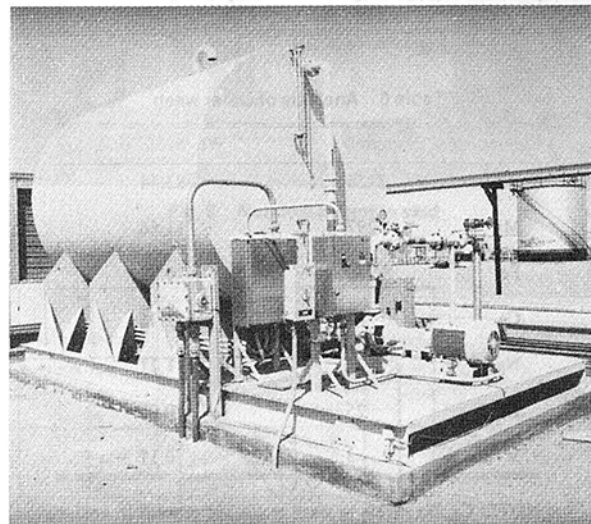
Operational results from sample analyses have consistently provided proof of significant sodium level reduction to levels below 1 ppmw after purification. Sodium reduction factors after purification have been observed to be as high as 10 with reduction factors of 4 to 6 being more common. (A reduction factor of 10 means that if sodium levels before purification are 5 ppmw, after purification they will be 0.5 ppmw.)



**Fig. 5 On-line sodium analyzer**



**Fig. 6 Water washing skid**



**Fig. 7 Water washing skid**

### Impact of Crude Oil Operation on Performance

Burning treated crude or other ash forming fuels invariably leaves deposits on the hot section components, which is undesirable for the following reasons:

- The accumulation of deposits, which increases with time,

**Table 4 Water wash time requirements (h)**

	Cool by Ratchet		Cool by Spinning*	
	Summer	Winter	Summer	Winter
Load Operation				
Cool Turbine to 150°C (300°F) Wheelspace Temperature	30	15	12	8
Set-Up for Water Wash	1	1	1	1
Water Injection	.5	.5	.5	.5
Drain Excess Water; Ready to Fire	.5	.5	.5	.5
<b>Total Down Time Required</b>	<b>32</b>	<b>17</b>	<b>14</b>	<b>10</b>

\*Three 20 minute spins at 20% speed

**Table 5 Deposit analysis**

As Measured		By Atomic Wt.		Probable Composition	
Substance	Wt.%	Substance	%	Substance	Wt.%
Na <sub>2</sub> O	.1	SO <sub>4</sub>	84.93	MgSO <sub>4</sub>	47.4
CaO	2.0	Mg	9.59	MgO	30.6
MgO	49.2	V	2.78	MgSiO <sub>3</sub>	6.7
FeO <sub>3</sub>	.5	Si	1.01	CaSO <sub>4</sub>	4.9
Al <sub>2</sub> O <sub>3</sub>	.8	Ca	0.64	V <sub>2</sub> O <sub>5</sub>	3.4
SO <sub>4</sub>	41.2	Ni	0.62	Al <sub>2</sub> SiO <sub>5</sub>	1.3
SiO <sub>2</sub>	4.5	Al	0.37	NiO	1.3
C	.2	Fe	0.22	Fe <sub>2</sub> O <sub>3</sub>	.5
NiO	1.3	Na	0.03		
V <sub>2</sub> O <sub>5</sub>	3.4	C	0.02		

**Table 6 Analysis of water wash**

Elements	ppmw	Wt. % of Total
SO <sub>4</sub>	2125	83.44
Mg	297	11.66
Fe	280	0.22
Ca	60	2.35
Na	31	1.21
K	25	0.98
V	3	0.11

NOTE: Ca, Na levels in wash water are present in analysis.  
Fe levels from pipe scale are present in analysis

restricts the throat area of the first stage nozzle through which the combustion gases must pass. This increases the operating pressure ratio and decreases the compressor surge margin. If allowed to accumulate indefinitely, these deposits will cause a forced outage.

• Deposit accumulation on turbine bucket airfoils compromises the ability of the turbine to extract work from the combustion gases and results in decreased turbine output.

• Deposit accumulation, by decreasing turbine efficiency, increases fuel consumption and hence generation costs.

The ash content in the treated fuel influences the rate at which deposits will accumulate. Inspection of the raw fuel analysis (Table 3) shows an ash content between 25 and 104 ppmw. Magnesium additive injection contributes the largest share of ash. Tapline crude currently contains 50 ppmw ash, but after magnesium additive injection this increases to 200–300 ppmw, which, when calculated at a yearly fuel consumption of 26,500 m<sup>3</sup> (7,000,000 gal) per unit, amounts to 6,800 kg (15,000 lbs.) of ash.

Three methods of removing these turbine deposits are employed: water washing, self-cleaning, and nutshell cleaning. The term self-cleaning is used to describe the phenomenon whereby the turbine deposits naturally spall off the turbine components upon the restart of a unit following a shutdown. Water washing is the process whereby water is used to clean the deposits from the turbine during a shutdown, before starting the unit. Nutshell cleaning is an on-line process whereby nutshells are periodically injected into the turbine flow path via the combustion chamber to remove a portion of the deposits.

The turbine water wash system consists of a water wash skid (Fig. 6 and 7), interconnecting pipe work from the skid to the turbine base, and an on-base water distribution manifold with valving. The skid contains a 19-m<sup>3</sup> (5000-gal) tank with submerged electric heating elements and a 380-l/m (100-gpm) pump. Once the unit has cooled, water is injected at 380 l/m (100 gpm) into the air side of the fuel nozzles for approximately 25 min while the turbine is cranking. Cleaning has been accomplished with as little as 3,800 l (1000 gal) of water. Excess water is drained and the turbine restarted. Borescope inspections, after waterwashing, but before refiring, have verified that most deposits are removed. Occasionally, it has been observed that small build-ups remain, particularly underneath the second stage turbine bucket shroud and on the 1st stage nozzle pressure surface. On subsequent start-up, if any deposits remain, the probability of their removal is high due to the fact that full power recovery is generally obtained.

The downtime loss associated with waterwashing is shown in Table 4. Allowing sufficient time so that the wheelspace temperature reduces to 150°C (300°F) prior to injection of 80°C (180°F) demineralized water avoids thermal shock. Cranking the unit to reduce the cool down period has not been necessary. When plant power availability is not a factor, a normal cool-down cycle to ambient will minimize starting package wear and allow the injection of unheated water. Provided the remaining plant generation capacity can meet system demand, availability loss is minimized by placing the turbine on standby status during the cool down period. Taking advantage of this, the availability loss during waterwashing is only one hour. If full power availability is essential, a unit will not be taken off for waterwashing; instead, nutshells will be injected more frequently.

Tables 5 and 6 show the chemical analyses of deposits and turbine wash water, respectively. The exact deposit composition is undetermined due to the analytical procedure used. The large percentage of deposits due to the crude oil sulphur content and the magnesium inhibitor can be noted. Tapline crude has 1.5–1.9 sulphur and at MS5001P part-load firing temperatures this probably accounts for the large accumulation of water soluble MgSO<sub>4</sub>, which is readily removed by washing. Changes in type or amount of additive dosage as well as changes in the firing temperature, will alter the type of deposit formed. Generally, the higher the firing temperature, the more difficult the deposits are to remove. The water wash contains predominantly MgSO<sub>4</sub>, as shown in Table 6.

Although water washing and self-cleaning are capable of

restoring full power, the unit must be shutdown, which is unacceptable during the critical summer months. On-line nutshell cleaning has been found to adequately control power loss during this period.

The turbine nutshelling system consists of a skid mounted hopper and interconnecting piping between the skid and the turbine (Fig. 8 and 9). The hopper is filled with 4.5 kg (20 lbs.) of nutshells and pressurized with air from the atomizing air system which results in the nutshells being propelled into the gas stream midway through a dilution hole in one of the ten combustion liners. The hopper is then refilled and the procedure repeated for the remaining liners.

The compressor is cleaned every month with nutshells injected through the inlet duct mounted hoppers. This resulted in negligible power recovery because of a lack of appreciable quantities of oil fouling and/or sand carryover from the automatic self-cleaning inlet air filtration system.

Figure 10 shows the turbine's output stabilizing at 93 percent capability after 800 hrs of continuous deterioration. Current turbine waterwashing and nutshelling intervals are 2500 hrs and 15 days, respectively. If waterwashing was performed at 800 hr intervals, the average power output would rise to 96.5 percent. However, because fuel cost is not a significant

factor and excess generating capacity exists throughout much of the year, this has not been done.

In 1981-83, performance tests were conducted to establish the power loss characteristics at nutshelling intervals of 3, 5, 8, and 15 days. No change in the rate of power loss was apparent.

The average nutshelling power recovery is 0.4 MW or 1.8 percent of capacity. The nutshelling power recovery factor, a measure of the cleaning effectiveness, is 50 percent.

Because both self-cleaning and water washing usually restore full power, the main difference between them appears to be only the method and time of deposit removal, i.e., deposit removal via water during shutdown for water washing or deposit removal via thermal expansion, aerodynamic, and/or rotating induced forces during start-ups for self-cleaning. The actual mode of deposit breakdown appears to be associated with the thermal cycling of the unit, i.e., extreme thermal fatigue of one cycle. Consequently, it is evident that the effectiveness of the self-cleaning method is dependent on the degree of the thermal cycle. This helps to explain the fact that not all shutdowns result in full restoration of power, as shown in Fig. 10. The first shutdown at 820 hrs, which has obviously not experienced a full thermal cycle has not recovered full power. The shutdown at 1800 hrs, however, was down for approximately sixty (60) hrs and resulted in full power recovery upon start-up.

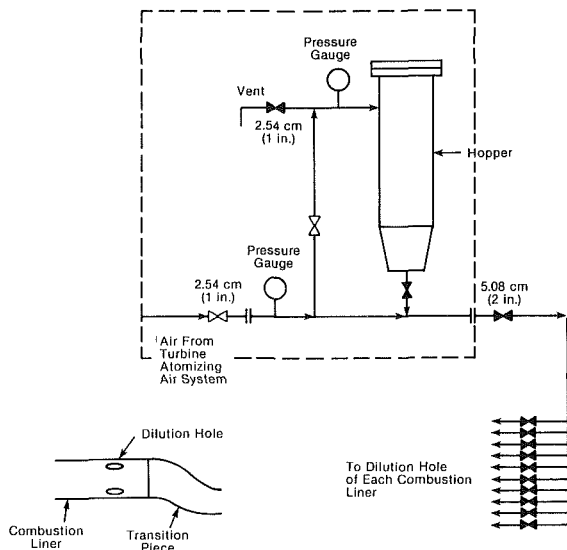


Fig. 8 Nutshell injection skid

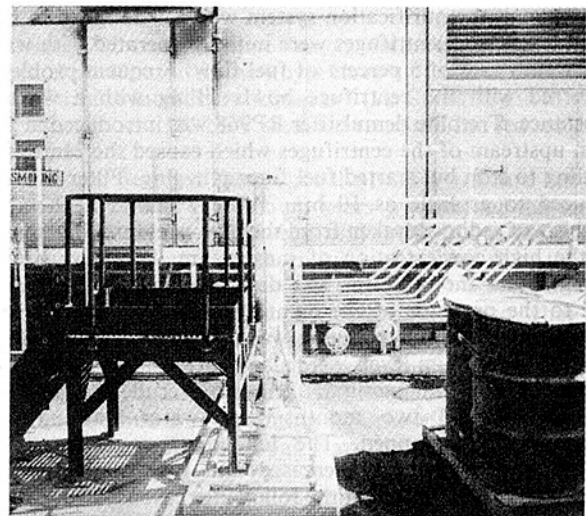


Fig. 9 Nutshell injection skid

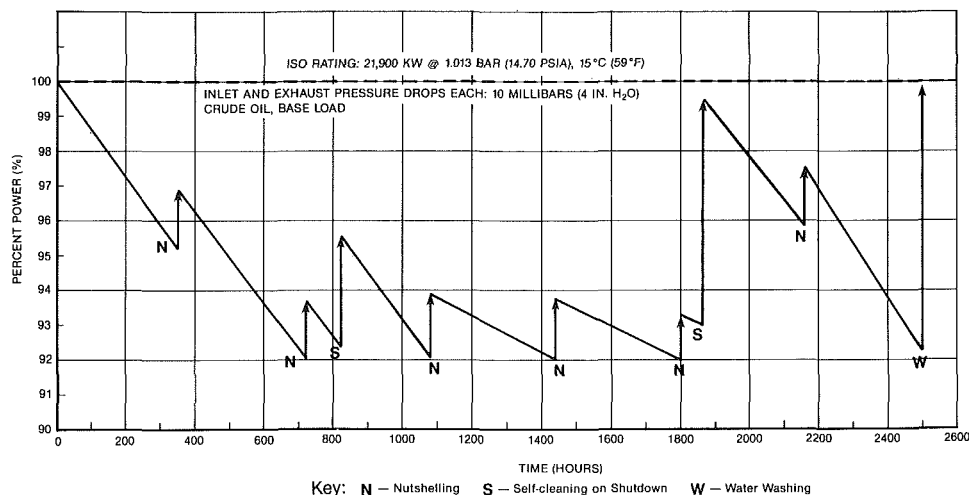


Fig. 10 Gas turbine performance loss and recovery



**Table 7 Analysis of sediment from turbine filter**

Component	Weight Percent of Total Sample %
MgCO <sub>3</sub>	35
MgSO <sub>4</sub>	21
Fe <sub>3</sub> O <sub>4</sub>	11
NaCl	2
CaCl <sub>2</sub>	2
FeS	nil
Potassium	nil
Vanadium	nil
Lead	nil
Organics & H <sub>2</sub> O	26

### Operation and Maintenance Impact of Crude Oil Operation

Although the purification system was not designed to mix wash water, the centrifuges were initially operated with wash water flow rate of 5 percent of fuel flow. Frequent problems occurred with the centrifuge bowls filling with a waxlike substance. Tretolite demulsifier RP968 was introduced at 200 ppm upstream of the centrifuges which caused the centrifuge fouling to stop but started fuel filter plugging. Filter life was reduced to as little as 10 hrs. Table 7 shows a chemical analysis of sediment taken from the high-pressure filters. Due to the high concentration of magnesium, it was originally thought that the inhibitor was destabilizing and coarsening due to the presence of the demulsifier. It was finally concluded that the filter plugging was due to a wax separation because the sodium levels were also concentrated to the same degree as the magnesium. The raw crude heater was recalibrated and two months later water washing and demulsification stopped. The immediate result was that centrifuge performance increased and fuel filter plugging stopped for one or more of the following reasons:

- The crude oil temperature was raised above the wax solubility temperature thus increasing centrifugal separation efficiency.
- Excessive demulsification interfered with the separation of oil and water inside the centrifuge, possibly being aggravated by the continued presence of wax.
- Wash water, being of questionable quality, possibly introduced more contaminants than were removed.

Since February 1981, fuel system plugging problems have all but disappeared. Only in isolated instances have any fuel nozzle check valves or high-pressure filters been replaced due to plugging. Centrifuge capacity had to be temporarily derated to maintain proper temperature due to the failure of one of the two crude oil heaters.

Operation of the centrifuge is automatic and can generally be run unattended; however, periodic inspections during start-up, shutdown, and during normal operation are made to minimize malfunctions. The centrifuges are operated only long enough to fill one of the two treated crude oil tanks. The capacity of 750 l/m (200 gpm) and availability of the fuel

purification system has precluded the need to transfer to distillate. Ninety-five percent of all fired hours have been on crude oil.

Maintenance items on the purification skid occur regularly but are generally minor repairs such as to change a defective valve, switch, damaged flexible crude hose, or to fix leaks. Centrifuge drive gears were changed on one unit due to noisy operation. Preventive maintenance on each centrifuge is performed on a monthly and yearly basis.

Because the load is constantly varying during the day, operations must adjust the magnesium flow rate correspondingly. Although each adjustment is not overly time consuming, an automated injection system which responds to changes in load is desirable. Care must be taken in the handling of the inhibitor as the magnesium compounds will tend to stratify, in time, if exposed to water and heat.

Combustion inspection intervals were initially scheduled at 1500 hr intervals but were increased to 3000 hrs during 1982. Starting in 1983, this was raised to 4500 hrs with further increases planned. Combustion liners and transition pieces have never been changed on any unit. One crossfire tube retainer was replaced in November 1980 and two ignitor shields in October 1981. On occasion, large deposit build-ups in the crossfire tubes have been observed. Since commissioning, there have been only two alarms for excessive exhaust gas temperature spread. As of July 1983, there were no visual indications of hot corrosion, cracking, or distortion in the hot gas path. A flow divider failed in October 1982, but this was attributed to normal wear and tear. Other than this, no major fuel system component has failed. There have been three to four mechanical breakdowns of the magnesium injection pumping unit. Plugging of the 125 micron high-pressure fuel filter and fuel nozzle check valves occurred quite frequently during initial operation but as soon as fuel washing and demulsification stopped so did the plugging problems. Fuel nozzle and/or fuel nozzle check valve replacement occurs very infrequently.

### Summary

The over 43,160 fired hrs of crude operation of the MS5001P units at the Qaisumah power plant is a significant demonstration of the effectiveness of centrifugal purification without the addition of wash water. Centrifugal purification has effectively reduced up to 8 ppmw of sodium plus potassium in the raw crude oil to less than 1 ppmw.

Full power is periodically restored by removing the ash formed from the crude oil and magnesium additive by either water washing and/or self-cleaning. When the shutdown of the units is prohibited due to periods of high-load demand, on-line nutshell cleaning has been proven to be able to successfully control power loss.

This performance combined with the high level of plant availability that has been achieved further demonstrates the ability of the gas turbines to operate on crude oil.

### References

- 1 Rose, R. S., Caruvana, A., Cohn, A., and Doering, H. vonE., "Application of Heavy Fuel Test Results to Gas Turbine Operation," ASME Paper No. 82-GT-193.
- 2 Barnum, B. M., and Duncan, R. L., "Gas Turbine Performance Deterioration and Water Wash Frequency," ASME Paper No. 81-JPGC-GT-10.
- 3 Lynch, J. R., Charron, M. A., and Baank, J., "Residual Fuel Experience on a General Electric MS7001 Gas Turbine in Suriname, South America," ASME Paper No. 82-GT-53.
- 4 Whitlow, G. A., Sherlock, T. P., Cohn, A., et al., "Combustion Turbine Deposition Observations from Residual and Simulated Residual Oil Studies," ASME Paper No. 82-GT-87.

**L. V. Shelton**  
Asst. Director,  
Marine Engineering.

**R. S. Carleton**  
Asst. Vice President  
Designers & Planners, Inc.,  
Arlington, Va. 22202

# The Marine Environment and Its Influence on Inlet System Design

*Historically, two of the principal hindrances to the design of effective marine gas turbine inlet systems have been the inability to define the marine environment and to identify the influence of this environment on the inlet system configuration. This paper summarizes the work done by the U.S. Navy to qualitatively and quantitatively define the composition of the marine atmosphere and identify inlet system design practices that can be employed to assist in designing an effective combustion air inlet system.*

## Introduction

The ingestion of airborne contaminants in the combustion air of gas turbine engines has proven to be the principal factor contributing to decreased engine performance and life. While the problems associated with contaminant ingestion have been experienced to some extent by all gas turbine, they appear to be most severe in the marine environment. This fact stems principally from the mobile characteristics of the installation. While most industrial engines tend to be stationary in nature and thereby subjected to the environmental conditions of one location, the marine engine can be subjected to all extremes of environment from open ocean conditions, to arctic conditions, to terrene conditions. In many instances these extremes of environment may be experienced simultaneously.

In an initial effort to support the installation of marine gas turbine engines as propulsion and generator prime movers aboard circa 1970-1980 surface ships, the U.S. Navy in 1965 initiated the Gas Turbine Combustion Air Aerosol Separation Program. The principal objectives of the Aerosol Separation Program were to assess the at-sea environment and evaluate various inlet filters under controlled test conditions. Under this program, U.S. Navy personnel conducted salt surveys aboard numerous U.S. Navy, Royal Navy, Royal Canadian Navy, and Royal Danish Navy destroyer type vessels in the North Sea, the Carribean Sea, and the North and South Atlantic Oceans. Although the data collected during these surveys were limited in nature, they provided the airborne salt loading data used to design the inlet systems aboard the DD 963 *Spruance* Class destroyers, the FFG 7 *Oliver H. Perry* Class frigate, and the PHM 1 *Pegasus* Class hydrofoils.

At the same time, the Royal Navy via the National Gas Turbine Establishment (NGTE), was conducting similar studies to support the Royal Navy's decision to go solely to gas turbine propulsion systems for surface combatants. The results of NGTE's work were published in a series of reports

in the 1972 to 1973 time frame, followed in 1974 by the formal publication of the Royal Navy's "Code of Practice for Gas Turbine Intakes and Uptakes" [1]. Contained in the Code of Practice was NGTE's assumed standard for sea salt levels in air, Fig. 1.

It should be noted that, while the NGTE standard has been accepted over the intervening years by most of the marine community as the referenced criteria defining the marine environment, it has never been fully subscribed to by the U.S. Navy. This nonacceptance of the NGTE standard stems primarily from a difference in philosophy as to what conditions should define the "average day" represented by the standard. The U.S. Navy with its multiple ocean Navy and global military commitments chose to design to inlet salt loading conditions representing a world-wide "average" day. NGTE, based on the Royal Navy's more limited military commitments, chose to base its standard on the worst case inlet loadings of "green-water" ingestion representative of winter conditions in the North Atlantic and Arctic Oceans, and the North Sea. Although this philosophical difference has

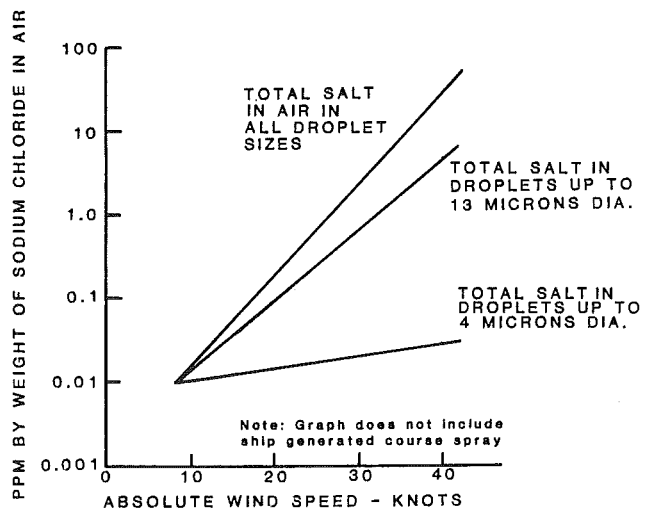


Fig. 1 NGTE salt aerosol test standard

Contributed by the Gas Turbine Division of THE AMERICAN SOCIETY OF MECHANICAL ENGINEERS and presented at the 29th International Gas Turbine Conference and Exhibit, Amsterdam, The Netherlands, June 4-7, 1984. Manuscript received at ASME Headquarters December 9, 1984. Paper No. 84-GT-137.

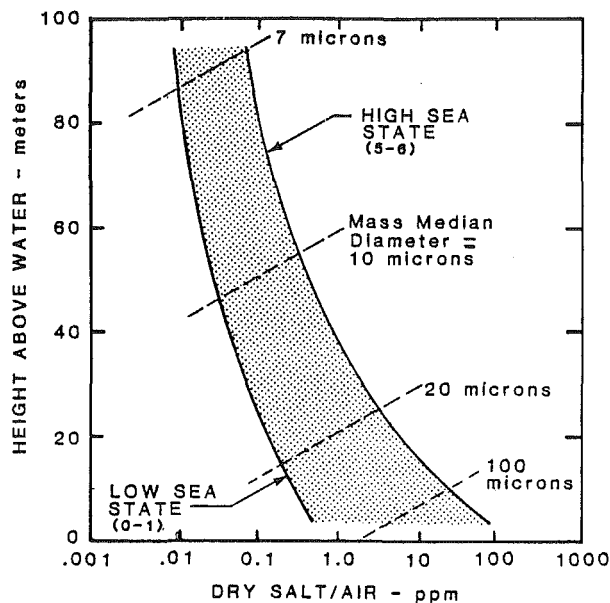


Fig. 2 Generalized characteristics of salt aerosol boundary layer above water/air interface

led to different approaches to inlet system design, the validity of each decision has been successfully proven in numerous practical applications.

In 1975, the U.S. Navy, via the Naval Sea Systems Command (NAVSEA), promulgated the Marine Gas Turbine Inlet Development Program. The principal objective of the program was to extend the operational life of marine gas turbine engines by improving the quality of the engine's inlet combustion air. In order to achieve this objective, NAVSEA undertook various research and development efforts, including:

- 1 Development of real-time instrumentation capable of measuring and cataloging the mass and particle size distribution of airborne salt aerosols
- 2 The accomplishment of at-sea salt measurement surveys to augment previously available marine salt-in-air data
- 3 The accomplishment of controlled environment tests of various moisture separators and combinations thereof to provide a common base for comparative performance analysis
- 4 The definition of the aerodynamic and boundary-layer characteristics of various ship configurations and how these characteristics influence the presence of ship generated aerosols at various locations aboard the ship

To date significant strides have been made in each of the four work areas. In conjunction with the Naval Research Laboratory, the University of Washington developed a portable sodium ion scintillation flame spectrophotometer which provided the capability of acquiring real-time salt aerosol concentration and particle size distribution data. Using the University of Washington spectrometer and other mass and particle distribution measuring instruments, U.S. Navy survey teams have conducted at-sea salt aerosol surveys aboard the gas turbine freighter GTS *Admiral William M. Callaghan*, the oceanographic research ship USNS *Hayes*, the USS *Spruance* (DD 963), the USS *Samuel Morison* (FFG 13), the fast patrol boat *Osprey* (PTF 25), and the Amphibious Assault Landing Craft *Jeff* (B). When coupled with data acquired during the Combustion Air Aerosol Separator Program [2], the data acquired during the Inlet Development Program provide a strong data base for predicting dynamic shipboard salt aerosol loadings. Comparison of these data with data collected by the Naval Research Laboratory aboard a static off-shore drilling rig provides information with respect to the influence of various ship's configuration and

the contribution of ship's dynamics to the loadings that can be expected at the inlet system intake.

## The Marine Environment

At-sea surveys and ships' operational data indicate the potential presence of three environmental elements that will affect the gas turbine and the subsequent design of the engine's combustion air inlet system. These elements include salt aerosols, sand, and ice.

**At-Sea Salt Aerosols.** The natural interaction between waves and the prevailing winds generate small bubbles of foam on the surface of the ocean. As these bubbles burst, small sea water droplets and aerosols are expelled into the atmosphere creating a salt-laden boundary layer directly above the water/air interface. The height and density of salt aerosols within this layer vary as a function of the size of the generated aerosol and the severity of the environmental conditions: i.e., the higher the sea and wind states, the larger the diameter of the aerosols generated and the greater the height and density of the boundary layer.

Additionally, the relative motion of any ship through the ocean will generate a bow wave and wake. As the foam bubbles in the bow wave and wake burst, additional droplets and aerosols will be expelled into the boundary layer. The diameter and quality of these ship-generated aerosols and droplets will be functions of sea and wind state, ship speed, heading, and even hull form.

In most instances, the larger natural and ship-generated droplets, defined herein as 50 microns in diameter or greater, will settle back into the ocean within seconds of their generation. The smaller aerosol particles, however, may become entrained in the ship's boundary layer and carried to any exposed deck surface.

The actual height and density profile of the aerosol laden boundary layer will vary as a function of ambient conditions. Although not specifically defined, Fig. 2 presents a generalized range of the boundary layer height/density relationship based on the at-sea survey data collected during the Gas Turbine Inlet Development Program. Also plotted is the average "wet" particle mass median diameter associated with the readings taken. It should be noted that Fig. 2 includes the effects of ship-generated spray present at the time that the survey readings were acquired.

As with any water droplets suspended in the atmosphere, ambient or atmospheric relative humidity will affect the actual diameter of the at-sea salt aerosol. As the relative humidity increases and decreases, the diameter of the suspended aerosol will correspondingly vary as the amount of water in the salt aerosol condenses and evaporates. It must be noted, however, that regardless of the amount of water present in the aerosol, its salt content remains constant under all conditions. Survey data have shown that aerosols tend to be "wet" or saturated within a humidity range of 80 to 100 percent with the greatest increase in diameter occurring as the humidity increases from 90 to 100 percent. As the humidity decreases below 80 percent and partial evaporation of the water in the droplet occurs, the remaining aerosol tends to take on a tacky character until at 40 percent humidity where the remaining aerosol becomes essentially a dry salt particle. In the case of increasing humidity, however, the reverse effect is not true. As the humidity increases above the 40 percent threshold, the salt aerosol will retain the basic characteristics of a dry particle until the humidity reaches 70 percent, where the aerosol will rapidly deliquesce back to its saturated state. This phenomenon is depicted graphically in Fig. 3.

Smaller, naturally generated open ocean salt aerosols will generally remain in suspension for sufficient time to reach equilibrium with respect to the relative humidity. Ship

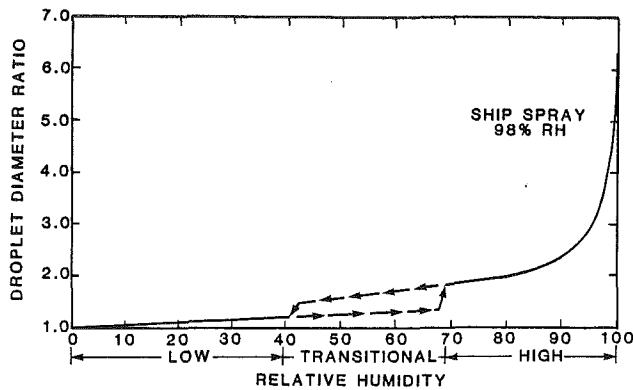


Fig. 3 Salt droplet size relation with humidity [3]

generated aerosols and those generated by the action of waves against a beach or solid wetted structure may not, however, have time to reach equilibrium. These aerosols and droplets will tend to be larger, heavier, and wetter than the stabilized natural aerosols and thereby tend to be found in the lower levels of the aerosol boundary layer.

The actual amount of salt contained in the salt aerosols present at the intake of the inlet system is referred to as the inlet concentration or loading. Concentration is measured in parts per million (ppm), the ratio of parts of salt per million parts of air on a mass basis. The average or mass median diameter (mmd) is the mean diameter of the population of aerosols contained in a sample of marine atmosphere. Mass median diameter is measured in microns (millionth of a meter [1 micron equals 0.000039 in.]). For reference purposes, visible fog ranges in mmd from 10 to 50 microns with light rain being of a mmd of approximately 100 microns.

As can be seen from the preceding discussion, the loading and mass distribution of the salt aerosols present at the inlet system ambient intake(s) can vary considerably depending upon ambient and operational conditions and the characteristics of the installation. Specifically, intake loadings will be dependent on the following factors:

- Ambient sea and wind conditions
- Inlet orientation with respect to the prevailing weather
- Inlet location and orientation within the installation (inboard versus outboard facing; sheltered versus outboard facing)
- Inlet height above water
- Installation type and configuration (stationary platform, wide beamed cargo vessel, high length to beam ratio combatant vessel)

One of the unwritten objectives pursued during the Gas Turbine Inlet Development Program was the definition of a single standard salt aerosol that would be representative of the ship and motion-generated aerosols present in the over-ocean aerosol boundary layer. This single aerosol standard would then have provided a fixed point design condition for the development of U.S. Navy gas turbine inlet combustion air systems.

Once initial at-sea survey data had been analyzed and the various factors influencing the system inlet loadings identified, however, the idea of developing and using a single-point standard was abandoned. In its place, a composite standard which defines the inlet loadings as a function of wet aerosol mass median diameter was developed. This standard (see Fig. 4) reflects typical inlet salt loadings as measured during the Combustion Air Aerosol Separator Program, during the six at-sea surveys conducted under the Inlet Development Program, and as presented in historical data from the open literature [4-8].

Of specific note is the fact that Fig. 4 presents the inlet loading as a function of wet particle mass median diameter,

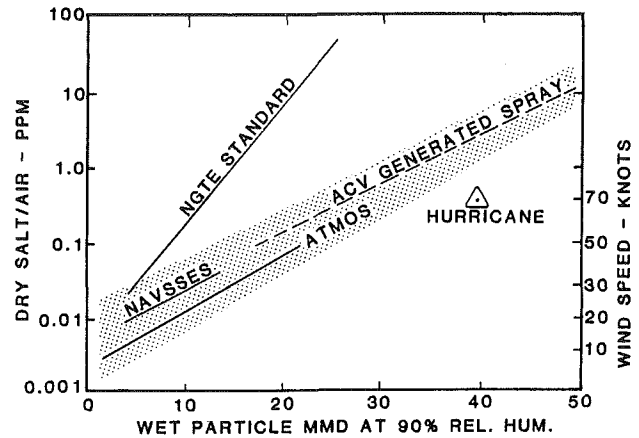


Fig. 4 U.S. Navy marine atmospheric salt aerosol concentration standard [3]

not as a function of some operational or ambient condition. Herein lies one of the major findings of the Inlet Development Program; whereas engine performance and life is a function of the total mass of salt ingested by the engine, filter performance is, within constraints, a direct function of the ingested aerosol size distribution.

It should also be noted that the salt aerosol concentrations are presented for a range of particle diameters rather than as a single line function of diameter. This has been done intentionally to reflect the influence of the numerous operational and ambient conditions discussed previously.

To identify the characteristics of the inlet loadings the following procedure is followed:

- 1 Based on preliminary platform design studies, enter Fig. 2 with the estimated height of the inlets above the water and read the dry salt/air loading in ppm.
- 2 Using the projected loadings, enter Fig. 4 and define the expected wet particle mass median diameter range.
- 3 Using Fig. 3, adjust the mmd range for any known influences of relative humidity.

The adjusted inlet salt aerosol loadings and mass median diameters calculated above now define the estimated airborne salt aerosol environment for which the inlet system should be designed.

**Sand.** In isolated cases, various ships and stationary marine platforms have been subjected to the influence of airborne sand and dust. Principally, these cases have been limited to geographical areas characterized by coastal deserts or arid regions such as the Persian Gulf area. In such instances, winds blowing off of the land have been known to carry fine airborne sand and dust particles out to sea for distances of up to 300 kilometers (approximately 200 miles). Additionally, air cushion vehicles will be subjected to sand loadings when operating on beaches or in shallow waters.

Similar to salt aerosols, sand particle diameters are measured in microns. Sand loadings, however, are measured in milligrams of solid mass per cubic foot of air. To date, the inlet sand loadings that may be experienced by various ship types have not been measured, except for the limited AALC Jeff(B) measurements taken along the Florida Gulf Coasts [9, 10]. These limited data, however, have been compared to and assimilated with sand loading data compiled for ACV applications by the British Hovercraft Corporation Limited [11], for various vehicular applications by the Donaldson Company, Inc. [12], and for various industrial applications by the American Air Filter Company [13]. Based on these compilations, the U.S. Navy has adapted the inlet sand loadings shown in Table 1 to be applied on an as required basis as defined by the operational requirements of the platform being designed.

**Table 1 U.S. Navy suggested sand/dust loadings**

Condition	Average particle dia	Inlet loading
Dust haze (off-shore)	1-3 microns	.0005-0.1 mg/ft <sup>3</sup>
Dust storm (beach proximity)	5-15 microns	0.1-4.0 mg/ft <sup>3</sup>
ACV over beach operation	98% > 150 microns	2.0-4.0 mg/ft <sup>3</sup>

**Ice.** A second geographically limited element that will influence inlet system design is ice. Ice in the marine environment occurs in two forms: glaze and rime ice. The principal sources precipitating the formation of ice at sea are freezing spray, precipitation, fog, and condensation. Glaze ice, resulting principally from spray or precipitation, is formed when large quantities of water freeze over an extended period of time. Glaze ice, characterized by its smooth, transparent appearance and high adhesive strength, presents a threat to the inlet system primarily from the potential blockage of the system inlet screens, louvers and potentially even filter elements. Rime ice, characterized by its opaque appearance, roughness, and low adhesive strength is precipitated principally by the impact of super-cooled sea water aerosols and droplets on system components. The principal threat rime ice poses to the inlet system and to the supported engine is the possibility of physical damage that could result from large sections of rime ice breaking away from a louver or duct wall and impacting the filter elements or being ingested by the supported engine.

**Icing Frequency.** Under sponsorship of the Gas Turbine Inlet Development Program, the U.S. Naval Air Propulsion Center, Trenton, N.J., conducted a survey to determine the frequency of encountering icing conditions [14]. This study was limited geographically to the Atlantic Ocean north of the 30th parallel. This limited area was selected principally because it provided the most complete meteorological data base of the world's oceans.

The study concluded that icing could occur if any or all of the following conditions were to occur simultaneously:

- Air temperature equal to or less than 0°C (32°F)
- Sea temperature equal to or less than 5°C (41°F)
- Windspeed equal to or greater than 9 m per s (17 knots)
- Wave height equal to or greater than 3 m (10 ft)

Based on these conditions, the study concluded that intake icing, while occurring infrequently, will be a problem that most ships and selected off-shore installations will encounter at some point during their operational life. For example, although actual icing did not occur, the above combination of environmental conditions which foster icing occurred in the same area off the coast of Newfoundland, Canada on 6 of the 30 days in January. In one instance, these conditions extended up to 1287 kilometers (800 miles) off-shore.

**Spray Icing.** Spray icing is responsible for approximately 75 percent of the icing conditions experienced at sea. Spray icing is generally encountered only under conditions where the following occur concurrently:

- The wind is greater than Beaufort Force 5
- Wave height exceeds 2.7 m (9 ft)
- Ambient air and sea temperatures are less than -2.2°C (28°F) and 7.8°C (46°F), respectively.

At air temperatures below -17.8°C (0°F), however, the possibility of ice formation at the level of the intakes is reduced as most of the droplets reaching the inlet will be in the frozen state. Within the -17.8°C to -2.2°C range, the spray generated by the ship and ambient conditions becomes supercooled during flight and freezes on contact with a cold surface. At the lower end of the temperature range rime ice is formed. At the higher end of the range, between ap-

proximately -10°C and -2.2°C, the spray being supercooled to a lesser degree may form glaze ice.

**Precipitation Icing.** Precipitation icing is promulgated by rain, sleet, and snow. All three elements can exist singly or in combination anywhere within the icing range, however, precipitation below -9.4°C (15°F) is usually in the form of dry snow.

Potentially the most hazardous form of precipitation to the inlet system is wet snow. Rain and sleet, due to their high density to diameter ratios will fall at relatively high velocities such that properly placed inlet louvers will shield the inlets from these droplets. Snow, however, having a high aerodynamic drag as a result of its characteristic high size to mass ratio, falls at a velocity of approximately 1 m per s. At this velocity the individual flakes of snow will tend to impact and adhere to the individual vane surfaces. As the amount of snow increases, the air passages between the individual vane elements will become blocked and flow to the engine effectively reduced. In the case of dry snow the majority of flakes induced into the inlets will bypass the louvers and become entrapped on the filter face. As the amount of snow on the filter face builds up it will effectively block the air flow path and increase system pressure loss.

**Fog Icing.** While fog may exist in three distinct types (radiation, advective, and frontal) only frontal fog will be experienced in the freezing range. Frontal fog can occur both on land and at sea. This type of fog results from the impact of a warm, humid air mass with a cold air front. Frontal fog is however, somewhat limited to coastal regions with a seaward limit of approximately 13-16 km (8-10 miles). The mass median diameter of sea fog at 0°C is approximately 45 microns, well within the separation capability of all currently available filters.

Steam fog or "Arctic sea smoke" may be encountered at sea in conditions where the air temperature is more than 9°C (16°F) colder than the surface water temperature. "Arctic frost" which is a special case of steam fog may occur when the ambient air temperature is below 0°C (32°F). "Arctic frost" is formed by suspended supercooled fog droplets that freeze on contact with a solid object. The occurrence of supercooled fog at sea, however, is extremely rare.

**Condensate Icing.** Condensate icing results from the freezing of free water in the air under static temperatures of 0°C (32°F) or below. Where other forms of icing primarily impact those areas and surfaces of the inlet system, condensate ice usually occurs on system internal components such as silence vanes, engine inlet screens, and in the engine inlet itself. Because of its potential to cause damage to the engine, condensate icing is of particular concern to the inlet system designer.

## Influence of Environment on Inlet System Design

The preceding paragraphs have discussed the U.S. Navy's work in defining the ambient marine environment. This environment, coupled with the engine manufacturer's contaminant ingestion limits and installation performance requirements, define the envelope for which the vessel or platform's inlet system must be designed.

In most land-based industrial gas turbine installations, the development of the inlet design will evolve directly from the defined requirements with only minimal regard for system volume and weight. In the marine installation, however, design constraints are commonly imposed on system weight and volume due to the overall space and stability restrictions characteristic of the application. In many instances, these design constraints will require a compromise in inlet system or

engine performance. In the long term, such compromises will invariably result in decreased engine performance and increased engine operating and overhaul costs. In most cases, the choice of compromise leads to a trade-off of engine performance versus engine life. In short, the compromise narrows down to a choice of designing a marginally effective inlet system with low pressure loss to gain immediate benefits in engine performance at the risk of engine life, or of designing a complicated system with high losses to gain engine life at the risk of performance.

Data acquired during the Aerosol Separator and Inlet Development Programs indicate the existence of three design variables which can be employed to decrease the inlet system loadings and thereby reduce the compromise which may have to be made. These factors are inlet height, orientation, and location.

**Height.** As discussed previously, the aerosol boundary layer exhibits decreasing density and particle size distribution with increasing height. During the Inlet Development Program, special attention was devoted to defining the variations in face loadings that occurred as the inlet height above the water was increased.

Data collected during the survey of an Osprey Class patrol boat indicate salt aerosol loadings at the level of the intakes, 3–6 m (10–20 ft) above the water, to be in the range of 0.5–50 parts per million (ppm) with a particle mass median diameter (mmd) of 15 microns [15].

In comparison, low sea state data acquired during the survey of the FFG 13 guided missile frigate USS *Morison* indicated salt loading at the bottom and top of the inlet louvers, 6–15 m (20–49 ft) above the water, to be 0.07 to 0.056 ppm at a mmd of 12 microns respectively (16). When extrapolated to high sea state conditions, typical inlet loading of 0.5 to 0.1 ppm are estimated. Thus a significant reduction can be seen between the measured Osprey and FFG 13 loadings.

Similarly, data collected during surveys of the DD 963 Class destroyer USS *Spruance* and the Roll-on, Roll-off vessel GTS *Admiral William M. Callaghan* indicate salt loadings at the intake levels, 15.2 and 27.5 m (50 and 90 ft) above the water respectively, to be in the range of 0.1 to 0.01 ppm at a mmd of 7 microns (17 and 18).

As can be readily seen, a significant reduction in inlet loading can be gained by locating the inlets as high above the waterline as possible. A similar benefit can be derived for stationary installations by locating the inlets as high above the water interface as possible. The determination of the actual height for the inlets, however, must be coordinated with other design features such as overall space arrangements, vessel/platform structure, and the installation requirements for other critical equipment and systems.

**Orientation.** Once inlet height has been selected, the orientation of the inlet faces should be established. Data developed from surveys conducted aboard the *Spruance*, *Callaghan* and the Danish destroyer *Peder Skram* indicate that for inlets installed 15 m (50 ft) or more above the water level, the physical orientation of the inlets will not have a measurable impact on the inlet loadings, except that the mmd of the loading particles will be slightly higher for forward and outboard facing inlets than for aft facing inlets.

Below the 15-m level, however, the orientation of the inlet can significantly impact loadings. Survey data taken during the Aerosol Separator Program aboard a 20-m (65-ft) gas turbine powered search and rescue boat having inboard and aft facing inlets reflected a high sea state inlet loading of 0.05 to 0.3 ppm at an average mmd of 10 microns [1]. When compared to the 0.1–0.5 ppm, 12 micron high sea state loadings estimated for the higher mounted outboard facing

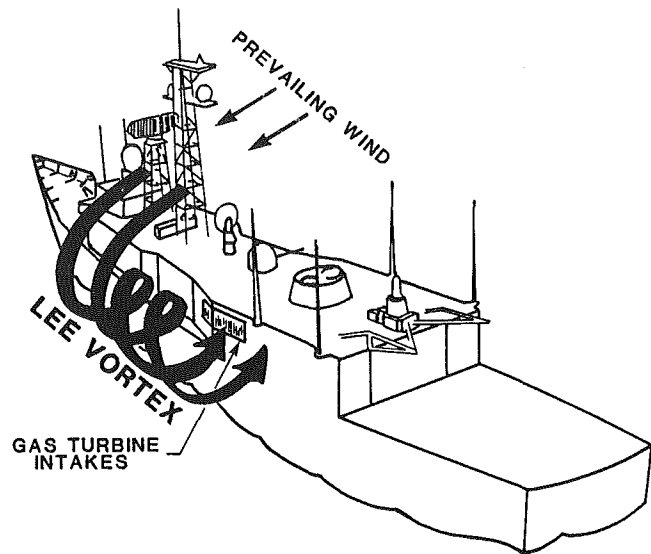


Fig. 5 Lee vortex effect

inlets aboard the FFG 13, the benefit to be gained as a result of inlet orientation can be seen. Although at-sea data for comparative height forward facing inlets are not available, survey data taken aboard the oceanographic research vessel USNS *Hayes* and aboard the USS *Meredith* indicate that forward facing inlets will be subjected to significantly higher inlet loadings consisting principally of large mmd ship generated spray droplets.

**Location.** During wind tunnel tests sponsored by the Inlet Development Program, it was noted that during cruising conditions with the prevailing winds approaching the ship from abeam, air passing over the ship's structure formed a lee vortex on the down wind side of the ship [19]. Under influence of this vortex, shown graphically in Fig. 5, wind passing over the ship was seen to fold down to the water surface where it would roll back into and up the lee side of the ship. During its passage along the water surface, salt aerosols from foam and spray became entrained in the air and were carried up the ship's hull.

During the Inlet Development Program surveys, inlet loadings on the lee side of the survey ship were measured in many instances to be as much as 2.5 times higher than the inlet loadings measured on the windward side. To minimize the effect of the lee vortex requires only that the inlet be inset from the side of the ship or that a nonperforated platform be installed outboard of the inlet. Survey data have indicated that an inset distance of twice the inlet height will remove the inlets from the influence of the lee vortex.

## Summary

The natural marine environment is comprised of three elements that historically have proven harmful to marine gas turbines: salt aerosols, sand/dust, and ice. Although present in varying concentrations, and in the case of sand/dust and ice isolated to selected geographical locations, each must be addressed in the design of any marine gas turbine combustion air inlet system. Failure to properly address these elements can result in decreased engine performance and increased engine operating and overhaul/replacement costs.

At-sea survey data collected during the U.S. Navy Gas Turbine Inlet Development Program have shown steady-state inlet salt loadings for conventional surface ships rarely exceed 0.1 parts per million. Inlet salt loadings for air cushion vehicle and small patrol craft will invariably be considerably higher

with short duration transient loads reaching as high as 500 parts per million. In either case, U.S. Navy measured marine salt aerosol loadings are substantially lighter than the universally accepted standard loadings published in 1973 by the Naval Marine Wing of the National Gas Turbine Establishment, U.K.

U.S. Navy survey and operational data also indicate that vessels and stationary installations operating under the influence of winds blowing off shore of arid coastal areas can be exposed to sand and dust loadings in addition to the normal salt loadings. Reports provided by vessels operating in the Persian Gulf area of the Indian Ocean document the presence of such sand laden air at distances of up to 322 km (200 miles) offshore.

The actual design of any combustion air inlet system must be a function of the application with the system design envelope being defined by the ambient inlet loadings, the engine contaminant limits, and the engine performance requirements. Inlet Development Program survey data indicate, however, that three design practices can be employed to lighten expected inlet loadings and ease the separation efficiency demands placed on the inlet system filter components. In general these practices and their benefits can be summarized as follows:

- The higher the system inlet face can be located above the vessel's waterline, the lighter the inlet loads
- The more sheltered the inlet face is from ambient and relative wind conditions, the lighter the inlet loads
- The further the inlet face can be set from the deck edge of the ship, the lighter the inlet loads

In summary, the design of any inlet system should be tailored to specifically address the expected environmental conditions to which the system will be exposed. In developing an inlet system design, however, the design engineer must remain flexible enough that he can make compromises in his design that will ultimately enhance the overall performance and cost of the total application.

## References

- 1 "Code of Practice for Gas Turbine Intakes and Exhausts," DG Ships/522/03/25/215, Report JB/JLN/RM, NGTE, Naval Marine Wing, Jan. 1973.
- 2 Kaufman, R. E., and Pollini, R. J., "Gas Turbine Combustion Air Salt Aerosol Separation Program," Subproject S-4617X, Task 105005, NAV-SECPHILADIV Project T-454, Naval Ship Engineering Center, Philadelphia, Pa., 10 December 1968, Defense Documentation Center AD 851951.
- 3 *Gas Turbine Inlet Design Handbook*, Department of the Navy, Naval Sea Systems Engineering Station, Philadelphia, Pa., Apr. 1983.
- 4 Woodcock, A. H., *J. Meter*, Vol. 10, 1953, pp. 362-371.
- 5 Fitzgerald, J. W., "On the Growth of Atmospheric Aerosol Particles With Relative Humidity," *Proceedings of the Fifth Meeting of the E-O Sensor Atmospheric Optics Working Group*, 4-5 April 1973, Las Cruces, N.M.
- 6 Durbin, W. G., and White, G. D., "Measurement of the Vertical Distribution of Atmospheric Chloride Particles," *Tellus*, 1961.
- 7 Lovett, R. F., "The Occurrence of Airborne Sea-Salt and Its Meteorological Dependence," M.Sc. thesis, Heriot-Watt University, Edinburgh, U. K., 1975.
- 8 Toba, Y., "On the Giant Sea Salt Particle in the Atmosphere, General Features of the Distribution," *Tellus*, 1965.
- 9 Lepple, R. K., and Ruskin, R. E., "Sea Salt Aerosol Survey Results on JEFF(B) Tests of 9 November 1978," NRL Letter Report 8320-281:be, 11 Dec. 1978.
- 10 Ruskin, R. E., Lepple, R. K., and Jeck, R. M., "Salt Comparison of Pressurized vs Ambient Deck Air Intakes on JEFF(B) Hovercraft," NRL Memorandum Report 4368, 2 Feb. 1981.
- 11 Gear, H. C., "Development of Air Filtration Systems for Gas Turbine Engines Installed in Amphibious Hovercraft," Filtration Society Meeting, Southampton, U.K., Apr. 1973.
- 12 Mund, M. G., and Guhne, H., "Gas Turbine-Dust-Air Cleaners: Experience and Trends," ASME Paper No. 70-GT-104, May 1970.
- 13 Hill, D. G. T., *Gas Turbine Intake Systems in Unusual Environments*, ASME, New York 1973.
- 14 Swan, K. T., "A Survey of Icing Conditions for Marine Gas Turbines," Report NAPTC-PE-114, Sept. 1977.
- 15 Lepple, F. K., "Preliminary Report to NAVSEC 6146B, Aerosol Samples Collected Aboard PTF 25 (OSPREY)," NRL Ltr. 8330-029; FKL-NSC, 3 Feb. 1978.
- 16 Ruskin, R. E., Lepple, R. K., and Jeck, R. M., "Sea Salt Spray Ingestion by FFG Gas Turbines," NRL Memorandum Report 4419, Nov. 1980.
- 17 Ruskin, R. E., Jeck, R. K., Lepple, R. K., and VonWald, W. A., "Salt Aerosol Survey at Gas Turbine Inlet Aboard USS *Spruance*," NRL Memorandum Report 3804, June 1978.
- 18 Ruskin, R. E., "Environmental and Salt Measurements in the Engine Air Stream on the GTS *William M. Callaghan*," 1977.
- 19 Phillippi, K. A., and Ozarko, H. S., "Experimental Study of Air Flow over a 2 Percent Model of the FFG-7," David Taylor Naval Ship Research and Development Center, Washington, D.C., 1976.

# Evolution of NO<sub>x</sub> Abatement Techniques Through Combustor Design for Heavy-Duty Gas Turbines

**M. B. Hilt**

Manager—Combustion Aerothermal Design.  
Mem. ASME

**J. Waslo**

Engineer—Combustion Development.  
Assoc. Mem. ASME

General Electric Company,  
Gas Turbine Division,  
Gas Turbine Engineering and  
Manufacturing Department,  
Schenectady, N.Y. 12345

*The role played by oxides of nitrogen in the formation of photochemical smog has been known for many years. However, because of the relatively small fraction of power generated by gas turbines, there were no significant attempts at limiting gas turbine NO<sub>x</sub> emissions in the United States until about 15 years ago. This paper outlines General Electric's experience with NO<sub>x</sub> abatement techniques from then until the present.*

## Introduction

Legislation was introduced in the State of California limiting the quantity of nitric oxide that could be discharged into the atmosphere by fossil fuel-burning power plants. The first regulation affecting customers of the General Electric Gas Turbine Division was the Los Angeles County Air Pollution Control District (LAAPCD) Rule 67 which limited sulfur dioxide, particulates, and stated "that a person shall not build, erect, install, or expand any nonmobile fuel burning equipment unit unless the discharge into the atmosphere of nitrogen oxide (NO<sub>x</sub>) does not exceed 140 pounds per hour calculated as nitrogen dioxide (NO<sub>2</sub>)" [1].

At about the same time the San Diego Air Pollution Control District (SDAPCD) issued Rule 68, which contained stringent regulations limiting NO<sub>x</sub> emissions from fossil fuel-burning power plants.

### Rule 68 – Effective 7/1/71[2]

Oil Fuel	Gas Fuel
225 ppm at 3% O <sub>2</sub> Dry Sample Basis	125 ppm at 3% O <sub>2</sub> Dry Sample Basis

Seventeen General Electric MS5001 gas turbines located in San Diego County were required to meet the newly enacted Rule 68, and five MS5001 machines in Los Angeles County came under Rule 67. The first General Electric NO<sub>x</sub> abatement work was a program in 1971 aimed at bringing the MS5001 machines into compliance with SDAPCD Rule 68. The early control methods, used for the San Diego and Los Angeles machines, were based on injecting water into the reaction zone, thus lowering flame temperature and inhibiting NO<sub>x</sub> production. From these beginnings, efforts were directed

toward reducing NO<sub>x</sub> through changes to the stoichiometry and fuel-air mixing in the reaction zone and toward alternate methods of water and steam injection for NO<sub>x</sub> control.

More advanced work, aimed at dry low NO<sub>x</sub> control, now makes use of staged combustion systems including rich-lean, lean-lean, and premixed combustors. Ultralow levels of NO<sub>x</sub> require even more exotic approaches, such as the catalytic combustors now being studied and tested.

The balance of this paper provides a general discussion of NO<sub>x</sub> formation and reduction, followed by a description of the use of each of these methods.

## NO<sub>x</sub> Formation and Reduction

Nitrogen oxides are divided into two classes according to their mechanism of formation. NO<sub>x</sub> formed from the oxidation of the diatomic nitrogen in the combustion air and fuel is called "thermal NO<sub>x</sub>" and is primarily nitric oxide (NO) with a small percentage of nitrogen dioxide (NO<sub>2</sub>). The formation rate is mainly a function of the stoichiometric adiabatic flame temperature as shown in Fig. 1 [3].

Emissions due to oxidation of organically bound nitrogen in the fuel [fuel-bound nitrogen (FBN)] are called "organic NO<sub>x</sub>." Only a few parts per million of the available diatomic nitrogen are oxidized to form nitrogen oxide, whereas the oxidation of FBN is very efficient. For conventional combustion systems the efficiency of conversion into nitrogen oxides is 100 percent at low FBN content (0.02% by wt) [4]. At higher levels of FBN (0.40 percent by wt), the efficiency falls off to approximately 20 percent. Organic NO<sub>x</sub> formation is less well understood than thermal NO<sub>x</sub> formation. However, it is known that measures which reduce flame temperature and thereby abate thermal NO<sub>x</sub> have little positive or even an adverse effect on organic NO<sub>x</sub>.

Examination of Fig. 1 shows that the rate of NO formation can be significantly reduced by operating the reaction zone of a combustor at either very lean or very rich equivalence ratios. Prior to the advent of NO<sub>x</sub> emission controls, gas turbine

Contributed by the Gas Turbine Division of THE AMERICAN SOCIETY OF MECHANICAL ENGINEERS and presented at the 29th International Gas Turbine Conference and Exhibit, Amsterdam, The Netherlands, June 4-7, 1984. Manuscript received at ASME Headquarters December 27, 1983. Paper No. 84-GT-48.



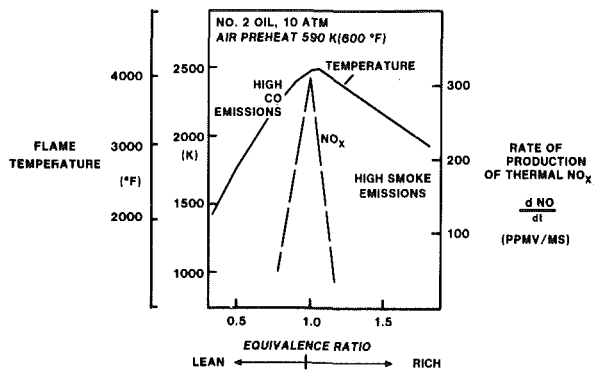


Fig. 1  $\text{NO}_x$  production rate

combustors were designed so that the reaction zone fuel/air ratio was near stoichiometric. A brief examination of Fig. 1 shows that the rate of  $\text{NO}_x$  formation tends to a maximum at this condition, and that the rate can be significantly reduced by moving the reaction zone equivalence ratio toward either lean or rich operation.

Since the overall combustion system equivalence ratio must be lean (to limit turbine inlet temperature), it was natural that the first efforts to lower  $\text{NO}_x$  emissions were directed toward designing a combustor with a leaner reaction zone.

It quickly became apparent that the reduction in primary zone equivalence ratio at full operating conditions was limited because of the large turndown in fuel flow (40 to 1), airflow (30 to 1), and fuel/air ratio (5 to 1) on industrial gas turbines. Further, the flame in a gas turbine is a diffusion flame since the fuel and air are injected directly into the reaction zone. Combustion occurs at or near stoichiometric conditions, and there is substantial recirculation within the reaction zone. The initial efforts to reduce  $\text{NO}_x$  by making the reaction zone of a conventional combustor lean gave about a 20 percent reduction in  $\text{NO}_x$ , but further efforts along this line did not prove fruitful.

Further reductions in  $\text{NO}_x$  can be achieved by designing staged combustors. A rich-burning first stage can minimize the fraction of a fuel-bound nitrogen converted to  $\text{NO}_x$ , but smoke emissions from such combustors are difficult to control. Staging also allows the designer to extend the operating envelope of a lean combustor by varying the fuel flow split between stages.

The third approach to reducing  $\text{NO}_x$  formation is to reduce the flame temperature by introducing a heat sink into the flame zone. Water or steam are extremely effective at achieving this goal. Of course, a penalty in overall efficiency must be paid for the additional fuel required to heat the water to combustor temperature, although gas turbine output is enhanced because of the additional mass flow through the turbine. The water must by necessity be of boiler feedwater quality to prevent deposits and corrosion in the hot turbine nozzle area downstream of the combustor. There are practical limits to the amount of water or steam that can be injected into the combustor before serious problems occur. This has been experimentally determined and must be taken into account in all applications if the combustor designer is to ensure long hardware life for the gas turbine user. The deterioration in performance is manifested primarily in two forms: excessive carbon monoxide (CO) and dynamic pressure increases. Although carbon monoxide has little negative effect upon operation, many agencies regulate the amount of this pollutant that can be discharged into the atmosphere. Also, increasing CO emissions indicate that the combustion process is deteriorating. Figure 2 shows typical curves of CO as a function of water injection rate.

Dynamic pressure oscillations occur in all diffusion flame

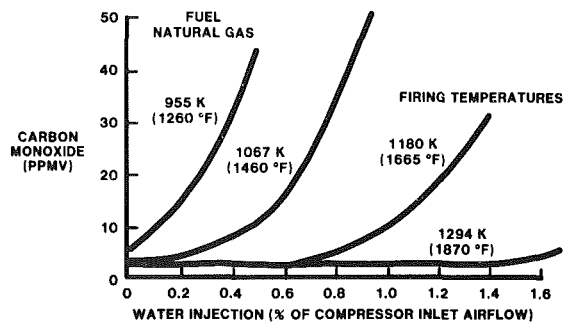


Fig. 2 Effect of water injection on carbon monoxide emissions at various firing temperatures

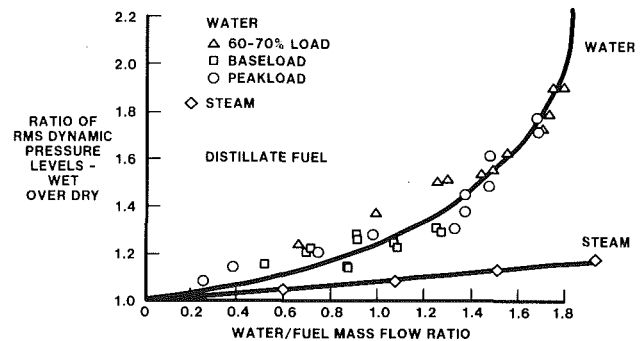


Fig. 3 MS7001E combustor dynamic pressure activity as a function of water/steam injection rate

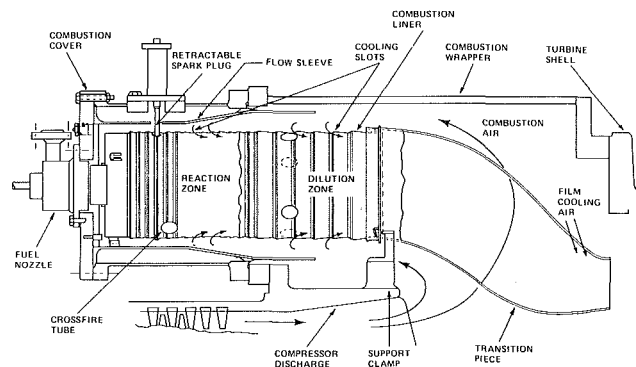


Fig. 4 Reverse-flow combustion system

combustors and are produced by the combustion process. These pressures can couple with the acoustic mode of the combustor and be amplified, thus causing increasing wear rates of the hardware or, in extreme cases, premature failure. Limits have been empirically established by field measurement and parts life experience. Exceeding these limits will impact upon the maintenance intervals for the combustion hardware. For this reason, combustor dynamic pressure levels are monitored in both the laboratory and field tests.

Figure 3 shows dynamic pressure activity for both water injection and steam injection. Water injection tends to excite the dynamic activity more than steam injection. Steam enters the combustor mixed with the air better than water does and thus has less impact on quenching the recirculating flame.

### $\text{NO}_x$ Control by Water Injection

1971-1972 San Diego County APCD Rule 68. The work conducted to satisfy the requirements of SDAPCD Rule 68 can be divided into two phases. The initial phase consisted of

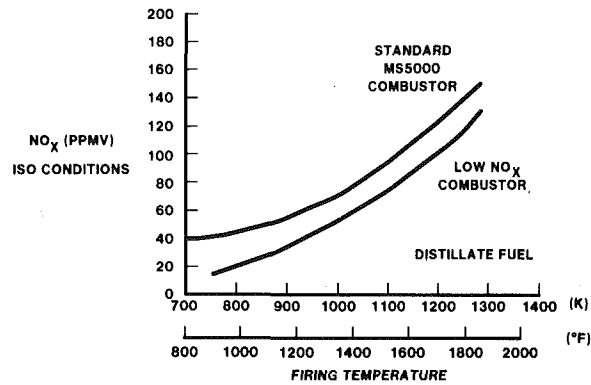


Fig. 5 MS5001 dry NO<sub>x</sub> abatement

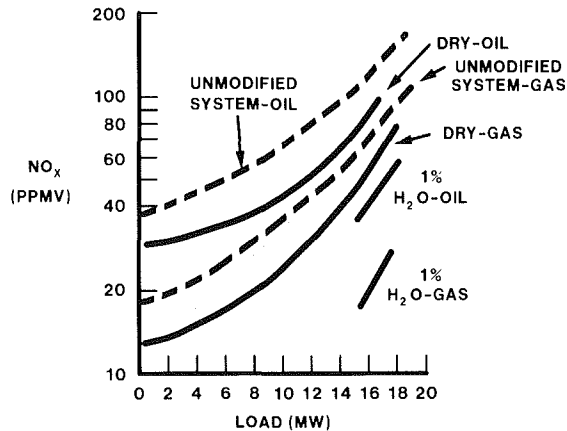


Fig. 6 Effect of water injection on nitric oxide emissions—MS5001 gas turbine

modifying reaction zone stoichiometry, as outlined in the preceding section, to reduce the NO<sub>x</sub> by lowering the peak flame temperatures in the combustor reaction zone [5]. Because of the schedule constraints, it was necessary to carry on parallel programs, one in the laboratory and the other using an actual operating gas turbine located at the customer's site.

The laboratory program was conducted in a single-burner test rig where the parameters affecting combustor performance could be accurately measured using laboratory instrumentation. The single-burner test rig is structured to use actual full-scale combustor hardware (Fig. 4), including fuel nozzle, cap and liner assembly, and transition piece. Combustor steady-state performance can be determined over the entire operating envelope from ignition to full load by simulating compressor and load characteristics of the actual machine. Oxides of nitrogen were measured from the exhaust of the combustor using a Dynascience Air Pollution Monitor Model NX130 NO<sub>x</sub> detector, and grab samples were taken for phenoldisulfonic acid (PDS) analysis. Similar measurements were made in the field to allow comparison of machine to test rig results.

The reaction zone stoichiometry of the combustor was modified by changing the combustor airflow splits in such a way that additional air was introduced into the head end of the combustor. Through experimentation, a practical limit was reached which reduced the NO<sub>x</sub> production by over 20 percent when compared to the original combustor. Figure 5 shows a comparison of the standard and low-NO<sub>x</sub> combustor NO<sub>x</sub> emissions over the load range while operating on distillate oil. Similar reductions were achieved on natural gas fuel operation.

Attempts were made to further decrease the equivalence

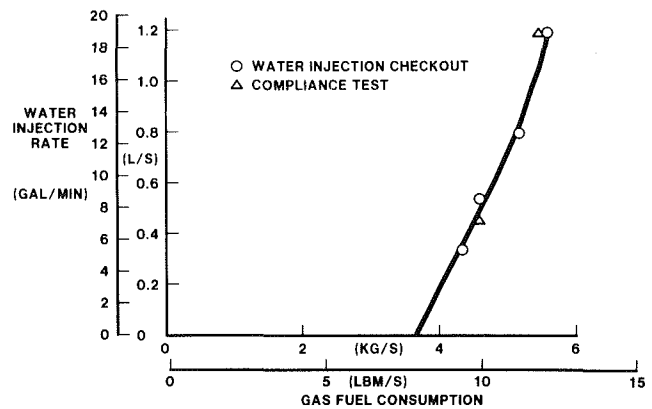


Fig. 7 MS7000 water injection schedule for compliance with US EPA New Source Performance Standards

Table 1 Compliance tests

Machine	Customer	Test
MS7001B	Santee Cooper	NO <sub>x</sub> -NSPS
MS5001P	City of Marquette	NO <sub>x</sub> -NSPS
MS7001E	Puget Sound Power and Light	NO <sub>x</sub> -NSPS
MS7001E	Missouri Public Service	NO <sub>x</sub> -NSPS
MS7001B	Modesto Irrigation District	NO <sub>x</sub> , Particulates, Stanislaus County, APCD

ratio of the reaction zone through the use of larger fuel nozzle air swirlers and the addition of more air holes near the cap end of the combustor. However, excessive start-up vapor resulted from these changes. Thus it was concluded that unless fuel staging or variable geometry configurations were introduced to control air admissions to the combustor, other means would be needed to control NO<sub>x</sub> emissions to the levels required to satisfy SDAPCD Rule 68. The method selected was injection of water into the combustor by means of a "shower head" (tubular ring with water spray holes) installed around the fuel nozzle. The water from the "shower head" entered the combustor through the air swirler slots, thus mixing to a limited degree with the incoming air. The system was evaluated in the lab and then added to a field machine for test. The resulting NO<sub>x</sub> reduction was dramatic, as shown in Fig. 6. Moreover, the water injection device was relatively simple and made it possible to retrofit existing machines by adding new fuel nozzles which incorporated water spray nozzles to replace the simple "shower head." A water supply system, including treatment facilities, and control modifications were provided to regulate the flow of water to ensure compliance at all load conditions.

The MS5001 machine was able to comply with LAAPCD Rule 67 without the use of water injection once the combustors were modified aerodynamically to the new lower NO<sub>x</sub> configuration.

Subsequent tests were conducted on the MS7001 machine, which also demonstrated the capability of water injection to reduce NO<sub>x</sub> to existing regulations.

**United States Environmental Protection Agency New Source Performance Standards (USEPA NSPS).** More recently, a number of gas turbines going into utility service have had to comply with the USEPA NSPS for NO<sub>x</sub> emissions. Compliance has been achieved using a water injection system similar to the original design first used in San Diego County.

A mobile van has been used to conduct a number of official compliance tests, as shown in Table 1.

A typical compliance curve depicting required H<sub>2</sub>O versus fuel flow is shown in Fig. 7. This particular curve has been

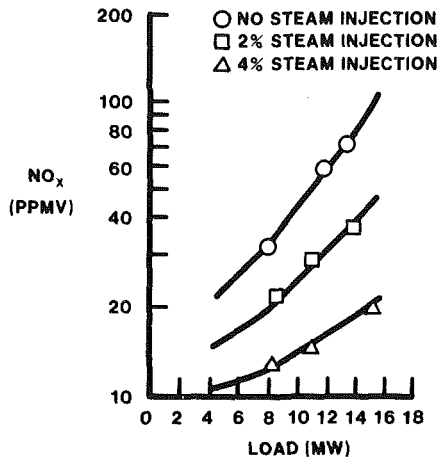


Fig. 8 Effect of compressor discharge steam injection on reducing nitric oxide emissions from MS5001 gas turbines

generated during field test and programmed into a microcomputer built into the gas turbine control system to meter the water into the combustor. The water or steam injection control system can be adjusted to increase or decrease the water injection rate as necessary to bring the unit into compliance.

### NO<sub>x</sub> Control by Steam Injection

Even prior to the successful experience gained in reducing NO<sub>x</sub> with water injection, it was determined that steam injection would have a beneficial impact upon reducing the NO<sub>x</sub> formation rate as well. A 1970 experiment was conducted using an MS5001 gas turbine utilizing steam injection into the compressor discharge plenum for power augmentation. The steam is injected through nozzles that penetrate the turbine shell between each transition piece. This practice has been used for many years by industrial users who find it desirable to maintain nearly constant load even at high ambient temperature or who have excess process steam that has no other use. Normally, steam injection into the compressor discharge air has been limited to approximately 5 percent by weight when compared to the inlet airflow. The MS5001 was operated over the load range at several exhaust temperatures, while the steam injection rate was varied over a range of flows. As shown in Fig. 8, a significant reduction in NO<sub>x</sub> while burning natural gas fuel was noted [6].

Because the steam is injected into the compressor discharge air, it follows that only a portion of the steam reaches the reaction zone while the remainder flows through cooling slots and in the liner dilution holes. About 40 percent of the steam actually passes through the swirler slots and primary mixing holes.

Subsequent to the foregoing work, a system was designed and developed to inject steam into the reaction zone air via the end cover of the combustor (Fig. 9) for three MS7001 machines placed into utility service in 1981. Extensive field measurements have been made on one of these units burning both natural gas and distillate oil fuel. Figure 10 is a plot of NO<sub>x</sub> abatement versus steam-to-fuel ratio on natural gas fuel. Similar results are achieved with distillate fuel. As mentioned earlier, the dynamic pressure response is much lower when steam injection is used for NO<sub>x</sub> abatement rather than water injection. These results are shown in Fig. 11 for natural gas fuel [7].

A similar combustion system was designed for an MS6001 machine to be used in a cogeneration industrial application. The results are similar to the MS7001 machine and are shown for natural gas fuel in Fig. 12. Identical seam injection

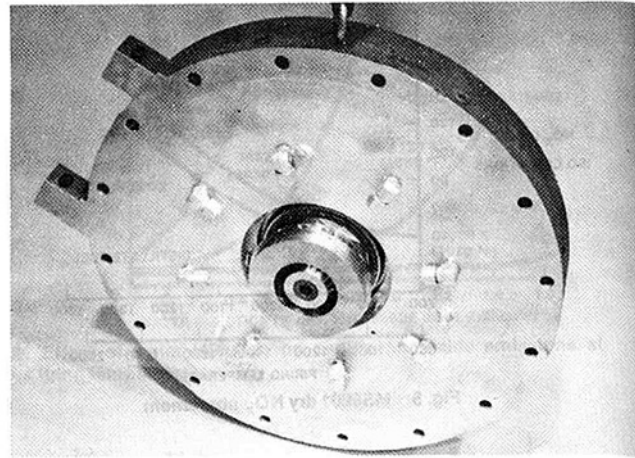


Fig. 9 MS7001 steam injection endcover

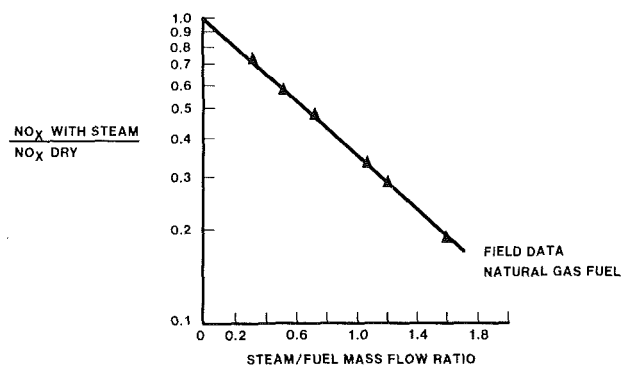


Fig. 10 MS7001E NO<sub>x</sub> abatement with steam injection

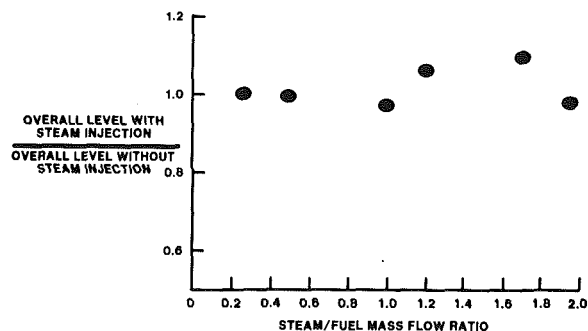


Fig. 11 MS7001E relative dynamic pressure level with steam injection for natural gas fuel

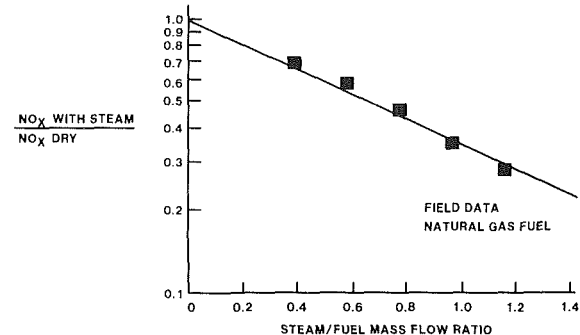


Fig. 12 MS6001 NO<sub>x</sub> abatement with steam injection

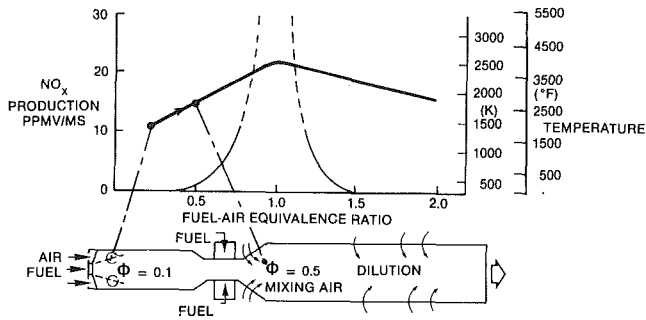


Fig. 13 Lean-lean combustor

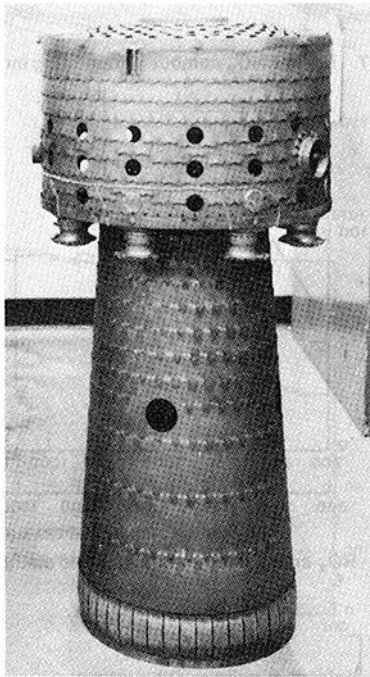


Fig. 14 Prototype dry low NO<sub>x</sub> combustor

configurations have been designed for gas-fired MS9001E machines used for electrical power generation. The NO<sub>x</sub> performance has been thoroughly mapped out in the single burner test stand in the laboratory.

### Dry Low NO<sub>x</sub> Combustors

Although water and steam injection are effective means for reducing NO<sub>x</sub> emissions, there are certain drawbacks to these techniques. For example, for an MS7001E simple-cycle machine operating at ISO conditions, baseload, on distillate fuel oil, 1 percent water injection (expressed as the weight percentage of compressor inlet airflow) has the following impact on performance:

Power output increases	2.7%
Efficiency decreases	2.0%
Fuel consumption increases	4.7%

Even though there is an advantage from an output standpoint, one can see that there is a fuel penalty associated with this NO<sub>x</sub> reduction. In addition, the quality of the injection water must be high, i.e., very low contaminant concentrations; thus the cost of water treatment can be significant. For the above reasons, it has been the desire for many years to meet the various NO<sub>x</sub> regulations without the use of water or steam injection.

A program to develop a combustor capable of meeting the California Bay Area Air Pollution Control District NO<sub>x</sub>

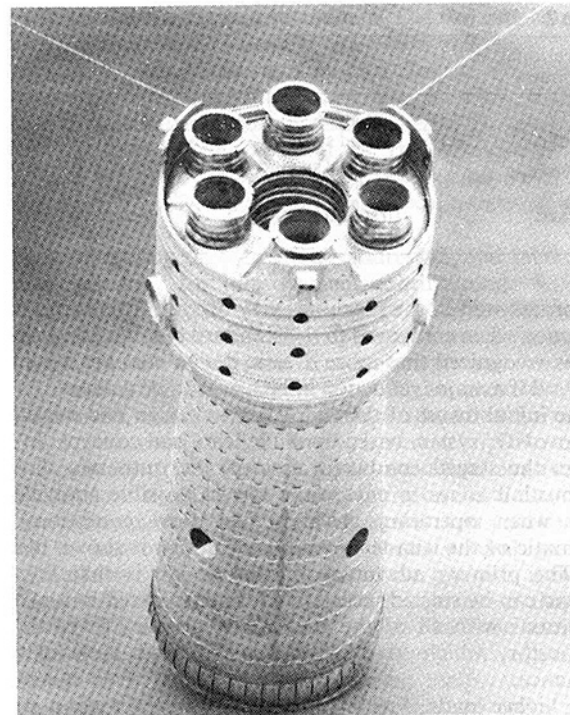


Fig. 15 Low NO<sub>x</sub> combustor configuration

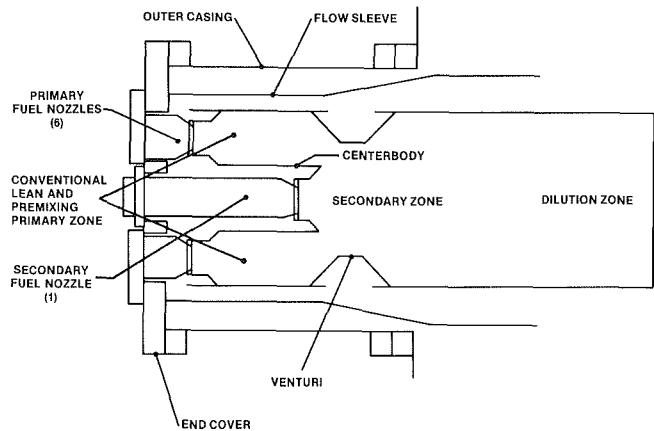


Fig. 16 Dry low NO<sub>x</sub> combustor

regulation of 75 ppmvd at 15 percent O<sub>2</sub> on both distillate and natural gas fuel operation was begun in the mid-1970s. The dry low NO<sub>x</sub> program had been underway for several years prior to this customer-related effort; therefore, a good foundation had been laid.

**Lean Design.** Early attempts to reduce reaction zone equivalence ratios to very low levels were only mildly successful. Because the basic concept consisted of a single fuel nozzle in a fixed-geometry combustor, it was not possible to lean out the reaction zone below a certain level without introducing low-speed ignition and blowout problems. In an attempt to minimize this condition, multiple fuel nozzle combustors were designed to attain better fuel distribution and air mixing within the reaction zone. In some cases, it was possible to achieve considerable NO<sub>x</sub> reduction at full-load conditions with acceptable CO and UHC emissions; however, CO and UHC at low-load conditions were still unsatisfactory. The multinozzle concept was designed and tested on both the MS5001 and MS7001 machines. For the final designs, the reaction zone stoichiometry was designed to offer full operating range capability. Although both of these designs

**Table 2 Dry low NO<sub>x</sub> combustor operation modes**

Operational mode	Fuel distribution	Flame distribution
primary	first stage	first stage
secondary	second stage	second stage
lean/lean	first and second stage	first and second stage
premixed	first and second stage	second stage

performed well in the machine, they offered little or no NO<sub>x</sub> reduction when compared to the standard combustion system. It was recognized that more drastic design changes would be required if a major reduction in NO<sub>x</sub> was to be achieved.

The initial thrust of this work was to design and develop a dry low NO<sub>x</sub> system based upon the lean-lean concept. In this design the staged combustor is separated into two distinct combustion zones to ensure the lowest possible equivalence ratio when operating at high fuel flow conditions. A schematic of the lean-lean combustor design is shown in Fig. 13. The primary advantage of this design is that the gas turbine can be started, accelerated, and operated at low-load conditions with all of the fuel in the primary stage of the combustor, which gives good ignition and blowout performance.

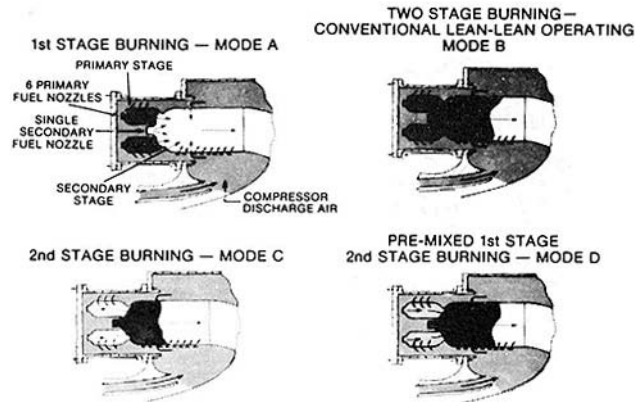
At higher loads, fuel is introduced into the second stage, and a fuel flow split is established which balances the equivalence ratio in each stage to minimize NO<sub>x</sub> formation and CO emissions. Even though NO<sub>x</sub> reduction was achieved, it still was not sufficient to satisfy the goals of the program.

Realizing that more drastic approaches to NO<sub>x</sub> reduction were required, more exotic combustors were designed, manufactured, and tested in the laboratory. The first truly successful dry low NO<sub>x</sub> combustor is shown in Fig. 14. The design incorporated a multinozzle system with forward facing primary fuel injection, coupled with a more conventional, large secondary fuel nozzle. The primary fuel was used for ignition and acceleration purposes and then, at part load, the remaining fuel requirements were introduced through the secondary fuel nozzle. This design allowed the combustor to be operated in two fuel lean zones and still have acceptable performance at part-load conditions through fuel staging. However, this design does not readily lend itself to machine production.

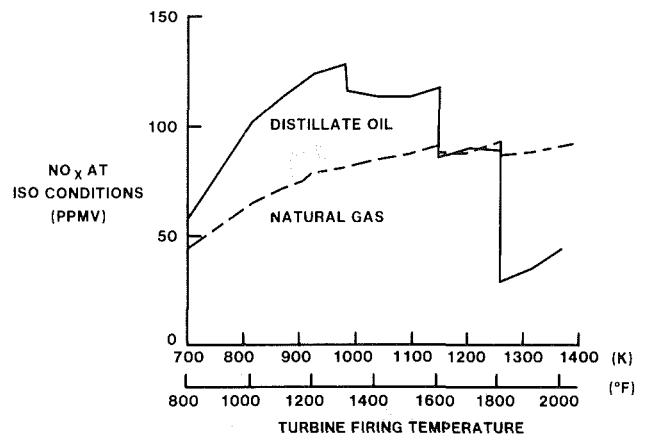
From the initial design, the combustor evolved into the configuration shown in Fig. 15. The principal change here was to unwrap the primary zone and put it in-line with the secondary combustor, thus simplifying the mechanical layout of the combustor. The primary zone of this combustor was fired at start-up and then used as an unfired fuel pre-mixer during dry low NO<sub>x</sub> operation. This work progressed rapidly through the laboratory development phase and then culminated in a demonstration in an actual operating gas turbine.

Low NO<sub>x</sub> development work had progressed to the point that by 1980 the dry low NO<sub>x</sub> combustor had evolved to a dual fuel, two-stage combustion system with six primary nozzles arranged in an annulus and one secondary nozzle in the centerbody (Fig. 16). This combustor has three zones: (i) the primary zone from the primary nozzles to the end of the centerbody; (ii) the secondary zone from the second stage cup to the dilution holes; and (iii) the dilution zone from the dilution holes to the end of the liner. The modes of operation of this combustor are summarized in Table 2 and Fig. 17 [8].

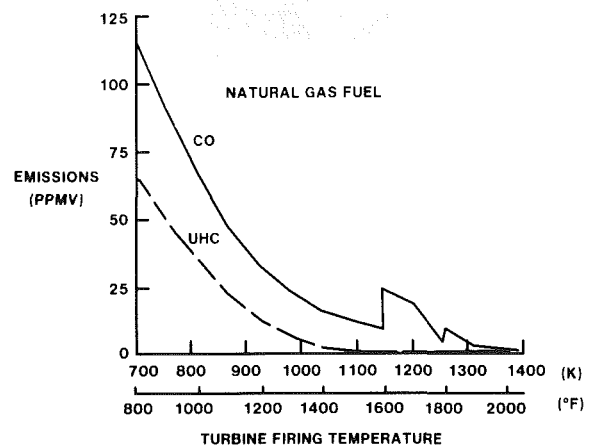
Ignition, acceleration, and low load operation take place with flame only in the primary zone. Fuel is then introduced into the secondary zone fuel nozzle and is ignited by the primary zone flame. This is conventional lean-lean operation. Fuel is increased to a preestablished flow rate at which point



**Fig. 17 Dry low NO<sub>x</sub> combustor operating modes**



**Fig. 18 NO<sub>x</sub> emissions - natural gas and distillate oil**



**Fig. 19 CO and UHC emissions**

the primary flow is gradually shut off until flame is entirely in secondary zone. Then fuel is again introduced to the primary zone, but is not ignited, while at the same time the secondary flow is reduced. During this pre-mixed operation, fuel splits can be varied to achieve optimum emissions.

These operating modes have different emission characteristics; distinct variations are seen when changing modes. Representative NO<sub>x</sub>, CO, and UHC emissions are shown in Figs. 18 and 19. The NO<sub>x</sub> emissions for distillate fuel are characteristic of operating the combustor in the primary only, lean-lean, and pre-mixed mode of operation. For natural gas, the system shown is operated in the primary only and lean-lean mode. Operating the combustor in the pre-mixed mode

when burning natural gas produces  $\text{NO}_x$  emission characteristics similar to the distillate curve.

Figure 19 shows the CO and UHC emissions for the combustor burning natural gas in the primary only and lean-lean mode. In general, the CO and UHC are higher when operating in the premixed mode, especially at reduced firing temperatures.

The hourglass-shaped low- $\text{NO}_x$  liner (Fig. 16) was tested

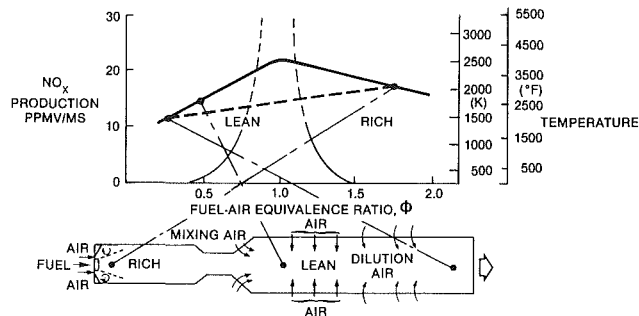


Fig. 20 Rich-lean hourglass combustor

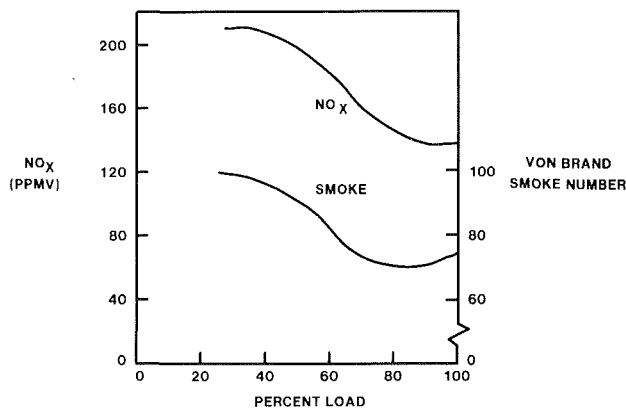


Fig. 21 Rich-lean  $\text{NO}_x$  and smoke emissions

both in the laboratory and in the field in the lean-lean and premixed modes on natural gas and distillate. Most significantly, this hardware met New Source Performance Standards (NSPS) on both fuels. However, some problems existed. In particular, smoke emissions were high on distillate at certain operating modes, and the flame tended to flash back into the premixing zone when running on distillate at high premixed levels. On natural gas, blowout occurred at low firing temperatures.

These operating problems were addressed, and laboratory testing was done for improvement confirmation. An axial swirler was added to the second-stage fuel cup to stabilize the flame and prevent blowout. The upstream cone of the venturi was replaced with a long tapered section to prevent flashback. By eliminating the flashback problem, higher premixed flows could be used, and lower  $\text{NO}_x$  emissions could be achieved. In addition, centerbody air addition was used to improve mixing in the primary zone. These last two modifications reduced  $\text{NO}_x$  emissions significantly when running on distillate oil.

Development of the dry low  $\text{NO}_x$  system has continued in order to improve performance on both natural gas and distillate fuels. Designs are in place for a gas-only lean-lean configuration which has  $\text{NO}_x$  performance lower than the USEPA NSPS over the entire load range. The same is true for distillate fuel if the operating range in the premixed mode is restricted to baseload and above firing temperatures. Additional work is required to expand the useful operating range of the system in the premixed mode on distillate fuel.

**Rich-Lean Design.** The rich-lean combustor concept takes advantage of the lower flame temperatures on the fuel rich side of stoichiometry because of insufficient oxygen present for the reactions to go to completion. The fuel is partially combusted and then this mixture of partially reacted combustion products is accelerated through a quick quench mixing zone into a zone where the stoichiometry moves to the fuel lean side. The rich zone is designed to operate at an equivalence ratio of between 1.2 and 1.4 and the lean zone at approximately 0.5. The combustor concept is shown in Fig. 20.

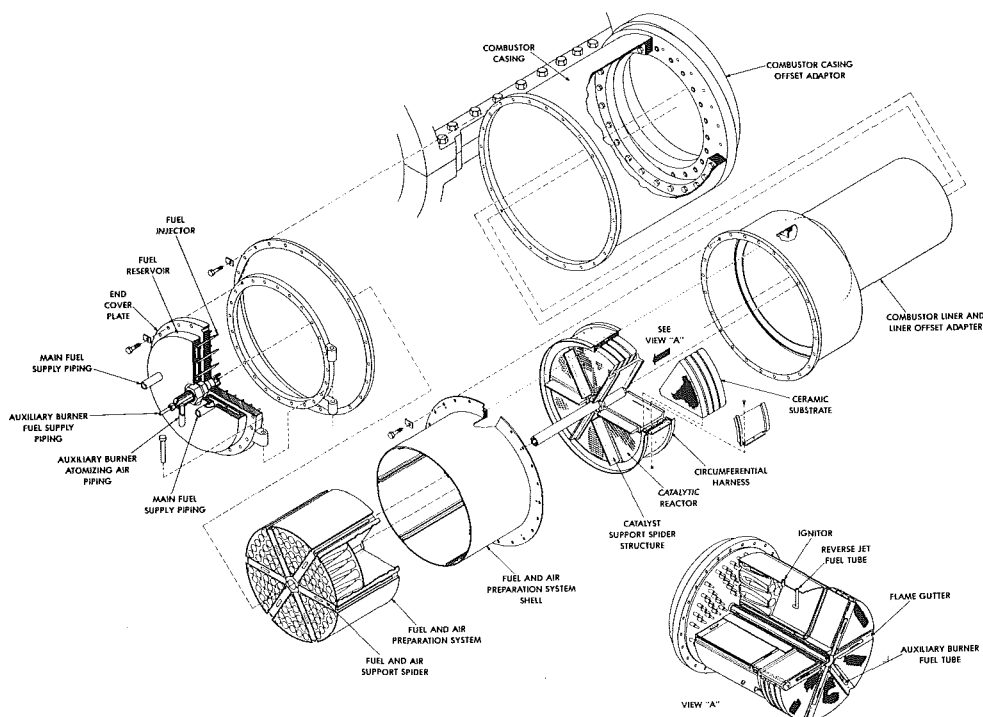


Fig. 22 Catalytic combustion system

A number of rich-lean configurations have been evaluated. Full-scale hardware was tested in an operating MS7001 gas turbine, which produced  $\text{NO}_x$  results as shown in Fig. 21. Unfortunately, the major difficulty in operating in the rich-lean mode is controlling smoke generated in the first stage. The smoke performance for this design is also shown in Fig. 21.

Further  $\text{NO}_x$  reduction is possible if cooling air is not introduced into the rich reaction zone as was the case with the preceding combustor. Additional work was carried out under a NASA-sponsored program [9] to develop a combustor capable of burning heavy fuels with significant fuel-bound nitrogen. This work was quite successful from an  $\text{NO}_x$  abatement standpoint; however, it pointed out the severity of the rich-zone liner-metal cooling problem and the requirement for exotic cooling techniques that would be required to produce a practical combustor.

In general, it has been concluded that rich-lean techniques have promise for  $\text{NO}_x$  abatement and are currently the only method thought practical for fuels containing significant quantities of fuel-bound nitrogen. For clean fuels, however, the lean-lean or premixed lean system has much to offer and is a more practical approach to  $\text{NO}_x$  abatement.

### Catalytic Combustion

The previously discussed work shows that ultralow  $\text{NO}_x$  emissions (20 ppmv) are not readily achieved using either conventional dry low  $\text{NO}_x$  or water or steam injection techniques. If it were possible to design a combustor to operate at very lean reaction zone equivalence ratios, then the  $\text{NO}_x$  production rate would be extremely low. The problem is that at these extremely low equivalence ratios it is very difficult to sustain flame within the combustor without having blowout problems because of the wide operating envelope of the system. One way of circumventing this situation is to use a combustion-enhancing catalyst within the combustor. One such combustor has been designed by the General Electric Company under sponsorship of the Southern California Edison Company [10]. Although the design has not yet been tested, it should offer great potential for  $\text{NO}_x$  abatement to levels well below those currently achievable.

The combustor design, depicted in Fig. 22, has several unique features worthy of note. First, the combustor incorporates an auxiliary combustor downstream of the catalyst that is used to start up and accelerate the gas turbine to full-speed conditions. This burner is placed after the catalytic segments to prevent raw, unburned fuel from splashing on the catalyst during the ignition sequence and to prevent hot combustion products from thermally shocking the delicate substrate material. The auxiliary combustor uses a flame gutter principle to stabilize the flame in the downstream zone of the combustor. These devices have been used successfully in jet engine afterburner designs for many years and have well-proven and demonstrated reliability. The flame gutters also serve as holding units for the individual catalytic segments.

The catalytic reactor is split into six segments to reduce the size of the individual catalytic substrates and to provide ample opportunity for fuel staging to capitalize on the improved catalytic efficiency at high bed temperatures. Each catalyst segment is supplied a well-mixed, uniform fuel/air mixture. The entire system has been designed to be fit into the envelope of an MS7001E combustion system through the use of a special offset adapter and combustor casing. The catalytic combustor offers great potential for  $\text{NO}_x$  reduction, and this work should be continued to advance the state of the art to a practical hardware design. However, the following concerns need to be addressed regarding the utility of catalytic combustion:

- The availability of reactor materials which will survive the required catalyst operating temperatures for a reasonable duty cycle
- The practical temperature limit for reliability
- The applicability of catalytic combustors to future gas turbines
- The cost of catalytic combustor development and application

### Summary

During the past 12 years, the General Electric Gas Turbine Division, other manufacturers, and government and private organizations have actively worked to lower  $\text{NO}_x$  production from gas turbines. Through work in cooperation with both environmental agencies and the needs of our customers, a great deal of progress has been made. From the aerodynamic  $\text{NO}_x$  reduction by "leaning" the reaction zone of conventional combustors, through the design and development of steam and water injection techniques, to sophisticated dry low  $\text{NO}_x$  combustors, it is possible to comply with all current emission regulations.

Development work is continuing to further reduce the  $\text{NO}_x$  emissions through additional refinements to the dry low  $\text{NO}_x$  system. Much has been learned from laboratory single burner tests at both atmospheric and full-pressure conditions. It is understood that a practical design for a low  $\text{NO}_x$  combustor requires excellent fuel/air premixing capabilities, acceptable flame stability in the secondary zone, and extremely high combustion efficiency to minimize CO emissions. These goals are achievable. However, extensive development is required, and the costs of additional hardware complexity must be evaluated against reduced operating costs when compared to conventional steam or water injection techniques.

Rich-lean combustion has potential for reduced  $\text{NO}_x$  emissions from gas turbines burning either liquid or gaseous nitrogen-bearing fuels. The technical barriers are formidable, and such systems require extensive development.

Finally, catalytic combustion, although still in the early development phases, has tremendous potential for ultralow  $\text{NO}_x$  emissions. Longer life and higher operating temperatures will be required to ensure practical maintenance intervals for gas turbine users. Because of its low  $\text{NO}_x$  potential, this work should continue, even if at a moderate pace, to the point where it can be determined if catalytic combustion will be the emission abatement technique of the 1990s.

### References

- 1 *Source Test Manual*, Air Pollution Control District, County of Los Angeles, 1972, p. 172.
- 2 Air Pollution Control District, County of San Diego, Nov. 5, 1982, Rule 68, p. IV-49.
- 3 Fenimore, C. P., "Formation of Nitric Oxide in Premixed Flames," 13th Symposium (International) on Combustion, The Combustion Institute, 1970.
- 4 Wilkes, C., "Fuel Property Effects on Gas Turbine Emission Control," General Electric TIS Report 74-GTD-75, Dec. 19, 1974.
- 5 Hilt, M. B., and Johnson, R. H., "Nitric Oxide Abatement in Heavy Duty Gas Turbine Combustors by Means of Aerodynamics and Water Injection," ASME Paper No. 72-GT-53, Mar. 1972.
- 6 Dibelius, N. R., Hilt, M. B., and Johnson, R. H., "Reduction of Nitrogen Oxides from Gas Turbines by Steam Injection," ASME Paper No. 71-GT-58, Dec. 1970.
- 7 Internal report, J. F. Savelli.
- 8 Washam, R. M., "Dry Low  $\text{NO}_x$  Combustion System for Utility Gas Turbine," ASME Joint Power Generation Conference, Sept. 1983.
- 9 Cutrone, M. B., Hilt, M. B., Goyal, A., Ekstedt, E. E., and Notardonato, J., "Evaluation of Advanced Combustors for Dry  $\text{NO}_x$  Suppression with Nitrogen Bearing Fuels in Utility and Industrial Gas Turbines," ASME Paper 81-GT-125, Mar. 1981.
- 10 Touchton, G. L., Szema, L. C., Cutrone, M. B., Cellamare, R., and Vonkleinsmid, W., "Design of a Catalytic Combustor for Heavy Duty Gas Turbines," ASME Paper 82-JPGC-GT-24, Nov. 1982.

# An Experimentally Verified $\text{NO}_x$ Prediction Algorithm Incorporating the Effects of Steam Injection

G. L. Touchton

Engineer,  
General Electric Company,  
Schenectady, N.Y. 12345

*A Perfectly Stirred Reactor model, kinetic rate data, and equilibrium adiabatic flame temperatures have been incorporated into a closed form  $\text{NO}_x$  prediction algorithm. The algorithm accounts for combustor inlet parameters and steam injection. Combining this model with the operating map for the gas turbine allows prediction of  $\text{NO}_x$  with variation in parameters such as inlet guide vane angle, ambient temperature, and load. If the actual values of the model input variables are measured, real time prediction of  $\text{NO}_x$  emissions may be generated using a microcomputer. This signal may then be used as an input to  $\text{NO}_x$  abatement systems such as Selective Catalytic Reduction. The semitheoretical technique is based upon the extended Zeldovich chain reaction kinetics for the production of  $\text{NO}_x$  in the post-flame zone. The temperature and concentration of major product species in the post-flame zone are taken to be those appropriate to equilibrium. Steam injection and inlet effects enter the model through their influence on the adiabatic equilibrium flame temperature. Mixing effects are accounted for empirically.*

## Introduction

An  $\text{NO}_x$  emissions model incorporating steam injection effects is needed for applications engineering predictions and for use as a control signal for Selective Catalytic Reduction of Nitrogen Oxides (SCR-De $\text{NO}_x$ ) in steam and gas turbine (STAG) combined cycle power plants.

SCR-De $\text{NO}_x$  technology is an exhaust gas clean-up method which utilizes the reduction of NO and  $\text{NO}_2$  by  $\text{NH}_3$  to form  $\text{N}_2$  and  $\text{H}_2\text{O}$  in the presence of a suitable catalyst. In addition to the proper proportions of  $\text{NH}_3$  and the catalyst, an appropriate temperature range is necessary. The combined steam and gas turbine cycle offers an excellent environment for SCR application. The steam cycle supplies steam for injection into the gas turbine combustor. This results in low inlet  $\text{NO}_x$  levels to the SCR-De $\text{NO}_x$  system and reduced ammonia consumption. Also, the temperature ranges needed are present within the heat recovery steam generator (HRSG). Such an application is shown schematically in Fig. 1. The features pertinent to the present study are the steam injection control loop and the ammonia injection control loop. The steam injection and ammonia injection control loops require a signal proportional to the mass flow of  $\text{NO}_x$  entering the De $\text{NO}_x$  system (exiting the gas turbine).

The signal proportional to  $\text{NO}_x$  mass flow must be generated by an  $\text{NO}_x$  measurement system and an exhaust flow measuring system, or calculated from gas turbine operating parameters. The present limitations of  $\text{NO}_x$

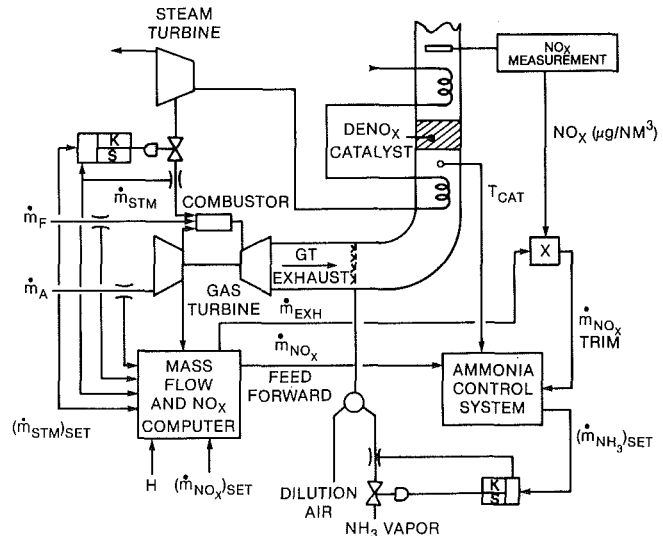


Fig. 1 Steam and gas turbine combined cycle with selective catalytic  $\text{NO}_x$  reduction

measurement systems—especially drift, stability, and response time—make them unsuitable for direct control of either  $\text{NH}_3$  or steam injection. Generating the  $\text{NO}_x$  signal from system operating parameters has advantages in terms of stability, reliability, and response time. The inputs to the computational algorithm are taken from highly reliable sensors which measure primarily pressures and temperatures. These sensors are much simpler than  $\text{NO}_x$  measurement systems and may be made redundant without unduly increasing maintenance and calibration time. Also,

Contributed by the Gas Turbine Division of THE AMERICAN SOCIETY OF MECHANICAL ENGINEERS and presented at the 29th International Gas Turbine Conference and Exhibit, Amsterdam, The Netherlands, June 4-7, 1984. Manuscript received at ASME Headquarters January 9, 1984. Paper No. 84-GT-152.



microcomputer-based controllers allow this time to be implemented in a functional form which incorporates all nonlinearities.

The algorithm used to calculate the  $\text{NO}_x$  level must be accurate over the load range of the gas turbine for wide variations in ambient temperatures and humidities. Also,  $\text{NO}_x$  must be predicted for a wide range of steam injection flows. The present paper describes an  $\text{NO}_x$  emissions model that is based upon combustor inlet parameters, and which meets the foregoing criteria. The order of presentation is:

1 A description of the model; its development from fundamental equilibrium and kinetic reaction principles; and the empirical modifications needed to accommodate mixing and residence time effects

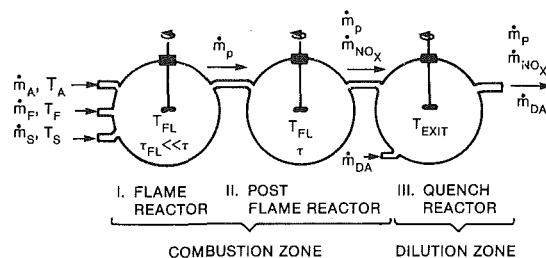
2 Fitting the model to single burner test results

3 A comparison of  $\text{NO}_x$  emission levels measured in field test of an MS7001E in combined cycle operation with levels predicted by the model

### Description of the Algorithm

The algorithm is based upon a Completely Stirred Tank Reactor (CSTR) model. Conceptually, the combustor is divided into three reactors as shown in Fig. 2. These reactors may be thought of as idealized subdivisions of the physical primary and dilution zones. The approximate physical locations of these zones are shown in Fig. 6. In the first reactor, the fuel is burned in a series of very fast steps that result in global equilibrium for all major species and for temperature. It is assumed that the residence time,  $\tau_F$ , is very short, that no appreciable "prompt" NO is formed and that atomic oxygen is at equilibrium before exiting Reactor I. There is evidence that, at least in shock tube experiments, O-atom overshoot may be important [1] and Fenimore [2] measured "prompt" NO levels in the earliest stages of combustion of complex hydrocarbons. However, these mechanisms are far less important than formation of NO by the Zeldovich mechanism [3] in the postflame zone, and they are not easily calculated for turbulent diffusion flames at gas turbine conditions. In the present study, where simplicity of the final expression is an important goal, many of these interesting but secondary effects are best absorbed into the empirically determined coefficients. The degree to which the measured emissions are predicted is then the final criterion for inclusion of additional effects.

The postflame reactor, which receives the products from the first reactor, is the site of NO formation. The NO is formed primarily from the Zeldovich chain reaction (Equations 1PF and 2PF) [3]. Reaction 3PF, which is important only under fuel-rich conditions, [4] is included for



FLAME REACTIONS	POST FLAME REACTIONS
$\text{CH}_4 + \text{AIR} + \text{H}_2\text{O} \rightarrow \text{EQ. PROD.}$	$\text{N}_2 + \text{O} \rightleftharpoons \text{NO} + \text{N} \quad (1 \text{ PF})$
$\text{EQ. (IF) } \text{O}_2 + \text{M} \rightleftharpoons \text{O} + \text{M}$	$\text{N} + \text{O}_2 \rightleftharpoons \text{NO} + \text{O} \quad (2 \text{ PF})$
$(k_{1PF})_{\text{eq}} = 2900e^{-60,755/R_u T} \text{ atm}^{1/2}$	$\text{OH} + \text{N} \rightleftharpoons \text{NO} + \text{H} \quad (3 \text{ PF})$
	$k_{1PF}^F = 1.35 \times 10^{14} e^{-74,500/R_u T}$
	$k_{1PF}^B = 3.10 \times 10^{13} e^{-334/R_u T}$
KINETIC RATE CONSTANTS FROM REF. [4].	$k_{2PF}^F = 6.43 \times 10^9 T e^{6250/R_u T}$
	$k_{3PF}^F = 7.25 \times 10^{11} T^{1/2}$

Fig. 2 Conceptual model of combustor

completeness (refer to Fig. 2 for equations 1PF, 2PF, and 3PF). All of the reactors are assumed to be completely stirred. In this model, the reaction is dominated by the kinetics and all mixing is complete and instantaneous. The concentration of NO appearing at the outlet is directly proportional to the product of the reaction rate and the residence time of a reactant parcel in the reactor. This last property is not true of CSTR's in general, but is due to the fact that the reactants, molecular nitrogen and atomic oxygen, are not depleted by the formation of the product NO. The concentration of the  $\text{N}_2$  is constant because of its great excess. Atomic oxygen concentration is maintained at the equilibrium value by the high temperature in the postflame zone. All  $\text{NO}_x$  is considered to be NO, so any  $\text{NO}_2$  found in the actual exhaust is considered to be formed from NO by oxidation.  $\text{NO}_2$  is important in industrial gas turbines only at low loads. At base load  $\text{NO}_2$  constitutes less than 5 percent of total  $\text{NO}_x$ . Thus, as with O-atom overshoot and "prompt" NO, this effect is

### Nomenclature

$A_1$  = scale factor for kinetic  $\text{NO}_x$  production  
 $A_2$  = scale factor for effective  $\text{NO}_x$  production (CSTR-3 model)  
 $B$  = empirical constant for effective residence time (CSTR-3 model)  
 $C$  = constant for effect of inlet air temperature on  $\text{NO}_x$  (CSTR-3 model)  
 $C_T$  = theoretical value of  $C$   
 $C_A$  = proportionality constant—fractional change in  $K_{STM}$  per degree change in inlet air temperature

$\bar{C}_{PY}$  = specific heat of component  $Y$   
 $C_{STM}$  = proportionality constant—fractional change in  $K_{STM}$  per degree change in steam inlet temperature  
 $D$  = constant for effect of apparent equivalence ratio on  $\text{NO}_x$  (CSTR-3) model  
 $e$  = Euler's logarithmic base, equal to 2.71828 . . .  
 $E_{\text{INO}_x}$  = mass of  $\text{NO}_x$  as  $\text{NO}_2/1000 \times$  mass of fuel  
 $f$  = mass fuel-to-air ratio  
 $g$  = coefficient for influence of air temperature on flame

temperature change with steam injection  
 $h$  = enthalpy per unit mass  
 $H$  = specific humidity  
 $k$  = kinetic activation energy  
 $K_{TOT}$  = total kinetic activation energy for Zeldovich mechanism  
 $K_{STM}$  = overall effectiveness constant for reduction in  $\text{NO}_x$  by steam  
 $K_1$  = change in product enthalpy per pound per degree change in flame temperature of products  
 $\dot{m}_X$  = mass flow of  $X$   
 $P_X$  = pressure at Station  $X$

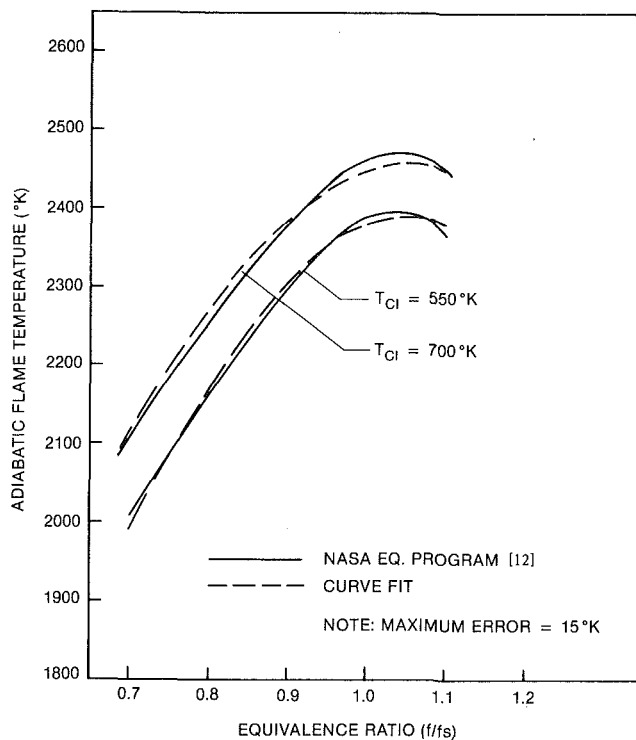


Fig. 3 Prediction of flame temperature (closed form)

lumped into the empirical parameters. Finally, only clean fuels are considered so no functions are needed to account for NO produced by oxidation of fuel bound nitrogen.

In Reaction III, the products of Reactor II are diluted instantaneously to combustor exit or machine exhaust conditions as appropriate. All reaction is "frozen" by the sudden drop in temperature.

Analytical solutions to equations 1F, 1PF-3PF have been presented by many investigators [2-5]. When combined with the CSTR model, they lead for suitably short (of the order of a few milliseconds) residence times to the following equation for the production of NO

$$X_{NO} = A_1 \tau \cdot \frac{P^{1/2}}{RT_{FL}} \cdot e^{-K_{TOT}/R_U T_{FL}} X_{N_2} X_{O_2}^{1/2} \quad (1)$$

As shown in Fig. 3, the equilibrium flame temperature of methane, considered as a function of inlet temperature and

#### Nomenclature (cont.)

$R_u$  = universal gas constant  
 $R$  = gas constant ( $R_u/MW$ )  
 $R_{HUM}$  = NO<sub>x</sub> ratio as a function of specific humidity  
 $R_{STM}$  = NO<sub>x</sub> ratio as a function of steam injection  
 $T_x$  = temperature at Station X  
 $V_R$  = reactor volume  
 $W/F$  = water-to-fuel mass (unless noted as mole) ratio  
 $X_y$  = mole fraction of constituent y  
 $\delta$  = degree of reaction  
 $\Delta X$  = change in variable X from datum state, equal to  $X - X^o$

$\eta$  = see equation (11)  
 $\eta_1$  = see equation (9)  
 $\phi$  = mass equivalence ratio, equal to ( $f/fs$ )  
 $\phi^o$  = equivalence ratio for maximum flame temperature  
 $\tau$  = residence time, equal to  $V_R P_R / \dot{m}_R R T_R$

#### Subscripts

A = inlet air  
 CI = combustor inlet station  
 CP = combustion products  
 DA = dry air  
 F = fuel

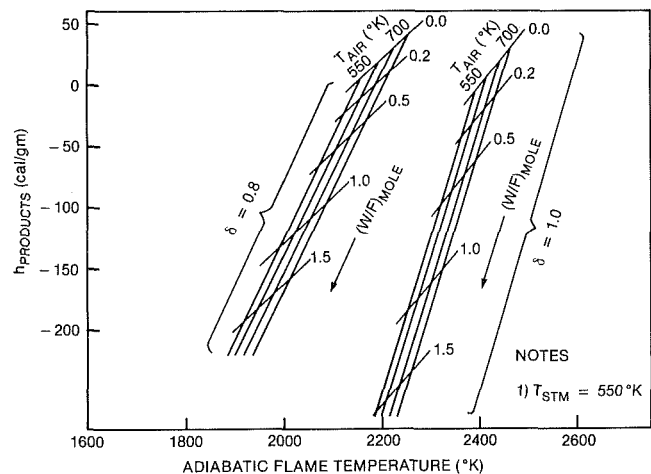


Fig. 4 Mixture enthalpy versus flame temperature

equivalence ratio, may be adequately represented as a parabola. For perfect gases, the equilibrium adiabatic flame temperature is pressure independent so long as dissociation is negligible. However, when dissociation is appreciable, pressure exerts an influence on the flame temperature through the LeChatlier effect. In this case, the pressure dependence of NO<sub>x</sub> production may differ from the square root even in a kinetic model. However, the range of pressures of the single-shaft industrial turbine from full-speed no-load to peak load is narrow and the square root dependence is adequate [6].

Fluid dynamic effects such as jet mixing and pressure loss (which in fact accomplish the stirring needed for the validity of the model) do not enter into equation (1). Therefore, there is no reason to expect it to model a practical combustor over a wide range of flows and pressure losses. However, in a gas turbine the flow variables are constrained by the choked condition at the first-stage nozzle. This condition holds the residence time constant. Because of this constraint, a large set of field test results are fitted by equation (1) [6]. A single-burner test, which was run over a wide range of independent pressures, flows, and inlet temperatures, showed that it was necessary to replace the residence time by an effective residence time as follows

$$\tau_{EFF} = \frac{\tau}{1 + B\tau} \quad (2)$$

FL = flame  
 N<sub>2</sub> = molecular nitrogen  
 O<sub>2</sub> = molecular oxygen  
 $P$  = combustion products plus injected water  
 $R$  = reactor  
 $S$  = stoichiometric  
 STM = steam  
 $W$  = water

#### Superscripts

$X^o$  = value of variable X for datum state  
 $X^i$  = value of variable X for initial state

CH<sub>4</sub>—DRY AIR—STEAM

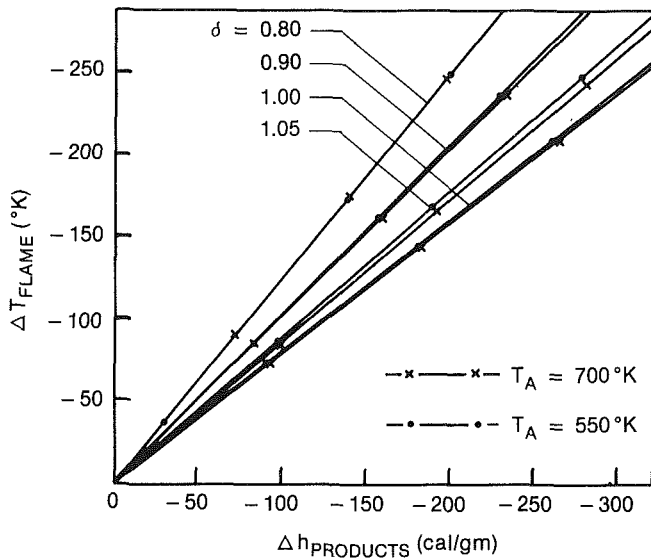


Fig. 5 Variation in mixture enthalpy versus variation in flame temperature

The model represents those points with short residence times (i.e., large pressure losses and intense stirring) best. As the residence time increases, equation (1) overpredicts the NO<sub>x</sub> emissions, an effect for which the effective residence time factor compensates.

When the parabolic flame temperature dependence and the effective residence time are combined with equation (1) as shown in Appendix A, there results

$$EINO_x = A_2 \cdot \frac{\tau}{1 + B\tau} \cdot P^{1/2} \cdot e^{-C\Delta T_{CI} - D(\phi - \phi^*)^2/T_{CI}} \quad (3)$$

To this model, which represents NO<sub>x</sub> production in dry air, we must add the effects due to inlet humidity and to water or steam injection.

Water or steam injection achieves NO<sub>x</sub> abatement by reducing the flame temperature, an effect accounted for through equation (1). The reduction in flame temperature comes about because of:

- 1 The change in the specific heat of the exhaust products
- 2 The change in the inlet air temperature due to the water or steam injection

In the case of ambient humidity, the second effect is not present. Many investigators have examined ambient humidity effects on NO<sub>x</sub> production from a theoretical and empirical standpoint [7-10]. When the NO<sub>x</sub> emissions are presented on a dilution free basis, the following relationship is found to best fit the data

$$\frac{EINO_x \text{ at } H}{EINO_x \text{ at } H^0} = e^{-19(H-H^0)} \quad (4)$$

If injected water or steam is completely mixed with the inlet air, then the change in inlet temperature may be computed and the effect of NO<sub>x</sub> production predicted from equations (3) or (4). Lewis, in a recent paper, has done this with reasonable success [11]. In order to go beyond an implicit approach, an expression for flame temperature change as an explicit function of combustor inlet parameters must be derived.

Combustor inlet conditions, including steam injection, will influence NO<sub>x</sub> mainly through their effect on flame temperature. In order to rank the interactions between steam injection and other inlet conditions, a parametric study of the influence of these variables on flame temperature was done

Table 1 Summary of equilibrium parameters

$\delta$	$\phi$	$\eta_1$	$K_1$ cal/gm	$\eta_1/K_1$ gm/cal
0.8	0.744	0.041	0.820	0.050
0.9	0.877	0.048	1.000	0.048
1.0	1.0	0.054	1.287	0.042

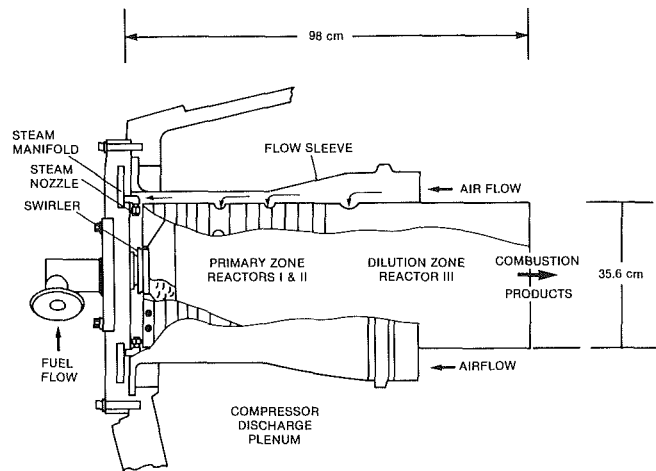


Fig. 6 Schematic of the MS9001E combustor

using the equilibrium computer code of Gordon and McBride [12]. Figure 4 shows the equilibrium adiabatic flame temperature for CH<sub>4</sub>-H<sub>2</sub>O-dry air combustion products for two degrees of reaction (equivalence ratios). The change in inlet enthalpy for any of the processes diagrammed equals the change in enthalpy of the products. Since the change in inlet enthalpy may be calculated from standard references [13, 14], the effect on flame temperature is readily found. As seen in Fig. 4, the curves of constant water to fuel ratio and constant inlet temperature are linear over the range of interest and may be replotted as shown in Fig. 5. The most interesting aspect of this figure is that inlet temperature has a weak effect, while the degree of reaction (or equivalence ratio) has a strong effect, with steam injection effectiveness reaching a minimum at stoichiometric ( $\phi = \delta = 1$ ), due to the maximum in the specific heat of the products.

A closed-form model for the effect of steam injection on NO<sub>x</sub> can be developed from these curves and the information presented in Table 1, by considering the process of mixing steam and combustion products in known proportion.

Since enthalpy is conserved

$$\dot{m}_w h_w^i + \dot{m}_{CP} h_{CP} = \dot{m}_p h_p \quad (5)$$

and mass is conserved

$$\dot{m}_p = \dot{m}_{CP} + \dot{m}_w \quad (6)$$

$$= \dot{m}_{DA} + \dot{m}_F + \dot{m}_w \quad (7)$$

From Fig. 5, the enthalpy of the products at any final flame temperature is

$$h_p = h_{CP} + K_1(T_{FL} - (T_{FL})_{CP}) \quad (8)$$

After some algebra, there results

$$\Delta T_{FL} = \frac{\eta_1}{K_1} \left[ \frac{h_w^i - h_{CP}}{1 + \eta_1 \left( \frac{W}{F} \right)} \right] \left( \frac{W}{F} \right) \quad (9)$$

where

$$\eta_1 = \frac{\phi}{\phi + (1/f_s)}$$

If datum values are introduced into this equation, the effects of variations in inlet air temperature and steam temperature may be made explicit:

$$\Delta T_{FL} = \frac{\eta_1}{K_1} \left[ \frac{(h_w^\circ - h_{CP}^\circ) + \bar{C}_{PSTM} \Delta T_{STM} - g \Delta T_{Cl}}{1 + \eta_1 \left( \frac{W}{F} \right)} \right] \left( \frac{W}{F} \right) \quad (10)$$

Where

$$g = \bar{C}_{PA} + 9.80 \times 10^{-5} K^{-1} (h_w^\circ - h_{CP}^\circ)$$

The coefficient  $g$  represents, correct to the first order, the combined effects of inlet air temperature on the enthalpy of the combustion products (first term on right) and on  $K_1$  (second term on right). Because it multiplies the entire expression, second-order corrections to  $K_1$  must be retained so that the final expression is correct to first order.

In applying equation (10) to a gas turbine combustor, some thought must be given to the physical process. As seen in Fig. 6, steam is introduced into a portion of the primary zone air and is unlikely to be well mixed. Fuel is introduced as a series of jets which burn as a turbulent diffusion flame with very little premixing. As Spalding has shown, a stoichiometric region will exist in this system irrespective of any details of mixing [15]. This region will dominate the  $NO_x$  production.

These lead to the following postulates:

1 The effective water to fuel ratio may differ substantially from the well mixed ratio. It is, however, a constant times the value calculated from inlet conditions.

2 The equivalence ratio in equation (10) is taken to be equal to unity.

Postulates 1 and 2 and the proportionality constant between flame temperature change and  $\ln NO_x$  production rate from Appendix A may be combined with equation (10) to give

$$R_{STM} = e^{-K_{STM} \left( \frac{1 + C_{STM} \Delta T_{STM} + C_A \Delta T_{Cl}}{1 + \eta \left( \frac{W}{F} \right)} \right)} \left( \frac{W}{F} \right) \quad (11)$$

where

$$\eta = \frac{1}{1 + (Vfs)}$$

The value of  $K_{STM}$  is estimated as 1.22 from Appendix A and Table 1. Similarly, the effects of steam temperature variation, inlet air temperature variation, and dilution by steam injection are estimated as  $C_{STM} = -1.44 \times 10^{-4} K$ ,  $C_A = +1.76 \times 10^{-4} K^{-1}$ , and  $\eta = .0544$ . Thus a 100 K change in steam temperature and inlet temperature changes steam effectiveness by -1.4 percent and +1.8 percent, respectively, while dilution alters steam effectiveness by -5.1 percent at a steam-to-fuel ratio of 1 to 1.

$R_{STM}$  is the ratio of  $NO_x$  on a dilution-free basis and at constant fuel flow. For this case, the combustor exit temperature will be lower with steam injection. If constant combustor exit temperature were maintained, more fuel would be injected to compensate for the steam injection and the apparent ratio would be larger—i.e., the apparent effectiveness would be less, as Lewis has noted [11].

The final model for  $NO_x$  production with steam injection is found by combining equations (3), (4), and (11) to give

$$EINO_x = A_2 \cdot \tau_{EFF} \cdot P_{Cl}^{1/2} e^{-C \Delta T_{Cl} - \frac{D(\phi - \phi^*)^2}{T_{Cl}}} \cdot R_{HUM} \cdot R_{STM} \quad (12)$$

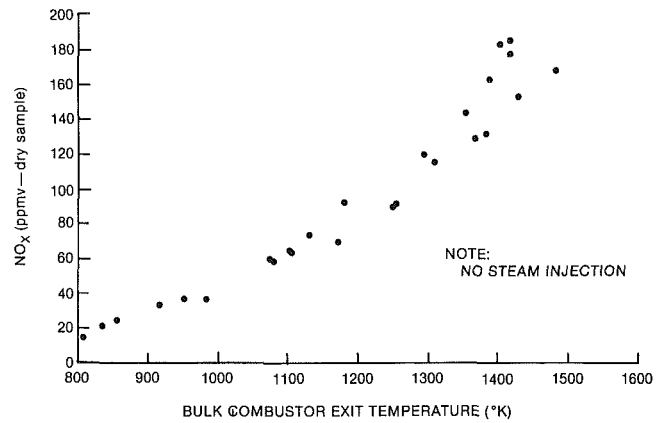


Fig. 7 Nitrogen oxide versus combustor exit temperatures

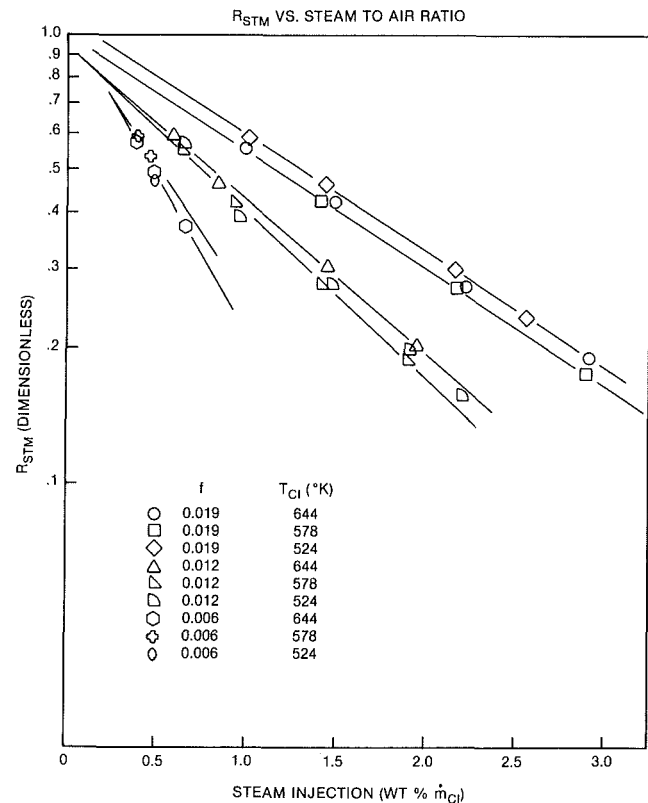


Fig. 8  $R_{STM}$  versus steam-to-air ratio

Where:

$$R_{HUM} = e^{-19\Delta H}$$

$$R_{STM} = e^{-K_{STM} \left( \frac{1 + C_{STM} \Delta T_{STM} + C_A \Delta T_{Cl}}{1 + \eta \left( \frac{W}{F} \right)} \right)} \left( \frac{W}{F} \right)$$

$$\tau_{EFF} = \frac{\tau}{1 + B\tau}$$

### Fitting The CSTR-3 Model To Single-Burner Test Results

Extensive tests were run in the General Electric single-burner test rig to characterize  $NO_x$  emissions burning methane with steam injection for  $NO_x$  abatement. The combustion system employed was the can system used in the GE MS9001E and MS7001E Gas Turbines. As shown

schematically in Fig. 6, the primary zone of this combustor is stirred by jets of air entering radially through rows of equally spaced holes. Recirculation in and stability of the primary zone are maintained by a swirler which is integral with the fuel nozzle. A dual fuel (liquid/gas) or gas only nozzle of conventional design was used. In these nozzles, gas is introduced into the swirler air stream via a series of holes between the vanes. Steam is introduced upstream of the liner cap through nozzles mounted on the endcover as shown.

The single burner test stands duplicated the pressure inlet temperature and flow path that a single combustor would see in a gas turbine. The inlet air was heated without vitiation by two indirectly fired preheaters. The facility is limited in air flow, however, to approximately 21 kg/s, which is 90 percent of the combustor flow of an MS9001E on an I.S.O. day with 84 deg inlet guide vane settings. The choked condition at the first-stage nozzle is simulated by a series of steam-cooled cylinders which provide an appropriate restriction downstream from the combustor. These nozzle bars were removed for a portion of the testing because, as noted above, the choked condition constrains the mass flow, pressure, and temperature so that they cannot be varied independently. Independent variation of the variables of a model is essential if the coefficients are to be uniquely determined [16, 17].

Data reduction is accomplished through an on-line computer system which converts the sensor outputs to engineering units and performs a mass energy balance between the measured fuel and air flow and the bulk average combustion system exit temperature. Combustion system exit temperatures are measured by a  $9 \times 7$  array of unshielded thermocouples located at the plane which corresponds to the first stage nozzle entrance. Thermocouple readings are corrected for radiation to the surroundings using an empirical factor [18]. Emissions measurements are made at a single point in this plane using an uncooled inconel probe.  $\text{NO}_x$  concentrations are corrected to bulk average values using the local oxygen concentration or local temperature. In either case, the correction is not large since the peak temperature at this plane exceeds the bulk average temperature by less than 15 percent.

The  $\text{NO}_x$  data are plotted against combustor exit temperature in Fig. 7. The ranges of fuel-to-air ratios, pressures, inlet temperatures, and mass flows for the test were selected to give a wide variation to the variables or because they represent contractual operating points. Subject to the limitation on airflow, they represent both open and closed inlet guide vane positions for the gas turbine. The steam effectiveness data are plotted against steam-to-air ratio in Fig. 8 and against steam-to-fuel ratio in Fig. 9. Two salient points are

- 1 Steam-to-fuel ratio correlates the data best
- 2 As predicted from the thermal model, inlet air temperature is a secondary influence on steam effectiveness.

The fact that the steam-to-fuel ratio correlates the data best confirms that the diffusion flame is the correct model for the gas turbine combustor. Steam-to-air ratio should be the appropriate parameter for a premixed flame.

Model coefficients were determined numerically using a nonlinear regression program based upon Marquardt's hypothesis [20]. In carrying out this analysis, a forward correction scheme was used in which the data were segregated into a set with no steam injection and a set with steam injection. Model coefficients for the data with no steam injection were determined first and then these were used as a correction to the data before determination of the steam injection coefficients.

The fit to the data with no steam injection is excellent with no appreciable systematic variation of the residuals when plotted against input parameters. More than 90 percent of the

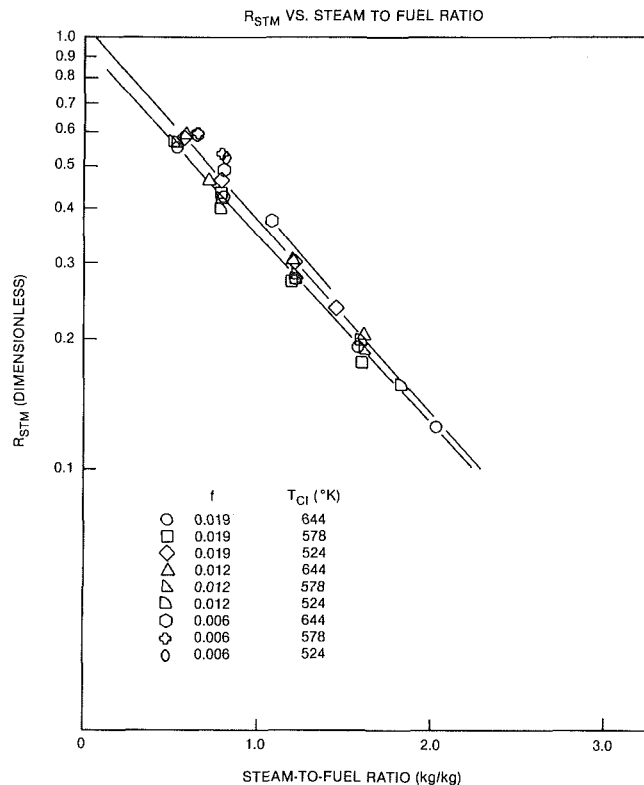


Fig. 9  $R_{STM}$  versus steam-to-fuel ratio

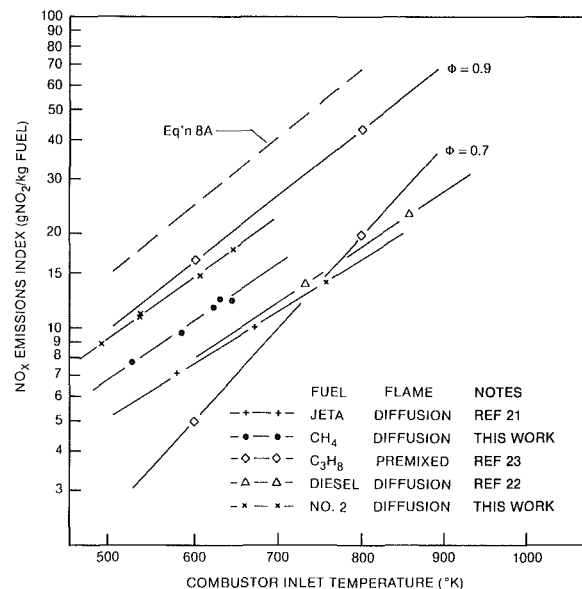


Fig. 10 Nitrogen oxides versus combustor inlet temperatures

total variation in the data is explained by the model, and the standard error of the estimate is only 9.5 percent of the mean EI (Table 2). Note that this number includes variation of the input parameters and the  $\text{NO}_x$  measurement system in addition to the deviations due to lack of fit of the model. Therefore, the error due to lack of fit is less than 9.5 percent of the mean.

The coefficients from above were used to correct the data with steam injection. These corrected values were used to determine the steam effectiveness coefficients. The standard error of the estimate (SEE) is 5.8 percent of the mean EI, and 98 percent of the total variation is explained by the model (Table 2).

**Table 2 Summary statistics**

	100( $r^2$ )	SEE
No steam injection	91.0%	9.5%
Steam injection	99.0%	5.8%
Field data set	98.2%	4.8%

Where:

$r^2$  = Coefficient of determination  
 SEE = Standard error of estimate of regression equation as a percent of mean EI

Note that  $r^2$  measures the fraction of the total variation of the random which is explained by the model.

**Table 3 Summary of model coefficients from data**

$$\begin{aligned}
 A_2 &= 19020/\text{MPa}^{1/2}\text{s} \\
 C &= 0.003810\text{K}^{-1} \\
 D &= 6.407 \times 10^5\text{K} \\
 K_{\text{STM}} &= +1.121 \\
 C_A &= +0.489 \times 10^{-4}\text{K}^{-1}
 \end{aligned}$$

90% simultaneous confidence intervals

Coefficient	Group 1	
	Lower limit	Upper limit
$A_2(\text{MPa}^{1/2}\text{s})^{-1}$	17598	20442
$C(\text{K}^{-1})$	0.002321	0.005299
$D(\text{K})$	$-8.069 \times 10^5$	$-4.745 \times 10^5$
Coefficient	Group 2	
	Lower limit	Upper limit
$K_{\text{STM}}$	1.136	1.106
$C_A$	-0.0001	0.0002

As a final test of the validity of the model, the parameters determined from the single-burner test stand were used to predict the results of a field test of an MS7001E in combined cycle service. The MS9001E and the MS7001E use the same combustor. There are 14 combustors per machine for the MS9000 versus 10 for the MS7000. The results of this comparison are shown in Table 2. More than 98 percent of the total variation is explained by the model. Again, since all errors, including measurement errors, are lumped into the SEE for the model, it is concluded that the error due to lack of fit is significantly less than 4.8 percent of the mean. The numerical values of the model coefficients are listed in Table 3. The agreement between the predicted and measured steam effectiveness coefficient  $K_{\text{STM}}$  (+1.22 versus +1.12) confirms the correctness of the postulated thermal model. It is clear that, in the range of steam-to-fuel ratios studied, effects of steam injection such as change in OH concentration have a negligible impact on  $\text{NO}_x$  formation. The second-order interaction term also shows fair agreement with the thermal model prediction.

## Summary and Conclusions

The CSTR-3 model had been shown in earlier work, to fit a large set of field tests using No. 2 distillate or JP fuels. Those tests include results from the MS7001B, MS5001N, CF6-50, CF6-6, and the JT9-D [19].

This model has been updated and extended by adding an empirical correction to the residence time to account for mixing effects and by accounting for  $\text{NO}_x$  abatement by steam injection. Steam injection was hypothesized to affect  $\text{NO}_x$  production through its effect on flame temperature alone, and a closed form model was derived. This model was then fit to an extensive test data base. The close agreement between the predicted values of the steam injection parameters and those which best fit the data, coupled with the fact that the thermal model explains all but 1 percent of the data variability, confirms that steam injection is a thermal effect.

The overall performance of the model, when used to

correlate actual field test data with steam injection, was within  $\pm 5$  percent (one standard deviation). This precision and its range of validity prove that the CSTR-3 model is fully satisfactory as a predictor of MS9001E performance. Therefore, the CSTR-3 model can be used with confidence in application engineering work or as an algorithm for control of steam and/or ammonia injection.

## References

- 1 Kollrack, R., and Aceto, L. D., "Radical Overshoot Phenomena in Liquid Fueled Gas Turbine Combustors," ASME Paper No. 77-GT-5, 1977.
- 2 Fenimore, C. P., "Formation of Nitric Oxide in Premixed Hydrocarbon Flames," *Proceedings of the 13th Combustion Symposium (International)*, The Combustion Institute, 1971, pp. 373-374.
- 3 Zeldovich, J., "The Oxidation of Nitrogen in Combustion and Explosions," *Acta Physicochimica*, U.R.S.S., Vol. 21, 1946, pp. 577-628.
- 4 Shaw, H., "The Effects of Water, Pressure, and Equivalence Ratio on Nitric Oxide Production in Gas Turbines," ASME JOURNAL OF ENGINEERING FOR POWER, Vol. 96, No. 3, July 1974, pp. 240-246.
- 5 Westenberg, A. A., "Kinetics of NO and CO in Lean, Premixed Hydrocarbon Air Flames," *Combustion and Science Technology*, Vol. 4, 1971, pp. 59-64.
- 6 Touchton, G. L., and Dibelius, N. R., "A Correlation of Nitrogen Oxides Emissions With Gas Turbine Operating Parameters," ASME Paper 76-GT-14, 1976.
- 7 Marchionna, N. R., "Effect of Inlet Air Humidity on the Formation of Oxides of Nitrogen in a Gas Turbine Combustor," NASA TMX-68209, Mar. 1973; (preliminary publication).
- 8 Sarli, V. J., Eiler, D. C., and Marshall, R. L., "Effects of Operating Variables on Gaseous Emissions," presented at the Air Pollution Control Specialty Conf. on Air Pollution Measurement, New Orleans, La., Oct. 1975.
- 9 Gleason, C. C., and Rogers, D. W., "Ambient Humidity Correction Factor for Gas Turbine Oxides of Nitrogen Emissions," G.E. Technical Memorandum 73-803, 1973.
- 10 Shaw, H., "The Effect of Water on Nitric Oxide Production in Gas Turbine Combustors," ASME Paper No. 75-GT-70, Houston, Texas, Mar. 1975.
- 11 Lewis, G. D., "Prediction of  $\text{NO}_x$  Emissions," ASME Paper No. 81-GT-119, 1981.
- 12 Gordon, S., and McBride, B. J., *Computer Program for Calculation of Complex Chemical Equilibrium Composition, Rocket Performance, Incident and Reflected Shocks and Chapman-Jouquet Detonations*, NASA SP-273, NASA Scientific and Technical Office, 1971.
- 13 Keenan, J. H., and Kaye, J., *Gas Tables*, John Wiley & Sons, New York, 1966.
- 14 Keenan, J. H., and Keyes, F. C., *Thermodynamic Properties of Steam*, John Wiley & Sons, New York, 1953.
- 15 Spalding, D. B., *Some Fundamentals of Combustion*, Academic Press, New York, 1955, p. 250.
- 16 Box, G. E. P., "Use and Abuse of Regression," *Technometrics*, Vol. 3, No. 4, Nov. 1966, pp. 625-629.
- 17 Hahn, G. J., "Regression for Prediction Versus Regression for Control," *General Electric Statogram Newsletter*, Vol. 21, No. 5, 1973.
- 18 Davis, L. B., "Gas Thermocouple Radiation Corrections," *General Electric TIC Report 75-GTD-10*, 1975.
- 19 Touchton, G. L., and Dibelius, N. R., "A Correlation of Nitrogen Oxides Emissions With Gas Turbine Operating Parameters Considering Variable Combustion Residence Time," *Proceedings of the Spring Technical Meeting*, New England Section of the Air Pollution Control Assoc., 1976, pp. 39-58.
- 20 Marquardt, D. W., "An Algorithm for Least Squares Estimation of Nonlinear Parameters," *J. Soc. Indust. Appl. Math.*, Vol. 11, No. 2, June 1963, pp. 431-441.
- 21 Marchionna, N. R., Diehl, L. A., and Trout, A. M., "Effect of Inlet Air Humidity, Temperature, Pressure, and Reference Mach Number on the Formation of Oxides of Nitrogen in a Gas Turbine Combustor," NASA Technical Note D-7396, Oct. 1973.
- 22 Gleason, C. C., Rogers, D. W., and Bahr, D. W., "Experimental Clean Combustor Program, Phase II, Final Report," NASA Report No. CR-134971, Aug. 1976.
- 23 Anderson, D., "Effects of Equivalence Ratio and Dwell Time on Exhaust Emissions from an Experimental Premixing Prevapourizing Burner," NASA Technical Memorandum, No. X-71592, presented at the ASME Twentieth Annual Int. Gas Turbine Conf., Houston, Texas, Mar. 1975.

## APPENDIX A

Over the range of temperatures of interest, the adiabatic flame temperature may be represented as

$$T_{\text{FL}} = T_F^\circ + \alpha \Delta T_{\text{Cl}} - \beta (\phi - \phi_F^\circ)^2 \quad (\text{IA})$$

When the reciprocal of this expression is taken and all but first order terms are discarded, there results

$$\frac{1}{T_{FL}} \approx \frac{1}{T_{FL}^{\circ}} \left[ 1 - \frac{\alpha}{T_{FL}^{\circ}} \Delta T_{CI} + \frac{\beta}{T_{FL}^{\circ}} (\phi - \phi_F^{\circ})^2 \right] \quad (2A)$$

To the first approximation the function  $\beta$  is proportional to the reciprocal of combustor inlet temperature so that

$$\frac{1}{T_{FL}} \approx \frac{1}{T_{FL}^{\circ}} \left[ 1 - \frac{\alpha}{T_{FL}^{\circ}} \Delta T_{CI} + \frac{b}{T_{CI}} (\phi - \phi_F^{\circ})^2 \right] \quad (3A)$$

Figure 4 shows that there is excellent agreement between this formula and the flame temperatures calculated from the NASA equilibrium formula. The values of the parameters for this fit are

$$\begin{aligned} T_{FL}^{\circ} &= 2414 \text{ K} \\ \alpha &= 0.424 \\ b &= 2.216 \times 10^6 \text{ K}^{-1} \\ T_{CI}^{\circ} &= 588 \text{ K} \\ \phi_F^{\circ} &= 1.05 \end{aligned}$$

These values agree very well with those calculated by other means. When the  $\text{NO}_x$  concentration is converted to  $\text{EINO}_x$  to eliminate dilution and (3A) is inserted into (1), we have

$$\text{EINO}_x = A \cdot \tau_{FL} \cdot P^{1/2} \cdot e^{C \Delta T_{CI} + \frac{D}{T_{CI}} (\phi - \phi^{\circ})^2} \cdot X \quad (4A)$$

Where

$$X = \left[ X_{\text{N}_2} X_{\text{O}_2}^{1/2} \left( \frac{1+f}{f} \right) \frac{1}{RT_{FL}} \right]$$

The factor  $X$  is essentially constant since  $f$  is assumed

stoichiometric and  $X_{\text{O}_2}$  is constant by assumption, so (4A) simplifies to

$$\text{EINO}_x = A_2 \cdot \tau_{FL} \cdot P^{1/2} \cdot e^{C \Delta T_{CI} + \frac{D}{T_{CI}} (\phi - \phi^{\circ})^2} \quad (5A)$$

From this it is easily seen that

$$C_T = \frac{K_{\text{TOT}} \alpha}{R_u (T_{FL}^{\circ})^2} \quad (6A)$$

The reference state for the present work is  $T_{CI} = 588 \text{ K}$ ,  $H = 0.006343 \text{ kg H}_2\text{O/kg dry air}$ ,  $P_{CI} = 1.013 \text{ MPa}$ . Therefore

$$C_T = (135255)(0.424)/(1.985(2394)^2) \text{ K}^{-1} \quad (7A)$$

$$= 0.00504 \text{ K}^{-1} \quad (8A)$$

$\text{NO}_x$  as a function of combustor inlet temperature for several diffusion flame combustors and one premixed combustor are shown in Fig. 10, along with a line of arbitrary intercept and a slope corresponding to (8A). It is clear that all the combustors have nearly the same slope without regard to design or fuel. This slope is approximately equal to the slope for  $\phi = 1$  from the premixed data so that the assumption of stoichiometric burning is supported. However, none of the data here can be reconciled with the predicted slope. The observed slope may be due to "prompt"  $\text{NO}_x$  production since the activation energy for this process is much lower than that for the Zeldovich mechanism. Whatever the underlying reason, the inlet temperature coefficient must be modified. The value appropriate to the present data is

$$C = 0.003810 \text{ K}^{-1} \quad (9A)$$

This implies a proportionality between  $\ln \text{NO}_x$  and flame temperature of

$$\Delta(\ln \text{NO}_x) = (0.008986 \text{ K}^{-1}) \Delta T_F \quad (10A)$$

# Water-Ethanol-Gasoline Blends—Physical Properties, Power, and Pollution Characteristics

S. Rajan

Associate Professor,  
Department of Thermal and  
Environmental Engineering,  
Southern Illinois University,  
Carbondale, Ill. 62901  
Mem. ASME

*Factors relevant to the utilization of nonanhydrous ethanol as a blending component with gasoline for use in current on-the-road spark ignition engines are investigated. Miscibility limits are determined and key physical properties important for proper engine operation are measured. Dynamometer tests on an unmodified production engine with hydrated ethanol-gasoline blends containing varying percentages of water show potential for increased thermal efficiency and reduced oxides of nitrogen emissions.*

## Introduction

Motivation for the addition of water or water-alcohol mixtures to petroleum-based internal combustion engine fuels has persisted for many years, often with widely differing objectives. Early interest in using water or water-ethanol mixtures stemmed from a need to inhibit detonation in high-performance engines [1, 2]. Another objective was to obtain internal engine cooling in the absence of a water jacket [3, 4]. Additionally, water-alcohol mixtures have been used to boost operating compression ratios of engines running on low octane fuel [5]. Even with the lower compression ratios, dictated by the stringent emission control regulations of current on-the-road vehicles, the addition of water-alcohol mixtures to liquid hydrocarbon fuels has found merit in reducing oxides of nitrogen emissions [6–10].

In recent years, with the emphasis on conservation and the need to find alternate transportation energy sources, ethanol has emerged as a practical and replenishable substitute for petroleum-based fuels such as gasoline [11, 12]. While some effort has been directed towards taking advantage of the higher compression ratio efficiency enhancement potential of neat ethanol [13], a more immediate application has been to use ethanol as a blending component with gasoline. The high cost of anhydrous alcohol used in the blend is, however, a deterrent to its more widespread application. The use of nonanhydrous ethanol or water-ethanol mixtures for blending with gasoline would lower the cost of the ethanol-gasoline blend if the associated miscibility and phase-separation problems could be properly addressed. Thus an additional and more recent motivation for the use of water-alcohol mixtures as a blending component is to reduce the overall cost of the alcohol-gasoline blend, while conserving and reducing our dependence on petroleum-based fuels.

While there has been a variety of motives for the addition

of water or water-alcohol mixtures to petroleum-based fuels, there are also several methods of introducing the water-alcohol-fuel mixture into the engine. Among the most common of the methods employed to add the water or water-alcohol mixtures to the parent hydrocarbon fuel is induction or injection into the hot intake manifold [7, 10]. Direct injection into the engine cylinder has also been employed [4, 6]. Another form of introduction, especially suitable for both gasoline and diesel engine applications, is injection directly into the cylinder of an emulsified mixture of the fuel components [14–16]. While dual carburetor systems have been suggested [17], the use of a single carburetor to deliver the alcohol-gasoline or water-alcohol-gasoline blend still provides the simplest introduction method [18, 19].

Since the majority of Otto-cycle engines in use today are equipped with carburetted fuel delivery systems, the economical advantages derived from less than 200 proof ethanol blended with gasoline will be feasible if such a blend can be substituted directly in place of the pure gasoline without requiring any engine hardware modifications. This poses certain problems, since nonanhydrous ethyl alcohol and gasoline do not mix very well. Very few data are available on the miscibility characteristics of nonanhydrous ethanol with gasoline and the physical properties of the resulting blends insofar as they influence engine performance. Also questions concerning power, emissions levels, driveability, and long-term materials stability need to be addressed before a nonanhydrous ethanol-gasoline blend can be utilized in current on-the-road vehicles. The aim of the present research was therefore to investigate the conditions under which less than 200 proof ethanol could be blended with gasoline to yield stable mixtures. In addition to miscibility characteristics, physical properties of the blend relevant to proper engine operation such as volatility, vapor pressure viscosity, and heating value were measured. Engine dynamometer tests were then conducted to evaluate the efficiency and comparative emissions performance of representative blends for use in a

Contributed by the Air Pollution Control Division for publication in the JOURNAL OF ENGINEERING FOR GAS TURBINES AND POWER. Manuscript received by the Air Pollution Control Division February 1, 1983.



production multicylinder engine under various regimes of engine operation.

## Experimental

**(a) Miscibility and Physical Properties.** An important consideration in the use of nonanhydrous ethanol as a blending component is an evaluation of its miscibility properties with gasoline. These miscibility properties were investigated by first preparing distilled water-anhydrous ethanol mixtures with the percentage by volume of water varying from 0–30 percent. A nonleaded summer gasoline was then blended with 100 cc of each water-ethanol mixture until phase separation into two immiscible components occurred. The volume of gasoline added to produce phase separation was determined, from which the individual percentages of water, ethanol, and gasoline in the blend could be calculated. The blends so obtained are referred to as "limit blends," since these are the limit proportions characterizing the miscibility of water-ethanol-gasoline mixtures.

Key physical properties of the limit blends important to proper operation of engines were then determined. Vapor pressure was measured using the Reid vapor pressure apparatus according to ASTM Test D 323-41 procedure. Fuel volatility was evaluated with the standard ASTM Test D 86-40 distillation apparatus. Viscosity of the blended fuels was measured with a Cannon-Fenske viscometer according to ASTM D 445 recommendations.

**(b) Engine Dynamometer Experiments.** To determine the suitability of substituting the limit blends containing less than 200 proof ethanol in place of gasoline in current on-the-road vehicles, a series of engine dynamometer experiments were performed. The test engine was a 2.3-L, four-cylinder, four-stroke Otto-cycle production engine with a compression ratio of 8.44 manufactured by the Ford Motor Company. To meet the requirement that the limit water-alcohol-gasoline blends be substituted directly in place of gasoline, no modification to the carburetor or any other engine component was undertaken. The power developed by the engine was measured by a Go Power water brake dynamometer coupled directly to the engine shaft. A surge tank served to reduce pulsations in the inlet air. The inlet air mass flow was measured with a standard ASME long radius nozzle. Fuel flow rates to the engine were measured with a rotameter calibrated for each particular fuel being tested.

Oxides of nitrogen emissions ( $\text{NO}_x$ ) were measured during the engine tests with a Thermo-Electron Model 10AR chemiluminescent analyzer fitted with a heated sample module. A Beckman Model 400 instrument equipped with a heated flame ionization detector was utilized to measure the exhaust unburnt hydrocarbons. Special attention was paid to the oxides of nitrogen and the unburnt hydrocarbons that are the pollutants largely responsible for smog formation; hence other engine exhaust components such as carbon dioxide, carbon monoxide, etc., are not reported.

Other engine parameters monitored were exhaust gas temperature, engine coolant temperature, inlet manifold gas temperature, intake manifold vacuum, lubricant pressure, etc.

In certain tests the comparative performance of the limit blends relative to gasoline was assessed through a series of three engine tests. In the first test, the engine was run on a no-lead gasoline to determine base level performance. Secondly, a limit blend with a given percentage of water in the alcohol was substituted in place of the no-lead gasoline, and the test was repeated under identical engine operating conditions. To determine specifically how water addition affected engine performance, the test was conducted for a third time with the engine now burning a mixture of ethanol and gasoline in the

same relative proportions as the limit blend of the second test, but without the water. In this way it was possible to delineate the influence of blending nonanhydrous ethanol with gasoline in terms of engine power and emission characteristics.

The engine operating conditions were varied during the tests in a manner that would permit the study of the combustion and emissions properties of the different fuels. Comparison of the performance of the water-ethanol-gasoline mixtures relative to that of the base gasoline was made under engine operating conditions simulating part load. Since the engine intake manifold vacuum was 45 cm of mercury under idle conditions and full-load conditions corresponded to a manifold vacuum of almost 0 cm of mercury, the engine tests were all performed at a constant part-load intake manifold vacuum of 25 cm mercury. If all other variables such as fuel density, fuel-air mixture temperature, pressure, etc., were the same, a constant intake manifold pressure during the tests would indicate an equal volume of fuel-air mixture inducted into the engine [20]. No attempt was made to externally control intake manifold temperature. However, by maintaining the intake manifold vacuum at a constant value of 25 cm mercury the engine operating conditions were chosen as far as possible without any extraneous control to yield a constant volumetric efficiency. Any observed variation in volumetric efficiency could then be attributed to the physical properties of the particular fuel. In addition, the data were taken such that the engine speed was very nearly the same for each test condition for the three fuels. In this manner, the mixing and turbulence characteristics of the gases in the cylinder were almost identical. Hence the observed variations in the measured power and emissions levels were the result of the combustion history of the particular fuel as influenced by its reaction kinetics.

An engine warm-up period at no load conditions ranging from 30 min to 1 hr preceded each test. After ascertaining that the engine was functioning normally, it was loaded by increasing the flow through the water brake dynamometer until the manifold vacuum reached 25 cm mercury. During some of the tests the spark advance was adjusted to the minimum value for best torque (MBT) within the knock limit. The engine was run at a given test condition until all engine operating parameters had stabilized, whereupon data pertinent to the test were recorded. In this manner the engine was tested under different operating conditions to study the influence of a variety of parameters, including spark advance, exhaust gas recirculation, speed, load, etc., to allow the performance characteristics of the fuels to be evaluated. Each test was repeated at least twice, not necessarily on the same day. The ambient temperature changed about 6°C during the tests and humidity variations were less than 4 percent.

## Results and Discussion

**(a) Physical Properties.** Figure 1 illustrates the miscibility characteristics of hydrated ethanol with gasoline depicting the relative proportions of each in the limit blends as a function of the volume percent of water in the hydrated alcohol. The data show that the volume percent of gasoline in the limit blend diminishes rapidly as the proof of the ethanol drops below 180, i.e., with 10 percent or more water in the alcohol. For the summer gasoline tested, the crossover point is 7.5 percent in the ethanol, which yields a 50–50 mixture of gasoline and hydrated ethanol in the limit blend.

The heating values of the limit blends as measured with a Parr adiabatic calorimeter exhibited a trend similar to the gasoline volumetric composition of the blend. However, the heating values did not drop as sharply as the gasoline volumetric composition of the limit blends. A 6 percent water in alcohol limit blend has a heating value of 39,920 kJ/kg,

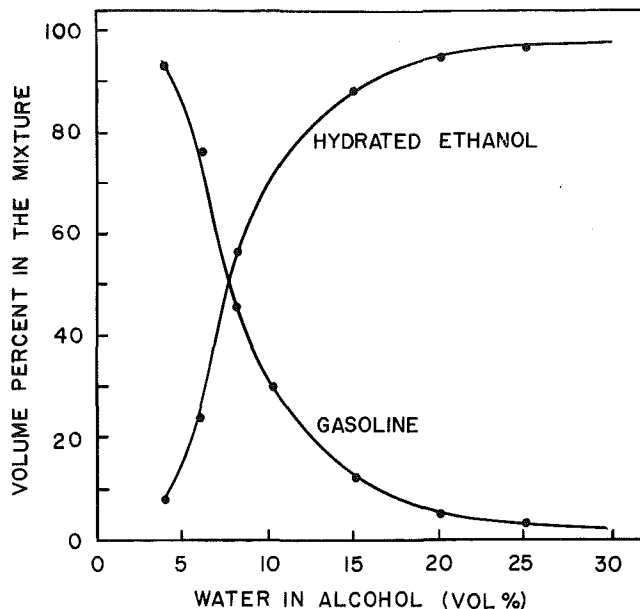


Fig. 1 Miscibility limits of hydrated ethanol-gasoline mixtures

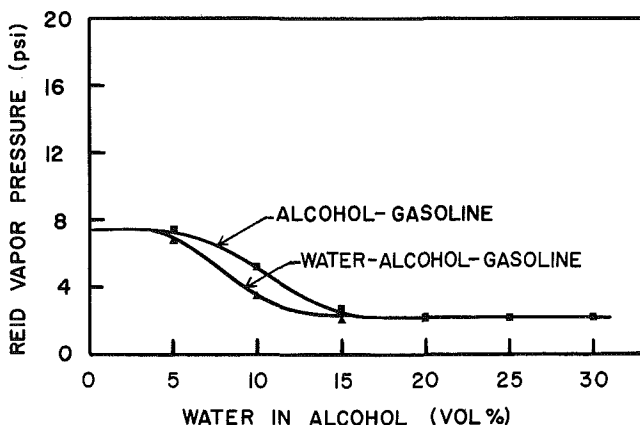


Fig. 2 Influence of water on the vapor pressure of water-ethanol-gasoline blends

while a 10 percent water in alcohol limit blend has a heating value of only 29,825 kJ/kg. For comparison, the heating value of the pure gasoline was 44,750 kJ/kg. The heating values of the limit blends are thus strongly influenced by the miscibility characteristics of the water-alcohol-gasoline mixture.

The volumetric composition of the limit blends, as shown in Fig. 1, were measured at an ambient temperature of 22.5°C. Other studies [21, 22] show that the water tolerance of alcohol-gasoline mixtures, while limited, improves both with the temperature of the blend and with increased aromatic content of the base gasoline. In general, the weight percent  $W$  of water in the blend can be related to the mixture temperature  $T$  in the range  $-23$  to  $+23$ °C by a quadratic expression of the form [22]

$$T = C_2 W^2 + C_1 W + C_0$$

where  $C_0$ ,  $C_1$ , and  $C_2$  are constants.

The miscibility characteristics of water-alcohol-gasoline blends are also influenced by the relative aromatic, paraffin, and olefinic content of the base gasoline. The aromatic hydrocarbons are the most water-tolerant, followed by the olefins and the paraffins. Within each group of hydrocarbons, the water tolerance  $W$  decreases with the average

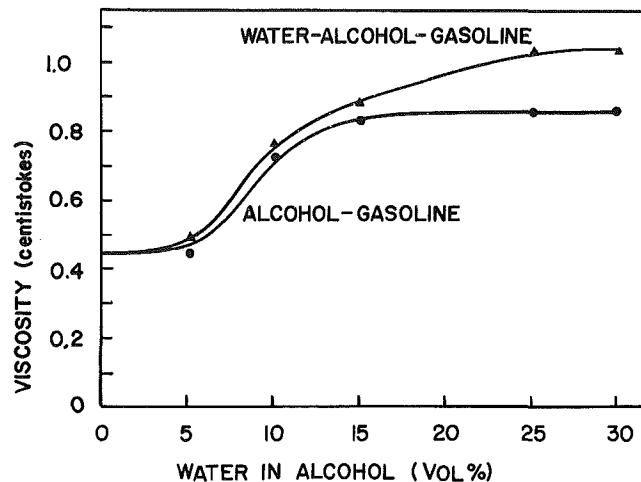


Fig. 3 Influence of water on the viscosity of water-ethanol-gasoline blends

weighted boiling point  $\bar{T}$  of the hydrocarbon group according to the empirical relationship

$$W = (C_5 + C_4 \bar{T}) T^2 + (C_3 + C_2 \bar{T}) + C_1 \bar{T} + C_0$$

In addition, the structure and concentration of the alcohol itself has a marked effect on the water tolerance of the blends. While increased gasoline hydrocarbon boiling point reduces the water tolerance of the blends, the converse is true for the alcohols. The higher alcohols, e.g., ethanol, propanol, butanol, possess much better miscibility characteristics with gasoline and improve the water tolerance of the water-alcohol-gasoline blends compared to methanol. Indeed, some of the higher alcohols can be employed as cosolvents to improve the water tolerance of ethanol-gasoline mixtures, their efficacy in this respect being a function of the relative influences of the hydrocarbon and hydroxyl groups in the alcohol molecular structure.

The vapor pressure of the limit blends as measured with the Reid vapor pressure apparatus at 100°F (37.8°C) is shown in Fig. 2. The vapor pressure of the summer gasoline was 7.4 psi (51.0 kpa), while that of the pure ethanol was 2.25 psi (15.5 kpa). Below 5 volume percent of water in the alcohol, the percentage of water-alcohol mixture in the limit blend is less than 10 percent as seen from Fig. 1. Hence the vapor pressure of the limit blend is not much different from that of the base gasoline. Also when the water in the alcohol exceeds 15 percent, the amount of gasoline in the limit blend is now less than 15 percent and the vapor pressure is close to the pure ethanol value. The vapor pressure of mixtures containing ethanol and gasoline only in the same relative proportions as found in a limit blend containing a given percentage of water is also shown in Fig. 2. The influence of water on vapor pressure is, therefore, to reduce the vapor pressure of pure ethanol-gasoline blends in the range of 5-15 volume percent of water in the ethanol. In the present study, the reported phenomenon [11] of boiling point depression from azeotrope formation of the alcohol with the lower boiling gasoline hydrocarbons was not observed, perhaps due to the lower concentration of these lighter hydrocarbons in the summer gasoline. Azeotrope formation of the alcohols with the low boiling point gasoline hydrocarbons has been shown to increase the vapor pressure of the blend [22] as measured by the micromethod [23]. Excessive vapor pressures in the fuel system can lead to vapor lock and rough engine operation. The data of Fig. 2 show that in cases where azeotrope formation produces an increase in the vapor pressure of the alcohol-gasoline blend, the use of hydrated ethanol as a

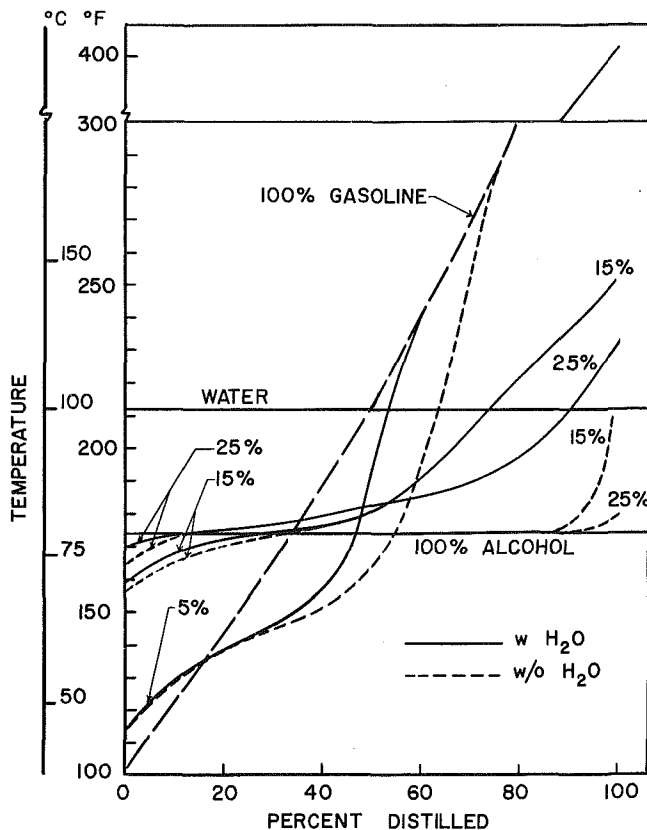


Fig. 4 Volatility characteristics of water-ethanol-gasoline blends

blending component can be beneficial in preventing vapor lock.

The influence of water on the viscosity of ethanol-gasoline blends is shown in Fig. 3 as a function of the volume percent of water in the ethanol. The lower curve in the figure represents the viscosity of the pure ethanol-gasoline blend where the ethanol and gasoline are in the same relative proportions as in a limit blend containing a given percentage of water in the ethanol. The use of hydrated ethanol as a blending component results in a slightly higher viscosity of the blend. In fuel injected engines this would produce a more uneven dispersion of droplets at a given cross section of the spray and would tend to increase the droplet size.

Figure 4 illustrates the effect of water on the volatility characteristics of ethanol-gasoline mixtures as determined with the ASTM distillation apparatus. The line with the long dashes running from bottom left to the top right represents the distillation characteristics of the pure gasoline, while horizontal lines at 100 and 77.8°C depict the boiling point temperatures of water and ethanol, respectively. The distillation curves for the limit blends containing 5, 15, and 25 percent of water in the alcohol are shown in full lines and are so labeled in Fig. 4. The dashed lines labeled 5, 15, and 25 percent are the distillation curves of the pure alcohol-gasoline blends in the same relative proportions as the corresponding limit blends but without the water.

The characteristics of the distillation curves in Fig. 4 can be attributed to three causes: (a) the relative proportions of ethanol and gasoline in the blend, (b) the presence of water, and (c) the possibility of ethanol/hydrocarbon azeotrope formation. Since a blend contains less gasoline overall, the fraction of blended fuel recovered at temperatures below the boiling point of the alcohol is less, resulting in the elevation of the front end distillation temperatures. This is readily seen in the distillation properties of the blended fuel in the range of 0-25 volume percent distilled. The influence of water addition

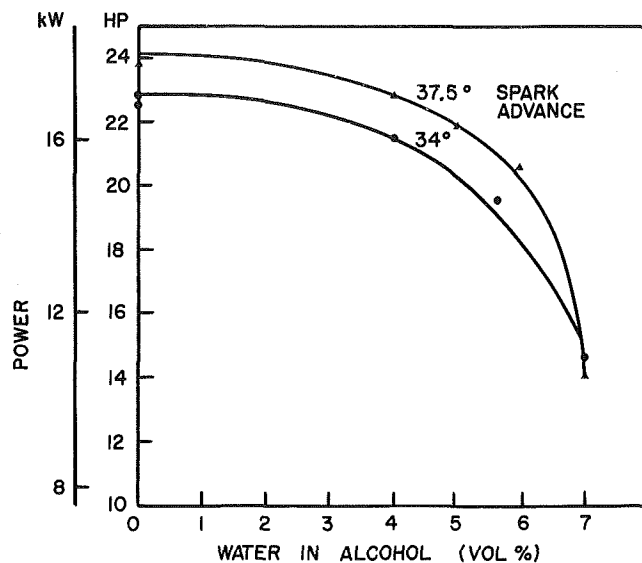


Fig. 5 Variation of engine brake power with volume percent water in the limit blend: speed = 2050 rpm

is minimal in the 5 volume percent water blend as seen by the closeness of the full and dashed lines in this region. With greater percentages of water in the hydrated ethanol, the volume of gasoline in the limit blend is drastically reduced (Fig. 1), causing the front end of the distillation curve to approach the horizontal pure alcohol line. Azeotrope formation of the ethanol with the low boiling point gasoline hydrocarbons will tend to alleviate the problem of elevated front end distillation temperatures by depressing the boiling point in this region.

The cold start and warm-up performance of engines operating on water-ethanol-gasoline blends will be less satisfactory than engines running on pure gasoline unless additional measures such as inlet manifold heating are undertaken to improve the front-end volatility of the blends. This tendency has been substantiated by fleet tests [24].

As the distillation temperatures are raised, Fig. 4 shows the distillation curves to be shifted to the right of the pure gasoline curve. This effect is less for the water-alcohol-gasoline limit blends than for the pure ethanol-gasoline blends and is especially pronounced at temperatures above the alcohol boiling point. This is due in some measure to the higher concentration of the gasoline in the test sample once the ethanol has largely distilled off. This should yield a faster engine response during acceleration and smoother operation in the normal power range.

**(b) Power and Pollution Characteristics.** The feasibility of utilizing less than 200 proof ethanol in the near term as a blending component was evaluated by engine dynamometer tests in an unmodified production engine. Limit blends containing various percentages of water in the alcohol were tested at a constant engine manifold vacuum of 25 cm of mercury as described earlier. The measured brake power realized with the limit blends is shown in Fig. 5 as a function of the volume percent of water in the ethanol for two values of the spark advance before top dead center. The point corresponding to 0 percent water represents the power developed with pure gasoline. The engine speed was kept constant at 2050 rpm in an effort to keep the turbulence levels uniform in the tests with the various fuels. Some difficulty was experienced in starting the engine with the 7 percent water in ethanol limit blend, as a result of the volatility characteristics of the blend as discussed above. Consequently the

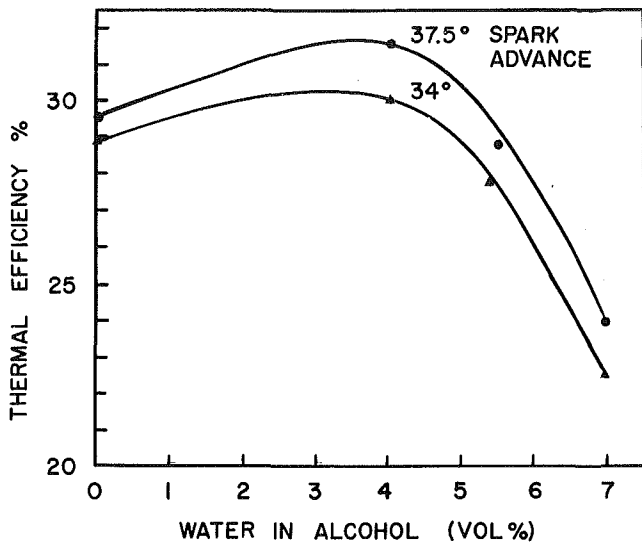


Fig. 6 Brake thermal efficiency variation with volume percent water in the limit blend: speed = 2250 rpm

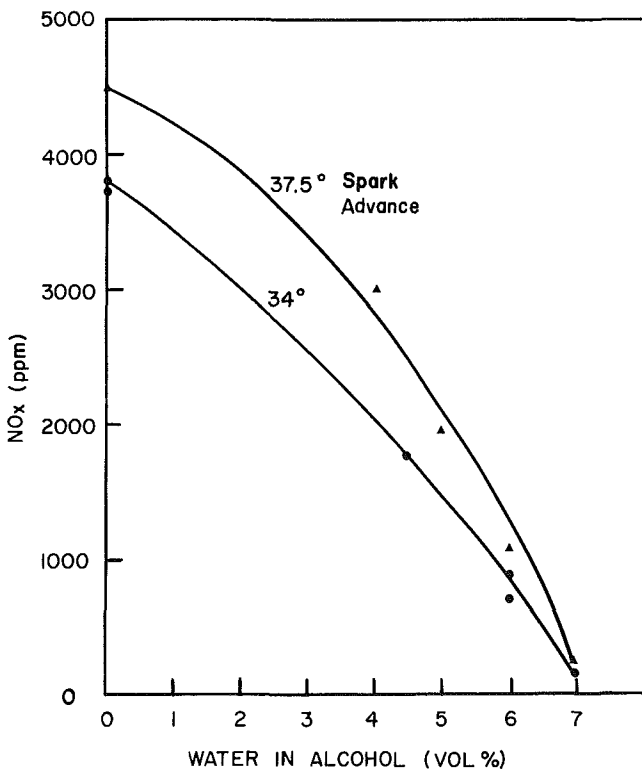


Fig. 7 Oxides of nitrogen emissions as a function of volume percent water in the limit blend: speed = 2050 rpm

engine was first started with pure gasoline and later switched over to the blended fuel once it had warmed up.

Figure 5 shows the engine brake power output drops significantly when the water in the blended ethanol increases beyond 6 percent by volume. This drop in power with increased volume percentages of water in the alcohol is predominantly the result of two factors. The first factor responsible for the low power output with the limit blends in the production engine is the blend leaning effect characteristic of unmodified production carburetors [8, 18]. For example, the stoichiometric air-fuel ratio for a 6 percent water in ethanol limit blend is about 13.5, but the production carburetor on the engine continues to supply air and fuel

corresponding to the stoichiometric air-fuel rate for gasoline, namely 15:1, with the blend substituted for gasoline. This reduction in power with the blends due to the blend leaning effect can be offset by simple retrofit measures such as the use of a larger metering jet in the carburetor.

Even with the proper air-fuel ratio being maintained, the power output with alcohol-gasoline mixtures has been shown to be lower than that with pure gasoline [18]. This is due to the smaller heating values of the alcohol-gasoline blends and is especially true for the limit blends tested here. To realize larger power outputs with the water-ethanol-gasoline blends would require operating the engine at higher speeds.

A somewhat different picture is presented when the brake thermal efficiency of the engine is considered. Figure 6 shows the thermal efficiency as a function of the volume percent of water in the alcohol for the limit blends. The 0 percent water in alcohol point corresponds to pure gasoline. It is found that a small amount of water up to 4 volume percent is actually beneficial in improving the conversion efficiency of heat to work. This increase in thermal efficiency derived from small amounts of water added to alcohol fuels, including methanol, has also been observed by other investigators [19, 25]. The present results show that the amount of the increase in thermal efficiency is a function of spark timing, as well as the percent of water in the alcohol. A longer spark advance is found to be beneficial as seen from the data for 37.5 deg spark advance as compared with 34 deg spark advance. However, there are limits to increasing the spark advance determined by the crank angle location of the peak power and possibly the occurrence of knock, beyond which further increases in spark advance will result in a reduction of thermal efficiency. The data of Fig. 6 also indicate that the addition of water to the ethanol of the limit blend beyond 5 volume percent results in reduction in the brake thermal efficiency.

The observed variation of thermal efficiency with increased water content of the alcohol as depicted in Fig. 6 is a result of a combination of factors that are not clearly understood at the present time. As seen from Fig. 1, for 5 volume percent of water, the limit blend consists of 80 percent gasoline, 19 percent ethanol, and 1 percent water. The combustion history in the engine cylinder of this blend as influenced by its components is largely instrumental for the observed variations in thermal efficiency. One possible factor influential in producing higher thermal efficiencies would be the higher flame speeds of the alcohol [19, 26] producing peak pressures close to the top dead center on the power stroke. However, other studies [10] have shown that both ignition delays and combustion intervals are increased when water is added to a hydrocarbon fuel, and this could offset any heat release rate gains realized by the faster combustion of the ethanol. Indeed these slower combustion rates could actually be beneficial if, even with a lower peak pressure, the average pressure during the expansion process was higher with a slower, controlled heat release rate in the presence of water. This can result in a larger torque on the crankshaft as seen by examining the dynamics of the slider-crank mechanism.

Also it is not clear why as the water content of the limit blend increases, the thermal efficiency decreases. This can be caused by altered heat transfer characteristics of the combustion gases resulting from increased quantities of water vapor in the system. Thermal dilution from increased quantities of water will lower chemical reaction rates leading to incomplete combustion. Also the catalytic activity of water vapor and the reactivity of increased OH radicals on the system is incompletely understood [27, 28]. Further work on elucidating the physical and chemical kinetic roles of water on the combustion of hydrocarbon fuels in engines is in progress.

Figure 7 shows the oxides of nitrogen ( $\text{NO}_x$ ) in the exhaust gases as measured with the Thermo-Electron 10AR chemiluminescent analyzer for two values of the ignition

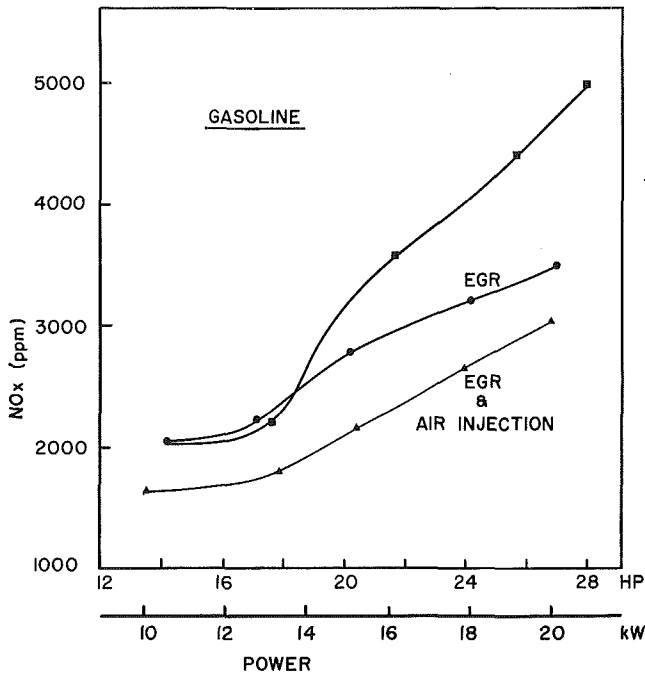


Fig. 8 Effect of EGR on  $\text{NO}_x$  emissions from the base gasoline: ■ no EGR or air injection

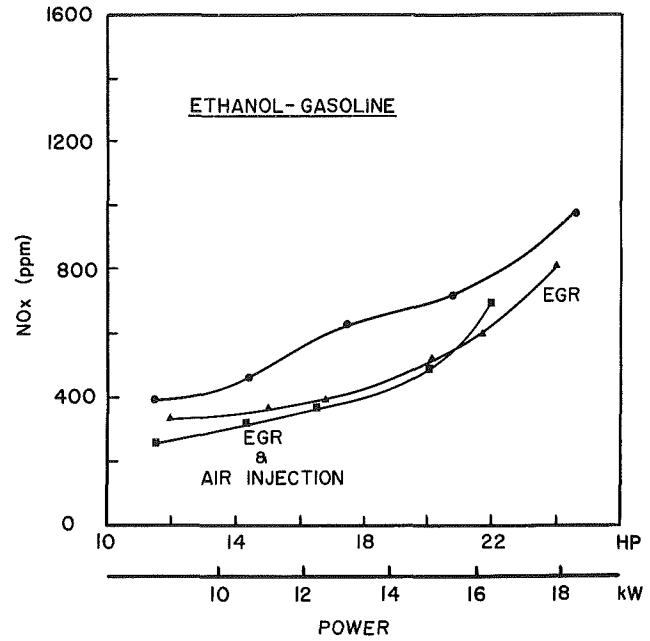


Fig. 10 Effect of EGR on the ethanol-gasoline blend alone: ● no EGR or air injection

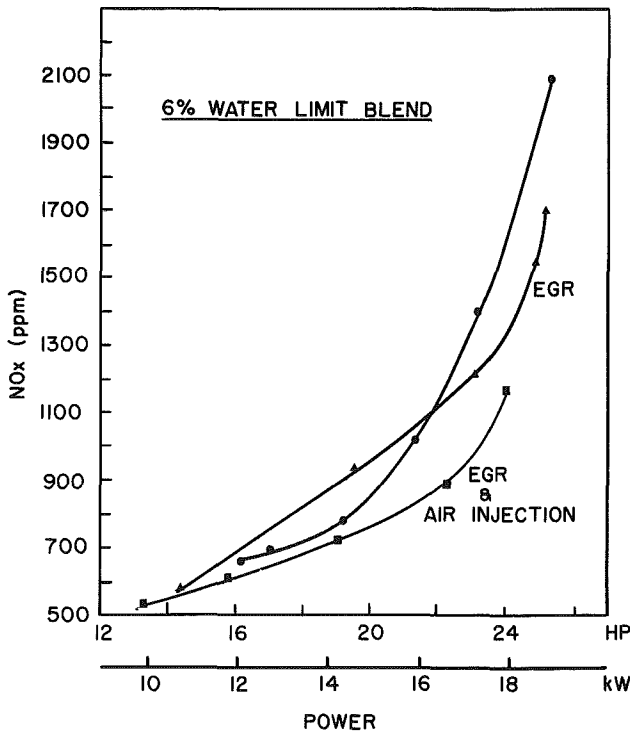


Fig. 9 Effect of EGR on  $\text{NO}_x$  emissions from 6 percent water in alcohol limit blend: ● no EGR or air injection

spark advance. The  $\text{NO}_x$  concentration drops sharply for the limit blends as compared with the value for pure gasoline. For the 6 to 7 volume percent water in alcohol limit blends the  $\text{NO}_x$  has been reduced by about 80 percent from the gasoline value. One reason for this reduction in  $\text{NO}_x$  concentration is the lower peak temperatures resulting from the lower energy densities of the charge in the combustion chamber. These temperature effects can be predicted by the basic Zeldovich mechanism [29] and have been investigated by a number of

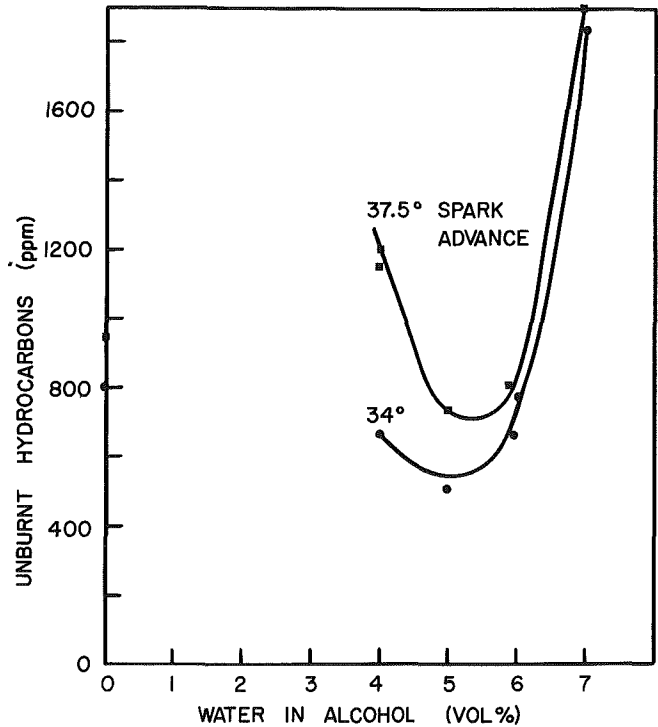


Fig. 11 Variation of unburnt hydrocarbon emissions with volume percent water in the limit blend: speed = 2050 rpm

workers [7, 30, 31]. Due to the presence of water in the limit blends, there is now a modification in the hydroxyl and oxygen atom concentrations during the combustion period [32]. These chemical kinetic effects also influence the formation of  $\text{NO}_x$  at a given temperature leading to a reduction in the observed  $\text{NO}_x$  emissions.

Tests were also conducted to evaluate the influence of water on the effectiveness of pollution control techniques such as exhaust gas recirculation (EGR) for the reduction of  $\text{NO}_x$  engine emissions. Figures 8 and 9 show the effect of EGR and air injection on measured  $\text{NO}_x$  emissions for pure gasoline

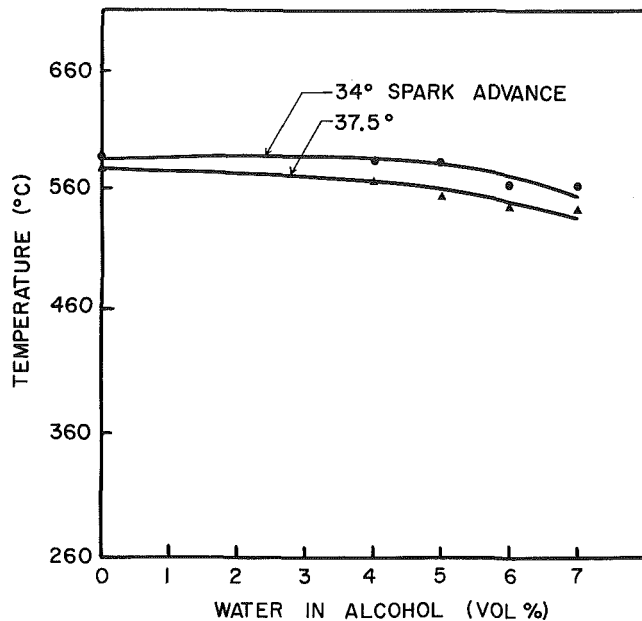


Fig. 12 Variation of exhaust gas temperatures with volume percent water in the limit blend: speed = 2050 rpm

and for the 6 percent water in alcohol limit blend. Figure 10 shows the  $\text{NO}_x$  emissions for an ethanol-gasoline blend containing ethanol and gasoline in the same relative proportions as a 6 percent water limit blend, but without the water. These data were obtained by operating the engine at various speeds while keeping the manifold vacuum at 25 cm of mercury. The engine was loaded at each speed until it began to knock and the load reduced just enough to eliminate the knock. Figure 8 shows that with the increased values of knock limited power, the  $\text{NO}_x$  emissions with gasoline increase quickly to 4000–5000 ppm at power outputs of about 20 kw. The effect of EGR is to reduce this value to 3000–3500 ppm at these loads. The curve for the combined effect of EGR and air injection is shown merely to indicate the dilution effects of air injection, since the temperatures in the exhaust manifold are probably too low to influence the formation of  $\text{NO}_x$  to any significant extent.

The measured emissions for the 6 percent water in alcohol limit blend indicate  $\text{NO}_x$  levels of less than 1000 ppm at these powers, and the influence of EGR is to reduce them still further. The effect of water in reducing  $\text{NO}_x$  emissions can be seen by comparing the data of Figs. 9 and 10. Figure 10 shows that  $\text{NO}_x$  emissions are of the order of 2000 ppm at these powers in the absence of water. Thus the influence of water is to reduce the  $\text{NO}_x$  emissions to about half the value of that obtained by using a simple ethanol-gasoline blend.

Figure 11 shows the unburnt hydrocarbon emission levels at a constant speed of 2050 rpm and a manifold vacuum of 25 cm mercury on a dry basis as measured with the Beckman 400 analyzer. Since the hydrocarbon oxidation reactions are highly temperature sensitive, the data of Fig. 11 indicate that gas temperatures in the cylinder are higher for a 34 deg spark advance than for a 37.5 deg advance. This is reflected in the measured exhaust gas temperatures shown in Fig. 12, which shows the exhaust temperatures to decrease somewhat as the water in the alcohol of the limited blends increases. However, the data of Fig. 11 show that even though in general the cylinder gas temperatures are decreasing, the exhaust unburnt hydrocarbons actually decrease in the range of 4–6 volume percent of water in the alcohol. This is the result of the variation in flame speeds and altered kinetic mechanisms in the presence of various percentages of water, ethanol, and

gasoline in the limit blends. Beyond 6 percent water in the limit blends, the combined influence of these factors produces a sharp increase in the observed exhaust unburnt hydrocarbons.

The sharpness of the observed increase in unburnt hydrocarbons when the water in the alcohol increases beyond 6 percent, taken in conjunction with the small decrease in the measured exhaust temperatures in this range, indicates that chemical kinetics plays a major role in increasing the level of exhaust unburnt hydrocarbons as the water content of the blended ethanol increases beyond 6 volume percent.

## Conclusions

1 Miscibility experiments indicate that it is not advisable to blend ethanol containing more than 5 to 6 volume percent of water with gasoline if the blend is to be utilized directly in current on the road Otto-cycle engines.

2 The distillation characteristics of the limit blends exhibit both advantages and disadvantages. Cold start and warm-up performance is adversely affected while economy and cruise ranges are somewhat benefitted.

3 Blending hydrated ethanol with gasoline would reduce the vapor pressure increase resulting from azeotrope formation.

4 Because of lower heating values per unit weight and the blend leaning effect of production carburetors, lower power outputs are realized when hydrated ethanol-gasoline blends are used in unmodified engines. However, this trend can be reversed by designing the engine and fuel delivery systems to take advantage of the special properties of these blends.

5 Water addition to ethanol-gasoline blends reduces the  $\text{NO}_x$  emissions appreciably. This is in part due to the leaner A/F ratios supplied by unmodified carburetors.

6 Measured total unburnt hydrocarbons were found to decrease somewhat when less than 4 volume percent water is included in the blended ethanol. With more than 4 volume percent water in the blended ethanol, the total unburnt hydrocarbons increased sharply.

## Acknowledgment

The assistance of Mr. Fariborz F. Saniee in obtaining the experimental data is gratefully acknowledged.

## References

- Ricardo, H. R., *The High-Speed Internal Combustion Engine*, Blackie and Sons, Ltd., 1953.
- Obert, E. F., "Detonation and Internal Coolants," *SAE Quarterly Transactions*, Vol. 2, 1948, pp. 52–59.
- Modak, A., and Caretto, L. S., "Engine Cooling by Direct Injection of Cooling Water," SAE Paper 700887, Fuels and Lubricants Meeting, 1970.
- Weatherford, W. D., and Quillian, R. D., "Total Cooling of Piston Engines by Direct Water Injection," SAE Paper 700886, Fuels and Lubricants Meeting, 1970.
- Van Hartesveldt, C. H., *SAE Quarterly Transactions*, Vol. 3, 1949, p. 277.
- Lestz, S. S., and Meyer, W. E., "The Effect of Direct Cylinder Water Injection on Nitric Oxide Emission from an S.I. Engine," *Proceedings of the 14th FISITA Congress*, London, 1972, pp. 2134–2141.
- Nichols, J. E., El-Messiri, I. A., and Newhall, H. K., "Inlet Manifold Water Injection for Control of Nitrogen Oxides—Theory and Experiment," *SAE Transactions*, Vol. 28, 1969, pp. 167–176.
- Melton, R. B., Jr., Lestz, S. J., and Quillian, R. D., Jr., "Direct Water Injection Cooling for Military Engines and Effects on the Diesel Cycle," Fifteenth Symposium (International) on Combustion, The Combustion Institute, 1975.
- Boekhaus, K. L., and Copeland, L. C., "Performance Characteristics of Stratified Charge Vehicles With Conventional Fuels and Gasoline Blended With Alcohol and Water," SAE Paper No. 760197.
- Harrington, J. A., "Water Addition to Gasoline—Effect on Combustion, Emissions, Performance and Knock," SAE Paper 820314, 1982.
- Freeman, J. H., et al., "Alcohols—A Technical Assessment of Their Application As Fuels," American Petroleum Institute Publication No. 4261, 1976.
- Allsup, J. R., and Eccleston, D. B., "Ethanol/Gasoline Blends As

Automotive Fuels," *Proceedings of the Third International Symposium on Alcohol Fuels Technology*, Vol. I, 1979.

13 Chiu, G., Anderson, R., and Baker, R., "Brazilian Vehicle Calibration for Ethanol Fuels," *Proceedings of the Third International Symposium on Alcohol Fuels Technology*, Vol. II, 1979.

14 Peters, D. B., and Stebar, R. F., "Water-Gasoline Fuels—Their Effect on Spark Ignition Engine Emissions and Performance," SAE Paper No. 760547, 1976.

15 Greeves, G., Khan, I. M., and Onion, G., "Effects of Water Introduction on Diesel Engine Combustion and Emissions," Sixteenth Symposium (International) on Combustion, 1977.

16 Murayama, T., Morishima, Y., Tsukahara, M., and Mujamoto, N., "Experimental Reduction of NO<sub>x</sub>, Smoke, and BSFC in a Diesel Engine Using Uniquely Produced Water (0–80%) to Fuel Emulsion," SAE Paper 780224.

17 Starke, F., "Operation of Otto-Type Engines on Gasoline-Methanol/Water," *Proceedings, International Symposium on Alcohol Fuels Technology*, Wolfsburg, W. Germany, 1977.

18 Rajan, S., and Sanjee, F. F., "Water-Ethanol-Gasoline Blends as Spark Ignition Engine Fuels," *Fuel*, Vol. 62, No. 1, 1983, pp. 117–121.

19 Johnson, R. T., "A Comparison of Gasoline, Methanol, and a Methanol/Water Blend as Spark Ignition Engine Fuels," *Proceedings, International Symposium on Alcohol Fuels Technology*, Wolfsburg, Germany, 1978.

20 Obert, E. F., *Internal Combustion Engines and Air Pollution*, Intext Educational Publishers, N.Y., 1973, pp. 388–389.

21 Keller, J. L., "Methanol and Ethanol Fuels for Modern Cars," American Petroleum Institute, Division of Refining Meeting, San Francisco, Calif., May 1979.

22 Cox, F. W., "The Physical Properties of Gasoline/Alcohol Automotive Fuels," *Proceedings of the Third International Symposium on Alcohol Fuels Technology*, Vol. II, 1979.

23 "Vapor Pressure of Petroleum Products by the Micromethod," D. 2551, American Society for Testing and Materials Book of Standards, 1974.

24 Brinkman, N. D., Gallopoulos, N. E., and Jackson, M. W., "Exhaust Emissions, Fuel Economy and Driveability of Vehicles Fueled with Alcohol-Gasoline Blends," SAE Paper 750120, 1975.

25 LaRusso, J. A., and Tabaczynski, R. J., "Combustion and Emissions Characteristics of Methanol, Methanol-Water and Gasoline-Methanol Blends in a Spark Ignition Engine," *Proceedings, 11th Intersociety Energy Conversion Engineering Conference*, Stateline, Nev., 1976.

26 Henein, N. A., Singh, T., Rozanski, J., and Husak, P., "Flame Speeds, Performance and Emissions With Methanol-Indolene Blends," *Proceedings, Fourth International Symposium on Automotive Propulsion Systems*, Vol. II, Washington, D. C., 1976.

27 Muller-Dethlefs, K., and Schlader, A. F., "The Effect of Steam on Flame Temperature, Burning Velocity and Carbon Formation in Hydrocarbon Flames," *Combustion and Flame*, Vol. 27, No. 2, 1976, pp. 205–215.

28 Dryer, F. L., "Water Addition to Practical Combustion Systems—Concepts and Applications," Sixteenth Symposium (International) on Combustion, The Combustion Institute, 1977.

29 Zeldovich, Ya B., "The Oxidation of Nitrogen in Combustion Explosions," *Acta Physicochimica U.R.S.S.*, Vol. 21, 1946, pp. 517–628.

30 Lavoie, G. A., Heywood, J. B., and Keck, J. C., "Experimental and Theoretical Studies of Nitric Oxide Formation in Internal Combustion Engines," *Combustion Science and Technology*, Vol. 1, 1970, pp. 316–326.

31 Caretto, L. S., Muzio, L. J., Sawyer, R. F., and Starkman, E. S., "The Role of Kinetics in Engine Emission of Nitric Oxide," *Combustion Science and Technology*, Vol. 3, 1971, pp. 53–61.

32 Bowman, C. T., "Nonequilibrium Radical Concentrations in Shock Initiated Methane Oxidation," Fifteenth Symposium (International) on Combustion, The Combustion Institute, 1975.

X. Q. Liu  
C. H. Wang  
C. K. Law

Department of Mechanical  
and Nuclear Engineering,  
Northwestern University,  
Evanston, Ill. 60201

# Simulation of Fuel Droplet Gasification in SI Engines

*The heating and gasification of a fuel droplet during the intake and compression strokes of an SI engine are modeled. Results show that the simultaneous increases in the gas temperature and pressure during compression tend to have compensatory effects on the droplet gasification rate such that it remains somewhat insensitive to changes in the cylinder environment. Generalized results are presented allowing for the assessment of the lower and upper bounds in the initial size of the droplet that can achieve complete gasification prior to the end of the compression stroke.*

## 1 Introduction

An important consideration in the design and optimization of liquid-fueled combustors is the extent the liquid fuel has gasified at the instant of ignition. This amount not only sensitively influences the ignitability and ignition delay of the mixture, but it also determines the extent of heterogeneous combustion that subsequently takes place. It is well known that droplet burning involves diffusion flames at which fuel and oxidizer react in near stoichiometric proportion. The resulting flame temperature is nearly the maximum possible, implying the formation of such highly temperature-sensitive pollutant species as thermal  $\text{NO}_x$ ,  $\text{SO}_x$ , and soot is significantly enhanced. Furthermore, even for those droplets which do not burn individually, as would be the case when they are situated in a dense spray, their relatively slow gasification rate becomes rate-limiting and thereby controls the bulk combustion behavior.

The foregoing factors generally are not considered to be relevant for the conventional reciprocating spark-ignition (SI) engines based on the belief that the high volatility of the liquid fuel ensures that complete gasification should occur during the carburetion process. Furthermore, for those droplets which fail to achieve complete gasification in the intake manifold, it is conjectured that they should still be totally gasified during the intake and compression strokes prior to spark discharge. The primary argument here being that the temperature-sensitive droplet gasification rate should be greatly accelerated as the gas is heated during the compression stroke.

There are, however, other factors which render the aforementioned consideration less conclusive. For example, it is reasonable to expect that during cold start, especially when the ambient temperature is low, the overall gasification rate can be significantly retarded such that the larger fuel droplets may survive until spark discharge. Secondary droplets may also be generated when the liquid film, deposited close to the intake valve through droplet impact, is sucked into the cylinder during intake. These droplets are expected to have larger sizes because of the relatively weak aerodynamic

stripping acting on the liquid film. They also have less time for gasification compared with the primary droplets generated by the carburetor.

Another important factor which has not been adequately recognized is the effect of pressure on the droplet gasification rate. That is, during the compression stroke, while the increasing gas temperature tends to enhance gasification, the simultaneously increasing pressure tends to retard it. Although it is not certain a priori which has the stronger influence, it is nevertheless clear that the droplet gasification rate can be substantially reduced from the value obtained by considering only the influence due to temperature increase.

These heterogeneous effects are also expected to become more serious with the utilization of such synthetic fuels as coal-derived oils. These synfuels have higher and wider distillation temperature ranges, and therefore are harder to vaporize. They also have higher contents of fuel-bound nitrogen, implying that it is even more important to control the thermal  $\text{NO}_x$  formation so as to reduce its overall level of emission.

In view of these considerations, we have formulated a model that simulates the droplet vaporization history when it is subjected to the highly-transient environment during the intake and compression strokes. We are especially interested in assessing the effect of increasing pressure on the droplet gasification rate, of resolving the possible existence of droplets at spark discharge, and of providing order-of-magnitude estimates of the sizes of these droplets. The model is presented in the next section and is followed by sample solutions in section 3.

## 2 Model Formulation

We present herein the model simulating droplet gasification during the intake and compression strokes. The simulation consists of two components: namely, a description of the droplet gasification process and rate in an environment of varying temperature and pressure, and a prescription of the temporally-varying environment within the cylinder.

For the droplet process, we adopt the classical  $d^2$ -Law model for droplet vaporization and combustion [1-5], modified to allow for droplet heating [4, 5], which is expected

Contributed by the Fuels Division for publication in the JOURNAL OF ENGINEERING FOR GAS TURBINES AND POWER. Manuscript received by the Fuels Division April 15, 1983.



to be an important element in controlling the droplet gasification rate. We do this because as the cylinder temperature and pressure continuously increase, the droplet temperature will also correspondingly increase. Therefore, only part of the heat absorbed by the droplet is used for gasification; the rest is expended in heating the droplet.

The controlling transport processes in delivering heat from the ambience to the droplet surface, and subsequently in dispersing the fuel vapor from the surface to the ambience, are diffusion and (radial) convection. Thus assuming gas-phase quasi-steadiness and spherical symmetry, conservation of fuel vapor and energy [1] require that

$$mY - 4\pi\rho Dr^2 \frac{dY}{dr} = m \quad (1)$$

$$mc_p(T - T_s) - 4\pi\lambda r^2 \frac{dT}{dr} = -mQ \quad (2)$$

where

$$m = 4\pi\rho v r^2 \quad (3)$$

is the instantaneous gasification rate;  $Y$ , the mass fraction of the fuel vapor;  $T$ , the temperature; and  $Q$ , to be specified later, is an *effective* latent heat of vaporization that includes the latent heat of vaporization plus the amount needed to heat the droplet interior per unit mass of fuel vaporized.

With the nondimensionalization  $\hat{m} = m/(4\pi\rho Dr_s)$ ,  $\hat{r} = r/r_s$ ,  $\hat{T} = c_p T/L$ , and  $\hat{Q} = Q/L$ , equations (1) and (2) become

$$\hat{m}Y_F - \hat{r}^2 \frac{dY_F}{d\hat{r}} = \hat{m} \quad (4)$$

$$\hat{m}(\hat{T} - \hat{T}_s) - \hat{r}^2 \frac{d\hat{T}}{d\hat{r}} = -\hat{m}\hat{Q} \quad (5)$$

Solving equations (4) and (5) subject to the boundary conditions

$$\hat{r} = 1: \hat{T} = \hat{T}_s, Y_F = Y_{Fs} \quad (6)$$

$$\hat{r} = \infty: \hat{T} = \hat{T}_\infty, Y_F = Y_{F\infty} \quad (7)$$

we obtained the fuel vapor and temperature profiles

$$Y_F(\hat{r}) = 1 + (Y_{Fs} - 1) \exp\left\{\hat{m}\left(1 - \frac{1}{\hat{r}}\right)\right\} \quad (8)$$

$$T(\hat{r}) = (\hat{T}_s - \hat{Q}) + \hat{Q} \exp\left\{\hat{m}\left(1 - \frac{1}{\hat{r}}\right)\right\} \quad (9)$$

and explicit expressions for the eigenparameters of interest

$$\hat{m} = \ln\{(1 - Y_{F\infty})/(1 - Y_{Fs})\} \quad (10)$$

$$\hat{Q} = \frac{(1 - Y_{Fs})(\hat{T}_\infty - \hat{T}_s)}{(Y_{Fs} - Y_{F\infty})} \quad (11)$$

Equations (10) and (11) show that  $\hat{m}$  and  $\hat{Q}$  are functions of  $Y_{Fs}$  and  $T_s$ . Since it is realistic to assume that the fuel vapor is saturated at the droplet surface,  $Y_{Fs}$  and  $\hat{T}_s$  are related through the Clausius-Clapeyron relation

$$Y_{Fs}(\hat{T}_s) = \{1 + (W_A/W_F)[p_\infty \exp[(c_p/R)(\hat{T}_s^{-1} - \hat{T}_b^{-1})] - 1]\}^{-1} \quad (12)$$

where  $T_b$  is the boiling point at one atmosphere, and  $p_\infty$  is the environment (i.e., cylinder) pressure expressed in the unit of atmosphere. Thus using equation (12) in equations (10) and (11),  $\hat{m}$  and  $\hat{Q}$  now depend only on the instantaneous droplet temperature,  $\hat{T}_s$ .

To follow the temporal variation of  $T_s$ , from our definition, we have

$$(Q - L) = \left[\frac{4}{3}\pi r_s^3 \rho_l c_p dT_s/dt\right]/m \quad (13)$$

where  $\rho_l$  is the liquid density. Since

$$m = -\left(\frac{d}{dt}\right)\left[\frac{4}{3}\pi r_s^3 \rho_l\right] \quad (14)$$

equation (13) becomes

$$\hat{Q}(\hat{T}_s) = 1 - \left(\frac{2}{3}\right)S \frac{d\hat{T}_s}{dS} \quad (15)$$

where  $S = (r_s/r_{so})^2$  is the normalized droplet surface area. Integrating equation (15), we obtain

$$S = \exp\left\{\int_{\hat{T}_{so}}^{\hat{T}_s} G(\hat{T}_s') d\hat{T}_s'\right\} \quad (16)$$

where

$$G(\hat{T}_s) = \left(\frac{2}{3}\right)/[1 - \hat{Q}(\hat{T}_s)] \quad (17)$$

in which  $\hat{Q}(\hat{T}_s)$  is given by equation (11).

Finally, expressing equation (14) as

$$\hat{m} = -\frac{dS}{dt} \quad (18)$$

where  $\hat{t} = [(2\rho D)/(\rho_l r_{so}^2)]t$ , the dependence of  $\hat{T}_s$  on time can be inversely expressed by integrating equation (18) and using equation (16)

$$\hat{t} = -\int_{\hat{T}_{so}}^{\hat{T}_s} [\hat{m}(\hat{T}_s')]^{-1} G(\hat{T}_s') \exp\left\{\int_{\hat{T}_{so}}^{\hat{T}_s''} G(\hat{T}_s'') d\hat{T}_s''\right\} d\hat{T}_s' \quad (19)$$

## Nomenclature

$c_p$  = specific heat at constant pressure  
 $D$  = mass diffusivity between fuel vapor and air  
 $G$  = function defined in equation (17)  
 $l_1, l_2, l_3$  = lengths of crank, connecting rod, and cylinder  
 $L$  = specific latent heat of vaporization  
 $m$  = droplet mass vaporization rate  
 $\hat{m} = m/(4\pi\rho Dr_s)$   
 $p$  = pressure  
 $Q$  = effective latent heat of vaporization  
 $\hat{Q} = Q/L$   
 $r$  = radial distance from droplet center

$\hat{r} = r/r_s$   
rpm = revolutions per minute  
 $r_v$  = compression ratio  
 $R$  = gas constant  
 $S$  = normalized droplet surface area,  $(r_s/r_{so})^2$   
 $t$  = time  
 $\hat{t} = t(2\rho D)/(\rho_l r_{so}^2)$   
 $\hat{t}_C$  =  $\hat{t}$  needed to complete the intake or compression stroke  
 $T$  = temperature  
 $\hat{T} = c_p T/L$   
 $T_r$  = residue temperature  
 $v$  = radial velocity from droplet  
 $W$  = molecular weight  
 $x, y$  = piston travel from top and bottom centers  
 $Y$  = mass fraction

$\tau$  = critical time for droplet to just complete gasification at end of compression stroke  
 $\rho$  = gas density  
 $\rho_l$  = liquid density  
 $\lambda$  = thermal conductivity  
 $\theta$  = crank angle  
 $\gamma$  = specific heat ratio  
 $\sigma$  = index for stroke

## Subscripts

$A$  = air  
 $b$  = normal boiling state  
 $e$  = ambient condition  
 $F$  = fuel  
 $s$  = droplet surface  
 $o$  = droplet initial state  
 $\infty$  = state within cylinder

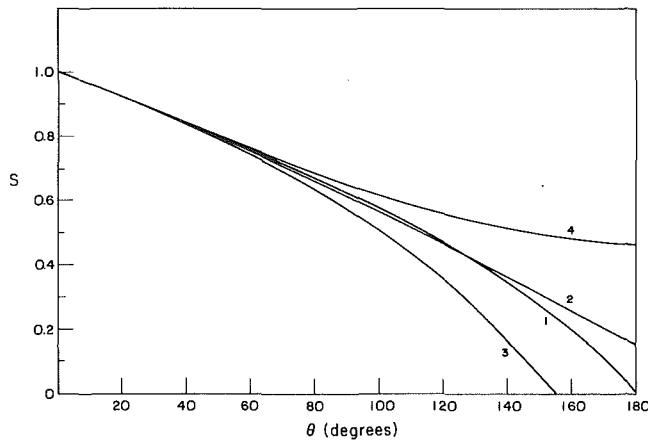


Fig. 1 Temporal variation of the nondimensional droplet surface area for various engine simulation modes: 1, standard case; 2, constant gas temperature and pressure; 3, only temperature varying; 4, only pressure varying

Formulation of the droplet vaporization model is complete at this stage. Thus given the droplet initial temperature,  $T_{s0}$ , its subsequent variations in temperature and vaporization rate can be traced for given environmental conditions  $p_\infty(t)$  and  $T_\infty(t)$ , which are to be supplied through the engine simulation process to be stated next.

To simulate the cylinder temperature and pressure, we use the idealized air standard cycle allowing the presence of the residue gas. Thus during intake,  $p_\infty$  is the outside pressure,  $p_e$ , while the temperature  $T_\infty$  is

$$T_\infty = \frac{T_r(l_3 - 2l_1) + xT_e}{l_3 - 2l_1 + x}$$

where

$$l_3 = \frac{2r_v l_1}{(r_v - 1)}$$

$l_2$  and  $l_1$  are, respectively, the lengths of the crank and the connecting rod,  $x$  is the distance of the piston travel from top dead center

$$x = l_2 - (l_2^2 - l_1^2 \sin^2 \theta)^{1/2} + l_1(1 - \cos \theta)$$

$\theta$  is the crank angle

$$\theta = \pi \hat{t} / \hat{t}_C$$

$\hat{t}_C$  is the time needed to complete the intake (or the compression) stroke, and  $T_r$  and  $T_e$  are, respectively, the residue and outside temperatures.

During the compression stroke, we have

$$p_\infty = \left( \frac{l_3}{l_3 - y} \right)^\gamma p_e$$

$$T_\infty = \left( \frac{l_3}{l_3 - y} \right)^{(\gamma-1)} \left\{ \frac{T_r(l_3 - 2l_1) + 2l_1 T_e}{l_3} \right\}$$

where

$$y = (l_2^2 - l_1^2 \sin^2 \theta)^{1/2} + l_1(1 + \cos \theta) - l_2$$

is the piston travel from bottom dead center.

This completes the description of the engine cylinder environment.

### 3 Results and Discussions

While a complete multiparametric mapping of the model obviously will be prohibitively extensive, we have nevertheless reduced the problem to a level such that a systematic,

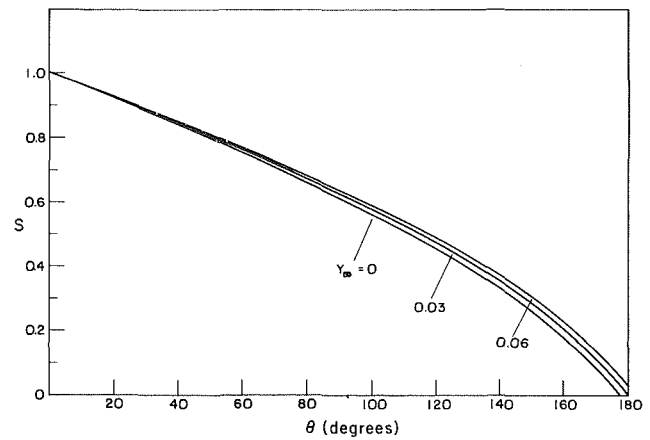


Fig. 2 Temporal variation of the nondimensional droplet surface area for different fuel vapor concentrations in the cylinder

reasonably general characterization of the phenomena of interest is possible.

The model fuel adopted for simulation is iso-octane, with  $L = 64$  cal/gm,  $T_b = 372^\circ\text{K}$ ,  $c_p = 0.675$  cal/gm $^\circ\text{K}$ , and  $R = 1.987 \times 10^{-2}$  cal/gm $^\circ\text{K}$ . For the gas properties, we have  $\gamma = 1.33$  and  $T_r = 1150^\circ\text{K}$ . For the engine configuration, we use  $l_1 = 42$  mm and  $l_2 = 155$  mm. We have found that a 10 percent variation in either  $l_1$  or  $l_2$  produces less than 1 percent in the nondimensional results presented in the following. Thus our results are quite insensitive to variations in  $l_1$  and  $l_2$ .

Noting that the initial droplet size  $r_{s0}$  and the engine speed are absorbed through nondimensionalization, the remaining parameters that could be of importance are the outside temperature  $T_e$ , the fuel vapor concentration  $Y_{F\infty}$ , and the compression ratio  $r_v$ . Their influences are studied in the following.

We first restrict the simulation to only the compression stroke such that effects due to the simultaneous variations in the cylinder temperature and pressure can be delineated. Physically, this corresponds to the situation involving a droplet entering the cylinder at the end of the intake stroke just before the intake valve is closed. We choose as our standard case  $T_e = 300$  K,  $Y_{F\infty} = 0.03$ ,  $r_v = 8.5$ , and compression time  $\hat{t}_C = 1.349$ , such that the droplet is completely vaporized at the end of the compression stroke. Figure 1 shows the variation of its surface area,  $S$ , with the crank angle  $\theta$ . For  $d^2$ -Law, such a plot yields a straight line. It is seen that while the initial variation is somewhat linear, the slope progressively increases after droplet half-life, implying that the vaporization rate is increased. This result demonstrates that the increasing cylinder temperature during compression does have a stronger, positive effect on the vaporization rate than the retarding influence of the simultaneous increase in the cylinder pressure. The net increase, however, is not too large. To illustrate this point, Fig. 1 also shows curves obtained by suppressing either the pressure or the temperature variations. It is seen that while their individual influences are quite significant, their opposite effects tend to be compensatory. Indeed, the standard curve with simultaneous variations in pressure and temperature agrees quite well with the curve obtained under the static situations of no changes in pressure and temperature, as shown in Fig. 1.

Figure 2 shows there is very little influence due to the presence of fuel vapor in the cylinder. The cases of  $Y_{F\infty} = 0$  and 0.06, respectively, correspond to the situations where practically no liquid fuel is vaporized to almost complete vaporization of a stoichiometric mixture. The vaporization

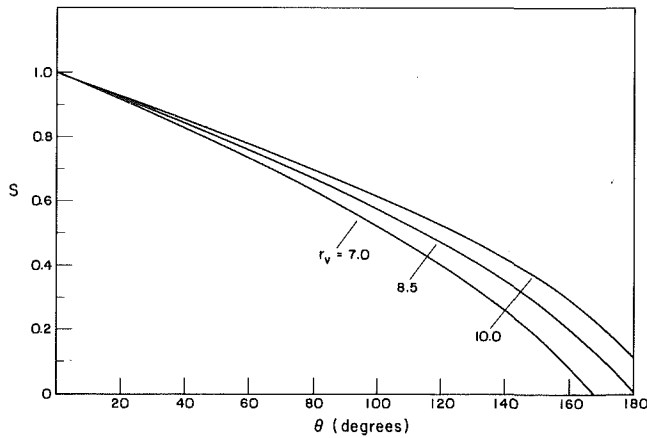


Fig. 3 Temporal variation of the nondimensional droplet surface area for various compression ratios

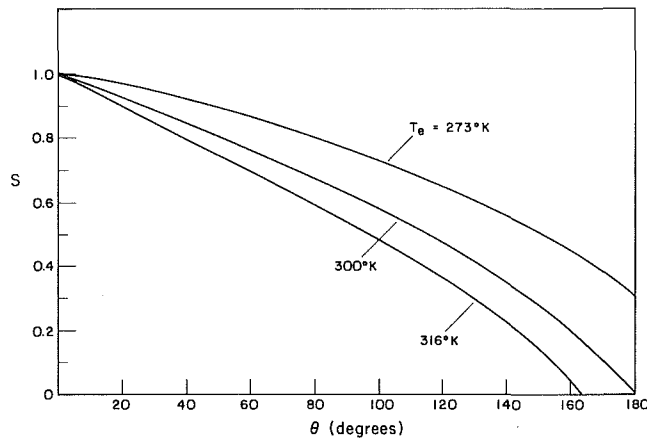


Fig. 4 Temporal variations of the nondimensional droplet surface area for various ambient temperatures

rate is slightly faster when the gas has less fuel vapor present, as would be expected.

Figure 3 shows that increasing  $r_v$  increases the gasification rate, hence corroborating the previous result that increasing temperature has a stronger influence than increasing pressure. Figure 4 shows that the ambient temperature has the greatest influence on the gasification rate, especially at low temperatures, as would be expected.

A particularly useful result of the present study is the identification of a nondimensional critical time  $\tau$ , corresponding to the situation where the droplet attains complete gasification at the end of the compression stroke. Thus, by definition,

$$\tau = \left( \frac{2\rho D}{\rho_l r_{so}^2} \right) t$$

$$= \left( \frac{\rho D}{\rho_l r_{so}^2} \right) \left( \frac{60}{\text{rpm}} \right) (2^\sigma) \quad (20)$$

where  $\sigma=0$  if only the compression stroke is simulated, while  $\sigma=1$ , if both intake and compression strokes are simulated. This critical time can be iteratively determined by equating the complete droplet gasification time with the compression time.

Figure 5 shows  $\tau$  as a function of  $T_e$  and  $r_v$ . It may be emphasized that these curves are general and useful in that, for a given fuel, all the important system parameters (e.g.,  $r_{so}$ , rpm,  $T_e$ ) are represented. For example, by giving the rpm,  $r_v$ , and  $T_e$ , we can readily determine the size of a droplet that can just achieve complete gasification at the end of the com-

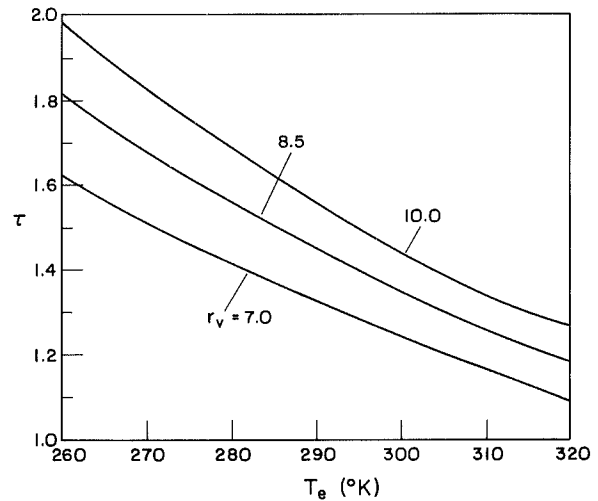


Fig. 5 Critical time to achieve complete gasification during compression stroke

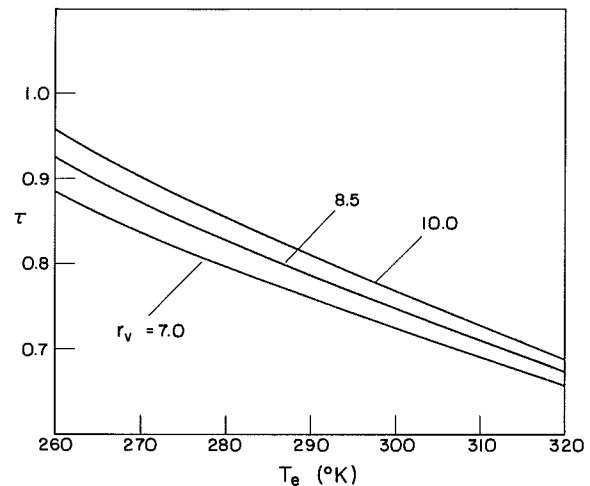


Fig. 6 Critical time to achieve complete gasification during intake and compression strokes

pression stroke here such that the droplet has the least available time for gasification. Thus any droplet which is smaller than that given by Fig. 5 will be able to completely vaporize.

Extending the foregoing concept, we have plotted the  $\tau$  obtained by including both the intake and compression strokes (Fig. 6). Since the droplet in this case is inducted at the beginning of the intake stroke and hence has the maximum time to achieve gasification, therefore any droplet which is larger than that given in Fig. (6) will not be able to achieve complete gasification. Thus Figs. 5 and 6 provide lower and upper bounds in the droplet size to achieve complete gasification.

Finally, we note that when determining the droplet radius  $r_{so}$  from  $\tau$ , equation (20) shows that we need the thermophysical "constant"  $(\rho D/\rho_l)$ . This can be either estimated or, more accurately, extracted by comparing the experimental and theoretical gasification rates of a single droplet in a constant environment, as governed by the  $d^2$ -Law behavior. Thus, using the calibrated results of Kent [6] for droplet vaporizing in environments similar to the present one, we have determined that  $(\rho D/\rho_l) = 1.8 \times 10^{-4} \text{ cm}^2/\text{s}$ .

By using the aforementioned value for  $(\rho D/\rho_l)$ , together with Figs. 5 and 6, we have determined the minimum and

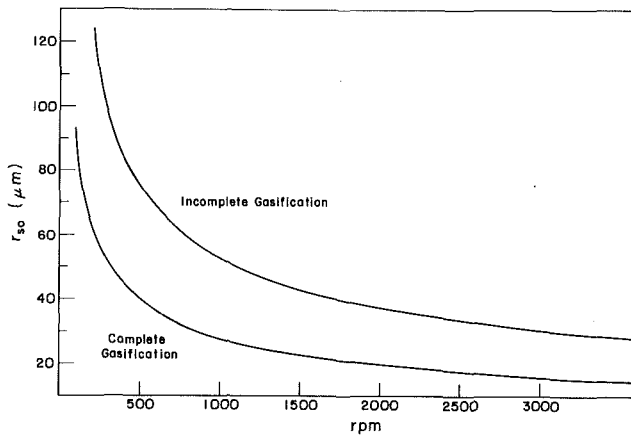


Fig. 7 Critical droplet size range to achieve complete gasification for the standard case

maximum initial droplet radii for the standard case, as shown in Fig. 7. Similar curves can be readily constructed by using Figs. 5 and 6. Figure 7 shows that, say during idling ( $\sim 800$  rpm), droplets with radii smaller than  $30 \mu\text{m}$  will achieve complete gasification, while those above  $60 \mu\text{m}$  will not. At 2000 rpm, the lower and upper bounds become  $20 \mu\text{m}$  and  $37 \mu\text{m}$ , respectively.

#### 4 Concluding Remarks

In the present investigation, we have modeled the heating and gasification of a fuel droplet in the temporally-varying environment during the intake and compression strokes of an SI engine. It is shown that the seemingly complex problem is

actually characterized by only a few parameters, such that a detailed and general parametric study and representation is possible. Results demonstrate that the simultaneous increases in the cylinder temperature and pressure have approximately compensatory effects on the gasification process, such that the net droplet gasification rate is minimally affected. Of particular utility is the identification and presentation of a critical gasification time corresponding to complete droplet gasification at the end of the compression stroke. This allows the assessment of the lower and upper bounds in the initial droplet size in order to achieve complete gasification.

#### Acknowledgment

During the course of this work, XQL was on sabbatical leave from the Chemical Machinery Research Institute, Lanzhou, People's Republic of China, while CHW and CKL were supported by the Army Research Office under Grant No. DAAG29-82-K-0023.

#### References

- 1 Williams, F. A., *Combustion Theory*, Addison-Wesley, Reading, Mass., 1965.
- 2 Spalding, D. B., "The Combustion of Liquid Fuels," *Fourth Symposium (International) on Combustion*, Williams and Wilkins, Baltimore, 1953, pp. 847-864.
- 3 Godsave, G. A. E., "Studies of the Combustion of Drops in a Fuel Spray: The Burning of Single Drops of Fuel," *Fourth Symposium (International) on Combustion*, Williams and Wilkins, Baltimore, 1953, pp. 818-830.
- 4 Law, C. K., "Mechanisms of Droplet Combustion," *Proc. of the Second International Colloquium on Drops and Bubbles*, JPL Publication 82-7, edited by D. H. Le Croisette, 1982, pp. 39-53.
- 5 Law, C. K., "Recent Advances in Droplet Vaporization and Combustion," *Prog. in Energy and Combustion Science*, Vol. 108, 1982, pp. 171-201.
- 6 Kent, J. C., "Quasi-Steady Diffusion-Controlled Droplet Evaporation and Condensation," *Appl. Sci. Res.*, Vol. 28, 1973, pp. 315-345.

F. M. Steele  
 Elmira, N.Y. 14901  
 Mem. ASME

# Contamination Control in Gas Turbine Oil Systems

## Introduction

Lube and fuel oils perform a variety of simultaneous functions in recirculating systems of gas turbines and accessories. They may burn, cool, dampen, flush, heat, lubricate, resist corrosion, and transmit power. For contamination control, the most significant function is flushing, which suspends and carries impurities or contaminants to various devices for isolation and removal.

Common contaminants such as solid particles, water, acids, air, corrosive gases, low-boiling hydrocarbons, and microorganisms accumulate in an oil system by environmental ingress and by component wear and deterioration. Contaminant accumulation impairs oil functions and leads to excessive wear and corrosion, malfunction, and failure of system components, unless contaminant concentrations are maintained below component tolerance levels.

Processes used for removal of contaminants from various oils include centrifugation, coalescence, demulsification, distillation, electrostatic precipitation, filtration, gravity separation, magnetic separation, and sparging or mass transfer. Four processes commonly applied to gas turbines and accessories are gravity separation, filtration, distillation, and centrifugation. In most cases, these provide effective contamination control when combined in suitable control programs.

## Contamination Control Technology

Contamination control in circulating oil systems of gas turbines is accomplished by installation of a suitable contaminant removal device (CRD) in each strategic location. Each CRD is selected to produce a contaminant level low enough to provide adequate life and reliability for the components it protects.

The rate of contaminant addition to an oil system is the sum of the rates of environmental ingress and system generation. The rate of contaminant removal by a CRD is proportional to its efficiency. The contaminant level at any time is the resultant of the addition and removal rates. The level increases when the addition rate exceeds the removal rate and vice versa. The level remains constant when the addition and removal rates are equal. This is the control level.

CRD efficiency is expressed commonly as percent reduction

in concentration of contaminant in oil flowing through a CRD. Filter efficiency also is stated as filtration or beta ( $B_x$ ) ratio.  $B_x$  is the upstream count divided by the downstream count of particles above  $x$  microns per milliliter of oil.  $B_{10} = 2$  describes a filter which reduces count of particles above 10 microns by a ratio of 2:1, or by 50 percent.

Filters are used in this paper to illustrate contaminant control for lube and fuel oil applications since they are the most widely used CRDs for turbine oil systems.

## Transfer Systems

In a transfer system, oil flows, with little or no contaminant addition, from a source through a CRD without return to the source.

There are four types of transfer systems (see Fig. 1):

1 In a single-stage, single-cycle system, oil flows from a dirty oil tank through a CRD to a clean oil tank.

2 In a single-stage, multiple-cycle system, oil flows from a dirty oil tank through a CRD to a clean oil tank. Some oil also cycles through the CRD for more contaminant removal.

3 In a multiple-stage, single-cycle system, oil flows from a dirty oil tank through two or more CRDs to a clean oil tank.

4 In a multiple-stage, multiple-cycle system, oil flows from

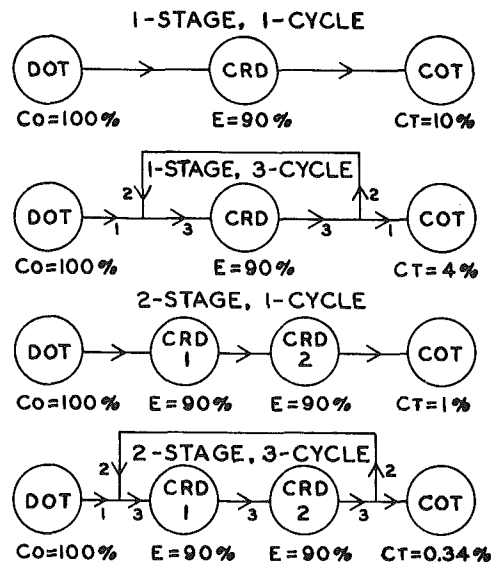


Fig. 1 Transfer systems

Contributed by the Gas Turbine Division of THE AMERICAN SOCIETY OF MECHANICAL ENGINEERS and presented at the 29th International Gas Turbine Conference and Exhibit, Amsterdam, The Netherlands, June 4-7, 1984. Manuscript received at ASME Headquarters January 11, 1984. Paper No. 84-GT-155.

**Table 1 Particulate levels in fuel transfer system**

Mech. filter	Efficiency		Size X UM	No. Parts/ML over X	
	%	Bx		upstream	downstream
MF1	99.9	1000	125	1	<1
MF1	0.0	1	124	1	1
MF2	99.9	1000	75	10	<1
MF2	0.0	1	74	10	10
1-MF3	99.9	1000	40	50	<1
1-MF3	90.0	10	30	100	10
1-MF3	50.0	2	10	4000	2000
2-MF3	90.0	10	30	10	1
2-MF3	50.0	2	10	2000	1000

a dirty oil tank through two or more CRDs in series. Some oil also cycles through the CRDs for additional contaminant removal.

The contaminant level in a transfer control system is expressed by equation (1).

$$C_T = C_o(1 - 0.01E)^T \quad (1)$$

Reduction in level is obtained either by increasing the number of transfers,  $T$ , or by increasing the CRD efficiency,  $E$ , or both. Efficiency is increased by replacing the existing CRD with one of higher efficiency, or by using more stages of or more cycles through the existing CRD, or both.

The dimensionless chart in Fig. 2 relates contaminant reduction to transfers and efficiencies. Contaminant levels can be shown on the right ordinate as particles per milliliter greater than a specified size, milligrams per liter, parts per million, etc. A time scale can be added to the abscissa in minutes, hours, days, etc. The chart then indicates the transfers and efficiency required to obtain the desired contaminant level in a given batch of fluid in the desired time.

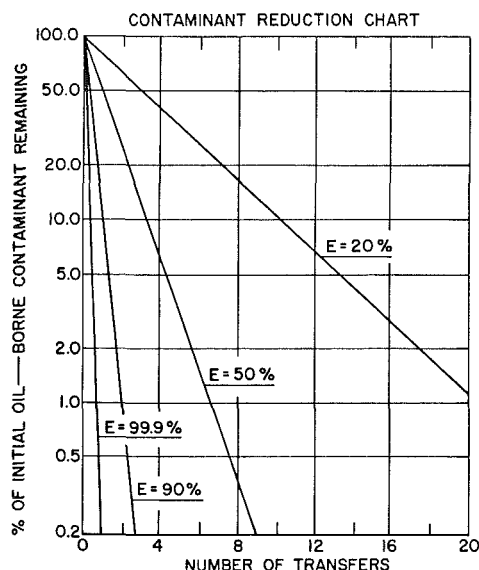
Typical transfer systems include filling containers at refineries and blending plants, transfer from storage to turbine reservoirs, and combustion chambers. Figure 3 [1] illustrates typical CRDs in a gas turbine, distillate fuel injection system, which is also a single-transfer, multiple-stage, single-cycle contaminant control system.

Gravity separation,  $G$ , in bulk storage and day tanks removes some large particles and droplets. An air filter-breather, AFB, on each tank minimizes ingress of airborne particulate matter and moisture. A coalescer, CO, sometimes is used between tanks to remove free water.

Mechanical filtration in several particle size ranges protects system components. Strainer MF1 provides surface filtration to protect low pressure transfer pump LP1. Strainer MF2 provides surface filtration to protect low pressure injection pump LP2. Filter MF3 provides both surface and depth filtration to protect high-pressure injection pump HP and its pressure regulating valve. A second filter MF3 provides surface and depth filtration to protect flow divider FD and injection nozzles N.

Minor recirculation through pressure regulating valves enhances contaminant reduction slightly, but does not justify classification of the system as multiple cycle.

The relationship of efficiencies to particle sizes and counts for the mechanical filters in Fig. 3 are shown in Table 1. Strainer MF1 removes practically all particles above and none



**Fig. 2 Contaminant reduction by transfer with no contaminant addition**

below 125 um. Strainer MF2 removes practically all particles above and none below 75 um. First filter MF3 removes 99.9 percent of particles over 40 um, 90 percent over 30 um, and 50 percent over 10 um. Second identical filter MF3 reduces residual contaminant from first filter MF3 by like percentages.

Assumed upstream particle counts used in Table 1 illustrate the effect of control system efficiency on contaminant reduction. Actual counts may vary considerably from assumed values, depending on the particulate level in untreated fuel.

If the operator of the fuel system in Fig. 3 wants a maximum count to the flow divider of 500 parts/ml over 10 um, or one-half the level in Table 1, he can increase the 10-um efficiency of 2nd MF3 from 50 percent ( $B_{10} = 2$ ) to 75 percent ( $B_{10} = 4$ ), possibly by changing to another cartridge type. Or, he can reduce 2nd MF3 upstream count by installing another  $B_{10} = 2$  filter anywhere upstream. For any filter, the downstream count varies in direct proportion to the upstream count.

**Nomenclature**

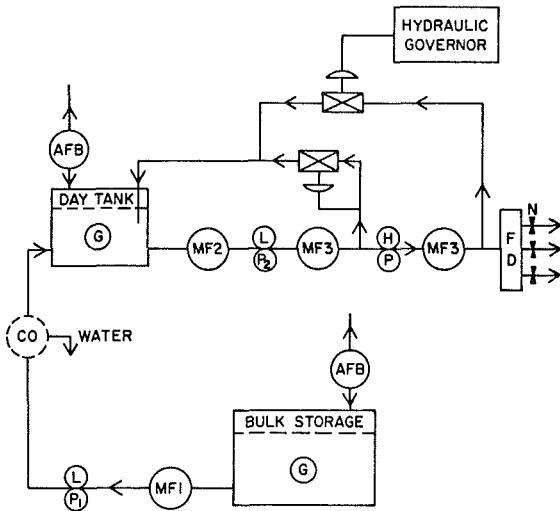
- $A$  = contaminant added
- $C_c$  = recirculation control level with addition
- $C_N$  = recirculation control level without addition
- $C_o$  = initial contaminant level
- $C_T$  = transfer control level without addition
- $E$  = percent efficiency
- $N$  = number of passes =  $Qt/V$
- $P$  = periods per pass
- $Q$  = circulating rate
- $t$  = time of circulation
- $T$  = number of transfers
- $V$  = volume

**Equations**

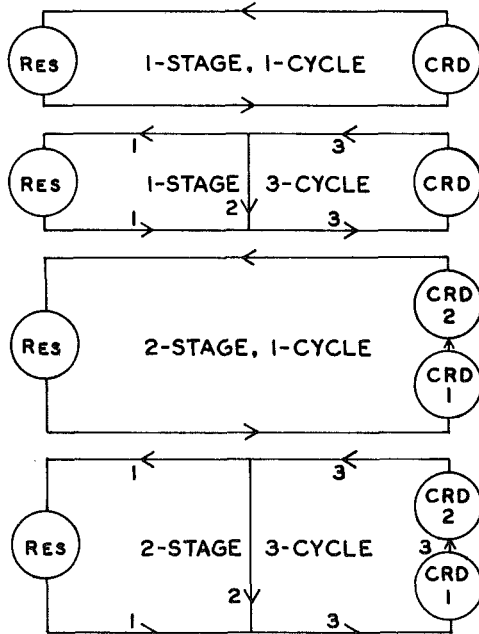
- (1)  $C_T = C_o(1 - 0.01E)^T$
- (2)  $C_N = C_o[1 - (0.01E/P)]NP$
- (3)  $C_c = \frac{A/NP}{0.01E}$

**Table 2 Comparison of transfer and recirculating systems**

System	% Efficiency	% Contaminant level at T or N			
		0	1	2	5
Transfer	99.9	100.0	0.1	0.01	0.01
Recirc.	99.9	100.0	34.9	12.2	0.52
Transfer	90.0	100.0	10.0	1.0	0.01
Recirc.	90.0	100.0	38.9	15.2	0.90
Transfer	50.0	100.0	50.0	25.0	3.13
Recirc.	50.0	100.0	59.9	35.9	7.69
Transfer	20.0	100.0	80.0	64.0	32.77
Recirc.	20.0	100.0	81.7	66.8	36.42



**Fig. 3 CRDS on distillate fuel system**

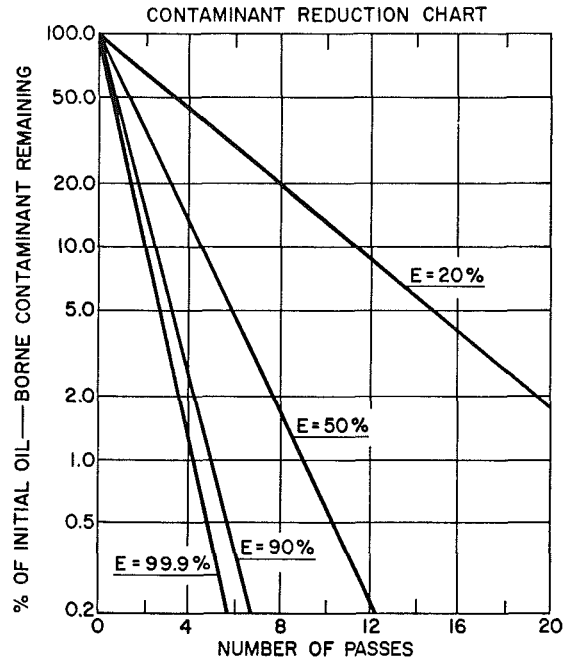


**Fig. 4 Recirculating systems**

The operator should verify periodically specification levels for particulates in fuel deliveries. Installing more efficient air filter-breathers on storage tanks to reduce environmental ingress may be helpful.

**Recirculating Systems**

A system in which oil flows continuously from and returns to the same point (e.g., an oil reservoir) is called a recir-



**Fig. 5 Contaminant reduction by recirculation with no contaminant addition**

culating system. When fitted with suitable CRDs, it becomes a multiple-pass contaminant control system.

One pass is completed when the volume of oil circulated through a CRD equals the total volume of oil in the system. Continued circulation, or recirculation, provides many passes during which some oil may never pass through the CRD. Nevertheless, multiple-pass recirculation provides adequate contaminant removal and control.

As with transfer systems, there are four types of multiple-pass systems (see Fig. 4). In each case, oil treated with a CRD is mixed continuously with untreated oil. Contaminant may or may not be added during recirculation.

1 In a single-stage, single-cycle system, oil makes one cycle through a CRD for each pass through the system.

2 In a single-stage, multiple-cycle system, oil makes several cycles through a CRD for each pass through the system.

3 In a multiple-stage, single-cycle system, oil makes one cycle through two or more CRDs in series for each pass through the system.

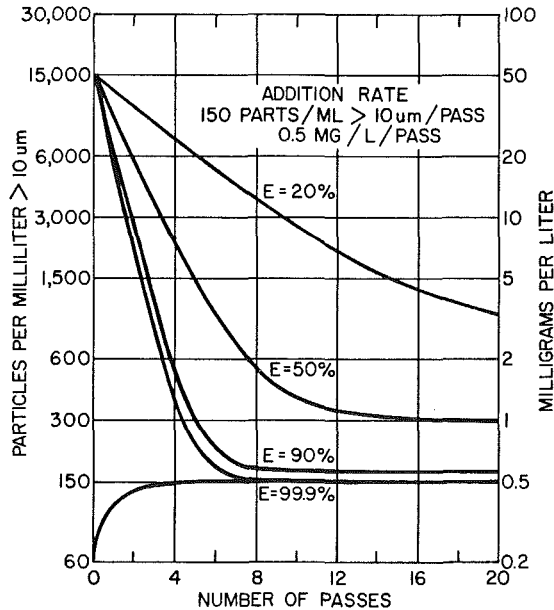
4 In a multiple-stage, multiple-cycle system, oil makes several cycles through two or more CRDs in series for each pass through the system.

The contaminant level in a multiple-pass system *without* contaminant addition is expressed by equation (2) which is similar to that used for calculating growth of principal with compound interest, except that the periodic increment is negative. For calculations *P* should be at least 10 for estimates and 100 for reasonable accuracy.

$$C_N = C_o [1 - (0.01E/P)]^{NP} \tag{2}$$

**Table 3 Particulate levels in oil recirculation system**

Mech. filter	Efficiency		Size XUM	No. parts/ML over X	
	%	Bx		upstream	downstream
MF1	99.9	1000	75	10	<1
MF1	0.0	1	74	10	10
MF2	99.9	1000	40	50	<1
MF2	90.0	10	30	100	10
MF2	50.0	2	10	4000	2000
MF2	20.0	1.25	5	8000	6400
MF3	99.9	1000	30	10	<1
MF3	99.9	1000	10	2000	2
MF3	99.0	100	5	6400	64



**Fig. 6 Contaminant reduction by recirculation with contaminant addition**

Reduction in level is obtained either by increasing the number of passes,  $N$ , or by increasing the CRD efficiency,  $E$ , or both. Efficiency is increased by replacing the existing CRD with one of higher efficiency, or by using more stages of or more cycles through the existing CRD, or both.

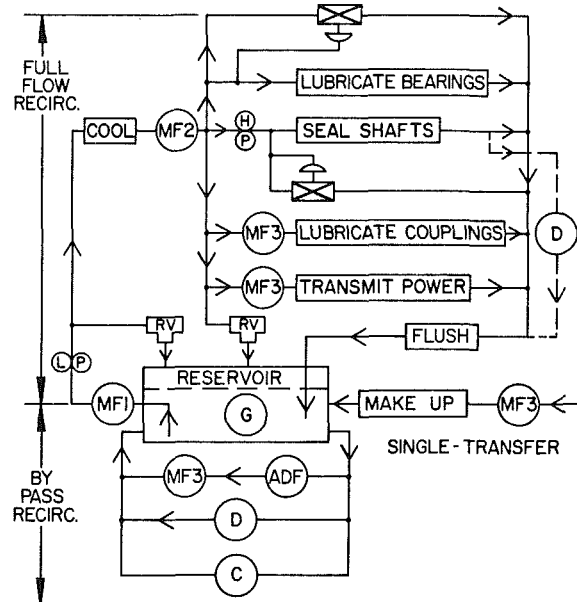
The dimensionless chart in Fig. 5 [1] relates contaminant reduction to passes and efficiencies. A specific contaminant level can be added to the right ordinate and a time scale can be added to the abscissa. The chart then indicates the passes and efficiency required to obtain the desired contaminant level in the desired time.

Although recirculation reduces contaminant level less rapidly than multiple-transfer, as shown in Table 2, recirculation is essential for an operating turbine from which oil cannot be removed.

The ultimate contaminant level in a recirculating system with contaminant addition is expressed by equation (3). Reduction in level is obtained either by decreasing the contaminant addition rate ( $A/NP$ ) or by increasing the CRD efficiency,  $E$ , or both.

$$C_c = \frac{A/NP}{0.01E} \quad (3)$$

The addition rate is decreased by reducing environmental ingress and/or system generation, or by increasing the rate of recirculation through the CRD, or both. Doubling the flow reduces the time per pass by 50 percent and the addition per pass by 50 percent, and hence the contaminant level by 50 percent. Efficiency is increased by replacing the existing CRD with one of higher efficiency, or by using more stages of or more cycles through the existing CRD, or both.



**Fig. 7 Relationships of CRDS to oil functions**

The chart in Fig. 6 relates particulate reduction to passes and efficiencies. At an arbitrary addition rate of 1 percent of the initial high level, the ultimate control level, represented by the flat, horizontal portion of each curve, is directly proportional to the addition rate, and is independent of the initial level as shown by the 99.9 percent curves.

Figure 7 (1) shows the relationships of typical CRDs to oil functions on a gas turbine-compressor in three modes: full-flow recirculation, by-pass recirculation, and single-transfer.

In the full-flow mode, gravity separation,  $G$ , in the reservoir provides minimal protection for the entire system by removing relatively large volume particles and droplets. Mechanical filtration in three particle size ranges enhances oil functions by protecting system components.

Strainer MF1 protects low-pressure pump LP, relief valve RV, and the cooler. Filter MF2 checks migration from a new or repaired cooler, protects bearings, high-pressure pump HP and shaft seals, pressure regulating and relief valves, and provides first-stage filtration for shaft couplings and hydraulic system components. Filters MF3 provide second-stage filtration for couplings and hydraulic components.

The relationship of efficiencies to particle sizes and counts for the mechanical filters in Fig. 7 are shown in Table 3. Strainer MF1 removes practically all particles above and none below 75  $\mu$ m. Filter MF2 removes 99.9 percent of particles over 40  $\mu$ m, 90 percent over 30  $\mu$ m, 50 percent over 10  $\mu$ m, and 20 percent over 5  $\mu$ m. Upstream counts are assumed for illustrative purposes. Downstream counts increase with contaminant generation and ingress.

If filters MF3 each handle 10 percent of the flow passing through filter MF2, 20 percent of the flow returning to the



**Table 4 Acceptable contaminant levels in turbine lube oils**

Contaminant	After flushing	During operation
Parts/ML > 10 UM		
Hydraulic	3-30	30-300
Lubricating	30-300	300-3000
Gravimetric-MG/L		
Hydraulic	0.01-0.1	0.1-1
Lubricating	0.10-1.0	1.0-10
Water-PPM		
Mineral oil	50-100	100-200
Phosphate ester	500-1000	1000-2000
Acid-MG KOH/G		
Mineral oil	0.05-0.1	0.1-0.2
Phosphate ester	0.10-0.2	0.3-0.7
LB hydrocarbons		
% visc. reduction	2-5	5-10
Bacteria/ML	$10^1-10^2$	$10^2-10^4$

reservoir comes from filters with 10-um efficiencies of 99.9 percent, and 80 percent comes from a filter with 10-um efficiency 50 percent. The combined efficiency is 60 percent.

If the contaminant addition per pass in the full-flow mode is 600 parts/ml over 10 um, and the filter efficiency is 60 percent, then the ultimate control level is 600/0.6 or 1000 parts/ml over 10 um.

If the operator of the oil system in Fig. 7 wants a maximum count to the bearing header of 1000 parts/ml over 10 um or one-half the downstream count from MF2 in Table 2, he can increase the 10-um efficiency of MF2 from 50 percent ( $B_{10} = 2$ ) to 75 percent ( $B_{10} = 4$ ), possibly by changing to another cartridge type. Or, he can install another  $B_{10} = 10$  filter anywhere upstream of the header.

If a turbocompressor is pumping sour gas, hydrogen sulfide and/or low boiling hydrocarbons ( $C_{3+}$ ) are dissolved in oil as it passes through shaft seals. Vacuum distillation,  $D$ , removes these contaminants from oil before it returns to the reservoir [2].

In the bypass mode CRDs are used for various requirements.

In some turbines conventional mineral oils have been replaced with fire resistant phosphate ester fluids. PE fluids tend to hydrolyze with formation of acids that are controlled by adsorbent filter ADF. Typical adsorbents are fuller's earth for low acid levels and activated alumina for high acid levels [3, 4]. Mechanical filter MF3 ( $B_5 = 100$ ) prevents migration of adsorbent fines into the turbine reservoir.

A centrifuge is used commonly for removal of most free water. Assume the reservoir of a turbine holding 10,000 L of mineral oil is equipped with a bypass centrifuge  $C$  which maintains the water level at 150 ppm, 10 ppm above the solubility level of 140 ppm at an operating temperature of 55°C.

During shutdown about 75 percent or 105 ppm of dissolved water precipitates as free water at 20°C, making the total free water content 115 ppm, or about 1 L dispersed perhaps as 10,000 droplets throughout the oil system. This condition, which promotes rapid corrosion especially of bearings and supports microbial growth, can be avoided by a vacuum distillation system  $D$ , which maintains water level during turbine operation below solubility at 20°C, and thus prevents precipitation of free water during shutdown [5].

In the single-transfer mode filter MF3 ( $B_5 = 100$ ) reduces particle counts of makeup oil to or below new oil values.

### Acceptable Contaminant Levels

A contamination control program requires periodic checks on the levels of principal contaminants—solid particles, water, acids, low boiling hydrocarbons—to insure continuing trouble-free operation, or to make necessary adjustments to CRDs.

High contaminant levels present potential problems for operating systems and components. Particulates can cause wear, malfunction, and failure. Equipment operating in a dusty environment is subject to high particulate ingestion rate and requires more protection by CRDs than equipment operating in a controlled atmosphere. Free water can cause rusting, bearing fatigue, pump cavitation, and oil degradation. Most dissolved water, which has no significant detrimental effect, becomes free water on cooling during shutdown when prolonged, static contact of water droplets greatly accelerates component corrosion [6].

Acids can cause component corrosion and disintegration and servovalve corrosion-erosion [4].

Low boiling hydrocarbons in seal oil can cause reduced viscosity, which can result in lubrication failure, and can reduce flash point which might cause an explosion [7].

Microbial growth can cause deposits on bearings and shaft seals and blockage of oil filters [8].

An ideal program would include continuous readout monitors with alarms for preset maximum contaminant levels. Some monitors exist but have restricted use because of high cost.

Most turbine manufacturers and larger users have established in-house standards for maximum desirable contaminant levels in lube oils based on many thousands of hours of operating experience. Manufacturers usually have tighter standards to insure shipment of clean equipment. Table 4 shows typical values which may require modification for specific installations.

Oil samples should be taken and tests run every 1500-2000 hrs for turbines operating continuously under relatively constant load and stable ambient conditions. Sampling frequency should increase when starting equipment rebuilt in the field, when operating intermittently, or when contaminant concentration is increasing above normal levels.

Test reports may be available within a few hours after sampling in plants with inhouse laboratories. Elapsed time for outside labs varies from a few days to a few weeks—sometimes too long for corrective action before problems develop.

### Summary

The designer of a fuel or oil system for a gas turbine has great flexibility in selecting and locating CRDs suitable to protect contaminant-sensitive components while the fluid is performing its intended functions.

For transfer systems and for recirculating systems without contaminant addition, he needs to know typical contaminant levels of untreated fluids and CRD efficiencies for the contaminants in order to project contaminant levels in treated fluids.

For recirculating systems with contaminant addition, he needs to know typical addition rates and CRD efficiencies in order to project cleanliness levels in operating systems.

Fluid contaminant levels are obtained from analyses. Addition rates are determined by difference in successive analyses of samples from a system without CRDs, or by calculation using equation (3). CRD efficiencies are obtained from the manufacturers.

Control of contamination in a circulating fuel or lube system is the responsibility of the operator who uses CRDs provided by the designer. Experience may suggest that some original CRDs be supplemented or replaced for suitable control. In this case, the operator should consult with the system designer, the CRD manufacturer, and the fluid supplier.

The benefits of contamination control include increased turbine reliability, availability, production, and decreased costs of labor and parts for repair and maintenance. The overall result is higher operating profit.

## Acknowledgments

The author wants to express his appreciation to The Hilliard Corporation for help in preparing and reviewing the manuscript.

## References

- 1 Steele, F. M., "Contamination Control in Turbomachinery Oil Systems," ASLE Annual Meeting, Houston, Texas, Apr. 1983.
- 2 Steele, F. M., "Seal Oil Degassing in Gas Turbine-Centrifugal Compressors," ASME Gas Turbine Division Annual Meeting, Amsterdam, Holland, June 1984.

- 3 Steele, F. M., "Filtration and Reclamation of Turbine Oils," *Lubrication Engineering*, Vol. 34, No. 5, 1978, pp. 252-257.
- 4 Steele, F. M., "Adsorbent Filter Media for Oil Reclamation," *BFPR Journal*, Oklahoma State University, Vol. 15, No. 3, 1982, pp. 307-315.
- 5 Steele, F. M., "Distillation Processes for Reclaiming and Upgrading Oils," *BFPR Journal*, Oklahoma State University, Vol. 15, No. 3, 1982, pp. 315-321.
- 6 Block, H. P., "Criteria for Water Removal from Mechanical Drive Steam Turbine Lube Oils," *Lubrication Engineering*, Vol. 36, No. 12, 1980, pp. 699-707.
- 7 Kelchner, J. R., and Stevens, V. S., "The Reclamation of Centrifugal Compressor Seal Oil," World Filtration Congress III, King of Prussia, Pa., 1982.
- 8 Summers-Smith, D., "Microbial Activity in Industrial Turbine Lubrication Systems," *Tribology International*, Vol. 15, No. 4, 1982, pp. 180-182.

F. J. Thomas

J. S. Ahluwalia

E. Shamah

Chevron Research Company,  
Richmond, Calif. 94802

G. W. van der Horst

Chevron Central Laboratories,  
Rotterdam,  
The Netherlands

# Medium-Speed Diesel Engineers: Part I—Design Trends and the Use of Residual/Blended Fuels

*Fuel costs can exceed 50 percent of the total diesel plant's operational expenditures. To reduce fuel costs, medium-speed engines are now available with improved fuel consumption and ability to burn residual fuels. Part I of this paper reviews these engine and design changes needed for both improved fuel consumption and the ability to burn poorer quality fuels. Characteristics of these fuels and international fuel specifications are discussed. Ignition quality of residual fuels by a modified ASTM D 613 procedure are presented and correlation shown to calculated diesel index and calculated carbon aromaticity index (CCAI). Residual fuel ignition delay effects on combustion pressure rise, fuel consumption, and piston temperature in a laboratory single-cylinder diesel engine are shown.*

## Introduction

Diesel engines are the most efficient power plant available today for mobile equipment in on- and-off-highway service, marine propulsion, drilling rigs, and railroad service and are increasingly being selected for industrial power plants. The cost of fuel for these engines can exceed 50 percent of the total operational power plant expenditures. This situation is a result of the two OPEC crises of 1973 and 1979, where fuel prices increased tenfold, as shown in Fig. 1.

Diesel engine designers have placed emphasis on improving the thermal efficiency of their designs to lower fuel consumption, and considerable development is underway to design medium-speed engines in the speed range of 600–1200 rpm that burn low-quality fuels of 180–380 cSt<sup>1</sup>/50°C viscosity.

Low-speed, two-stroke diesel engines and large bore, 400–620 mm, four-stroke, medium-speed diesel engines have proven performance on such residual intermediate fuels and can operate on even heavier fuels. Thermal efficiencies exceeding 50 percent and specific fuel consumption (SFC) of 160 g/kWh are now a reality with these large, two-stroke engines. Figure 6 shows SFC rates and relationship to cylinder bore size. This figure confirms the effect of bore size on SFC stated by Voisard [1].

This paper will discuss the development trends of medium-speed engines in the speed range 600–1200 rpm and cylinder bore range 200–350 mm designed to operate on either distillate, blended, or residual intermediate-type fuels. For existing engines, which currently operate on distillate fuel, the development activities to operate these engines on blended fuels or distillates with some residual content are discussed. Figure 2 illustrates these areas of activity for existing and new

engine designs, and Fig. 3 shows the particular types of engines and applications to be discussed.

With the foreseen changes in future residual fuel quality [2], engine designers and major users have proposed various future level standards [3]. These standards of CIMAC, British standards, and the proposed International Organization for Standardization (ISO) fuel standards are summarized.

To successfully operate medium-speed diesel engines on these fuels depends upon the particular fuel's characteristics, the fuel preparation/purification and handling facilities, and the selection of the appropriate lubricant for the engine, fuel, and operating service conditions. In selecting the lubricant, account must be taken of how the used oil will be renewed or purified of the contaminants from combustion, and the risk

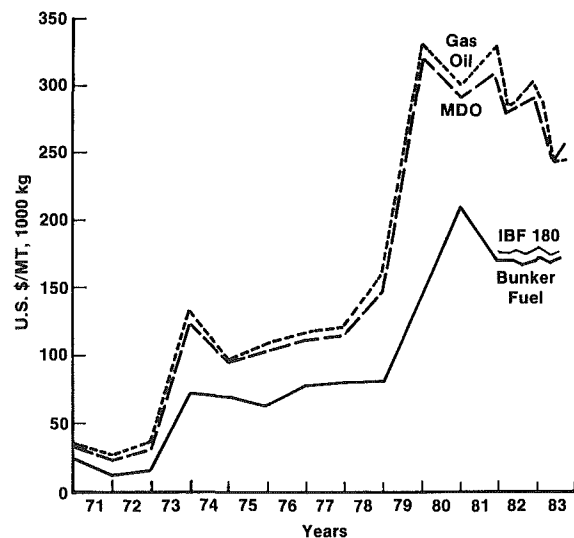


Fig. 1 Evolution of fuel oil prices

<sup>1</sup>cSt = mm<sup>2</sup>/s

Contributed by the Diesel and Gas Engine Power Division and presented at the Energy Sources Technology Conference and Exhibition, New Orleans, Louisiana, February 12–16, 1984. Manuscript received by the Diesel and Gas Engine Power Division December 5, 1983. Paper No. 84-DGP-15.

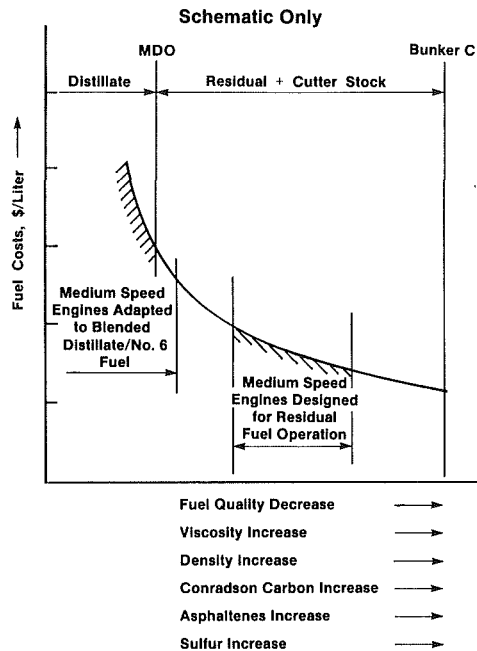


Fig. 2 Fuel quality versus cost

of water leakage must be considered. Lubricants and these factors will be covered in Part II of this paper. A simplified diagram showing the interrelationship of these factors is shown in Fig. 4, and the detailed relationships between these factors that are discussed in Parts I and II are shown in Fig. 5.

### Medium-Speed Engines – Trends in Designs

There are over 100 engine designs on the international market which fit into the medium-speed diesel engine 600–1200 rpm, 200–350 mm cylinder bore range covered in this paper. These designs cover applications for industrial power plants, compressors, drilling rigs, fishing vessels, railroad locomotives, towboats, and main and auxiliary power of ships.

To compare engine designs, the following parameters are used in Tables 1–3:

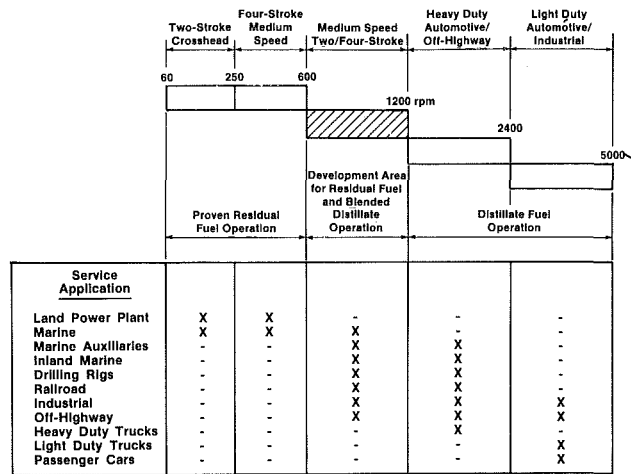


Fig. 3 Typical diesel engine speed ranges versus fuel type

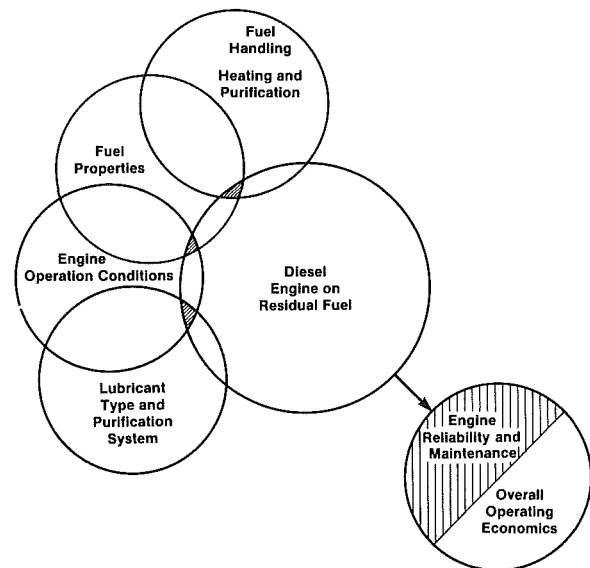


Fig. 4 Interaction of engine-fuel-lubricant on overall operating economics – schematic

### Nomenclature

$A$  = percent mass of ash  
 $A_p$  = piston area, cm<sup>2</sup>  
 $C_m$  = mean piston speed, m/s  
 CCR = Conradson carbon residue of fuel  
 $D$  = cylinder bore, mm  
 $I_F$  = inertia factor, m<sup>2</sup>/s<sup>2</sup>  
 $L$  = piston stroke, mm  
 $N$  = engine speed, rpm  
 $N_{ref}$  = engine speed at reference conditions, rpm  
 $P$  = power output, kW/cylinder  
 $P_A$  = power factor, kW/cm<sup>2</sup>  
 $P_i$  = engine power output, kW  
 $P_s$  = specific power output, kW/L  
 $Q_H$  = gross specific energy (higher calorific value) of fuel, MJ/kg

$Q_L$  = net specific energy (lower calorific value) of fuel, MJ/kg  
 $S$  = percent mass of fuel sulfur  
 $T_F$  = piston thermal factor, kW/m  
 $V$  = kinematic viscosity, cSt at 50°C  
 $V_d$  = cylinder piston displacement, L  
 $W$  = percent mass of water in fuel  
 $Z$  = number of revolutions per power stroke  
 $b_e$  = effective specific fuel consumption, g/kWh  
 $b_i$  = indicated specific fuel consumption, g/kWh  
 $i$  = number of cylinders

$p_a$  = charge air pressure, Bar  
 $p_e$  = brake mean effective pressure, Bar  
 $p_o$  = ambient air pressure, Bar  
 $p_r$  = frictional mean effective pressure, Bar  
 $\Delta t_{OL}$  = lubricant temperature change from reference conditions, °C  
 $\Delta t_w$  = coolant temperature change from reference conditions, °C  
 $\eta_b$  = effective brake thermal efficiency, %  
 $\eta_i$  = indicative thermal efficiency, %  
 $\eta_m$  = mechanical efficiency, %  
 $\rho$  = fuel density at 15°C, kg/m<sup>3</sup>

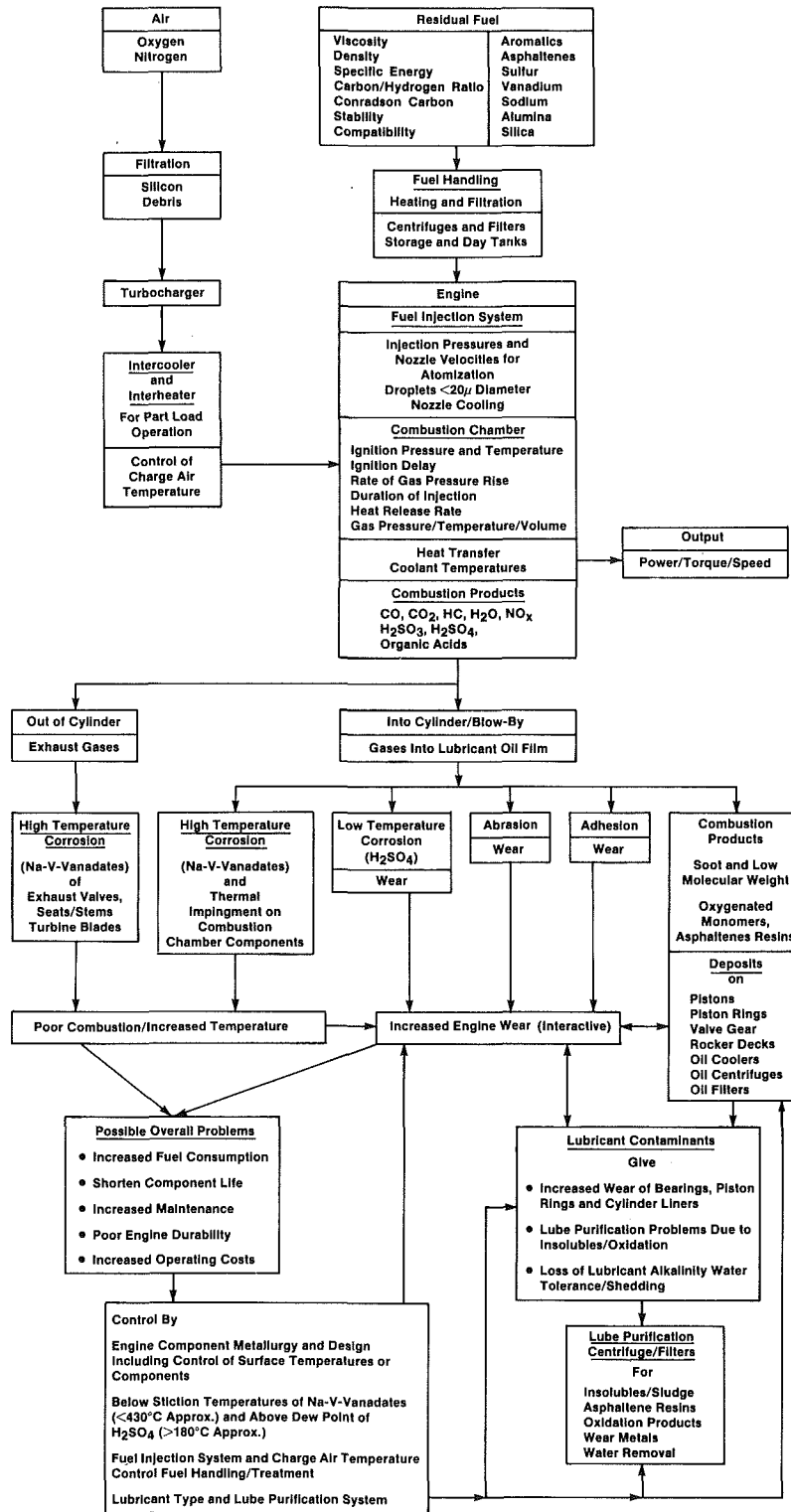


Fig. 5 Schematic of residual fuel effects on engine wear and corrosion and lubricant purification systems effects – medium-speed diesel engines

Specific power output (kW/L displacement)

$$P_s = \left( \frac{P_i}{V_d \cdot i} \right) = 50 \left( \frac{p_e \cdot C_m}{L \cdot Z} \right) \quad \text{kW/L} \quad (1)$$

Brake mean effective pressure (bar)

$$p_e = 600 \left( \frac{P_i \cdot Z}{V_d \cdot N \cdot i} \right) \quad \text{bar} \quad (2)$$

Mean piston speed (m/s)

$$C_m = \left( \frac{L \cdot N}{30,000} \right) \quad \text{m/s} \quad (3)$$

Power factor (kW/Cm<sup>2</sup> piston area)

$$P_A = \left( \frac{P_i}{A_p \cdot i} \right) = \left( \frac{P_e \cdot C_m}{200 \cdot Z} \right) \quad \text{kW/Cm}^2 \quad (4)$$

**Table 1 1983/1984 ratings: examples of medium-speed engines in service in North America: speed range 750-1200 rpm, bore range 205-275 mm**

Designer	Model	Bore, mm D	Stroke, mm L	L/D Ratio	Output, kW/Cylinder	Speed, rpm	Specific Output, kW/Liter	bmp, Bar	Mean Piston Speed, m/Sec.	Inertia Factor, m <sup>2</sup> /Sec. <sup>2</sup>	Power Factor, kW/cm <sup>2</sup>	Thermal Factor, kW/m
APE - Allen	S12-F	241	305	1.26	176.0	1000	12.63	15.15	10.16	81.6	0.386	101.0
Bombardier	251	229	267	1.17	165.7	1100	15.07	16.44	9.79	82.2	0.402	100.4
Bergen	KVMB	250	300	1.20	183.4	825	12.45	18.12	8.25	56.7	0.374	101.3
Burmeister and Wain	U28 LU	280	320	1.14	195.0	775	9.90	15.32	8.27	59.8	0.317	97.7
Cooper-Superior	40-X-16	254	267	1.05	123.5	1000	9.13	10.95	8.90	75.4	0.244	76.0
Daihatsu	6DS-26A	260	300	1.15	183.9	750	11.55	18.47	7.50	48.8	0.346	98.8
EMD*	645 EC	230	254	1.10	153.8	900	14.60	9.70*	7.62	52.6	0.370	95.0
EMD*	645 FB	230	254	1.10	177.2	950	16.80	11.00*	8.04	58.6	0.428	104.9
EMD*	710	230	279	1.21	184.1	900	15.83	10.56*	8.38	57.9	0.442	107.7
Fairbanks Morse*	38 TD 81/8	206	254 x 2	1.23	350.0	900	20.60	13.73	7.62	47.1	0.476	112.3
GE	7PDL	229	267	1.17	184.0	1050	16.80	19.20	9.34	74.9	0.448	108.0
GEC-ALCO	251F	229	267	1.17	184.3	1100	16.80	18.40	9.79	82.2	0.448	108.1
GEC-ALCO	270	270	305	1.13	240.6	1000	13.78	16.54	10.17	91.6	0.420	116.1
KHD-Deutz	BV 16 M 628	240	280	1.17	196.3	1000	15.49	18.59	9.33	74.6	0.434	109.6
Krupp-Mak	M 282	240	280	1.17	200.0	1000	15.79	18.95	9.33	74.6	0.442	110.8
Mirrlees Blackstone	MB 275	275	305	1.11	287.5	1000	15.92	19.10	10.20	93.8	0.484	129.9
Mirrlees Blackstone	ESL MK2	222	292	1.31	165.1	1000	14.57	17.48	9.73	72.0	0.427	102.3
Murphy-MWM	TBD 441	230	270	1.17	150.0	1000	13.37	16.05	9.00	69.0	0.361	93.3
Murphy-MWM	TBD 444	230	320	1.39	165.0	750	12.41	19.86	8.00	46.0	0.397	99.8
Nohab	F 30A	250	300	1.20	170.0	750	11.54	18.47	7.50	46.9	0.346	96.1
SEMT-Pielstick	PA 5 V 255	255	270	1.06	220.0	1000	15.96	19.15	9.00	76.5	0.431	113.5
SEMT-Pielstick	PA 6 V 280CL	280	350	1.25	294.2	750	13.65	21.84	8.75	61.3	0.478	130.3
SWD	SW 240	240	260	1.08	171.7	1000	14.60	17.51	8.67	69.4	0.380	99.6
Wartsila	VASA 22HF	220	240	1.09	147.5	1000	16.17	19.40	8.00	58.7	0.388	95.2
Waukesha	P 8894 D51VHP	232	216	0.93	113.1	1200	12.38	12.38	8.64	80.2	0.268	76.1
Waukesha-Sulzer	AT 25	250	300	1.20	220.7	1000	14.98	17.98	10.00	83.3	0.450	115.4

\*Two-stroke.

**Table 2 1983 ratings: examples of four-stroke, medium-speed engines rated at 1000 rpm**

Designer	Model	Bore, mm D	Stroke, mm L	L/D Ratio	Output, kW/Cylinder	Specific Output, kW/Liter	bmp, Bar	Mean Piston Speed, m/Sec.	Inertia Factor, m <sup>2</sup> /Sec. <sup>2</sup>	Power Factor, kW/cm <sup>2</sup>	Thermal Factor, kW/m
Anglo-Belgian	D 2	256	320	1.25	224.0	13.60	16.30	10.70	91.6	0.435	114.7
APE-Allen	S 12-F	241	305	1.26	176.0	12.63	15.15	10.16	81.6	0.386	101.0
APE-Allen	S1ze	240	280	1.17	160.0	12.63	15.16	9.33	87.0	0.354	94.8
H. Cegielski	a 8C 22	220	270	1.23	110.0	10.72	12.86	9.00	66.0	0.289	77.5
Cockerill	240 CO	240	305	1.27	231.3	16.76	20.11	10.17	81.4	0.511	122.7
Cooper-Superior	40-X-16	254	267	1.05	123.5	9.14	10.97	8.90	75.4	0.244	76.0
Crepelle	SN 3L	280	320	1.14	203.8	10.34	12.41	10.67	99.6	0.331	100.8
Daihatsu	8DV-22A	220	280	1.27	137.9	12.96	15.55	9.33	68.4	0.363	90.8
Daihatsu	6PS HTC-20	200	250	1.25	61.3	7.80	9.37	8.33	55.5	0.195	55.0
Franco Tosi	Q12 BSS	220	300	1.36	138.9	12.18	14.62	10.00	73.3	0.365	91.2
Fuji	M 23C	230	260	1.13	137.9	12.77	15.32	8.67	66.5	0.332	88.0
GEC-ALCO	270D	270	305	1.13	240.6	13.78	16.54	10.17	91.6	0.420	116.1
GEC-Ruston	RKC	254	305	1.20	233.1	15.09	18.11	10.17	86.1	0.460	118.5
GEC-Ruston	RK 270	270	305	1.13	285.2	16.33	19.60	10.17	91.6	0.498	130.8
GEC-Ruston	AP 230	230	273	1.19	179.0	15.80	18.90	9.10	69.8	0.431	105.6
KHD-Deutz	BA 8 M 528	220	280	1.27	137.5	12.92	15.50	9.33	68.4	0.362	90.6
KHD-Deutz	BV 16 M 628	240	280	1.17	196.3	15.49	18.59	9.33	74.6	0.434	109.6
Krupp-Mak	M 282	240	280	1.17	200.0	15.79	18.95	9.33	74.6	0.442	110.8
MAN- B & W	20/27	200	270	1.35	100.0	11.79	14.15	9.00	60.0	0.318	77.5
MAN- B & W	25/30	250	300	1.20	220.0	14.94	17.93	10.00	83.3	0.448	115.1
MTU	1163 TB 62	230	280	1.22	220.0	18.91	22.69	9.33	71.5	0.530	112.0
MWM	TBD 440/441	230	270	1.17	129.0	11.50	13.80	9.00	69.0	0.310	84.0
Mirrlees-Blackstone	MB 275	275	305	1.11	287.5	15.92	19.10	10.20	93.8	0.484	129.9
Mirrlees-Blackstone	ESL MK 2	222	292	1.31	165.1	14.57	17.48	9.73	72.0	0.427	102.3
Nohab	F 30	250	300	1.20	188.0	12.80	15.30	10.00	83.3	0.383	103.1
SEMT-Pielstick	PA 5 V 255	255	270	1.06	220.0	15.96	19.15	9.00	76.5	0.431	113.5
SEMT-Pielstick	PA 6 V 280	280	350	1.04	294.0	16.46	19.76	9.67	90.3	0.477	130.5
SKL	VD 26/20 AL2	200	260	1.30	110.4	13.51	16.22	8.67	57.8	0.351	83.1
SKL	VDS 24/24 AL1	240	240	1.00	150.0	13.62	16.58	8.00	64.0	0.332	90.6
Sulzer	A 20/24	200	240	1.07	103.0	13.66	16.39	8.00	53.3	0.328	79.1
SWD	SW 280	280	300	1.07	295.0	15.97	19.16	10.00	93.3	0.479	130.6
SWD	SW 240	240	260	1.08	171.7	14.60	17.51	8.67	69.4	0.380	99.6
Wartsila	VASA 22 HF	220	240	1.09	147.5	16.17	19.40	8.00	58.7	0.388	95.2
Waukesha-Sulzer	AT 25	250	300	1.20	223.7	15.19	18.23	10.00	83.3	0.456	116.5

Piston thermal factor (kW/m)

$$T_F = \left( \frac{1000 \cdot P}{D} \right)^{0.7} = 1.2074 \left( \frac{D \cdot L \cdot p_e \cdot N \cdot i}{10^6 \cdot Z} \right)^{0.7} \text{ kW/m} \quad (5)$$

Inertia factor (m<sup>2</sup>/s<sup>2</sup>)

$$I_F = \frac{(C_m)^2}{L/D} \text{ m}^2/\text{s}^2 \quad (6)$$

The specific power output, brake mean effective pressure, and mean piston speed parameters are widely used in comparing engines. The power factor, equation (4), is often used for a relative ranking of the loading on the piston from a thermal

viewpoint. An alternative parameter can be used: the piston thermal factor (equation (5)), developed by Stikei [5] and based on experimental data that indicated that thermal load increases with increasing piston diameter for engine with identical specific output (kW/L).

The inertia factor, developed by Henshall [4] can be used as a first approximation to relative bearing loads.

Table 1 shows examples of some engine designs used in North American service for engines in the 205-280 mm (8-11-in.-dia) bore size.

The 1983-1984 ratings show cylinder power output is in the range 112-350 kW, with specific power output range of 9.0-16.8 kW/L. The higher specific outputs relate to locomotive service where space is important.

**Table 3 1983 ratings: examples of four-stroke, medium-speed engines rated at 750 rpm**

Designer	Model	Bore, mm D	Stroke, mm L	L/D Ratio	Output, kW/Cylinder	Specific Output, kW/Liter	bmep, Bar	Mean Piston Speed, m/Sec.	Inertia Factor, $\text{m}^2/\text{Sec.}^2$	Power Factor, kW/m	Thermal Factor, $\text{m}^2/\text{Sec.}^2$
APE-Allen	VS 27G	325	370	1.14	328.1	10.69	17.10	8.00	56.2	0.396	126.7
APE-Allen	VS 12-FX	241	305	1.27	132.0	9.49	15.18	7.63	45.9	0.289	82.6
Daihatsu	6PL-24	240	320	1.33	153.2	10.58	16.93	8.00	48.0	0.339	91.9
Daihatsu	6DS-26A	260	300	1.15	183.9	11.55	18.47	7.50	48.8	0.346	98.8
Daihatsu	8DV-26	260	320	1.23	165.5	9.74	15.59	8.00	52.0	0.312	91.8
Daihatsu	6DS-28	280	340	1.21	232.9	11.12	17.80	8.50	59.5	0.378	101.7
Franco Tosi	QT 320SS	320	380	1.19	262.5	8.59	13.74	9.50	76.0	0.326	109.6
Fuji	V 27.5G	275	320	1.16	220.7	11.61	18.58	8.00	55.0	0.372	107.9
Fuji	M 28	280	350	1.25	251.3	11.66	18.66	8.75	61.3	0.408	116.7
Fuji	M 30	300	350	1.17	294.2	11.89	19.03	8.75	65.6	0.416	124.2
Lindholmen	CN 275	275	330	1.20	220.0	11.22	18.50	8.25	56.7	0.370	107.7
MaK	M 35	350	380	1.09	441.0	12.06	19.30	9.50	83.1	0.458	148.0
MAN-B & W	23/30	230	300	1.30	135.0	10.83	17.33	7.50	43.1	0.325	86.7
MAN-B & W	28/32	280	320	1.14	220.0	11.17	17.86	8.00	56.9	0.357	106.3
MAN-B & W	32/36	320	360	1.13	405.0	13.99	22.38	9.00	72.0	0.504	148.5
MWM	TBD 444	230	320	1.39	165.0	12.41	19.86	8.00	46.0	0.397	98.8
MWM	TBD 510BV	330	360	1.09	385.0	12.50	20.01	9.00	74.3	0.450	140.2
Mirrlees	ESL MK2	222	292	1.31	123.9	10.94	17.50	7.30	40.5	0.319	83.7
Nohab	F 30A	250	300	1.20	170.0	11.54	18.47	7.50	46.9	0.346	96.1
Niigata	MG 25CX	250	320	1.28	171.6	10.93	17.48	8.00	50.0	0.350	96.7
SEMT-Pielstick	PA 6-280CL	280	350	1.25	294.2	13.65	21.84	8.75	61.3	0.478	130.3
SWD	SW 240	240	280	1.17	147.5	11.63	18.60	7.00	42.0	0.326	89.5
SWD	SW 280	280	300	1.07	228.6	12.38	19.80	7.50	52.5	0.371	109.2
Wartsila	VASA 32	320	350	1.09	341.1	12.12	19.39	8.75	70.0	0.424	131.6

**Table 4 1983 rating: examples of four-stroke, medium-speed engines with increased stroke/bore ratio for improved fuel economy**

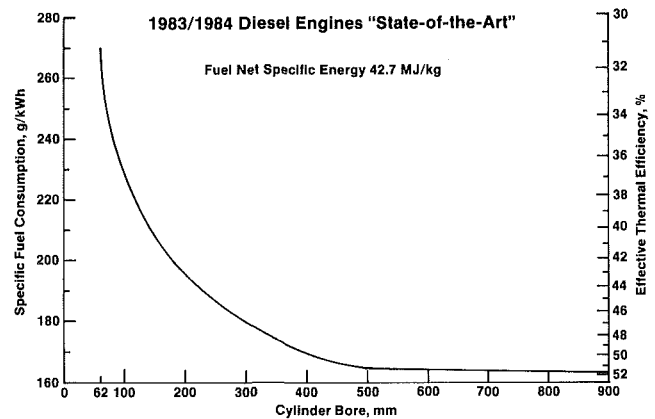
Designer	Model	Bore, mm D	Stroke, mm L	L/D Ratio	Output, kW/Cylinder	Speed, rpm	Mean Piston Speed, m/Sec.	Specific Output, kW/Liter	bmep, Bar	Inertia Factor, $\text{m}^2/\text{Sec.}^2$	Power Factor, kW/m	Thermal Factor, kW/m	Specific Fuel Consumption, g/kWh
GMT	230B	230	270	1.17	200.0	1200	10.80	17.83	17.83	99.4	0.481	114.2	222
	230BL	230	310	1.35	200.0	1050	10.85	15.53	17.75	87.3	0.481	114.2	212
SEMT-Pielstick	PA 6-280	280	290	1.04	294.2	1000	9.67	16.48	19.77	99.5	0.478	130.3	199
	PA 6-280CL	280	350	1.25	294.2	750	8.75	13.65	21.84	61.3	0.478	130.3	185

For four-stroke designs, the bmep ranges from 11.0–21.8 bar<sup>2</sup> (315 psi) and for two-stroke designs, 9.7–11.0 bar (160 psi). Mean piston speeds range from 7.6–10.2 m/s and the inertia factor 46–94 m<sup>2</sup>/s<sup>2</sup>

The power factor ranges from 0.24–0.48 kW/cm<sup>2</sup>, and the piston thermal factor 76–130 kW/m. Engines with high power factors and piston thermal factors require good piston cooling using thermally stable lubricants in order to avoid the formation of piston deposits on the piston undercrown or in the piston oil cooling channels.

Table 2 shows a similar comparison for four-stroke engine designs in the international market rated at 1000 rpm engine speed. This speed represents the area where a majority of medium-speed engines of 200–280 mm bore operate. Most of these engines burn distillate fuels, although an increasing number can now operate on distillate fuels blended with some residual fuel or use residual intermediate fuels up to 180 cSt/50°C viscosity. The specific output at a speed of 1000 rpm ranges from 7.8 kW/L to 18.9 kW/L, with the most recent designs above 12 kW/L. The bmep ratings range from 9.3–22.7 bar (330 psi), with recent designs exceeding 17 bar for four-stroke engines. The mean piston speed is in the range of 8.0–10.7 m/s and power factors 0.2–0.53 kW/cm<sup>2</sup>, with recent designs exceeding 0.40 kW/cm<sup>2</sup>. The inertia factors and thermal factors vary widely, depending upon the main application of the design and the degree of supercharging. Naval and railroad designs represent engines with the higher factors. Stroke/bore ratios mostly range between 1.1 and 1.25 for recent designs.

<sup>2</sup> 1 Bar = 14.5 psi = 100 kPa = 10<sup>5</sup> N/m<sup>2</sup>



**Fig. 6 Specific fuel consumption and thermal efficiency versus cylinder bore**

Table 3 is a similar analysis for engine designs rated at 750 rpm. Many designs [6, 7, 8] are now offered at 750-rpm speed when residual-intermediate fuels are to be burnt. Reducing the speed also has the advantage of improving fuel economy due to lower frictional losses. Two examples of designs that have increased piston stroke to maintain the same power output, with improved fuel economy at lower speeds, are shown in Table 4. It is noted that the new longer stroke/bore ratios are in the range 1.25–1.35. In addition, specific outputs are reduced, and SFC improvements of 4.7–7.0 percent have been obtained with these longer stroke/bore ratios.

**Specific Fuel Consumption.** The current state-of-the art of SPC for recent designs is shown in Fig. 6 for engines with cylinder bores from 62–900 mm. This figure is based on the best of the two-stroke and four-stroke designs. Thermal efficiencies are in the range 40–45 percent for engines in the group covered in this paper’s review, resulting in a SFC range of 187–211 g/kWh using a standard fuel specific energy reference of 42.7 MJ/kg using the relationship:

$$\text{Thermal Efficiency } \eta_b = \left( \frac{3600}{b_e \cdot Q_L} \right) 100 = \left( \frac{84.31}{b_e} \right) 100 \% \quad (7)$$

Von Schnurbein [47] has reported on the relationship of bore size, bmep, mean piston speed, and engine speed on frictional mep ( $p_r$ ) for four-stroke engines, equation (10), valid for cylinder bore >100 mm and mean piston speeds <10 m/s. The relationships of frictional mep, mechanical efficiency, and SFC are shown by equations (8) and (9)

$$b_e = b_i \cdot \eta_m \quad (8)$$

$$\eta_m = \frac{1}{1 + \left( \frac{p_r}{p_e} \right)} \quad (9)$$

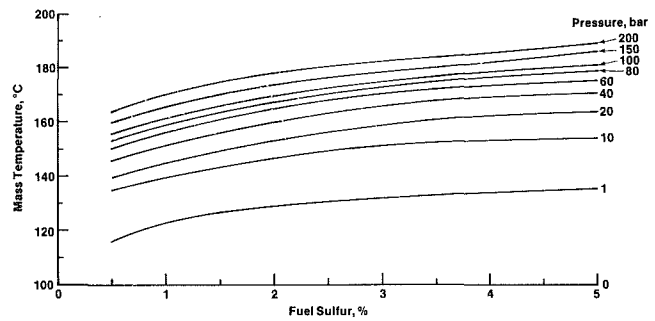
$$p_r = 6.7(D)^{-0.329} - 89(D)^{-0.943} \left[ 1 - \left( \frac{N}{N_{\text{ref}}} \right)^2 \right] + 0.0002(p_e)^3 - 0.006(p_e) + \left( \frac{p_a}{p_o} - 1 \right) \sqrt{0.1874 - 0.018(C_m)} - 0.005(\Delta t_{\text{OL}}) - 0.0055(\Delta t_w) \quad (10)$$

The subscript “ref” refers to reference conditions. ISO reference conditions are:

Net specific energy, MJ/kg	42.700
Intake air temperature, °K	300 (27°C)
Water for charge air cooler, °K	300 (27°C)
Atmospheric pressure, millibar	1000
Exhaust back pressure, millibar	25

**Design Changes to Use Lower Cost Fuels.** Engine designs shown in Tables and can operate on residual intermediate-fuels. This has been achieved by improving the fuel injection systems to atomize the fuel droplets to below 20  $\mu$ . Paro [9] has reported on a 220-mm bore engine capable of operating on residual fuels over the range 0–20 bar bmep, that satisfactory combustion was obtained, provided injection pressures at idle exceed 500 bar; this corresponds at full load to above 1000 bar. Injection pressure systems with 1200–1700 bar pressures are now offered on medium-speed engine designs for residual fuels. These designs require heating facilities for the fuel so the fuel can circulate through the low-pressure system and injection pumps. Preheating is required, up to 150°C may be necessary to bring the viscosity at the injectors to about 12 cSt. The temperature required depends upon the fuel viscosity. Figure 9 shows the viscosity/temperature relationship of fuels and their relationship at the different temperature, 40, 50, 80, and 100°C, used by the industry, ASTM, British standards, CIMAC, and ISO. Herzog [10] has reported on the effect of viscosity on injection and the relationship of viscosity to density and fuel injection pressures.

Further advances are expected in fuel injection systems incorporating electronically controlled high-pressure fuel injection systems. Little [11] reports such systems can give over 6 percent improvement in SFC, and variable injection timing is possible. The use of high injection pressures for fuel



Source: Ref. (14) Belcher, P. R.

**Fig. 7 Dew point temperature—effect of fuel sulfur content and combustion pressure**

**Table 5 Medium-speed diesels – design trends for:**

<p>1. <u>Improved Specific Fuel Consumption by:</u></p> <ul style="list-style-type: none"> <li>Lower Engine Speed</li> <li>Increased Stroke/Bore Ratio</li> <li>Increased Maximum Combustion Pressures</li> <li>Increased Ratio of Maximum Pressure/bmep</li> <li>Increased bmep</li> <li>Increased Cylinder Bore</li> <li>Improved Turbocharger Efficiencies</li> </ul>
<p>2. <u>Improved Ability to Burn Residual Fuels by:</u></p> <ul style="list-style-type: none"> <li>Increase Injection Pressures</li> <li>Reduce Fuel Droplet Size, &lt;20 Micron</li> <li>Electronic Controlled Injection Rates and Duration</li> <li>Controlled Charge Air Temperature for Compression Temperature for Minimum Ignition Delay</li> <li>Reduced Engine Speed - Longer Time for Combustion</li> <li>Metallurgy Selection for Power Assembly and Turbine Blade</li> <li>Fuel Purification - Handling Tanks and Heating</li> <li>Selection of Lubricant and Lube Purification System</li> </ul>

atomization and controlled injection with short injection duration, together with controlled fuel viscosity at the injectors, eliminates many of the problems associated with digesting residual fuels in medium-speed engines. These engines have a relatively short time available to complete combustion. The effect of the fuels used in medium-speed engines and their characteristics on engine wear and deposits will be discussed in the next section.

Advances in turbocharger design continue to allow single-stage turbochargers to cover medium-speed engine requirements up to a bmep rating of 25 bar, with turbocharger pressure ratios up to 4.5. Significant advancement in improving turbocharger efficiencies is allowing engine designers to further reduce the SFC of engine designs. New designs favor increased maximum combustion pressures as high as 120–150 bar with resulting improved SFC. Typical pressure ratios of such engines show maximum pressure/bmep in the range 6.5–7.5 and charge air pressure/bmep ratios of the range 0.18–0.22. Piston manufacturers [12] are developing pistons with higher top piston rings, closer crownland clearances, and reduced piston skirt bearing area capable of withstanding increased firing pressures [13] to further help in reducing SFC.

Medium-speed engines can successfully operate on lower-cost residual fuels, provided care is taken to ensure temperatures of the cylinder walls and piston ring area remain above the dew point of sulfuric acid,  $H_2SO_4$ , which is related to combustion pressure and fuel sulfur content, as shown in Fig. 7, reported by Belcher [14] and Simonetti [15]. The critical temperature range is 160–190°C; above these temperatures, low temperature corrosive wear is minimized.

Most of these designs have four valve cylinder heads usually



of nodular cast iron, and the valve seats are cooled in the areas close to the combustion space. Exhaust valve face and valve seat temperatures are controlled below 450°C; this minimizes the high temperature corrosion effects of the fuel compounds of vanadium and sodium salts. Details of these corrosive compounds will be discussed in the fuel section of this paper. The exhaust valves are usually the limiting factor

for maintenance. Many engines use Nimonic 80A-type material, or similar armor plus valve rotators, to extend exhaust valve life. Many designs have cast iron or steel-crown pistons with aluminum piston skirts when operating on heavy fuels. Wear in the piston groove area is minimized by such designs.

At part-load operation, it is important to control the charge air temperature entering the cylinders for good combustion of residual fuels. Whereas at full load, the charge air temperature is cooled after leaving the turbocharger by passing through an intercooler; at part load, recent designs arrange to heat the charge air to as high as 75°C. This is especially beneficial at idle/light-load conditions as it helps to minimize the ignition delay.

In summary, medium-speed engines are now available to operate on residual fuels up to 180 cSt/50°C grade; and some designs are able to operate on even higher viscosity grades. Table 5 summarizes key design criteria for the successful operation on residual fuels.

### Types of Fuels

In order to understand the characteristics of distillates and residual-type fuels, it is appropriate to look first at the crude oil/refinery streams shown in Fig. 8. This figure shows how crude petroleum is separated into fractions depending upon the boiling range. Atmospheric distillation is the first step. The crude is heated in a pipe still, vaporized, and the fractions separated in a fractionating tower. The more volatile hydrocarbons are taken from the top of the tower (gas, naphtha, and gasoline), and other distillates are separated lower down the tower at various levels (kerosine, diesel, gas oil, and heating oil) until the undistilled portion of the crude oil is withdrawn from the bottom of the tower.

To obtain higher valued products, the residue is often vacuum distilled and some fractions are converted to gasoline, light and heavy cycle oils, by using fluid catalytic cracking. The residue from this process (FCC) can become a component of residual fuel products. Lubricant base stocks are obtained from the residue of the atmospheric distillation by using

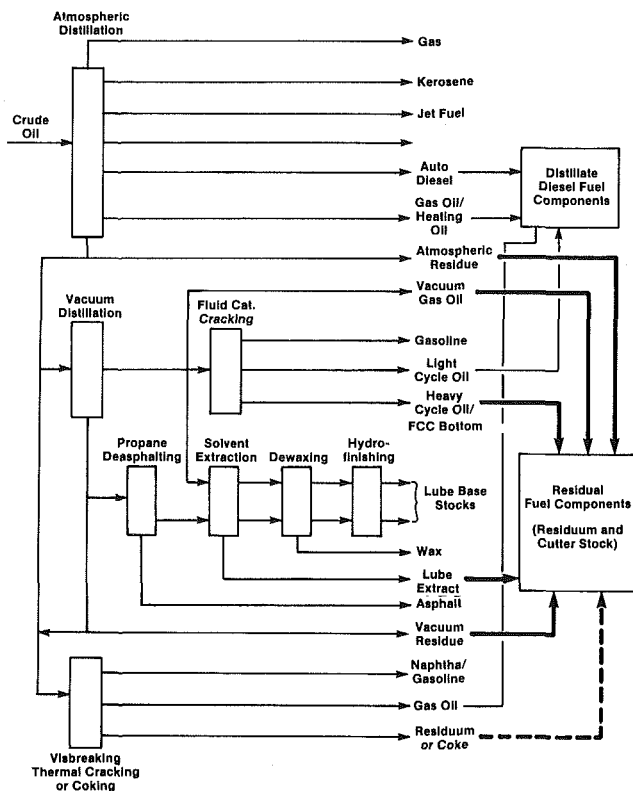


Fig. 8 Simplified modern conversion refinery processing scheme for distillate and residual fuels

Table 6 ISO proposed fuel grades, June 1983

Parameter	Test Method	Limit	Distillate Fuels				Residual Fuels															
			DM-X	DM-A	DM-B	DM-C	RM-10A	RM-10B	RM-10C	RM-15D	RM-25E	RM-25F	RM-35G	RM-35H	RM-35K	RM-35L	RM-45H	RM-45K	RM-45L	RM-55H	RM-55L	
Density at 15°C, kg/m <sup>3</sup>	ISO 3673	Max.	-	900	900	920	975	991	991	991	991	991	991	991	991	-	-	991	-	-	991	-
Viscosity at 40°C, cSt	ISO 3104	Min.	1.4	1.5	-	-	-	-	-	-	-	-	-	-	-	-	-	-	-	-	-	-
Viscosity at 100°C, cSt	ISO 3104	Max.	-	-	-	-	10	10	10	15	25	25	35	35	35	35	35	45	45	45	55	55
Flash Point, °C	ISO 2719	Min.	43	60	60	60	60	60	60	60	60	60	60	60	60	60	60	60	60	60	60	60
Pour Point (Upper), °C, Winter	ISO 3016	Min.	-	-6	0	0	0	24	24	30	30	30	30	30	30	30	30	30	30	30	30	30
Pour Point (Upper), °C, Summer	ISO 3016	Max.	-	0	6	6	6	24	24	30	30	30	30	30	30	30	30	30	30	30	30	30
Cloud Point, °C	ISO 3015	Max.	-16	-	-	-	-	-	-	-	-	-	-	-	-	-	-	-	-	-	-	-
Carbon Residue, Ramsbottom on 10% Residue, % m	ISO 4262	Max.	0.20	-	-	-	-	-	-	-	-	-	-	-	-	-	-	-	-	-	-	-
Carbon Residue, Ramsbottom, % m	ISO 4262	Max.	-	0.20	0.25	2.5	-	-	-	-	-	-	-	-	-	-	-	-	-	-	-	-
Conradson Carbon Residue, % m	ISO 6615	Max.	-	-	-	-	10	10	14	14	15	20	18	22	22	-	22	22	-	22	-	
Ash, % m	ISO 6245	Max.	0.01	0.01	0.01	0.05	0.10	0.10	0.10	0.10	0.10	0.15	0.15	0.20	0.20	0.20	0.20	0.20	0.20	0.20	0.20	
Sediment by Extraction, % m	ISO 3735	Max.	-	-	0.07	0.07	-	-	-	-	-	-	-	-	-	-	-	-	-	-	-	
Water, % Vol.	ISO 3733	Max.	-	-	0.4	0.4	0.50	0.50	0.15	1.0	1.0	1.0	1.0	1.0	1.0	1.0	1.0	1.0	1.0	1.0	1.0	
Cetane Index	ISO 4264	Min.	45	40	35	35	35	35	35	4.0	5.0	5.0	5.0	5.0	5.0	5.0	5.0	5.0	5.0	5.0	5.0	
Sulfur, % m		Max.	1.0	1.5	2.0	2.0	3.5	3.5	3.5	4.0	5.0	5.0	5.0	5.0	5.0	5.0	5.0	5.0	5.0	5.0	5.0	
Vanadium, mg/kg		Max.	-	-	-	100	150	150	300	350	200	500	300	600	600	600	600	600	600	600	600	
Approximate Equivalent Grades/Viscosities																						
CIMAC Fuel BS HA100:1982			-	-	-	1	4	3	2	5	6	7	-	8	9	-	10	11	-	12	-	
Viscosity, cSt/80°C	Max.		H1	-	H2	M3	-	-	M4	M5	-	M6	-	M7	-	M10	M8	-	M11	M9	M12	
Viscosity, cSt/50°C	Max.						15	15	15	25	45	45	75	75	75	100	100	100	100	130	130	
Viscosity Redwood No. 1, 100°F	Max.						40	40	40	80	180	180	380	380	380	380	380	500	500	700	700	
Current Fuel Type							80	300	300	600	1500	1500	3000	3000	3000	3000	5000	5000	5000	7000	7000	
							11	1BF 40	1BF 40	1BF 40	1BF 80	1BF 180	1BF 180	1BF 380	1BF 380	1BF 380	1BF 500	1BF 500	1BF 500	1BF 700	1BF 700	

<sup>1</sup>Can contain some residual fuel.

$$\text{Fuel Specific Energy (MJ/kg): Gross } Q_H = [52,140 - 8,802, \rho^2] \left[ 1 - \left( \frac{W + A + S}{100} \right) \right] + 9,420 \left( \frac{S}{100} \right)$$

$$\text{Net } Q_L = [46,704 - 8,802, \rho^2 + 3,167 \rho] \left[ 1 - \left( \frac{W + A + S}{100} \right) \right] + 9,420 \left( \frac{S}{100} \right) - 2,449 \left( \frac{W}{100} \right)$$

Where:  $\rho$  = Density at 15°C in kg/Liter = kg/m<sup>3</sup> 1000; W = Water, % m; A = Ash, % m; S = Sulfur, % m

propane deasphalting, solvent extraction, dewaxing, and hydrofinishing.

In recent years, visbreaking/thermal cracking or coking processes are becoming common in obtaining higher quality products. These processes leave less residuum. This residuum can be used in fuels for diesel engines. However, in the case of coking, no residuum is available for use in diesel engines. It can be expected that in the long term, due to these processes to obtain higher valued products, heavy fuels will decrease in quantity and quality [2].

Fuels are a complex mixture of compounds of carbon and hydrogen; they are difficult to classify or define by chemical formula or physical properties. In practice, fuels for diesel engines are generally defined by their applications. The most widely used fuel classifications are:

U.S.	ASTM D 975-81	Standard classification of diesel fuel oils
	ASTM D 396	Standard specifications for fuel oils - No. 6 fuel
British	BS 2869-83	Specification for fuel oils for oil engines and burners for nonmarine use
	BS MA 100, 1982	Petroleum fuels for marine oil engines and boilers

**Table 7 Variations in average quality of fuels with viscosities from 101-250 CST at 50°C delivered in various areas of the world during 1983 (first 8 months)**

Test	U.S.A.	Europe	South Africa	Middle East	Far East
Density at 15°C, g/ml	0.982	0.966	0.985	0.951	0.964
Viscosity at 50°C, cSt	187	172	167	148	177
Water, % by Volume	0.2	0.3	0.1	0.3	0.2
Conradson Carbon, % by Mass	13.3	11.3	16.2	9.0	11.6
Sulfur, % by Mass	2.58	2.89	3.30	3.08	3.19
Ash, % by Mass	0.06	0.04	0.04	0.03	0.03
Vanadium, mg/kg	139	69	87	34	50
Sodium, mg/kg	40	50	47	57	37
Aluminum, mg/kg	12	6	10	3	4
Silicon, mg/kg	21	13	19	7	9
Specific Energy, Net, MJ/kg	40.11	40.20	39.89	40.35	40.17
Number of Fuels	253	271	46	101	111

Source: Reference (16).

Two new standards, which in the future will influence the selection of fuels for diesel engines, were recently issued: (i) CIMAC fuel recommendation and (ii) the ISO fuel standard for heavy fuels [3]. This latter ISO standard is still a tentative draft under preparation by Working Group 6 of Subcommittee 4, Classification and Specifications, of ISO Technical Committee ISO/TC 28, Petroleum Products and Lubricants. The draft is very similar to BS MA 100 1982. Table 6 summarizes the proposed ISO fuel grades for 4 distillate and 15 residual fuel grades. Cross reference to the CIMAC and BS MA 100 1982 standards are shown also in Table 6. Examples of commercial fuels of viscosity range 101-250 cSt/50°C, which average close to IF 180-type fuels used in different parts of the world reported by Det Norske Veritas [16], are shown in Table 7.

Table 8 compares the proposed ISO distillate fuel grades with the current ASTM D 975-81 standards and BS 2869 and BS MA 100 1982 standards. This table also shows the recently proposed ASTM "3D" fuel, which was intended as an extender fuel at times of ASTM 2D fuel shortage, as occurred during the OPEC 1973 and 1979 crisis. To avoid recurrence of problems caused by such fuel shortages, the American Association of Railroad (AAR) [17] has sponsored full-scale locomotive fuel studies at the Southwest Research Institute to look at: (i) supplementing ASTM No. 2D fuel for use in emergency, and (ii) broadening the fuel specification range for lower cost alternatives to ASTM No. 2D diesel fuel [18]. Our experience shows the major problem to be overcome in using Blended No. 2D/No. 6 fuels relates to railroad service where prolonged idling operation exists. It is common in cold climates in Canada and the U.S. for locomotives to idle 48-72 hr continuously. Combustion of blended fuels at prolonged idle is difficult, particularly in elevated mountain regions like the Rockies (3500-m altitudes). Under prolonged idling, exhaust system and turbocharger deposits become serious problems as reported by Jackson [19] and confirmed in our recent field tests on two-stroke and four-stroke engines. Results of our tests, including studies of engine deposits from operating on blended fuels, are discussed in the lubricant section, Part II.

To understand why blended and residual fuels are more difficult to burn and the effects they have on engine durability, it is appropriate to look at fuel characteristics as shown in Tables 9 and 10. The fuel properties are grouped in Table 9 for those related of fuel handling and combustion, and Table 10 shows the effects of fuel impurities on engine

**Table 8 Distillate fuel specifications**

	ASTM D 975-81				Proposed ISO, June 1983				BS 2869:1983		BS MA 100:1982		
	1D	2D	"Proposed" 3D	4D <sup>1</sup>	DM-X	DM-A	DM-B	DM-C	A1	A2	M1	M2	M3 <sup>1</sup>
Density at 15°C, kg/m <sup>3</sup>	-	-	-	-	-	890	900	920	-	-	-	900	900
Viscosity at 40°C, cSt	Min. 1.3	1.9	-	5.5	1.4	1.5	-	-	1.5	1.5	1.5	-	-
	Max. 2.4	4.1	7.5	24.0	5.5	6.0	11.0	14.0	5.0	5.5	5.5	11.0	14.0
Cetane Index	Min. 40	40	37	40	45	40	35.0	-	50	45	45	35	-
Carbon Residue on 10% Residue, %	Max. 0.15	0.35	0.40	-	0.20	-	-	-	-	-	0.20	-	-
Carbon Residue, Ramsbottom, %	Max. -	-	-	-	-	0.20	0.25	2.5	0.20	0.20	-	0.25	2.5
Flash Point, FM, °C	Min. 38	52	55	55	43	60	60	60	56	56	43	60	60
Cloud Point, °C	Max. -	-	-	-	-	-	-	-	-	-	-16	-	-
Pour Point (Upper), °C	Max. -	-	-	-	-	-6	0	0	-9 <sup>2</sup>	-9 <sup>2</sup>	-	0	0
December 1-March 31	Max. -	-	-	-	-	0	6	6	0 <sup>2</sup>	0 <sup>2</sup>	-	6	6
April 1-November 30	Max. -	-	-	-	-	0.01	0.01	0.02	0.01	0.01	0.01	0.02	-
Sediment, %	Max. -	-	-	-	0.05	0.01	0.30	0.30	0.05	0.05	0.05	0.25	0.30
Water, % V	Max. 0.05	0.05	-	0.50	-	-	-	-	-	-	-	-	-
Water and Sediment, % V <sup>2</sup>	Max. 0.01	0.01	-	0.10	0.01	0.01	0.01	0.05	0.01	0.01	0.01	0.01	0.05
Ash, % m	Max. 0.50	0.50	0.70	0.2	1.90	1.50	2.00	2.0	0.30	0.50	1.00	2.00	2.00
Sulfur, % m	Min. -	282	-	-	-	-	-	-	#3	#3	-	-	-
Distillation Temperature, °C, at 90%	Max. 288	338	-	-	-	-	-	-	-	-	-	-	-
Copper Strip Corrosion	Max. No. 3	No. 3	-	-	-	-	-	-	1	1	-	-	-
Vanadium, mg/kg	Max. -	-	-	-	-	-	-	100	-	-	-	-	100
Approximate Viscosity at 100°F, SUS	Min. -	32.6	-	45.0	-	-	-	-	-	-	-	-	-
	Max. 34.4	40.1	50.4	125.0	44.0	45.6	62.4	73.5	44.0	44.0	44.0	62.4	73.5

<sup>1</sup>Small amounts of residuum permitted.

<sup>2</sup>Cold filter plugging, BS 6188 method.

<sup>3</sup>85% minimum at 350°C.

**Table 9 Fuel characteristics—influence of engine operation and remedial measures handling and combustion**

Characteristics	Effect	Remedial Measure
Viscosity	Fuel atomization and injector lubrication.	Residual fuels up to 1000 cSt/50°C viscosity can be satisfactorily atomized at temperatures up to 150°C. Heating above 150°C promotes reformation of asphalt. Heat fuels to 12-20 cSt/50°C range for satisfactory operation. Viscosities above this can cause fuel pump drive overloading. Delayed combustion and poor atomization can occur if viscosities above/below range. Low viscosities can give poor injector lubrication.
Density	Related to specific energy of fuel. Centrifuge separating effect falls as density increases. More abrasive and corrosive constituents get into engine, leading to higher wear and heavy ash deposits.	Below 991 kg/m <sup>3</sup> density, increase fuel heating, use lower flow rates through centrifuge and recirculation to settling tanks. Above 991 kg/m <sup>3</sup> to 1010 kg/m <sup>3</sup> , use either chemical additive treatment or special centrifuges.
Compatibility	Asphaltene deposits can result as precipitates. This leads to sludge formation in the fuel system and filter clogging.	Use one bunkering in storage tank until empty. Use onboard fuel blending only if compatibility can be checked. Include shearing-blender or homogenizer in blending system. Fuel additives in storage tank may help.
Conradson Carbon Residue	Abrasive carbon deposits can result from incomplete combustion, especially at part load. Fouling and smoke can occur resulting in ring sticking and/or heavy piston, valve, and port deposits.	Requires good fuel/air mixture formation and atomization. Good component cooling. At part load increased cooling water temperatures and preheating of charge air to 35°C/40°C minimum. Variable injection timing, load related, is helpful (electronic control of injection).
Asphaltenes	Slow burning and smoke leads to increased soot formation and residue	
Cetane Number	Low cetane number (<35) gives poor starting and rough engine running, ignition delay, and high combustion temperatures.	Increase charge air temperature at low loads, increased compression ratio, heating of fuel, fuel additives, variable timing with loads to match fuel ignition qualities (electronic injection).
Aromatics	Aromaticity in fuels control ignition delay. High values delay ignition causing problems listed under cetane number.	
Flash Point	Safety in handling, fire hazard.	ISO propose minimum of 60°C flash point. Emergency fuels 43°C minimum.
Pour Point and Cloud Point	Low temperature operation.	ISO propose specification to ensure winter and summer low temperature. Operability is satisfactory. Completely heated fuel system.

**Table 10 Fuel characteristics influence on engine operation and remedial measures: impurities**

Characteristics	Effect	Remedial Measure
Water and Dirt	Corrosion and vapor lock in the fuel system impairs atomization. High temperature corrosion, if seawater (Na), wear increase.	Centrifuge fuels to separate water and impurities.
Vanadium and Sodium	High temperature corrosion, dependent upon V/Na ratio and level of vanadium. Corrosion can occur at temperatures in 430-650°C range. Deposits form on exhaust valve seats, turbochargers, and piston crowns.	Avoid high temperatures by cooling critical parts. Increase turbocharger air flow to cool exhaust valves, use rotocaps. Select exhaust valve and turbocharger blade material (Nimonic), use armor protected seats.
Sulfur	Low temperature corrosion from H <sub>2</sub> SO <sub>4</sub> reduces piston rings, piston groove, and cylinder liner life.	Keep component temperature above the dew point of H <sub>2</sub> SO <sub>4</sub> , approximately 180-190°C (see Figure 7), Depends upon sulfur level and combustion pressure. Select a lubricant with adequate neutralization capacity (TBN - ASTM D 2896). Design for good lubricant distribution. Avoid too low an oil consumption rate.
Ash and Catalytic Fines (Aluminum and Silicates)	Excessive abrasive wear of fuel injection system and piston rings/grooves and cylinder liners. Ash deposits and abrasive wear.	Centrifuge fuel, can eliminate particles above 7.5 microns.* Lubricant viscosity/EP properties may help to maintain film thickness and surface protection of rings and liners. Selection of materials for components and surface finish.

\*Source: References (30) and (42).

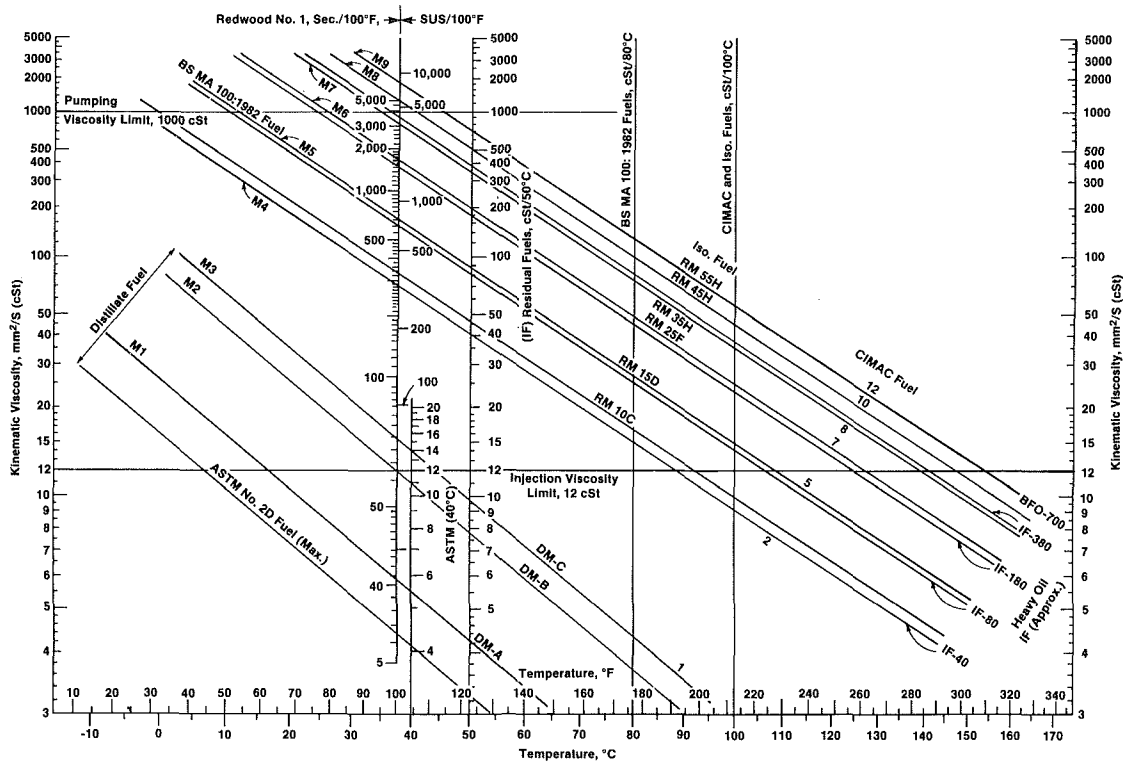


Fig. 9 Fuel specifications – viscosity/temperature relationships

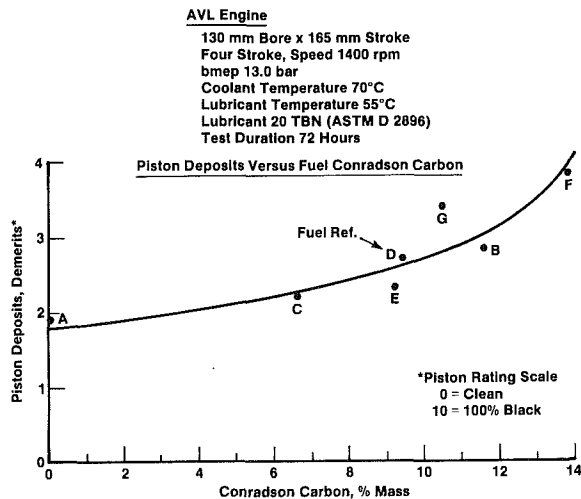


Fig. 10 Residual fuel studies in a medium-speed laboratory diesel engine

wear and corrosion. Remedial measures are also listed which reflect the changes offered by the latest engine designs and installations and fuel handling equipment. The importance of these fuel characteristics is discussed below. The relationships between the engine, fuel, and installation for handling residual fuels and the resultant effects of residual fuel combustion products on corrosion and wear, engine deposits, lubricant insolubles, and their purification are shown in Fig. 5.

### Fuel Viscosity

It is difficult to pump viscous residuum fuels; and the practical limit, as shown in Fig. 9, is about 1000 cSt. Installations must have heating facilities to handle residuum fuel. The fuel viscosity at the fuel injectors is important for

good atomization and combustion; typical viscosity at the injectors is 12 cSt. The engine builders design their injection equipment for an optimum injection viscosity and pressure. If fuel viscosity is too high, fuel jets can impinge on cylinder walls and pistons from overpenetration into the combustion air, and delayed ignition and burning can also occur. The increased fuel system pressures resulting from too viscous a fuel can overload fuel pump drives. If too high a fuel temperature is used, the low viscosity of the fuel can result in poor fuel droplet penetration and poor combustion. Both cases will result in nonoptimum combustion and increased SFC. Furthermore, if fuels are heated above 150°C, asphalts can form, leading to soot formation and increased engine deposits. Viscosity, pressure, and fuel density interactions in fuel systems were recently reported by Herzog [10].

### Density

Density is an indicator of the energy available in a fuel. The proposed ISO fuel specification [3] recommends the following equation for the specific energy when measured values are not available:

$$Q_H = \left[ 52.190 - 8.802 \left( \frac{\rho}{1000} \right)^2 \right] \left[ 1 - \left( \frac{W+A+S}{100} \right) \right] + 9.420 \left( \frac{S}{100} \right) \quad (11)$$

$$Q_L = \left[ 46.704 - 8.802 \left( \frac{\rho}{1000} \right)^2 + 3.167 \left( \frac{\rho}{1000} \right) \right] \left[ 1 - \left( \frac{W+A+S}{100} \right) \right] + 9.420 \left( \frac{S}{100} \right) - 2.449 \frac{W}{100} \quad (12)$$

$$\frac{1}{3} \text{ MJ/kg Fuel} = \frac{4.1868}{1000} \times (\text{Kcal/kg}) = \frac{2.2360}{1000} \times (\text{Btu/Lb})$$

**Table 11 Examples of diesel engine builders guides on fuel**

Fuel Type	Blended Distillate Fuels				Residual Intermediate Fuels									
	229	230	209	230	240	250	250	255	270	280	280	320	330	350
Engine Bore, mm	267	254	279	300	280	300	300	270	305	320	350	350	360	380
Engine Stroke, mm	184	177	100	135	165	220	224	220	240	195	295	341	368	441
Engine Output, kW/Cylinder	1050	900	1000	750	1000	1000	1000	1000	775	750	750	750	750	750
Engine Speed, rpm	19.2	11.0**	14.2	17.3	15.6	17.9	18.2	19.1	16.5	15.5	21.8	19.4	19.1	19.3
Engine bmep, Bar														
Fuel Type	No. 2D/No. 6	No. 2B/No. 6	IF 60	IF 380	IF 180	IF 120	IF 120	IF 180	IF 180	IF 180	IF 380	IF 380	IF 380	IF 420
Viscosity at 50°C, cSt	Max. 1.9-8.4*	1.9-8.9*	6 <sup>1</sup>	380	180	120	120	180	180	180	380	380	380	420
Fuel Sulfur, % m	1.0	1.8	2.5	4.0	4.0	3.0	3.0	4.0	3.5	3.5	4.0	4.0	4.0	4.0
Conradson Carbon, % m	2.0	4.0	7	12	10	9	16	10	9	12	12	12	12	14
Asphaltenes, % m	1.0	1.0	4.72	-	6	6 <sup>2</sup>	-	8	7	-	-	-	-	9
Ash, % a	0.02	0.02	0.05	0.10	-	0.05	0.05	0.10	0.15	0.10	0.10	-	0.10	-
Water, % Vol.	0.20	0.25	9.50	0.50	-	0.5	0.5	-	0.75	0.50	-	-	0.5	-
Vanadium, mg/kg	Max. 30	30	100	150	200	100	100	300	100	150	-	-	350	400
Sodium, mg/kg	Max. 10	10	35 <sup>3</sup>	100	-	35 <sup>3</sup>	20 <sup>4</sup>	-	30	50	-	-	-	-
Aluminum, mg/kg	Max. 5	10	-	-	-	-	-	30 <sup>1</sup>	-	-	20 <sup>1</sup>	-	-	-
Cetane Number	Min. 37	37	-	-	-	-	-	30	-	-	-	-	-	-
Distillation at 371°C, 4 Vol	Min. 90	90	-	-	-	40	-	-	-	-	-	-	-	-
Distillation 90%, °C	Max. -	358	-	-	-	-	-	-	-	-	-	-	-	-
Distillation Recovery, %	Min. 90	90	-	-	-	-	-	-	-	-	-	-	-	-

<sup>1</sup>Includes (Al + Si).  
<sup>2</sup>Two-thirds of CCR.  
<sup>3</sup>One-third of vanadium.  
<sup>4</sup>One-fifth of vanadium.  
\*At 40°C, range in viscosity.  
\*\*Two stroke.

**Fuel Stability**

Fuel stability relates to the solubility of the components of an individual fuel. Oil companies conduct stability tests on fuels to ensure that a fuel remains stable in storage.

**Compatibility of Fuels**

Mixing of fuels from different supply sources can lead to incompatibility, even though each fuel is stable by itself. Likewise, mixing fuel components for blended or light intermediate fuels from different crude sources, due to the differences in chemical composition, can give compatibility problems. The asphaltenes tend to precipitate due to the low solvent power of the main fuel component. Heating the fuel within practical temperature limits will not significantly alter the solubility. The asphalt deposits lead to sludge formation in the fuel system, filter clogging, and impairment of the fuel injection system resulting in poor atomization and incomplete combustion. Oil companies mix components and carefully check compatibility by their quality control tests, usually centrifuge or hot spot tests. With the increasing use of residual fuels from catalyst cracking and visbreaking, the risk of fuel incompatibility increases. Where possible, it is advisable to use fuel storage tanks with only one bunkering and use until empty.

**Conradson Carbon Residue (CCR)**

CCR relates to the tendency to form carbon deposits from combustion residues. These abrasive deposits [20] usually are located on the piston crown and in the piston ring grooves, leading to wear and sticking of piston rings [21]. Smoke and engine fouling are particularly of concern under part-load operational conditions. Our work shows increasing CCR gives higher deposits [22, 23], as shown in Fig. 10.

The design precautions taken with respect to the fuel injection system and preheating the charge air are similar to those needed to handle asphaltenes and aromatics discussed below. Medium-speed engine designers generally place a limiting value on the CCR value for their engine fuels, as shown in Table 11. This table covers examples of blended distillate/No. 6 fuels and residual fuels, IF 60-380 type, for medium-speed engines of 200-350 mm bore.

**Asphaltenes**

Asphaltenes are high-molecular-weight, resin-type

materials found in residual fuels. They are insoluble in naphtha but soluble in benzene and normally exist in colloidal dispersions in the fuel oil and cannot be removed by centrifuging [24]. Asphaltene is completely combustible but is slow burning and can cause poor combustion in diesel engines unless the fuel injection system is designed for good atomization with fuel droplets below 20 μ [21]. Syassen [21] has shown that the ignition of an injected fuel droplet is influenced mainly by its size, vapor pressure, temperature of the compressed air, and its density; all events that the relevant to droplet heating, evaporation, diffusion, and ignition, take place within about 1 ms. For a medium-speed engine at 1000 rpm rotational speed, this is equivalent to 6 deg of crank angle. Droplet size is one of the key factors for satisfactory combustion of residual fuel in medium-speed engines. For example [21], a droplet of 10-μ dia heated to 300°C (at a compression temperature of 500°C) requires about 0.18 ms for heating, evaporation, diffusion, and ignition; if the droplet was 20 μ, the time required is about 0.53 ms. To ensure fuel droplet size is below 20 μ at part-load operation and 10 μ at full load, engine builders are using high fuel injection pump pressures of 1000-1700 bar. Part-load operation below 30 percent load may also require the charge air temperature to be heated to above 40°C. Designs are now available utilizing intercooler cooling water systems to preheat the air at light loads.

Increasing levels of asphaltenes can lead to increased temperatures in the combustion chamber [25] due to sluggish heat release. Our work [22, 23, 26] has shown piston deposits can increase with increased levels of asphaltenes. Asphaltene effect can be minimized by good air to fuel mixing [25]. Our work shows, in medium-speed engines, that used oil insolubles increase with increasing level of asphaltenes [22, 23].

**Aromatics**

Aromatics affect combustion, particularly the ignition delay and rate of pressure rise at the start of combustion. For distillate fuels, the ignition performance has been defined since the 1930s by the ASTM D 613 cetane number test using the Waukesha CFR single-cylinder engine. The cetane number is useful for high-speed diesel ignition performance. It relates to a blend ratio of N-cetane (assigned the Number 100) and heptamethylnonane (assigned the Number 15). Often when the CFR engine test cetane number is not available, an estimate is used known as the cetane index (ASTM method D 976), which used an empirical equation based on the API

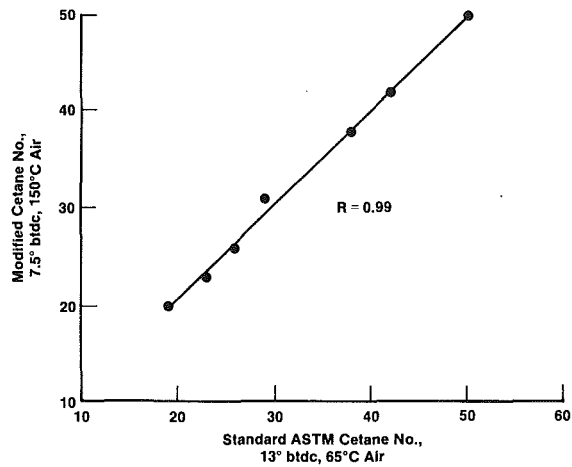


Fig. 11 Cetane number at modified versus standard conditions

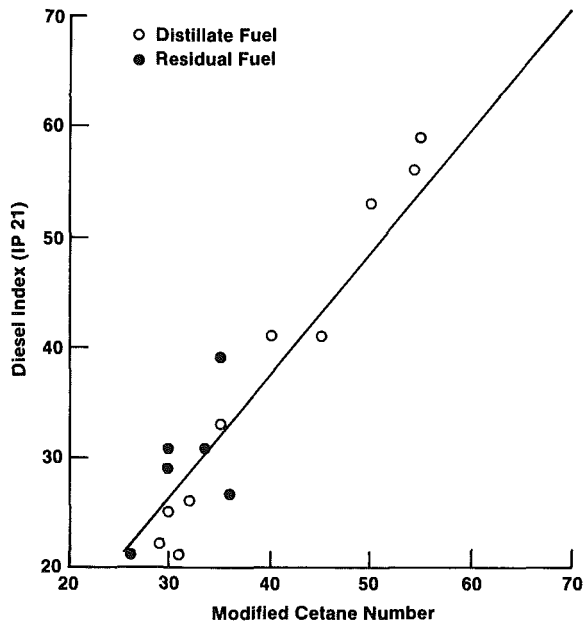


Fig. 12 Correlation between diesel index and cetane number

gravity and midboiling point of the distillation curve. For residual fuel, midboiling point is not applicable as the residual fraction by definition cannot be distilled. A second empirical equation often used is the diesel index (IP 21), which relates the API gravity and the aniline point, that involves the observations of a cloudy transition through the fuel. This is not possible with some residual fuels. In our work [22, 23, 26], evaluating the ignition qualities of residual fuels required a modification to the ASTM D 613 method. It is possible to evaluate both the ignition qualities of distillate fuels and residual fuels by modifying the D 613 method. This requires installing heating equipment for the residual fuels, changing the air charge temperature from 60 to 150°C, and changing the fuel injection timing from 13 deg BTDC to 7.5 deg BTDC to overcome the unstable combustion of residual fuels under standard ASTM D 613 conditions. Figure 11 shows the correlation for distillate fuels of the ASTM D 613 method and our modified D 613 method taken from work reported by Hold [26]. When the diesel index (IP 21) can be obtained, we find it correlates with the modified cetane number (MCN), as shown in Fig. 12. Zeelenberg [27] has suggested an ignition index suitable for residual fuels based on the carbon aromaticity of the fuel known as the CCAI. Figure 13, taken

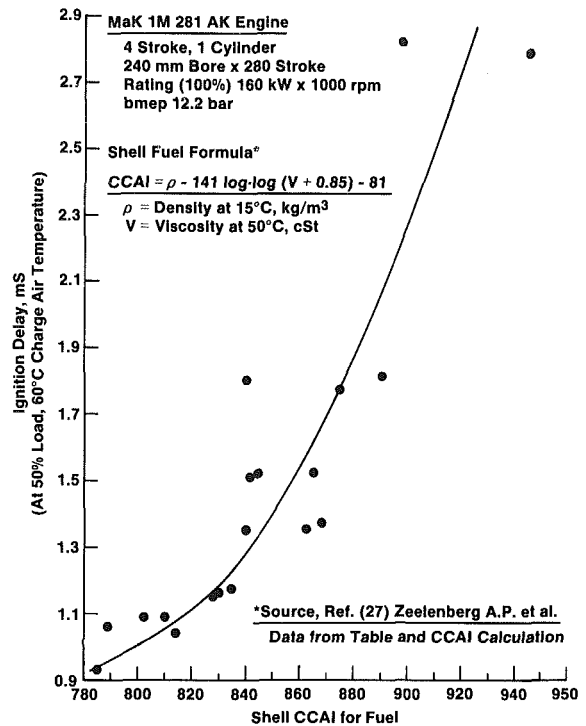


Fig. 13 Ignition delay versus calculated carbon aromaticity index (CCAI) of fuel

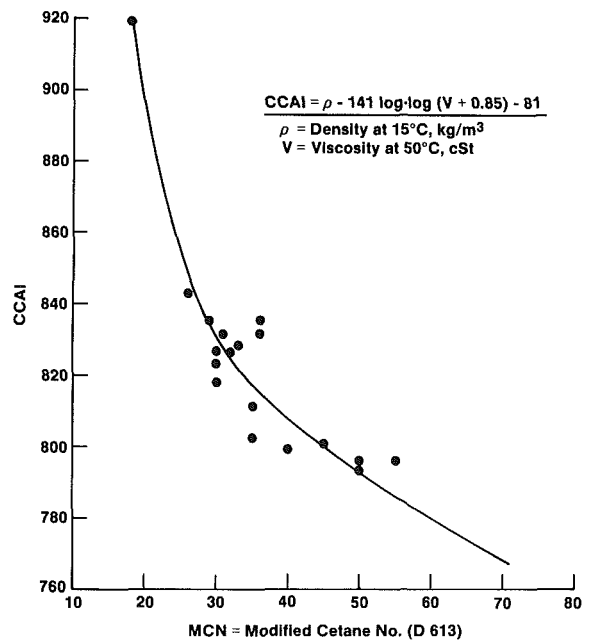


Fig. 14 Modified cetane number (ASTM D 613) versus calculated carbon aromaticity index (CCAI)

from the data reported in [27], shows the measured ignition delay (ms) of wide range of fuels in a four-stroke MaK IM 281 AK engine of 240-mm bore at a speed of 1000 rpm and the CCAI values of these fuels. We have applied equation (13), proposed by Zeelenberg [27], to a wide range of fuels where we have established their ignition characteristics using the modified D 613 method discussed above. Figure 14 shows the correlation with equation (13). Our data confirms Zeelenberg's [27] work. It appears that residual fuels can be evaluated in a modified ASTM D 613 engine test, which is also suitable for distillate fuel [22, 23, 26]; and either the

Table 12 Fuel properties – AVL-CAT study<sup>1</sup>

Fuels	F1	F2	F3	F4	F5	F6	F7	F8	F9
Density, kg/m <sup>3</sup> at 15°C	828	971	965	966	895	963	973	961	945
Viscosity, cSt at 50°C	475	451	370	737	18.0	370	305	163	223
Flash Point (PM), °C	107	93	90	232	83	56	56	125 <sup>1</sup>	148
Pour Point, °C	+18	-3	-3	+9	+3	-9	-9	-18	+24
Conradson Carbon, % m	0.8	16.4	13.2	9.7	3.3	17.6	18.9	7.6	7.1
Asphaltenes, % m	0	8.8	4.5	1.4	1.5	8.0	10.8	1.7	1.1
Ash, % m	0	0.06	0.02	0.01	0.01	0.01	0.01	0.03	0.01
Sulfur, % m	0.09	1.81	4.02	2.86	2.16	3.50	3.74	1.05	2.53
Water and Sediment, % Vol	0.05	0.10	Trace	0.40	0.01	0.05	0.05	0.10	-
Distillation D 86, °C									
IBP	190	214	213	402	199	191	186	196	230
10%	285	251	319	-	266	276	362	268	399
30%	309	311	427	-	332	436	463	376	459
50%	325	-	-	-	412	-	-	458	509
70%	341	-	-	-	494	-	-	-	-
90%	371	-	-	-	-	-	-	-	-
EP	392	-	521	478	-	-	489	524	550
Recovery, % Vol	97	-	40	5	-	-	32	65	64
Metals, mg/kg									
Al	0	10	0	0	0	0	0	3	-
Ca	2	46	0	2	1	4	2	7	-
Fe	1	61	0	5	4	4	4	16	-
Mg	0	51	0	2	0	1	2	2	-
Na	5	80	2	16	7	16	17	18	16
Ni	0	92	15	0	14	12	14	44	-
Si	0	0	0	0	0	0	0	0	-
V	0	34	28	10	38	51	57	19	36
Source	China	U.S.	Kuwait	Holland	Russia	Bahrain	Bahrain	U.S.	Holland
Fuel Type	Low Sulfur	Experimental Blend	High Sulfur	High Viscosity	Borderline Stability	High Sulfur	High Sulfur		

<sup>1</sup>By CCL method, Reference (29).

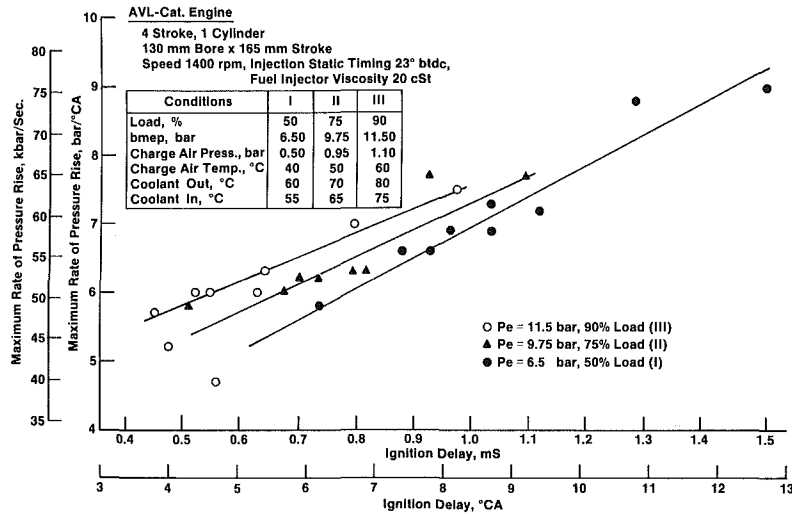


Fig. 15 Ignition delay versus maximum combustion pressure rise

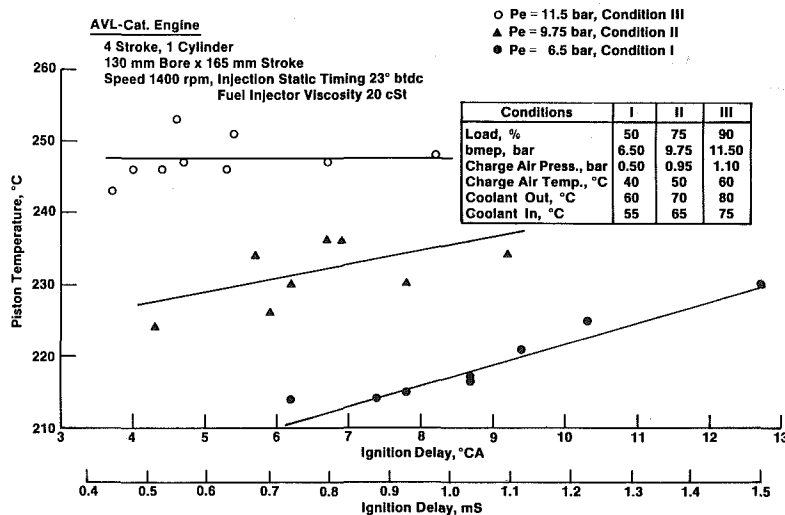


Fig. 16 Piston temperature versus ignition delay

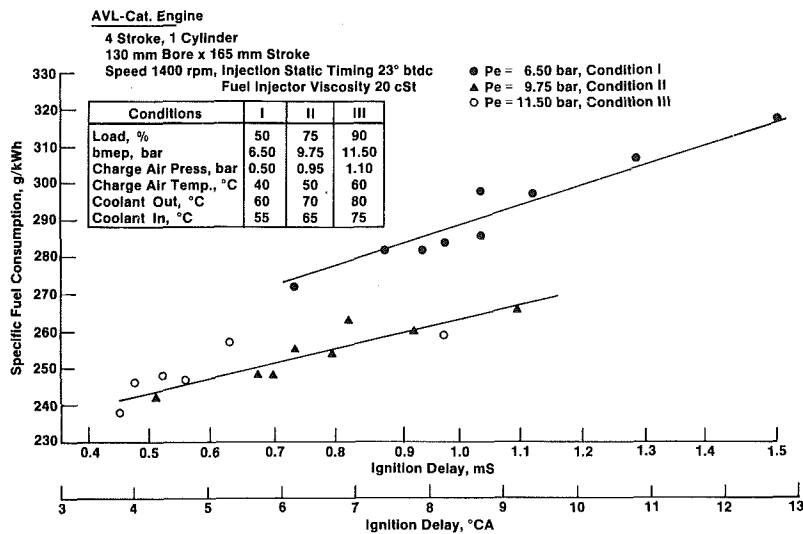


Fig. 17 Specific fuel consumption versus ignition delay

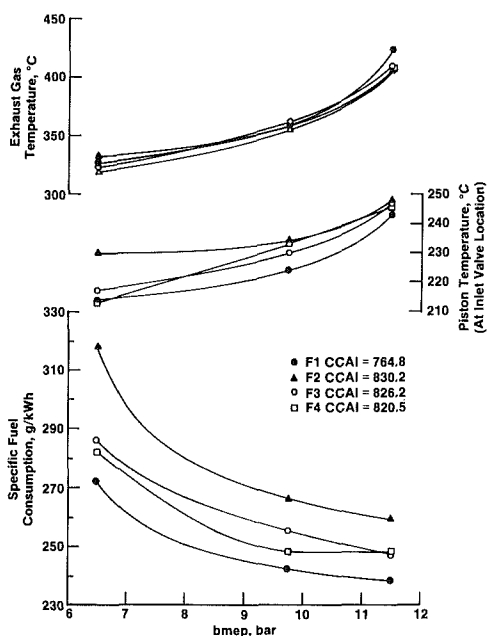


Fig. 18 Study of residual fuels

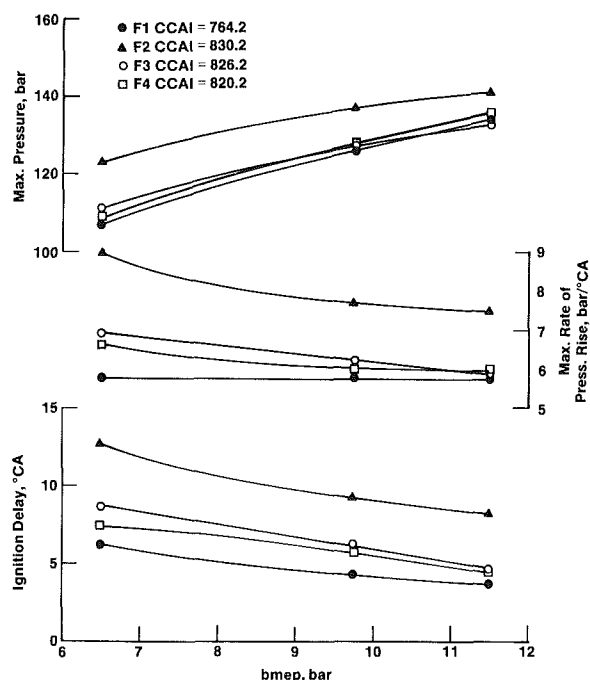


Fig. 19 Study of residual fuels

diesel index (IP 21) or the CCAI [27] value can be used as an approximate guide when the modified cetane test data (D 613) are not available. Due to the difficulty of noting the aniline point for residual fuels, it is not always possible to calculate the diesel index. The CCAI value, however, is computed from the fuel density and fuel viscosity, which are available on all fuels:

$$CCAI = \rho - 141 \log \cdot \log(V + 0.85) - 81 \quad (13)$$

It should be noted, we found the calculated cetane index (ASTM D 976) to have a poor correlation with the ignition qualities of residual fuels [26].

The influence of fuel aromatics on ignition delay in medium-speed and slow-speed engines of 220–700-mm bore has been reported by Hafner [25]. The effect of fuels with cetane numbers from 30–50 in medium-speed engines (re maximum combustion pressures), pressure rise, and ignition delay has been reported by Daugas [28]. The findings in these reports are similar to our work [22, 23, 26] discussed below.

## Fuel Study in a Medium-Speed AVL Direct-Injection Engine

Nine fuels from the U.S., Middle East, Europe, Russia, and China were evaluated; these were selected to include fuels with: high viscosity, high sulfur, low sulfur, high Conradson carbon, high asphaltenes, low flesh, and high boiling point.

Table 12 shows the fuel properties of the fuels designated F1 to F9. The AVL engine was instrumented to record piston crownland temperature using a Karl Schmit linkage system; and ignition was monitored by: needle lift, rate of pressure rise, combustion pressure, and injection pressure against crankshaft angle. Three test conditions of 50, 75, and 90 percent load were studied at 1400 rpm. With fuel injector viscosity controlled at 20 cSt, coolant and charge air temperatures were reduced at part load to simulate field service. Figure 15 shows the observed relationship between ignition delay and maximum pressure rise ( $dp/d\theta$ ) for the three load conditions. Figure 16 shows the piston temperature remained



**Table 13 Residual fuel studies in a medium-speed laboratory diesel engine\***

Fuel	A	B	C	D	E	F	G
<b>Fuel Properties</b>							
Viscosity, cSt at 50°C	2.46	62.4	288	306	317	426	900
Density, kg/Liter at 15°C	0.8369	0.9485	0.9384	0.9601	0.9562	0.9827	0.9653
Sulfur, % Mass	1.00	4.02	1.04	3.28	2.90	3.47	2.86
Conradson Carbon, % Mass	0	11.6	6.6	9.4	9.2	13.9	10.5
Asphaltenes, % Mass	0	8.5	0.8	2.6	2.2	5.9	2.1
Ash, % Mass	0	0.006	0.005	0.009	0.008	0.015	0.008
Flash Point, °C	70	84	224	190	192	120	256
Pour Point, °C	-30	-30	36	12	18	3	9
Distillation, IBP °C	175	194	326	289	292	216	340
Distillation, 90% EF	388	527	577	571	571	524	572
Distillation Recovered, % Vol	97	63	68	65	67	48	47
Aniline Point, °C	69.0	-	94.8	83.6	85.2	76.0	95.2
Diesel Index, IP21	59	27	39	29	21	21	31
Cetane No., D 613 Mod**	55	36	35	30	26	30	30
Cetane Index, D 976	57	50	68	61	-	-	-
Heat of Combustion, MJ/kg	45.194	42.603	44.087	42.921	43.036	42.441	43.194
<b>Metals, mg/kg</b>							
Vanadium	<1	11	13	29	24	30	6
Aluminum	<1	<1	<1	<1	<	1	1
Sodium	<1	1	7	6	5	12	9

\*Reference (23).

\*\*Chevron Method; see Reference (23) for details.

**Table 14 Deposits and corrosion from combustion gases containing V, Na, and S<sup>1</sup>**

Temperature	Temperature Range	Combustion Gases/Deposits	Corrosion By
Low	Below Dew Point of SO <sub>3</sub> ~150°C (Depends on Pressure/ Temperature)	SO <sub>3</sub>	Sulfuric Acid (H <sub>2</sub> SO <sub>4</sub> )
Intermediate	Above Dew Point of SO <sub>3</sub> Range ~150-400°C Below 250°C Low Deposit	Na <sub>2</sub> SO <sub>4</sub> V <sub>2</sub> O <sub>5</sub> SO <sub>3</sub>	Na <sub>2</sub> S <sub>2</sub> O <sub>7</sub>
High	Above About 400°C to the Dew Point of Na <sub>2</sub> SO <sub>4</sub> and V <sub>2</sub> O <sub>5</sub> Above Dew Point of Na <sub>2</sub> SO <sub>4</sub> and V <sub>2</sub> O <sub>5</sub>	Na <sub>2</sub> SO <sub>4</sub> V <sub>2</sub> O <sub>5</sub> None	Na <sub>2</sub> V <sub>2</sub> O <sub>4.5</sub> V <sub>2</sub> O <sub>5</sub> *

<sup>1</sup>Reference (35).

\*Chemical reaction at high temperature of V<sub>2</sub>O<sub>5</sub> and Na<sub>2</sub>SO<sub>4</sub>.  
 $6V_2O_5 + Na_2SO_4 + Na_2O \cdot V_2O_4.5 + SO_3 + 1/2 O_2$

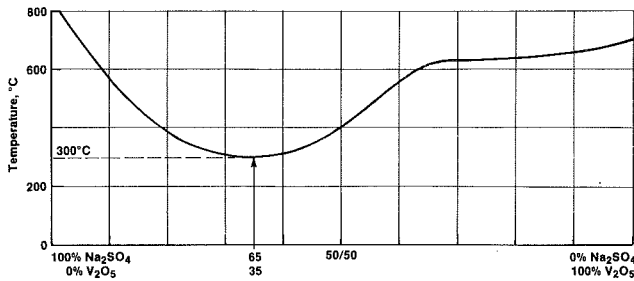
constant at full load with various ignition delays; however, at part load, piston temperature increased with increasing ignition delay. Figure 17 shows SFC can be affected by the ignition delay qualities of a fuel. The relationship of load (bmep) to ignition delay at 1400 rpm for four of the fuels, F1 to F4, are shown in Figs. 18 and 19, which illustrate fuels with a range of 765-830 CCAI values [27] representing fuels of low sulfur (F1), high Conradson carbon (F2), high sulfur (F3), and high viscosity (F4). From our co-workers fuel studies [29] and our previously reported studies on another seven widely different fuels, Table 13, for ignition delay [22, 23, 26], we conclude:

- 1 A modified ASTM D 613 method ranks residual and distillate fuels for ignition delay.
- 2 Cetane index does not correlate for residual fuels.
- 3 Diesel index, if it can be computed, correlates with the modified D 613 method.

**Table 15 Examples of vanadium and sodium salts and their low melting points**

Compounds	Melting Point, °C
Sodium Metavanadate (NaVO <sub>4</sub> )	625
Sodium Pyrovanadate (Na <sub>2</sub> V <sub>2</sub> O <sub>7</sub> )	632-754
Sodium Pyrosulfate (Na <sub>2</sub> S <sub>2</sub> O <sub>7</sub> )	682
Vanadium Pentoxide (V <sub>2</sub> O <sub>5</sub> )	664-691
Sodium Sulfate (Na <sub>2</sub> SO <sub>4</sub> )	880-885
<b>Eutectic Mixtures of:</b>	
V <sub>2</sub> O <sub>5</sub> and Na <sub>2</sub> SO <sub>4</sub>	538
V <sub>2</sub> O <sub>5</sub> and NaVO <sub>3</sub>	566
NaVO <sub>3</sub> and Na <sub>4</sub> V <sub>2</sub> O <sub>7</sub>	577

\*Source: Reference (33).



Source: Motorship, March 1978

Fig. 20 Melting temperature of  $V_2O_5 - Na_2SO_4$  mixtures

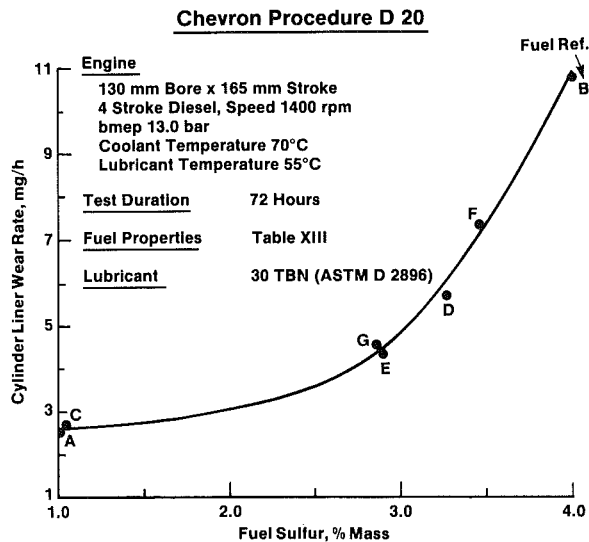


Fig. 21 Cylinder liner wear rate versus fuel sulfur (residual fuel studies in a medium-speed diesel engine)

4 Calculated carbon aromaticity index, CCAI, may give a guide to ignition delay performance based on a fuel's density and viscosity.

5 Specific fuel consumption does not correlate with viscosity, Conradson carbon residue, sulfur, or asphaltene of a fuel. At low loads, specific fuel consumption can relate to the ignition delay characteristic of a fuel.

6 The ratio of combustion pressure rise relates to ignition delay and is most pronounced at light loads.

7 The piston temperature increases with increasing ignition delay at part-load operation but remains constant at full load.

### Fuel Impurities

Table 10 shows a summary of fuel impurities, their effect on engine performance, and the remedial measures that can be taken to minimize their effects on engine wear, corrosion, and deposition on components. These impurities are discussed below.

**Water and Dirt.** These contaminants can be removed by careful fuel treatment, which includes utilizing both a storage tank and a day-settling tank. Facilities to heat the fuel close to  $98^\circ C$  are needed in order to centrifuge the fuel at a temperature which maximizes the difference between the fuel density and the water density. It is desirable to use fuels with densities below  $991 \text{ kg/m}^3$ . However, for heavier fuels, techniques [30, 31, 32] are now available to successfully remove water from fuels with densities up to  $1013 \text{ kg/m}^3$ .

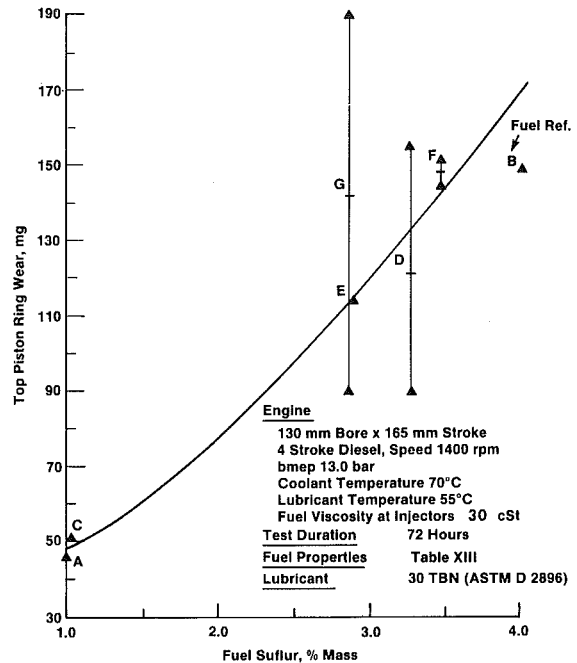


Fig. 22 Effect of BMEP on ring wear for several residual fuels

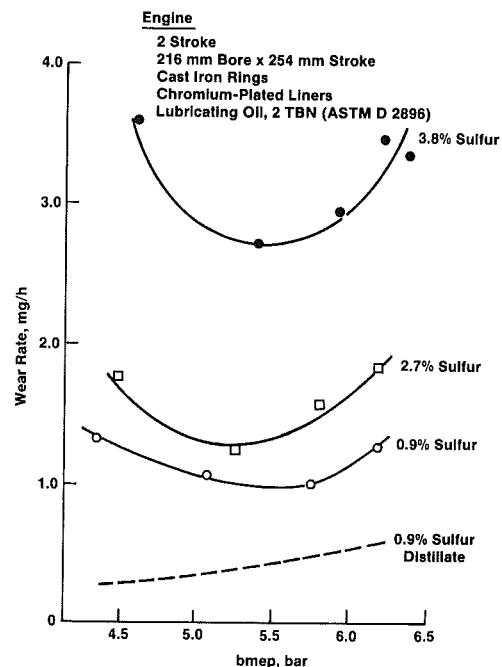


Fig. 23 Top piston ring wear versus fuel sulfur (residual fuel studies in a medium-speed diesel engine)

**Vanadium and Sodium.** Residual fuels can contain a small amount of metallic constituents, including vanadium, sodium, and nickel. Rust particles ( $FeO$ ) and sand (silica) also show up with ash measurements. The vanadium and sodium elements oxidize [33] during the combustion process to form vanadium oxides ( $V_2O_5$ ), sodium oxide ( $Na_2O$ ), and other oxides [34, 35]. These oxidize, react with each other to form low melting salts which can deposit on exhaust valves [36, 37, 38] and piston crowns [37]. These salts may include sodium sulfate ( $Na_2SO_4$ ) and sodium vanadates of various compositions, as shown in Tables 14 and 15. From [33], the melting temperatures of the  $V_2O_5 - Na_2SO_4$  mixtures can be

**Table 16 Distribution of ash particles in a fuel oil<sup>1</sup>**

Diameter, $\mu$	Catalyst Particles			Carbon-Like Particles		
	Centrifuging		Removal Efficiency, %	Centrifuging		Removal Efficiency, %
	Before	After		Before	After	
>20	1,020	20	98.0	750	0	100
10-20	885	90	89.8	4,360	205	95.3
7.5-10	885	20	97.7	17,320	705	95.9
5.0-7.5	-	-	-	23,300	1,200	94.8
2.5-5.0	-	-	-	49,500	11,500	76.8

<sup>1</sup>Reference (42).

**Table 17 Fuel ash composition**

	Total Ash, Wt %	SiO <sub>2</sub> , mg/kg	Al <sub>2</sub> O <sub>3</sub> , mg/kg
Before Centrifuging	0.0491	206	34
After Centrifuging	0.0385	114	17

<sup>1</sup>Reference (42).

as low as 300°C, as shown in Fig. 20. These liquid salts dissolve protective oxides on the exhaust valve alloy surfaces and cause accelerated corrosion and degradation of the valve materials [36]. An extensive study of the effect of high-temperature corrosion on exhaust valves and the characterization of the valve face deposits is reported by Kvernes et al. [37]. Deposits were found to have two layers. The inner layer is enriched in vanadates and the outer layer in sodium sulfate. Exhaust valve degradation generally starts on the valve seats, and the following factors are involved in the formation of blow-through channels:

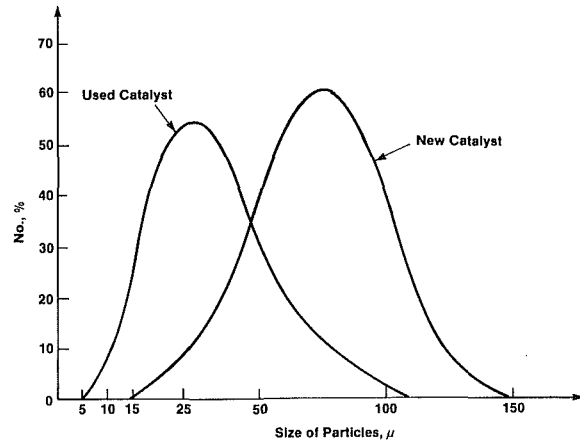
- Mechanically formed dents on the valve seat
- Partial spalling of salt layers on the valve seats
- Corrosion on the valve seat

To minimize the risk of high-temperature corrosion, engines operating on residual fuels usually have cooled exhaust valve seats [39, 40] and sufficient excess charge air to keep valve face temperatures below 450°C.

Valves can have rotators fitted and use alloy steel materials like Nimonic 80A or Deloro Alloy 60-type materials. Many designs use plasma-coating technology to further extend valve life.

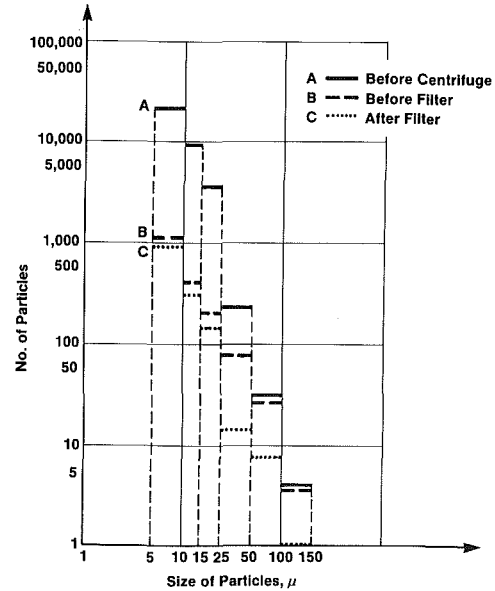
Engine builders limit the level of vanadium and the ratio of vanadium to sodium in the residual fuels suitable for use in medium-speed engines, as shown in Table 11. The current CIMAC and British Standards MA 100 1982 and the proposed ISO standards separate residual fuels by vanadium level, in addition to parameters like viscosity, density, sulfur, Conradson carbon, etc., as shown in Tables 6 and 8.

**Sulfur.** The sulfur element in the fuel oxidizes during the combustion process to form SO<sub>2</sub> and SO<sub>3</sub>. With the water present from combustion, sulfuric acid (H<sub>2</sub>SO<sub>4</sub>) can form if the vapors fall below the acid dew point, 140–190°C, range [14, 15]. The dew point depends upon fuel sulfur level and combustion gas pressure, as shown in Fig. 7 from Belcher [14]. Low-temperature corrosion occurs on the cylinder liners, piston rings, and piston grooves. For cylinder liners, the temperature from the top ring zone falls rapidly in the areas not exposed to the radiant flame of combustion, temperatures can fall to 160–120°C range. Fortunately, the combustion pressure also falls rapidly, resulting in the temperature remaining above the local dew point [14, 15]. Experience



Source: Ref. (30) Bontour M. and Chapuy J. F.

**Fig. 24 Size distribution of catalyst powder (Si and Al)**



Source: Ref. (30) Bontour M. and Chapuy J. F.

**Fig. 25 Treatment of slurry with centrifuge and filter**

shows cylinder liners usually wear in the area of top ring reversal due to corrosion/abrasion/adhesive wear. Increasing the sulfur level usually results in increased wear, as shown in Figs. 21–23 from our studies on residual fuels. Part II of this paper discusses how the selection of suitable lubricants can control most of the wear, particularly by the choice of suitably high alkaline (TBN) lubricants.

**Catalytic Fines.** Residual, or blended, fuels containing any abrasive material, naturally occurring or as catalyst fines may cause increased wear in medium-speed diesel engines, depending upon the engine, concentration, size, and abrasiveness of the particles. Pratt [41] has shown that particles as small as  $3 \mu$  can embed in the piston ring surfaces and lead to piston ring scuffing. Other engine builders [30] have reported damage affecting injection pump plungers, injector orifices, cylinder liner wear, and piston ring wear.

The catalyst fines come from the residuum of the FCC unit of a refinery. A refiner may blend this residuum, also called FCC bottoms or slurry, in the residual fuel meant for boilers. Only by accident would it get into diesel intermediate fuels. The concentration of catalyst fines in the FCC bottoms and the quantity blended would determine the amount of catalyst fines in the residual fuel. FCC units use fine-powdered, alumina-silica based catalysts. The particles are about  $75\text{-}\mu$  dia for new catalyst [2]. They, however, reduce in size after recovery and reuse. There is no fixed size distribution. One example is shown in Fig. 24 from Bontour [30].

It is difficult to measure the catalyst fines in a fuel. There is no recognized test method. The concentration of aluminum in the fuel ash cannot truly represent the presence of catalyst fines, as aluminum can originate from naturally occurring or foreign impurities and the catalysts can differ in composition. A debate is going on regarding the validity of a numerical value of 30 ppm of aluminum, maximum, indicated in the proposed ISO, CIMAC, and BS MA 100 1982 specifications, to minimize the risk of abrasive wear from catalyst fines in the absence of a standard test method. Table 11 shows some engine builder precautionary guidelines in respect of maximum aluminum or aluminum-silica content.

Centrifuging of residual fuels, is an essential step to reduce the concentration of abrasive impurities. Work [30, 42, 43, 44] by engine builders and centrifuge manufacturers has shown that the bulk of catalyst fines can be removed by centrifugal separation with high separation efficiencies under proper operating conditions. Tables 16 and 17, from work reported by Endo [42], give an example of removal efficiencies of catalyst particles using a centrifuge. The advantage of combining a centrifuge operating at 10 percent capacity and a filter to reduce catalyst fines is shown in Fig. 25. The data are significant in the  $5\text{-}25 \mu$  range, where a large number of particles were present.

**Lubricants.** The ability of a medium-speed diesel engine to burn residual and blended fuels is closely associated with the selection of a suitable lubricant to control wear and deposits [45, 46]. Part II of this paper will discuss these lubricants and their characteristics together with performance in engines and in purification equipment.

## Conclusions

Medium-speed diesel engines of 200–350 mm cylinder bore operating at 600–1200 rpm design speeds are available to operate on blended or intermediate residual fuels.

For operation on intermediate residual fuels, engines must have facilities to heat the fuel, purify the fuel, and keep fuel bunkers separated to a void fuel incompatibility problems. Engine designs for operation on these fuels include components to resist the high-temperature corrosion of the fuel impurities, vanadium and sodium, which occurs above  $450^\circ\text{C}$ . These engines must maintain sufficiently high temperatures (above  $160\text{-}190^\circ\text{C}$ ) of cylinder liner walls, piston, and piston rings to minimize low-temperature corrosion from the fuel sulfur. For good atomization of these fuels, injection pressures must be sufficiently high to ensure droplet sizes below  $20 \mu$  and the inlet charge air to the cylinders may have to be heated to above  $40^\circ\text{C}$  to avoid ignition delay at part-load conditions.

Our work shows that the relative ignition quality of intermediate residual fuels can be ranked by a modified ASTM D 613 method or estimated from the fuel density and viscosity values. We also found that ignition quality of fuels can affect the fuel consumption of the engine at light-load conditions.

Our studies on blended fuels and intermediate residual fuels indicate higher quality lubricants are needed to combat the potential for increased wear relative to ASTM No. 2 fuel. Part II discusses these lubricants.

## Acknowledgment

The authors wish to thank the management of Chevron Chemical Company, Chevron Central Laboratories, Chevron U.S.A., Chevron International Oil Company, and Chevron Research Company for permission to publish this paper.

They also wish to thank the staff of Chevron Central Laboratories who carried out most of the work on residual fuel evaluations and developed the modified ASTM 613 procedures to evaluate residual fuel ignition qualities and the staff of Chevron Research Company and Chevron Chemical Company and affiliates, Orobis Limited, Orogil S.A., Aditivos Mexicanos S.A., Karonite Chemical Company, and Nomura Jimusho Inc. who contributed much of the work described in this paper.

## References

- 1 Voisard, O., "Money and Ships," (Extract Commentary, the Motor Ship), London Sea Trade Conference, London, May 1983.
- 2 Casale, P. G., Davidson, D., Graham, M., and Thompson, R. H., "Some Considerations on Marine Residual Fuels," Institute of Marine Engineers, London, Nov. 1982.
- 3 "Marine Fuel Oils, Specifications Working Group of Subcommittee, Classifications and Specifications," ISO Technical Committee, ISO/TC 28/SG 4, Petroleum Products and Lubricants, June 1983.
- 4 Henshall, S. H., "Medium- and High-Speed Diesel Engines for Marine Use," The Institute of Marine Engineers, London, 1972.
- 5 Stikei, G., "Hoátadá És Hóterhelé Belsoégésu Motordkban," Akadémiai Kiadó, Budapest, 1962; (English translation: "Heat Transfer and Thermal Loading in Internal Combustion Engines").
- 6 "Longer Stroke PA6 from Pielstick Cuts Speed at 750 rpm," *Marine Engineers Review*, Jan. 1983.
- 7 "Long Stroke Diesel Series Developed, MWM," *Diesel and Gas Turbine Worldwide*, Jan.-Feb. 1983.
- 8 Drei, V., "B-230 Engine: Research and Experiments for Widening the Speed and Output Range for Utilizing Alternative Fuels," CIMAC Paper D 7.2, 1983.
- 9 Paro, D., and Liljenfeldt, G., "Injection Equipment for a 900-1000 rpm Heavy Fuel Engine," CIMAC Paper D 16, 1981.
- 10 Herzog, P., and Stipek, T. H., "Studies on Heavy Fuel Operated Injection Pumps," CIMAC Paper D 11, 1981.
- 11 Little, C. M. D., and Scott, P. F., "An Electronically Controlled High Pressure Fuel Injection System for Improved Performance of Medium-Speed Engines," CIMAC Paper D 33, 1981.
- 12 Travaille, J., and Munro, R., "Diesel Engine Piston Design for Fuel Economy and Reliability Improvements," ASME Paper 83-DGEP-7, Oct. 1983.
- 13 Reipert, P., Moebus, H., and Schellmann, K., "Computer Design of a Steel-Nodular Cast Iron Piston Capable of Withstanding High Loads for Application in Medium-Speed Diesel Engines," ASME Paper 83-DGEP-8, Oct. 1983.
- 14 Belcher, P. R., "The Function of Lube Oil in Fighting Corrosion in Medium-Speed Engines," *Marine Engineers Review*, London, Apr. 1983.
- 15 Simonetti, G., "Forty Years Experience in the Lubrication of Large and Medium Bore Diesel Engines Operating on Boiler Oil," ASLE, Summer Meeting, 1966.
- 16 Royle, D., (Det Norske Veritas), "A Review of the Quality of Residual Fuels Supplied to Motorships Worldwide," Paper 39, *Trans. I Mar. E.*, (TM), Vol. 95, 1983.
- 17 Harris, J. W., "Association of American Railroad Alternate Fuel Program, Fuel Committee Status," AAR Report, Mar. 9, 1983.
- 18 Sefer, N. R., and Baker, Q. A., "Characterization of Residual Fuels and Their Blends with Railroad Diesel Fuel," ASME Paper 83-DGP-6, 1983.
- 19 Jackson, D. R., and Blevins, W. G., "Possibilities for Locomotive Diesel Fuels—A Railway Overview," ASME Paper 83-DGEP-3, Oct. 1983.
- 20 McConnell, G., and Nathan, W. S., "A Wear Theory for Low Speed Diesel Engines Burning Residual Fuel," *Wear*, Vol. 5, 1962, pp. 43-54.
- 21 Syassen, O., "Adapting Medium-Speed Engines to Future Fuel Qualities," *Diesel and Gas Turbine Worldwide*, Nov. 1981.

- 22 Van der Horst, G. W., Sundermeijer, J. J. H., and Hold, G. E., "The Impact of Changing Fuel Characteristics on Marine Diesel Engine Operation," CIMAC Paper D 102, 1981.
- 23 Van der Horst, G. W., and Hold, G. E., "Diesel Engine Lubrication with Poor Quality Residual Fuels," ASME Paper 83-DGP-11, 1983.
- 24 Seth, B. N., and Clark, G. H., "Lubricants for Medium-Speed Trunk Piston Diesel Engines Operating on Distillate and Residual Fuels," Diesel Engine and Users Association, London, Oct. 1968.
- 25 Hafner, R., "High Economy Four-Stroke Engines—Approaches to Heavy Fuel Oil Compatibility, Low Consumption Rates, and High Reliability," CIMAC Paper D 9.3, 1983.
- 26 Hold, G. E., and Van der Horst, G. W., "Effects of Fuel Characteristics on Marine Diesel Engine Operation," Japan Society of Lubrication Engineers, Tokyo, Nov. 1980.
- 27 Zeelenberg, A. P., Fijn Van Draat, H. J., and Barker, H. L., "The Ignition Performance of Fuel Oils in Marine Diesel Engines," CIMAC Paper D 13.2, 1983.
- 28 Daugas, C. F., and Bastenhof, D., "Combustion of Future Residual Fuels and New Fuels in a Four-Stroke, Medium-Speed Engine," CIMAC Paper D 92, 1981.
- 29 Notermans, J. J. A., "Internal Chevron Central Laboratories Report No. 283 Marine Fuels Study, Physical, Chemical, and Combustion Properties," July 1982.
- 30 Bontour, M., and Chapuy, J. F., "Contribution to the Treatment of Low-Grade Fuel Oils and Evaluation of Their Influence on Engine Wear," CIMAC Paper D 6.1, 1983.
- 31 "Alfa-Laval Breaks 991 Density Barrier with ALCAP Centrifugal Separator," *The Motorship*, July 1983, pp. 41-42.
- 32 "A Self-Thinking Fuel Treatment System," *The Motorship*, Aug. 1983, pp. 32, 46.
- 33 "Corrosion in Diesel Engines Operating with Residual Fuel," *Gas and Oil Power*, June 1969, pp. 130-133.
- 34 Tipler, W., "Fuel Oil Ash Deposition and Corrosion in Steam Boilers," Shell OPD Report No. 206/62M, 1962.
- 35 Ishigai, S., Nishikawa, E., and Yamauchi, S., "Study of Gas-Side Fouling of Oil-Fired Boilers by Means of Controlled Temperature Tubes in a Test Furnace," *Bulletin of the MESJ*, Vol. 3, No. 1, Mar. 1975.
- 36 Henry, A., and Lees, D. J., "Corrosion of Austenitic Steels in Molten Sulfate Deposits," *Corrosion Science* 20, 1980, pp. 405-412.
- 37 Kvernes, I., Kofstad, P., Seirsten, M., "High-Temperature Corrosion and Protection of Diesel Engine Exhaust Valves," CIMAC Paper D 101, 1981.
- 38 Fiedler, H., Groth, K., and Hesse, A., "Investigations on High-Temperature Corrosion of Exhaust Valves and on Combustion of High Viscosity Residual Fuels in Medium-Speed, Four Stroke Diesel Engines," CIMAC Paper D 69/70, 1981.
- 39 Olsson, I., Thorn, L. E., and Lundin, A., "Development of a Heavy Fuel Version of the Nohab F-Type Medium-Speed Engine," CIMAC Paper D 105, 1981.
- 40 Eckert, B. O., "Service Experience with Z-40-Type Medium-Speed Engines Running on Heavy Fuel Oils and Related Design Aspects for the ZA-40 Engine," CIMAC Paper D 2.3, 1983.
- 41 Pratt, T. N., "The EMD 645 Engine and Blended Fuels," Maritime America '83 Conference, Mar. 1983.
- 42 Endo, T., Murakami, S., Nagita, Y., and Obara, T., "Combustion Tests of Low Grade Fuel Oils on a Medium-Speed Diesel Engine," *Journal of Marine Engineering Society of Japan*, Vol. 15, No. 2; Translation in *Bulletin of the MESJ*, Vol. 8, No. 4, 1980.
- 43 Van Shultz, B., "Separation of Particles from Marine Heavy Fuel Oil," Fourth International Marine Propulsion Conference, London, Mar. 1982.
- 44 Giffin, K., and Loodenkemper, F. J., "Centrifugal Separation," Fourth International Marine Propulsion Conference, London, Mar. 1982.
- 45 Thomas, F. J., and Hold, G. E., "Modern Marine Diesel Engine Lubricants and Their Development," ASME Paper 80-DGP-10, Feb. 1980.
- 46 Van der Horst, G. W., Polman, J., and Sundermeijer, J. J. H., "Improved Wear and Deposit Control in Medium-Speed Marine Diesel Engines," Euorport 1973 Conference, Amsterdam, Institute of Marine Engineers (United Kingdom), Nov. 1973.
- 47 Von Schnurbein, E., and Bucker, J., "Experience with the Rating and Operation of Medium-Speed, Four-Stroke Engines Under Extreme Site Conditions," CIMAC Paper D 64, 1981.

F. J. Thomas  
J. S. Ahluwalia  
E. Shamah

Chevron Research Company,  
Richmond, Calif. 94802

G. W. van der Horst  
Chevron Central Laboratories,  
Rotterdam, The Netherlands

## Medium-Speed Diesel Engines: Part II—Lubricants, Their Characteristics and Evaluation

*Fuel costs can exceed 50 percent of the total diesel plant's operational expenditures. To reduce fuel costs, medium-speed engines are now available with improved fuel consumption and ability to burn residual fuels. Part II of this paper reviews characteristics of lubricants suitable for use with distillate, residual, and blended fuels in medium-speed engines. Examples are shown of how lubricants and their additives control engine wear, deposits, and oxidation, and how fuel consumption is affected by viscosity. Control of insolubles and the purification of used lubricants are discussed.*

### Introduction

Lubricants for the medium-speed diesel engines of 600–1200 rpm and 200–350-mm bore dia, discussed in Part I, must be carefully selected depending upon fuel used, type of service, and the system used for oil purification and oil replacement. Due to the wide range of designs, ratings, service application, and fuel used, there is no simple system for oil classification like the widely used API system of CD and CC lubricants. Lubricants for medium-speed diesel engines must be developed by cooperation between the oil industry, additive suppliers, and engine builders. This requires screening lubricants in a wide range of bench tests for oxidation control, volatility, EP performance, rust, foaming, water tolerance, demulsibility, bearing metal corrosion, etc. Performance in laboratory diesel engines using distillate, blended, or residual fuels is normally the next stage of evaluation. In order to interpret the bench and engine tests, it is necessary to know the performance in the particular screening test of good and poor reference lubricants selected from current or previous field test experience. Table 18 summarizes some of the tests we have developed and are using to evaluate medium-speed diesel lubricants.

This paper discusses the important characteristics required in a lubricant and how the additives and base stock components are balanced to impart the required characteristics. It is shown, dependent upon the fuel used, service operation, and lubricant purification system, that different lubricants should be utilized for optimized plant operation and engine durability. The wide variety of lubricant characteristics requires a careful balance among the constituents of the formulated lubricant to ensure satisfactory service results.

Figure 26 shows how the lubricant systems of medium-speed diesel engines can be divided into various categories. The total oil charge system usually lies between 0.3–1.4 L of oil per kilowatt of power. The higher ratios generally relate to

the larger engines of above 3500 kW, which usually use a dry sump and purify the oil by a centrifuge with three to five full lubricant passes in a 24-hr period; the flow rate for modern detergent/dispersant/inhibitor lubricants through the centrifuge is recommended at about 1/5–1/3 of the centrifuge maximum capacity rating. Smaller engines usually have a wet-sump system relying upon filters to purify the used oil or utilize a centrifuge on a bypass basis to extend oil life.

The oil life depends upon the lubricant system. However, the oil consumption rate is a major factor which must be considered in estimating the lubricant life. Fresh oil makeup renews the additives circulating in the system. It is possible today, with oil consumption rates of 0.4–0.7 percent of the fuel consumption rate and the appropriate lubricant, to have, for example, an oil life of two years in North America railroad service using distillate fuels of <0.5 percent sulfur content. Most earlier drains in such service are due to contamination from coolant or fuel dilution.

Table 19 summarizes the fuel and lubricant systems for medium-speed diesel engines using either distillate, blended distillate with residual, or residual fuels. The fuel systems were described in Part I; the lubricant properties and how lubricants and their additives are evaluated will be discussed below.

### Lubricant Properties

A basic function of the lubricant is to lubricate the moving parts of the engine and carry away the heat generated by friction. In addition, a lubricant must have properties to provide:

- Adequate viscosity
- Oxidation resistance
- Bearing corrosion protection
- Volatility control
- Wear protection
- Engine deposit control
- Efficient water separation
- Efficient filtration

Contributed by the Diesel and Gas Engine Power Division and presented at the Energy Sources Technology Conference and Exhibition, New Orleans, Louisiana, February 12–16, 1984. Manuscript received by the Diesel and Gas Engine Power Division December 5, 1983. Paper No. 84-DGP-17.

**Table 18 Summary of tests used by Chevron to evaluate medium-speed diesel engine lubricants**

Chevron Procedure Number	Test	Brief Description
B 12-2/3	Cyclic Panel Coker Test	315°C, 5 Hr and 24 Hr
B 16	Rust Test	60°C, 24 Hr, ASTM D 665 Test
B 17	Soda Four-Ball Wear Test	NDS XXK 2740 Step-Load Method
B 18	Oxidation Test	165.5°C, 48 Hr, JIS K 2514 Test
B 19	Bearing Corrosion Test	140°C, 100 Hr, Mirreles Test
B 20	Centrifuge Demulsibility Test	60°C, 5 Hr, Water Separation Test
B 21	Centrifuge Hydrolytic Stability Test	60°C, 3 Hr, Emulsification/TBN Retention
B 21	Oxidation Test	200°C, 30 Hr, Modified IP 48 Test
B 29	Electron Photomicrography	2500X and 10,000X Lubricant Particle Dispersion
B 37-1	Oxidation Test	Proprietary Oxygen Absorption Test, 171°C
B 52-1	High Speed Insolubles Test	Insolubles Determination
B 10-1	Filter Blockage Test	
D 7	Two-Stroke, 1.0% Sulfur Fuel Test	Oxidation and TBN Loss
D 17	Four-Stroke, 1.0% Sulfur Fuel Test	Deposits, Oxidation, TBN Loss
D 18-3D	Two-Stroke, 2.5% Sulfur Fuel* Test	Wear, Deposits
D 20	Four-Stroke, 2.5% Sulfur Fuel* Test	Deposits and Wear Test
D 32	Four-Stroke, 0-4% Sulfur Fuel Test	TBN Loss, Oxidation, and Wear Test
G 18-1	Four-Stroke, Leaded Gasoline	Copper-Lead Corrosion and Oxidation Test

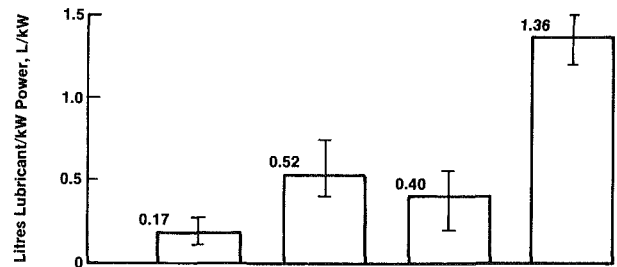
\*Residual fuel.

### Viscosity

Viscosity must remain reasonably constant if an engine is to function satisfactory. Too high a viscosity from oxidation of the lubricant or from the thickening effect of combustion insolubles can cause problems; and if periodic shutdowns occur, bearing oil starvation and/or filter plugging can occur. Lubricants are designed to be within a specific viscosity grade, defined by SAE J300, September 1980 standards, shown in Table 20. Most medium-speed engines use SAE 30 or SAE 40 oils, although a recent survey [48] indicated 79 percent of the engine builders favored a SAE 35-type lubricant of 12-13 cSt/100°C, if this grade were available. Too low a viscosity can lead to excess wear due to operation in the boundary region depicted in Fig. 27 and too high a viscosity can lead to increased fuel consumption. Viscosity influences the startability, particularly in low temperature climates such as in Canada, Northern Europe, and Russia. Multigrade SAE 20W-40 lubricants are under evaluation in railroad service where prolonged idling periods (up to 72 hr) exist, as in Canada. Our co-workers show that these type of lubricants give improved fuel consumption [49], particularly at light load conditions, improved oil consumption over SAE 30 grade oils, and improved low-temperature starting.

**Fuel Consumption and Lubricant Viscosity.** The lubricant viscosity can influence the fuel consumption of the engine. The lower the viscosity, the lower the viscous drag of the lubricant between moving parts. However, there is a critical viscosity below which hydrodynamic and

Diesel Engine	High Speed	Medium Speed		
		<5000	<3500	>3500
Power, kW	<700	Railroad	Marine	Marine
Service	Trucks and Industrial			
Sump Type	Wet	Wet	Wet	Dry
Filtration of Lubricant	Spin-on Filters	Candle Filters	Filters and Centrifuge in By-Pass	Centrifuge 3 to 5 Passes Per 24 Hr
Oil Life, Hr	100 to 500	2,000 to 8,000	2,000 to 16,000	10,000 to 24,000



**Fig. 26 Lubricant system of medium-speed engines capacity ratio (L/kW)**

semihydrodynamic lubrication changes to boundary lubrication and metal-to-metal contact can occur, which leads to increased friction, scuffing, and possible engine seizure. To study this region [50], we used a two-stroke, 190-mm bore

### Nomenclature

$C_m$ = mean piston speed, Meter/Second	$P_z$ = maximum combustion pressure, Bar	$TBN_0$ = lubricant initial total base number (TBN), ASTM D 2896, mg KOH/g oil
$K_I$ = constant, dependent upon the engine combustion system and service conditions	$Q$ = lubricant system total quantity, kg	$TBN_t$ = lubricant total base number (TBN) at time $t$ , ASTM D 2896, mg KOH/g oil
$K_T$ = constant, dependent upon the engine combustion system and rate of neutralization of the lubricant	$R$ = lubricant consumption, G/kW-hr	$b_e$ = effective specific fuel consumption, g/kWh
$P_i$ = engine power output, kW	$S$ = percent mass of sulfur in fuel	$t$ = time, hr
	$T_R$ = average temperature value of the cylinder liner at the top position ring reversal (TDC) and the temperature of the first piston ring groove face, °C	$x_t$ = percent mass, insolubles at time $t$
		$x_0$ = percent mass, insolubles at time $t=0$
		$x_{max}$ = percent mass, maximum insolubles

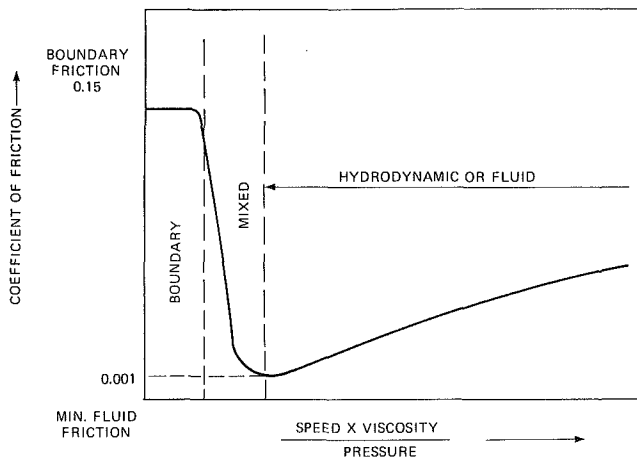
**Table 19 Fuel and lubricant systems for medium-speed diesel engines using various fuels**

Fuel	Distillate	Blended (Distillate Plus Residual)		Heavy (Residuum Plus Cutter Stock)
Application				
Railroad	x	x		
Industrial	x	x		x
Inland Marine	x	x		x
Marine	x	x		x
Insolubles Control	Low	Medium		High
Insolubles Level				
Fuel System	No	Yes		Yes
Dual Fuel	No	Yes		Yes
Fuel Purification		Centrifuge Residual		Centrifuge
Installation				
Heat Intake Air at Part Load	No	Yes		Yes
Lube System	Small Sump Short Drain	Small Sump Short Drain	Large Sump Long Drain	Large Sump Long Drain
Water Contamination Risk	Low	Low	Moderate to High	High
Lube Purification	Filter	Filter	Centrifuge and Filter	Centrifuge and Filter
Lube Quality				
Detergent/Dispersant	High	High	Moderate	Moderate
Emulsion Resistance	-	-	Important	Important
Water Shedding	-	-	Important	Important
Wear Control				
Corrosion				
Low Temperature	Low	Medium		High
Fuel Sulfur, % Mass	<0.5	<1.8		<4.0
Lube Quality, TBN (ASTM D 2896)	10-15	15-30		20-40
Adhesive/Abrasive Wear				
Fuel Purification, Sludge/Catalyst Pines	No	No	Yes	Yes
Lube Quality			Centrifuge	Centrifuge
Antiwear/EP Additive	Yes	Yes		Yes
Corrosion				
High Temperature	No	Low		Low
Engine Design-Metallurgy	Standard	Standard		High
Engine Operation	Standard	Standard		Special Design
Lube Quality	Not Important	Not Important		Below Stiction Temperature
				Not Important

**Table 20 Engine oil viscosity classification, SAE J300 Sept. 1980**

High Temperature Kinematic Viscosity, cSt at 100°C	ASTM Method	SAE Viscosity Number									
		0W	5W	10W	15W	20W	25W	20	30	40	50
Min.	D 445	3.8	3.8	4.1	5.6	5.6	9.3	5.6	9.3	12.5	16.3
Max.	D 445	NR	NR	NR	NR	NR	NR	<9.3	<12.5	<16.3	<21.9
Low Temperature Absolute Viscosity, CP Temperature, °C	D 2602	3250	3500	3500	3500	4500	6000	NR	NR	NR	NR
Borderline Pumpability, Maximum Temperature, °C	D 3829	-30	-25	-20	-15	-10	-5	NR	NR	NR	NR
		-35	-30	-25	-20	-15	-10	NR	NR	NR	NR

NR = not required.  
Multigrade oils based on individual low temperature and high temperature specifications.



**Fig. 27 Types of lubrication**

where this engine would move into the critical region of boundary lubrication, the viscosity of the lubricant was varied from 270 to 20 cSt at 50°C, as shown in Fig. 28. The shape of this curve is similar to that in Fig. 27, which is the classical Stribeck curve used to illustrate types of lubrication regions, suggesting that specific fuel consumption and the coefficient of friction are directly related.

To improve the fuel consumption of an engine by choice of a lubricant, the effect of base stock components, V.I. improvers, and friction modifiers have been studied in diesel engines by our co-workers [49, 51]. Wall [51] confirmed the fuel consumption relationship to viscosity and showed for non-Newtonian multigrade lubricants, which contain viscosity index improvers, that high-shear-stress, hydrodynamic viscosity must be measured to correctly rank these lubricants on a Newtonian scale. This is due to the temporary shear, which results from the use of V.I. improver additives in multigrade oils [52, 53, 54].

The effect of friction reduction by either viscosity reduction or surface friction modifiers is most pronounced at part-load conditions.

Our work on lubricant effects on fuel consumption in a medium-speed, 16-cylinder, 230-mm-bore two-stroke engine has been reported by Logan [49]. Figure 29 shows the effect of a multigrade SAE 20W-40 lubricant relative to a SAE 40

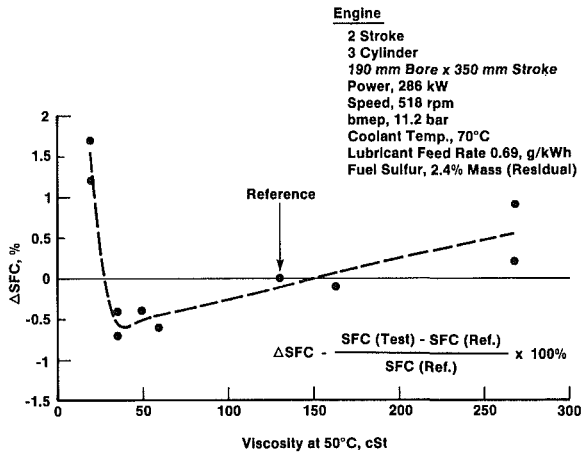
engine which normally operates at 518 rpm engine speed at a bmp of 11.2 bar under the Chevron D 18-3DA procedure summarized in Table 21. This engine has separate cylinder quill lubricators, which allow control of the quantity of lubricant to the piston ring zone. To establish the region



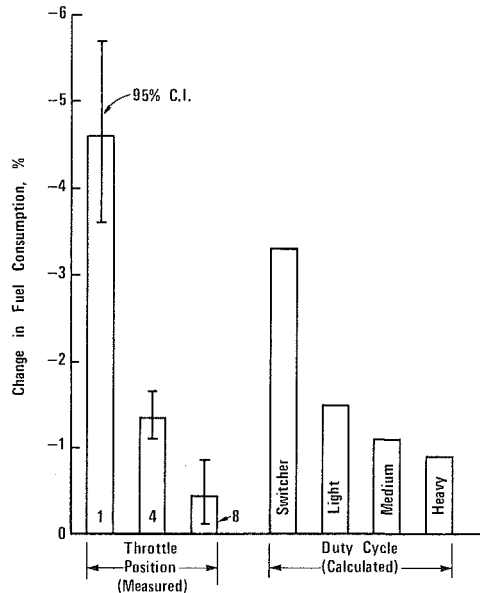
**Table 21 Laboratory test procedures**

Procedure	D 7	D 18-3DA	D 17	D 32	D 20	D 20-1
Engine	Two Stroke		Four Stroke			
Number of Cylinders	3	3	1	1	1	1
Bore, mm	114.3	190	130.2	130.2	130.2	130.2
Stroke, mm	127	350	165.7	165.1	165.1	165.1
Test Duration, Hr	200	72	100	150	72	72
Power, kW	56	286	30.7	29.4	32.8	48
bmp, Bar	4.8	11.2	15.9	15.2	13.0	19.0
Speed, rpm	1800	518	1050	1050	1400	1400
Oil Temperature, °C	138	70	149	118	55	70
Coolant (Out) Temperature, °C	96	70	82	46	70	70

**Chevron Procedure D 18-3DA**



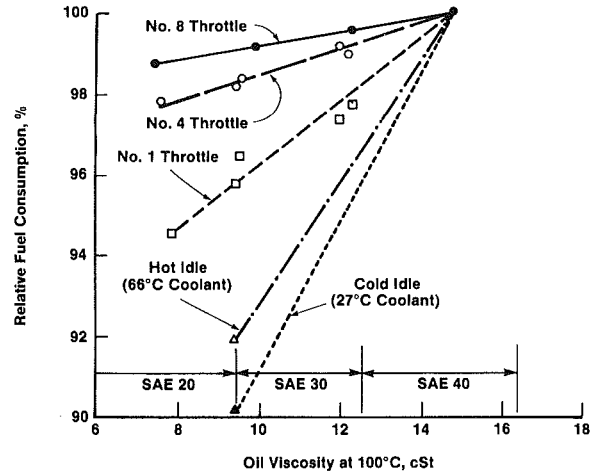
**Fig. 28 Fuel consumption versus lubricant viscosity**



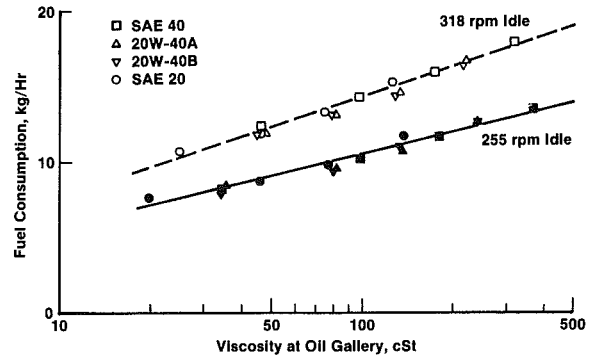
**Fig. 29 Fuel savings of SAE 20W-40 relative to MVI SAE 40**

grade lubricant on change in fuel consumption at various railroad engine throttle positions. Also shown are the estimated fuel savings (1-3 percent) for typical North American railroad duty cycles.

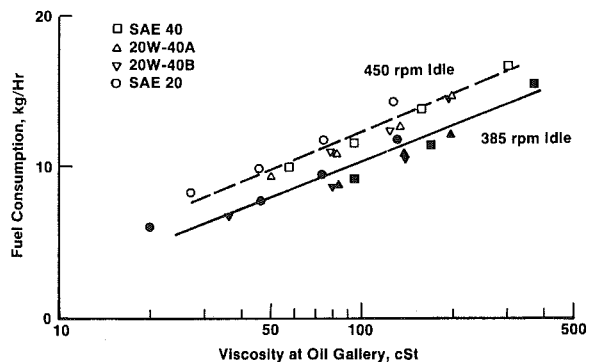
Our recent studies on the effects of lubricant viscosity on fuel consumption in a two-stroke, 230-mm bore engine are shown in Figs. 30 and 31. Figure 30 shows the viscosity effect is largest at cold idle, giving up to 10 percent fuel savings. The



**Fig. 30 Effect of lubricant viscosity on fuel consumption of two-cycle locomotive engine (230-mm bore x 254-mm stroke)**

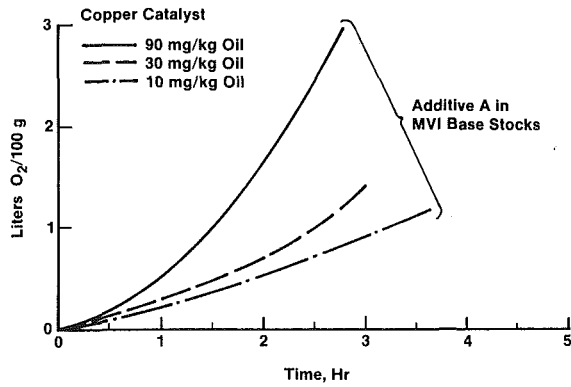


**Fig. 31 Effect of lubricant viscosity on fuel consumption at idle - two-cycle locomotive engine (230-mm bore x 254-mm stroke)**



**Fig. 32 Effect of lubricant viscosity on fuel consumption at idle - four-cycle locomotive engine (229-mm bore x 267-mm stroke)**

**Chevron Procedure B 37-1, Temperature 171°C**



**Fig. 33 Lubricant oxidation – effect of copper catalyst**

fuel consumption tests at idle in the above two-stroke engine were conducted at several engine coolant temperatures between 25°C and 70°C [55]. The results, plotted in Fig. 31, show that oil viscosity computed at the measured oil gallery temperature for the respective tests correlates with fuel consumption. This work was also repeated in a four-stroke, 229-mm-bore engine which gave similar results shown in Fig. 32. These figures also show the quantity of fuel saved at lower idling speeds.

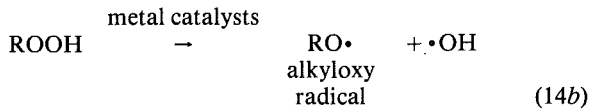
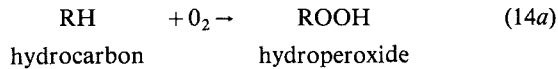
With the increasing combustion pressure of new fuel-efficient engine designs, selection of the engine oil viscosity will become more critical to ensure adequate bearing protection; and in the case of multigrade lubricants, the effect of temporary viscosity shear must be considered with caution.

**Oxidation Resistance**

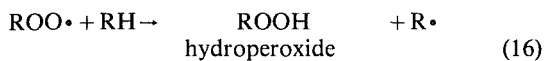
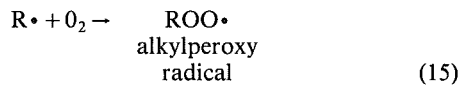
Oxidation takes place when a lubricating oil comes in contact with air (oxygen). This process becomes significant at temperatures above 80°C, particularly in the presence of used oil metals or oil decomposition products, which act as catalysts. The oxidation process leads to the formation of acidid corrosive compounds, varnish, and sludge deposits, and an increase in the viscosity of the lubricating oil.

Oxidation of hydrocarbon molecules of a lubricating oil is a free radical chain reaction. It can be represented by the following equations:

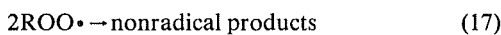
Initiation:



Propagation:



Termination:

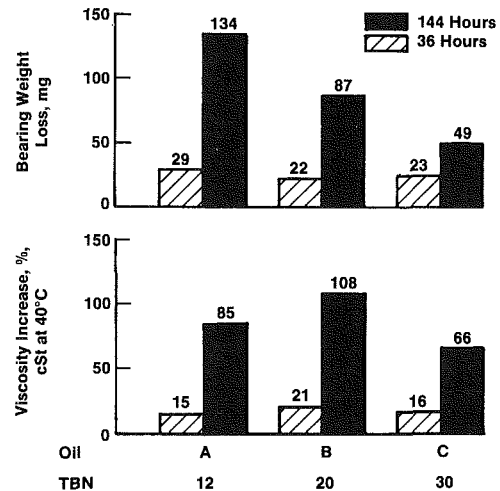


Decomposition of the hydroperoxides can lead to further free radical reactions which produce highly oxygenated hydrocarbons. These can agglomerate and drop out on engine surfaces, forming varnish and sludge deposits.

In order to keep engine deposit levels low and prevent oil

Bearing Material	Composition	New Specimen	Good Lubricant 25 TBN	Typical Failure
Copper-Lead	30% Lead 0.6% Max. Tin Balance Copper			
Phosphor-Bronze	10% Min. Tin 0.5% Min. Phosphorus 0.25% Max. Lead 0.05% Max. Zinc Balance Copper			
Aluminum-Tin	20% Tin 1.0% Copper 0.3% Max. Iron, Silicon, Other Balance Aluminum			
White Metal	8.5-10% Antimony 3.5-5.0% Copper 0.35% Max. Lead Balance Tin			

**Fig. 34 Mirreles bearing corrosion test, Chevron procedure B 19**



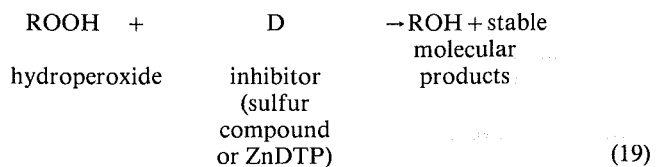
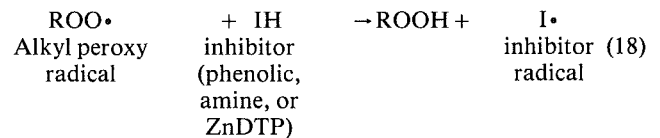
**Fig. 35 Copper-lead bearing corrosion and oxidation tests, Chevron procedure G 18-1, oil temperature 137°C**

viscosity increase, the foregoing processes must be interrupted at some point. Oxidation inhibitors are used to:

- Break the chain of free radical reactions
- Decompose hydroperoxides

Equation (14) depicts the initiation phase in the oxidation process. The catalyst may be copper or iron. Figure 33 shows an example of copper catalyst level effect on lubricant oxidation. The uptake of oxygen increases with the increase in copper concentration.

Typical oxidation inhibitors are zinc dialkyl-dithiophosphates, hindered phenols, and compounds of nitrogen and sulfur. Compounds like hindered phenols or amines are effective in breaking the peroxide chains (equation (18)), sulfur compounds decompose hydro-peroxides (equation (19)), zinc dithiophosphates are effective in both stages.



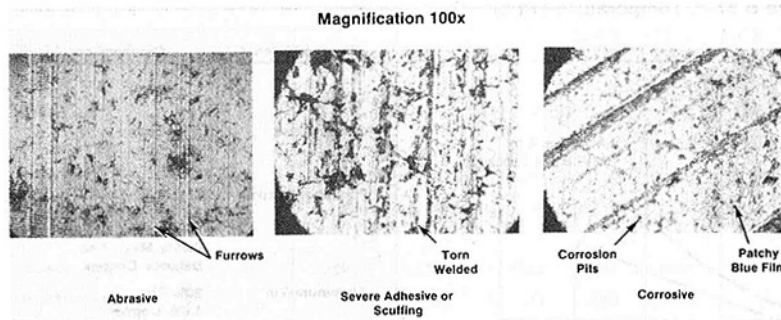
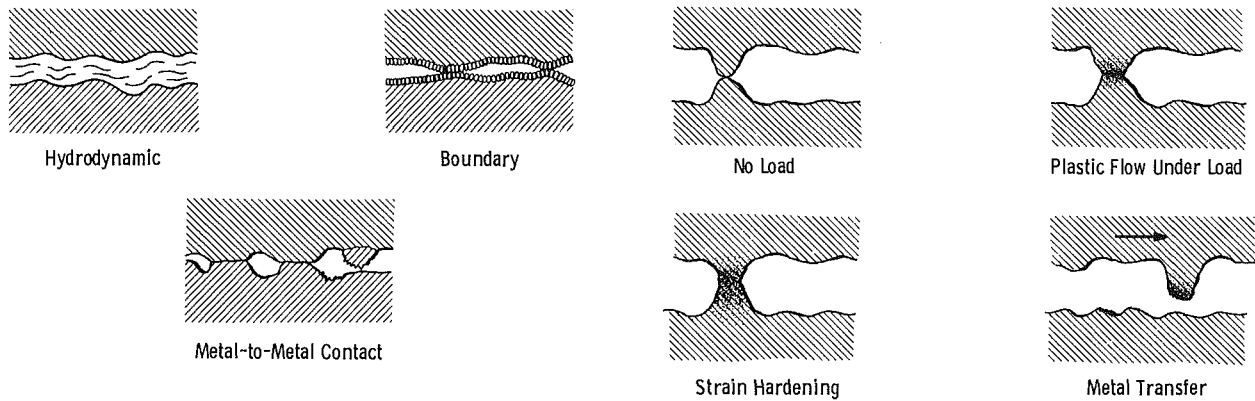


Fig. 36 Micrographs of used engine cylinder liners showing types of wear



If metal transfer severe, then scuffing or galling occurs.

Fig. 38 Wear metal transfer

With the increasing thermal ratings of new designs, the lubricant may be exposed to higher temperatures in the piston ring and piston undercrown zones. Higher temperature greatly accelerates the rate of oxidation. Lubricant oxidation is reflected by viscosity and acidity measurements of used oil. Oil viscosity may, however, be masked by insolubles from combustion products, which enter the crankcase and thicken the oil. Laboratory techniques are used to separate the insolubles effect, and differential infrared analysis at the  $5.8 \mu$  waveband can confirm the degree of oxidation.

### Bearing Corrosion Protection

The bearings of medium-speed diesel engines incorporate alloys of metals like copper, lead, tin, and aluminum. Acidic contaminants in the lubricating oil, primarily from oil oxidation and fuel combustion, attack these alloys. Reference [56] shows examples of bearing failures.

The inhibitors selected for bearing corrosion protection must be compatible with the nonferrous materials of the bearings. Inhibitors, like zinc dithiophosphates, are not compatible with bearings containing silver due to excessive silver sulfide corrosion reactions. Laboratory methods for lubricant performance with silver bearings are discussed by Bowman [57]. White metal bearings materials can suffer copper cuboid grain boundary attack with some inhibitors. Copper-lead bearings corrosion can be controlled by inhibitors like zinc dithiophosphates. It is therefore, necessary to run bench corrosion tests on bearing material or to run engine oxidation/bearing corrosion tests like the Petter WI test or the Labeco CLR L-38 test.

Figure 34 illustrates the effect of a good and a poor lubricant in a 100-hr Mirrlees bearing corrosion test using four bearing materials; copper-lead, phosphor-bronze, aluminum-tin, and white metal. The lubricant temperature is controlled at  $140^{\circ}\text{C}$ . Examples of engine evaluation of lubricants for copper-lead corrosion tendency by the modified Petter WI test (Chevron Procedure G18-1) are shown in Fig. 35.

### Volatility

Lubricants can have the same viscosity but, different volatility. This depends upon the distillation characteristics of the base stock components of the finished oil. A lubricant which has high volatility can give poor oil consumption. Keyworth [58] has reported on controlled turbocharged medium-speed, four-stroke, 400-mm-bore engine tests which demonstrates the relationship between oil volatility and oil consumption. Two SAE 30 oils gave oil consumptions of 0.67 g/kWh and 1.67 g/kWh; these oils at  $450^{\circ}\text{C}$  showed distillations of 4 and 30 percent, respectively. For future very highly rated high-speed and medium-speed engines, including semiadiabatic designs, hydrocarbon-type lubricants may not be satisfactory. Research is, therefore, active on synthetic and partial synthetic lubricants. A 12-TBN synthetic [58] medium-speed diesel engine oil has been evaluated successfully in some highly rated European four-stroke engines.

### Wear

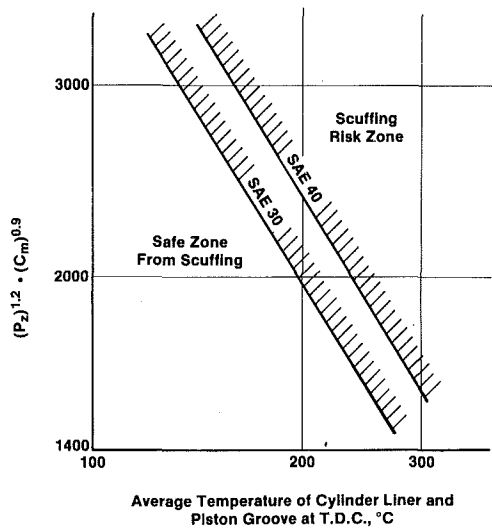
A diesel engine is subject to three types of wear [59] in the power assembly of the cylinder liner, piston, and piston rings:

- Adhesive Wear
- Abrasive Wear
- Corrosive Wear

Fig. 36 shows examples of the surface condition of cylinder liners resulting from these basic wear categories.

**Adhesive Wear.** The adhesive wear depends upon the type of lubrication conditions prevailing: hydrodynamic, boundary, or metal-to-metal contact as illustrated in Fig. 37.

Adhesive wear occurs due to metal transfer at junctions, as shown in Fig. 38, which depicts the metal transfer process from plastic flow and strain hardening to metal transfer.



Reference 63 Nakano et al.

Fig. 39 Scuffing criteria chart for four-stroke engines

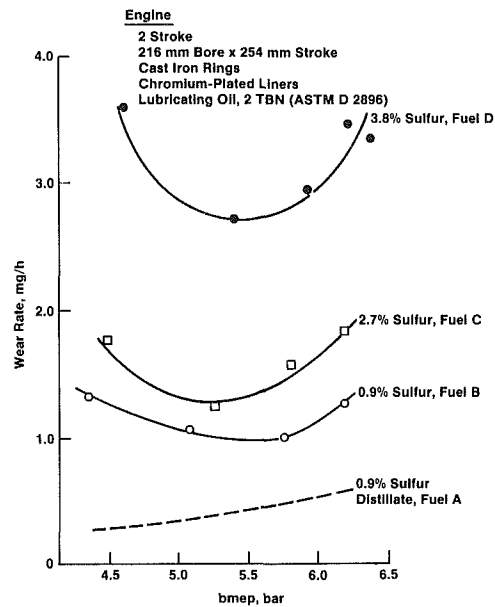


Fig. 41 Effect of BMEP on ring wear for several residual fuels

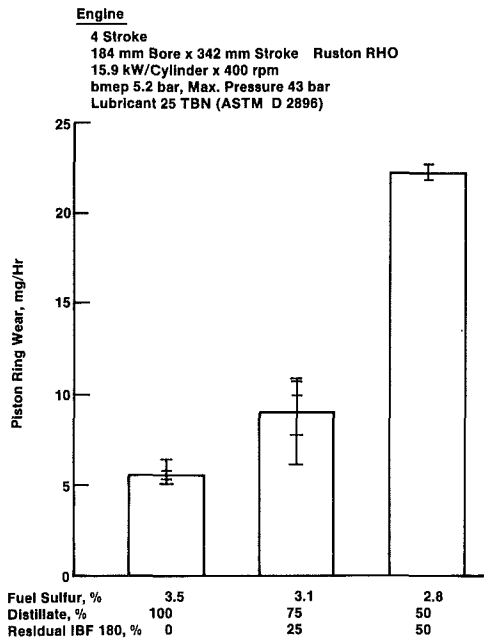


Fig. 40 Mixed fuel effect on piston ring wear

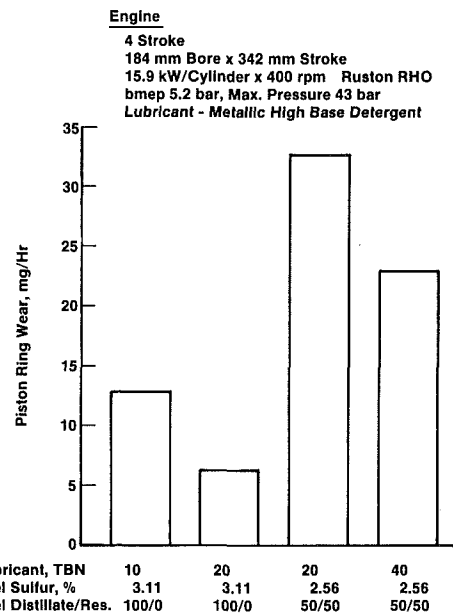


Fig. 42 Mixed fuel effect and lubricant alkalinity effect on piston ring wear

Extremely small oxide wear fragments can result from severe conditions of high pressures and temperatures where the lubricant film ruptures. Large metallic wear fragments also can form which can be loose or attached to the surface. These abrasive particles can lead to scuffing or galling.

From an engine designer's viewpoint, adhesive wear control, particularly scuffing, is very much a state-of-the-art progress with the engine being used as the final acceptance criteria of materials, design, surface finish, and lubricants. At higher ratings of bmep and piston speed, piston ring scuffing [60, 61] can become the limiting factor.

Willn [62], using a special test rig to study cylinder liner and ring scuffing, covered the influence of lubricants, materials, and surface finish on scuffing failure. Recently Nakano [63] expanded Willn's work and established a guide (Fig. 39) for scuffing using the following equation:

$$P_z^{1.2} C_m^{0.9} T_R = \text{constant} \quad (20)$$

Nakano [63] assumed the piston ring face pressure is proportional to the maximum cylinder combustion pressure

$P_z$ , and the oil film temperature  $T_R$  between the piston ring and cylinder liner to be related to the generation of scuffing. Unfortunately, insufficient information was known on the lubricants used in the engines which led to the development of Fig. 39. It is not possible, from this study, to separate lubricants by their additive and base stock characteristics.

Additives can provide improved boundary lubrication in zones where the mating metal surfaces are under very high loads and temperatures and where the oil has very low viscosity. These additives, known as antiwear/extreme pressure (EP) additives, can protect the metal surfaces by forming a coat of adsorbed, chemisorbed, or deposited molecules on them.

The risk of scuffing of piston ring/liner may increase for a given specific output (kW/L) in the new lower speed/longer bore-stroke engines with higher combustion pressures. Future lubricants may, therefore, need improved boundary lubrication as imparted by the antiwear/EP properties of

**Table 22 Radioactive locomotive engine wear study, 216-mm-bore engine**

Fuel	Distillate Fuel	Residual Fuel			
	A	B	C	D	
Reference					
Fuel Sulfur, % m	0.93	0.90	2.7	3.8	
Density, Kg m <sup>3</sup>	887.1	979.2	974.5	977.2	
Viscosity, cSt/37.8°C	2.56	131.2	58.1	46.2	
Conradson Carbon Residue	-	13.2	7.9	4.9	
Distillation, °C ASTM D 158					
1BP	207	202	177	197	
10%	242	243	223	271	
50%	258	370	353	351	
90%	284	-	-	-	
EP	318	-	-	-	
Calculated Carbon, Aromaticity Index <sup>1</sup>	767.5	944.2	928.5	927.7	

<sup>1</sup>See Equation (13), Part I.

additives in suitable base stocks. Zinc dithiophosphates, sulfurized olefins, chlorinated waxes, phosphates, amine salts of phosphate esters, and borates are some of the examples of antiwear/SP compounds. Keyworth [58] has also reported high ash oils to be beneficial for antiscuffing properties.

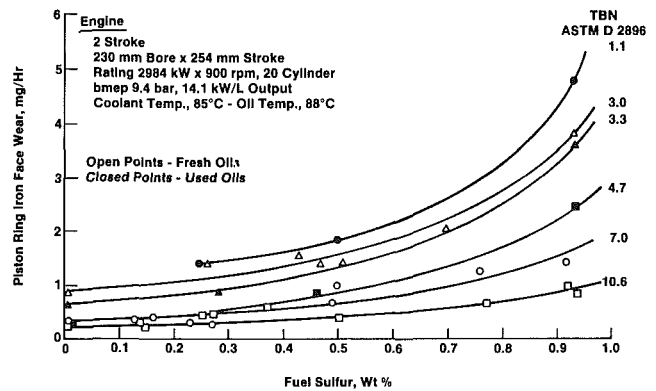
**Abrasive/Corrosive Wear.** Assuming that adhesive wear has been minimized by proper lubricant selection, the principal cause of piston ring and cylinder liner wear appears to be from the simultaneous action of corrosive compounds and abrasives on the moving parts. This is noted in engines when comparing residual or blended fuels with distillate fuels of the same fuel sulfur level, i.e., under similar corrosive wear risk conditions. Figures 40-42 show that wear with distillate fuels is lower than that with residual fuels at a constant fuel sulfur level.

Figure 40 shows how wear rates increase with residual fuel content in a blended fuel with fuel sulfur held in the range 2.8-3.5 percent mass. The cause of this increase wear for the same lubricant has not been satisfactorily explained due to the many variables complexed within each fuel which cannot be isolated.

Burtenshaw [64] suggested corrosive and abrasive wear using residual fuels were related to fuel sulfur, fuel ash, and fuel Conradson carbon residue. Our work reported by van der Horst [22, 23] and Hold [26] does not confirm this.

McConnell [20] proposed a hypothesis for abrasive wear. Tests on a used lubricant sample from an engine operated on residual fuel has shown it contained abrasive particles, which could scratch a metal surface having a hardness of 900 Vickers Pyramid Number (VPN). Iron oxide prepared in the laboratory both from ferrous sulphate and from iron, had also been capable of scratching a 900 VPN surface, whereas "coke," prepared from residual fuel, would not have marked any surface which has been harder than 200 VPN. McConnell [20] suggested that the surfaces of the cast iron piston rings and cylinder had been weakened by a sulfuric acid attack and that the resulting ferrous debris had been heated in the combustion flame to form ferric oxide, this oxide then was the abrasive which had subsequently produced heavy scuffing on ring and liner surfaces.

He concluded that engine wear, when running on residual fuels, is caused by an interaction of corrosion and abrasion with corrosion playing the dominant part. It is postulated that the carbon particles produced by poor combustion carry the sulfuric acid to the metal surface, or they may provide an abrasive which removes the ferrous sulfate layer on that



**Fig. 43 Radioactive wear test, piston ring wear versus fuel sulfur and lubricant alkalinity fresh and used oils**

surface. Either mechanism explains the increase of corrosive wear with poor fuel combustion. Corrosive attack can, therefore, be eliminated either by neutralizing the acid or by eliminating the carbon particles. The carbon particles produced during combustion do not contribute alone to the abrasive process. The abrasive wear is controlled by the degree of acid attack, which weakens the wearing surfaces, thus producing iron and iron sulphate which can be converted to ferric oxide. This oxide is extremely hard and produces severe abrasion. Recent studies by our co-worker D. Godfrey [65, 66] suggest this mechanism could also apply to engines using distillate fuels.

For a given fuel sulfur level, the above mechanism suggests wear will increase when poor combustion exists, such as at low load operation. Figure 41 from our earlier work [67] using radioactive piston rings in a locomotive engine confirms wear increases at low load with residual fuel, whereas with distillate fuel wear decreases. Table 22 shows the analysis of these fuels. Figure 41 and Table 22 show the residual fuel B increased wear at low loads higher than distillate fuel A, at the same 0.9 percent sulfur level. Fuel B has high Conradson carbon content and high aromaticity, i.e., poor ignition qualities. From the discussions on fuels in Part I, it is probable that residual fuels with proper ignition qualities will give higher insolubles. Under poor combustion conditions, such as low loads, increased wear could, therefore, result as explained above. If wear was only related to fuel sulfur; wear at low loads would be reduced, similar to the distillate fuel experience (Figs. 41 and 43) due to the lower fuel flow rates.

Increased wear was reported [67, 68, 69, 70] in the first

Table 23 Comparison of TBN methods ASTM D 664 versus D 2896

ASTM Method	D 664	D 2896
Acid	HCl	HClO <sub>4</sub> (Perchloric)
Titration	Manual	Automatic
Time	Slow	Fast
Cost	High	Low
Comments	<p>Low Values Often Due to Incomplete Neutralization</p> <p>Large Variation Among Laboratories, Particularly on Used Oils</p> <p>Sample Size and Titration Speed Affects Results</p>	<p>Values Close to Theory</p> <p>Better Reproducibility Among Laboratories</p>

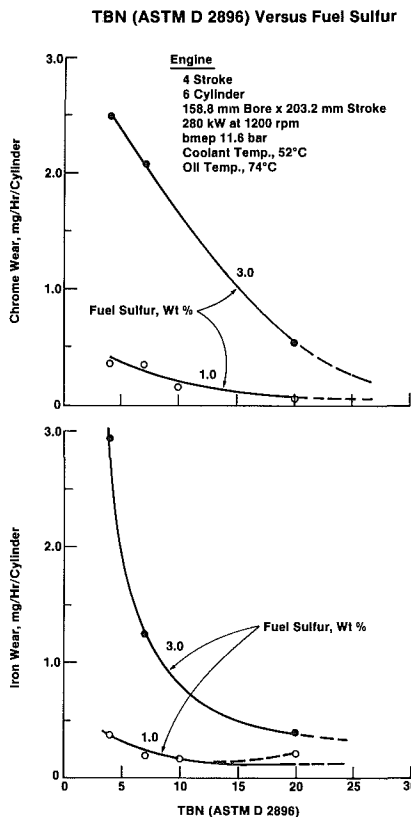


Fig. 44 Radioactive wear study on a four-stroke diesel engine

attempts in the 1950s to burn residual fuels in locomotives where light load and idling was a major part of the service life. In 1983, in cooperative tests with the Union Pacific Railroad, we studied blended distillate/residual fuels in laboratory engine tests and two-stroke and four-stroke locomotive tests. Increased wear relative to distillate fuels was again confirmed.

In addition to abrasive wear from fuel combustion effects, ingested dust particles can be abrasive if poor air filtration occurs, as reported by Pinotti [68], Watson [71], and Thomas [72].

In summary, to minimize abrasive wear it is necessary to have good air filtration and good combustion. The latter prevents combustion particles acting as a carrier for sulfuric acid to attack the metal surfaces leading to corrosive wear, which as described above, can further lead to iron oxide formation resulting in abrasive wear.

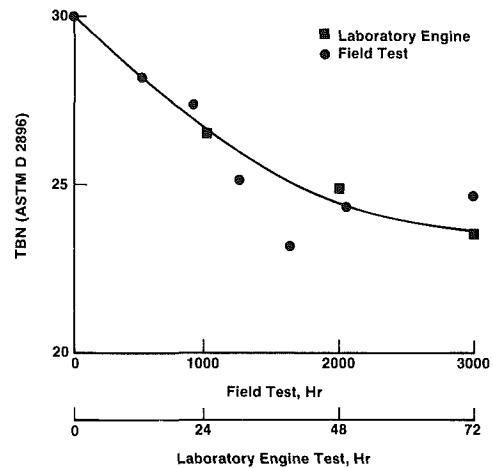


Fig. 45 Correlation between laboratory engine Chevron D 20 procedure and field tests

**Corrosive Wear.** The neutralization of sulfuric acid from the combustion process of the fuel is key to controlling corrosive wear. Lubricants for medium-speed diesel engines contain alkaline additives to neutralize these acids. A measure of a lubricant's ability to neutralize acids is the total base number (TBN) in mg KOH/g oil usually measured by either ASTM D 2896 or the older method, ASTM D 664. A comparison of these methods is shown in Table 23. The ASTM D 2896 is a more precise method, is faster to conduct, and can be automated. It uses perchloric acid (HClO<sub>4</sub>) to titrate the lubricant. The ASTM D 664 method, when run as outlined, has good precision. It uses hydrochloric acid (HCl) as titrant. However, most laboratories run variants of this method to overcome the slow time normally required for manual titrations. In the following discussions, we use TBN values obtained by the ASTM D 2896 method, which correlates with engine wear, as shown in Fig. 43. These data are from our co-worker's radioactive wear studies [73] in a 20-cylinder, 2984-kW, 230-mm-bore, two-stroke engine. This figure covers both fresh and used oils. Additional radioactive wear studies [74] in the six cylinder, four-stroke engine are shown in Fig. 44 for the lubricant range 4–20 TBN and for distillate fuels of sulfur level 1.0 percent mass and 3.0 percent mass. These data confirm earlier findings above.

As mentioned earlier, no standard engine lubricant test procedures are available for the development of medium-speed diesel engine lubricants. Our company has developed a number of screening engine tests, as summarized in Table 21. These tests evaluate oils with respect to wear, TBN retention, oxidation, and insolubles control. These parameters will be discussed below. However, to utilize these tests, it is necessary

sal = Low Sulfur, Low Alkalinity, Low Load  
 SAL = High Sulfur, High Alkalinity, High Load

Engine	Commercial	D 20-3
No. of Cylinders	4	1
Cycle	4	4
Bore, mm	480	130
Stroke, mm	520	165
(100%) Max. Rating, kW	2863	37.0
(90%) Continuous Rating, kW	2515	33.3
Speed, rpm	450	1400
Specific Output, kW/L	7.43	16.4
bmp, 100% Load, bar	19.8	14.4
bmp, 90% Load, bar	17.8	13.0
bmp, 70% Load, bar	13.9	10.1
Fuel Temp. at Injector, °C	93-98	100
Fuel Vis. at Injector, cSt	30-35	36
Coolant Temp., °C	82	74
Oil Temp., °C	60	55

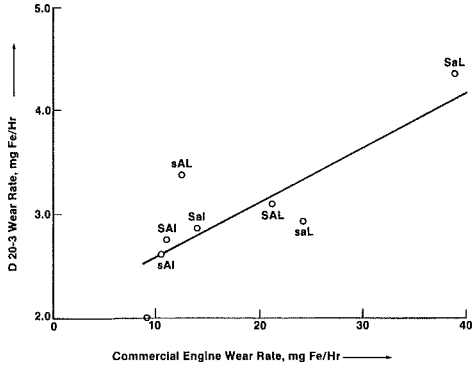


Fig. 46 Correlation of Chevron D 20 procedure and four-stroke, 480-mm-bore engine

Chevron Test Procedure D 20-2

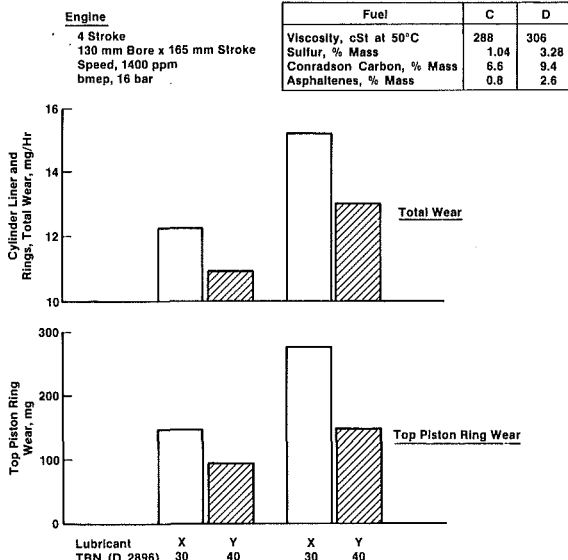


Fig. 47 Residual fuel studies in a medium-speed laboratory diesel engine effect of lubricant and fuel quality on engine wear

to have field correlations. Fig. 45 illustrates the correlation between field and our laboratory D 20 engine test procedure for studying TBN retention. This 72-hr procedure predicts 3000-hr field conditions. Applications of this procedure was discussed by van der Horst [22, 26, 46]. A similar correlation for our D 20 engine test procedure shows cylinder wear rates in Fig. 46, reported by Vrolijk [75]. Figure 47 shows the effect of two lubricants of 30 and 40 TBN with two different residual fuels in our laboratory tests.

The level of TBN of the lubricant is important in controlling corrosive wear. In service, a number of factors control the lubricant's TBN, and an approximation for

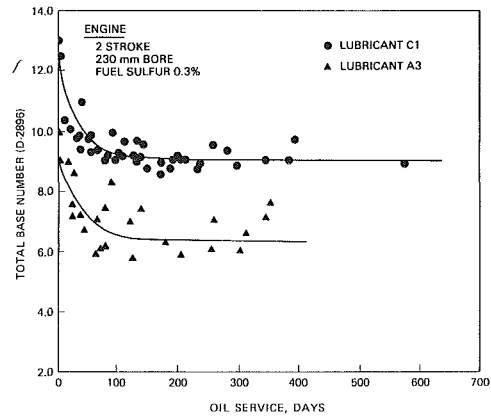


Fig. 48 Lubricant alkalinity retention in railroad service

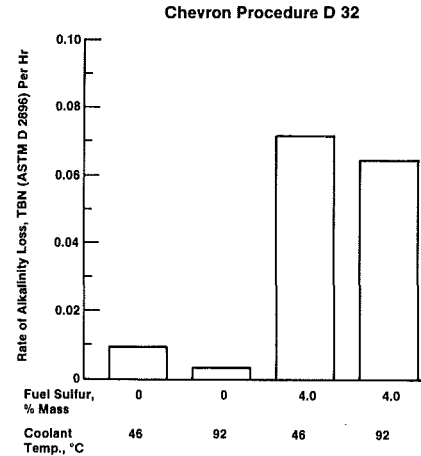


Fig. 49 Effect of fuel sulfur and coolant temperature on rate of alkalinity loss

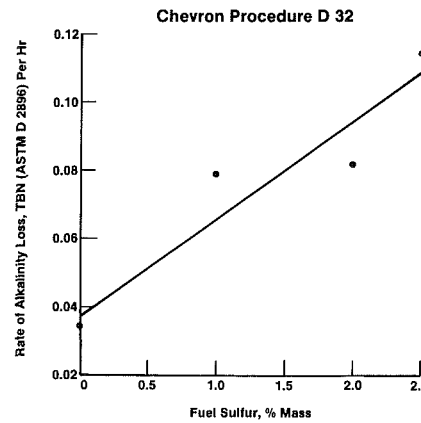


Fig. 50 Effect of fuel sulfur on rate of alkalinity loss

estimating TBN levels in service can be made using equation (21) reported by Thomas [45], for normal service conditions where fresh oil makeup is at regular intervals.

$$TBN_t = TBN_0 - K_T \left( \frac{b_e \cdot S}{R} \right) \left[ 1 - e^{-\left( R \cdot P_i / 1000Q \right) t} \right] \quad (21)$$

The condition of adequate alkalinity conditions depends upon the value of:

$$TBN_t = TBN_0 - K_T \left( \frac{b_e \cdot S}{R} \right) \quad (22)$$

Equation (22) shows the importance of selecting a suitable alkalinity level of a lubricant ( $TBN_0$ ) to match the fuel sulfur ( $S$ ) level and recognize the importance of the ratio oil con-

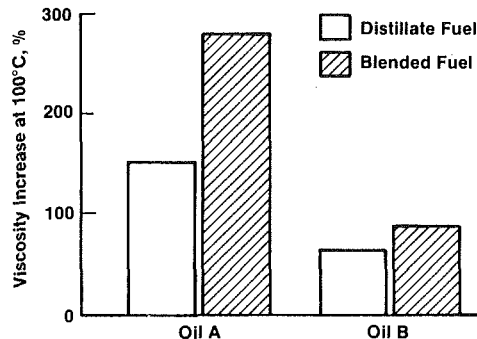


Fig. 51 D 17 viscosity increase for distillate and blended fuels

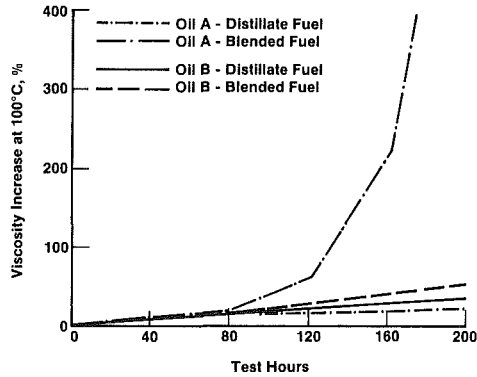


Fig. 52 D 7 viscosity increase with distillate and blended fuels

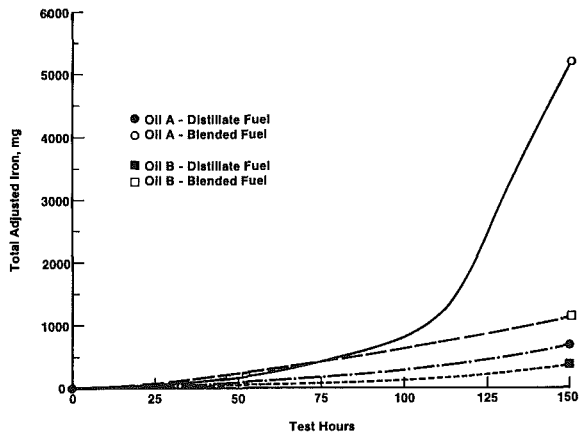


Fig. 53 Wear with distillate and blended fuels, Chevron D 32 procedure

sumption to fuel consumption ( $R/b_e$ ) and engine design/service factor ( $K_T$ ).

Typical examples of equilibrium TBN curves are shown in Fig. 48 representing railroad service.

In developing lubricants with good corrosive wear control, the rate of alkalinity loss, TBN/hour must be considered. Our engine test procedure D 32 is used for this purpose. An example of the effect of fuel sulfur level, 0 percent m and 4 percent m, together with changes in coolant temperature, 46°C and 92°C, is shown in Fig. 49. The effect of fuel sulfur level on the rate of TBN loss for a particular lubricant is linear with respect to fuel sulfur, as shown in Fig. 50. The line does not go through zero for this lubricant, as some alkalinity is lost due to oxidation reactions.

### Lubricants for Blended Fuel Service

Our experience in the field and in laboratory engine tests with blended fuels shows the need for improved lubricants to control deposits, insolubles, and wear. An example will illustrate the benefits of using an improved lubricant. This lubricant was developed [76] with improved dispersancy, wear control and oxidation control. A comparison of the performance of this improved lubricant (Oil B) with a commercial railroad Generation IV lubricant (Oil A), both with No. 2 diesel and blended fuel (30 percent No. 6, 70 percent No. 2-D fuel), is discussed below.

The Chevron D 17 engine procedure (Table 21) is a severe test designed to correlate with railroad service. Figure 51 shows with distillate fuel a viscosity increase of 60 percent for the newly developed Oil B, compared with 150 percent for the commercial Oil A. However, with the blended fuel operation, the new Oil B gave 90 percent viscosity increase; and the commercial Oil A gave over 280 percent viscosity increase. This evaluation was also repeated in the Chevron D 7 engine test, detailed in Table 21. Similar viscosity increases were noted for the two oils with distillate fuel; again we noted a very significant increase for Oil A when blended fuel was used (Fig. 52). Our D 32 engine test (Table 21) was also used to evaluate these lubricants. Figure 53 shows significant wear improvement, from 700 mg iron for Oil A to 300 mg iron for Oil B, with distillate fuel. With blended fuel, the high wear rate of 5500 mg iron for Oil A was significantly reduced to 1000 mg iron for Oil B.

Several field tests with blended fuels have been run in the United States. In one railroad, a fuel consisting of 20 percent No. 6 in 80 percent No. 2 (Table 24) was run for 15 months in locomotives with two-stroke and four-stroke engines. The primary objective of the test was to quantify the problems associated with mixed fuel operation. A commercial Generation IV lubricant was used in both locomotives [77].

Table 24 Chevron engine test and field test fuels

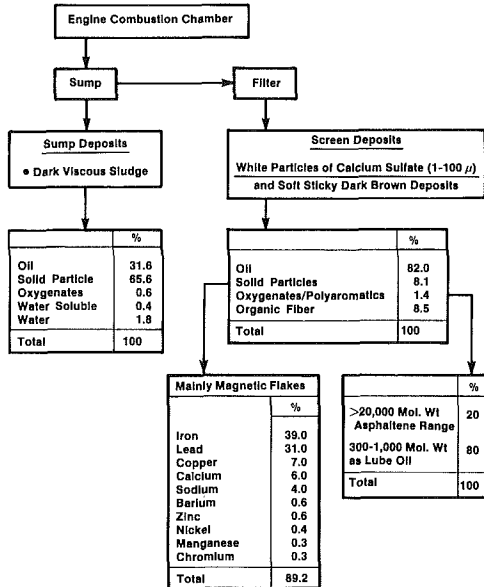
Test Procedure	D 7, D 17, D 32		D 20	Field Test
	Distillate Fuel	Blended Fuel (30% Resid)	Residual Fuel	Blended Fuel (20% Resid)
Properties				
Specific Gravity	0.87	0.895	0.9503	0.899
Viscosity, cSt at 40°C	3.2	8.9	-	8.1
Viscosity, cSt at 50°C	-	-	228.3	-
Conradson Carbon, % Mass	0.1	4.2	8.2	3.8
Asphaltenes, % Mass (IP 143)	-	0.86	3.2	0.9
Distillation, °C				
1BP	195	186	452	216
10%	224	234	766	245
50%	276	310	960	289
75%	310	383	-	321
90%	334	-	-	-
EP	359	-	-	-
Recovered, % Vol	-	78	-	86
Sulfur, % Mass	1.03	1.39	2.43	0.55
Metals, mg/kg				
Sodium	-	2	12	-
Vanadium	-	17	9	42
Aluminum	-	<1	-	-
Cetane No.	43	42	-	39



**Table 25 Used oil analyses: 15-month locomotive field test (four-stroke, 229-mm-bore engine)**

	Fresh Oil	Average of 90-Day Drain Oil	
		Unit On Distillate Fuel	Unit On Blended Fuel
Viscosity, cSt at 100°C	14.9	16.2 (1.0)*	17.5 (2.2)
Alkalinity Value (D 2896)	13	11.0 (0.7)	10.2 (0.6)
Coagulated Pentane Insolubles, %	0	3.8 (1.6)	4.6 (1.5)
Iron, mg/kg	<5	26.0 (8.6)	47.0 (14.6)

\*Standard deviation.



\*Courtesy of Semt-Plietlick

**Fig. 54 Analysis of deposits from engine sump and lubricant filter four-stroke marine engine**

It soon became apparent that this service, which included long periods of idle and dynamic breaking, was very severe for blended fuel operation. One locomotive lost turbochargers due to the ignition of deposits in the exhaust system formed during prolonged cold idle periods. The other locomotive also had to have its turbochargers changed for cleaning; they were coated with heavy tarlike material attributed to incomplete combustion at idle.

At the conclusion of this test, higher wear of the piston rings was measured for the locomotives running on blended fuel compared with the reference locomotive using No. 2D distillate fuel in the same service. This wear could not be attributed to corrosion since the fuel sulfur was not high and the oil alkalinity values remained high, see Table 25. These data lend support to the wear mechanism discussed in the preceding section.

### Oil Purification

**Insolubles Control.** The lubricant in a trunk piston diesel engine becomes contaminated with dirt, soot, oxygenated products, wear metal particles, additive-metal salts, water, etc. A typical analysis of medium-speed marine trunk piston engine filter screen and sump tank deposits is given in Fig. 54.

The rate and degree of contamination depend upon the engine, type of application, operating conditions, quality of fuel, fuel purification, quality of lube oil, and lube oil purification system. The level of contamination is much higher in highly rated medium-speed engines burning blended or residual fuels, as compared to distillate fuels. This would result in increased deposits and sludge formation, more

frequent plugging of filters and purifiers and increased engine wear. It is, therefore essential to control these insoluble contaminants within tolerable limits to ensure satisfactory equipment and oil life.

Insolubles buildup in an engine lubricant system without purification, generally follows the relationship:

$$x_t = K_L \left( \frac{b_e}{R} \right) \left[ 1 - e^{-\left( \frac{RP_i}{1000Q} \right) t} \right] + x_0 \left[ e^{-\left( \frac{RP_i}{1000Q} \right) t} \right] \quad (23)$$

Equation (23) indicates a maximum level of insolubles would be reached, if no oil drain occurs, equal to

$$x_{Max.} = K_L \left( \frac{b_e}{R} \right) \quad (24)$$

Equation (24) illustrate the importance of the ratio of oil consumption to fuel consumption ( $R/b_e$ ) and engine design/service factor ( $K_L$ ). Purification of the lubricant or oil drains at selected times will ensure the maximum level of insolubles remains within the capabilities of the lubricant dispersant-detergent system.

Various factors pertaining to the fuel and lube oil system influence insolubles control of medium-speed engine lubricants are summarized in Table 19. Essentially, they are:

- Purification of blended/residual fuel
- Purification of lube oil
- Lube oil additives balance

The purification of fuel is accomplished by way of settling tanks and by properly designed centrifuge and filter systems to remove impurities, such as dirt, catalyst fines, scale, water, and sludge. Sludge can be formed due to instability of the fuel or incompatibility of the blend. If not removed, it would not only cause engine operational problem, but would further increase the level of insolubles and deposits during the combustion process.

The roles of lube oil additives and lube oil purification system are complementary. For example, in a railroad system, where only filters are used for oil purification, insolubles are controlled by an increase in dispersant additives level. Unlike railroad practice, in marine propulsion installations, the engine oil purification is done primarily by a centrifuge. The function of the filter is to protect the engine, particularly the bearings, against any large contaminants in the oil supplied to the engine. In such a system, a moderate level of dispersant would normally suffice.

The lube oil life is, however, limited. It must be changed when the additives get depleted or no longer perform their intended function. But the drain period, as depicted in Fig. 26, can vary depending upon the lubrication system and the method of oil purification.

The lube oil additives that are effective in the control of insolubles and deposits are the well-known detergent--dispersant additives. These additives are, however, present in combination with other additives. A typical medium-speed engine lubricant would contain metal detergents, ashless dispersant, oxidation inhibitor, antiwear or EP agent, V.I. improver (for multigrade oils), rust inhibitor, foam inhibitor,

**Table 26 Lubricant contaminants and means of control**

Contaminant	Particle Size, Micron	Control by
1. Smaller Particles: (Carbonaceous and Wear Metals)	0-1.5	. Additives (Metallic Detergents and Ashless Dispersants)
2. Larger Particles: (Agglomerates of Soot, Resins, Asphaltenes, Calcium Sulfate, Etc., and Wear Metals)	>(1-5) <10 >10	. Centrifuge . Filters (Micro) . Filters (Cloth, Fiber, Screens, Strainers)
3. Water		. Demulsifier Additive . Centrifuge

**Table 27 Factors affecting filter plugging**

Filter	Type, material, porosity, structural stability, water tolerance.
Plugging Material	
Particulate	Number, size, nature of particles. (Crystalline/fibrous, amorphous.)
From Additives	Sediment due to hydrolytic instability. Thermal degradation products.
Contaminants	Agglomerates of soot and resins, wear metals, calcium sulfate, foreign matter.
Emulsion	Stability.
Water	Extent of contamination. Removal by centrifuge.
Operating Factors	Rate of flow. Temperature (viscosity of oil). Pressure
Mechanism	Bridging, packing of small particles.

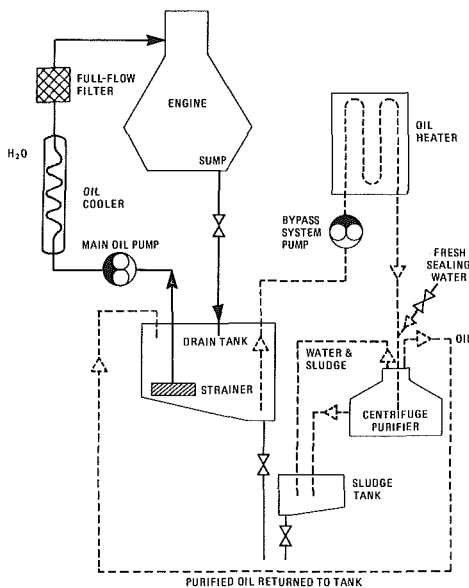
- Facilitate separation of water and insolubles without depletion of additives
- Facilitate the process of filtration without premature plugging

Metallic detergents/dispersants (e.g., sulfonates, phenates, salicylates) and ashless dispersants, such as succinimide, succinate ester, alkyl amine, and phosphonate ester, peptize small particulate solid material and prevent particle agglomeration. A dispersant or detergent peptizes, or disperses, particles up to 0.05- $\mu$  size by forming an adsorbed film on the surface of the particle. The hydrophobic tail of the additive molecule prevents coagulation by providing a physical barrier to contact with other particles. Adsorption of metallic sulfonate detergents on larger particles (0.5-1.5- $\mu$  size) charges the surface of the particles. The coagulation in this case is prevented by repulsion between similarly charged particles. Ashless dispersants also function in a similar manner. Their longer tails, compared to metallic detergents, provide physical barrier to particles (0.05- $\mu$  size).

The size of various contaminants and the means of controlling them are presented in Table 26. Particles, or agglomerates, which exceed the additive control limit, have to be strained with the help of filters, screens, or centrifugal purifiers. The choice depends upon the engine and the type of service. For example, in marine application, centrifuges are invariably used in conjunction with 25-30- $\mu$  size metallic filters. A schematic of a typical marine engine lubricant oil purification system is shown in Fig. 55. The insolubles and water are primarily controlled by the centrifuge. Any malfunction, or poor quality of lubricating oil in terms of water tolerance, would cause the centrifuge to be prematurely blocked or plugged.

A railroad oil purification system generally consists of full flow pleated paper filter elements. Each design of locomotive requires a filter matched to its own system. For example, an EMD engine uses a 13- $\mu$  size basic filter element, whereas GE uses a 30- $\mu$  size element. The life of the filter is limited. It is discarded when the pressure across it exceeds a predetermined limit.

**Water Tolerance of Additives.** Water can be one of the major contaminants in a medium-speed engine oil, particularly in the marine environment. Water comes from blow-by gases, from coolant system leakages, from improper operation of the lube oil automatic purifiers, or through accidental contamination. The condensing limit for water in most applications is 0.5 percent by volume, maximum, although detergent-dispersant oils can sometimes solubilize up to about 1 percent of water. Excessive water can cause troublesome emulsions, which are difficult to separate and can promote the coagulation of insolubles to form sludge. Water may react with certain additives in the package or hydrolyze them resulting in sedimentation and additive depletion. Emulsions and additive sediment, along with other contaminants, can cause serious problems of filter plugging, excessive back flushings in automatic filters, deposits, and



**Fig. 55 Typical marine engine lubricant purification system**

and a pour point depressant. These additives are complex chemical compounds. They have to be carefully selected and balanced to remove all possible incompatibility and antagonism in the performance of their basic functions of wear, deposits, lubricant viscosity, and insolubles control.

From the point of view of insolubles control, the additives have to perform the following functions:

- Keep the insolubles in suspension and prevent their agglomeration

Table 28 Chevron marine centrifuge tests

Chevron Test Procedure	B 21-1	B 21-2
Objective	Water Tolerance	Water Shedding
Duration, Hr	3	5
Apparatus		
Centrifuge Model	Westfalia LG 205-3	Westfalia LG 205-3
Capacity, Liters/Hr	300	300
Oil Volume, Liters	5.7	5.7
Oil Circulation Rate, Liters/Hr	50	50
Oil Inlet Temperature, °C	80	80
Water, Demineralized, % Vol	2	5
Water, Rate Added, Liters/Hr	1	0

problems of dischargeability of sludge in modern automatic centrifuges. In addition, emulsions have a detrimental effect on the lubrication of highly loaded main and conrod bearings.

**Filter Plugging.** The phenomenon of railroad and marine filter plugging has been studied in order to develop medium-speed lubricating oils with good filterability characteristics. Ouvrier-Buffet [78] has also reported on demulsibility, hydrolysis resistance, and filterability of medium-speed engine lubricants.

Field problems, with respect to filter blocking, have been reported from time to time. In a survey [48] conducted by the European CEC Project Group CL 16 on crankcase oils for medium-speed engines using heavy fuels, 10 of the 14 engine manufacturers reported that they had occasionally experienced lube oil filter clogging.

The plugging of paper or metallic mesh filters reveals that the mechanism of filter plugging is complex. Factors involved, connected with the lube oil formulation or with the filter and operating conditions, are summarized in Table.

The effect of water on fresh oils formulated with different medium-speed additive packages has been studied [78]. It was observed that additives that give amorphous, or small, crystalline particles and resist the formation of stable emulsions have a lesser tendency to block filters.

**Centrifuge Performance.** A centrifuge is important for the control of insolubles and also water removal. But if the lubricant is not properly formulated for good hydrolytic stability and demulsibility or water release properties, a centrifuge cannot perform its function properly. The result would be:

- Incomplete removal of water
- Additive depletion and loss of TBN
- Excessive deposits in the centrifuge
- Incomplete discharge of sludge from automatic centrifuges
- Decrease in the efficiency of the centrifuge

The water shedding and water tolerance properties of a medium-speed engine oil are evaluated in a laboratory centrifuge by the Chevron Marine Centrifuge Test Procedure B 21-1 and B 21-2, described in Table 28. To simulate bulk contamination and system leakage situations, the procedures incorporate both premixing and continuous addition of water in lubricant circuits similar to the schematic circuit shown in Fig. 56. At the end of the test, the centrifuge is dismantled and disks and bowl are inspected, deposits are observed and weighed. Water content, calcium content, and alkalinity (TBN) of the oil are measured.

Van der Horst has described the centrifuge tests on ten oils with a TBN range of 10-30 by the foregoing procedure [79].

Excessive loss of TBN reflecting additive depletion occurred with two oils that had encountered service problems.

### Conclusions

- Compared with medium-speed diesel engines operated on distillate fuel, blended and residual fueled engines place more severe demands on the lubricant with respect to oxidation, insolubles handling, deposit control, and wear.

- Satisfactory engine durability can be obtained when medium-speed diesel engines are operated with blended or residual fuels by using suitably designed lubricants.

- Proprietary bench and laboratory engine tests that relate to field service experience must be utilized to design suitable lubricants for the service described above. Chevron has developed several useful tests for this purpose.

- It is hypothesized that carbonaceous particles from incomplete combustion, generally greater with blended and residual fuels, help promote higher rates of iron corrosion by sulfur acids; and those corrosion products, in turn, lead to formation of hard iron oxides and increased abrasive wear.

- Engine fuel consumption relationships to engine idle speed, coolant temperature, and lubricant viscosity were established for two-stroke and four-stroke locomotive engines.

- Lubricants must be carefully balanced to handle insolubles from combustion and oxidized products in order for satisfactory purification by centrifuges to be achieved. The additive balance must be able to tolerate water and avoid emulsions, agglomeration, and hydrolysis.

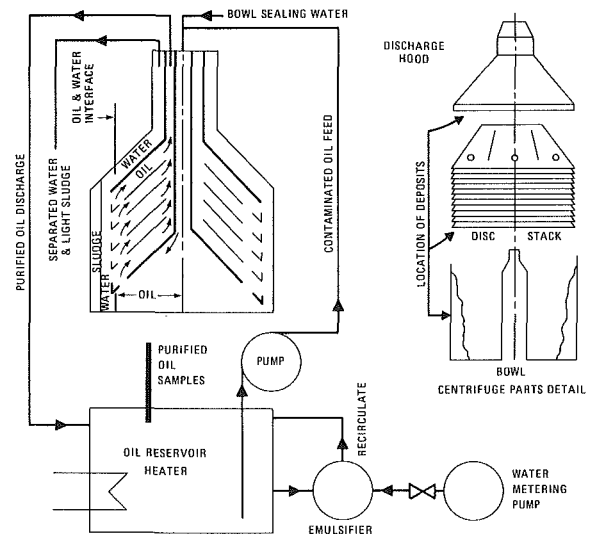


Fig. 56 Lubricant centrifuge test circuit

## Acknowledgment

The authors wish to thank the management of Chevron Chemical Company, Chevron Central Laboratories, Chevron U.S.A., Chevron International Oil Company, and Chevron Research Company for permission to publish this paper.

They also wish to thank the staff of Chevron Central Laboratories; Chevron Research Company; Chevron Chemical Company and affiliates; Orobis Limited; Orogil S.A.; Aditivos Mexicanos, S.A.; Karonite Chemical Company; and Nomura Jimusho, Inc.; who contributed much of the work described in this paper.

## References

- 45 Thomas, F. J., and Hold, G. E., "Modern Marine Diesel Engine Lubricants and Their Development," ASME Paper 80-DGP-10, Feb. 1980.
- 46 Van der Horst, G. W., Polman, J., and Sundermeijer, J. J. H., "Improved Wear and Deposit Control in Medium-Speed Marine Diesel Engines," Europort 1973 Conference, Amsterdam, Institute of Marine Engineers United Kingdom, Nov. 1973.
- 47 Von Schnurbein, E., and Bucher, J., "Experience with the Rating and Operation of Medium-Speed, Four-Stroke Engines Under Extreme Site Conditions," CIMAC Paper D 64, 1981.
- 48 Fleischhack, G. C., "Interactions Between Medium-Speed Engine and Its Fuels and Lubricants," CIMAC Paper 6.5, 1983.
- 49 Logan, M. R., Parker, C. K., and Pallesan, L. C., "Improved Fuel Economy Through Lubricant Technology in Medium-Speed Railroad Diesel Engines," ASLE Annual Meeting, May 1982.
- 50 Vrolijk, D. J. E., "Bolnes Lubrication Study," Chevron Central Laboratories Internal Report (unpublished), Apr. 1981.
- 51 Wall, J. C., "Influence of Crankcase Lubricant Viscosity on Fuel Consumption in a Medium-Speed Diesel Engine," SAE Paper 821148, 1982.
- 52 Stambaugh, R. L., and Kopko, R. J., "Behavior of Non-Newtonian Lubricants on High Shear Rate Applications," SAE Paper 730487, 1973.
- 53 McMillan, M. L., and Murphy, C. K., "Temporary Viscosity Loss and Its Relationship to Journal Bearing Performance," SAE Paper 780374, 1978.
- 54 Dancy, J. H., Marshall, H. T., and Oliver, C. R., "Determining Frictional Characteristics of Engine Oils by; Engine Friction and Viscosity Measurements," SAE Paper 800364, 1984.
- 55 Shamah, E., "Fuel Consumption Studies in Two-Stroke and Four-Stroke Medium-Speed Diesel Engines at Idle Conditions," Chevron Research Internal Report (unpublished), November 1983.
- 56 "Bearings, Main and Connecting Rod," Technicians Guide, Detroit Diesel Allison, Publication MGS-CL10M5183, 1983.
- 57 Bowman, L. O., and Savage, M. W., "Laboratory Methods for Predicting Silver Bearing Performance of Lubricating Oils," SAE Paper 110B, Jan. 1960.
- 58 Keyworth, R. O., "Current Trends and Future Development in Medium-Speed Diesel Lubricant Technology," DEUA Publication 403, London, January 1981.
- 59 Eberle, M. K., "The Marine Diesel Engine - The Answer to Low Grade Fuels," ASME Paper 80-DGP-16, 1980.
- 60 Piston Ring Scuffing Conference, Publication CP5-1975, Institution of Mechanical Engineers, London, May 1975.
- 61 Aue, G. K., "Piston Ring Scuffing—General Review, Piston Ring Scuffing Conference Paper C63/75, I Mech. E., London, May 1975.
- 62 Willn, J. E., and Brett, P. S., "An Investigation into Piston Ring Scuffing During Running-In," Piston Ring Scuffing Conference Paper C70/75, I Mech. E., London, May 1975.
- 63 Nakano, H., Osu, T., Nakayama, N., Fugi, T., and Tokunaga, Y., "Critical Criterion of Piston Ring Scuffing," (in Japanese), *Junkatsu*, Vol. 27, No. 5, 1982, pp. 386-391.
- 64 Burtenshaw, R. P., and Lilly, L. R. C., "Towards Wear Reduction in Engines Using Residual Fuel," *Trans. I. Mar. E.*, Vol. 84, 1972, pp. 389-422.
- 65 Godfrey, D., "Mechanism of Caterpillar Piston Ring and Liner Wear Run on 1% Sulfur Fuel," Chevron Research Internal Report (unpublished), May 1983.
- 66 Godfrey, D., "Tribological Examinations of Detroit Diesel Piston Rings and Liners Run on 1% Sulfur Fuel," Chevron Research Internal Report (unpublished), June 1983.
- 67 Jones, D. R., Kipp, K. L., and Goodrich, J. E., "Performance of Residual Fuels in High Speed Diesel Engines," ASTM Second Pacific Area National Meeting, Sept. 1956.
- 68 Pinotti, P. L., Garin, P. V., and Jones, D. R., "Radioactive Rings Solve Wear Problems in Diesel Locomotives," SAE Paper 362A, 1961.
- 69 McBrain, R., "The Use of Economy Fuels on Diesel Locomotives," ASME Paper No. 57-RR-6, 1957.
- 70 Neely, G. L., Griep, E. F., and Pinotti, P. L., "Dark Diets for Diesels," SAE National West Coast Meeting, Aug. 1956.
- 71 Watson, C. E., Hanly, F. J., and Burchell, R. W., "Abrasive Wear of Piston Rings," *SAE Trans.*, Vol. 63, 1955.
- 72 Thomas, G. E., and Culbert, R. M., "Ingested Dust, Filters, and Diesel Engine Ring Wear," SAE Paper 680536, 1956.
- 73 Tennyson, T. A., and Parker, C. K., "Locomotive Radioactive Ring Studies of Fuel, Lubricant, and Operating Variables," SAE Paper 700892, 1970.
- 74 Sam, F., Hall, K. L., and Painter, L. J., "Corrosive Wear in a Diesel Engine," Chevron Research Internal Report (unpublished), July 8, 1974.
- 75 Vrolijk, D. J. E., and Hall, K. L., "RF 2 Test—The Effects of Fuel Sulfur, Oil TBN, and Engine Load on Wear," Chevron Central Laboratories Internal Report (unpublished), 1978.
- 76 Hance, V. M., "Study of Blended and Distillate Fuels in the Chevron D 7, D 17, and D 32 Engine Test Procedure," Chevron Chemical Company Internal Report (unpublished), Nov. 1983.
- 77 Hudgens, D. D., "Changes in Fuels and Lubricants," Report of the Committee on Fuels and Lubricants, Annual Proceedings, Locomotive Maintenance Officers Association, Sept. 1983.
- 78 Ouvrier-Bufferet, C., "Demulsibility, Hydrolysis Resistance, and Filterability of Medium-Speed Engine Lubricants," Marine International Symposium, Lub Marine, Nice, Sept. 1981; also *The Motorship*, Feb. 1982, pp. 27-29.
- 79 Van der Horst, G. W., "Development of Modern Lubricants for Medium-Speed Diesel Engines," *ASLE*, Vol. 33, No. 11, Nov. 1977.

## Acknowledgment

The authors wish to thank the management of Chevron Chemical Company, Chevron Central Laboratories, Chevron U.S.A., Chevron International Oil Company, and Chevron Research Company for permission to publish this paper.

They also wish to thank the staff of Chevron Central Laboratories; Chevron Research Company; Chevron Chemical Company and affiliates; Orobis Limited; Orogil S.A.; Aditivos Mexicanos, S.A.; Karonite Chemical Company; and Nomura Jimusho, Inc.; who contributed much of the work described in this paper.

## References

- 45 Thomas, F. J., and Hold, G. E., "Modern Marine Diesel Engine Lubricants and Their Development," ASME Paper 80-DGP-10, Feb. 1980.
- 46 Van der Horst, G. W., Polman, J., and Sundermeijer, J. J. H., "Improved Wear and Deposit Control in Medium-Speed Marine Diesel Engines," Europort 1973 Conference, Amsterdam, Institute of Marine Engineers United Kingdom, Nov. 1973.
- 47 Von Schnurbein, E., and Bucher, J., "Experience with the Rating and Operation of Medium-Speed, Four-Stroke Engines Under Extreme Site Conditions," CIMAC Paper D 64, 1981.
- 48 Fleischhack, G. C., "Interactions Between Medium-Speed Engine and Its Fuels and Lubricants," CIMAC Paper 6.5, 1983.
- 49 Logan, M. R., Parker, C. K., and Pallesan, L. C., "Improved Fuel Economy Through Lubricant Technology in Medium-Speed Railroad Diesel Engines," ASLE Annual Meeting, May 1982.
- 50 Vrolijk, D. J. E., "Bolnes Lubrication Study," Chevron Central Laboratories Internal Report (unpublished), Apr. 1981.
- 51 Wall, J. C., "Influence of Crankcase Lubricant Viscosity on Fuel Consumption in a Medium-Speed Diesel Engine," SAE Paper 821148, 1982.
- 52 Stambaugh, R. L., and Kopko, R. J., "Behavior of Non-Newtonian Lubricants on High Shear Rate Applications," SAE Paper 730487, 1973.
- 53 McMillan, M. L., and Murphy, C. K., "Temporary Viscosity Loss and Its Relationship to Journal Bearing Performance," SAE Paper 780374, 1978.
- 54 Dancy, J. H., Marshall, H. T., and Oliver, C. R., "Determining Frictional Characteristics of Engine Oils by; Engine Friction and Viscosity Measurements," SAE Paper 800364, 1984.
- 55 Shamah, E., "Fuel Consumption Studies in Two-Stroke and Four-Stroke Medium-Speed Diesel Engines at Idle Conditions," Chevron Research Internal Report (unpublished), November 1983.
- 56 "Bearings, Main and Connecting Rod," Technicians Guide, Detroit Diesel Allison, Publication MGS-CL10M5183, 1983.
- 57 Bowman, L. O., and Savage, M. W., "Laboratory Methods for Predicting Silver Bearing Performance of Lubricating Oils," SAE Paper 110B, Jan. 1960.
- 58 Keyworth, R. O., "Current Trends and Future Development in Medium-Speed Diesel Lubricant Technology," DEUA Publication 403, London, January 1981.
- 59 Eberle, M. K., "The Marine Diesel Engine - The Answer to Low Grade Fuels," ASME Paper 80-DGP-16, 1980.
- 60 Piston Ring Scuffing Conference, Publication CP5-1975, Institution of Mechanical Engineers, London, May 1975.
- 61 Aue, G. K., "Piston Ring Scuffing—General Review, Piston Ring Scuffing Conference Paper C63/75, I Mech. E., London, May 1975.
- 62 Willn, J. E., and Brett, P. S., "An Investigation into Piston Ring Scuffing During Running-In," Piston Ring Scuffing Conference Paper C70/75, I Mech. E., London, May 1975.
- 63 Nakano, H., Osu, T., Nakayama, N., Fugi, T., and Tokunaga, Y., "Critical Criterion of Piston Ring Scuffing," (in Japanese), Junkatsu, Vol. 27, No. 5, 1982, pp. 386-391.
- 64 Burtenshaw, R. P., and Lilly, L. R. C., "Towards Wear Reduction in Engines Using Residual Fuel," *Trans. I. Mar. E.*, Vol. 84, 1972, pp. 389-422.
- 65 Godfrey, D., "Mechanism of Caterpillar Piston Ring and Liner Wear Run on 1% Sulfur Fuel," Chevron Research Internal Report (unpublished), May 1983.
- 66 Godfrey, D., "Tribological Examinations of Detroit Diesel Piston Rings and Liners Run on 1% Sulfur Fuel," Chevron Research Internal Report (unpublished), June 1983.
- 67 Jones, D. R., Kipp, K. L., and Goodrich, J. E., "Performance of Residual Fuels in High Speed Diesel Engines," ASTM Second Pacific Area National Meeting, Sept. 1956.
- 68 Pinotti, P. L., Garin, P. V., and Jones, D. R., "Radioactive Rings Solve Wear Problems in Diesel Locomotives," SAE Paper 362A, 1961.
- 69 McBrain, R., "The Use of Economy Fuels on Diesel Locomotives," ASME Paper No. 57-RR-6, 1957.
- 70 Neely, G. L., Griep, E. F., and Pinotti, P. L., "Dark Diets for Diesels," SAE National West Coast Meeting, Aug. 1956.
- 71 Watson, C. E., Hanly, F. J., and Burchell, R. W., "Abrasive Wear of Piston Rings," *SAE Trans.*, Vol. 63, 1955.
- 72 Thomas, G. E., and Culbert, R. M., "Ingested Dust, Filters, and Diesel Engine Ring Wear," SAE Paper 680536, 1956.
- 73 Teanyson, T. A., and Parker, C. K., "Locomotive Radioactive Ring Studies of Fuel, Lubricant, and Operating Variables," SAE Paper 700892, 1970.
- 74 Sam, F., Hall, K. L., and Painter, L. J., "Corrosive Wear in a Diesel Engine," Chevron Research Internal Report (unpublished), July 8, 1974.
- 75 Vrolijk, D. J. E., and Hall, K. L., "RF 2 Test—The Effects of Fuel Sulfur, Oil TBN, and Engine Load on Wear," Chevron Central Laboratories Internal Report (unpublished), 1978.
- 76 Hance, V. M., "Study of Blended and Distillate Fuels in the Chevron D 7, D 17, and D 32 Engine Test Procedure," Chevron Chemical Company Internal Report (unpublished), Nov. 1983.
- 77 Hudgens, D. D., "Changes in Fuels and Lubricants," Report of the Committee on Fuels and Lubricants, Annual Proceedings, Locomotive Maintenance Officers Association, Sept. 1983.
- 78 Ouvrier-Bufferet, C., "Demulsibility, Hydrolysis Resistance, and Filterability of Medium-Speed Engine Lubricants," Marine International Symposium, Lub Marine, Nice, Sept. 1981; also *The Motorship*, Feb. 1982, pp. 27-29.
- 79 Van der Horst, G. W., "Development of Modern Lubricants for Medium-Speed Diesel Engines," *ASLE*, Vol. 33, No. 11, Nov. 1977.

## DISCUSSION

### Dr. J. M. Conway-Jones<sup>1</sup>

The authors are to be congratulated on the wide ranging review of the problems that arise in the lubrication systems of diesel engines burning residual/blended fuel with high sulphur content, and also on giving information on how to deal with these problems.

I am interested in the reference to calcium sulphate particles in Fig. 54, in the size range 1-100/ $\mu$ . We have found many particles embedded in the soft overlay on crankshaft bearings, and there appears to be a tendency toward increased wear of overlays in engines operating with residual fuels. The mechanism of wear may be partly corrosive, but there is evidence (Fig. 57) of abrasive wear. Typically, the particles are in the size range 5-15/ $\mu$ m, i.e., larger than the minimum oil film thickness, which may be 2-3/ $\mu$ m and smaller than the mesh of the full flow filter.

Regarding the nature of these particles, many elements are detected, and as an example, Fig. 58 is a scanning electron microscope view of a particle found in the surface of a bearing from a residual fuel engine, together with the output from an energy dispersive X-ray analyser. Many elements are present which, in this case, appear to be agglomerated with carbon. Such agglomerates may be hard or soft, and some may be relatively harmless to the bearing.

However, there are also other particles which plough through the soft overlay, Fig. 59. The analysis shows a high concentration of calcium and sulphur. While some of the hard particles may be ash or catalytic fines the majority, as illustrated here, are probably calcium sulphate with entrained

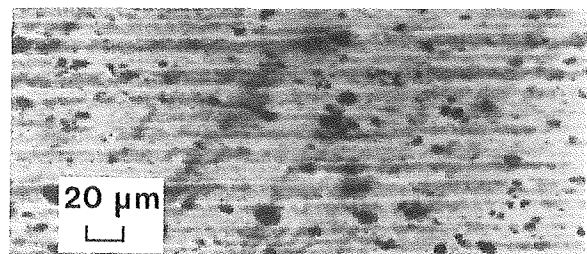


Fig. 57 Abraded overlay with embedded particles

<sup>1</sup>Manager, R&DO The Glacier Metal Co Ltd., Wembley, England.

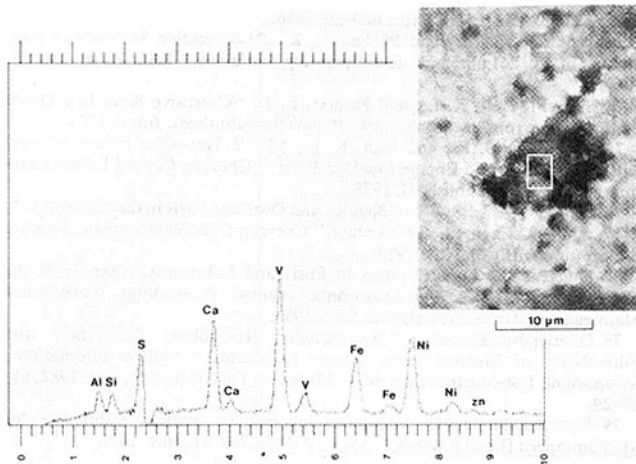


Fig. 58 Agglomerate embedded in bearing operating with residual/blended fuel

carbon. (The X-ray analyser was not capable of detecting oxygen or carbon).

The authors give information on measurements of wear in cylinders and piston rings. It would be interesting to know if they have data on the effects of the sulphur content of the fuel on the wear of crankshaft bearings. I would also be interested to know if they have seen similar particles embedded in the bearing surface, and have an explanation as to why the particles should grow so large prior to embedment. If indeed they are calcium sulphate, they are presumably spent TBN additives which have correctly neutralized the sulphuric acid produced by combustion. Initially, the calcium sulphate so produced will be in the form of very fine particles, but I would be interested to know if the authors have an explanation as to what causes them to grow so large.

One method of removing these fine particles is to use the Glacier bypass centrifuge. This uses the pressure of the engine oil issuing from jets to spin the rotor, and oil insolubles are collected in the rotor bowl by the centrifugal action produced.

Figure 60 illustrates typical particles collected from a bypass centrifuge fitted to an engine operating with residual fuel, and demonstrates its ability to collect particles down to  $2/\mu\text{m}$  and below, thereby contributing to extending the life of engine components.

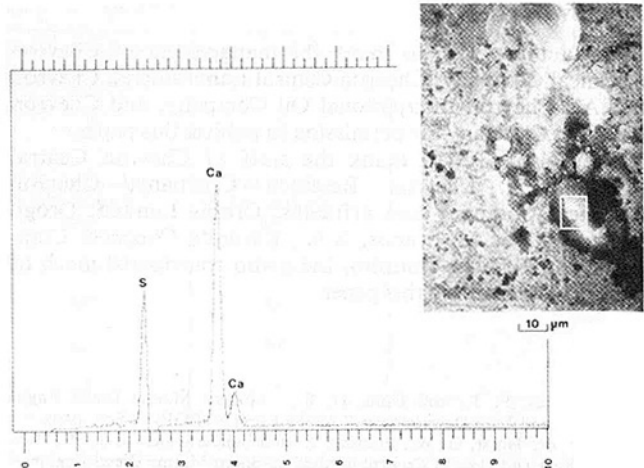


Fig. 59 Relatively hard particle containing calcium and sulphur which ploughed into softer overlay

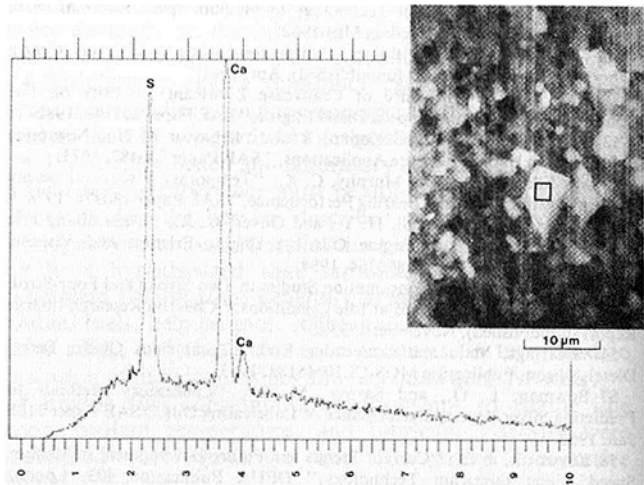


Fig. 60 Particles collected in bypass centrifuge from engine operating with residual/blended fuel

# Centrifugal Fan Performance With Distorted Inflows

T. Wright<sup>1</sup>

Westinghouse Fluid Systems Laboratory,  
West Lafayette, Ind. 47906

S. Madhavan

J. DiRe

Westinghouse Sturtevant Division  
Hyde Park, Mass.

*Efforts to quantify degradation of the performance of a centrifugal fan subjected to distorted inflows are presented. The study centered on examination of pressure rise, efficiency, and onset of stall for a backwardly-inclined, airfoil-bladed fan. Nonuniform flow patterns were generated in an adjustable countervane damper assembly installed upstream of the inlet box, and systematic families of performance curves were generated. Results of these tests show that significant degradation in efficiency and pressure rise—as much as 10 to 15 percent—may result from moderately to severely distorted inflow patterns. Onset of stall was significantly influenced by severely distorted inflows.*

## Introduction

The problem of determining how much a turbomachine is affected by poor inlet flow conditions is an old one. It arises in HVAC design and installation, layout of hydraulic pumping systems, and in the design of inlet configurations for both ground-based and airborne gas turbine compressors. In the case of aircraft configurations, some extensive studies [1] of inlet flow mapping and engine performance have been done. Investigations of inlet flows in fans used in heating/cooling and ventilation applications have been carried out as well [2]. However, for heavy duty centrifugal fan equipment, the information on performance has been largely qualitative or related to a specific installation with the exception of the unsteady work sponsored by EPRI [3].

A recent example of a centrifugal fan being subjected to poor inlet flow occurred in a power plant. Field measurements of fan performance indicated that both efficiency and pressure rise of the fans were several percentage points short of expected performance. Surveys of the flow entering the inlet boxes of the fans showed significant velocity variations across the inlet planes. To check on the relationship of the distorted inflow to the apparent performance shortfall, a scale-model test was set up. Results from that test indicated that the fan performance was degraded by several percent when subjected to an inflow distortion pattern similar to those measured in the field. On the basis of these limited laboratory results, it was decided that a specification on required inflow quality should be developed. In order to define this specification with any certainty, more extensive information relating performance to inflow was required.

## Analysis

In order to quantify the influence of inlet flow distortion on fan performance in a way which can be generalized and scaled to other sizes of equipment or to similar equipment, it is

useful to describe inlet flow patterns in simple, compact terms. An example of poor inlet flow is illustrated in Fig. 1 along with the basic features of the fan inlet system. The figure shows the kinds of flow distortion that may arise as a result of "poor" inlet ducting. The ductwork problems may result from severe space constraints that affect the layout of the delivery of air/gas to the fan, or from awkward routing requiring too many turns of the flow or turns and transitions being too close to the fan. Distortions of inflow may include nonuniform velocity profiles along the axial ( $x$ ) dimension of the inlet plane or along the transverse ( $z$ ) dimension. It may also include coherent vorticity, or various combinations of these flow patterns, as well as differences in volume flow rate through the halves of a double width fan (flow imbalance). Based on field observations and experience, it appears that the transverse component of distortion is both common and severe in its effects compared to the others. While vorticity, flow imbalance, and axial distortion are not considered negligible, it was decided to limit initial investigations to

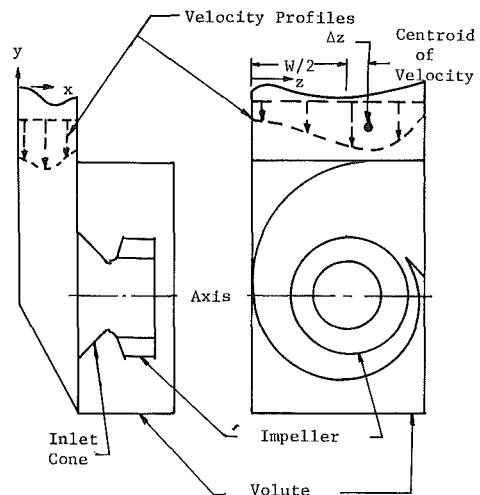


Fig. 1 Examples of poor inlet flow profiles shown with basic fan geometry

<sup>1</sup>Currently with the Mechanical Engineering Department, University of Alabama at Birmingham.

Contributed by the Gas Turbine Division and presented at the Joint Power Generation Conference, Indianapolis, Indiana, September 25-29, 1983. Manuscript received by the Gas Turbine Division June 29, 1983. Paper No. 83-JPGC-GT-5.

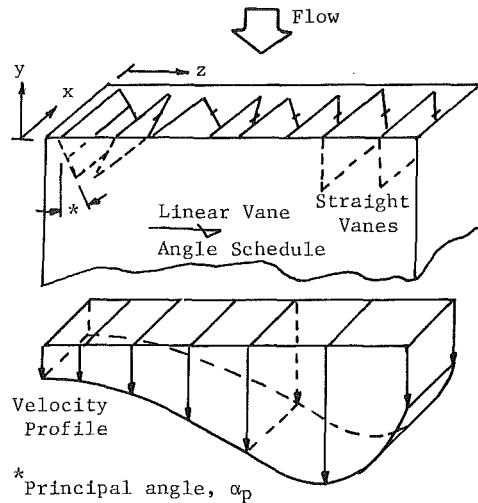


Fig. 2 Vane box geometry, nomenclature, and velocity profile shown for an asymmetrical vane schedule

examining the influence of systematic families of velocity profiles that vary strongly in the  $z$ -direction, are reasonably uniform in the  $x$ -direction, and whose vectors all lie approximately along the  $y$ -direction. Such an approach was meant to provide extensive data on the most important form of distortion and to maximize return of information with somewhat limited resources.

The work was restricted to the kind of inflow profile shown in Fig. 2. The vane box is shown schematically as an array of adjustable vane pairs that can be used to generate high impedance in part of the inlet plane and lower impedance elsewhere. In order to characterize a family of such profiles, three descriptive parameters were developed – a velocity ratio, a centroidal location, and a loss coefficient.

The velocity ratio is a measure of the overall amplitude of the disturbance compared to uniform flow and employs a normalized standard deviation calculation to provide a means of smoothing for irregular flows.

Using  $\hat{V}$  to represent the amplitude, then

$$\hat{V} = \left( \sum_{i=1}^n (V_i - \bar{V})^2 / n \right)^{1/2} / \bar{V} \quad (1)$$

where

$$\bar{V} = \sum_{i=1}^n V_i / n. \quad (2)$$

The  $\Sigma$  form of these equations permits correlation of a set of discrete measurements and can be applied to any number of measurements along the  $z$ -axis of various locations of  $x$ . The  $y$ -location is specified as the entrance plane of the fan inlet box.

Centroidal location of the velocity profile is an important parameter because of the way in which it may induce a preswirl component into a fan impeller. If  $\Delta z$  is the centroidal offset of the velocity (see Fig. 1) and  $\bar{V}$  is the mean velocity, then a swirling moment exists that has a magnitude  $\Gamma$  equal to the product of  $\bar{V}\Delta z$ . This moment will then induce a swirl velocity  $u_i$  at the leading edge of the impeller blades which is proportional to  $\Gamma$ , so that  $u_i \cong \Gamma/d$  with the algebraic sign of  $\Gamma$  (or  $\Delta z$ ). From the Euler ideal pressure rise equation [4],  $\Delta p_T = \rho U_T u_T - \rho U_i u_i$  [( )<sub>T</sub> refers to o.d., ( )<sub>i</sub> refers to i.d.]. The influence of  $\Delta z$  on pressure rise can be approximated by combining these results. That is, a change  $\delta$  in pressure rise can be written as  $\delta = (\Delta p_T (\Delta z \neq 0) - \Delta p_T (\Delta z = 0)) / \Delta p_T (\Delta z = 0)$  so that  $\delta \cong -\bar{V}\Delta z / u_T D$ . Introducing  $\phi$  and  $\Psi_T$  (see Nomenclature),  $\delta \cong -(2\phi / \Psi_T) (\Delta z / D)$ . The convention for positive  $\Delta z$ , illustrated in Fig. 2, is for positive  $\Gamma = \bar{V}\Delta z$  when  $\Gamma$  has the same sense of rotation as the impeller. Using typical values for  $\phi$  and  $\Psi_T$  (see Fig. 7) yields  $\delta \cong \Delta z / 2D$ .

If  $\Delta z$  is one-fourth of the inlet box width (which is about twice the impeller diameter  $D$ ), then  $\delta$  will be about 0.25 – that is, pressure rise may be increased or decreased by roughly 25 percent for large values of ( $\pm$ )  $\Delta z$ . If the fan is fitted with a set of inlet guide vanes in the inlet cone, then the magnitude of  $\Gamma$  will be significantly reduced by the straightening of the swirling inflow by the vanes. The influence of  $\Delta z$  on pressure rise will be reduced, but a significant penalty in pressure loss across the vane row will occur, impacting both net pressure rise and efficiency.

For convenience in representing the experimental data, a normalized centroidal offset parameter is defined by  $\hat{\epsilon} = 2\Delta z / W$  where  $W$  is the width of the inlet box. So  $\hat{\epsilon}$  has the range  $-1 \leq \hat{\epsilon} \leq +1$ . In terms of a velocity survey across the inlet plane,  $\hat{\epsilon}$  is defined by

$$\hat{\epsilon} = 2 \sum_{i=1}^n (V_i z) / \sum_{i=1}^n (V_i) / W - 0.5 \quad (3)$$

## Nomenclature

$A$  = fan reference area,  
 $A = (\pi/4)D^2, m^2$   
 $D$  = fan impeller diameter, m  
 $d$  = fan impeller inlet diameter, m  
 $i$  = index of velocity survey point, dimensionless  
 $N$  = fan rotational speed, rpm  
 $n$  = number of velocity survey points, dimensionless  
 $\Delta p_l$  = local value of total pressure loss, mm H<sub>2</sub>O  
 $\Delta p_T$  = fan total pressure rise, mm H<sub>2</sub>O  
 $Q$  = volume flow rate, L/s  
 $Q_0$  = reference value of  $Q$ , L/s  
 $U_T$  = fan tip speed,  $U_T = \pi ND/60$ , m/s  
 $U_i$  = fan inlet speed,  $U_i = \pi ND/60$ , m/s  
 $u_T$  = tangential discharge velocity of fan, m/s  
 $u_i$  = tangential inlet velocity of fan, m/s

$V$  = inflow velocity, m/s  
 $V_y$  =  $y$ -component of inflow velocity, m/s  
 $\bar{V}$  = averaged value of  $V$ , m/s  
 $\hat{V}$  = normalized rms inflow velocity, dimensionless  
 $W$  = width of fan inlet box, cm  
 $x$  = axial dimension of inlet plane, cm  
 $y$  = streamwise dimension of inlet plane, cm  
 $z$  = transverse or width dimension of inlet plane, cm  
 $\Delta z$  = offset of velocity centroid, cm  
 $\alpha_p$  = principal angle of distortion vane schedule, deg  
 $\Gamma$  = velocity moment or vortex strength, m<sup>2</sup>/s  
 $\delta$  = change in normalized ideal pressure rise due to  $\Gamma$ , dimensionless

$\hat{\epsilon}$  = normalized offset of centroid of inlet velocity profile, dimensionless  
 $\eta_s$  = static efficiency,  
 $\eta_s = (\Psi_s / \Psi_T) \eta_T$ , dimensionless  
 $\eta_{s0}$  = reference value of  $\eta_s$ , dimensionless  
 $\eta_T$  = total efficiency, dimensionless  
 $\phi$  = flow coefficient,  $\phi = Q / U_T A$ , dimensionless  
 $\Psi$  = total pressure rise coefficient,  
 $\Psi_T = (\Delta p_T / (\frac{1}{2} \rho U_T^2))$ , dimensionless  
 $\Psi_s$  = static pressure rise coefficient,  $\Psi_s = \Psi_T - \phi^2$ , dimensionless  
 $\rho$  = air/gas weight density, Kg/m<sup>3</sup>  
 $\zeta_T$  = total pressure loss coefficient, dimensionless



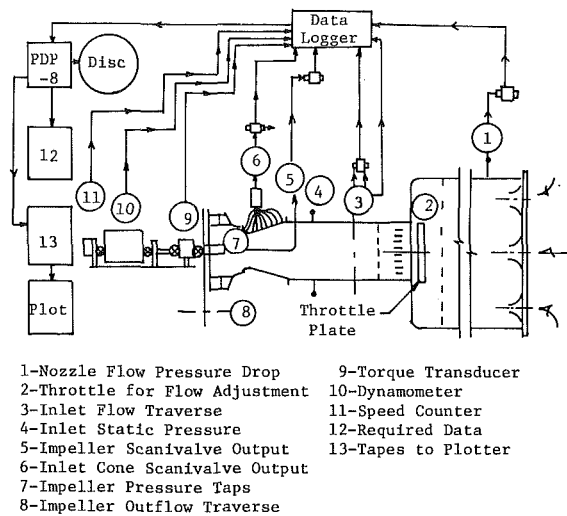


Fig. 3 Schematic of the fan test stand, showing instrumentation and data acquisition path

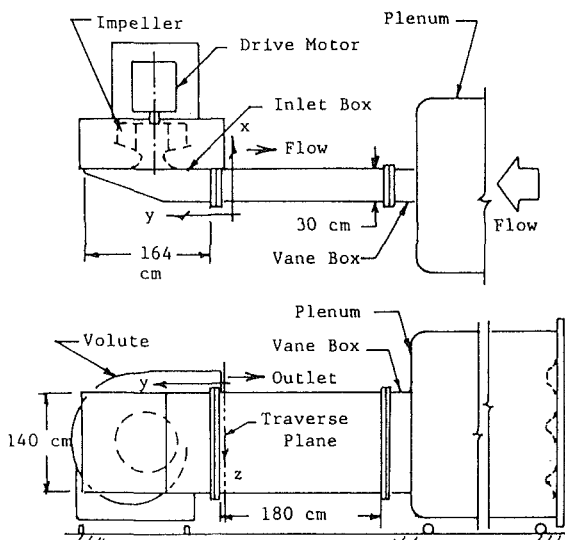


Fig. 4 Inflow test stand arrangement

In defining the performance response of the fan to variations in  $\hat{V}$  and  $\hat{\epsilon}$ , it is important to credit the fan with the work associated with artificially generating the pattern of inflow distortion. The pressure rise of the fan is defined as the change in total pressure from the inlet box flange to the discharge plane of the fan housing. Thus it is necessary to define total pressure losses across the countervane distortion assembly to be used in simulating poor entry flow and to include these losses as another characteristic of the flow distortion system in order to correctly define the fan performance. In surveying the inflow patterns, any decrements in total pressure across the vane row are recorded along with  $V$  and  $z$ , so that a mass-averaged loss may be estimated. Defining the local value of the loss as  $\Delta p_l$ , a loss coefficient  $\zeta_T$  is calculated by

$$\zeta_T = \left( \sum_{i=1}^n \Delta p_l V_i / \sum_{i=1}^n V_i \right) / \frac{1}{2} \rho \bar{V}^2 \quad (4)$$

For the studies undertaken in this work, the dependent variables—the effects of distortion—are described by the ratio of pressure rise to pressure rise at  $\hat{V} = \hat{\epsilon} = \zeta_T = 0$ , and by the ratio of efficiency to efficiency at  $V = \hat{\epsilon} = \zeta_T = 0$ . More specifically, these variables are  $(\Psi_c / \Psi_{s0})$  and  $(\eta_s / \eta_{s0})$ . The  $( )_0$  value corresponds to  $\hat{V} = \hat{\epsilon} = \zeta_T = 0$ .

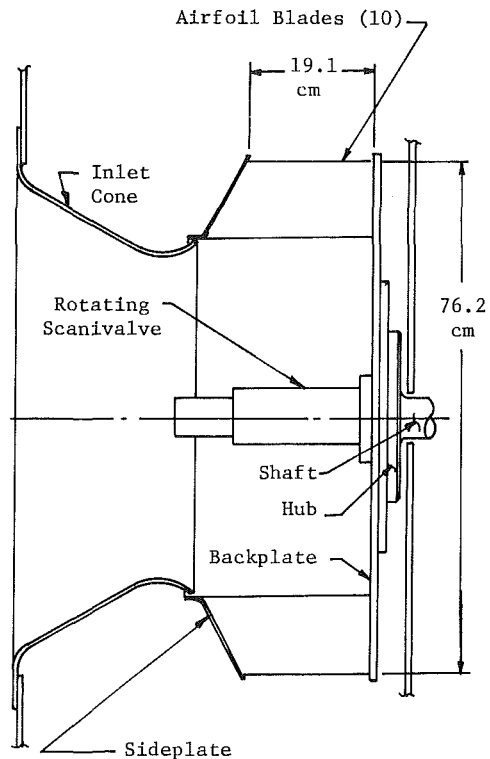


Fig. 5 Impeller showing inlet cone geometry (from [6])

Summarized results use the reference  $( )_0$  values corresponding to operation of the fan with no distortion at its “design point” or point of best efficiency. For the test fan, operation  $( )_0$  is at  $\phi = .176$ . Since the fan to be used in the experimental phase of this work was already equipped with dynamic pressure instrumentation, determination of the onset of severe pressure pulsation [5, 6] associated with rotating stall in the impeller would require very little extra effort or cost. It was decided to measure this stall onset as a function of the flow distortion parameters— $\hat{V}$ ,  $\hat{\epsilon}$ —and to assess their influence on stable fan operation. Rotating stall is manifested most clearly by a rapid increase in magnitude of the pressure pulse near fan running frequency. In addition, the frequency of pulsation begins to decrease as amplitude increases. This process continues until very severe pulsation is occurring at approximately two-thirds running frequency. It was decided for this work to establish a common basis for comparing fan performance with inflow distortion to the reference case, by forcing the fan to operate with a pulsation frequency of 14.6 Hz (running frequency is 20 Hz) and comparing flow-pressure rise performance. Stopping at 73 percent considerably reduces the worst vibrational stress on our relatively fragile and expensive instrumented impeller.

## Experiment

While much of the detail on the experimental equipment, test procedures, and data acquisition will be referred to an earlier paper [7], those elements which are unique to this work will be discussed in more depth.

Figure 3 is a schematic representation of the test stand. It illustrates the layout, instrumentation, and flow of information to final reduction of the test data. The inlet arrangement for the fan was modified for this work as shown in Fig. 4. Here the inlet box for the fan is shown installed along with the inlet flow distortion device (the distorter). All data derived from this test stand were acquired and reduced according to conventional industry standards [8].

Additional instrumentation used in this work consisted of

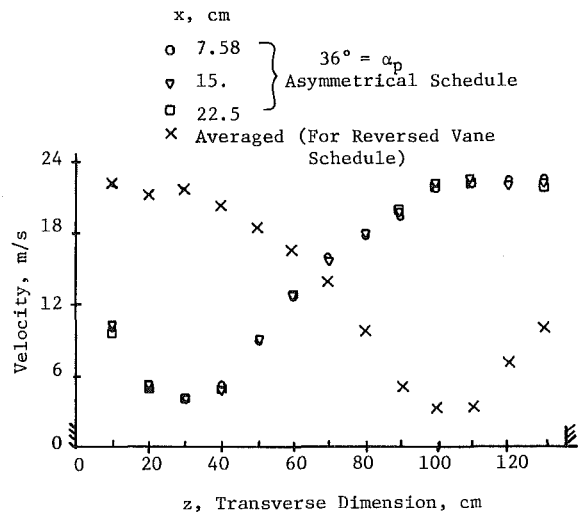


Fig. 6 A distorted velocity profile at the entrance of the inlet box

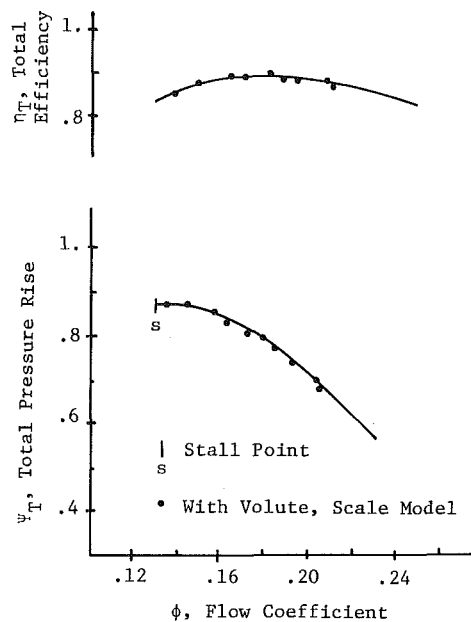


Fig. 7 Fan overall performance (from [6])

an Endevco piezoresistive pressure transducer, installed in the cutoff of the fan housing, and a real time analyzer used to monitor the unsteady pressure measurements. The layout of impeller and volute housing is detailed elsewhere [7], but Fig. 5 provides major dimensions of the configuration.

The heart of the apparatus for this experiment is the distorter, which consisted of 14 equally-spaced vanes arrayed across the  $x$ -dimension of the box. The  $\sim 30\text{-cm} \times 140\text{-cm}$  cross-section of the distorter corresponds to the dimensions of the inlet box, and its length of 180 cm allows substantial decay of the sharply irregular velocity distribution that exists just downstream of the vanes. Velocity surveys used to establish the distortion parameters were carried out using Kiel and wedge-type probes at a distance of 150 cm from the trailing edges—that is, just upstream of the entry plane of the fan inlet box. The vanes were arranged in systematic “schedules” of offset angles (relative to the flow direction) with linear variation of the characteristic angle of a vane pair across the width ( $z$ ) dimension of the distorter.

Vane schedules are identified by the “principal” vane angle,  $\alpha_p$ . The distorter was connected to an exhaust blower

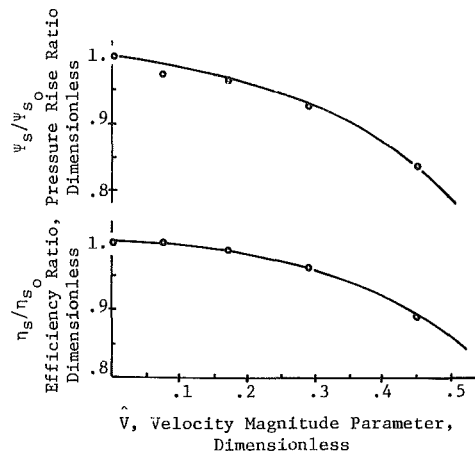


Fig. 8 Summary of the influence of symmetrical inlet profiles on fan performance at reference flow rate ( $\hat{\epsilon} = 0$ , no IGVs installed)

for calibration of distortion parameters  $\hat{V}$ ,  $\hat{\epsilon}$ , and  $\zeta_T$  (as described in the Analysis section of this paper).

Examples of velocity profiles generated at  $\phi = .176$  are shown in Fig. 6. For the base case with all vanes at 0 angle, the measurements gave  $\hat{V} = .02$ ,  $\hat{\epsilon} = .01$ , and  $\zeta_T = .025$ —a flow of high uniformity.

Systematic testing of the various vane arrangements and reduction of the velocity surveys to the bulk distortion parameters were carried out.

A set of inlet guide vanes (IGVs) to be installed in the inlet cone of the fan were fabricated. The IGVs are fixed in the wide-open position (vanes aligned with the fan axis) and are intended to provide a measure of their influence on performance with distorted inlet flow at or near design point operation.

The fan performance curves, in terms of pressure rise and efficiency as functions of volume flow rate, and the stall onset points, were generated for the range of distortion parameters calibrated. Additional tests were run by using vane settings between and beyond those assigning interpolated or extrapolated values of  $\hat{V}$ ,  $\hat{\epsilon}$ , and  $\zeta_T$  to these tests.

All pressure transducers and pressure-type probes used in this work were calibrated using a micromanometer (20-in. Meriam with graduations of 0.001 in.-H<sub>2</sub>O) and a free-jet air source for the probes (jet diameter was 0.1 m with velocities to 33.5 m/s). The cradled dynamometer and torque transducer were calibrated using deadweight moment measurements, and bearing losses were approximated by measuring torque required to run the drive train without the fan impeller installed. Data values were accessed in groups of 20, 40, or 80 successive readings of a given signal in order to remove unsteadiness from the signals by averaging. Based on calibration information and reproducibility checks, the accuracy of pressure, pressure-rise, flow, and velocity data are within  $\pm 1/2$  percent of values at design point. Power measurements are within  $\pm 1$  percent of the design point value, so that efficiency data are within about  $\pm 1.5$  percent.

Results for the fan configured with the IGVs are shown in Fig. 8. Here normalized pressure rise and efficiency are shown for symmetrical distortion patterns as a function of  $\hat{V}$  ( $\hat{\epsilon} \approx 0$ ). For values of  $\hat{V} > 0.1$ , measurable loss of efficiency is observed; the loss approaches 15 percent for distortions as large as 60 percent of the mean velocity. Degradation of pressure rise is more rapid and can yield seriously impaired performance for relatively small distortions.

Figure 9 summarizes results for asymmetrical inflow patterns without IGVs. The influence of  $\Gamma$  on pressure rise is clearly seen for positive and negative values of  $\hat{\epsilon}$ . Again falloff in efficiency is significant with measurable loss oc-

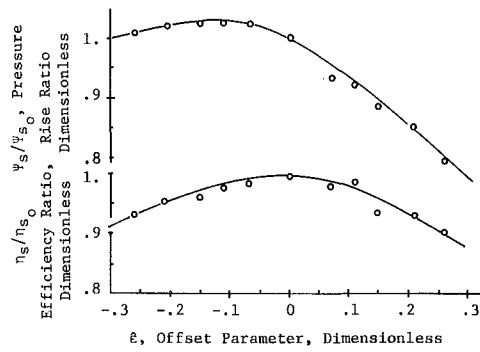


Fig. 9 Summary of the influence of asymmetrical inlet profiles on fan performance at reference flow rate (no IGVs installed)

- Original Tests
- Repeat Tests
- △ Case A
- ▽ Case B
- ◇ Case C

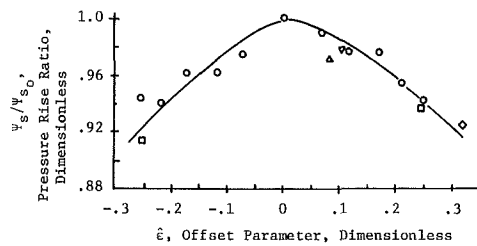


Fig. 10 Summary of the influence of asymmetrical inlet profiles on fan pressure rise at reference flow rate (with IGVs installed)

- Original Tests
- Repeat Tests
- △ Case A
- ▽ Case B
- ◇ Case C

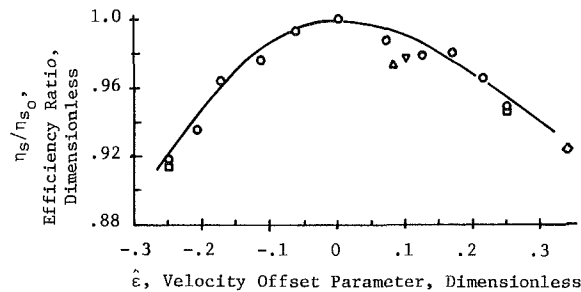


Fig. 11 Summary of the influence of asymmetrical inlet profiles on fan efficiency at reference flow rate (with IGVs installed)

curing for small values of  $\hat{\epsilon}$  with very large penalties for  $|\hat{\epsilon}| > .15$ .

When tested with IGVs installed, the fan yielded a significantly different response to inlet flow distortion. Figure 10 shows the trend in pressure rise with asymmetrical inflow profiles. As compared to the results of Fig. 9, the influence of  $\Gamma$  is virtually eliminated. Figure 11 shows the corresponding efficiency performance. The results are very similar. The results for efficiency variation with  $\hat{V}$  are summarized in Fig. 12. Here the results show a constant trend of falling efficiency. As compared to the data taken without IGVs installed, the loss in efficiency seems to show little difference within the apparent experimental uncertainty and scatter of the data. Figure 13 gives the corresponding result for pressure rise.

The simulation of the field performance problem men-

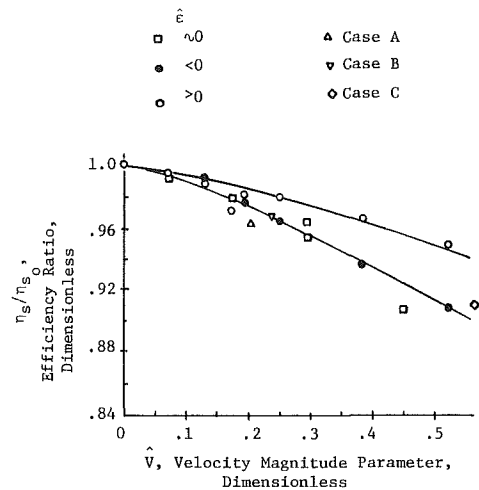


Fig. 12 Summary of the influence of inlet flow distortion on fan efficiency at reference flow rate (with IGVs installed)

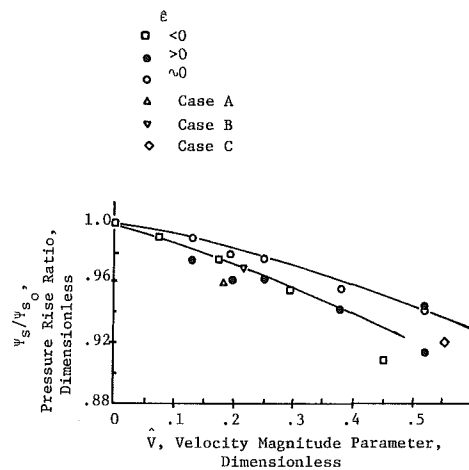


Fig. 13 Summary of the influence of inlet flow distortion on fan pressure rise at reference flow rate (with IGVs installed)

tioned earlier resulted in additional data points for Figs. 10 and 11, Case A. Tests were run on a similar but larger fan with inflow surveys run downstream of a distortion assembly in the manner described above. In addition, a laboratory simulation of a fan and inflow ductwork configuration was tested to determine the influence of two upstream elbows on the fan performance. The test layout is shown in Fig. 14, illustrating the single turning vane used in each elbow to improve the inflow. The fan was tested with open inlet, with the ductwork connected, and again with the turning vanes installed. In each case, the inflow patterns were measured and characterized as prescribed above and the performance was normalized. Average values of performance and distortion parameters were used; flow imbalance was not considered. Results are shown in Figs. 11 and 12 as Case B and Case C. These results are in substantial agreement with the systematic data.

Finally, Figs. 15 and 16 provide a summary of the influence of the distortion parameters on the onset of severe pressure pulsation—the 14.6 Hz rotating stall point. The influence, as seen in the figures, is not very strong except at the largest values of distortion. In general, both pressure and flow rate appear to consistently decrease with increasing  $|\hat{\epsilon}|$  or  $\hat{V}$ , but the shifts are confined to a few percent of the undistorted performance. It appears that stall onset is dominated by variables other than distortion, at least for moderately distorted inflows.

The overall view of these results shows that distortion of the

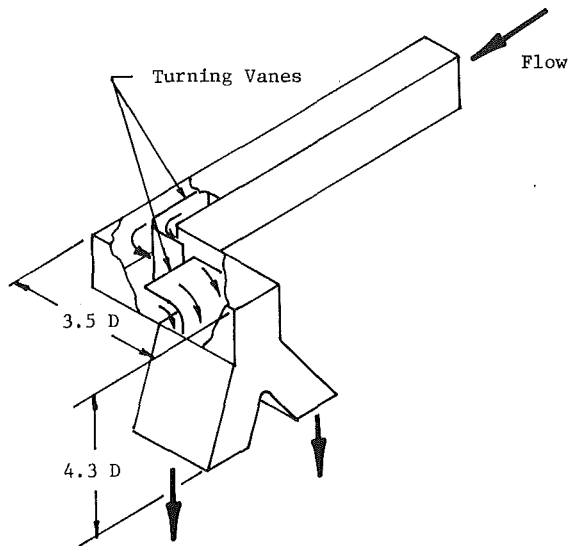


Fig. 14 Inlet flow duct geometry with two abrupt turns; tested with (Case B) and without (Case C) the turning vanes installed. Proportions are given in fan diameters.

inlet profile to a centrifugal fan has a serious impact on efficiency. With the exception of a mild increase for negative  $\Gamma$  (accompanied by a penalty in efficiency), pressure rise suffers as well. For moderate distortions— $\hat{V} \sim .25$ ;  $\hat{\epsilon} \sim .25$ —typical losses in efficiency and pressure rise may be expected to range between 5 and 10 percent. In terms of performance evaluated against energy cost over the life of the equipment, these are large losses. For example, a large forced-draft fan requiring a shaft power of 3000 KW would waste about 300 KW at a 10 percent penalty associated with poor inflow. Current estimates for evaluated life cost of a kilowatt range around 2000 dollars/KW, so that 300 KW is evaluated at a cost penalty of 600,000 dollars. This number is of the same magnitude as the first cost of the fan, and is large compared to the cost of modifications to improve inflow.

## Conclusions

Distortion of the inflow to the centrifugal fan tested reduces the level of efficiency for all conditions studied.

In virtually every situation, pressure rise performance is reduced as well.

Even moderate levels of distortion—10 to 15 percent velocity variation or 10 to 15 percent lateral offset of the flow entering the inlet box—can lead to significant penalties in performance—5 percent in efficiency and pressure rise.

Relatively severe distortion—30 to 50 percent velocity variation or flow offset—can cause serious deterioration in fan performance—10 to 12 percent reductions in efficiency and pressure rise.

For the airfoil-bladed fan tested in this work, the onset of severe pressure pulsations associated with rotating stall is strongly affected only by severe inflow distortion.

The results of this study should be used to formulate provisional guidelines for allowable levels of inflow distortion for centrifugal fans.

This work should be extended to include several significantly different fans: a single-thickness, backwardly inclined blade, an airfoil-bladed fan of lower specific speed, and a radial-tip blower.

Future studies should be done to include other types of distortion patterns: multilobed symmetrical patterns, distortion in the axial position on the inlet plane, and coherent vorticity.

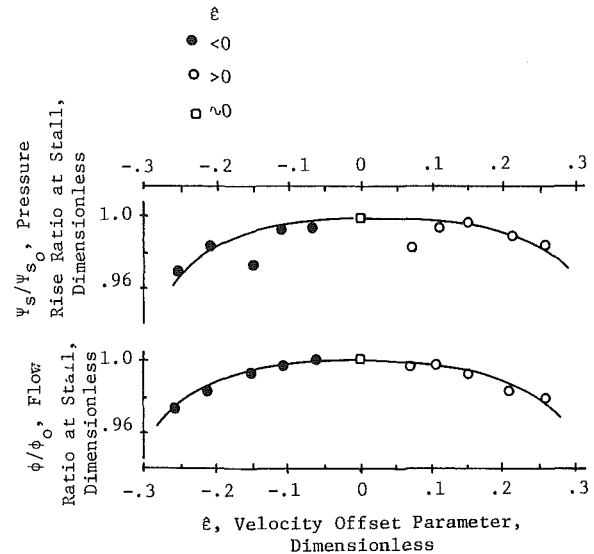


Fig. 15 Summary of stall onset (at 14.6 HZ) with inlet flow distortion (with IGVs installed)

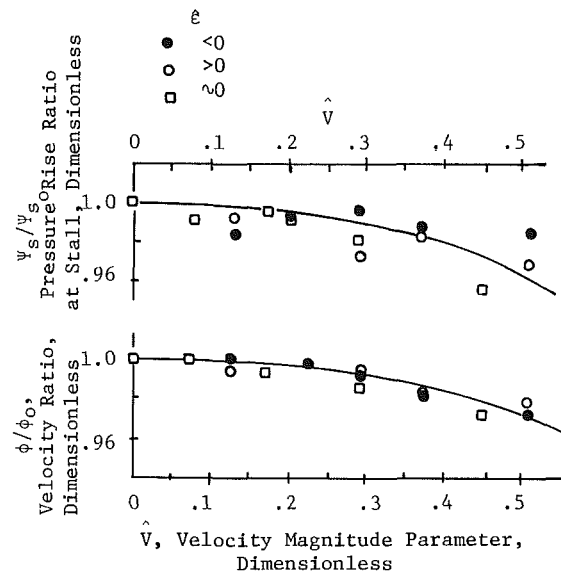


Fig. 16 Summary of stall onset (at 14.6 HZ) with inlet flow distortion (with IGVs installed)

## References

- 1 Carta, F. O., "Analysis of Unsteady Aerodynamic Effects on an Axial Flow Compressor Stage with Distorted Inflows," Project Squid Technical Report UARL-1-PU, July 1, 1972.
- 2 Gessner, F. B., "An Experimental Study of a Centrifugal Fan Inlet Flow and Its Influence on Fan Performance," ASME Paper No. 67-FE-21.
- 3 Goldschmied, F. R., Wormley, D. N., and Rowell, D., "Air/Gas System Dynamics of Fossil Fuel Power Plants, Vol. 5: System Excitation Sources," Research Project 1651, Westinghouse/Massachusetts Institute of Technology, Oct. 1981.
- 4 Wislicenus, G. F., *Fluid Mechanics of Turbomachinery*, Dover Publications, New York, 1965, pp. 119-125.
- 5 Wormley, D. N., Rowell, D., and Goldschmied, F. R., "Air/Gas System Dynamics of Fossil Fuel Power Plants—Pulsations," EPRI Report CS-2206, Jan. 1982, pp. 3-57, 3-78.
- 6 Greitzer, E. M., "The Stability of Pumping Systems—The 1980 Freeman Scholar Lecture," ASME *Journal of Fluids Engineering*, Vol. 103, June 1981, pp. 193-242.
- 7 Wright, T., Tsou, K. T. S., Greaves, K. W., and Madhavan, S., "The Internal Flow Field and Overall Performance of a Centrifugal Fan Impeller—Experiment and Prediction," ASME Paper 82-JPGC-GT-16.
- 8 *AMCA Standards*, Bulletin 210, 1975.

# Axial Fan Performance With Blade-Base Clearance

T. Wright<sup>1</sup>

Westinghouse Fluid Systems Laboratory,  
West Lafayette, Ind. 47906

*A study to evaluate the influence of increasing the clearance between blade and hub on a controllable pitch axial fan (CPAF) is presented. Fan performance was measured over a range of increasing clearance for several settings of blade pitch angles. The resulting variations of pressure rise, flow rate, and efficiency have been correlated as functions of established clearance parameters with good results. The study shows that large base clearances may result in reductions in efficiency and flow rate of 5 percent or greater in a typical CPAF configuration.*

## Introduction

In designing and developing products for sale in the industrial, commercial, and utility markets, a careful balance must be maintained between the initial cost of the product and the quality of its performance. A high first cost can often be accommodated if the product operates with a high enough efficiency and reliability so that savings in power costs or the benefits of increased availability can offset the incremental cost. Conversely, low first cost can cause the end user of the product to lose money by paying for lost wattage or production associated with low efficiency or reduced availability.

In developing a controllable pitch axial fan (CPAF) for industrial and utility applications, the questions of quality versus cost arose many times. The fundamental role of a CPAF in such applications is the inherent ability of the fan to provide excellent control over a very wide range of flow delivery while maintaining high efficiency over the same range of performance (relative to other types of fans). When pressure developed to find ways to reduce the cost of a CPAF, any benefit analysis must be tempered by knowing whether the cost-reduced product can still deliver the inherent advantages it was designed to provide. One question which arose was whether the tolerance on the running clearance between the bases of the movable blades and the surface of the fan hub could be relaxed. Since most designs include a spherically ground hub surface to maintain constant base clearance over the full range of pitch control, and require controlled tolerances for grinding the undersurface of the blade bases, relaxation of small clearance requirements in this region could yield significant savings in manufacturing costs. To develop the complete answer to this question it was necessary to supply a confident estimate of the effect of increased base clearances on the performance—both pressure rise and efficiency—of the fan. In a general sense, it is clear that increasing clearance will degrade performance. Quantifying the degree of degradation requires an available theoretical or experimental basis for accurate estimation. It was decided to examine the literature on gas turbine axial compressor per-

formance to seek disciplined information on base clearance, and if possible to apply these results to the CPAF. However, since the performance parameters and application requirements of high-speed, multistage axial compressors differ considerably from those of the typical CPAF, it was felt that at least a limited test program would be required to build the required degree of confidence into these results.

The earliest studies of the influence of the end walls (hub and outer casing) approached the problem from two-dimensional and annular cascade aerodynamics. These studies [1] considered the effects of endwalls and secondary flows on turning the fluid in terms of end wall boundary layers and passage and corner vortices—and virtually no systematic information on the effect of clearances on these parameters was available. Other investigations [2, 3] provided a measure of the complexity of the problem in terms of measurement and amenability to analysis. Recent investigations [4–6] point out the limitations of the classical secondary flow theory and boundary layer approach and highlight the overwhelming importance of tip clearance on endwall flow development. A good review of this work is provided by Hunter and Cumpsty [7]. Of particular interest in design analysis, the work of Smith [8], Koch and Smith [9], and Koch [10] provide practical guidelines for assessing endwall effects in general, and clearance effects in particular, on compressor performance. It was decided to use these results as basic guidelines in assessing the influence of blade base clearance, and to use thier correlation parameters to generalize—to the extent possible—limited but systematic measurements of clearance effects in a model CPAF experiment.

## Analysis

In determining the effect of base clearance on CPAF performance, the primary concern was what happens to flow rate, pressure rise, and efficiency in the region of best efficiency for a given blade pitch setting. Blade base clearance was to be imposed as a perturbation on the configuration of the fan with normal tip clearance and tolerances, so that measurement of relatively small changes in performance would be required to characterize this influence.

Figure 1 illustrates the parameters involved. Based on the prior work [8–10], it was clear that the primary influence of clearance would be reflected in the endwall or hub surface

<sup>1</sup>Currently with the Mechanical Engineering Department, University of Alabama at Birmingham

Contributed by the Gas Turbine Division and presented at the Joint Power Generation Conference, Indianapolis, Indiana, September 25–29, 1983. Manuscript received by the Gas Turbine Division June 29, 1983. Paper No. 83-JPGC-GT-6.

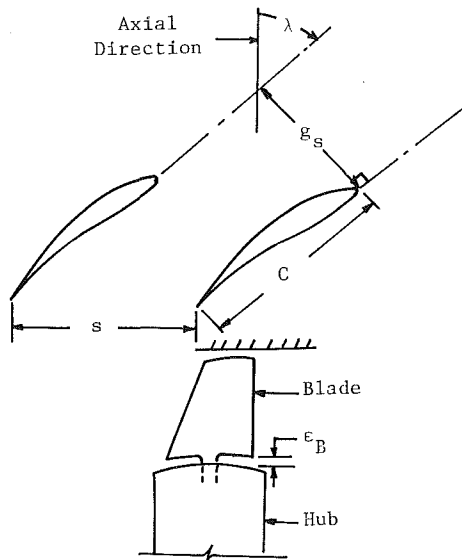


Fig. 1 Illustration of blade base cap and nomenclature

boundary layer displacement thickness or blockage of the ideal flow through the fan stage. In turn, the degree of annulus blockage would be governed by a diffusion parameter and an appropriately normalized gap value. Based on analogy to axial diffusers, the diffusion parameter should be a ratio of static pressure rise (recovery) to incoming dynamic pressure. The extensive earlier efforts [8-10] indicate that the best geometrical parameter to represent the clearance gap is the ratio of the gap height to the staggered spacing as shown in Fig. 1. (Some controversy concerning the proper gap normalization parameter exists [7].)

For the CPAF, the conventional definitions for normalized performance parameters are stated in terms of the shaft power  $P$ , the total pressure rise  $\Delta p_T$ , static pressure rise  $\Delta p_s$ , and volume flow rate  $Q$ . They are normalized by tip speed  $V_T$  and overall area or annulus area of the blade row  $A$ . Performance coefficients are then defined as:

$$\text{Flow coefficient: } \phi = Q / (A V_T)$$

$$\text{Total pressure rise coefficient: } \psi_T = \Delta p_T / (\frac{1}{2} \rho V_T^2)$$

$$\text{Static pressure rise coefficient: } \psi_s = \psi_T - \phi^2$$

$$\text{Power coefficient: } C_p = P / (\frac{1}{2} \rho V_T^3 A)$$

$$\text{Total efficiency: } \eta_T = \phi \psi_T / C_p$$

The diffusion parameter [11] for this analysis is the ratio  $\psi_s / \phi^2$  and is analogous to the parameter used by Koch and

Smith [9]. The normalized gap parameter is defined as  $\bar{\epsilon}_B = \epsilon_B / g_s$  where  $\epsilon_B$  is the blade base clearance and  $g_s = s \cos \lambda_B$ .

A combined parameter to characterize the incremental blockage of the fan annulus associated with opening up the blade base clearance is defined as  $\delta = \bar{\epsilon}_B (\psi_s / \phi^2)_0$ . Here, the  $( )_0$  notation refers to the reference condition with  $\epsilon_B = 0$ . The rationale for correlating blockage is to measure the pressure rise/flow rate performance of the fan at a given pitch setting at zero base clearance. Successive testing at increasing values of  $\epsilon_B$  shows reduced volume flow rate at a given value of pressure rise. This difference,  $Q_0 - Q$ , may be normalized as  $(Q_0 - Q) / Q_0$  so that the incremental blockage is defined as  $B' = (1 - Q / Q_0)$ . Additional testing at other values of  $\lambda_B$  is similarly treated to create a body of data in terms of  $B'$  versus  $\delta$ .

Treatment of the influence of  $\epsilon_B$  on efficiency also follows the form suggested by Koch and Smith [9]. In that work  $\eta$  was shown to behave according to  $\eta = \eta' (1 - \delta^* / h) / (1 - v / h)$ . Here  $\eta$  is a "free-stream" efficiency ("i.e., the efficiency that would exist if there were no end-wall losses" [9]).  $\delta^*$  and  $v$  are displacement and tangential force deficit thicknesses, including both end walls.  $h$  is annulus height. Smith [8] suggests that  $v$  will be roughly  $.65 \delta^*$ ; Koch and Smith [9] suggest a form where  $.45 \delta^* < v < .50 \delta^*$ , depending on pressure rise; and Hunter and Cumpsty [7] show that  $.4 \delta^* < v < .6 \delta^*$  (roughly). For the purpose of this study,  $\bar{\eta}$  is defined as  $\bar{\eta} = \eta_T / \eta_{T0}$  and is the incremental influence of  $\epsilon_B$  on efficiency. Assuming some average relationship between  $v$  and  $\delta^*$ , that is,  $v \propto \delta^*$ , then  $\bar{\eta}$  should be uniquely related to  $B'$  and hence to  $\delta$ .

However,  $B'$  is to be defined as incremental blockage at a given pressure rise while degradation of efficiency is most usefully defined for a CPAF at or near a specified flow rate. Operation at fixed speed in a flow system of nearly constant resistance will cause a fan to degrade along a very steep load-line path as clearance is increased. To relate efficiency to  $\delta$  and maintain fixed flow rate requires an estimate of the slope of the pressure rise curve. A very simple manipulation of the Euler equation for head rise [12] shows that this slope will be proportional to the flow rate at least near the design or "best efficiency" point. This approximation allows correlation of pressure rise or efficiency against the product  $\phi \delta$ , or more simply, against  $\phi_0 \delta$ .

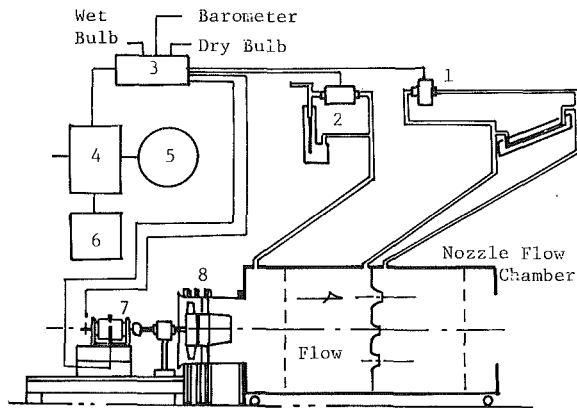
Having used the best available basis for defining the expected fan behavior with base clearance, it remained to test a typical CPAF configuration. Correlation of test results could then be carried out using the above relationships.

## Experiment

Experimental data for this work were acquired using a scale-model CPAF installed in the test stand shown

## Nomenclature

$A$ = fan annulus area, $m^2$	$s$ = circumferential spacing, m	$\eta'$ = free-stream efficiency, dimensionless
$B'$ = incremental blockage factor, $B' = (1 - Q / Q_0)$ , dimensionless	$V_T$ = tip speed, m/s	$\eta_T$ = total efficiency, $\eta_T = \phi \psi_T / C_p$ , dimensionless
$C$ = blade or vane chord, m	$t$ = blade or vane maximum thickness, m	$\bar{\eta}$ = ratio of efficiency to value with $\epsilon_B = 0$ , dimensionless
$C_p$ = power coefficient, dimensionless	$v$ = end wall boundary layer tangential force deficit thickness, m	$\lambda_B$ = stagger angle at blade base, deg
$C_{l_0}$ = design lift coefficient, dimensionless	$x$ = normalized blade radial location, dimensionless	$\lambda$ = local blade stagger angle, deg
$g_s$ = staggered spacing, $g = s \cos \lambda_B$ , m	$\delta$ = clearance parameter, $\delta = \bar{\epsilon}_B (\psi_s / \phi^2)_0$ , dimensionless	$\phi$ = flow coefficient, dimensionless
$h$ = blade height, m	$\delta^*$ = end wall boundary layer displacement thickness, m	$\psi_T$ = total pressure rise coefficient, dimensionless
$P$ = shaft power, kW	$\epsilon$ = blade-base clearance, m	$\psi_s$ = static pressure rise coefficient, dimensionless
$\Delta p_T$ = total pressure rise, mm $H_2O$	$\bar{\epsilon}_B$ = normalized clearance, $\bar{\epsilon}_B = \epsilon_B / g_s$ , dimensionless	$\rho$ = air or gas density, $kg/m^3$
$\Delta p_s$ = static pressure rise, mm $H_2O$	$\eta$ = stage efficiency, dimensionless	$\sigma$ = blade or vane row solidity, $\sigma = C / s$
$Q$ = volume flow rate, $L/s$		



1. Nozzle Flow Pressure Drop
2. Static Pressure Drop
3. Data Logger
4. Computer
5. Disk Storage
6. Reduced Data
7. Dynamometer/Speed Counter
8. Test Fan

Fig. 2 Schematic test stand arrangement

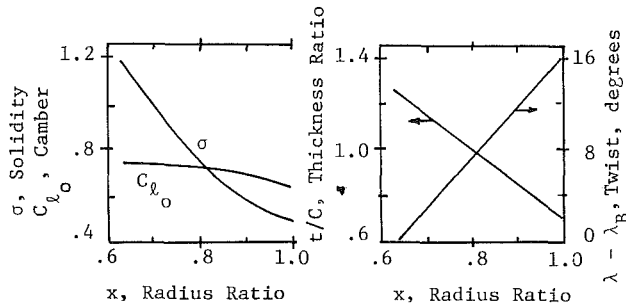


Fig. 3 Blading parameters for small-scale developmental CPAF.  $x = .631$  is hub station,  $x = 1.0$  is tip station.

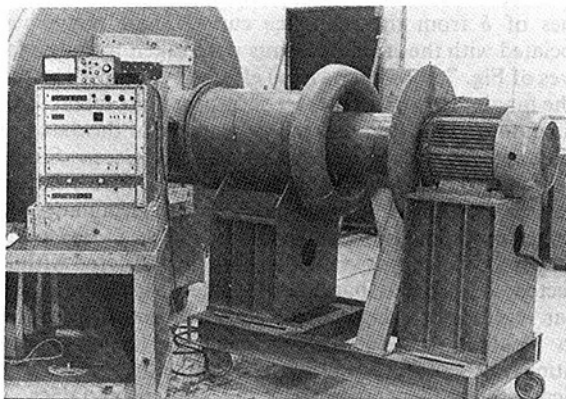


Fig. 4 Photograph of the fan test stand and data acquisition module

schematically in Fig. 1. The fan as configured for these tests is a single-stage unit with an o.d. of 0.508 m, hub-tip diameter ratio of 0.631 with 16 blades and 23 stator vanes. Tip clearance was ground in place to be 0.1 percent of the fan diameter with the movable blades set at flat pitch at the blade tips. Additional geometric detail for the stage is given in Table 1 and Fig. 3, and the fan and test stand are shown in Fig. 4. The fan is driven by a two-pole induction motor at a nominal speed of 3600 rpm. Blade chord Reynolds number at the tip speed of 95.8 m/s is  $5.0 \times 10^5$ , while blade tip relative Mach number is 0.28 (both based on standard sea level conditions [13]—1 atm, 15°C).

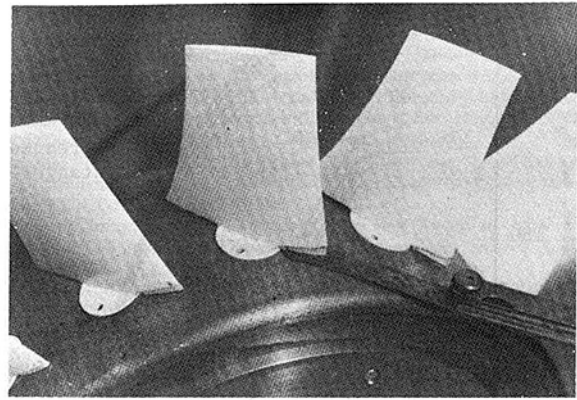


Fig. 5 Photograph of the fan showing base clearance

Table 1 Fan geometry

- Blades: Based on NACA 63-Series [15] airfoils with wedge-thickening to provide a trailing edge thickness of approximately .7 mm
- Stator vanes: Constant chord, constant cross section based on NACA 65-(1.6)14 airfoil [15] with tip solidity,  $\sigma$ , equal to 1.16
- Axial separation: Approximately 0.3 blade chords at midspan with  $\lambda_B = 50$  deg

Table 2 Array of test combinations of base clearance and blade pitch

$\epsilon_B$ (mm)	$\lambda_B$		
	40°	50°	60°
0	*	*	*
.76	*	*	*
1.52	*	*	-
1.90	-	-	*
2.28	*	*	-
3.04	-	-	*

\*tested  
-not tested

In order to vary the base clearance of the blades of the fan, wooden blocks were installed between the base airfoil sections and the surface of the hub. At a given blade pitch setting, the blades were tested, a finite gap was opened by sanding away the base surface of the wooden wedges, and the fan was retested. The procedure was repeated to the largest clearance. Blade pitch was then reset, new wedges installed, and the whole procedure was repeated. Figure 5 illustrates the clearance setting. While some error in gap height was necessarily incurred, repeated measurements of a given clearance gap indicated an accuracy and uniformity of clearance within about  $\pm 5$  to  $\pm 10$  percent of the nominal gap height.

Volume flow rate and pressure rise were determined from pressure measurements at the plenum chamber piezometer rings as indicated in Fig. 2. Torque and speed were acquired using a calibrated brushless (induction-type) torque transducer with magnetic proximity pickup of rotational speed from a 60-tooth gear. Pressure measurements, flow rate, and power were all corrected to a common speed and air density basis according to industry standards [14]. The rather small CPAF model used for these tests was built as a flexible test bed for parametric testing to evaluate a broad range of designs. Ultimate accuracy in test results and final detail in fan configuration were subordinated to examination of parametric trends. Based on instrument calibrations and reproducibility of data, the accuracy of data from this test stand is estimated as:  $\pm 1/2$  percent of design point values for flow and pressure rise;  $\pm 1$  percent for power.

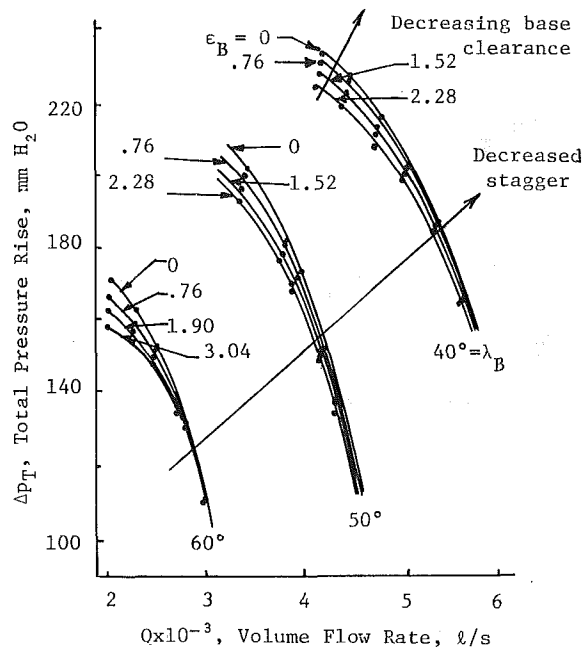


Fig. 6 Pressure rise performance of model CPAF at three pitch angles with varying base clearance ( $\epsilon_B$  in mm)

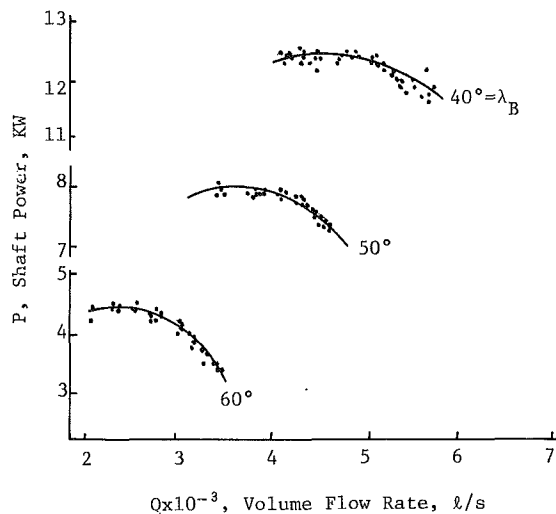


Fig. 7 Required shaft power at the three pitch angles

Table 2 summarizes the array of tests which were run. Twelve complete performance curves were developed over a full range of flow from stall to maximum flow rate at minimum measuring system resistance. Figure 6 shows the flow-pressure rise results, and Fig. 7 gives the corresponding shaft power requirements. In general, the flow-pressure rise data are well-behaved with only minor scattering, while the power data shows considerably greater scatter. There were no recognizable trends in power with base clearance at a given blade pitch setting; rather, the collection of power measurements falls within a  $\pm 1$  percent band. Apparently, any trend associated with clearance was lost within the resolution of the torque measurement. The solid lines in both figures represent "best fit" fairing through the data.

### Correlation of Data

The organization of the experimental results follows the rationale outlined in the analysis section. The zero-clearance curves of Fig. 6 were used as reference at a given pitch angle.

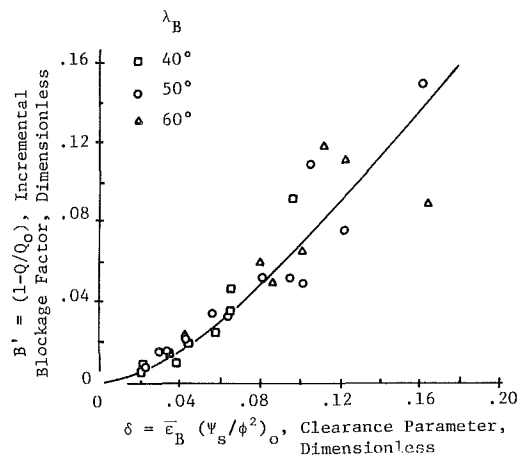


Fig. 8 Behavior of the incremental annulus blockage associated with base clearance

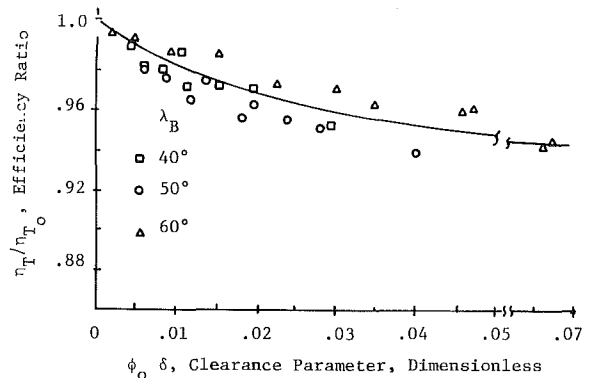


Fig. 9 Dependence of efficiency of blade base clearance

At constant pressure rise, crossings of the curves for finite clearance were used in calculating  $B'$  (incremental blockage), and these values were associated with the corresponding values of  $\delta$  from the reference curve. Shaft power values associated with the crossing points were taken from the faired curves of Fig. 7 to calculate local efficiency values. The results of the manipulation of data are shown in Figs. 8 and 9.  $B'$  as a function of  $\delta$  shows a reasonable collapse of the data in Fig. 8, although increasing scatter for large  $\delta$  is seen. Since the largest values of  $\delta$  were taken very near stall, with flattening off of the flow-pressure curves, accurate determination of  $B'$  becomes more and more difficult. In Fig 9, a clear trend of decreasing efficiency is seen. The data are scattered within the expected  $\pm 1$  percent band seen earlier. Applying a simple linear regression, using a quadratic function of  $\delta$ , to the  $B'$  data yields a correlation coefficient of 0.87. A similar treatment of  $\eta$  yields a value of  $-0.87$ . In either case the result indicates clear dependence on the chosen variables, particularly in light of the need to difference and ratio values of performance with small geometrical changes. Considering the generic nature of the parameter  $\delta$  and the acceptable quality of correlation of these results, it should be possible to estimate with reasonable confidence the influence of blade base clearance on CPAF performance over a broad range of design conditions. For example, if a fan with  $\psi_T = .46$ ,  $\phi = .2$  has a very close base clearance (say,  $\epsilon_B = .005$ ), then the price paid for minimum clearance for blade movement is perhaps 1 percent in incremental blockage and about a point in total efficiency. Opening up the base clearance to four times that value leads to an additional loss of about three points in efficiency and a serious reduction in flow rate at fixed pressure rise (perhaps 10 percent). Further increases appear to



be limited to a loss of perhaps five points in efficiency compared to a very well-executed design. Now, five points on a large fan absorbing about 2000 KW costs the end-user 100 KW. Evaluated at 2000 dollars/KW, the penalty associated with large base clearance is 200,000 dollars. Since such a cost is comparable to the first cost of the entire fan, it is clear that blade-base clearance must be treated as a serious design parameter.

### Conclusions

It is concluded from the results of this rather limited study that the influence of blade base clearance on the performance of a controllable pitch axial fan is significant. Opening up the gap can lead to serious degradation of efficiency and achievable flow and pressure rise. The influence of the base clearance correlates well with established variables based on extensive data from multistage axial flow compressors, so that it is reasonable to use existing correlations in design evaluations for controllable pitch fans with one or two stages. The curves for incremental blockage and efficiency ratio associated with the clearance parameters should be useful in estimating the penalties in operating cost when larger clearances are used to reduce first cost.

### References

- 1 "Secondary Flows in Turbomachines," *Lecture Series 72*, Von Karman Institute for Fluid Dynamics, Brussels, Belgium, Jan. 1975.
- 2 Herzig, H. Z., Hansen, A. G., and Costello, G. R., "A Visualization Study of Secondary Flows in Cascades," NACA Report 1163, 1954.

- 3 Johnson, I. A., and Bullock, R. O., *Aerodynamic Design of Axial Compressor Aerodynamics*, NASA SP-36, 1965, pp. 385-413.
- 4 Lakshminarayana, B., Pouagare, M., and Davino, R., "Three-Dimensional Flow Field in the Tip Region of a Compressor Rotor Passage—Part I: Mean Velocity Profiles and Annulus Wall Boundary Layer," *ASME JOURNAL OF ENGINEERING FOR POWER*, Vol. 104, No. 4, Oct. 1982, pp. 760-771.
- 5 Lakshminarayana, B., Davino, R., and Pouagare, M., "Three-Dimensional Flow Field in the Tip Region of a Compressor Rotor Passage—Part II: Turbulence Properties," *ASME JOURNAL OF ENGINEERING FOR POWER*, Vol. 104, No. 4, Oct. 1982, pp. 772-781.
- 6 Gregory-Smith, D. G., "Secondary Flow and Losses in Axial Flow Turbines," *ASME Journal of Engineering for Power*, Vol. 104, No. 4, Oct., 1982, pp. 819-823.
- 7 Hunter, I. H., and Cumpsty, N. A., "Casing Wall Boundary-Layer Development Through an Isolated Compressor Rotor," *ASME JOURNAL OF ENGINEERING FOR POWER*, Vol. 104, No. 4, Oct. 1982, pp. 805-818.
- 8 Smith, L. H., Jr., "Casing Boundary Layers in Multistage Axial-Flow Compressors," *Flow Research in Blading*, edited by L. S. Dzung, Elsevier Publishing, Amsterdam, Netherlands, 1970, pp. 275-300.
- 9 Koch, C. C., and Smith, L. H., Jr., "Loss Sources and Magnitudes in Axial-Flow Compressors," *ASME JOURNAL OF ENGINEERING FOR POWER*, Vol. 98, Series A, No. 3, July 1976, pp. 411-424.
- 10 Koch, C. C., "Stalling Pressure Rise Capability of Axial Flow Compressor Stages," *ASME JOURNAL OF ENGINEERING FOR POWER*, Vol. 103, No. 4, Oct. 1981, pp. 645-656.
- 11 Sovran, G., and Klomp, E. D., "Experimentally Determined Optimum Geometries for Rectilinear Diffusers with Rectangular, Conical or Annular Cross Section," *Fluid Mechanics of Internal Flow*, Elsevier Publishing, Amsterdam, Netherlands, 1967.
- 12 Wislicenus, G. F., *Fluid Mechanics of Turbomachinery*, Dover Publications, New York, 1965, pp. 119-125.
- 13 Perkins, C. D., and Hage, E. H., *Aircraft Performance, Stability, and Control*, John Wiley and Sons, New York, 1960, pp. 481-482.
- 14 *AMCA Standards*, Bulletin 210, 1975.
- 15 Abbott, I. H., and von Doenhoff, A. E., *Theory of Wing Sections*, App. III., Dover Publications, New York, 1959.

# Centrifugal Fan Performance With Inlet Clearance

T. Wright<sup>1</sup>

Westinghouse Fluid Systems Laboratory,  
West Lafayette, Ind. 47906

*This paper describes a systematic study of the influence of the inlet clearance gap on the performance of a centrifugal fan. Overall fan performance in terms of volume flow rate, pressure rise, stall margin, and efficiency were measured over a range of values of the radial clearance between the impeller and the stationary inlet cone. These data have been correlated as functions of lumped clearance parameters. Additional data on velocity surveys in the impeller discharge are presented and discussed in relation to overall performance.*

## Introduction

In the traditional market for centrifugal fans in industrial, commercial, and utility applications, strong emphasis has long been placed on the first cost of these fans. Questions of how performance could be controlled or improved have been tempered with considerations of ease of manufacturing and installation and maintenance of the equipment in the field.

One design parameter for these fans which frequently takes center stage in discussions of improved performance versus first cost is the clearance to be maintained between the rotating impeller of the fan and the stationary inlet flow cone (see Fig. 1). While a very large radial gap between these elements can seriously degrade fan performance, reducing the clearance for improvement of overall performance can quickly lead to difficulties in manufacturing tolerances and installation procedures. If really tight clearances are to be maintained, then consideration must be given to structural rigidity and vibration of all components, and to problems associated with manufacture, shipment, and field assembly of very large machines. However, if the cost of the means to overcome these difficulties (for example, large-scale precision machining, hydraulic explosion forming, use of highly rigid sandwiched materials, centerline support designs) can be offset by reduced operating costs associated with improved efficiency, then tight clearances become feasible. The question to be answered first is: how much can be gained?

Historically, the attitude maintained has been to settle for "adequately small" gaps as a compromise between increased cost and good performance. Arguments based on the concept of a Coanda effect [1] where the gap leakage flow causes a "latching" of the inflow to the rotating sideplate of the impeller have supported the idea of an optimum value of radial clearance. That is, a too large clearance causes excessive recirculating leakage while a too small clearance destroys the favorable Coanda effect. This may be too simplistic a view of the real flow, since it fails to take into

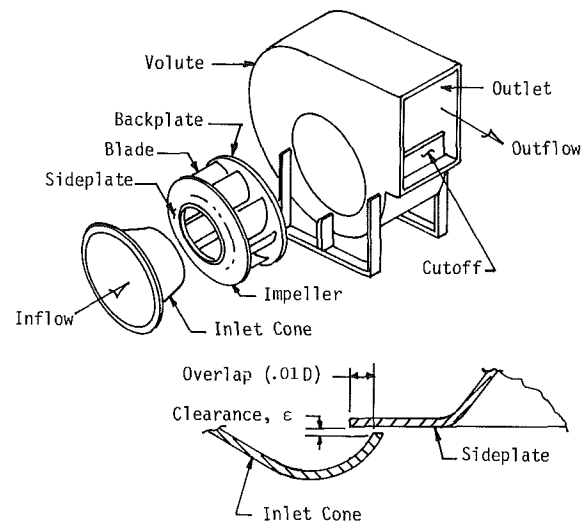
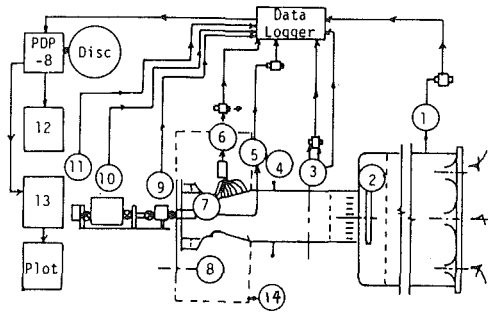


Fig. 1 Centrifugal fan components with details of the inlet clearance geometry

account the strongly three-dimensional flow which characterizes centrifugal fan impellers [2, 3]. The relationship between leakage velocity (stationary frame) and impeller surface (rotating frame) relative velocities must be considered as well. In particular, control (or lack of control) of leakage flow through the inlet clearance gap may interact strongly with the spanwise migration of low energy fluid along blade suction surfaces [4, 5]. Since for high specific speed centrifugal fans this effect may significantly influence flow near the sideplate of the impeller, interaction between gap leakage flow and the low energy spanwise flow may be a dominant aspect of the influence of inlet gap clearance. That is, gap flow may amplify disturbances caused by the accumulation of low energy flow near the sideplate by causing this disturbed region to occupy a greater spanwise portion of the blade channel. Measurements of sideplate surface pressures [2] at large and small clearances show an effect on stability of the flow in this region as well. These considerations lead one to suspect that fan performance—pressure rise, flow rate, efficiency, and stall margin—might be expected to improve

<sup>1</sup>Currently with the Mechanical Engineering Department, University of Alabama at Birmingham.

Contributed by the Gas Turbine Division of THE AMERICAN SOCIETY OF MECHANICAL ENGINEERS and presented at the 29th International Gas Turbine Conference and Exhibit, Amsterdam, The Netherlands, June 4-7, 1984. Manuscript received at ASME Headquarters January 12, 1984. Paper No. 84-GT-186.



- |                    |                  |                   |
|--------------------|------------------|-------------------|
| 1. Nozzle          | 6. Cone Output   | 11. Speed Readout |
| 2. Throttle        | 7. Impeller Taps | 12. Data          |
| 3. Traverse        | 8. Traverse      | 13. Tapes         |
| 4. Inlet Static    | 9. Torque        | 14. Volute        |
| 5. Impeller Output | 10. Dynamometer  |                   |

Fig. 2 Schematic of the fan test, showing instrumentation and data acquisition path

monotonically with decreasing inlet clearance and leakage flow. This is clearly true in axial flow equipment [6-8].

Recent work [9-11] with small centrifugal compressors for gas turbine applications has shown trends which are similar to those seen for axial compressors. Here, the clearance parameter is the axial separation between an unshrouded impeller and stationary casing, so that the flow field behavior may differ considerably from that of a fully shrouded centrifugal fan impeller with an inlet gap. While the influence of increasing the axial gap in an unshrouded compressor should be more severe, these very systematic experiments [9-11] show clearly monotonic trends of performance degradation with increased clearance.

The nagging suspicion persists that the "optimum" clearance may not really exist, and a clear, systematic quantification of how much could be gained by reducing inlet clearance is not available. Since a great deal (if not most) of the literature on high specific speed centrifugal impellers is held proprietary, it was decided that an orderly and careful series of experiments was required to answer the question posed earlier. The necessary experimental facility already existed [2], so a small program was initiated to investigate inlet gap influences.

### Analysis

While the main thrust of this work was concerned with accurate measurement of fan performance with systematically varied clearance, a preliminary study of the details of the

impeller flow was made. The fan was originally configured with an open impeller [2] so that detailed traverses of the impeller discharge flow could be carried out. Probing of the flow with a five-hole cone-type probe provided circumferentially averaged distributions across the span of the blade row. Additional measurements using hot-film probes with high-frequency response yielded details of the blade-to-blade variations in velocity at different spanwise stations across the impeller.

Results from the pressure probe were normalized by reference pressure based on fan tip speed to yield pressure coefficients  $\Psi$  according to

$$\Psi = \Delta p / (\frac{1}{2} \rho V_{tip}^2) \quad (1)$$

where  $\Delta p$  is  $p - p_i$ , and  $p_i$  is the measured inlet pressure of the fan. Hot-film velocity surveys were measured by averaging successive traces to remove the random influences of turbulence in the flow. Ensemble averaging with a shaft-speed encoded trigger signal [12] was employed with 128 successive traces of the voltage signals.

These measurements were made over a range of clearances in order to establish some insight into the suspected interaction between leakage flow and the migration of low-energy fluid through the blade suction surface boundary layer toward the sideplate of the fan. High-specific speed centrifugal fans are characterized by wide (axially) blade channels with very tight curvature on the sideplate in the axial to radial bend region. In addition, relative velocities are high. The Rossby number, defined as  $W/\omega R_n$ , can thus be expected to be very large (compared to those associated with centrifugal pumps and compressors) so that secondary flow of low-energy fluid will move strongly to the sideplate of the fan [4, 13]. The presence of strong leakage flow moving counter to the low-energy fluid migration should provide an interaction observable in the spanwise discharge surveys with systematic variation of clearance and leakage.

Treatment of the overall performance of the fan is more straightforward. A conventional volute housing was added to the test stand in order to carry out standard performance measurements with a range of values of the radial height of the inlet clearance gap. Total pressure rise of the fan and the total efficiency were developed from  $p_i$ , measured at the inlet (below barometric pressure) and the barometric back pressure at the open exit of the fan housing, along with volume flow rate determination and torque-speed measurements. A mean velocity pressure based on flow/discharge area was added to the measured static pressure rise to yield total pressure. Finally, a total pressure rise coefficient  $\Psi_T$  was determined by

$$\Psi_T = \Delta p_T / (\frac{1}{2} \rho V_{tip}^2) \quad (2)$$

### Nomenclature

$A_d$ = disk area of fan impeller, $A_d = (\pi/4)D^2$	$SM$ = stall margin, $SM = 1 - \phi_{st}/\phi_{D0}$	$\bar{\eta}$ = normalized efficiency, $\bar{\eta} = \eta_T/\eta_{T0}$
$B$ = blockage of flow due to leakage, $B = 1 - \phi/\phi_0$	$V_{abs}$ = absolute impeller discharge velocity	$\phi$ = flow coefficient, $\phi = Q/(A_d V_{tip})$
$C_p$ = power coefficient, $C_p = P/(\frac{1}{2} \rho V_{tip}^2 A_d)$	$V_{tip}$ = impeller tip speed, $V_{tip} = \omega D/2$	$\rho$ = fluid density
$D$ = fan impeller diameter	$W$ = relative velocity	$\Psi$ = pressure rise coefficient, $\Psi = \Delta p / (\frac{1}{2} \rho V_{tip}^2)$
$P$ = shaft power	$\beta$ = blade inlet angle relative to a radius	$\omega$ = rotational speed
$p$ = outlet pressure	$\delta$ = inlet radial clearance parameter, $\delta = \bar{\epsilon}(\Psi_s/\phi^2)_0$	<b>Subscripts</b>
$p_i$ = inlet pressure	$\epsilon$ = radial height of inlet clearance gap	$D$ = design point of fan
$\Delta p$ = pressure rise, $\Delta p = p - p_i$	$\bar{\epsilon}$ = normalized gap height, $\bar{\epsilon} = \epsilon/s$	$0$ = reference point at "zero" clearance
$Q$ = volume flow rate	$\cos \beta_i$	$s$ = static value
$R_n$ = radius of curvature of streamline	$\eta$ = efficiency	$st$ = stall
$S$ = blade spacing at leading edge		$T$ = total value

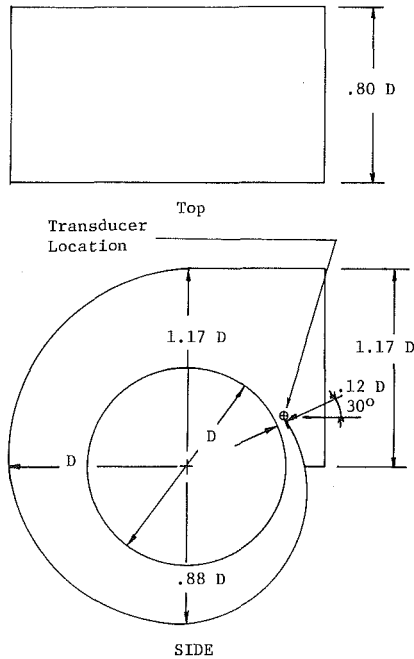


Fig. 3 Overall layout of volute

Volume flow rate was normalized to yield a flow coefficient  $\phi$  according to

$$\phi = Q / (A_d V_{tip}) \quad (3)$$

Defining a power coefficient  $C_p$  as normalized measured shaft power by

$$C_p = P / (\frac{1}{2} \rho V_{tip}^3 A_d) \quad (4)$$

the total efficiency  $\eta_T$  is calculated by

$$\eta_T = \phi \Psi_T / C_p \quad (5)$$

The body of data acquired at various clearance values was cross plotted to yield extrapolated performances and efficiency curves at "zero" clearance. These curves with values denoted by a  $( )_0$  subscript were used to normalize the influence of increasing clearance. Reductions in flow  $B$  (blockage) at a given pressure rise were defined according to

$$B = 1 - \phi / \phi_0 \quad (6)$$

Efficiency values were normalized by the "zero" values to yield  $\bar{\eta}$  according to

$$\bar{\eta} = \eta_T / \eta_{T0} \quad (7)$$

Additional measurements were made to establish the value of flow rate at which the impeller began to undergo severe pulsations in pressure at a frequency slightly lower than the running frequency. This condition is associated with development of rotating stall in the impeller channels [14, 15] and is a critical performance parameter of any fan. The pulsations in pressure associated with this phenomenon can lead to events which are catastrophic to a fan and the system in which it operates [16]. A stall margin parameter,  $SM$ , was defined based on the difference between  $\phi_{D0}$  and  $\phi_{st}$ .  $\phi_{D0}$  is the value of  $\phi$  where best total efficiency occurs as extrapolated to "zero" clearance.  $\phi_{st}$  is the value where strong pulsations begin. Here the  $( )_{st}$  value is the value at which a roughly 25 decibel increase in pressure fluctuation (over the fluctuation at running speed) is seen at about 73 percent of rotating frequency. While 67 percent frequency is the accepted value for rotating stall, running at this value caused severe cracking and degradation in the plastic and aluminum impeller used for these tests [2]. Tests were run at 73 percent

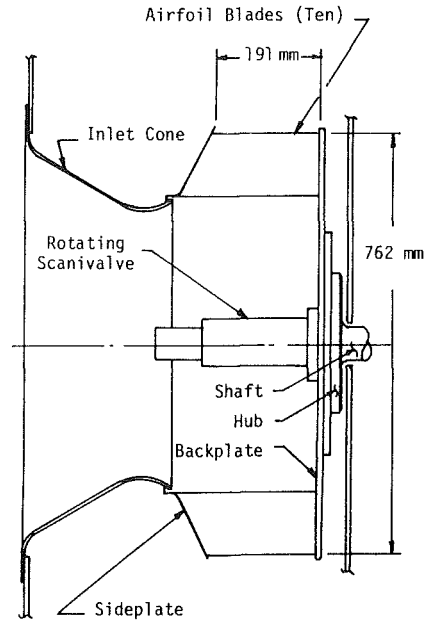


Fig. 4 Impeller showing overall dimensions (from [2])

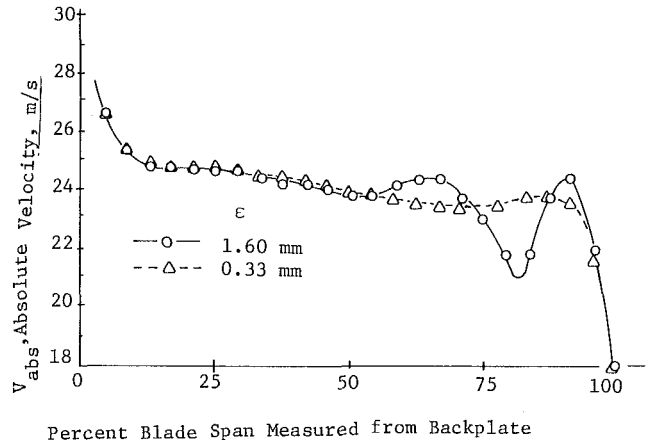


Fig. 5 Absolute discharge velocity at design point flow with large and small clearance: cone probe

frequency to provide a consistent measure of the influence of clearance on this stall inception point.  $SM$  is thus defined as

$$SM = 1 - \phi_{st} / \phi_{D0} \quad (8)$$

and may be normalized by  $SM_0$ .

These dependent variables were correlated against the primary independent parameter of the study—the radial height of the inlet clearance gap,  $\epsilon$ . Although the data presented in this work were derived from a single fan geometry, the clearance was normalized in a form conventional in the literature on axial compressors. That is,  $\bar{\epsilon}$  was defined by

$$\bar{\epsilon} = \epsilon / (s \cos \beta_i) \quad (9)$$

$s \cos \beta_i$  is the staggered spacing [6–8, 17] which, for this work, was 84 mm. In order to relate performance more closely to the baseline fan performance, a diffusion parameter [8, 17] was introduced as  $(\Psi_s / \phi^2)_0$ . This ratio is the static pressure rise of the baseline, "zero" clearance extrapolation, divided by the related velocity pressure. Thus the primary independent variable is given as  $\delta$  by

$$\delta = \bar{\epsilon} (\Psi_s / \phi^2)_0 \quad (10)$$

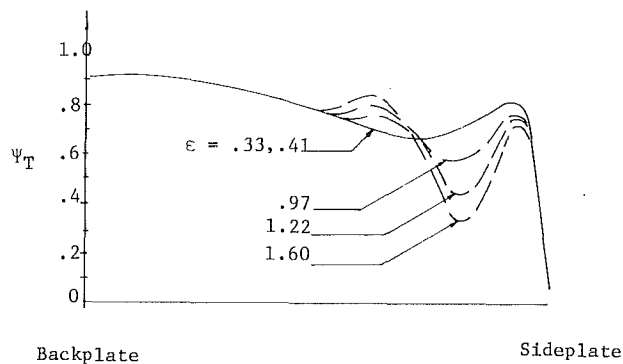


Fig. 6 Influence of clearance gap on spanwise blade performance

Again following the axial literature, efficiency is correlated against the product of  $\phi_0\delta$  in order to relate behavior at a given flow rate.

The experimental data for this work, once acquired and reduced to normalized form, were extensively manipulated using an interactive BASIC language computer program operating on a small microcomputer. The program included statistical and graphical (screen and printer) routines, as well as an interactive mode for modifying the functional form between dependent and independent variables. Use of this program provided the opportunity to examine a wide range of hypothetical relationships with immediate evaluation of merit in terms of correlation coefficients and visual results of the scatter of the data in a given formulation.

### Experiment

While much of the detail on the experimental equipment, test procedures, and data acquisition will be referred to earlier papers [2, 18] those elements which are unique to this work will be discussed in more depth.

Figure 2 is a schematic representation of the test stand. It illustrates the layout, instrumentation, and flow of information to final reduction of the test data. The volute housing used in measuring overall performance of the fan is shown in Fig. 3, and major dimensions of the impeller are given in Fig. 4.

Additional instrumentation included a three-element hot-film probe with linearizers capable of response to a 100-KHz signal, and a five-hole conical pressure probe used for time-averaged measurements. A miniaturized piezoresistive pressure transducer, capable of a flat response to 10 KHz, was installed in the cutoff of the fan housing (Fig. 3) for monitoring pressure pulsations associated with rotating stall.

All pressure transducers and the probes used in this work were calibrated using a micromanometer with graduations of 0.001 in.-H<sub>2</sub>O and a free-jet air source for the probes (jet diameter was 0.1 m with velocities to 33.5 m/s). Frequency response of the piezoresistive transducer was checked using an acoustic calibration source (1 kHz). The cradle-type dynamometer was calibrated using deadweight moment measurements, and bearing losses were approximated by measuring the torque required to run the drive train at 1200 rpm without the fan impeller installed. Based on calibration data and checks on reproducibility, the accuracy of pressure, flow rate, and pressure rise data are estimated to be within  $\pm 1/2$  percent of values at design point. Determination of fan power is estimated to be with  $\pm 1/2$  percent so that efficiency data are accurate to  $\pm 1.5$  percentage points. All data were adjusted to standard air density and nominal fan speed (1200 rpm) according to industry standards [19]. Repeatability of these measurements was considerably better—about .1 percent in each primary variable.

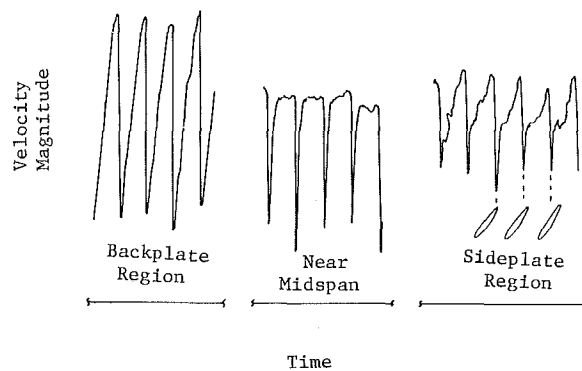


Fig. 7 Representative hot-film voltage traces taken across the impeller discharge at design point flow rate

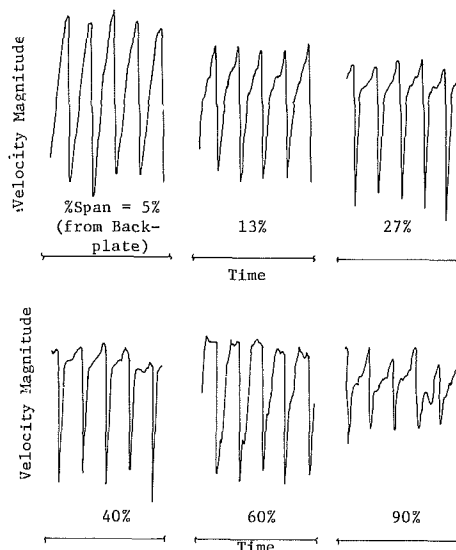


Fig. 8 Velocity traces across impeller at design flow with  $\epsilon = 1.60$  mm

In varying the inlet clearance radial height, some effort was taken to insure accurate geometry. The inlet cone and rotating sideplate were both machined to accurate roundness ( $\pm 0.05$  mm). The inlet cone was mounted and aligned to the impeller using radial jacking screws to within  $\pm 0.05$  mm, based on average clearance from the impeller. Then four circumferential shimming points were adjusted until roundness of the somewhat flexible cone was within  $\pm .1$  mm. Overall accuracy of the clearance as installed is estimated to be within  $\pm .1$  mm. Variations in clearance were achieved by sliding the impeller along its shaft, away from the inlet cone, applying layers of aluminum tape (0.1 mm thick) to the inlet cone surface, and moving the impeller back into its correct position. Following securing of the impeller, clearances were then measured between sideplate and cone by: (i) rotating the impeller and measuring at four equally spaced points around the periphery; and (ii) holding the impeller fixed and measuring clearance at eight points around the periphery. If variations in clearance about the mean value exceeded 0.1 mm, the cone was readjusted and checked until this tolerance was met. Although an acceptable minimum clearance of .1 mm could be achieved in this manner, mild vibration during running (not so mild while searching for the stall point) prevented using a clearance smaller than about 0.25 mm.

### Results

Preliminary investigations consisted of pressure and

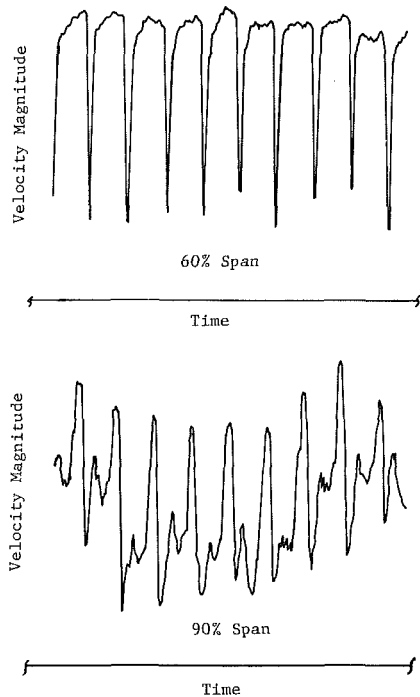


Fig. 9 Velocity traces at design flow with  $\epsilon = 0.41$  mm (qualitative velocity magnitude)

velocity traverses across the axial span of the impeller discharge, and hot-film velocity traverses of the time-dependent absolute discharge velocities at various spanwise positions across the impeller exist. The probe sensing heads were located approximately 6 mm from blade training edges.

Figure 5 shows a selection of two absolute velocity distributions for the fan operating at design point (with impeller only),  $\phi = .18$ , at a small clearance (.33 mm) and a large clearance (1.60 mm). The profile seen for the small clearance is smooth and regular with a significant region of low activity very close to the sideplate. For the large clearance, a much different velocity pattern is seen. Two strongly defined regions of low velocity exist; one near the sideplate and the other standing well out into the blade channel. Although the mechanism is not well understood at this time, it appears that the increased volume of leakage flow through the larger clearance is interacting strongly with the core flow in the blade channel. It is hypothesized here that the region of low activity standing away from the sideplate represents a strong interaction with low energy flow which has migrated from the blade suction surface boundary layers. However, considering the magnitude of the defect region (about 50 percent larger than the sideplate region defect), there seems to be some amplification occurring. Figure 6 shows total pressure rise distributions for five values of clearance over the same range, with  $\phi = .18$ . These results more clearly show the influence of increasing gap height, since they provide a measure of net usable work done across the blade span (data points have been removed for clarity). The same trend is seen as was seen in Fig. 5, although magnitudes of the irregularities are more pronounced. Based on the regular progression of the curves to the relatively uniform distribution seen for the tightest clearance, it was tentatively concluded that an optimum clearance would not be found. The regular, progressive buildup of a second defect region where none was expected lends support to the idea of a secondary interaction of the gap leakage flow with either the main channel flow or the migrating boundary layer fluid.

Hot-film velocity surveys, again taken with the impeller operating near design point (with volute removed), are shown

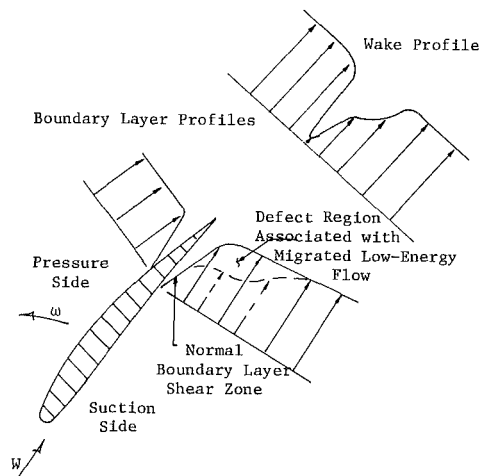


Fig. 10 Concept of relation of wake profile to boundary layer behavior with migrated low-energy flow

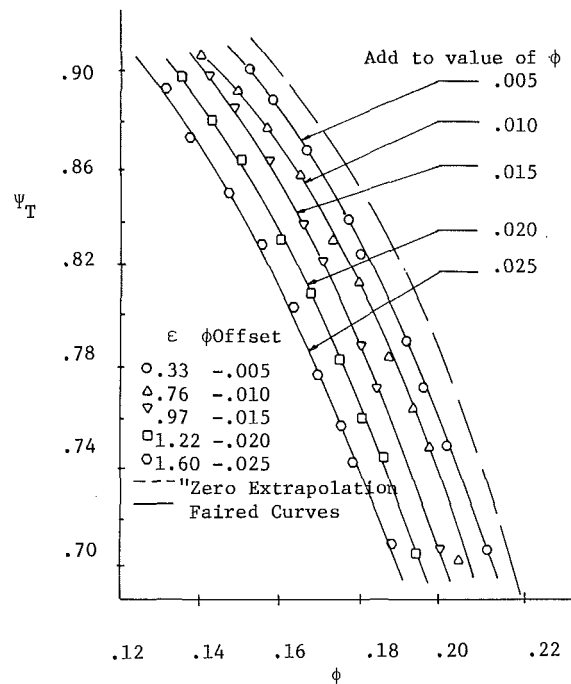


Fig. 11 Flow-pressure rise results

as averaged traces in Fig. 7 for a large clearance configuration. These traces are typical for flow near the backplate, midspan, and sideplate, representing three distinct types of flow. Near the backplate strong wake-jet behavior is observed; near midspan, relatively clean potential core-boundary layer flow is seen; and near the sideplate, a strong secondary loss region is seen. Figure 8 provides more detail for a large clearance configuration ( $\epsilon = 1.60$  mm). In successive surveys moving away from the sideplate, the double-lobed velocity shape persists well into the blade channel. Figure 9 shows similar results for a small clearance test ( $\epsilon = 0.41$  mm). Here, near the sideplate the perturbed behavior of the velocity shape is very strong, but as the survey is taken farther out into the channel, the flow soon assumes the midspan shape shown in Fig. 7. Figure 10 represents a possible interpretation of these results. The secondary wakelike shape is interpreted as the imposition of low energy flow that has migrated from regions nearer the backplate portions of the blade. The spanwise region exhibiting this characteristic is more extensive for the large clearance test

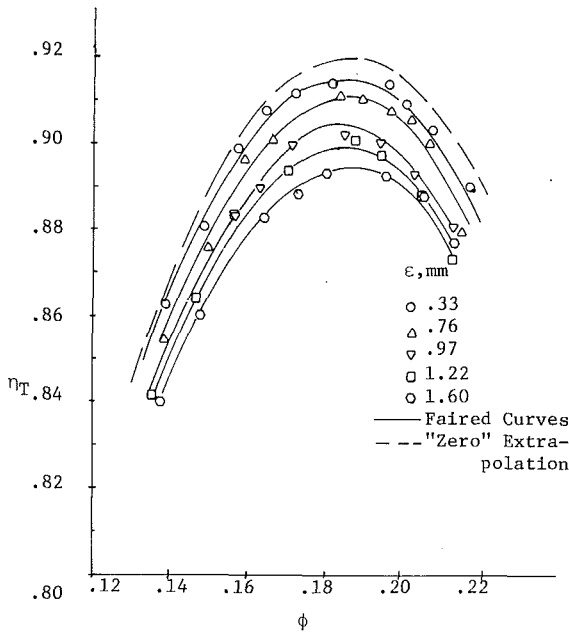


Fig. 12 Efficiency results

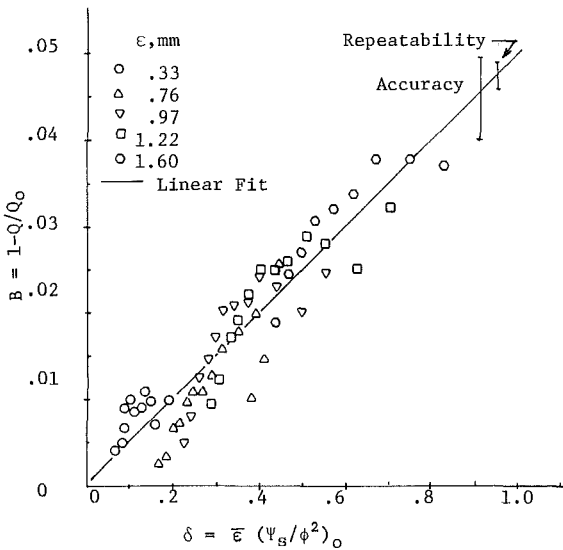


Fig. 13 Correlation of flow reduction with clearance

than for the test with the smaller clearance. Although not enough data are available, this observation seems to support the hypothesis of interaction of leakage and spanwise flows.

The results of the main thrust of this work are taken from the standard pressure rise and flow rate performance measurements with the volute in place. Figure 11 shows the measured pressure rise values as functions of volume flow rate at five values of the radial inlet clearance (data were not acquired for  $\epsilon = 0.41$  mm). Note that volume flow rate for each curve is offset for clarity of the figure. It is seen that the differences in flow rate at a given pressure rise are actually rather small, but that a clear trend is apparent. Figure 12 gives the corresponding value of total efficiency reflecting the results of the power measurements. In both Figs. 11 and 12 the extrapolated "zero" clearance curves are included. The faired lines given in these figures were used to generate a large number of values for  $B$  and  $\bar{\eta}$  in the manner described in the Analysis. These values are plotted in Figs. 13 and 14. The linear regression techniques [20] contained in the data manipulation program yielded correlation coefficients of .92

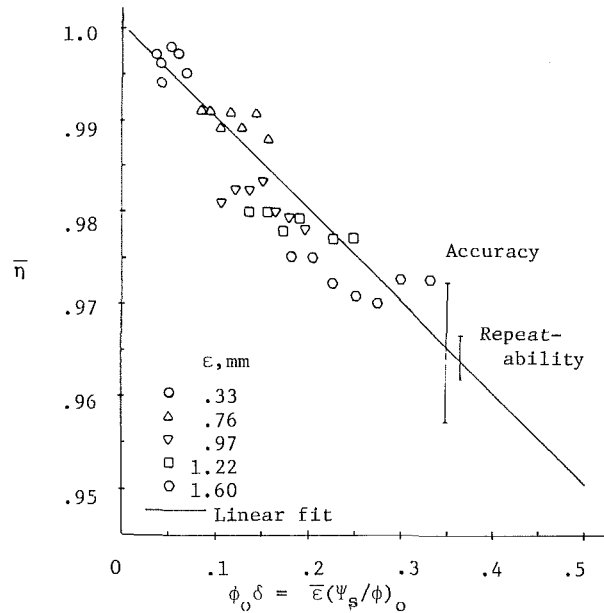


Fig. 14 Correlation of efficiency reduction with clearance

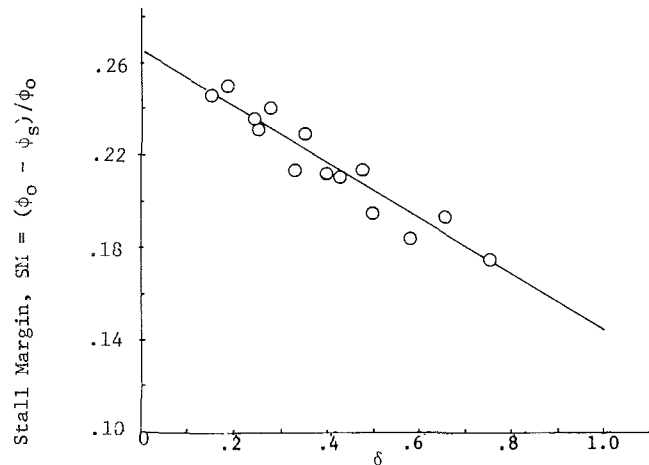


Fig. 15 Correlation of stall margin reduction with clearance

for  $B$  versus  $\delta$  and .91 for  $\bar{\eta}$  versus  $\phi_0 \delta$  (determinations of about .85 and .82). Figure 14 illustrates qualitative agreement with the work of Klassen et al. [10] for unshrouded compressor impellers, which showed similar monotonic trends. Close examination of the data for a given clearance shows that a secondary trend seems to lie within the grouping of the overall collection of data, particularly for the values of  $B$ . However, considerable manipulation of the correlation variable failed to provide any further collapse of the data.

One of the very many other correlations which were examined is mentioned, not because it is a good correlation, but because it illustrates the amplification effect of leakage flow on overall fan performance. If it were assumed that the influence of leakage is purely favorable (Coanda effect) except for the lost volume flow rate due to recirculation, then  $B$  should correlate directly with the product of leakage velocity and gap height. Assuming a constant loss coefficient for the gap, leakage velocity should be proportional to the square root of the total pressure rise of the fan. That is,  $B$  should correlate with the product  $\bar{\epsilon} \Psi_T^{1/2}$ . These were the data considered, and the result was not good (correlation coefficient was .75). Comparison to the result in Fig. 13 shows that other factors are more important; specifically, the value

of volume flow rate or the diffusion effect through the blade row. The diffusion parameter is in turn closely related to the development of low energy fluid on blade surfaces and the effect of clearance is amplified by the diffusion factor in the product  $\bar{\epsilon}(\Psi_s/\phi^2)_0$ .

There does not seem to be an optimum value for clearance for the fan tested. Results are very linear and clearly monotonic to very small values of clearance. However, examining the value of  $\bar{\eta}$  in the range of typical "good" clearance (.1-.15 on  $\phi_0\delta$ ), it appears that halving the clearance would provide only about 1 point improvement in peak efficiency for the fan with  $\phi = .18$ ,  $\Psi_T = .80$ . For a fan of lower specific speed (say,  $\phi = .10$ ,  $\Psi_T = .80$ ) with similar clearance, halving the gap height could yield only about 1/2 a point.

Results for determining the stall margin of the fan based on pressure oscillations at 73 percent of running frequency are summarized in Fig. 15. Here the data are normalized by the extrapolated value for "zero" radial clearance (26.5 percent flow rate reduction). Correlation with  $\delta$  is good (correlation coefficient was  $-.96$ ). Again, in the range of normal "good" clearance, no great gains will be made by significant reductions in clearance. About 70 percent of the ideal "zero" clearance margin is obtained (about 20 percent stall margin). Note that no case is presented for increasing or doubling the clearance as a cost reduction measure. The results shown here indicate that both efficiency and stall margin could suffer appreciably.

## Conclusions

Based on the results presented here, the concept concerning interaction between inlet leakage flow and spanwise migration of low energy fluid from the suction surface boundary layers of the fan blades remains more of a suspicion than an established fact. The hypothesis warrants greater study and will probably require detailed velocity traverses within the blade channels for a family of inlet clearance values.

The results for variation of overall fan performance with clearance (with the volute in place) indicate that the "optimum" clearance concept is probably not valid. At least for the fan tested, results showed continually improving performance with decreasing clearance.

The trends in efficiency improvement with decreasing clearance indicate that a fan with reasonable inlet geometry will not improve dramatically with greatly reduced clearance. While stall margin is more substantially improved by reducing clearance, it is doubtful if such gains can be used to justify the cost and field problems which will result from trying to maintain really small gaps. If the future brings greatly increased energy costs, the potential gains in efficiency may require a careful cost evaluation of fans with reduced radial clearances.

## Acknowledgments

The author wishes to thank the Westinghouse Sturtevant

Division for their financial support of this work. Mr. A. P. Mascia, Mr. K. W. Greaves, Mr. J. DiRe, and Dr. S. Madhavan were particularly helpful in the course of the work. Mr. D. Ariewitz, Mr. P. A. Chovan, and Dr. M. A. Wright (currently at Purdue University) of the Fluids Systems Laboratory staff all supported the experimental efforts.

## References

- 1 Fox, R. W., and McDonald, A. T., *Introduction to Fluid Mechanics*, 2d ed., John Wiley and Sons, New York, 1978, p. 207.
- 2 Wright, T., Tzou, K. T. S., Greaves, K. W., and Madhavan, S., "The Internal Flow Field and Overall Performance of a Centrifugal Fan Impeller—Experiment and Prediction," ASME Paper No. 82-JPGC-GT-16.
- 3 Prince, T. C., and Bryans, A. C., "Three-Dimensional Inviscid Computation of an Impeller Flow," ASME Paper No. 83-GT-210.
- 4 Johnson, M. W., and Moore, J., "Secondary Flow Mixing Losses in a Centrifugal Impeller," ASME JOURNAL OF ENGINEERING FOR POWER, Vol. 105, Jan. 1983, pp. 24-32.
- 5 Johnson, M. W., and Moore, J., "The Influence of Flow Rate on the Wake in a Centrifugal Impeller," ASME JOURNAL OF ENGINEERING FOR POWER, Vol. 105, Jan. 1983, pp. 33-39.
- 6 Smith, L. H., Jr., "Casing Boundary Layers in Multistage Axial-Flow Compressors," *Flow Research in Blading*, edited by L. S. Dzung, Elsevier Publishing, Amsterdam, Netherlands, 1970, pp. 275-300.
- 7 Koch, C. C., and Smith, L. H., Jr., "Loss Sources and Magnitudes in Axial-Flow Compressors," ASME JOURNAL OF ENGINEERING FOR POWER, Vol. 98, No. 3, July 1976, pp. 411-424.
- 8 Koch, C. C., "Stalling Pressure Rise Capability of Axial Flow Compressor Stages," ASME JOURNAL OF ENGINEERING FOR POWER, Vol. 103, No. 4, Oct. 1981, pp. 645-656.
- 9 Klassen, H. A., Wood, J. R., and Schwann, L. F., "Experimental Performance of a 16.10-Centimeter-Tip-Diameter Backswept Centrifugal Compressor Designed for 6:1 Pressure Ratio," NASA TM X-3552, June 1977.
- 10 Klassen, H. A., Wood, J. R., and Schwann, L. F., "Experimental Performance of a 13.65-Centimeter-Tip-Diameter Tandem-Bladed Sweptback Centrifugal Compressor Designed for a Pressure Ratio of 6," NASA TP-1091, Nov. 1977.
- 11 Beard, M. G., Pratt, C. M., and Timmis, P. H., "Recent Experience on Centrifugal Compressors for Small Gas Turbines," ASME Paper No. 78-GT-193, Apr. 1978.
- 12 Lakshminarayana, B., Pouagare, M., and Davino, R., "Three-Dimensional Flow Field in the Tip Region of a Compressor Rotor Passage—Part I: Mean Velocity Profiles and Annulus Wall Boundary Layer," ASME JOURNAL OF ENGINEERING FOR POWER, Vol. 104, No. 4, Oct. 1982, pp. 760-771.
- 13 Hawthorne, W. R., "Secondary Vorticity in Stratified Compressible Fluids in Rotating Systems," (as quoted in [4], A-Turbo/TR63, Cambridge University Engineering Department, Cambridge, 1974.
- 14 Greitzer, E. M., "The Stability of Pumping Systems—The 1980 Freeman Scholar Lecture," ASME Journal of Fluids Engineering, Vol. 103, June 1981, pp. 193-242.
- 15 Wormley, D. N., Rowell, D., and Goldschmied, F. R., "Air/Gas System Dynamics of Fossil Fuel Power Plants—Pulsations," EPRI Report CS-2206, Jan. 1982, pp. 3-57, 3-78.
- 16 Goldschmied, F. R., Wormley, D. N., and Rowell, D., "Air/Gas System Dynamics of Fossil Fuel Power Plants, Vol. 5: System Excitation Sources," EPRI Research Project 1651, Westinghouse/Mass. Institute of Technology, Oct. 1981.
- 17 Wright, T., "Axial Fan Performance with Blade-Base Clearance," ASME Paper No. 83-JPGC-GT-6, Sept. 1983.
- 18 Wright, T., DiRe, J., and Madhavan, S., "Centrifugal Fan Performance with Distorted Inflows," ASME Paper No. 83-JPGC-GT-5, Sept. 1983.
- 19 *AMCA Standards*, Bulletin 210, 1975.
- 20 Mendenhall, W., *Introduction to Probability and Statistics*, Wadsworth Publishing Co., Belmont, Calif., 1971, pp. 259-288.



# Flow in a Centrifugal Fan Impeller at Off-Design Conditions

T. Wright<sup>1</sup>

Westinghouse Fluid Systems Laboratory  
West Lafayette, Ind. 47906

K. T. S. Tzou

Westinghouse R&D Center  
Pittsburgh, Pa.

S. Madhavan

Westinghouse Sturtevant Division  
Hyde Park, Mass.

*Predicted and measured surface velocity and pressure distributions in the internal flow channels of a centrifugal fan impeller are presented for volume flow rates between 80 and 125 percent of design flow rate. Predictions are based on a fully three-dimensional, finite element analysis of the inviscid, incompressible blade channel flow. Additional predictions using a conventional quasi-three-dimensional analysis are presented for comparison. Experimental results were developed using extensive blade and sidewall surface pressure taps installed in a scale model of an airfoil-bladed centrifugal fan impeller designed for heavy industrial and power generation applications. The results illustrate the ability of both flow analyses to predict the dominant features of the impeller flow field, including peak blade surface velocities and adverse gradients at flows far from the design point. In addition, the experimental results provide valuable insight into the limiting channel diffusion values for typical centrifugal cascade performance, and the influence of viscous effects as seen in deviations from the ideal flow predictions.*

## Introduction

In an earlier paper [1], the results of an experimental and analytical investigation of a centrifugal fan impeller were reported. These results were restricted primarily to the flow and velocities in the impeller at the design flow rate of the fan. That investigation has been extended to cover a range of off-design flow conditions between 80 and 125 percent of design flow. The purpose of this work was twofold. Good baseline data on the details of the flow in a high-specific-speed fan impeller were needed to enhance understanding of limiting flow conditions in such an impeller. These data could serve as well for evaluation of current and future calculational techniques. The work also provided an evaluation of the ability of inviscid analysis codes to yield useful predictions of velocity and pressure distributions inside the impeller.

As noted elsewhere [2], the quasi-three-dimensional solution techniques have become the standby methods for analysis of turbomachines, particularly where strongly three-dimensional flows exist. Although the literature on this subject goes back to the turn of the century, more recent and thorough treatment was presented by Wu [3-6]. Power series methods for analysis of the blade-to-blade flow were proposed fairly early on [7, 8] and have been successfully used [9]. More recent implementation of quasi-three-dimensional methods has been done by Katsanis [10, 11] and by Novak [12]. For this work, the centrifugal fan impeller was analyzed using the meridional solution of Novak [12] and the blade-to-blade solutions of Katsanis [10, 11] as these codes were well-tested and readily available.

<sup>1</sup>Currently with the Mechanical Engineering Department, University of Alabama at Birmingham

Contributed by the Gas Turbine Division of THE AMERICAN SOCIETY OF MECHANICAL ENGINEERS and presented at the 29th International Gas Turbine Conference and Exhibit, Amsterdam, The Netherlands, June 4-7, 1984. Manuscript received at ASME Headquarters January 12, 1984. Paper No. 84-GT-182.

Fully three-dimensional methods have more recently become available, many relying on finite-element calculation procedures [13, 2, 1]. Some are restricted to incompressible [1, 14], others can handle compressibility [13, 15], and some include the effects of rationality of the flow [16, 17]. This work employed an existing computer code [1, 14] which restricted the study to inviscid, incompressible analysis of the flow in the fan impeller. However, since part of the purpose of the study was to determine the adequacy of quasi-three-dimensional analysis (neglecting viscosity) to describe the flow, the finite element code used effectively provided a testing of the quasi-three-dimensional assumptions. Considerable use is made of this analytical technique, and more recent refinements of such methods [18, 19] ensure its continued use.

## Analysis

The finite element analysis code used in this work is described in earlier papers [1, 14]. Representation for the flow reduces to  $\nabla_R^2 \Phi = 0$ . Here, the potential function  $\Phi$  is for the absolute velocity and the Laplacian operator is written in terms of the relative coordinate system moving with the impeller. Solution of the potential equation is subject to inhomogeneous Neumann boundary conditions on the moving solid surfaces of the impeller (impermeable surfaces), over the inflow and discharge boundaries (to establish volume flow), and across surfaces of peripheral symmetry (flux matching). In addition, the Kutta condition must be applied to the blade surface velocity or pressure distributions at trailing edges in order to obtain a unique solution to the problem with lifting surfaces. This is done by linearly combining solutions using a collocation procedure which meets the Kutta condition exactly at certain points and ap-

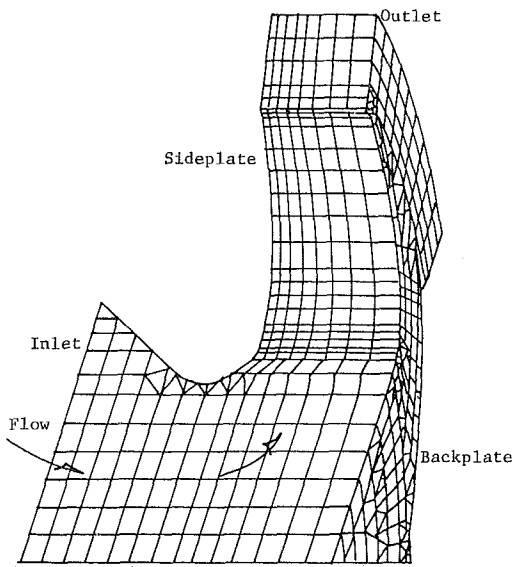


Fig. 1 Finite element grid for the impeller

proximately at other points. That is, a parameter,  $\Delta\Phi$ , was added to the exit plane distribution of  $\Phi$  to allow for adjustment of trailing edge velocity at a single point on the blade trailing edge. Combinations of several (usually three) solutions obtained in this manner were developed to insure uniqueness in the solution of the flow. Because of the structure of this program, it was not possible to exactly match the procedure used in the quasi-three-dimensional solution. An illustration of the grid used is given in Fig. 1.

To meet the specific needs of centrifugal fan aerodynamic design and analysis, this calculational method was developed, based on the proprietary computer code WECAN (Westinghouse Electric Computer Analysis). This finite element program is capable of representing the full three-dimensional geometry of a centrifugal fan and solves the three-dimensional, incompressible, inviscid flow field in the impeller or other sections of a fan.

The quasi-three-dimensional analysis used in this work includes a meridional analysis code, developed by Novak [12] based on a streamline curvature technique for circumferentially averaged surfaces of revolution through the impeller. The code was used in its incompressible form without estimates of the various loss parameters which may be employed. Five congruent stream surfaces were used across the span of the impeller as shown in Fig. 2. The mean values of the flow deviation from blade surfaces in the impeller discharge were based on the method of Stodola [20]. Results from the meridional analysis were used to establish stream tube thickness and incidence angle distributions for use in the blade-to-blade analysis [11]. This analysis embodies a finite-difference solution of the stream function in the blade channel (for this work the incompressible option was used). In defining the finite difference grid for this solution, a total of 35 streamwise mesh lines was used, with 10 lines defining the

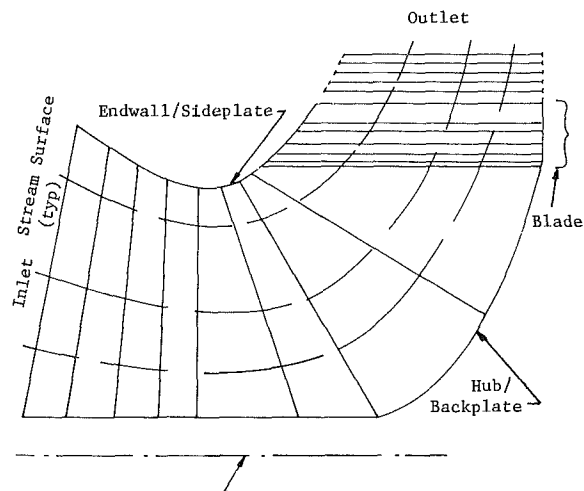


Fig. 2 Meridional streamlines and normals

region upstream of the blade (extending one blade chord upstream), 15 lines dividing up the blade channel, and 10 lines downstream of the blade (one chord length). The cross-channel grid consisted of 30 mesh lines defining the stream normal spacing. The Kutta condition for flow near the blade trailing edges is imposed on the solution through iterative matching of pressure and suction surface velocities near the trailing edge. The structure of the quasi-three-dimensional code does not allow imposition of a Kutta condition in the same form as was used in the finite element analysis. Here, the flow angle at the exit station must be specified, and adjustment of this angle is used to force velocity matching in the stream tube (or blade spanwise station) being analyzed. If the deviation angles so calculated differ significantly ( $\pm 0.5$  deg) from those used in the meridional solution, the meridional flow field is recalculated using the values from the blade-to-blade results. Information is thus passed back and forth between the two codes until a solution is obtained within the tolerance on change of deviation angles. At this point, boundary value information is transferred from the blade flow solution to a third code [11] which solves the flow around a magnified leading edge region in order to refine the calculation for the influence of blade leading edge incidence. The leading edge region analyzed in this work consisted of a zone defined by the 8th and 13th streamwise mesh lines, and the 2nd and 15th normal grid lines, using an amplification factor of four.

It was necessary to carry out minor smoothing of velocity and pressure distribution calculated by both the finite element and quasi-three-dimensional codes. For the finite element results, the mesh points nearest a surface were used to extrapolate to the surface value. For the quasi-three-dimensional result, jaggedness cropped up in the matching region for the magnified leading edge solution. A simple three-point moving average calculation was employed to smooth the results.

Results for the flow solutions are presented in terms of

### Nomenclature

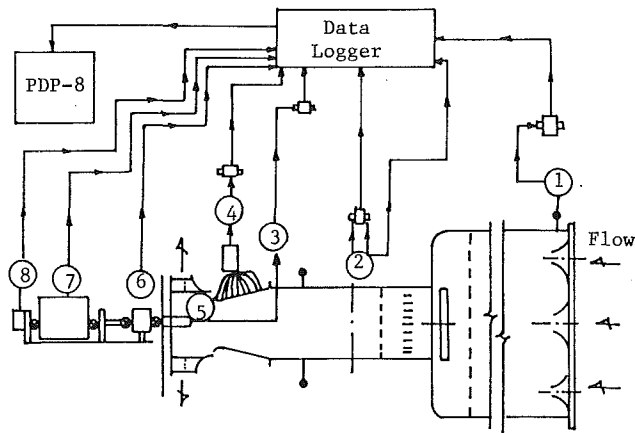
$A$  = fan reference area,  $\pi D^2/4$   
 $C$  = blade surface length  
 $D$  = fan diameter  
 $L$  = total length along end wall path  
 $\Delta p$  = static pressure rise,  $p_s - p_i$   
 $P_s$  = surface static pressure  
 $P_i$  = inlet static pressure  
 $Q$  = volume flow rate

$s$  = distance along end wall path  
 $V_{tip}$  = tip speed of impeller,  $\omega D/2$   
 $V_s$  = blade surface velocity  
 $x$  = distance along blade surface  
 $\nabla^2_R$  = Laplacian operator in relative coordinate system  
 $\rho$  = fluid density  
 $\psi_s$  = static pressure rise coefficient,  $\Delta p / \frac{1}{2} \rho V_{tip}^2$

$\Phi$  = potential function for absolute velocity  
 $\phi$  = flow coefficient,  $Q / AV_{tip}$   
 $\omega$  = rotational speed

### Subscripts

$P$  = peak value on suction surface  
 $T$  = trailing edge value on suction surface



1. Nozzle Flow Pressure Drop
2. Inlet Flow Traverse
3. Impeller Scanning Valve Output
4. Inlet Cone Scanning Valve Output
5. Impeller Pressure Taps
6. Torque Transducer
7. Dynamometer
8. Speed Counter

Fig. 3 Schematic layout of instrumentation for the test stand

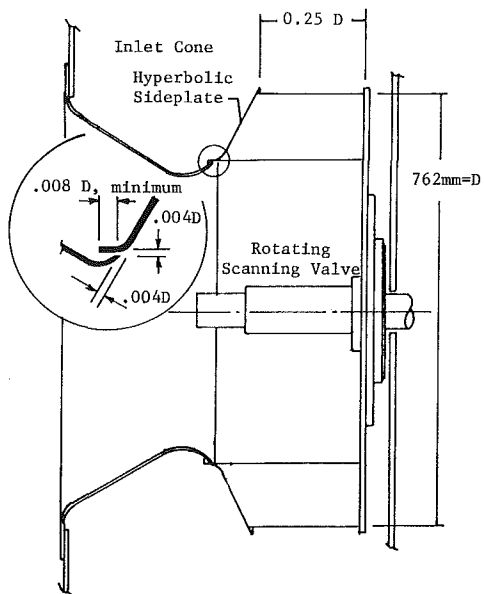


Fig. 4 Scale model impeller with detail of allowable clearance

blade surface velocity distributions, as  $V_s$  versus  $x/c$ , where  $x/c$  is normalized surface length along the blade contour. Static pressure distributions along the impeller endwall—from the fan inlet to the impeller discharge—are given as  $\psi_s$  versus  $s/L$  where  $s/L$  is the normalized path length.  $\psi_s$  is the static pressure coefficient defined by  $\psi_s = \Delta p / \frac{1}{2} \rho V_{tip}^2$ ;  $\Delta p = p_s - p_i$ , where  $p_i$  is the inlet static pressure. A velocity ratio defining suction surface peak velocity,  $V_{sp}$ , normalized by trailing edge velocity,  $V_{ST}$ , is used to characterize blade loading or diffusion levels. Finally, the volume flow rate of the fan is presented in coefficient form as  $\phi = Q / AV_{tip}$ ;  $Q$  is volume flow rate and  $A$  is the fan reference area defined as  $A = \pi D^2 / 4$ .

### Experiment

The experimental apparatus and instrumentation developed to provide a practical evaluation of the calculational methods

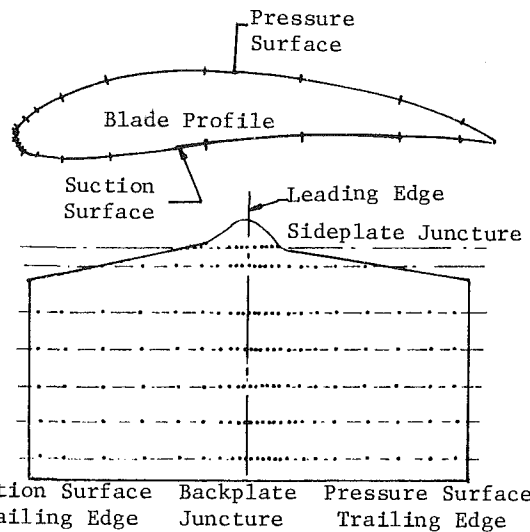


Fig. 5 Location of pressure taps on blade profile and developed blade skin

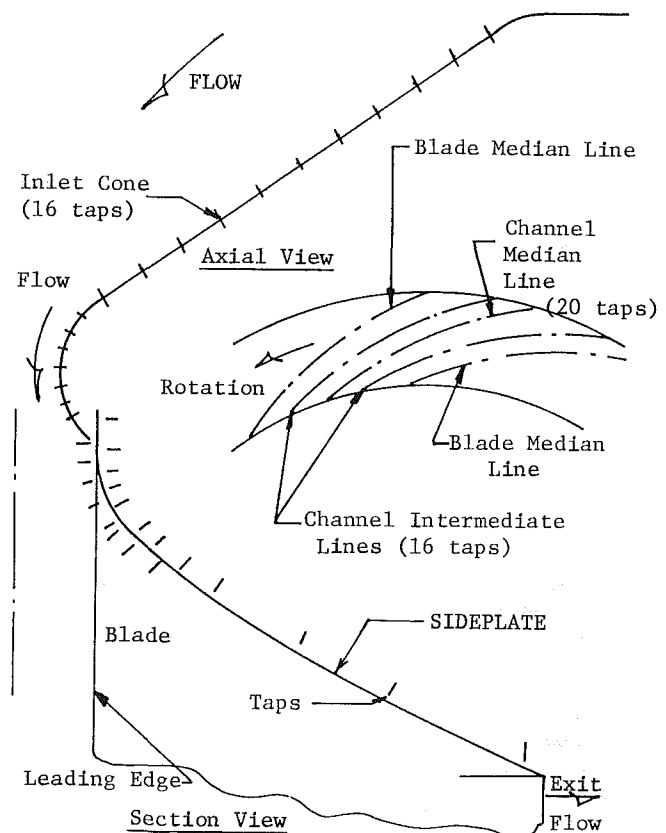


Fig. 6 Two views of sideplate showing tap locations

are shown schematically in Fig. 3. More detail is available in an earlier paper [1]. The "test section" is configured to achieve flexibility in mounting fan impellers, inlet sections, and volute scrolls of various geometries. Emphasis is placed on using stationary and rotating static pressure taps and on detailed probing of the pressure and velocity field of the impeller discharge using hot-film and conventional pressure-type, three-axis probes. Motive power is provided by a cradled dynamometer (using a six-pole induction motor).

For this work the test section configuration consists of a scale model of an airfoil-bladed centrifugal fan impeller and inlet cone (single width, single inlet). The configuration of the impeller, scaled to a diameter of 762 mm (30 in.) to run at a

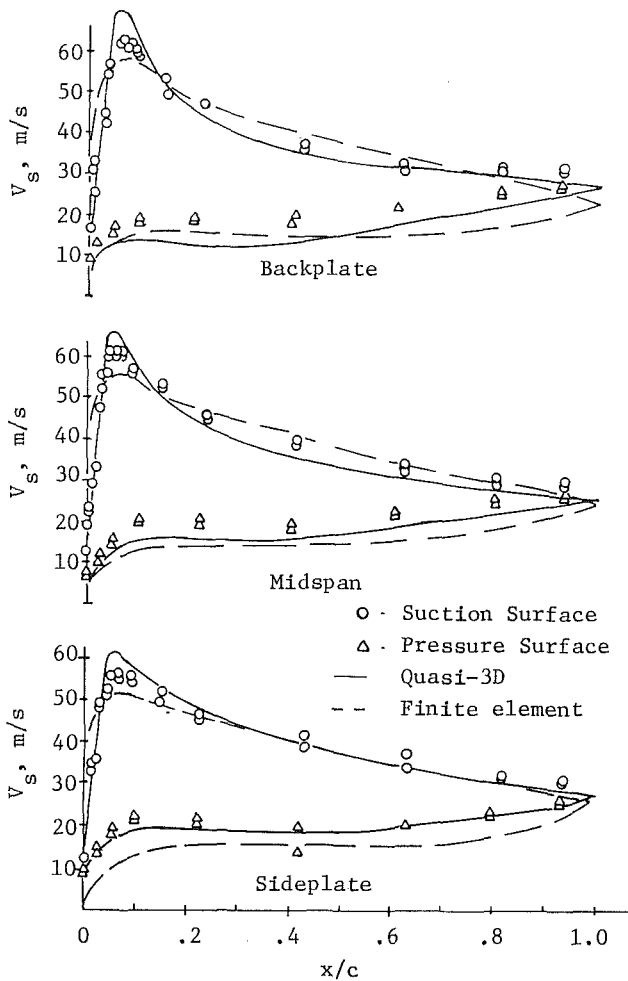


Fig. 7 Velocity distributions at  $\phi = 0.14$

nominal 125.7 radians per s (1200 rpm), is shown in Fig. 4. The inlet cone was fitted to the impeller with a nominal radial clearance to represent standard installation practice. The blade surface tap array is illustrated in Fig. 5 (on the developed blade surface). One hundred fifty-one taps on 7 of the 10 blades were augmented by 4 redundant taps at similar locations for checking purposes. The hyperbolic sideplate of the fan was fitted with 36 pressure taps located in a blade-to-blade channel as shown in Fig. 6. The 16 taps installed on the stationary inlet cone are also shown in Fig. 6. Additional dimensions are available [1]. The static pressures from the blade and sideplate surface taps were routed to the rotating scanning valve on the fan axis as shown in Fig. 3. The pressure signals were processed through a strain-gage transducer and logged electrically as indicated in the schematic diagram. In the course of data reduction and analysis, all pressure measurements were corrected for the influence of centrifugal force on the hydrostatic column between the fan centerline and the particular tap location, and the data were all corrected to a common base of speed and density. Velocity pressures were derived from these measurements by differencing from the rotating total energy associated with inlet static pressure and the whirl component.

All pressure transducers and pressure-type probes used in this work were calibrated using a micromanometer (20-in. Meriam® with graduations of 0.001 in.-H<sub>2</sub>O) and a free jet air source for the probes (jet diameter was 0.1 m [4 in.] with velocities to 33.5 m/s [110 ft/s]). The cradled dynamometer and torque transducer were both calibrated using dead weight moment measurements and bearing losses were approximated

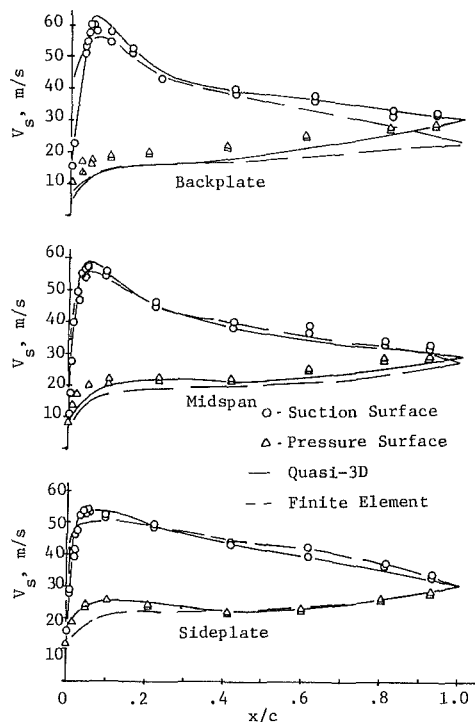


Fig. 8 Velocity distributions at  $\phi = 0.176$

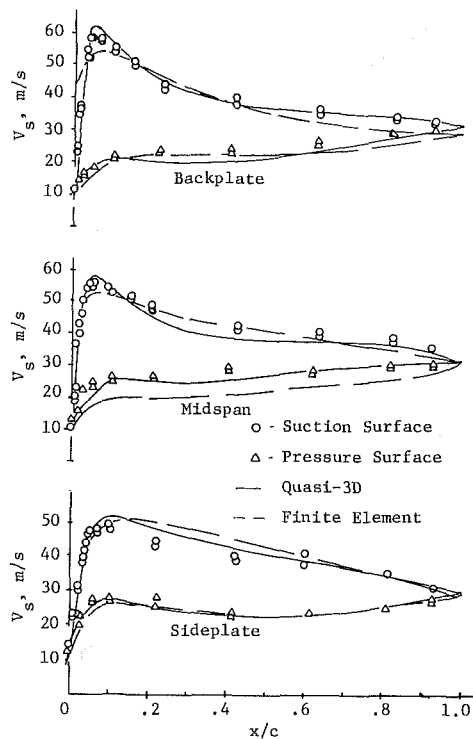


Fig. 9 Velocity distributions at  $\phi = 0.21$

by measuring the torque required to run the drive train without the fan impeller installed. Based on both calibration information and reproducibility checks, the accuracy of pressure, flow and pressure-rise measurements are within  $\pm 1/2$  percent of values at design point. The determinations of fan power by torque measurement vary by  $\pm 1$  percent, so that efficiency data are accurate to  $\pm 1.5$  percent.

## Results

Partial results for the two calculational procedures are

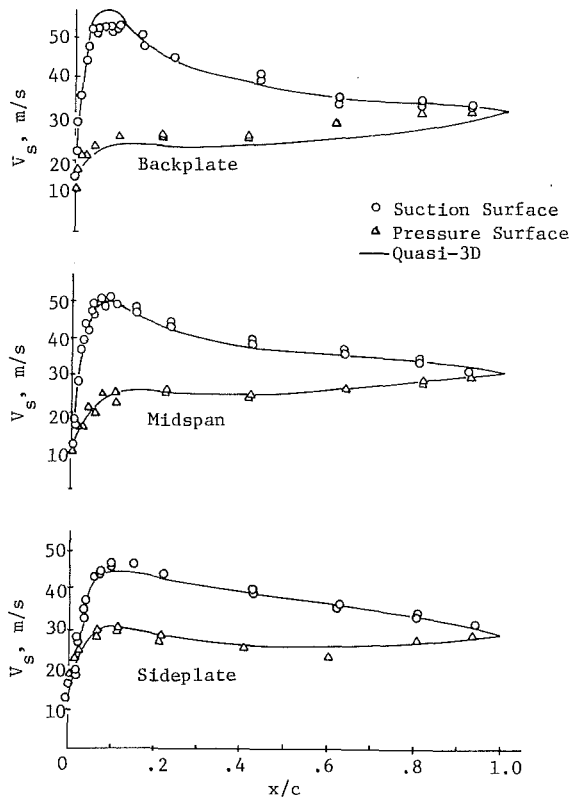


Fig. 10 Velocity distributions at  $\phi = 0.22$

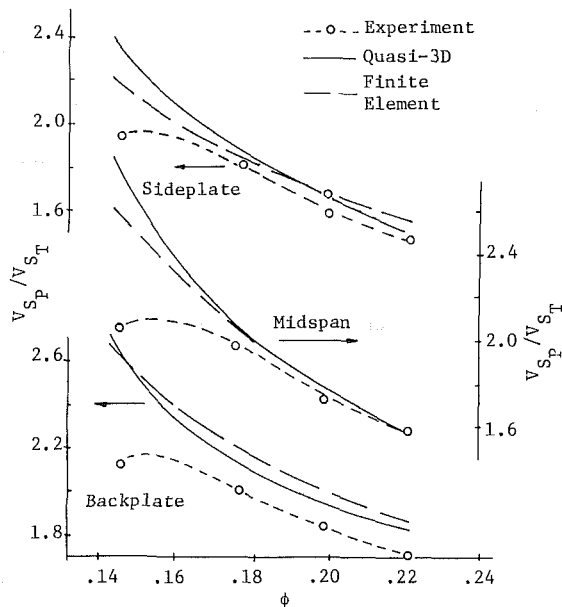


Fig. 11 Comparison of velocity ratio determinations

presented in Figs. 7, 8, 9, and 10. Here the blade surface velocity distributions are given for four different flow rates—from near stall ( $\phi = .14$ ) to 125 percent of design flow ( $\phi = .22$ ). The experimental data show the influence of the strong three-dimensionality of the flow across the blade span associated with the sharp bend around the sideplate-inlet cone juncture. The minimum radius of curvature in the fan is much less than is typical in pumps and compressors, causing relatively large changes in incidence angle across the blade leading edge. Suction surface velocity peaks are quite high in the backplate region of the blade and are considerably alleviated near the sideplate. While both of the prediction

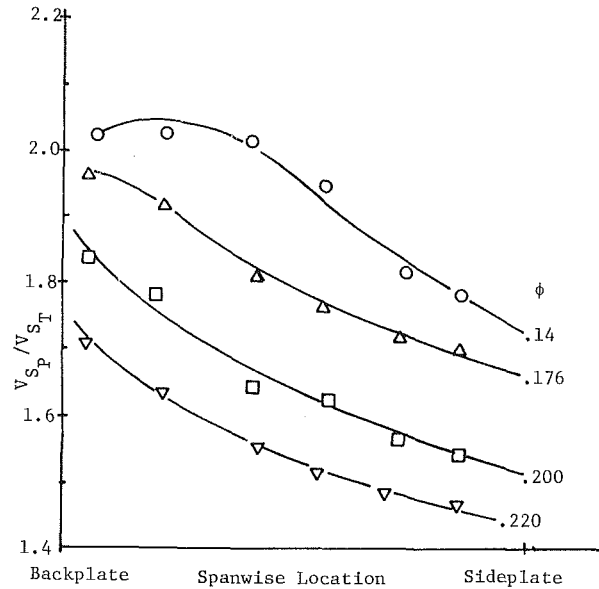


Fig. 12 Experimental values of velocity ratios along blade span

methods correctly predict this trend, the quasi-three-dimensional method consistently exaggerates the sharpness of the suction surface velocity peak, and the finite-element calculation underestimates the sharpness of the experimental results.

The quasi-three-dimensional analysis seems to provide better agreement with the experimental data near the blade trailing edges. Inspection of the curves in Figs. 7, 8, 9, and 10 show that the trailing edge velocities are nearly constant across the blade span for a given flow rate (experimentally and by the quasi-three-dimensional calculation). The finite element analysis predicts considerable spanwise variation which may be traceable to the method used to impose the Kutta constraint. Superposition of only three solutions differing by an incremental potential on the (perhaps too close) exit plane may not be adequate to accurately define the trailing edge condition. Using five stream tubes in the quasi-three-dimensional analysis and imposing a trailing edge velocity match in each tube appears to provide better constraint. Further, the agreement between experiment and quasi-three-dimensional analysis is not unreasonably good in view of the very high impeller efficiency (low losses) over the range of these data (efficiency was above 90 percent [1]).

Figure 11 is a collection of peak-to-trailing-edge velocity ratios taken from the suction surface velocity results—analysis and experiment. As functions of volume flow rate at the backplate, midspan, and sideplate regions of the fan blade, both methods predict trends in substantial agreement with the experimental data. At low flow rates, both inviscid methods (particularly the quasi-three-dimensional) yield velocity ratios in excess of experimental measurements. In fact, the experimental data shown in Fig. 12 indicate that allowable diffusion has been exceeded ( $V_{S_p}/V_{S_T} \cong 2$ ) resulting in a falling off of the velocity ratio. This is particularly true near the backplate of the fan.

Figures 13 and 14 show analytical and experimental results for the endwall pressure distributions. At the lower flow rates, these distributions are well-behaved except near the leakage slot at the sideplate-inlet cone juncture. Considerable scatter is seen in the data taken near the leakage slot. The flow appears to be unsteady in this region as a result of minor variations in clearance, measured statically, and due to a small amount of runout and vibration while running. Analytical results are in substantial agreement with experiment, again indicating the ability of the analysis to

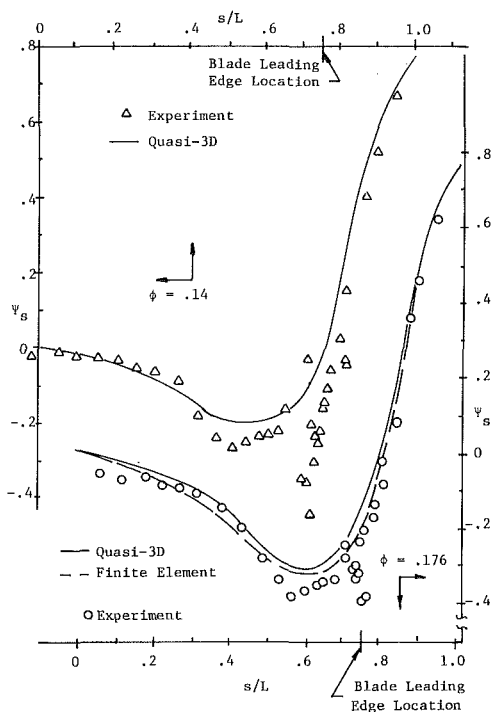


Fig. 13 Endwall pressure profiles

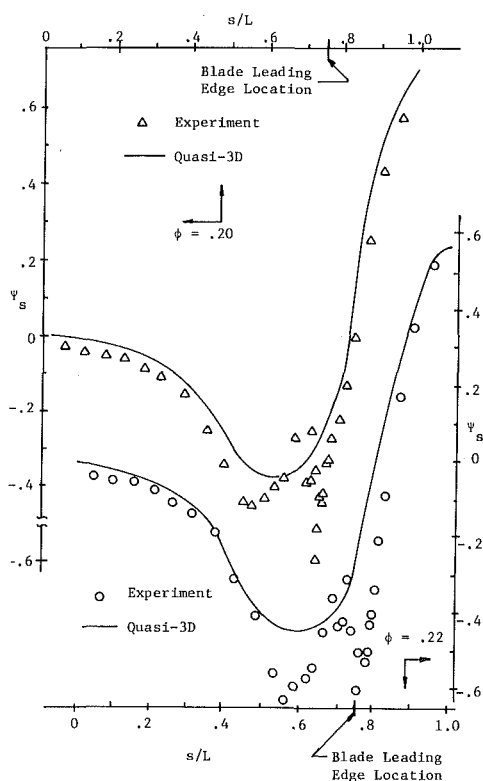


Fig. 14 Endwall pressure profiles

correctly predict the three-dimensional nature of the flow. However, for the higher flow rates (Fig. 14), experimental results are more irregular, indicating that the viscous effects associated with very rapid pressure recovery from the minimum pressure seen at the throat of the inlet are beginning to dominate the flow. Recovery of static pressure along the sideplate contour is remarkable in view of the behavior in the throat region and must reflect on the stabilizing influence of the rotating flow field on seemingly separated flows.

## Conclusions

The experimental results given here and in an earlier paper [1] provide fairly extensive data on a centrifugal machine whose geometry is not typical in terms of pump and compressor literature. The information provides new insight into the detailed behavior of airfoil centrifugal fans of high specific speed.

Analysis of the flow in the impeller using a conventional quasi-three-dimensional technique shows that the dominant features and trends in flow behavior can be reasonably predicted. Given sufficient care in using the three analysis codes, and the patience to iterate between them, very good solutions may be generated for strongly three-dimensional flows relatively quick and at modest cost. However, considering the need to interact between the results of several computer programs to arrive at a "converged" solution, a very objective view of the results must be maintained to avoid seeking a "reasonable" prediction, as mentioned in a recent paper [2].

The finite element calculations presented here indicate the real ability of such methods to handle flows in complex geometries. Additional refinement in mesh description can be expected to improve agreement with experimental data. More careful attention to the exit boundary and trailing edge conditions and increased mesh refinement in the leading edge and near-surface regions of the blade channel will allow better definition of velocity gradients in the critical regions. Unfortunately, the financial resources provided for the finite element work did not allow these refinements to be investigated. Perhaps the real advantage of such a solution lies in the isolation of the investigator from the calculational process.

Future work in fan analysis will rely on use of the simpler and less expensive quasi-three-dimensional codes to perform the yeoman duty of design investigations and parametric trade-off studies. These studies may then be checked and verified using the full three-dimensional finite element analysis, followed by application of boundary layer analysis in critical portions of the flow field [1].

## Acknowledgments

The authors wish to thank the Westinghouse Sturtevant Division for their financial support of this work. Mr. A. P. Mascia and Mr. K. W. Greaves were particularly helpful in the course of the work. Mr. D. Ariewitz, Mr. J. S. Orisich, Dr. M. A. Wright (currently at Purdue University), and Mr. G. R. Howland (currently of MEPCO, West Lafayette, Ind.) of the Fluid Systems Laboratory staff all supported the effort.

## References

- 1 Wright, T., Tzou, K. T. S., Greaves, K. W., and Madhavan, S., "The Internal Flow Field and Overall Performance of a Centrifugal Fan Impeller—Experiment and Prediction," ASME Paper No. 82-JPGC-GT-16, Oct. 1982.
- 2 Prince, T. C., and Bryans, A. C., "Three-Dimensional Inviscid Computation of an Impeller Flow," ASME Paper No. 83-GT-210, Feb. 1982.
- 3 Wu, Chung-Hua, and Wolfenstein, L., "Application of Radial-Equilibrium Condition to Axial-Flow Compressor and Turbine Design," NACA Technical Report 955, 1950.
- 4 Wu, Chung-Hua, "A General Throughflow Theory of Fluid Flow with Subsonic or Supersonic Velocity in Turbomachines of Arbitrary Hub and Casing Shapes," NACA Technical Note 2302, 1951.
- 5 Wu, Chung-Hua, "A General Theory of Three-Dimensional Flow in Subsonic and Supersonic Turbomachines of Axial-, Radial-, and Mixed-Flow Types," NACA Technical Note 2604, 1952.
- 6 Wu, Chung-Hua, "Matrix and Relaxation Solutions That Determine Subsonic Through-Flow in an Axial-Flow Gas Turbine," NACA Technical Note 2750, 1952.
- 7 Dreyfus, L. A., "A Three-Dimensional Theory of Turbine Flow and Its Application to the Design of Wheel Vanes for Francis and Propeller Turbines," *ACTA Polytechnica*, Mech. Eng. Ser., Vol. 1, No. 1, 9146.
- 8 Reissner, H., "Blade Systems of Circular Arrangement in Steady

Compressible Flow," *R. Courant Anniversary Volume*, Interscience Publications, 1948, pp. 307-327.

9 Novak, R. A., "A Computer Program for the Mean Streamsheet Design and Analysis of Turbomachinery," Dyna Tech R/D Co., Cambridge, Mass., Mar. 1, 1974.

10 Katsanis, T., "Computer Program for Calculating Velocities and Streamlines on a Blade-to-Blade Stream Surface of a Turbomachine," NASA TN D-4525, 1968.

11 Katsanis, T., and McNally, W. D., "Revised Fortran Program for Calculating Velocities and Streamlines on a Blade-to-Blade Stream Surface of a Turbomachine," NASA TM X-1764, 1969.

12 Novak, R. A., "Streamline Curvature Computing Procedures for Fluid Flow problems," *ASME JOURNAL OF ENGINEERING FOR POWER*, Oct. 1967, pp. 478-490.

13 Laskaris, T., "Finite-Element Analysis of Three-Dimensional Potential Flow in Turbomachines," *AIAA Journal*, Vol. 16, No. 7, July 1978, pp. 717-722.

14 Whirlow, D. K., Goldschmied, F. R., and Farn, C. L. S., "Analysis of

the Three-Dimensional Potential Flow of Centrifugal Draft Fans," *EPR Symposium on Power Plant Fans* (EPRI Publication CS-2206), Oct. 1981.

15 Ecer, A., Akay, H. U., and Mattai, S., "Finite Element Analysis of Three-Dimensional Flow Through a Turbocharger Compressor Wheel," *ASME Paper No. 83-GT-92*, Feb. 1983.

16 Denton, J. D., and Singh, V. K., "Time-Marching Methods for Turbomachinery Flow Calculations," (as quoted in [2]), *VKI Lecture Series 7*, 1979.

17 Akay, H. U., and Ecer, A., "Applications of a Finite Element Algorithm for the Solution of Steady Transonic Euler Equations," *AIAA Paper No. 82-0970*.

18 Wu, Chung-Hua, and Baogno, W., "Matrix Solution of Compressible Flow on  $S_1$  Surface Through a Turbomachine Blade Row with Splitter Vanes or Tandem Blades," *ASME Paper No. 83-GT-10*, Feb. 1983.

19 Mao, S. K., and Li, D. T., "A Streamline Curvature Method for Calculating  $S_1$  Stream Surface Flow," *ASME Paper No. 83-GT-16*, Feb. 1983.

20 Wislicenus, G. F., *Fluid Mechanics of Turbomachinery*, Dover Publications, New York, 1965, pp. 261-286.

# ERRATA

Corrections to "Analysis of an Axial Compressor Blade Vibration Based on Wave Reflection Theory," by J. A. Owczarek, published in the January 1984 issue of the JOURNAL OF ENGINEERING FOR GAS TURBINES AND POWER, pp. 57-64.

## APPENDIX B

### Phase Angle Between Vibrating Rotor Blades

For the wave of the type  $(1W \times nV)$ , the phase angle  $\sigma$  between the rotor blade  $N_B = 0$  and a blade  $N_B$  of the same family ( $N_B/n_1 = \text{an integer}$ ) can be determined from equation

$$\begin{aligned} 360j + \sigma &= 360f_N \frac{\Delta x}{W} \\ &= \frac{360f_N}{n_V} \frac{60}{N} \frac{\Delta x}{t_V} \end{aligned} \quad (1B)$$

For the waves of the type  $(1W \times nR)$ , the phase angle  $\sigma$  between the rotor blade  $N_B = 0$  and blade  $N_B$  of the same family ( $N_B/n = \text{an integer}$ ) can be determined from equation

$$\begin{aligned} 360j + \sigma &= 360f_N \frac{\Delta x_S}{W} \\ &= \frac{360f_N}{n_S} \frac{60}{N} \frac{\Delta x_S}{t_S} \end{aligned} \quad (4B)$$



H. R. Wyssmann

T. C. Pham

R. J. Jenny

Sulzer-Escher Wyss, Ltd.,  
Zurich, Switzerland

# Prediction of Stiffness and Damping Coefficients for Centrifugal Compressor Labyrinth Seals

*A theory is presented for the calculation of stiffness and damping coefficients of the fluid-rotor interaction in centrifugal compressor labyrinth seals based on turbulent flow calculations. The theory has been confirmed by measurements on labyrinth test stands and on a centrifugal compressor impeller shroud seal at pressures up to 140 bar. Predicted rotor stability limits based on the theory are in agreement with those observed in real compressors.*

## Introduction

With the increase of pressure in centrifugal compressors, rotor instability problems caused by the working fluid-rotor interaction have emerged. It has been conjectured for some time that the leakage fluid passing through the labyrinth seals on impeller shrouds and balance pistons is a main source of self-excitation.

Several authors have worked on theories for the calculation of the destabilizing forces in labyrinth seals. The work of Alford [1] for a single cavity neglects the circumferential velocity of the leakage flow and predicts no self-excitation if the discharge area is larger than the entrance area of the labyrinth. Spurk and Keiper [2] find the opposite result having taken into account the influence of the leakage swirl. Both models show no excitation for a constant gap width labyrinth.

The result of Kostyuk [3] shows that a self-exciting force does not exist if the rotor has eccentricity parallel to the axis. This contradicts well established measurements. An extension of this model has been used by Iwatsubo [4]. Other authors have produced theories using stream tube models [5, 6].

Measurements have already been made by Rosenberg [5] and an extensive experimental investigation was carried out by Benckert [7] with different types of labyrinth geometries. His measurement showed that the labyrinth cross-coupling force is strongly dependent on the swirl velocity of the leakage flow.

A first model for the calculation of labyrinth cross-coupling forces has been given by the present authors some time ago [8, 9]. The theory has been reworked and extended, in particular it includes now the calculation of labyrinth damping coefficients.

## Theory

**Principle.** The theory presented calculates the circumferential pressure distribution as a function of lateral rotor displacement and displacement time rate in multistage labyrinth seals. The theory has been developed for the following labyrinth types as shown in Fig. 1:

- The straight-through labyrinth with caulked strips on the rotor or on the stator
- The straight-through labyrinth with milled strips on the stator as used for high pressure differentials
- The staggered and the full labyrinth

The theory starts with three-dimensional flow calculations of the turbulent flow in a concentric labyrinth chamber with the aid of a computer program due to Spalding [10]. The program solves the time-averaged Navier-Stokes equations employing the  $k-\epsilon$  turbulence model and has been correlated with labyrinth flow measurements by Stoff [11]. The results as given in Fig. 2 are used in the following for modeling the flow profiles for the eccentric labyrinth and to correlate the turbulence parameters used in the equations for the eccentric labyrinth.

Continuity and momentum equations will be formulated for a single eccentric labyrinth chamber with a simplified flow configuration as suggested by Fig. 2. The nonstationary pressure is then sought by integration of the equations linearized in the rotor displacement and displacement time rate. The final results are two displacement-dependent coefficients, i.e., stiffness and cross-coupling stiffness, and two velocity dependent coefficients representing the damping for each labyrinth chamber. By summation over the length of the labyrinth, the coefficients for the entire seal are obtained.

**Assumptions.** The following assumptions are made:

- (a) The fluid in the labyrinth behaves as an ideal gas.
- (b) The temperature of the fluid is constant along the seal.
- (c) Pressure fluctuations within each gland are sufficiently small compared to the pressure difference of adjacent glands.
- (d) The boundary layers may be described by wall friction laws.

Contributed by the Gas Turbine Division of THE AMERICAN SOCIETY OF MECHANICAL ENGINEERS and presented at the 29th International Gas Turbine Conference and Exhibit, Amsterdam, The Netherlands, June 4-7, 1984. Manuscript received at ASME Headquarters January 6, 1984. Paper No. 84-GT-86.

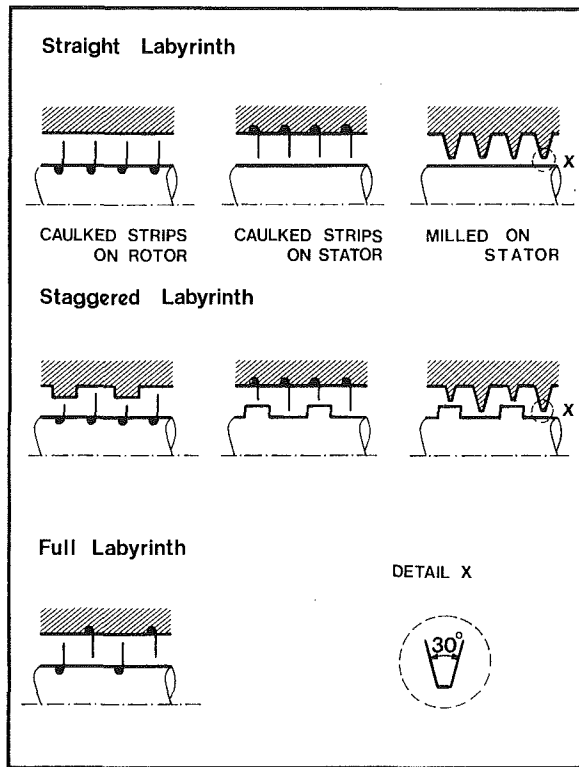


Fig. 1 Labyrinth types

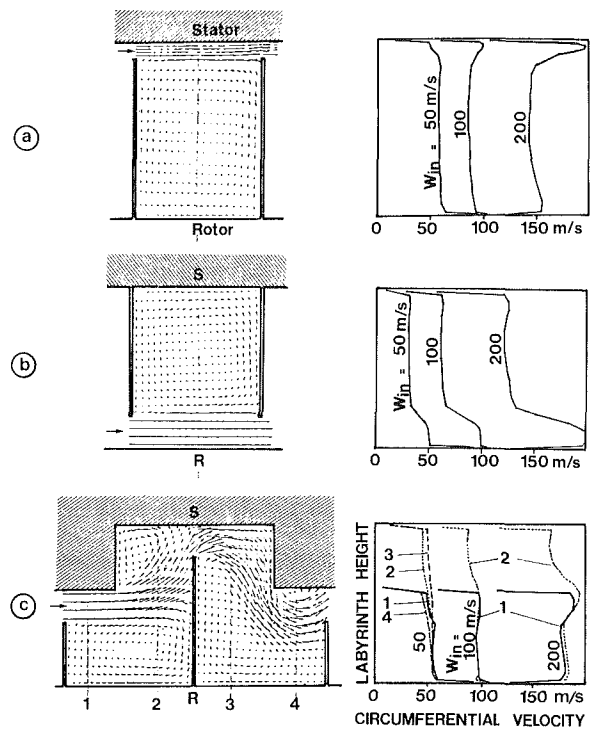


Fig. 2 Three-dimensional flow calculation of the concentric labyrinth for three geometries: (a) straight rotor labyrinth; (b) straight stator labyrinth; (c) staggered labyrinth

### Straight Labyrinth.

**Flow Configuration.** The calculation of the three-dimensional flow within a labyrinth chamber for the straight labyrinth (see Fig. 2(a) and 2(b)) reveals the following distinctive flow regions, schematically depicted in Fig. 3:

(A) Core flow with nearly uniform circumferential velocity

(B) Leakage flow of jet flow type passing through the labyrinth chamber

(c) Thin boundary layers at the stationary and rotating walls

(D) Shear flow region in the mixing zone between jet and core flow.

Hence the following flow model will be used:

• The circumferential flow is represented by two velocities in the circumferential direction  $w_i$  for region A and  $w_m$  for region B. The shear flow region D is described by free shear stresses and the boundary layers by wall shear stresses.

• The meridian flow is given by the well-known labyrinth equations as given by several authors [13, 14].

**General Equations.** The following derivation of the flow equations is valid for the labyrinth with strips on the rotor. For stator labyrinths the reasoning is analogous, important differences will be mentioned.

The continuity and momentum equations in circumferential direction for the control volumes I and II in Fig. 4 read: Continuity equations:

### Nomenclature

$a$  = area of the cross section between 2 strips  
 $A$  = area of the cross section of labyrinth channel  
 $B$  = mixing thickness  
 $b_Q$  = cross-coupling damping  
 $B_Q$  = nondimensional cross-coupling damping  
 $b_R$  = direct damping  
 $B_R$  = nondimensional direct damping  
 $c_f$  = friction coefficient  
 $C_{ax}$  = axial velocity  
 $d$  = distance between 2 strips  
 $e$  = eccentricity  
 $h$  = labyrinth strip height  
 $i$  = number of labyrinth chamber

$k_Q$  = cross-coupling stiffness  
 $K_Q$  = nondimensional cross-coupling stiffness  
 $k_R$  = direct stiffness  
 $K_R$  = nondimensional direct stiffness  
 $l$  = mixing length  
 $\dot{m}$  = leakage flow rate through labyrinth  
 $\dot{m}_r$  = mass rate exchange between 2 control volumes  
 $p$  = pressure  
 $Q$  = cross-coupling force  
 $R$  = direct force  
 $r$  = labyrinth radius  
 $\Delta r$  = radial clearance of concentric labyrinth  
 $t$  = time  
 $w$  = circumferential velocity

$W$  = nondimensional circumferential velocity  
 $z$  = number of labyrinth strips  
 $\beta$  = mixing factor  
 $\delta$  = radial clearance of eccentric labyrinth  
 $\mu$  = labyrinth flow coefficient  
 $\nu$  = viscosity  
 $\pi_p$  = pressure ratio of labyrinth  
 $\rho$  = density  
 $\tau$  = stress  
 $\varphi$  = angle

### Subscripts

in = inlet  
 $j$  = jet  
 $r$  = rotor or radial  
 $s$  = stator  
 out = outlet

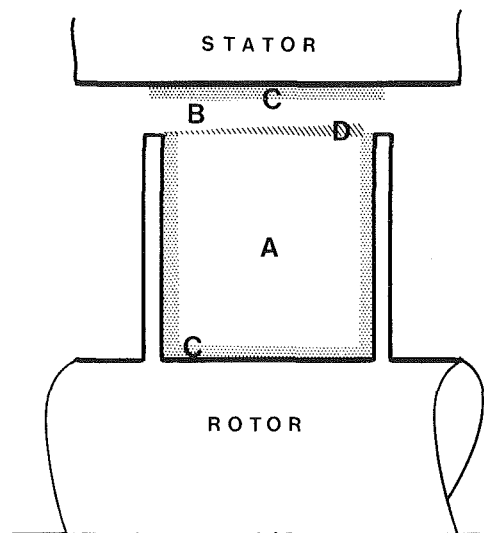


Fig. 3 Different flow regions in the labyrinth chamber

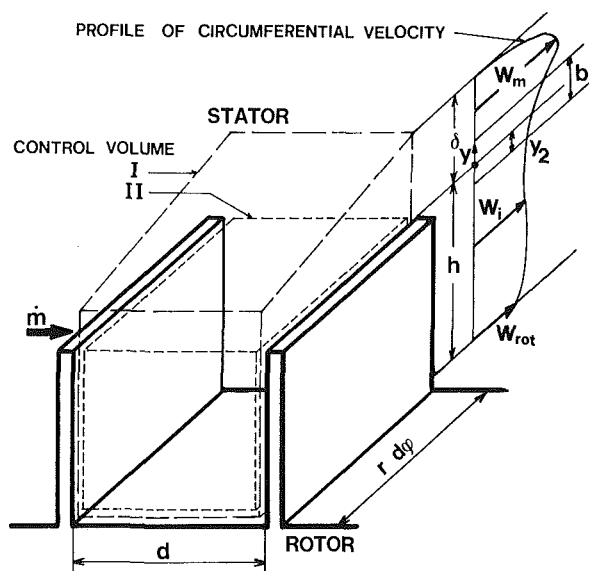


Fig. 4 Control volumes and profile of circumferential velocity of the straight labyrinth

$$\text{Volume I : } a \frac{\partial w_i}{\partial \varphi} + \delta d \frac{\partial w_m}{\partial \varphi} - w_m d \frac{\partial \delta}{\partial \varphi} - r \frac{\partial A}{\partial t} = 0 \quad (1)$$

$$\text{Volume II: } a \frac{\partial w_i}{\partial \varphi} - \dot{m}_r / \rho = 0 \quad (2)$$

Momentum equations:

$$\begin{aligned} \text{Volume I : } & -2a w_i \frac{\partial w_i}{\partial \varphi} - 2\delta d w_m \frac{\partial w_m}{\partial \varphi} - w_m^2 d \frac{\partial \delta}{\partial \varphi} \\ & + \dot{m} / \rho (w_{in} - w_{out}) - \tau_r / \rho a_r r \\ & - \tau_s / \rho a_s r - r d \frac{\partial (\delta w_m)}{\partial t} - r a \frac{\partial w_i}{\partial t} = \frac{A}{\rho} \frac{\partial p}{\partial \varphi} \end{aligned} \quad (3)$$

$$\begin{aligned} \text{Volume II: } & -2a w_i \frac{\partial w_i}{\partial \varphi} + \dot{m}_r / \rho w_0 - \tau_r / \rho a_r r \\ & - \tau_s / \rho d r - r a \frac{\partial w_i}{\partial t} = \frac{a}{\rho} \frac{\partial p}{\partial \varphi} \end{aligned} \quad (4)$$

where  $w_i$  is the circumferential velocity of core flow (region

A);  $w_m$ , the circumferential velocity of the free jet (B); and  $w_0$ , the circumferential velocity in the interface between volume I and volume II.

The leakage flow rate  $\dot{m}$  is taken from Neumann [14]:

$$\dot{m} = 2\pi\mu r \delta \rho_0 \sqrt{p_0 / \rho_0} \sqrt{(1 - \pi_p^2) / z} \quad (5)$$

where  $p_0$  and  $\rho_0$  are the pressure and the density of the fluid before the labyrinth seal,  $\pi_p$  is the pressure ratio of the labyrinth seal, and  $z$  is the number of labyrinth strips.

The flow coefficient  $\mu$  of the labyrinth in equation (5) follows the definition of Neumann [14] and takes into account the influence of the labyrinth strip geometry on the leakage flow.

The turbulent wall shear stresses  $\tau_r$  and  $\tau_s$  are given by the following equations:

$$\begin{aligned} \tau_r &= \frac{1}{2} c_{fr} \rho |w_i - w_{rot}| (w_i - w_{rot}) \text{ (rotor)} \\ \tau_s &= \frac{1}{2} c_{fs} \rho \sqrt{c_{ax}^2 + w_m^2} w_m \text{ (stator)} \end{aligned} \quad (6)$$

where the friction coefficients  $c_{fr}$  and  $c_{fs}$  are calculated with Prandtl's universal law for the tube flow [15].

The Reynold's number  $Re$  depends on the flow conditions at the labyrinth entrance and may be defined as

$$Re = \sqrt{w_{rot}^2 + w_{in}^2} (h + \Delta r) / \nu$$

The free shear stress  $\tau_j$  is introduced to characterize the shear flow region D. Following Abramovich [16], the velocity profile is given by

$$(u - u_m) = (u_i - u_m) \left[ 1 - \left( \frac{y + y_2}{b} \right)^{1.5} \right]^2 \quad (7a)$$

where the local coordinate  $y$ , the boundary layer thickness  $y_2$ , and the mixing thickness,  $b$ , are defined in Fig. 4.;  $u$ ,  $u_i$ , and  $u_m$  are the flow velocities in this region. Neglecting the laminar shear stresses, the free shear stress  $\tau_{j,u}$  is given by Prandtl's mixing length hypothesis [15] and reads

$$\tau_{j,u} = \rho l^2 \left| \frac{\partial u}{\partial y} \right| \left| \frac{\partial u}{\partial y} \right| \quad (7b)$$

where the mixing length  $l$  is assumed to be proportional to a characteristic length in the shear flow region. For free jets, an obvious choice for  $l$  is the mixing thickness  $b$ . For the obstructed jet flow at hand, a proportionality factor,  $\beta$ , called mixing factor is defined, hence  $l$  reads

$$l = \beta \cdot b \quad (8)$$

The mixing factor  $\beta$  is determined by correlation with the general three-dimensional calculations for the concentric labyrinth and by experiments. This will be discussed in the next section.

The free shear stress  $\tau_{j,u}$  is therefore obtained from equations (7a) and (7b), where  $y_2$  has been set equal to  $b/2$

$$\tau_{j,u} = 9\rho\beta^2 |u_i - u_m| (u_i - u_m) \cdot \left[ 1 - \left( \frac{y_2}{b} \right)^{1.5} \right]^2 \left( \frac{y_2}{b} \right) \quad (9)$$

The free shear stress  $\tau_j$  is finally obtained by taking the component of  $\tau_{j,u}$  in the circumferential direction

$$\tau_j = 1.881\rho\beta^2 \sqrt{(w_i - w_m)^2 + c_{ax}^2} (w_i - w_m) \quad (10)$$

The circumferential velocity  $w_0$  in the interface between volume I and volume II is then obtained from equation (7a)

$$w_0 = w_m + 0.418(w_i - w_m) \quad (11)$$

Finally, the circumferential component  $w_m$  of the leakage flow is taken constant in the axial direction within a labyrinth chamber and is obtained by taking the mean value of inlet and outlet velocity

$$w_m = (w_{in} + w_{out}) / 2 \quad (12)$$

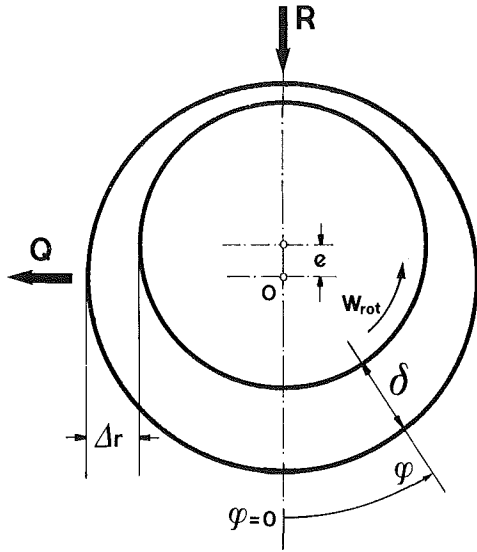


Fig. 5 Labyrinth positioned eccentrically

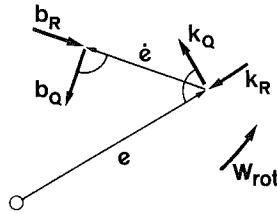


Fig. 6 Definition of labyrinth excitation coefficients

**Concentric Labyrinth.** For the concentric case,  $w_i$ ,  $w_m$  and  $\dot{m}$  are independent of  $\varphi$ , and  $\dot{m}_r$  is zero. Denoting all quantities of the concentric solution by a bar, equations (3) and (4) now become

$$\bar{m}(\bar{w}_{in} - \bar{w}_{out}) = \frac{1}{2} \rho c_{fr} |\bar{w}_i - \bar{w}_{rot}| (\bar{w}_i - \bar{w}_{rot}) a_r r + \frac{1}{2} \rho c_{fs} \sqrt{\bar{w}_m^2 + \bar{c}_{ax}^2} \bar{w}_m a_s r \quad (13)$$

$$\frac{1}{2} \rho c_{fr} |\bar{w}_i - \bar{w}_{rot}| (\bar{w}_i - \bar{w}_{rot}) a_r r = -1.881 \rho \beta^2 \sqrt{(\bar{w}_i - \bar{w}_m)^2 + \bar{c}_{ax}^2} (\bar{w}_i - \bar{w}_m) d r \quad (14)$$

and equation (5) for leakage rate reads with  $\delta = \Delta r$

$$\bar{m} = \bar{\mu} r \Delta r \rho_0 \sqrt{p_0 / \rho_0} \sqrt{(1 - \pi_p^2) / z} \quad (15)$$

The pressure in the labyrinth chamber  $i$  is taken from Neuman [14]

$$p_i = p_0 \sqrt{1 - \frac{(1-j)i+j}{(1-j)z+j} (1 - \pi_p^2)} \quad (16)$$

where  $j$  is a function of  $\Delta r/d$ .

For an ideal gas, the density  $\rho$  in the labyrinth chamber reads

$$\rho = \rho_i = \rho_0 \frac{p_i}{p_0} \quad (17)$$

Equations (13–17) determine the circumferential velocities in the labyrinth if the mixing factor  $\beta$  is known. Based on the results obtained from the three-dimensional calculations,  $\beta$  has been correlated to the labyrinth type and geometry

$$\beta = \beta_0 \cdot \text{function}(r, \Delta r, h, d)$$

The factor  $\beta_0$  takes account of the free jet contraction and

from measurements has been found to lie between 0.027 and 0.050, depending on labyrinth type.

All necessary equations are now given. The next step will be the derivation of the equations for the labyrinth coefficients.

**Labyrinth Coefficients.** A variable pressure distribution results when the rotor is displaced in a direction perpendicular to the axis by a small amount  $e(t)$  (see Fig. 5). The corresponding force acting on the rotor may be decomposed into two components  $Q$  and  $R$  perpendicular and parallel to  $e$ , respectively. The eccentricity  $e$  and its time rate  $\dot{e}$  are small compared to the radial clearance of the concentric labyrinth. The gap  $\delta$  can therefore be written as

$$\delta = \Delta r + e(t) \cos \varphi \quad (18)$$

and consequently the flow quantities and the pressure read:

$$w_i = \bar{w}_i + \tilde{w}_i(\varphi, t), \quad w_m = \bar{w}_m + \tilde{w}_m(\varphi, t) \\ \dot{m} = \bar{\dot{m}} + \tilde{\dot{m}}(\varphi, t), \quad p = \bar{p} + \tilde{p}(\varphi, t) \quad (19)$$

where the quantities with the tilde denote small deviations from the concentric solutions.

Introducing (18) and (19) into equations (1–5) and neglecting terms of second and higher order in  $e$  and  $\dot{e}$ , the resulting equations may be solved for the pressure variation  $\tilde{p}$

$$\tilde{p} = \hat{p}_1 \dot{e} \sin \varphi + \hat{p}_2 \dot{e} \cos \varphi + \hat{p}_3 e \sin \varphi + \hat{p}_4 e \cos \varphi \quad (20)$$

where the  $\hat{p}_i$  are functions of geometry and the flow parameters for the concentric labyrinth.

The force components  $Q$  and  $R$  are obtained by integration of the pressure around the rotor

$$Q = \int_0^{2\pi} \tilde{p} \sin \varphi r d \varphi, \quad R = \int_0^{2\pi} \tilde{p} \cos \varphi r d \varphi \quad (21)$$

This may be written as

$$Q = k_Q e + b_Q \dot{e}, \quad R = k_R e + b_R \dot{e}$$

where

$$k_R = -\pi r d \hat{p}_4, \quad k_Q = \pi r d \hat{p}_3, \\ b_R = -\pi r d \hat{p}_2, \quad b_Q = \pi r d \hat{p}_1 \quad (22)$$

are the labyrinth stiffness and damping coefficients (for the sign convention see Fig. 6). In particular,  $k_R$  is the direct stiffness (conservative part of the stiffness matrix);  $k_Q$ , the (circulatory) cross-coupling stiffness;  $b_R$ , the (dissipative) direct damping; and  $b_Q$  the (gyroscopic) cross-coupling damping. The words given in brackets are the notation of Ziegler [17].

**Staggered Labyrinths.** Here the tangential flow is almost uniform across the labyrinth chamber, due to the increased mixing of the leakage flow by the stepped passage. Hence a single circumferential velocity  $w_i$  is assumed.

The continuity and momentum equations now read

$$\text{Continuity: } -A \frac{\partial w_i}{\partial \varphi} - w_i \frac{\partial A}{\partial \varphi} - r \frac{\partial A}{\partial t} = 0 \quad (23)$$

$$\text{Momentum: } -2A w_i \frac{\partial w_i}{\partial \varphi} - w_i^2 \frac{\partial A}{\partial \varphi} + \dot{m} / \rho (w_{in} - w_{out}) - \tau_r / \rho a_r r + \tau_s / \rho a_s r - r \frac{\partial (w_i A)}{\partial t} = \frac{A}{\rho} \frac{\partial \rho}{\partial \varphi} \quad (24)$$

with the same notation as for the straight labyrinth. Again, the leakage rate  $\dot{m}$  is given by equation (5).

The uniformity of the circumferential flow imposes that the outlet velocity  $w_{out}$  is equal to the core velocity  $w_i$ :

$$w_{out} = w_i$$

The shear stresses  $\tau_r$  and  $\tau_s$  are given by equations (6).

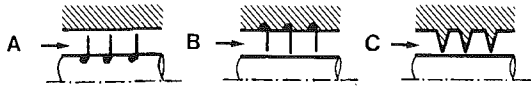


Fig. 7 Labyrinth types in Figs. 8, 9, and 10

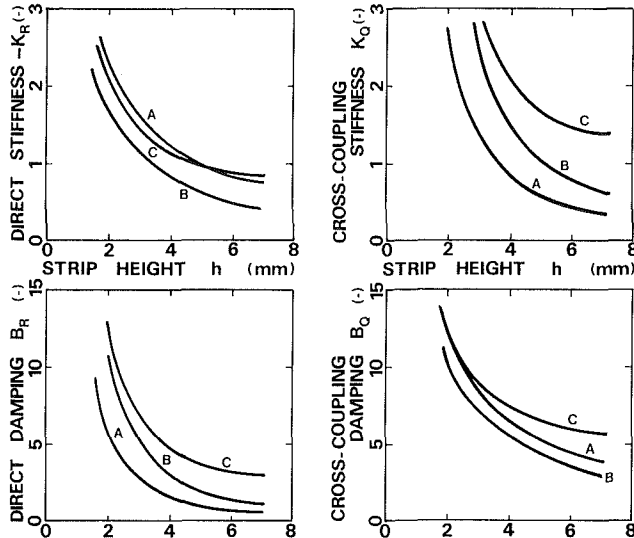


Fig. 8 Influence of labyrinth strip height  $h$  on nondimensional labyrinth coefficients

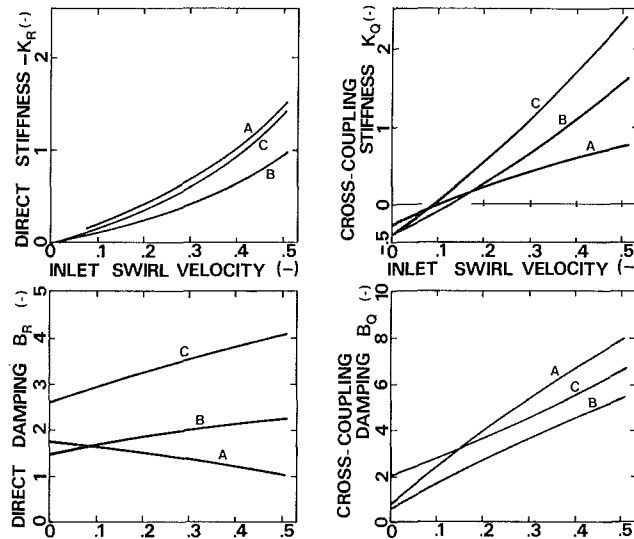


Fig. 9 Influence of nondimensional inlet swirl velocity on nondimensional labyrinth coefficients

However, the friction coefficients calculated with Prandtl's universal law are approximately 20 percent too high compared to experimental results for this type of flow. This will be accounted for in the numerical calculations.

## Results

This theoretical model allows the influence of different labyrinth geometries, operating conditions, and gas characteristics on labyrinth excitation coefficients to be studied. The discussion will focus on seals on impeller shroud labyrinths. The labyrinth coefficients, and the velocities have been made dimensionless by setting

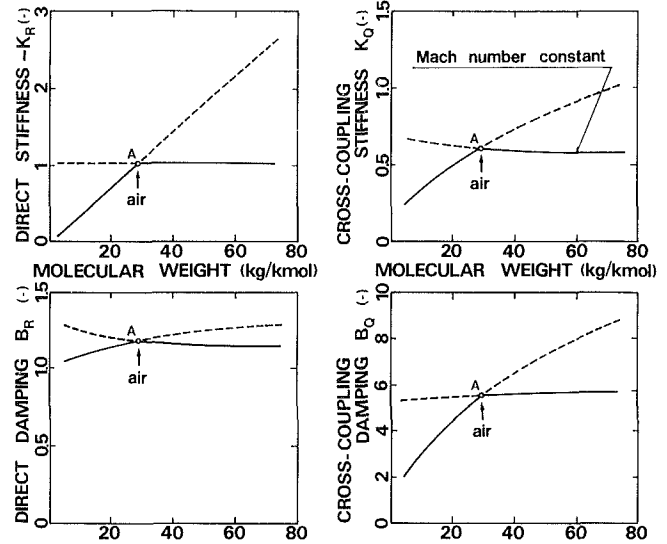


Fig. 10 Influence of gas molecular weight on nondimensional labyrinth coefficients

$$K_R = k_R / p_0 r, K_Q = k_Q / p_0 r,$$

$$B_R = b_R \sqrt{p_0 / \rho_0} / p_0 r^2, B_Q = b_Q \sqrt{p_0 / \rho_0} / p_0 r^2$$

$$W = w / \sqrt{p_0 / \rho_0} \quad (25)$$

The labyrinth types which will be discussed are defined in Fig. 7. The relevant parameters in the calculation are:  $r = 100$  mm;  $\Delta r = 0.25$  mm;  $d = 4$  mm;  $h = 4$  mm;  $z = 4$ ;  $\pi_p = 0.8$ ;  $W_{rot} = 0.5$ ,  $w_{in}/w_{rot} = 0.8$ . The results show that the cross-coupling stiffness, which is responsible for self-excitation is always larger for the stator labyrinth with milled strips compared to the other labyrinth types, but this is also true for the (direct) damping as Fig. 8-10 show. Therefore, when comparing labyrinth types with regard to rotor stability, the effective self-excitation action of the labyrinth has to be looked at, which may be estimated by calculating the difference of cross-coupling and damping force

$$F_Q = (k_Q - b_R \omega_k) e$$

where  $\omega_k$  is the first natural frequency of the rotor-bearing system. The other two coefficients  $k_R$  and  $b_Q$  have only little influence on rotor stability.

**Influence Of Labyrinth Geometry.** The labyrinth coefficients are strongly dependent on the strip height  $h$  as may be seen in Fig. 8, this is especially true for the cross-coupling stiffness.

The calculations reveal little influence of strip distance  $d$  and radial clearance  $\Delta r$  (results not given here). However, since an increase in  $\Delta r$  also increases the swirl velocity of the leakage fluid entering the labyrinth, the coefficients are indirectly affected by a change in  $\Delta r$  as will be seen below.

**Influence Of Operating Conditions.** It has been known for some time [7, 8] that the most important parameter affecting self-excitation due to labyrinth seals is the inlet swirl velocity of the leakage flow. This is confirmed in Fig. 9. A most interesting result is the fact that the damping of the labyrinth is hardly affected by a change in swirl velocity. Hence, reducing swirl velocity eliminates the destabilising cross-coupling while retaining the desired labyrinth damping, thus drastically improving rotor stability. This may be achieved by putting swirl brakes at the labyrinth entrance [8].

The phenomenon that the cross-coupling stiffness  $k_Q$  becomes negative even before the swirl velocity is zero may be explained as follows: the sign of  $k_Q$  mainly depends on the difference of inlet and outlet circumferential momentum, as

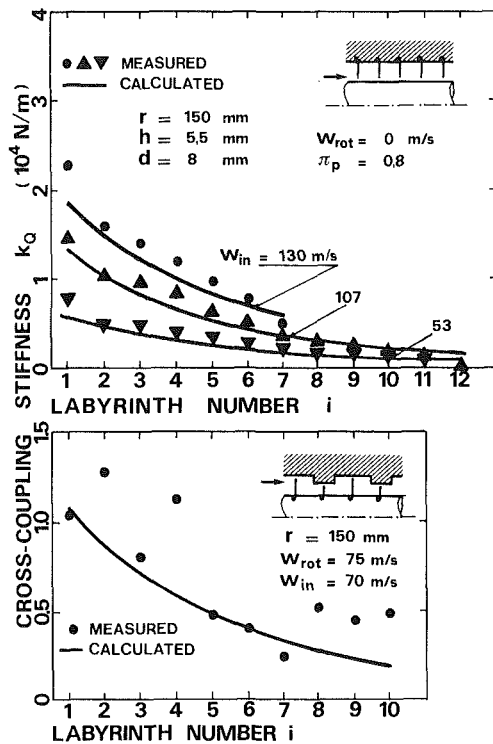


Fig. 11 Distribution of cross-coupling stiffness along the labyrinth

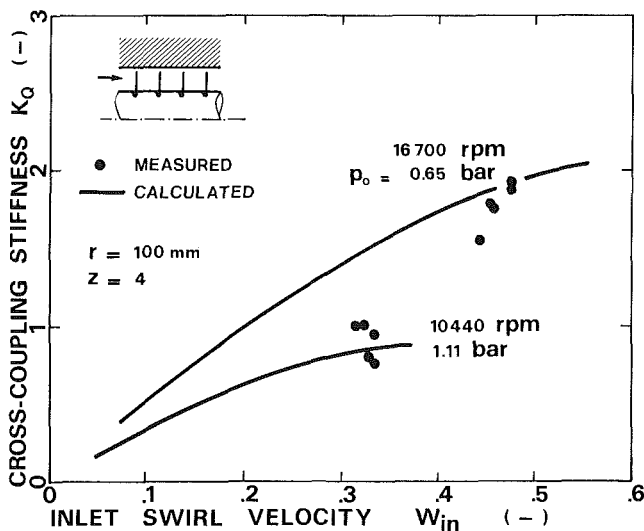


Fig. 12 Nondimensional total cross-coupling stiffness versus nondimensional inlet swirl velocity

an investigation of the basic equations reveals. At small inlet swirl the circumferential momentum is increased by the shaft rotation, this difference becomes negative before the inlet swirl does.

**Influence Of Gas Molecular Weight.** Assuming that an impeller has been originally designed to be used for air, two different cases have to be considered:

If the application is for gases lighter than air, the impeller speed is given by the strength of the material, i.e., it will be the same as for air. Therefore, the nondimensional velocities  $W_{in}$  and  $W_{rot}$  decrease with decreasing molecular weight and the labyrinth coefficients follow the curves to the left of point A in Fig. 10. On the other hand, if gases heavier than air are used the speed must be reduced to keep the Mach number constant and therefore the nondimensional speed, being

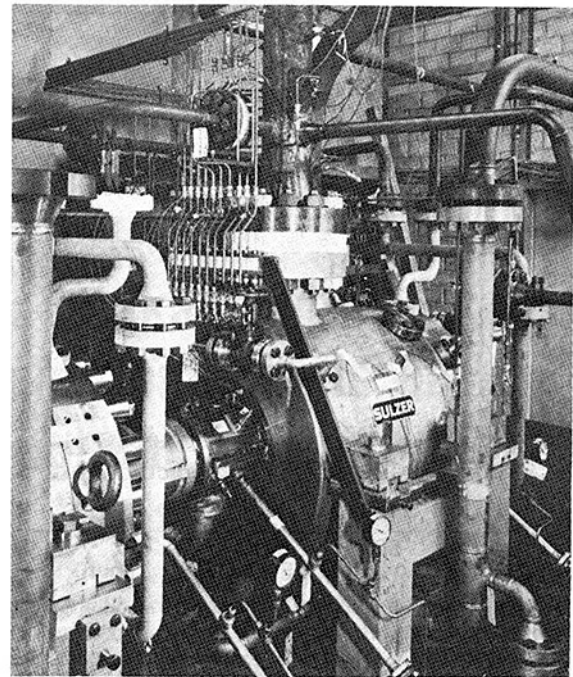


Fig. 13 Measurement of cross-coupling coefficients on high-pressure centrifugal compressor

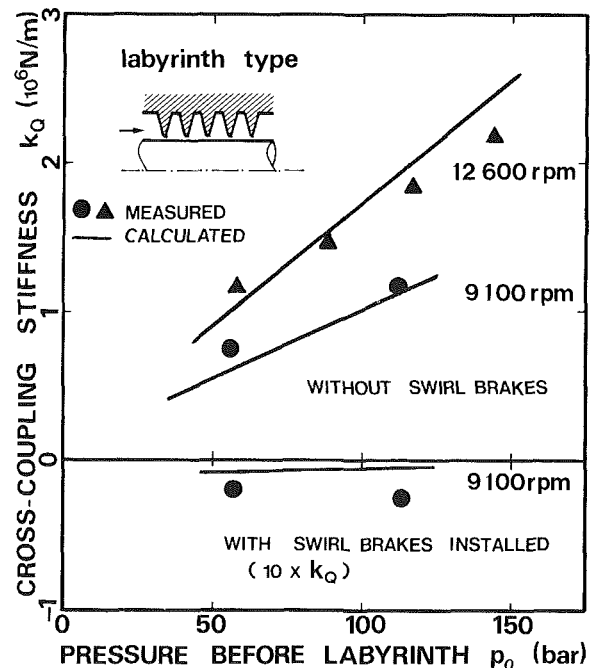


Fig. 14 Total cross-coupling stiffness versus pressure

directly related to Mach number, remains constant leading to nondimensional labyrinth coefficients practically independent of molecular weight (the curves to the right of point A in Fig. 10). From its definition (25), it follows that the dimensional damping then increases with molecular weight, hence a rotor used for gases heavier than air will tend to have better stability with increasing molecular weight if all other parameters remain the same.

### Comparison With Measurement

Since the influence of direct stiffness on rotor stability is small and measurements of labyrinth damping are not

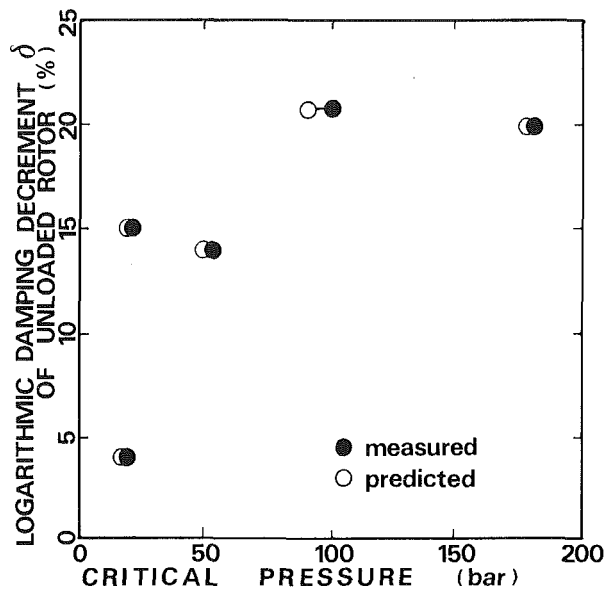


Fig. 15 Comparison of predicted and measured stability limits of five different compressors

available, only comparison of measured and calculated cross-coupling stiffness will be given.

The measurements in Fig. 11 are labyrinth tests at low pressure levels due to Benckert [7]. The variation of  $k_Q$  along the seal is given for two different types of labyrinths. The decrease of  $k_Q$  is a consequence of the reduction in swirl velocity in downstream direction. The agreement with calculated results is less satisfactory for the staggered than for the straight labyrinth. Here the assumption of a uniform circumferential velocity may be an oversimplification. However, the scattering of measured data makes the comparison difficult.

Figure 12 shows measurements of total cross-coupling stiffness of a shroud labyrinth with strips on the rotor carried out by the authors on an impeller test stand for different flow conditions.

Measurements of cross-coupling stiffness in a high-pressure centrifugal compressor have been carried out by the authors. For different rotor eccentricities, the pressure distribution in the labyrinth chambers of the first interstage shroud labyrinth at pressures up to 140 bar have been measured (Fig. 13). This has been repeated with a mounted swirl brake, reducing the inlet swirl velocity,  $w_{in}$ . The results shown in Fig. 14 fully confirm the theory, which predicted a sign reversal of the cross-coupling stiffness due to the swirl brake.

The present theory of labyrinth coefficients has also been checked against observations of instabilities of real compressors in test runs and the field (Fig. 15). The linear stability analysis taking into account the labyrinth coefficients calculated by the present theory gives the logarithmic damping decrement  $\delta$  of a rotor as a function of discharge pressure. Instability sets in when  $\delta$  becomes negative, the amplitude growing unboundedly. In practice, the transition from stability to instability is rather smooth due to nonlinearities and moreover may be obscured by stochastic

phenomena. The observed critical pressures in Fig. 15 are defined as the pressure when the Fourier analysis of the rotor vibration shows a distinctive although small peak at the first natural frequency. Again the theory is fully confirmed by experience.

## Conclusions

A theoretical model which allows the calculation of the labyrinth coefficients for rotor dynamics, including damping, has been presented. The good agreement with measured data taken from laboratory investigations and from measurements carried out on a high pressure centrifugal compressor confirm the reliability of the model. In addition, the comparison of critical discharge pressures observed on real compressors with the predicted stability limits shows good agreement.

If a swirl brake is installed to reduce the inlet swirl of the leakage flow, then the labyrinth cross-coupling stiffness is eliminated as predicted by theory and confirmed by measurements. The damping action of the labyrinth is retained. Hence for a rotor stability analysis this should be taken into account if rotor design should not be overly conservative.

## References

- 1 Alford, J. S., "Protecting Turbomachinery From Self-Excited Whirl," ASME JOURNAL OF ENGINEERING FOR POWER, Vol. 38, 1965, pp. 333-344.
- 2 Spurk, H. H., and Keiper, R., "Selbsterregte Schwingungen bei Turbomaschinen infolge Labyrinthströmung," *Ingenieurarchiv*, Vol. 43 (174), pp. 127-135.
- 3 Kostyuk, A. G., "A Theoretical Analysis of the Aerodynamic Forces in the Labyrinth Glands of Turbomachines." *Teploenergetika*, 1972, No. 419 (11), pp. 29-33.
- 4 Iwatsubo, T., "Evaluation of Instability Forces of Labyrinth Seals in Turbines or Compressors," NASA Conference Publication 2133, 1980, pp. 139-167.
- 5 Rosenberg, S., Orlik, W. G., and Marcenks, U. A., "Investigation of the Aerodynamic Transverse Force in Labyrinth Seals with Eccentric Rotor," *Energomaschinenstrojen*, Vol. 8, 1974, pp. 15-17.
- 6 Ulrichs, K., "Die Spaltströmung bei thermischen Turbomaschinen als Ursache für die Entstehung schwingungsanfängerischer Querkräfte," *Ingenieur-Archiv*, Vol. 45, 1976, pp. 193-208.
- 7 Benckert, H., "Spaltströmung," *Forschungsberichte Forschungsvereinigung Verbrennungskraftmaschinen*, Frankfurt, Vol. 253, 1978.
- 8 Jenny, R., and Wyssmann, H., "Lateral Vibration Reduction in High Pressure Centrifugal Compressors," *Proceedings of the 9th Turbomachinery Symposium*, Texas A and M University, 1980, pp. 45-56.
- 9 Jenny, R., "Labyrinth as a Cause of Self-excited Rotor Oscillations in Centrifugal Compressors," *Sulzer Technical Review*, No. 4, 1980, pp. 149-156.
- 10 Lauder, B. E., and Spalding, D. B., *Mathematical Models of Turbulence*, Academic Press 1972.
- 11 Stoff, H., "Calcul et mesure de la turbulence d'un écoulement incompressible dans le labyrinthe entre un arbre en rotation et un cylindre stationnaire," Thesis No. 342 (1979) Swiss Federal College of Technology, Lausanne, Juris Verlag Zurich, 1979.
- 12 Boymann, T., and Suter, P., "Transport Phenomena in Labyrinth Seals of Turbomachines," AGARD Conference, London, Apr. 1978; *Proceedings Seal Technology in Gasturbine Engines*.
- 13 Trutnovsky, K., "Berührungsfreie Dichtungen." *VDI Verlag*, 1973.
- 14 Neumann, K., "Zur Frage der Verwendung von Durchblickdichtungen im Dampfturbinenbau," *Maschinentechnik*, Vol. 13, 1964, Nr. 4
- 15 Schlichting, H., *Boundary Layer Theory*, McGraw-Hill, New York 1979.
- 16 Abramovich, G. N., *The Theory of Turbulent Jets*, MIT Press, Cambridge, Mass., 1963.
- 17 Ziegler, H., *Principles of Structural Stability*, Ginn-Blaisdel, Waltham, Mass., 1968.

# Analysis for Leakage and Rotordynamic Coefficients of Surface-Roughened Tapered Annular Gas Seals<sup>1</sup>

C. C. Nelson

Mechanical Engineering Department,  
Texas A&M University,  
College Station, Texas 77843

*In order to soften the effects of rub, the smooth stators of turbine gas seals are sometimes replaced by a honeycomb surface. This deliberately roughened stator and smooth rotor combination retards the seal leakage and may lead to enhanced rotor stability. However, many factors determine the rotordynamic coefficients and little is known as to the effectiveness of these "honeycomb seals" under various changes in the independent seal parameters. This analysis develops an analytical-computational method to solve for the rotordynamic coefficients of this type of compressible-flow seal. The governing equations for surface-roughened tapered annular gas seals are based on a modified Hirs's turbulent bulk flow model. A perturbation analysis is employed to develop zeroth and first-order perturbation equations. These equations are numerically integrated to solve for the leakage, pressure, density, and velocity for small motion of the shaft about the centered position. The resulting pressure distribution is then integrated to find the corresponding rotor-dynamic coefficients. Finally, an example case is used to demonstrate the effect of changing from a smooth to a rough stator while varying the seal length, taper, preswirl, and clearance ratio.*

## Introduction

Figure 1 illustrates the basic geometry of the convergent tapered annular turbine gas seal. In this figure both the rotor and the stator elements of the seal are shown to have the same nominally smooth surfaces. In practice, however, the smooth stator is sometimes replaced by a honeycomb or other deliberately roughened surface. The purpose of this roughened surface is to soften the effects of rub from the rotor and to retard leakage. But in addition, the smooth rotor and rough stator combination may have significant influence on the seal's rotordynamic coefficients. In fact, von Pragenau [1] suggests just such a concept for an incompressible-flow "damper seal" which he believes will enhance rotor stability.

As related to rotordynamics, seal analysis has the objective of determining the reaction force acting on the rotor as a result of the shaft motion. For small motion about a centered position, the relation between the reaction-force components and the shaft motion can be written

$$-\begin{Bmatrix} F_x \\ F_y \end{Bmatrix} = \begin{bmatrix} \mathcal{K} & k \\ -k & \mathcal{K} \end{bmatrix} \begin{Bmatrix} X \\ Y \end{Bmatrix} + \begin{bmatrix} \mathcal{C} & c \\ -c & \mathcal{C} \end{bmatrix} \begin{Bmatrix} \dot{X} \\ \dot{Y} \end{Bmatrix} + \begin{bmatrix} \mathfrak{M} & m \\ -m & \mathfrak{M} \end{bmatrix} \begin{Bmatrix} \ddot{X} \\ \ddot{Y} \end{Bmatrix} \quad (1)$$

The off-diagonal coefficients ( $k$ ,  $c$ ,  $m$ ) are referred to as the cross-coupled stiffness, damping, and added-mass terms, respectively. These cross-coupled terms arise from the fluid's circumferential velocity component. This phenomenon is usually referred to as the effects swirl. The circumferential velocity component is in part a function of the stator and rotor surface roughness. A rough stator and smooth rotor will tend to reduce the circumferential velocity, leading to a reduction in the destabilizing cross-coupled terms.

Fleming [2, 3] made a separate analysis for the direct stiffness  $\mathcal{K}$ , and for the direct damping  $\mathcal{C}$  of smooth-tapered annular gas seals. However, he did not include the effects of swirl and thus could not obtain the cross-coupled terms. Childs [4] developed an analysis for both direct and cross-coupled terms of incompressible-flow by using Hirs's [5] turbulent bulk-flow model and a perturbation technique. Nelson [6] used a similar approach to develop a numerical solution for the direct and cross-coupled stiffness and damping of smooth compressible-flow seals. The present analysis modifies the solution of [6] to include the effects of

<sup>1</sup>This work is being supported by NASA Grant NAG3-181 from the Lewis Research Center.

Contributed by the Gas Turbine Division of THE AMERICAN SOCIETY OF MECHANICAL ENGINEERS and presented at the 29th International Gas Turbine Conference and Exhibit, Amsterdam, The Netherlands, June 4-7, 1984. Manuscript received at ASME Headquarters December 19, 1983. Paper No. 84-GT-32.



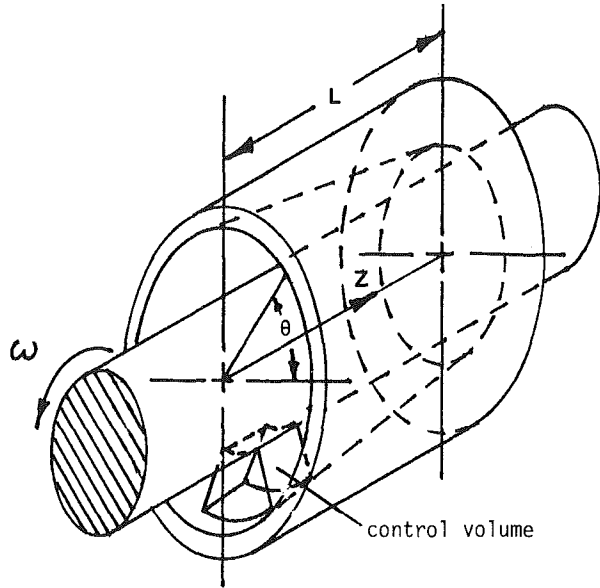


Fig. 1 Smooth tapered annular seal

different stator and rotor surface conditions and then demonstrates the analysis on a specific seal example.

### Governing Equations

The control volume element shown in Fig. 1 has been enlarged and redrawn in Fig. 2. Note that the smooth stator surface has been replaced by a roughened honeycomb surface. The shear stresses  $\tau_s$  and  $\tau_r$  are the net wall shear stresses resulting from both the pressure induced flow and the drag induced flow. Hirs's turbulent bulk-flow model assumes that these stresses can be written as

$$\tau = \frac{1}{2} \rho U_m^2 n_o \left( \frac{2\rho U_m H}{\mu} \right)^{m_o} \quad (2)$$

where  $U_m$  is the mean flow velocity relative to the surface upon which the shear stress is acting. Hirs's constants  $n_o$  and  $m_o$  are generally empirically determined from pressure flow experiments. For the control volume in Fig. 2,  $n_s$  and  $m_s$  represent Hirs's constants relative to the stator surface and  $n_r$  and  $m_r$  represent those relative to the rotor surface. Substituting the mean flow velocity relative to each surface into

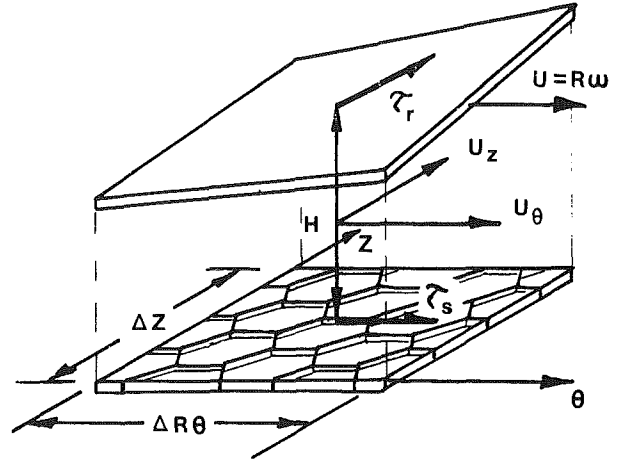


Fig. 2 Control volume for a seal with a honeycomb stator

equation (2) and then taking the appropriate component of the shear stress in the Z- and  $\theta$ -direction, the axial and circumferential momentum equations are

$$\begin{aligned} -H \frac{\partial p}{\partial Z} = & \rho \left\{ \frac{n_s}{2} \left( \frac{2\rho H}{\mu} \right)^{m_s} U_z (U_\theta^2 + U_z^2)^{\frac{m_s+1}{2}} \right. \\ & \left. + \frac{n_r}{2} \left( \frac{2\rho H}{\mu} \right)^{m_r} U_z [(U_\theta - U)^2 + U_z^2]^{\frac{m_r+1}{2}} \right\} \quad (3a) \\ & + \frac{\partial(\rho U_\theta H)}{\partial t} + \frac{1}{R} \frac{\partial(\rho U_\theta U_z H)}{\partial \theta} + \frac{\partial(\rho U_z^2 H)}{\partial Z} \end{aligned}$$

$$\begin{aligned} -\frac{H}{R} \frac{\partial p}{\partial \theta} = & \rho \left\{ \frac{n_s}{2} \left( \frac{2\rho H}{\mu} \right)^{m_s} U_\theta (U_\theta^2 + U_z^2)^{\frac{m_s+1}{2}} \right. \\ & \left. + \frac{n_r}{2} \left( \frac{2\rho H}{\mu} \right)^{m_r} (U_\theta - U) [(U_\theta - U)^2 + U_z^2]^{\frac{m_r+1}{2}} \right\} \quad (3b) \\ & + \frac{\partial(\rho U_\theta H)}{\partial t} + \frac{1}{R} \frac{\partial(\rho U_\theta^2 H)}{\partial \theta} + \frac{\partial(\rho U_\theta U_z H)}{\partial Z} \end{aligned}$$

The bulk-flow continuity equation is

$$0 = \frac{\partial(\rho H)}{\partial t} + \frac{1}{R} \frac{\partial(\rho U_\theta H)}{\partial \theta} + \frac{\partial(\rho U_z H)}{\partial Z} \quad (3c)$$

And for adiabatic flow the energy equation is

### Nomenclature

$C(Z)$  = centered position seal clearance  
 $\bar{C}$  = nominal seal clearance,  $(C_e + C_x)/2$   
 $\bar{c}$  = dimensionless nominal seal clearance,  $\bar{C}/R$   
 $c_v$  = specific heat at constant volume  
 $\mathcal{C}, \mathcal{c}$  = direct and cross-coupled damping coefficients of equation (1)  
 $\tilde{\mathcal{C}}, \tilde{\mathcal{c}}$  = dimensionless direct and cross-coupled damping coefficients defined by equation (26)  
 $D$  = shaft diameter  
 $H(Z, \theta, t)$  = local seal clearance  
 $h = H/\bar{C}$  = dimensionless clearance  
 $k$  = entrance loss coefficient  
 $\mathcal{K}, \mathcal{k}$  = direct and cross-coupled stiffness coefficients of equation (1)  
 $\tilde{\mathcal{K}}, \tilde{\mathcal{k}}$  = dimensionless direct and cross-coupled

stiffness coefficients defined by equation (25)

$L$  = seal length  
 $l$  = dimensionless seal length,  $L/R$   
 $M$  = Mach number,

$$U_z \sqrt{\frac{\rho}{\gamma p}}$$

$m_s, m_r$  = coefficients for Hirs's turbulent lubrication equations  
 $n_s, n_r$

$$P_c = \text{pressure coefficient, } \frac{p_a}{(R\omega)^2 \rho_a}$$

$p$  = pressure  
 $\bar{p}$  = dimensionless pressure,  $p/p_a$   
 $R$  = shaft radius

$$0 = \frac{\partial}{\partial t} \left[ \left( c_v T + \frac{U_\theta^2}{2} + \frac{U_z^2}{2} \right) \rho H \right] + \frac{1}{R} \frac{\partial}{\partial \theta} \left[ \left( c_v T + \frac{U_\theta^2}{2} + \frac{U_z^2}{2} + \frac{p}{\rho} \right) U_\theta \rho H \right] + \frac{\partial}{\partial z} \left[ \left( c_v T + \frac{U_\theta^2}{2} + \frac{U_z^2}{2} + \frac{p}{\rho} \right) U_z \rho H \right] \quad (3d)$$

$$+ U(U_\theta - U) \frac{\rho n_r}{2} \left( \frac{2\rho H}{\mu} \right)^{m_r} \left[ (U_\theta - U)^2 + U_z^2 \right]^{\frac{m_r+1}{2}}$$

Assuming a perfect gas ( $c_v T = p/\rho(\gamma - 1)$ ) and using the dimensionless parameters defined in the Nomenclature, the foregoing governing equations take the following dimensionless working form:

Momentum:

$$\frac{-P_c}{\bar{\rho} l} \frac{\partial \bar{p}}{\partial z} = \frac{u_z}{\bar{c} h} [f_s + f_r] + \frac{D u_z}{D \tau} \quad (4a)$$

$$\frac{-P_c}{\bar{p}} \frac{\partial \bar{p}}{\partial \theta} = \frac{1}{\bar{c} h} [u_\theta f_s + (u_\theta - 1) f_r] + \frac{D u_\theta}{D \tau} \quad (4b)$$

Continuity:

$$0 = \frac{\partial(\bar{p} h)}{\partial \tau} + \frac{\partial(\bar{p} u_\theta h)}{\partial \theta} + \frac{1}{l} \frac{\partial(\bar{p} u_z h)}{\partial z} \quad (4c)$$

Energy:

$$\frac{\bar{p}}{h} \frac{\partial h}{\partial \tau} = u_\theta \left( \frac{\partial \bar{p}}{\partial \theta} + \frac{\bar{p}}{P_c} \frac{D u_\theta}{D \tau} \right) + u_z \left( \frac{1}{l} \frac{\partial \bar{p}}{\partial z} + \frac{\bar{p}}{P_c} \frac{D u_z}{D \tau} \right) + \frac{1}{\gamma - 1} \left( \frac{D \bar{p}}{D \tau} - \frac{\gamma \bar{p}}{\bar{\rho}} \frac{D \bar{p}}{D \tau} \right) + \frac{\bar{p}}{\bar{c} h P_c} (u_\theta - 1) f_r \quad (4d)$$

where

$$f_s = \frac{n_s}{2} (u_\theta^2 + u_z^2)^{\frac{m_s+1}{2}} (2R_c)^{m_s}$$

$$f_r = \frac{n_r}{2} [(u_\theta - 1)^2 + u_z^2]^{\frac{m_r+1}{2}} (2R_c)^{m_r} \quad (4e)$$

$$\frac{D}{D \tau} = \frac{\partial}{\partial \tau} + u_\theta \frac{\partial}{\partial \theta} + \frac{u_z}{l} \frac{\partial}{\partial z}$$

## Perturbation Analysis

The governing equations (4a-d) define the relationship between the dimensionless clearance, pressure, density, axial velocity, and circumferential velocity ( $h, \bar{p}, \bar{\rho}, u_z, u_\theta$ ) as functions of the independent dimensionless spatial variables ( $\theta, z$ ) and the dimensionless time  $\tau$ . Expansion of these equations in the perturbation variables

$$h = h_0 + \epsilon h_1 \quad \bar{p} = \bar{p}_0 + \epsilon \bar{p}_1 \quad u_\theta = u_{\theta 0} + \epsilon u_{\theta 1}$$

$$\bar{\rho} = \bar{\rho}_0 + \epsilon \bar{\rho}_1 \quad u_z = u_{z 0} + \epsilon u_{z 1} \quad (5)$$

yields the zeroth and first-order equations as shown in Appendix A.

**Zeroth-Order Solution.** The zeroth-order equations describe the steady flow resulting from a centered position rotating shaft. Before these equations can be integrated, values for Hirs's constants  $m_s, n_s, m_r,$  and  $n_r$  must be established. Lacking experimental data for these constants, values can be approximated by the use of Colebrook's formula [7].

$$\frac{1}{\sqrt{4n_0 R_a^{m_0}}} = -2 \log \left( \frac{e/2\bar{C}}{3.7} + \frac{2.51}{R_a \sqrt{4n_0 R_a^{m_0}}} \right) \quad (6)$$

For a given relative roughness a least-squares fit is used to determine  $n_0$  and  $m_0$  over a range of  $R_a$  (say  $5000 < R_a < 1000000$ ).

Integration begins by guessing an entrance zeroth-order Mach number  $M_0(0)$ . Defining an entrance loss coefficient  $k$  in a manner similar to Zuk [8], the following equations give the initial zeroth-order pressure and density.

$$\bar{p}_0(0) = \frac{1}{\left[ 1 + \frac{(\gamma - 1)(1 + k) M_0^2(0)}{2} \right]^{\gamma(\gamma - 1)}} \quad (7)$$

$$\bar{\rho}_0(0) = \frac{1 + \left[ \frac{(\gamma - 1) M_0^2(0)}{2} \right]}{\left[ 1 + \frac{(\gamma - 1)(1 + k) M_0^2(0)}{2} \right]^{\gamma(\gamma - 1)}} \quad (8)$$

In the first application,  $k$  is assumed to be 0.1. Expanding the Mach number as defined in the Nomenclature in terms of the

## Nomenclature (cont.)

$R_{ao}$	= centered position, axial Reynolds number, $\frac{2\rho U_z \bar{C}}{\mu}$
$R_c$	= circumferential Reynolds number, $\frac{\rho(R\omega)\bar{H}}{\mu}$
$R_{co}$	= centered position, nominal circumferential Reynolds number, $\frac{\rho(R\omega)\bar{C}}{\mu}$
$R_g$	= perfect gas constant
$T$	= temperature
$t$	= time
$U$	= velocity of rotor surface, $R\omega$
$U_z, U_\theta$	= fluid velocity in the $z$ and $\theta$ directions
$(u_\theta = U_\theta/(R\omega))$	= dimensionless tangential and axial velocities
$(u_z = U_z/(R\omega))$	= dimensionless tangential and axial velocities
$Z, R\theta$	= axial and circumferential seal coordinates illustrated in Fig. (1)
$z$	= dimensionless seal coordinates, $Z/L, \theta$

$\gamma$	= specific heat ratio, $c_p/c_v$
$\epsilon$	= dimensionless seal eccentricity ratio
$e/2\bar{C}$	= relative surface roughness
$\mu$	= viscosity
$\rho$	= density
$\bar{\rho}$	= dimensionless density, $\rho/\rho_a$
$\tau_s, \tau_r$	= shear stress illustrated in Fig. (2)
$\tau$	= dimensionless time, $t\omega$
$\Omega$	= shaft orbital velocity
$\Omega$	= shaft whirl ratio, $\Omega/\omega$
$\omega$	= shaft angular velocity

## Subscripts

a, e, x, b	= reservoir, entrance, exit, and sump conditions, respectively
0, 1	= zeroth and first-order perturbations in the dependent variables
s, r	= stator surface and rotor surface, respectively

perturbation variables gives the following zeroth-order entrance equation

$$M_0^2(0) = \frac{u_{z0}^2(0)\bar{\rho}_0(0)}{\gamma\bar{p}_0(0)P_c} \quad (9)$$

From this equation, the initial zeroth-order axial velocity  $u_{z0}(0)$  can be found. Having now  $\bar{p}_0(0)$ ,  $\bar{\rho}_0(0)$ , and  $u_{z0}(0)$ , the centered position axial Reynolds number  $R_{a0}$  is determined and used to approximate a new loss coefficient from the data of Deissler [9] as

$$k = \sqrt{5.3/\log_{10} R_{a0}} - 1.0 \quad (10)$$

For  $R_{a0} > 200,000$ ,  $k$  is set equal to zero. This new loss coefficient is then used to determine new entrance conditions and the procedure repeated until a consistent result for  $k$  is found. Finally, the initial zeroth-order circumferential velocity,  $u_\theta(0)$ , is a given independent variable which indicates the amount of prerotation given to the entering fluid.

Having now the zeroth-order initial conditions, equations (A.1a-d) are numerically integrated along the seal length. The guess for the entrance Mach number is continually adjusted until: (a) the Mach number at the exit just reaches one and the exit pressure remains greater than the sump pressure for choked flow, or (b) until the exit pressure just matches the sump pressure and the Mach number remains less than 1 for unchoked flow. All intermediate values of the pressure, density, and velocities and their derivatives are then stored for later use in solving the first-order perturbation equations. Also, the leakage is determined from these zeroth-order values.

**First-Order Solution.** The first-order equations (A.2a-d) define  $\bar{p}_1(z, \theta, \tau)$ ,  $\bar{\rho}_1(z, \theta, \tau)$ ,  $u_{z1}(z, \theta, \tau)$ , and  $u_{\theta 1}(z, \theta, \tau)$ , resulting from the seal clearance function  $h_1(z, \theta, \tau)$ . If the shaft center moves in an elliptical orbit, then the rotation displacement vector to the shaft center has coordinates

$$X = Cx_0 \cos \Omega t, \quad Y = Cy_0 \sin \Omega t \quad (11)$$

and the clearance function is

$$h_1 = -x_0 \cos \bar{\Omega} \tau \cos \theta - y_0 \sin \bar{\Omega} \tau \sin \theta \quad (12)$$

The assumed harmonic response is

$$\begin{aligned} \bar{p}_1 &= (\bar{p}_x^c \cos \bar{\Omega} \tau + \bar{p}_x^s \sin \bar{\Omega} \tau) \cos \theta + (\bar{p}_y^c \cos \bar{\Omega} \tau \\ &\quad + \bar{p}_y^s \sin \bar{\Omega} \tau) \sin \theta \\ \bar{\rho}_1 &= (\bar{\rho}_x^c \cos \bar{\Omega} \tau + \bar{\rho}_x^s \sin \bar{\Omega} \tau) \cos \theta + (\bar{\rho}_y^c \cos \bar{\Omega} \tau \\ &\quad + \bar{\rho}_y^s \sin \bar{\Omega} \tau) \sin \theta \\ u_{z1} &= (u_x^c \cos \bar{\Omega} \tau + u_x^s \sin \bar{\Omega} \tau) \cos \theta + (u_y^c \cos \bar{\Omega} \tau \\ &\quad + u_y^s \sin \bar{\Omega} \tau) \sin \theta \\ u_{\theta 1} &= (v_x^c \cos \bar{\Omega} \tau + v_x^s \sin \bar{\Omega} \tau) \cos \theta + (v_y^c \cos \bar{\Omega} \tau \\ &\quad + v_y^s \sin \bar{\Omega} \tau) \sin \theta \end{aligned} \quad (13)$$

Substitution of equations (12) and (13) into the first-order equations (A.2a-d) yields sixteen first-order ordinary differential equations which can be written in the form

$$[A(z)] \frac{d\mathbf{X}}{dz} + [B(z)] \mathbf{X} = x_0 \mathbf{C}(z) + y_0 \mathbf{D}(z) \quad (14)$$

where

$$\mathbf{X} = (\bar{p}_x^c, \bar{p}_x^s, \bar{p}_y^c, \bar{p}_y^s, \bar{\rho}_x^c, \bar{\rho}_x^s, \bar{\rho}_y^c, \bar{\rho}_y^s, u_x^c, u_x^s, u_y^c, u_y^s, v_x^c, v_x^s, v_y^c, v_y^s).$$

The coefficients of  $[A]$ ,  $[B]$ ,  $\mathbf{C}$ , and  $\mathbf{D}$  are given in Appendix B. These coefficients are completely determined from the values obtained in the zeroth-order solution.

The necessary sixteen boundary conditions for equation (14) are now written by examining the perturbation conditions that must exist at the entrance and exit for choked or unchoked flow. For ease in writing these conditions, the following definitions are made

$$\mathbf{p}_1 = \begin{Bmatrix} \bar{p}_x^c \\ \bar{p}_x^s \\ \bar{p}_y^c \\ \bar{p}_y^s \end{Bmatrix}, \quad \bar{\rho}_1 = \begin{Bmatrix} \bar{\rho}_x^c \\ \bar{\rho}_x^s \\ \bar{\rho}_y^c \\ \bar{\rho}_y^s \end{Bmatrix}, \quad \mathbf{u}_{z1} = \begin{Bmatrix} u_x^c \\ u_x^s \\ u_y^c \\ u_y^s \end{Bmatrix}, \quad \mathbf{u}_{\theta 1} = \begin{Bmatrix} v_x^c \\ v_x^s \\ v_y^c \\ v_y^s \end{Bmatrix} \quad (15)$$

(a.1) For choked flow, the first-order perturbation in the exit Mach number is set equal to zero. Using the definition of the Mach number, the first-order perturbation is

$$M_1 = M_0 \left( \frac{\bar{p}_1}{2\bar{p}_0} + \frac{u_{z1}}{u_{z0}} - \frac{\bar{\rho}_1}{2\bar{\rho}_0} \right) \quad (16)$$

This yields

$$\frac{\bar{p}_1(1)}{2\bar{p}_0(1)} + \frac{u_{z1}(1)}{u_{z0}(1)} - \frac{\bar{\rho}_1(1)}{2\bar{\rho}_0(1)} = 0 \quad (17)$$

(a.2) For unchoked flow, the first-order perturbation in the exit pressure is zero giving

$$\bar{p}_1(1) = 0 \quad (18)$$

(a) At the entrance, the circumferential velocity perturbation is zero, i.e.,

$$u_{\theta 1}(0) = 0 \quad (19)$$

(b) Expansion of the pressure loss equation (7) in terms of the perturbation pressure and the perturbation Mach number from equation (16) yields the following first-order pressure loss equation which must be satisfied at the entrance

$$\bar{p}_1(0) + \frac{r\bar{p}_0(0)}{2\bar{p}_0(0) - r} \left( \frac{\bar{p}_1(0)}{\bar{\rho}_0(0)} + \frac{2u_{z1}(0)}{u_{z0}(0)} \right) = 0 \quad (20)$$

where

$$r = \frac{\gamma(k+1)\bar{p}_0(0)M_0^2(0)}{1 + (\gamma-1)(k+1)\frac{M_0^2(0)}{2}} \quad (21)$$

(c) A similar expansion for the density change at the entrance defined by equation (8) gives

$$\bar{\rho}_1(0) + \frac{rs\bar{\rho}_0(0)}{2\bar{\rho}_0(0) + rs} \left( \frac{2u_{z1}(0)}{u_{z0}(0)} - \frac{\bar{p}_1(0)}{\bar{\rho}_0(0)} \right) = 0 \quad (22)$$

where

$$s = 1 + (\gamma-1) \frac{[M_0^2(0)(k+1) - 2]}{2\gamma(k+1)} \quad (23)$$

Solution of the differential equation (14) in terms of the above sixteen boundary conditions can be found by numerical integration techniques. The solution will take the form

$$\mathbf{X} = x_0 \mathbf{f}(z) + y_0 \mathbf{g}(z) \quad (24)$$

**Dynamic Coefficient Definitions.** As shown in [6] if the added mass terms are neglected, the dynamic seal coefficients can be obtained by numerically integrating the appropriate solution component of equation (24), i.e.,

$$\bar{\mathcal{K}} = \frac{\mathcal{K}\bar{C}}{p_a RL} = \pi \int_0^1 f_1(z) dz \quad \bar{\mathcal{L}} = \frac{\bar{k}\bar{C}}{p_a RL} = -\pi \int_0^1 f_3(z) dz \quad (25)$$

$$\bar{\mathcal{C}} = \frac{\mathcal{C}\bar{C}\bar{\Omega}}{p_a RL} = \pi \int_0^1 g_3(z) dz \quad \bar{\mathcal{C}} = \frac{\bar{c}\bar{C}\bar{\Omega}}{p_a RL} = \pi \int_0^1 g_1(z) dz \quad (26)$$

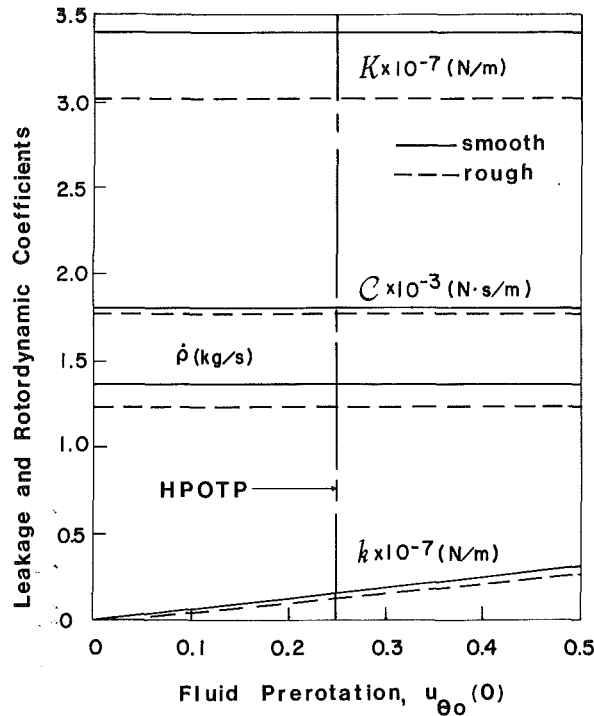


Fig. 3 Leakage and rotordynamic coefficients versus fluid prerotation (unchoked flow)

### Numerical Example

For the compressible flow seal with different stator-rotor surface roughness treatments, there are fourteen independent geometric and fluid dynamic seal variables. Assuming a perfect gas, these variables can be reduced to ten dimensionless parameters. One possible set is  $P_c = p_a / (\rho_a \omega^2 R^2)$ ,  $R_{coa} = \rho_a C \omega R / \mu_a p_a / p_b$ ,  $\gamma$ ,  $L/D$ ,  $C_e/C_x$ ,  $C/R$ ,  $e_s/2\bar{C}$ ,  $e_r/2\bar{C}$  and  $u_{\theta}(0) = U_{\theta}(0)/(\omega R)$ . Due to this large number of independent parameters, it is unreasonable to attempt to describe the leakage and dynamic coefficient's dependence in the form of a complete set of design charts. Thus a specific seal geometry and flow condition was chosen, and only the length, taper, fluid prerotation, and clearance ratio ( $L/D$ ,  $C_e/C_x$ ,  $u_{\theta}(0)$ , and  $\bar{C}/R$ ) were independently varied. The particular seal selected is equivalent to the turbine interstage seal of the High-Pressure Oxidizer Turbopump (HPOTP) of the Space Shuttle Main Engine operating at Rated Power Level. The rotor is smooth and the stator is a honeycomb surface, resulting in the following seal parameters as supplied by Jackson [10]

$$\begin{aligned}
 p_a &= 34.05 \text{ MPa (4938 psia)} \\
 p_b &= 26.41 \text{ MPa (3830 psia)} \\
 T_a &= 773^\circ \text{K (1391}^\circ \text{R)} \\
 R &= 7.282 \text{ cm (2.867 in)} \\
 C_e &= 0.381 \text{ mm (0.015 in)} \\
 C_x &= 0.254 \text{ mm (0.010 in)} \\
 L &= 2.527 \text{ cm (0.995 in)} \\
 \gamma &= 1.4 \\
 R_g &= 2480 \text{ m} \cdot \text{N/kg}^\circ \text{K (461 ft} \cdot \text{lb/lbm}^\circ \text{R)} \\
 \mu &= 2.05 \times 10^{-5} \text{ Pa} \cdot \text{s (1.38} \times 10^{-5} \text{ lb}_m/\text{ft} \cdot \text{s)} \\
 U_{\theta}(0) &= 0.25 \\
 \omega &= 28352 \text{ rpm} \\
 e_s/2\bar{C} &= 1.54 \times 10^{-2} \Rightarrow m_s = -0.0251, n_s = 0.01534 \\
 e_r/2\bar{C} &= 3.08 \times 10^{-4} \Rightarrow m_r = -0.1691, n_r = 0.03976
 \end{aligned}$$

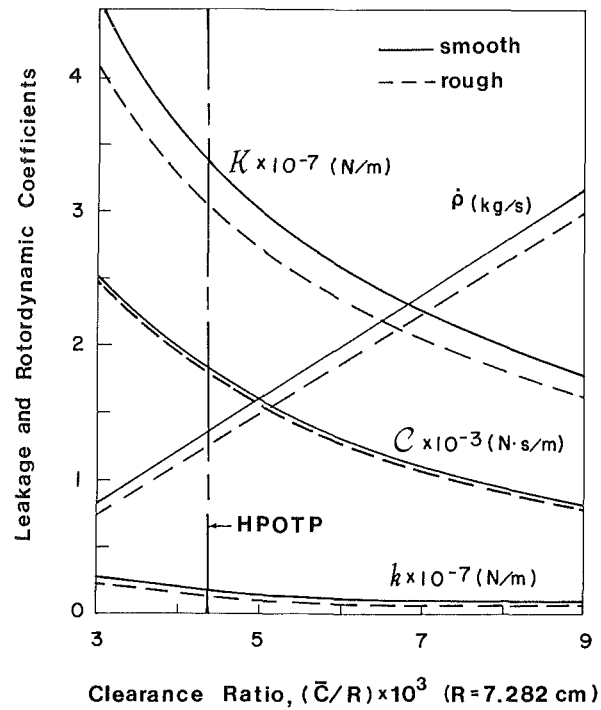


Fig. 4 Leakage and rotordynamic coefficients versus clearance ratio (unchoked flow)

Table 1 Leakage and rotordynamic coefficients for the HPOTP turbine interstage seal

	$\dot{\rho}$ (kg/s)	$\mathcal{K} \times 10^{-7}$ (N/m)	$k \times 10^{-7}$ (N/m)	$\mathcal{C}$ (N·s/m)	$n_c$ (N·s/m)
rough	1.23	3.07	0.147	1770	13.0
smooth	1.35	3.40	0.160	1800	-0.9

Results obtained for this seal are shown in Table 1. The first row of data represents the seal with the given smooth rotor and rough stator. The second row represents the results if both the stator and rotor are smooth. As expected, the rough stator decreases the leakage and cross-coupled stiffness. However, it also has the effect of significantly reducing the direct stiffness and slightly decreasing the direct damping.

Results obtained by varying the seal geometry are plotted in Figs. 3-6. In these graphs, the broken lines represent the given rough stator and the continuous lines represent a smooth stator. The vertical broken line represents the actual value of the independent variable for the HPOTP seal. Cross-coupled damping is not shown, since it was found to be relatively insignificant.

Figure 3 shows the effect of fluid prerotation (preswirl). Clearly, prerotation has no effect on  $\dot{\rho}$ ,  $\mathcal{K}$ , or  $\mathcal{C}$ . However, there is a direct linear relationship for  $k$ .

Figure 4 shows the effect of changing the nominal clearance  $\bar{C}$  (convergent taper was held constant). Within the range shown, decreasing the clearance results in an exponential increase in all coefficients and a linear decrease in leakage.

Figure 5 shows the effect of convergent taper,  $C_e/C_x$ . For these results, the exit clearance was held constant and the entrance clearance increased. It should be noted that this also has the effect of increasing the nominal clearance. Thus  $1.0 \leq C_e/C_x \leq 2.5$  results in  $0.0035 \leq \bar{C}/R \leq 0.0061$ . As might be expected from Fig. 4, increasing the taper in this manner increases  $\dot{\rho}$  and decreases  $k$  and  $\mathcal{C}$ . However,  $\mathcal{K}$  shows roughly a 50 percent increase when the seal is changed from straight to having a convergent taper ratio of  $C_e/C_x = 2$ .

Finally, Fig. 6 shows the effect of seal length. Generally, as

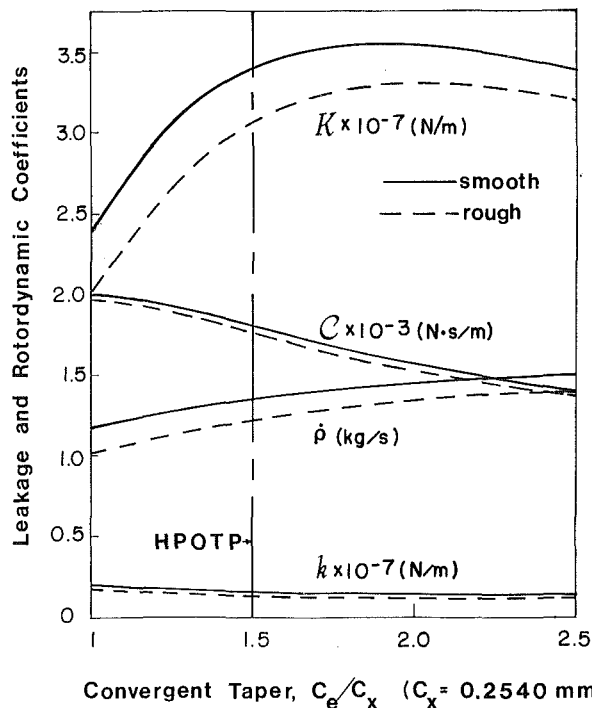


Fig. 5 Leakage and rotordynamic coefficients versus convergent taper (unchoked flow)

$L/D$  increases, the coefficients increase and the leakage decreases. However, for a very long seal (i.e.,  $L/D=0.8$ ),  $\mathcal{K}$  does reach a maximum and thereafter decreases.

### Concluding Remarks

An analysis has been presented which calculates the leakage and rotordynamic coefficients for tapered annular gas seals in which the rotor and stator have different surface roughness treatments. To demonstrate this analysis, the effect of changes in seal length, taper, clearance, and fluid prerotation was shown for the HPOTP turbine interstage seal. Generally, changes in the abovementioned seal parameters resulted in major changes in the leakage and rotordynamic coefficients.

In terms of the honeycomb stator enhancing rotor stability, the results appear mixed. There is a favorable 9 percent reduction in cross-coupled stiffness and leakage. But at the same time, direct damping decreases almost 2 percent and direct stiffness decreases 10 percent. Thus, general statements concerning the problems of instability and critical speeds can only be addressed by considering the entire rotordynamic system – clearly a problem outside the scope of this analysis. It should also be kept in mind that the selection of Hirs's constants may not accurately reflect the actual shear stresses developed over the honeycomb surface. Experimental tests need yet to be performed to determine the correct values for these constants.

### References

- 1 von Pragenau, G. L., "Damping Seals for Turbomachinery," NASA Technical Paper-1982, George C. Marshall Space Flight Center, Ala. 35812.
- 2 Fleming, D. P., "Stiffness of Straight and Tapered Annular Gas Path Seals," *J. Lubr. Technol.*, Vol. 101, No. 3, July 1979, pp. 349-355.
- 3 Fleming, D. P., "Damping in Ring Seals for Compressible Fluids," NASA, Lewis Research Center.
- 4 Childs, D. W., "Finite Length Solutions for the Rotordynamic Coefficients of Convergent-Turbulent Annular Seals," Mechanical Engineering, Texas A&M University, 1982.
- 5 Hirs, G. G., "Fundamentals of a Bulk-Flow Theory for Turbulent Lubrication Films," Ph.D. dissertation, Delft Technical University, The Netherlands, July 1970.

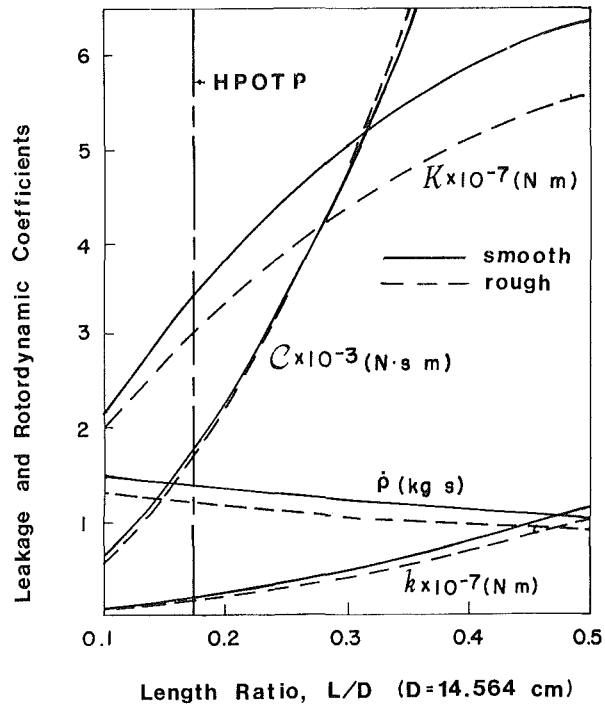


Fig. 6 Leakage and rotordynamic coefficients versus length ratio (unchoked flow)

- 6 Nelson, C. C., "Rotordynamic Coefficients for Compressible Flow in Tapered Annular Seals," Mechanical Engineering, Texas A&M University, 1983.
- 7 White, F. M., *Fluid Mechanics*, McGraw-Hill, 1979.
- 8 Zuk, J., Ludwig, L. P., and Johnson, R. L., "Quasi-One-Dimensional Compressible Flow Across Face Seals and Narrow Slots," NASA Technical Note D-6668, May 1972.
- 9 Deissler, R. G., "Analysis of Turbulent Heat Transfer and Flow in the Entrance Regions of Smooth Passages," NACA TN 3016, 1953.
- 10 Jackson, E. D., Manager, Rotating Machinery Analysis, Rockwell International, Rocketdyne Division, personal correspondence, 1983.

## APPENDIX A

### Perturbation Equations

#### Zeroth-Order Equations.

$$-\frac{P_c}{\bar{\rho}} \frac{\partial \bar{p}_0}{\partial z} = \frac{u_{z0}}{ch_0} [f_{s0} + f_{r0}] + \frac{u_{z0}}{l} \frac{\partial u_{z0}}{\partial z} \quad (A1a)$$

$$0 = \frac{1}{ch_0} [u_{\theta 0} f_{s0} + (u_{\theta 0} - 1) f_{r0}] + \frac{u_{z0}}{l} \frac{\partial u_{\theta 0}}{\partial z} \quad (A1b)$$

$$0 = \bar{\rho}_0 u_{z0} \frac{\partial h_0}{\partial z} + \bar{\rho}_0 h_0 \frac{\partial h_{z0}}{\partial z} + u_{z0} h_0 \frac{\partial \bar{p}_0}{\partial z} \quad (A1c)$$

$$0 = u_{\theta 0} \frac{\partial u_{\theta 0}}{\partial z} + u_{z0} \frac{\partial u_{z0}}{\partial z} + \frac{P_c \gamma}{\bar{\rho}_0 (\gamma - 1)} \left( \frac{\partial p_0}{\partial z} - \frac{p_0}{\bar{\rho}_0} \frac{\partial \rho_0}{\partial z} \right) + \frac{l(u_{\theta 0} - 1) f_{r0}}{ch_0 u_{z0}} \quad (A1d)$$

where

$$f_{s0} = \frac{n_s}{2} \frac{m_s + 1}{(u_{\theta 0}^2 + u_{z0}^2)^2} (2R_{c0})^{m_s}$$

$$f_{r0} = \frac{n_r}{2} \frac{m_r + 1}{[(u_{\theta 0} - 1)^2 + u_{z0}^2]^2} (2R_{c0})^{m_r}$$

### First-Order Equations.

$$\begin{aligned} \frac{-P_c}{\bar{\rho}_0 l} \frac{\partial \bar{p}_1}{\partial z} &= \frac{-P_c \bar{p}_1}{\bar{\rho}_0^2 l} \frac{\partial \bar{p}_0}{\partial z} + \frac{1}{\bar{c} h_0} \left[ u_{z0} (f_{s1} + f_{r1}) \right. \\ &\quad \left. + \left( u_{z1} - u_{z0} \frac{h_1}{h_0} \right) (f_{s1} + f_{r1}) \right. \\ &\quad \left. + \frac{\partial u_{z1}}{\partial \tau} + u_{\theta 0} \frac{\partial u_{z1}}{\partial \theta} + \frac{u_{z0}}{l} \frac{\partial u_{z1}}{\partial z} + \frac{u_{z1}}{l} \frac{\partial u_{z0}}{\partial z} \right] \end{aligned} \quad (\text{A2a})$$

$$\begin{aligned} \frac{-P_c}{\bar{\rho}_0} \frac{\partial \bar{p}_1}{\partial \theta} &= \frac{1}{\bar{c} h_0} \left[ u_{\theta 0} \left( f_{s1} - \frac{h_1}{h_0} f_{s0} \right) \right. \\ &\quad \left. + (u_{\theta 0} - 1) \left( f_{r1} - \frac{h_1}{h_0} f_{r0} \right) + u_{\theta 1} (f_{s0} + f_{r0}) \right. \\ &\quad \left. + \frac{\partial u_{\theta 1}}{\partial \tau} + u_{\theta 0} \frac{\partial u_{\theta 1}}{\partial \tau} + \frac{u_{z0}}{l} \frac{\partial u_{\theta 1}}{\partial z} + \frac{u_{z1}}{l} \frac{\partial u_{\theta 0}}{\partial z} \right] \end{aligned} \quad (\text{A2b})$$

$$\begin{aligned} 0 &= \frac{\bar{p}_0}{h_0} \frac{\partial h_1}{\partial \tau} + \frac{\partial \bar{p}_1}{\partial \tau} + \frac{\bar{p}_0 u_{\theta 0}}{h_0} \frac{\partial h_1}{\partial \theta} + \bar{p}_0 \frac{\partial u_{\theta 1}}{\partial \theta} + u_{\theta 0} \frac{\partial \bar{p}_1}{\partial \theta} \\ &\quad + \frac{1}{l h_0} \left[ h_1 \frac{\partial (\bar{\rho}_0 u_{z0})}{\partial z} + \frac{\partial (\bar{\rho}_0 u_{z1} h_0)}{\partial z} + \frac{\partial (\bar{\rho}_1 u_{z0} h_0)}{\partial z} \right] \end{aligned} \quad (\text{A2c})$$

$$\begin{aligned} \frac{P_c \bar{p}_0}{\bar{\rho}_0 h_0} \frac{h_1}{\partial \tau} &= u_{z0} \left[ \frac{\partial u_{z1}}{\partial \tau} + u_{\theta 0} \frac{\partial u_{z1}}{\partial \theta} + \frac{1}{l} \left( u_{z0} \frac{\partial u_{z1}}{\partial z} \right. \right. \\ &\quad \left. \left. + 2u_{z1} \frac{\partial u_{z0}}{\partial z} + u_{\theta 1} \frac{\partial u_{\theta 0}}{\partial z} \right) + u_{\theta 0} \left[ \frac{\partial u_{\theta 1}}{\partial \tau} \right. \right. \\ &\quad \left. \left. + u_{\theta 0} \frac{\partial u_{\theta 1}}{\partial \theta} + \frac{1}{l} \left( u_{z0} \frac{\partial u_{\theta 1}}{\partial z} + u_{z1} \frac{\partial u_{\theta 0}}{\partial z} \right) \right] \right. \\ &\quad \left. + \frac{\gamma P_c}{\bar{\rho}_0 (\gamma - 1)} \left\{ \frac{1}{\gamma} \frac{\partial \bar{p}_1}{\partial \tau} + u_{\theta 0} \frac{\partial \bar{p}_1}{\partial \theta} + \frac{u_{\theta 0}}{l} \frac{\partial \bar{p}_1}{\partial z} \right. \right. \\ &\quad \left. \left. + \frac{1}{l} \frac{\partial \bar{p}_0}{\partial z} \left( u_{z1} - u_{z0} \frac{\bar{p}_1}{\rho_0} \right) - \frac{\bar{p}_0}{\rho_0} \left[ \frac{\partial \bar{p}_1}{\partial \tau} \right. \right. \right. \\ &\quad \left. \left. + u_{\theta 0} \frac{\partial \bar{p}_1}{\partial \theta} + \frac{u_{z0}}{l} \frac{\partial \bar{p}_1}{\partial z} + \frac{1}{l} \frac{\partial \bar{p}_0}{\partial z} \left( u_{z1} \right. \right. \right. \\ &\quad \left. \left. \left. + u_{z0} \left( \frac{\bar{p}_1}{\bar{\rho}_0} - \frac{2\bar{p}_1}{\bar{\rho}_0} \right) \right) \right] \right\} \\ &\quad \left. + \frac{\bar{p}_0 (u_{\theta 0} - 1) f_{r0}}{\bar{c} h_0 P_c} \left[ \frac{\bar{p}_1}{\bar{\rho}_0} + \frac{u_{\theta 1}}{(u_{\theta 0} - 1)} + \frac{f_{r1}}{f_{r0}} - \frac{h_1}{h_0} \right] \right] \end{aligned} \quad (\text{A2d})$$

where

$$f_{s1} = f_{s0} \left[ m_s \left( \frac{\bar{p}_1}{\bar{\rho}_0} + \frac{h_1}{h_0} \right) + a (u_{\theta 0} u_{\theta 1} + u_{z0} u_{z1}) \right]$$

$$f_{r1} = f_{r0} \left[ m_r \left( \frac{\bar{p}_1}{\bar{\rho}_0} + \frac{h_1}{h_0} \right) + b ((u_{\theta 0} - 1) u_{\theta 1} + u_{z0} u_{z1}) \right]$$

$$a = (m_s + 1) / (u_{\theta 0}^2 + u_{z0}^2)$$

$$b = (m_r + 1) / [(u_{\theta 0} - 1)^2 + u_{z0}^2]$$

## APPENDIX B

### Matrix Coefficients

All coefficients are zero, except those defined below. Also,  $\gamma' = \gamma P_c / [\bar{\rho}_0 (\gamma - 1)]$  and  $q = \bar{p}_0 (u_{\theta 0} - 1) f_{r0} / (\bar{c} h_0 P_c)$

### Matrix [A].

$$a_{i,i+4} = u_{z0}/l \quad i=1,2,3, \dots, 12$$

$$a_{i,i+8} = \bar{p}_0/l \quad i=2,3,4$$

$$a_{i+4,i} = \frac{P_c}{\bar{\rho}_0 l} \quad i=1,2,3,4$$

$$a_{i+12,i} = \gamma' u_{z0}/l \quad i=1,2,3,4$$

$$a_{i+8,i} = \frac{-\gamma' \bar{p}_0 u_{z0}}{\bar{\rho}_0 l} \quad i=5,6,7,8$$

$$a_{i+r,i} = \frac{u_{z0}^2}{l} \quad i=9,10,11,12$$

$$a_{i,i} = \frac{u_{z0} u_{\theta 0}}{l} \quad i=13,14,15,16$$

### Matrix [B].

$$b_{i,i+4} = \frac{1}{l h_0} \frac{d(u_{z0} h_0)}{dz} \quad i=1,2,3,4$$

$$b_{i,i+5} = -b_{i+1,i+4} = \bar{\Omega} \quad i=1,3,5, \dots, 11$$

$$b_{i,i+6} = -b_{i+2,i+4} = u_{\theta 0} \quad i=1,2,5,6,9,10$$

$$b_{i,i+8} = \frac{1}{l h_0} \frac{d(\bar{\rho}_0 h_0)}{dz} \quad i=1,2,3,4$$

$$b_{i,i+14} = -b_{i+2,i+12} = \bar{p}_0 \quad i=1,2$$

$$b_{i,i} = \frac{u_{z0}}{\bar{c} h_0 \bar{\rho}_0} (m_s f_{s0} + m_r f_{r0}) - \frac{P_c}{\bar{\rho}_0^2 l} \frac{d\bar{p}_0}{dz} \quad i=5,6,7,8$$

$$\begin{aligned} b_{i,i+4} &= \frac{1}{\bar{c} h_0} \{ f_{s0} [1 + u_{z0}^2 a] + f_{r0} (1 + u_{z0}^2 b) \} \\ &\quad + \frac{1}{l} \frac{du_{z0}}{dz} \quad i=5,6,7,8 \end{aligned}$$

$$b_{i,i+8} = \frac{u_{z0}}{\bar{c} h_0} [u_{\theta 0} f_{s0} a + (u_{\theta 0} - 1) f_{s0} b] \quad i=5,6,7,8$$

$$b_{i+6,i} = -b_{i+8,i-2} = P_c / \bar{\rho}_0 \quad i=3,4$$

$$b_{i+4,i} = \frac{1}{\bar{c} h_0 \bar{\rho}_0} [u_{\theta 0} m_s f_{s0} + (u_{\theta 0} - 1) m_r f_{r0}] \quad i=5,6,7,8$$

$$b_{i,i} = \frac{u_{z0}}{\bar{c} h_0} [u_{\theta 0} f_{s0} a + (u_{\theta 0} - 1) f_{r0} b] + \frac{1}{l} \frac{du_{\theta 0}}{dz} \quad i=9,10,11,12$$

$$b_{i,i+4} = \frac{1}{\bar{c} h_0} [f_{s0} (1 + u_{\theta 0}^2 a) + f_{r0} (1 + (u_{\theta 0} - 1)^2 b)] \quad i=9,10,11,12$$

$$b_{i+12,i} = \frac{-\gamma u_{z0}}{\bar{\rho}_0 l} \frac{d\bar{p}_0}{dz} \quad i=1,2,3,4$$

$$b_{i+11,i} = -b_{i+12,i-1} = \frac{\gamma' \bar{\Omega}}{\gamma} \quad i=2,4$$

$$b_{i+10,i} = -b_{i+13,i-1} = \gamma' u_{\theta 0} \quad i=3,4$$

$$b_{i+8,i} = \frac{\gamma' u_{z0}}{l \bar{\rho}_0} \left( \frac{2\bar{p}_0}{\bar{\rho}_0} \frac{d\bar{p}_0}{dz} - \frac{d\bar{p}_0}{dz} \right) + \frac{q(1+m_r)}{\bar{p}_0} \quad i=5,6,7,8$$

$$b_{i+7,i} = -b_{i+8,i-1} = -\gamma' \frac{\bar{p}_0 \bar{\Omega}}{\bar{\rho}_0} \quad i=6,8$$

$$b_{i+6,i} = -b_{i+9,i-1} = -\gamma' \frac{\bar{p}_0 u_{\theta 0}}{\bar{\rho}_0} \quad i=7,8$$

$$b_{i+4,i} = \frac{\gamma'}{l} \left( \frac{d\bar{p}_0}{dz} - \frac{\bar{p}_0}{\bar{\rho}_0} \frac{d\bar{\rho}_0}{dz} \right) + \frac{2u_{z0}}{l} \frac{du_{z0}}{dz} + \frac{u_{\theta 0}}{l} \frac{du_{\theta 0}}{dz} + qf_{r0}u_{z0} \quad i=9,10,11,12$$

$$b_{i+3,i} = -b_{i+4,i-1} = u_{z0}\bar{\Omega} \quad i=10,12$$

$$b_{i+2,i} = -b_{i+5,i-1} = u_{z0}u_{\theta 0} \quad i=11,12$$

$$b_{i,i} = \frac{u_{z0}}{l} \frac{du_{\theta 0}}{dz} + q \left( \frac{1}{u_{\theta 0} - 1} + bu_{\theta 0} \right) \quad i=13,14,15,16$$

$$b_{i,i+1} = -b_{i+1,i} = u_{\theta 0}\bar{\Omega} \quad i=13,15$$

$$b_{i,i+2} = -b_{i+2,i} = u_{\theta 0}^2 \quad i=13,14$$

#### Vectors C and D.

$$c_1 = d_4 = \frac{1}{lh_0} \frac{d(\bar{\rho}_0 u_{z0})}{dz}$$

$$c_2 = -d_3 = -\bar{\rho}_0 \bar{\Omega} / h_0$$

$$c_3 = -d_2 = -\bar{\rho}_0 u_{z0} / h_0$$

$$c_5 = d_7 = \frac{u_{z0}}{ch_0^2} [(m_s - 1)f_{s0} + (m_r - 1)f_{r0}]$$

$$c_9 = d_{12} = \frac{1}{\bar{c}h_0^2} [u_{\theta 0}(m_s - 1)f_{s0} + (u_{\theta 0} - 1)(m_r - 1)f_{r0}]$$

$$c_{13} = d_{13} = \frac{q(m_r - 1)}{h_0}$$

$$c_{14} = -d_{15} = \frac{P_c \bar{p}_0 \bar{\Omega}}{\bar{\rho}_0 h_0}$$

# Development of a Case Vibration Measurement System for the DC-990 Gas Turbine

H. A. Kidd

Senior Controls Design Engineer,  
Dresser Industries,  
Dresser Clark Division,  
Olean, N. Y.

*The continued use of gas turbines in industrial applications and increased customer desires for trend analysis has led gas turbine suppliers to develop sophisticated, reliable, cost-effective vibration monitoring systems. This paper discusses the application of case vibration monitoring systems and the design criteria for each component. Engine installation, transducer mounting brackets, types of transducers, interconnecting cables and connectors, charge amplifiers, and signal conditioning and monitoring are considered. Examples are given of the benefits experienced with the final system in several of Dresser Clark's engine development programs, by manufacturing and production testing, and by Dresser's field service staff.*

## Introduction

The DC-990 was introduced to the industrial marketplace in 1978 as a state-of-the-art, cold end drive, two-shaft gas turbine. Within a year, five engines were installed and eleven more were in various stages of production. Not uncommon to a newly developed gas turbine, as operating time increased Dresser became aware of several mechanical problems. One of the problems, thermal bowing of the power turbine shaft after shutdown, required an improved vibration monitoring system to protect the engine when restarting. The new system was defined, designed, built, and finally verified at the same time the development work was done to resolve the shaft thermal bowing problem. As a result, the final vibration monitoring system and several alternatives were evaluated for several months and well over one-hundred operating hours in test cells. The engineers responsible for the design changes that resolved the shaft thermal bowing problem found the information the vibration monitoring system rendered consistent and reliable. When we introduced the vibration system to the field, we had the highest level of confidence in its performance.

Briefly, the solution to the power turbine shaft thermal bowing problem was:

- To upgrade the vibration monitoring system
- To reduce the diameter of the power turbine shaft
- To install a viscous damped power turbine bearing at the exhaust end

This combination of hardware was offered to existing customers and introduced to manufacturing.

## The Original Vibration System

The original case vibration monitoring system employed on the 990 consisted of a total of three velocity transducers. They were located on the accessory gear box, the gas generator (engine midframe) and the power turbine (engine rear). Each transducer was wired back to the signal conditioner in the unit control panel located approximately 250 ft away. The velocity signal was filtered and integrated and displacement was displayed. The system configuration is defined in Fig. 1.

By 1980, the power turbine shaft thermal bowing problem mandated a higher quality vibration monitoring and protection system. At this time the following system shortcomings were identified:

- The velocity transducer low frequency (below 45 Hz) sensitivity was questionable. During engine warmup, the power turbine rotates at 1500–2000 rpm, just below the first critical of  $2300 \pm 100$  rpm. The velocity transducer could not reliably detect high vibration levels during warm up and when accelerating through the critical to the operating power turbine speed range of 3000–7200 rpm.

- The high temperature connection on the velocity transducer had proven to be an unreliable electrical connection.

- The velocity transducer has a short life (6 months). When it failed, its output was extremely low.

- The temperature rating of the velocity transducer was borderline for the gas generator position.

To improve the system, Dresser Clark established a research project to analyze gas turbine vibration monitoring systems, then specify a system suitable for the DC-990, and qualify vendors through a rigorous test program. Since high-temperature eddy current probes were not available, the system had to measure case vibration.

## Components of a Case Vibration Monitoring System

**Mounting Bracket.** Starting at the engine and working

Contributed by the Gas Turbine Division of THE AMERICAN SOCIETY OF MECHANICAL ENGINEERS and presented at the 29th International Gas Turbine Conference and Exhibit, Amsterdam, The Netherlands, June 4–7, 1984. Manuscript received at ASME Headquarters January 9, 1984. Paper No. 84-GT-143.



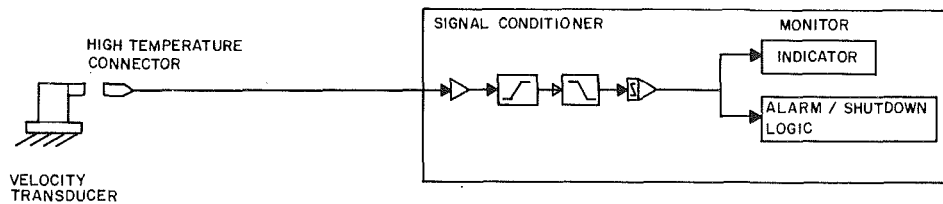


Fig. 1 Original 990 vibration system

towards the monitor, the first component in the system under consideration is the transducer mounting bracket. The bracket should be small, rigid, have a very high resonant frequency ( $\geq 10$  times running frequency), and be of a material suitable for the temperatures expected. The bracket should include facilities for manifolding cooling air for very high temperature applications and be attached to a bearing housing support member. The transducer mounting surface should be smooth (32 RMS). The size of the screws that attach the transducer to the bracket will probably be defined by the transducer manufacturer. Allen screws, 1/4-28, are recommended; smaller screws tend to break off during maintenance after temperature cycling has occurred.

**Velocity Transducers.** The velocity transducer consists of a coil that is physically fixed to the transducer case and a seismic mass (magnet). The magnet may be supported by a spring system and the transducer may employ jeweled bearings to minimize any friction on the moving part. Temperature compensation and hermetic sealing are standard features.

The advantages of a velocity transducer system are:

- lower system cost
- fewer system components
- strong output signal (100 mV/in./s typical)

The disadvantages of velocity transducer system are:

- limited useful frequency range
- difficult to calibrate at low frequencies
- reduced life because of moving parts
- low tolerance for cross axis movement
- not suitable for high temperature ( $> 650^\circ\text{F}$ )

**Accelerometers.** An accelerometer consists of a compressed stack of piezoelectric crystals and a mass that generates a charge output when excited. It is necessary to locate a charge amplifier near the accelerometer (within 15 ft) to amplify the low-level signal. Low-temperature ( $< 250^\circ\text{F}$ ) accelerometers can incorporate the charge amplifier in the same housing as the crystal. However, higher temperature applications require a remote charge amplifier, because the charge amplifier electronics cannot tolerate the heat. The physical size of the accelerometer is determined by the maximum temperature it is designed for and its output sensitivity. Output ranges are available from 5 to over 1000 pC/g. A reasonable output sensitivity for a 900°F accelerometer is 50 pC/g. Lower output sensitivities will result in an undesirable signal/noise ratio. Higher output levels at this temperature will require too physically large a transducer. The crystal should be designed with a resonant frequency no less than 5 times the maximum operating frequency. Harold Bredin discusses accelerometers in greater detail in his paper [1].

An accelerometer can be expected to have a service life of 20,000–40,000 hr. Like velocity transducers, accelerometers are available with hermetic seals.

Figure 2 compares the useful range of a typical ac-

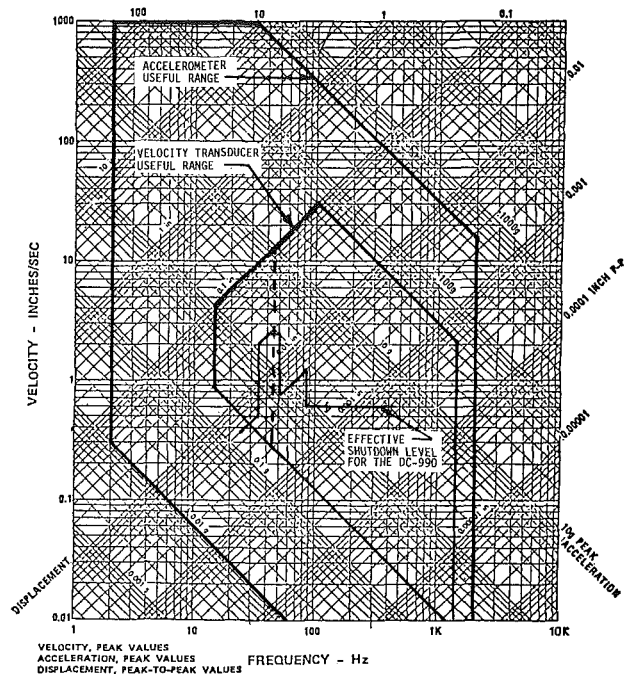


Fig. 2 Frequency response comparison

celerometer with a typical velocity transducer. It can readily be seen that the accelerometer has a much wider range of operation. With this wider range of operation comes the blessing of increased machinery protection and the responsibility of employing sophisticated filtering to eliminate unwanted information. This filtering is required in the charge amplifier and monitor.

The advantages [2] of an accelerometer system are:

- wide useful frequency range
- suitable for high temperature (900°F) applications
- long life
- no moving parts

The disadvantages of an accelerometer system are:

- high system cost
- required sophisticated filtering and signal conditioning
- requires special interconnecting wiring

**Interconnecting Cables and Connectors.** High-temperature twisted shielded cable should be used for the velocity transducer. Mineral insulated cable or graphite impregnated twisted shielded cabling should be used for accelerometer applications. This type of cable is used to minimize cable capacitance effects on the charge signal output of the accelerometer. Hard-line/soft-line cable combinations should be avoided. The cables should be routed so that they do not come in contact with very high-temperature parts. Locating

### Nomenclature

C = coulombs

g = acceleration  
NGG = gas generator speed

NPT = power turbine speed  
P = pico

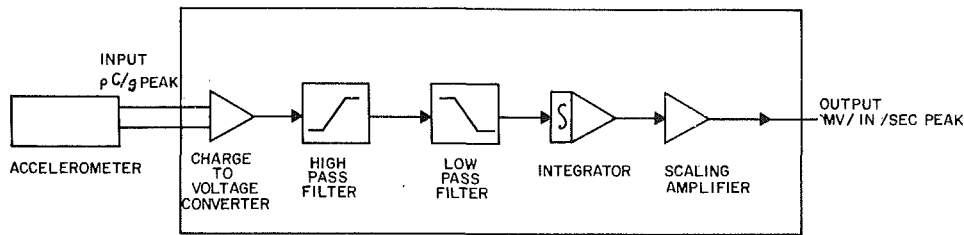


Fig. 3 Charge amplifier/integrator

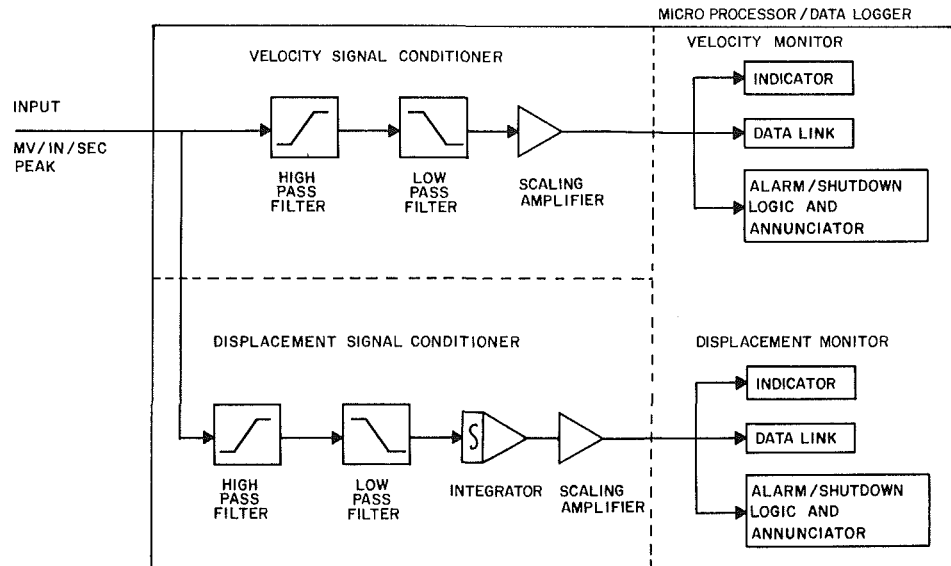


Fig. 4 Signal conditioner/monitor

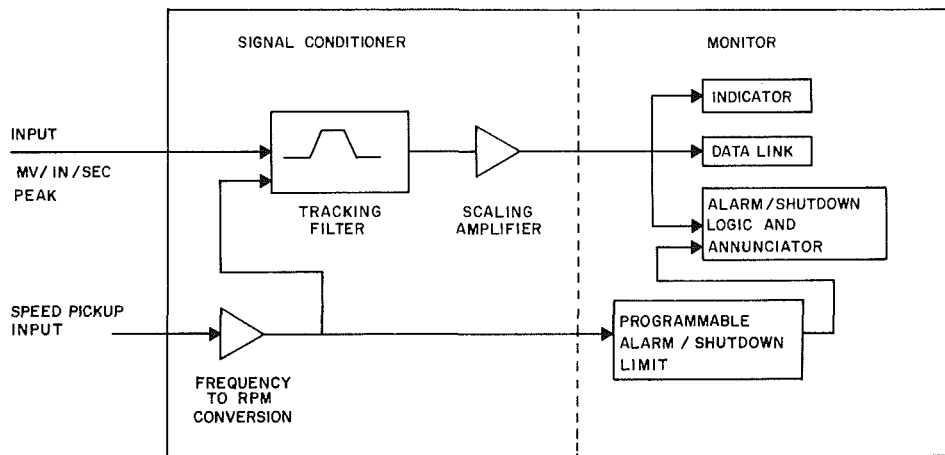


Fig. 5 Alternate signal conditioner/monitor schemes

transducers on the bottom of the engine will help make this possible. The cable should be secured every 12-18 in. to eliminate noise generated by cable whip.

Connectors are always a problem. The most reliable industrial system does not employ "connectors," but rather terminates wires on terminal strips. Unfortunately, this is not always possible. To eliminate the connector on the engine, the soft-line graphite impregnated cable can be potted to the transducer and the hard line mineral insulated cable can be hermetically welded to the transducer.

**Charge Amplifier.** Since low-temperature accelerometers are not useable on a gas turbine, only remote charge amplifiers are considered. A block diagram of a charge amplifier/integrator is shown in Fig. 3.

The first stage of the amplifier is a charge to voltage

converter. The next stage, the high-pass filter, is required to eliminate the unwanted low-frequency components of the accelerometer output. This filter is the most critical of all the filters. The 3 db point frequency must be carefully selected to eliminate as much of the low-frequency component as is possible without minimizing protection near critical speeds. The filter should have a very sharp roll-off (60 db/octave). The low pass filter 3 db frequency is selected to be above any operating speed or multiple of interest. A 36 db/octave roll-off is adequate. This low-pass filter is used to eliminate any undesired input signal from blade-pass frequencies or other high-frequency sources.

After the filtering is complete, the acceleration signal may be integrated to a velocity signal. The final stage of the charge amplifier/integrator is the scaling amplifier.

**Signal Conditioner and Monitor.** The signal conditioner and

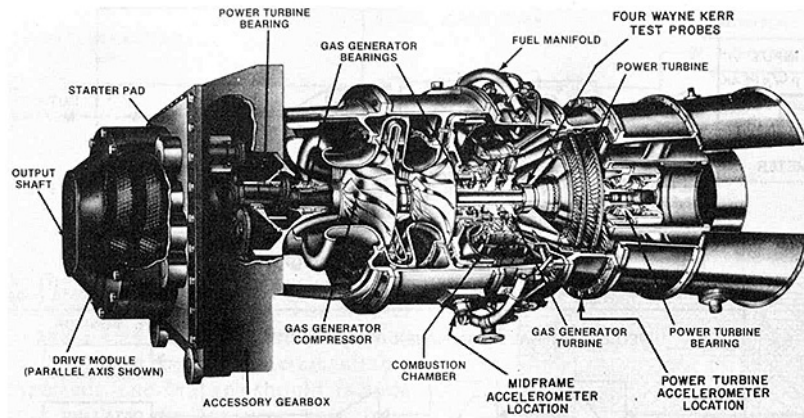


Fig. 6 DC-990 cross-sectional view

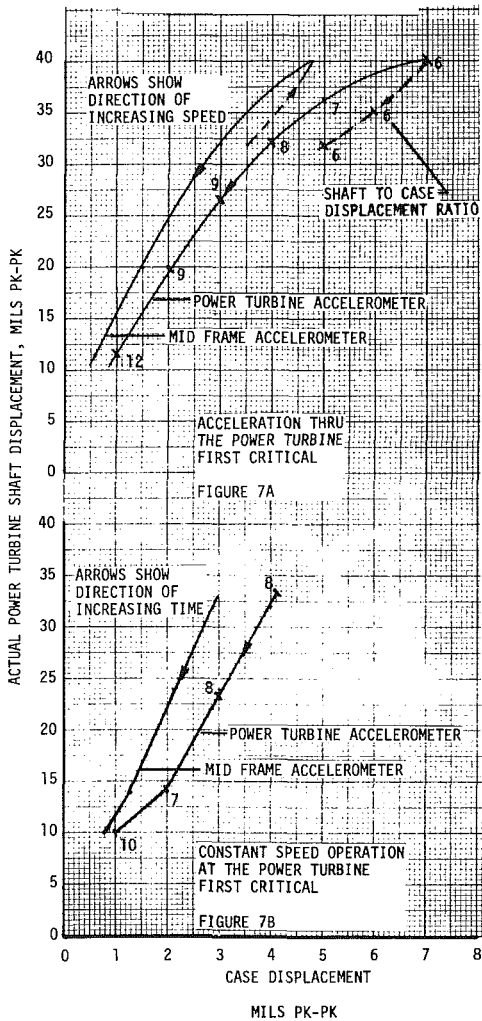


Fig. 7 Comparison of sensed case movement to actual shaft movement after an induced distortion

monitor, Fig. 4, is designed to accept an input signal from either a velocity transducer or a charge amplifier/integrator. The velocity signal is filtered again in the velocity signal conditioner and also filtered then integrated in the displacement signal conditioner. Velocity and displacement are both continuously monitored, since velocity monitoring offers protection at high or normal operating speeds and displacement monitoring offers protection at lower speeds. This protection scheme can be adjusted to suit the specific needs of the gas turbine by altering alarm and shutdown levels and high pass filter 3 db points. Refer again to Fig. 2 and note

the effective shutdown levels achieved with the DC-990 vibration system. High-pass filter 3 db points are 25 Hz on the displacement channel and 83 Hz on the velocity channel.

The velocity and displacement signal conditioner input is an a-c signal. The signal conditioner high-pass and low-pass filters should be more restrictive than those in the charge amplifier to take full advantage of the continuous velocity and displacement monitoring. After the actual measurement if performed, a scaling amplifier is used to convert the output to a convenient d-c level.

The monitor may be as simple or as sophisticated as is desired. The requirements shown in Fig. 4 are considered minimal.

Several alternate signal conditioning schemes are available. The most interesting, effective, and expensive scheme is the tracking filter shown in Fig. 5. The tracking filter combines the high-pass and low-pass filters and causes them to follow the speed of the rotor producing the equivalent of a sliding band pass filter. This eliminates all signals except the main running component. A second scheme shown in Fig. 5 is the altering of alarm and shutdown limits as a function of speed. This could be used to allow for higher vibration levels at lower speeds and achieve a somewhat constant *g*-level.

### DC-990 System Configuration

The system configuration employed on the DC-990 is a combination of Figs. 3 and 4 with programmable alarm and shutdown logic. A 50 *pC/g* accelerometer was chosen as the primary sensing device because of its ability to withstand high temperatures, its excellent low frequency response, and its long life. Two accelerometers were employed: one on the midframe location and one on the power turbine location.

The charge amplifiers are the same for each transducer with high-pass filter 3 db points located 13 Hz below the first critical at 25 Hz and slopes of 60 db/octave. The low-pass filter 3 db point is 450 Hz and has a slope of 36 db/octave. The output of the charge amplifier was made equal to the output of velocity transducers in the field to facilitate equipment retrofits.

The signal conditioner and monitor are also the same for each transducer. The velocity high-pass filter 3 db point is at 83 Hz and has a slope of 36 db/octave. The low-pass filter 3 db/octave point, is 450 Hz, and also has a slope of 36 db/octave. This filter arrangement covers the normal gas generator operating range of 12,000–18,000 rpm. Alarm and shutdown levels were established at .4 and .6 in./s. The displacement channel high-pass filter 3 db point is 25 Hz and the low-pass filter 3 db point is a 350 Hz. Both filters have a slope of 36 db/octave. Alarm and shutdown levels are 3 and 5 mils.

The programmable alarm and shutdown logic allows for higher limits while passing through the power turbine first

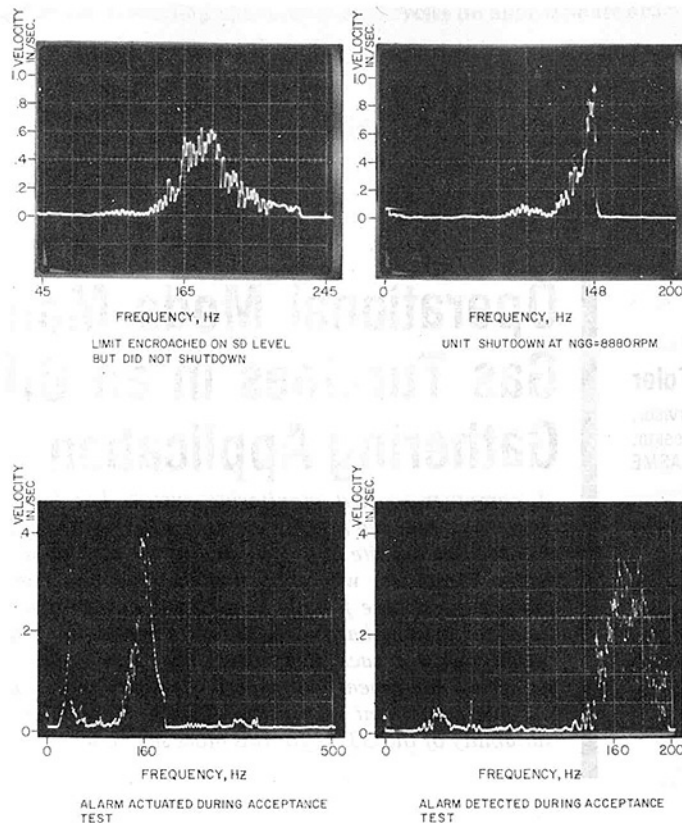


Fig. 8 Detection of gas generator rotor unbalance

critical. At these low speeds, bearing loads are moderate and higher vibration levels are acceptable.

### Test Program

The acceptance testing of the vibration monitoring system took place over approximately three months. The goals of the program were:

- To determine the reliability of the entire system
- To establish a correlation between the actual rotor displacement and the case displacement
- To establish a reference for alarm and shutdown setpoints

During the test program, various shaft and bearing configurations were evaluated. Each engine was instrumented with velocity transducers and accelerometers in the horizontal and vertical planes at the midframe and power turbine location. An assembly of four Wayne Kerr noncontact probes were installed 90 deg apart from each other at one location on the power turbine shaft. (The typical life of these probes was less than 10 fired hr.) Figure 6 identifies the major components of the DC-990 engine, the final location of accelerometers, and the location of the Wayne Kerr probes.

After an imbalance was intentionally introduced to the power turbine shaft, the engine was operated at the power turbine critical or accelerated through the critical. Figure 7 demonstrates the type of correlation obtained between case displacement and shaft displacement. No correlation at all was discernible below the critical because of the charge amplifier high-pass filter. There was a correlation between case/rotor displacement at and above the power turbine critical speed; however, it cannot be defined any more precisely than somewhere between 1:6 and 1:20 for all DC-990 engines and all operating speeds. At or near the power turbine critical, the range is between 1:6 and 1:12. (The weight ratio of the power turbine rotor to the engine casing weight is around 1:4.)

Several types of engine mounting techniques were tested. It was found that large variations in case measurements exist in the horizontal plane but readings in the vertical plane were consistent.

Although the ratio of shaft displacement to case displacement varies, the relationship is more than adequate to define conservative alarm and shutdown setpoints, especially since the higher ratios exist only at lower displacement amplitudes. The viscous damped bearing was designed such that with a power turbine rotor displacement of 160 mils PK-PK the loading is only 210 psi at at the first critical.

### Experience

The system has proven useful for analyzing both Gas Generator and Power Turbine rotor critical speeds. Figure 8 shows examples of gas generator rotor unbalance on new and rebuilt engines that was detected in the test cell prior to shipment. The engines shutdown on high velocity levels. Several engines were rebuilt in the field and shutdown immediately when placed into service as the vibration monitoring system detected a misassembly.

### Acknowledgments

The author would like to acknowledge the excellent cooperation and assistance during test phases of this project of Jerry Hoover, supervisor of Product Design, Dresser Clark and the cooperation of Don Schneider, President of Diagnostic Systems Corporation.

### References

- 1 Bredin, H., "Measuring Shock and Vibration," *Mechanical Engineering*, Feb. 1983, pp. 30-36.
- 2 Jackson, C., *The Practical Vibration Primer*, Gulf Publishing Co., 1979, pp. 4-7.

# Operational Mode Monitoring of Gas Turbines in an Offshore Gas-Gathering Application

**D. F. Toler**  
Supervisor,  
Gas Turbine Design.  
Mem. ASME

**R. N. Yorio**  
Supervisor,  
Solid Mechanics  
Turbo Division.  
Ingersoll-Rand Company,  
Phillipsburg, N.J. 08865

*A computer-assisted monitoring system has been implemented on GT-61 Gas Turbines employed in offshore gas gathering. Operating load data are continuously recorded at the site and evaluated at the turbine manufacturer's plant on a main-frame computer, where existing analysis and testing techniques are utilized to predict the service fatigue lives of the power turbine structural components. The data acquisition hardware, the data reduction software, and the life prediction techniques are each described. The data collected indicate that offshore gas gathering equipment will experience many more operating load cycles than comparable equipment in pipeline service. The fatigue life predictions reaffirm the suitability of the GT-61 for this more severe service.*

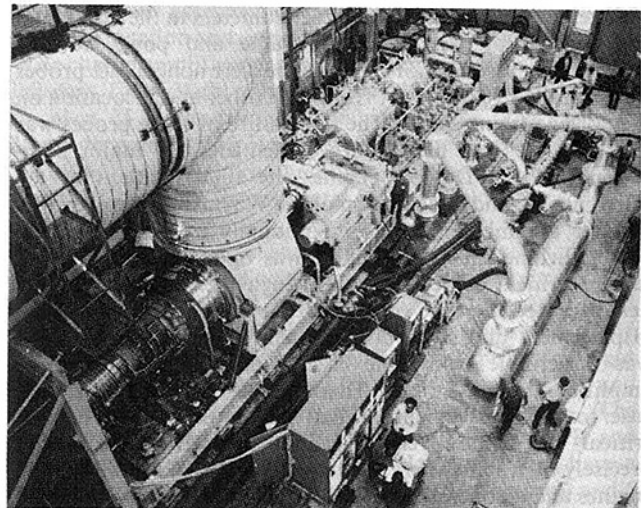
## Introduction

An accurate assessment of the operating load characteristics of a gas turbine can help extend hardware inspection intervals, preclude premature removal of parts from service, and prevent excessive conservatism in future designs. Knowledge of the operating load history holds particular significance for a multibody gas turbine driven train (see Fig. 1) integrated into an overall complex process such as offshore gas gathering. The system complexity gives rise to a myriad of possible events that require gas turbine response. The turbine, in reacting to these demands, can accumulate low cycle fatigue (LCF) damage and may be subject to fracture in critically stressed areas of structural components. In the design phase, component LCF life prediction must be based on an assumed load history. However, the actual operating load excursions may differ considerably from those assumed. If the service loads experienced are less severe than the design assumptions, inspection intervals and replacement times can be extended, while more severe service will necessitate shorter inspection intervals and limited service lives.

Operating logs, start counters, and hour meters have traditionally provided gas turbine manufacturers with some measure of a unit's service experience. However, transient operating conditions which can produce significant fatigue damage are usually not logged. Start counters record only start attempts and do not record other potentially damaging load excursions. The hour meter provides no breakdown of operating time at various operating loads. The authors' company has attempted to obtain more detailed operating data (outlined in Table 1) through extensive surveys of operating logs and the addition of part-speed counters.

However, gas turbine rotating components undergo significant excursions in both centrifugal and thermal loads – the latter being time-dependent. Therefore, as a minimum, it is necessary to monitor both rotor speed and operating temperature with time. Component analysis with test calibration makes it possible to fully characterize the load history of the major structural components with just these two parameters.

An automated data acquisition and reduction system has been conceived and implemented on eight (8) GT-61 gas turbine driven compressor trains in an offshore gas gathering application. This type of service is a prime candidate for operational mode monitoring since process variables are not



**Fig. 1** As seen during the factory performance test, two compressors and an electric generator are driven through a gear by the GT-61 gas turbine.

Contributed by the Gas Turbine Division of THE AMERICAN SOCIETY OF MECHANICAL ENGINEERS and presented at the 29th International Gas Turbine Conference and Exhibit, Amsterdam, The Netherlands, June 4-7, 1984. Manuscript received at ASME Headquarters January 5, 1984. Paper No. 84-GT-77.

**Table 1 Parameters for evaluating operational load cycles (in approximate order of importance)**

	At 500 hrs	At 5000 hrs
1 Total number of starts	90	260
2 Percent of start attempts where loaded condition is not attained	9%	16%
3 Percent hot starts (typically one-half hour or less after shutdown)	55%	46%
4 Percent cold starts (typically hours between shutdown and start-up)	36%	38%
5 Maximum operating speed during a cycle	4800 rpm	4900 rpm
6 Normal power turbine inlet temperature	1415°F (768°C)	1415°F (768°C)
7 Frequency of trips from load to idle followed by return to load	2 per start	2 per start
8 Hours of operation	500 hrs	5000 hrs
9 Normal operating speed	4650 rpm	4800 rpm
10 Typical time at idle after a trip prior to returning to load	2 min	2 min
11 Minimum operating speed during a cycle	1200 rpm	1100 rpm
12 Time at idle during a normal start before increasing power	15 min	15 min
13 Time at idle during a normal shutdown	15 min	15 min
14 Typical time from idle to load	2 min	2 min
15 Operating speed at idle	1200 rpm	1100 rpm
16 Maximum power turbine inlet temperature during a cycle	1415°F (768°C)	1415°F (768°C)
17 Percent emergency shutdowns	90%	95%
18 Percent normal shutdowns	10%	5%
19 Power turbine inlet temperature at idle	750°F (399°C)	790°F (421°C)

well known prior to start-up and gas field conditions can change appreciably with field depletion. The system was formulated to attain the highest level of monitoring capability practical while utilizing low-cost, off-the-shelf hardware. The recorded load histories are integrated with existing engineering analysis and materials testing techniques to provide accurate component life predictions.

### Data Acquisition

The primary component of the data acquisition system is a DATEL LPS-16 Data Logger which records power turbine rotor speed and inlet temperature on a Phillips cassette tape. The data logger is mounted in the control panel and uses the control system scaled output of 0 to +5 V<sub>dc</sub> as the signal source for both parameters. The LPS-16 has a 16-channel multiplexer with the sequencer/programmer modified by DATEL Intersil to permit two-channel operation. The two input signals from the control system are scanned consecutively by the multiplexer and processed by a sample hold circuit. The maximum voltage detected is digitized by a 12-BIT unipolar (0 to +5 V<sub>dc</sub>) Analog-to-Digital (A/D) converter. The output of the A/D converter is recorded on a magnetic cassette tape along with a 4-BIT channel identifier from the sequencer/programmer. This results in a serial record of data in a predefined format of hexadecimal characters, which is easily processed by computer. Internal electronic circuitry accurately controls the scan rate, which was selected such that two data channels will be consecutively scanned and recorded each minute. This is sufficient to accurately describe all anticipated load excursions, yet permit 35

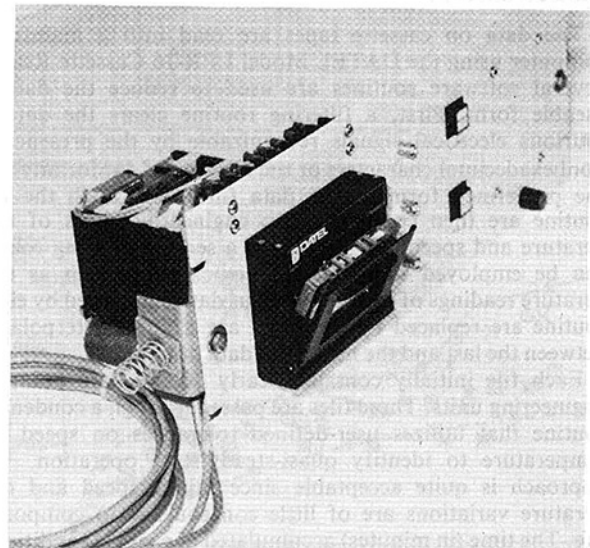
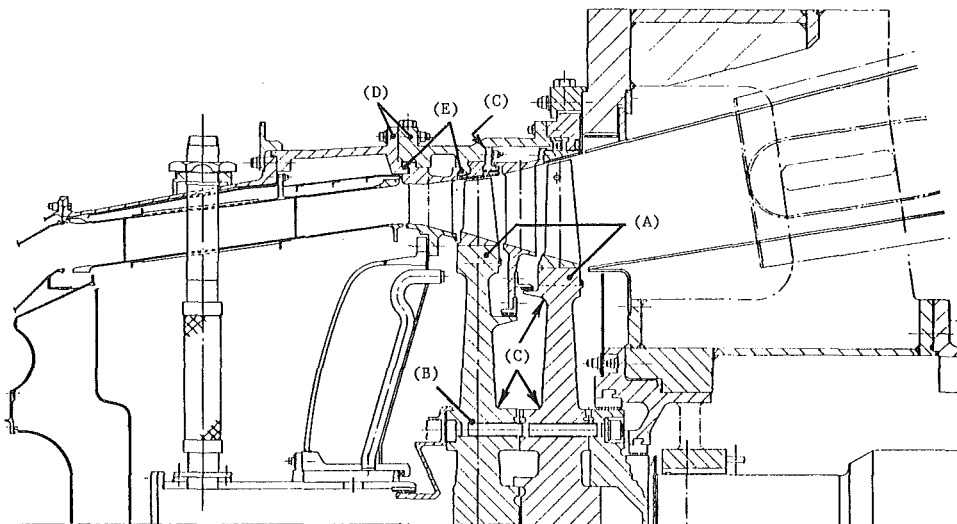


Fig. 2 The LPS-16 data logger prepared for installation

days of continuous recording per tape. The LPS-16 is shown in Fig. 2 ready for installation.

The tape cassettes utilized are DATEL Model 12123-2 Phillips cassettes, which have an extended temperature range from -40°F to +140°F (-40°C to +60°C) and are certified for digital recording. This, in addition to conformally coating all circuitry, helps to maintain reliable data recording in the harsh offshore environment. Continuous operation is ensured



**Fig. 3 The GT-61 Power Turbine cross section illustrating some component locations with geometric notches; (A) blade to disk "firtree" attachments; (B) rotor tiebolt holes; (C) fillet radii; (D) casing bolt holes; and (E) stator attachments**

by utilizing the power turbine skid battery and charger system and incorporating an oversized DC-DC converter in the circuitry.

A DATEL Model BPM-12 converter (+28 V<sub>dc</sub> to +12 V<sub>dc</sub>) powers the LPS-16 from the +28 V<sub>dc</sub> skid batteries. The oversized BPM-12 will continue to supply +12 V<sub>dc</sub> during low state-of-charge periods for the skid battery system to as little as +22 V<sub>dc</sub>. However, the battery system is very reliable and is continuously recharged by the platform electrical system.

Data acquisition is completed by periodic readings taken by site personnel from the start counter, hour meter, and part-speed counter. These data can be correlated with taped data and will provide continuity should tape change-out not occur or should the tape system become inoperative.

### Data Reduction

The data on cassette tapes are read into a mainframe computer using the DATEL Model LPR-16 Cassette Reader. Several software routines are used to reduce the data to useable form. First, a filtering routine clears the data of spurious electrical signals recognizable by the presence of nonhexadecimal characters or the absence of conformity with the predefined format. The data filtered through the first routine are then converted into engineering units of temperature and speed. At this point, a second filtering routine can be employed to eliminate illogical data such as temperature readings of zero. Erroneous data eliminated by either routine are replaced by data that are a linear interpolation between the last and the next valid data points.

Each file initially contains nearly 50,000 data points in engineering units. These files are passed through a condensing routine that utilizes user-defined tolerances on speed and temperature to identify quasi-steady-state operation. This approach is quite acceptable since minor speed and temperature variations are of little consequence to component life. The time (in minutes) accumulated at a single condition is determined simply by counting the number of successive data points within the specified tolerance, based on the data acquisition rate of one point per minute. Depending on the actual operating history, the condensed file should contain only a few hundred points.

The condensed file of data points (each representing a rotor speed, an inlet temperature, and a duration) can be printed in tabular form or plotted as speed versus time and inlet temperature versus time. The time scale plotted is such that 1 min intervals are discernible during transients, but continuous

operation at steady-state temperature and speed is represented by a fixed span and labeled with the actual time spent at that condition. The total operating time, or the total time spent at any given condition can be determined and printed. The maximum temperature and speed can be determined and printed for each excursion above idle.

### Life Prediction

Having documented the power turbine operating load history in terms of two performance parameters, rotor speed, and inlet temperature, it is then necessary to relate excursions in these parameters to life predictions for the various power turbine components. To do this, the operating load experience of a component must first be determined from the load history of the unit. Rotor speed is clearly a direct measure of the centrifugal load within a rotating part. The thermal load experienced by a component is not so easily quantified since metal temperature depends upon local gas temperature, mass velocity, and nature of the flow, as well as cooling effects. Still, excursions in component metal temperatures can be related to inlet temperature data alone, with reasonable accuracy, for a given power turbine configuration. This is achieved by applying conservative simplifying assumptions to turbine performance and heat transfer analyses conducted in conjunction with corroborative full-scale transient testing.

Low cycle fatigue damage is incurred when cyclic loading produces plastic strain in a component. In a power turbine with uncooled airfoils, plastic strain usually occurs only in components with geometric notches (see Fig. 3). The finite element method is used to solve for the pseudo-elastic stresses in the component's notched locations at the peak thermal load found for that excursion. This peak thermal load is determined by finite element or finite difference techniques calibrated by full-scale, in-house testing, particularly for transient operation. The local strain approach [1] (Neuber Notch Analysis) is used to predict the local stress-strain response in the areas of stress concentration.

An internally developed computer program, similar to those of [2] and [3], predicts the fatigue lives of notched members subjected to complex load histories. This program determines the material stress-strain response at the notch root accounting for cyclic hardening and softening, duplicates material "memory," assesses cumulative fatigue damage based on closed hysteresis loops, and predicts life to crack initiation based on a mean-stress-corrected linear damage rule. Figure 4 shows the computer-predicted cyclic stress-

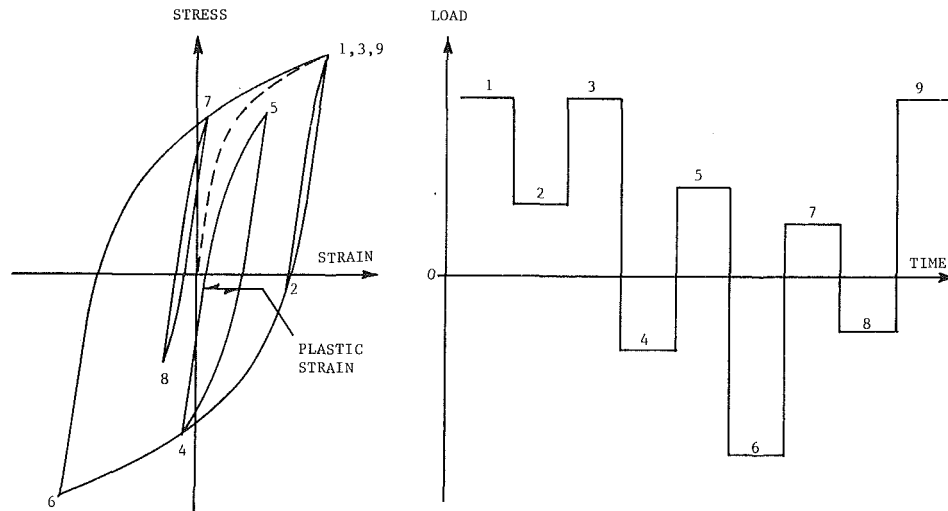


Fig. 4 Cyclic stress-strain response at a typical notch due to a sample load history as predicted by an in-house computer program

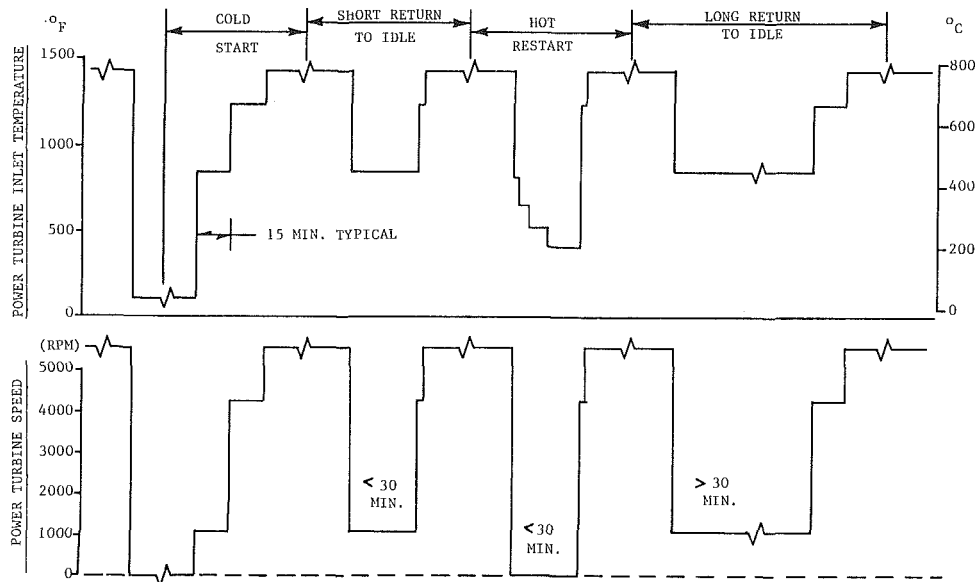


Fig. 5 Four unique cycles used in the design phase to represent the anticipated service

strain response at a typical notch due to a sample load history. Note that as the part is loaded from point 5 to 6, the stress-strain response follows the outer loop, thus resuming the same path it was taking prior to being interrupted at point 4 and thereby simulating material "memory."

It is difficult by merely observing the load history to determine which load excursions are damaging. Fatigue damage due to cyclic plastic strain accumulation can, in fact, be properly assessed only from the stress-strain hysteresis loops. For a given notch, these loops must be determined for each load cycle. This can be accomplished through elasto-plastic finite element analysis, but is greatly facilitated through the use of the modified Neuber approach [4], which provides conservative, but reasonably accurate estimates of the notch root stress-strain response.

The available life associated with a given cycle is determined from material strain-life data, which are obtained from constant-strain-amplitude fatigue tests of smooth specimens. The local strain approach asserts that the life of the notched member will be the same as a smooth specimen undergoing the same cyclic stress-strain history. Corroborative test data [5] indicate the validity of this premise. For each type of cycle

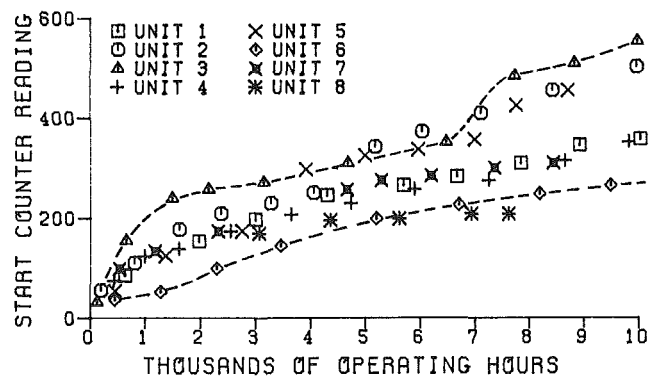


Fig. 6 Counted starts versus operating hours for monitored units

encountered, damage is assessed by dividing the number of such encounters by the available life. The Palmgren-Miner linear damage rule [6, 7] is employed in determining the total fatigue damage and expected fatigue life of each notch.

This system is capable of very detailed complex load history analysis, but this is neither practical nor necessary. The task of predicting the fatigue lives of power turbine components





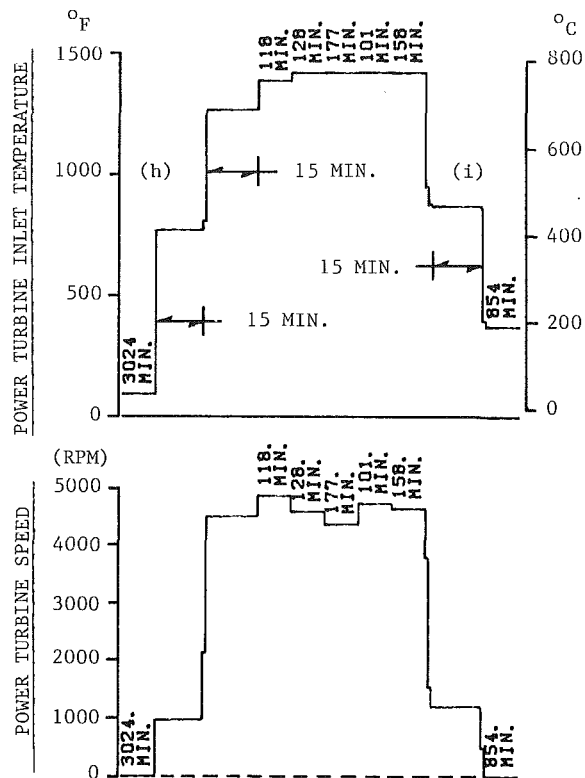


Fig. 8 An operating history segment illustrating cold start and normal stop characteristics

gas generator ignition) will have added 5 starts, yet 15 significant speed excursions (including accels and decels) can be seen. Note that the so-called "complete" shutdowns, such as at (b), were not sufficiently long to bring the inlet temperature down to ambient levels of 95°F (35°C).

Returns-to-idle can also be observed in Fig. 7, such as at (f). Such excursions will tend to unload the thermal gradients in gas turbine components as lower temperature gas is passed through the machine. The longer the time spent at idle, the more the thermal gradients will unload. Incomplete loading sequences, as at (d), will not significantly alter the thermal gradients due to the rapid unload-reload sequence. For any return to idle, if reloading is not attempted within 15 min after returning to idle, the unit will be automatically shut down and the rate of cooling will be dramatically reduced.

The presence of erroneous data can often be recognized by the unlikely relationships between temperature and speed as noted at (g) (up to this point the data had only been filtered by the first routine to eliminate spurious electrical signals).

There is reason to believe that the unit was available during the shutdown periods, since no zero temperature readings occurred which would be produced by turning the control system off. Daily reports from the site indicate that the unit was not available for one day while crude oil deposits were cleaned from an interstage scrubber. The unit was not operating 149 hrs of the 25 days represented by the data.

Figure 8 illustrates a cold start at (h) with a 15-min gas generator warm-up at idle and a 15 min power turbine warm-up at 4500 rpm. The power turbine warm-up is clearly seen here, but is often masked by continued operation at or near that condition after the timer ends. This is a result of the maximum operating speed being typically low for this installation. If a start follows a complete shutdown from load within 30 min, the timers are bypassed as illustrated at (e) in Fig. 7. The normal stop at (i) in Fig. 8 is the product of a return to idle followed by an automatic shutdown when no attempt is made to reload the unit within 15 minutes.

Early feedback of the monitored data revealed that power

turbine warm-up was occurring at higher operating temperature than desired. This was due to the power required to operate the compressors in a recirculation mode. This was corrected by changing the sequence to close the recirculation valves as soon as intercooler fans were on line, producing the start illustrated at (h). This type of feedback on the machine's actual response to the control system logic is a valuable by-product of operational mode monitoring.

In comparing the recorded data of Figs. 7 and 8 to the four representative cycles anticipated (Fig. 5), all the recorded excursions can be easily classified by type except, perhaps, the incomplete load sequence represented at (d) in Fig. 7. Closer examination confirms that the return to idle at (d) is the same as the "short return to idle" cycle of Fig. 5 and is superimposed on the cold start. This short return to idle will form a small stress-strain hysteresis loop inside the larger loop generated by the cold start.

For a given component, the fatigue damage associated with each recorded load cycle can readily be determined for each area of interest within the component (fillets, bolt holes, etc.). This is a direct consequence of classifying each actual operating cycle as one of the four predefined cycles of Fig. 5, since the fatigue damage associated with those cycles has been determined in the design phase. Such fatigue damage accumulation analysis can be carried out over the entire recorded history. However, in order to predict service lives, the load experience must be extrapolated into the future. To do this the characteristics of the last month's operation are assumed to exist over the remaining life of the unit. Based on this technique, the life predictions indicate that low cycle fatigue will not limit the service lives of the major structural components of GT-61 power turbines for this application.

## Conclusions

A continuous monitoring system has been shown to provide new insight into the operating load characteristics of gas turbines employed in offshore gas gathering. Sufficient data has been accumulated to provide a firm basis for component fatigue life predictions for this type of application. In addition, feedback of the actual load histories has permitted the optimization of operational sequences, such as compressor recirculation valve closing and turbine cooling air valve opening, to minimize low cycle fatigue damage to turbine components.

## Acknowledgments

The authors wish to acknowledge the efforts of Turbo Customer Service personnel for their field support of the data acquisition system, Andy Gruss for the development of the data acquisition system, and Gary Nemeč for the data reduction software.

## References

- 1 Dowling, N. E., Brose, W. R., and Wilson, W. K., "Notched Member Fatigue Life Predictions by the Local Strain Approach," *Fatigue Under Complex Loading*, Vol. 6, SAE, Warrendale, Pa., 1977, pp. 55-84.
- 2 Landgraf, R. W., Richards, F. D., and Lapoint, N. R., "Fatigue Life Predictions for a Notched Member Under Complex Load Histories," *Fatigue Under Complex Loading*, Vol. 6, SAE, Warrendale, Pa., 1977, pp. 95-106.
- 3 Tucker, L. E., "A Procedure for Designing Against Fatigue Failure of Notched Parts," Paper No. 720265, presented at SAE Automotive Engineering Congress, Detroit, Mich., Jan. 1972.
- 4 Topper, T. H., Wetzel, R. M., and Morrow, J., "Neuber's Rule Applied to Fatigue of Notched Specimens," *JMLSA Journal of Materials*, Vol. 4, No. 1, March 1969, pp. 200-209.
- 5 Wetzel, R. M., ed. *Fatigue Under Complex Loading*, Vol. 6, SAE, Warrendale, Pa., 1977.
- 6 Palmgren, A., "Die Lebensdauer von Kugellagern," *ZVDI*, Vol. 68, No. 14, 1924, pp. 339-341.
- 7 Miner, M. A., "Cumulative Damage in Fatigue," *Journal of Applied Mechanics*, ASME, Vol. 12, 1945, pp. A159-A164.

# Lateral Gear Shaft Dynamics Control Torsional Stresses in Turbine-Driven Compressor Train

**H. R. Simmons**

Senior Research Engineer.  
Mem. ASME

**A. J. Smalley**

Institute Engineer.  
Mem. ASME

Southwest Research Institute,  
San Antonio, Texas 78284

*An experimental evaluation of a gas turbine/compressor train yielded excellent correlation between measured and predicted torsional critical speeds. Torsional strain signals acquired at a coupling location provide basic data from which damping factors at resonance are found to vary from 1 to 6 percent, depending on mode shape. Resonant stress levels for the mode with low damping would be a factor of 2 higher than predictions based on industry accepted assumptions. Other modes are found to have considerably more damping than expected. Experimental data and a coupled torsional-lateral damped eigenvalue analysis show that this damping variation is related to pinion and gear lateral bearing motion. Conservative damping values are predicted by the coupled analysis.*

## Introduction

The usual methods for analyzing the torsional dynamics of turbine driven trains [1] ignore the effects of lateral gear dynamics. The prediction of torsional critical speeds by these conventional methods is relatively accurate for the majority of typical petrochemical systems, such as that shown in Fig. 1. There is, however, a lack of reliable damping and excitation data and this has led to rule of thumb assumptions and recommendations for most torsional systems. Wright [2] recommends that damping of 1.25 percent be used for nongearred torsional systems, while 2 percent should be assumed for trains with gearboxes. Smalley [3] shows that measured data on a variety of trains indicates torsional damping in the range 1-3.5 percent. Routine assumptions in the industry reach as high as 4 percent of critical damping. Smalley has further shown, using coupled lateral torsional eigenvalue analysis, that under realistic conditions lateral motion in the gearbox bearings can provide substantial torsional damping. Lateral gear dynamics has been addressed in the literature; Remmers [4] addresses the problem of gear tooth meshing quantity and dynamic loads on the gear teeth. Lund [5] describes a computational procedure for predicting coupled lateral/torsional response and eigenvalues, but does not present quantitative data on the important effects of this coupling.

In the present paper, a wide variation in measured torsional damping is shown for different modes of a turbine driven compressor train. Undamped analysis predicts the critical speeds with remarkable accuracy. However, the coupled lateral torsional damped eigenvalue analysis is required to

correlate this damping to observed lateral motion at the gearbox.

## Torsional Systems Analysis

The system under study was a gas-turbine-driven compressor train for pipeline service. As shown in Fig. 1, there are two compressor casings with a total power consumption of 26,000 hp. The compressors run at a maximum speed of 11,000 rpm and are driven through a speed increaser.

In order to respond most efficiently to changes in output requirements, the train operator should have maximum flexibility to vary train speed. Troublesome torsional critical speeds should be located as far as possible below nominal train speed. This requirement is complicated by the fact that both turbine and compressor shaft speed can excite torsional resonances.

The present study of torsional critical speeds was undertaken after the train was upgraded to include the second compressor casing. Even with careful system optimization, torsional critical speeds were predicted at 66 and 70 percent of running speed. These occur when the second torsional mode is

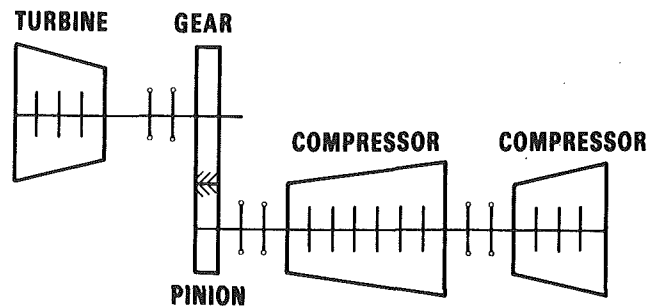


Fig. 1 Turbine compressor train model

Contributed by the Gas Turbine Division of THE AMERICAN SOCIETY OF MECHANICAL ENGINEERS and presented at the 29th International Gas Turbine Conference and Exhibit, Amsterdam, The Netherlands, June 4-7, 1984. Manuscript received at ASME Headquarters December 19, 1984. Paper No. 84-GT-28.

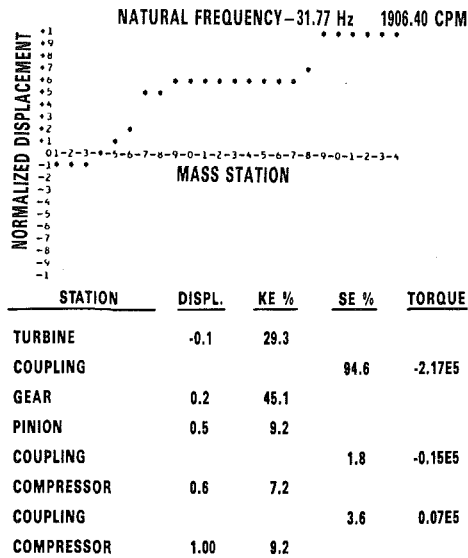


Fig. 2 Undamped torsional resonant mode shape and energy distribution - Mode 1

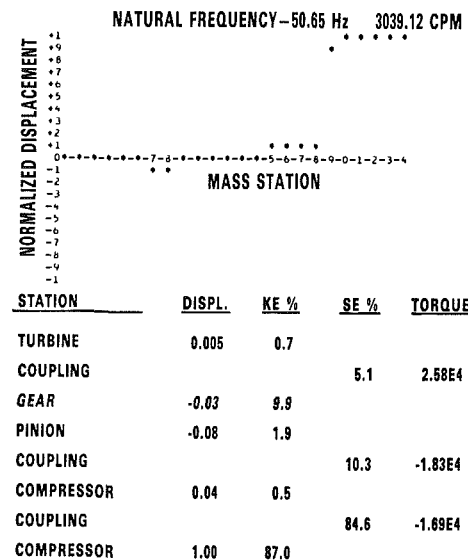


Fig. 3 Undamped torsional resonant mode shape and energy distribution - Mode 2

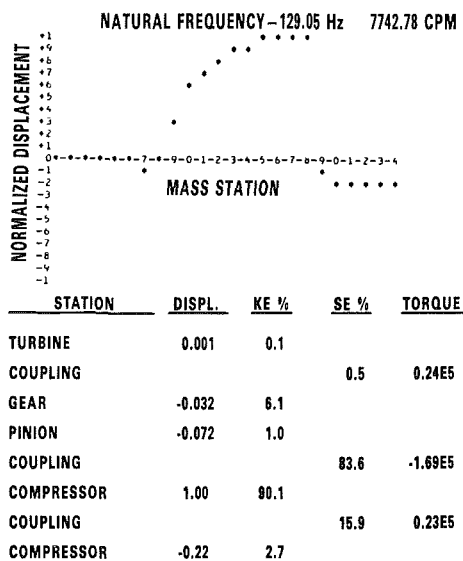


Fig. 4 Undamped torsional resonant mode shape and energy distribution - Mode 3

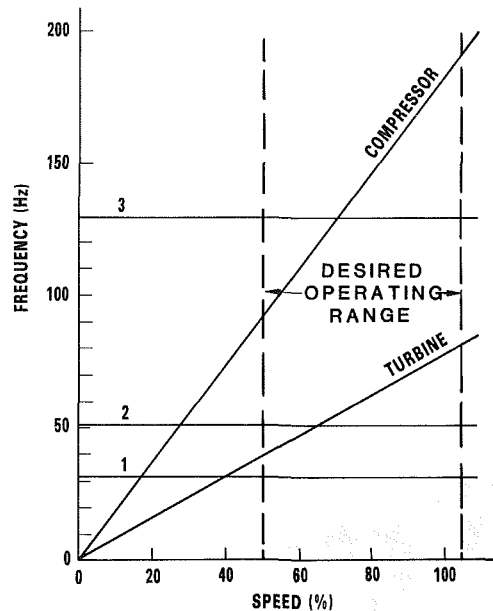


Fig. 5 Torsional critical speed interference diagram

excited by the turbine, and when the third torsional mode is excited by the compressor.

Mode shapes and strain energy distributions for the first three modes are shown in Figs. 2-4. Based on methods presented by Simmons [6], this information may be interpreted to guide design optimization. High strain energies indicate that the second mode is most effectively controlled by the coupling stiffness between the two compressors, and the third mode is most effectively controlled by the coupling stiffness between pinion and first compressor.

The interference diagram in Fig. 5 shows clearly how the turbine and compressor excitations give rise to criticals in the desirable operating range. Because of the low torsional amplitudes shown by the second and third mode shapes at the gearbox, there was some concern that either of these modes might be lightly damped and have high resonant stresses. As a result, some compromise in compressor operation might be necessary to ensure satisfactory life expectancy of the machine.

A test program was undertaken with two objectives in mind:

1 To verify the predicted critical speeds and thereby establish the extent of speed range that is free of critical speeds

2 To establish the severity of the torsional critical speeds below running speed so that safe minimum governor and warmup speeds could be set

There was at this time no a priori way of assuring the magnitude of torsional system damping. Subsequent analysis will show that consideration of lateral coupling at the gearbox gives more complete indication of likely torsional damping levels.

## Test Procedure

Prior to initial startup, the train was instrumented with a variety of torsional and lateral vibration transducers. The primary transducer was a torsional strain telemetry system, shown in Fig. 6. A full bridge strain gage set was mounted on the second high-speed coupling spool piece such that strains due to torsion would be additive and strains due to bending or axial forces would cancel. The Accurex<sup>1</sup> rotating transmitter mounted in a high-strength fiberglass collar provides bridge excitation and signal amplification. Stationary components of

<sup>1</sup>Accurex is a corporation located in Mountainview, California.

the system receive, condition, and scale the strain signal as well as provide power for the rotating module.

The strain gage bridge was calibrated by shunting one leg with a precision resistor as is standard practice. System calibration and accuracy was eventually verified when the unit was brought to full load and the measured torque corresponded to compressor load expectations from other sources.

Additional torsional information was obtained by frequency demodulation of gear tooth passage and tachometer pulse signals. Although this signal-to-noise level is low, a voltage signal proportional to instantaneous shaft speed can be recovered by proper filtering and amplification. One difficulty to be expected with this type of instrumentation is that gear tooth spacing errors and lateral shaft dynamics can also modulate tooth pass signals. Thus, it is usual practice

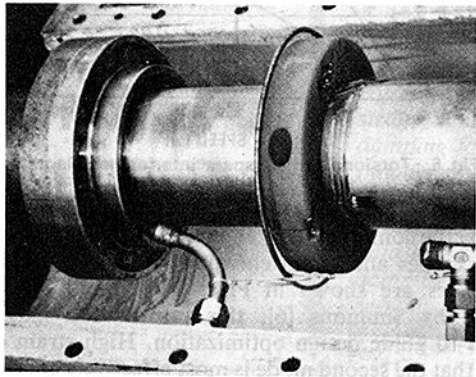


Fig. 6 Detail of typical strain gage telemetry system installation on coupling spool piece

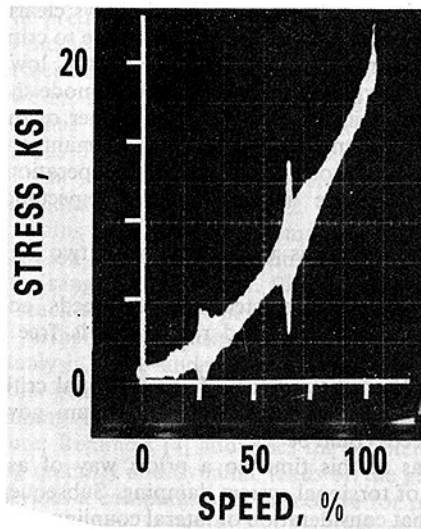


Fig. 7 Coupling stress results

to obtain at least one tooth pass signal from each gear and to also record shaft motion. To evaluate lateral dynamics of all the various components, shaft proximity probe signals and compressor case vibrations were recorded.

The test consisted of recording the various dynamic signals with a multichannel tape recorder while the train was brought up to 105 percent of operating speed in the normal manner. Close attention was paid to the shaft strain signal to avoid dwelling at high-stress conditions.

### Test Results

Total strain signal results versus speed are presented in Fig. 7. Comparison of this figure with Fig. 5 indicates that the high dynamic stresses near 65 percent speed are due to turbine excitation of the second torsional critical speed. Furthermore, compressor excitation of this mode occurs at near 30 percent speed, where low compressor load allows coupling backlash to occur which limits the stress excursions.

The results of all torsional criticals are more clearly seen in the tracking analyses of strain signals presented in Fig. 8. The overall stress level throughout the speed range consists primarily of the sum of first-order compressor speed and first-order turbine speed components. The second critical speed is highly responsive to both turbine and compressor excitations, although the compressor response is limited by backlash.

The broad responses of the first and third criticals indicate high damping. Damping values for each mode are presented in Table 1 for three generally accepted methods for the determination of damping from experimental data (Appendix A). Considering the nature of experimental data, all three methods agree remarkably well, except for compressor excitation of the second mode. The severe backlash associated with this mode violates the linearity assumptions implicit in the damping calculations based on single degree of freedom systems.

Repeated runup tests produced essentially identical results. Furthermore, the turbine-excited, second-mode spectrum

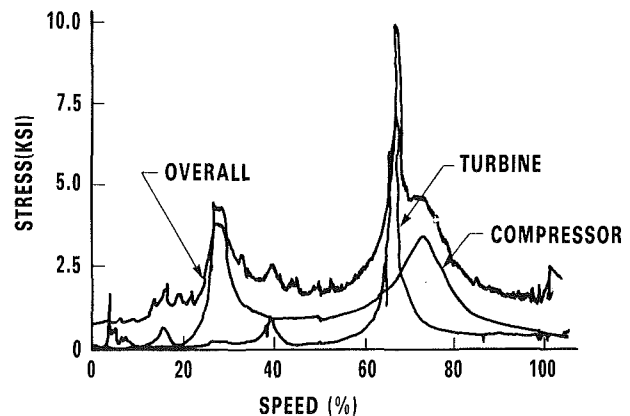


Fig. 8 Tracking plots of coupling oscillatory stress

Table 1 Measured torsional damping data

Exciting shaft	mode	Freq (Hz)	Speed (%)	Critical Damping (%)		
				Phase slope	Half power	Real peaks
Compressor	1	30	16.3	4.34	6.75	3.1
	2	51	27.8	23.1 <sup>a</sup>	6.67 <sup>a</sup>	4.2 <sup>a</sup>
	3	130	70.8	5.8	6.21	5.5
Turbine	1	30	38.6	2.85	2.3	2.3
	2	51	65.5	1.08	0.95	1.37

<sup>a</sup>Clipped data

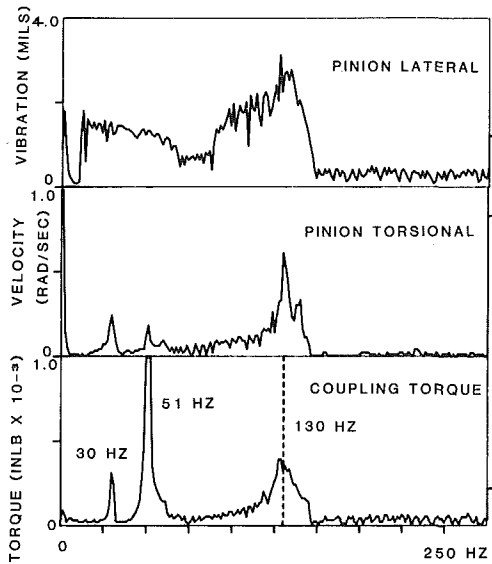


Fig. 9 Spectral record of maximum torsional and lateral vibration during turbine runup

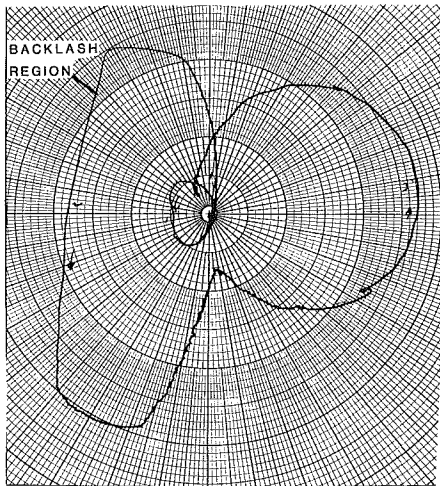


Fig. 10 Nyquist plot of high-speed shaft excitation during turbine runup

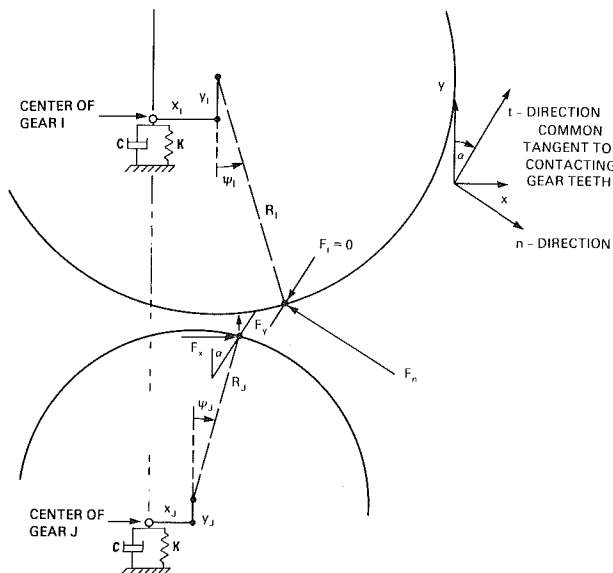


Fig. 11 Coupled torsional-lateral model of gearbox

Table 2 Predicted frequencies and system damping

Critical speed %	mode	Freq (Hz)		Damping (%)	
		pred	meas	pred	meas
38.6	1	31.1	30	1.4	2.85
65.5	2	50.3	51	0.62	1.08
70.8	3	123.	130	2.3	5.8

virtually traced over the compressor-excited data (constant frequency basis), except in the backlash region. The first-mode response is also very similar regardless of excitation source.

Comparison of Table 1 data would imply that conservative analyses must assume 1 percent of critical damping for all modes. Conversely, considerable design and operational freedom would evolve if the maximum measured damping could be utilized for all modes. The wide variation in damping could be related to specific modes suggesting that lateral gear and bearing dynamics (primarily the pinion) could have a significant effect.

To evaluate this hypothesis, peak hold spectra of a startup event are presented in Fig. 9 for comparing coupling torque oscillations with pinion torsional and lateral vibration. The pinion torsional data indicate responses at the first and third criticals that are comparable to coupling torque. Only a slight pinion torsional response appears at the highly responsive second mode, verifying the existence of a node near that location.

The pinion lateral vibration signal was obtained with a proximity probe, where shaft runout creates considerable noise in the spectrum that may hide or distort many facets in the data. Nevertheless, a strong lateral response at 130 Hz indicates that torsional lateral coupling occurs for the third critical speed, which accounts for its high damping. No similar lateral motion can be detected at 51 Hz, indicating that the second mode response does not benefit from bearing damping.

Well defined Nyquist (Fig. 10) and phase plots indicate that the coupling torque signals were phase related to angular locations on both the compressor and turbine shafts. This fixed angular force location and similar vibration levels from both compressor and turbine shafts suggest gear eccentricity may be the primary excitation source.

### Torsional Lateral Analysis

A coupled torsional lateral analysis of the system was performed some time after the original data was obtained. The torsional portion of the model is identical to that used for the original design analysis. The torsional-lateral vibration model (Appendix B) is shown in Fig. 11, where lateral motion was limited to the gearbox since the turbine and compressor are decoupled by flexible couplings. Both bullgear and pinion run on tilting pad bearings where

$$\begin{aligned}
 K_{xx} &\neq K_{yy} \\
 C_{xx} &\neq C_{yy} \\
 K_{xy} &= K_{yx} = C_{xy} = C_{yx} = 0
 \end{aligned}$$

The bearings loads, stiffness, and damping were calculated as a function of speed, accounting both for weight and transmitted torque loads. The lateral damping of the bearings was the only source of torsional damping in the eigenvalue analysis. Damped eigenvalues were calculated for the operating speeds at which each of the three highest torsional criticals occur; results are shown in Table 2, together with measured values using the phase slope method.

The following comments can be made with regard to these predictions and correlations:

**Table 3 Normalized amplitudes of pinion and bull gear for first three torsional modes**

Mode no.	Lateral amplitude		Torsional amplitude	
	pinion	bull gear	pinion	bull gear
1	.102	.211	.570	.214
2	.044	.063	.08	.034
3	.233	.178	.101	.033

1 Measured and predicted frequencies agreed closely as they did for the undamped analysis.

2 Predicted system damping values based on gearbox lateral damping alone are about half the measured damping values.

3 Predicted ranking of damping for the three criticals gives the same order of severity and similar relative severity as the measured data.

4 In all cases, predicted damping based on gearbox alone is conservative and could safely be used in design.

5 Other sources, such as turbine and compressor damping, would add to the predicted system damping.

6 In light of the fact that predictions of bearing damping are not generally considered precise, this correlation should be viewed as encouraging.

Further insight can be obtained from the normalized mode shapes for these three modes. In particular, predicted amplitudes for torsional and lateral amplitudes of bullgear and pinion are presented in Table 3. Considering that integration of pinion torsional velocity will attenuate the higher-frequency modes, the measured torsional and lateral vibrations of Fig. 9 are consistent with the predictions in Table 3.

The predicted gearbox amplitudes for Mode 2 are low for both lateral and torsional motion, providing a convincing explanation for the low damping of this mode. Conversely, the first mode has high torsional amplitudes and moderate lateral amplitudes, while the third mode has torsional amplitudes comparable to the second mode, but high lateral amplitudes. Thus, both predicted and measured data verify that high lateral vibrations of the gearbox bearings provide the most effective damping mechanism for the first and third torsional resonance.

A comparison of Table 3 and the uncoupled analysis presented in Figs. 2-4 indicates that the additional lateral degrees of freedom have only a slight effect on the torsional mode shape. Furthermore, the presence of torsional nodes near the gear set for both the lightly damped second mode and highly damped third mode indicates that a reliable damping criterion can not be established using the noncoupled analysis.

## Conclusions

The results of this investigation support the following conclusions:

1 Experimentally determined torsional damping for the turbine-compressor train were found to vary considerably from the constant values of 2 to 4 percent that are normally considered to be conservative for gear driven systems. Average experimental values were 3 percent, 1 percent, and 6 percent for the first, second, and third modes, respectively.

2 High torsional damping values were found to be associated with high lateral gear shaft vibrations. A rather direct correlation was shown between the measured damping and measured vibration amplitudes, indicating that squeeze film action at the bearings provides the most effective mechanisms for torsional resonances where torsional-lateral coupling occurs.

A coupled torsional-lateral damped eigen-value analysis further supports the relationship between torsional damping and lateral bearing vibration amplitudes in the gearbox.

Noncoupled torsional models cannot provide realistic estimates of gear shaft lateral coupling or damping.

4 Damped eigenvalue analysis based on gearbox lateral damping alone correctly ranks the severity of torsional vibration modes, but underestimates the absolute system damping level by about one-half. Design analysis based on gearbox lateral damping alone therefore provides a more effective but conservative design approach than the constant 2 to 4 percent values normally used.

5 In the tests run, the predominant torsional vibrations were observed to be phase locked with first-order running speed of both turbine and compressor, indicating that gear eccentricity is the most probable excitation source.

6 A strain gage telemetry system located at an active dynamic component provides a more sensitive, consistent indicator of torsional vibration characteristics than gear tooth demodulation or gearbox lateral vibration measurements. Field vibration measurement using telemetry techniques is at present the most reliable and versatile method for establishing torsional vibration severity and identifying safe operational speed ranges.

## References

- Harris, L. M., and Crede, C. E., *Shock and Vibration Handbook*, McGraw-Hill, section 38, 2nd ed., 1976.
- Wright, J., "A Practical Solution to Transient Torsional Vibration in Synchronous Motor Drive Systems," ASME Paper No. 75-DE-15.
- Smalley, A. J., "Torsional System Damping," presented at the 1983 Vibration Institute 7th Annual Meeting, Houston, Texas, Apr. 1983.
- Remmers, E. D., "The Dynamics of Gear Pair Systems," ASME Paper No. 71-DE-23.
- Lund, J. W., "Critical Speeds, Stability and Response of a Geared Train of Rotors," ASME Paper No. 77-DET-30.
- Simmons, H. R., "Vibration Energy: A Quick Approach to Rotor Dynamic Optimization," ASME Paper No. 76-DET-60.

## APPENDIX A

### Damping Analysis Methods

System damping (critical damping ratio) can be easily determined from vibration response data by the following three methods:

(i) **Half-Power Method** The critical damping ratio is calculated from frequency bandwidth between the half-power points on the forced response curve, i.e.,

$$\zeta = \frac{f_2 - f_1}{2f_n}$$

where:

$f_n$  = resonant frequency  
 $f_1, f_2$  = the frequencies at the half-power points ( $X_1, X_2$ ) on either side of resonance

$$X_1 = X_2 = \frac{X_n}{\sqrt{2}} = \text{magnitude of the half-power points}$$

$X_n$  = magnitude at resonance

(ii) **Phase Slope Method.** The critical damping ratio is calculated from the slope of the phase ( $d\theta/df$ ) at resonance, i.e.,

$$\zeta = \frac{180 \text{ deg}}{\pi f_n \left( \frac{d\theta}{df} \right)_n}$$

(iii) **Real Peak Method.** The critical damping ratio is calculated from the frequency bandwidth between the peaks of the real part of the response function, i.e.,

$$\zeta = \frac{(f_a/f_b)^2 - 1}{2[(f_a/f_b)^2 + 1]}$$

where:

- $f_a$  = frequency where the real part of the response peaks above resonance  
 $f_b$  = frequency where the real part peaks below resonance.

## APPENDIX B

### Torsional-Lateral Vibration Model

The present analysis is a simplification of [5] to address the effects of lateral gear dynamics on torsional eigenvalues. The rotor system for torsional and lateral motion is treated as a series of lumped inertias connected by inertialess springs. The model is simplified by allowing lateral motion at the gear shafts only and neglecting rotary inertia and gyroscopic effects.

Gearbox bearings are described by the low stiffness and low damping coefficients  $K_{xx}, K_{xy}, K_{yx}, K_{yy}, C_{xx}, C_{xy}, C_{yx}, C_{yy}$ .

For the results presented in this paper, the gearbox bearings are the only source of damping.

The coupled torsional-lateral motion at the gears are developed by ensuring that the gear teeth in contact provide no resistance to relative motion of the gear teeth along the common tangent, but develop resistance to normal relative motion based on a normal tooth stiffness,  $K_n$ .

In Fig. 11, the  $Y$ -direction is parallel in the line of centers at gear  $I$  and  $J$ .

With reference to Fig. 11, the normal force acting on gear  $I$  in the direction opposite to the  $n$ -direction is

$$F_n = K_n [(x_I - x_J) \cos \alpha - (y_I - y_J) \sin \alpha + (R_I \psi_I - R_J \psi_J) \cos \alpha] \quad (1)$$

The tangential force acting on gear  $I$  in the  $t$ -direction is

$$F_t = 0 \quad (2)$$

The  $x$ -force acting on gear  $I$  (opposite to the  $x$ -direction) is

$$F_x = F_n \cos \alpha + F_t \sin \alpha \quad (3)$$

$$F_x = K_n [(x_I - x_J) \cos^2 \alpha - (y_I - y_J) \sin \alpha \cos \alpha + (R_I \psi_I - R_J \psi_J) \cos^2 \alpha] \quad (4)$$

The  $y$ -force acting on gear  $I$  (opposite to the  $y$ -direction) is

$$F_y = -F_n \sin \alpha + F_t \cos \alpha \quad (5)$$

$$F_y = -K_n [(x_I - x_J) \sin \alpha \cos \alpha - (y_I - y_J) \sin^2 \alpha + (R_I \psi_I - R_J \psi_J) \sin \alpha \cos \alpha] \quad (6)$$

Where

- $K_n$  = the normal tooth stiffness  
 $x_I, y_I$  = the translations of gear  $I$   
 $x_J, y_J$  = the translations of gear  $J$   
 $R_I, R_J$  = the pitch circle radii of gears  $I, J$   
 $\alpha$  = the gear pressure angle

Based on torsional equations of motion for the entire rotor train, lateral equations of motion of the gearbox rotors, coupled torsional lateral motion at the gear teeth, and damped cross-coupled motion of the gearbox bearings, the system equations of motion are developed in the following form

$$[m]\{\ddot{x}\} + [c]\{\dot{x}\} + [k]\{x\} = 0 \quad (7)$$

or

$$\{\ddot{x}\} + [\bar{c}]\{\dot{x}\} + [\bar{k}]\{x\} = 0 \quad (8)$$

where

$$[\bar{c}] = [m]^{-1}[c] \quad [\bar{k}] = [m]^{-1}[k]$$

Equation (8) can be written in the following form

$$\begin{bmatrix} \{\dot{x}\} \\ \{\ddot{x}\} \end{bmatrix} = \begin{bmatrix} [0] & [I] \\ -[\bar{k}] & -[\bar{c}] \end{bmatrix} \begin{bmatrix} \{x\} \\ \{\dot{x}\} \end{bmatrix} \quad (9)$$

Where

$$[0] = \text{null matrix} \quad [I] = \text{identity matrix}$$

Take  $x_i = X_i e^{st}$ , and put  $\dot{X}_i = sX_i$  and  $\ddot{X}_i = s^2 X_i$

Substituting into (9), we have

$$S \begin{bmatrix} \{x\} \\ \{\dot{x}\} \end{bmatrix} = [A] \begin{bmatrix} \{x\} \\ \{\dot{x}\} \end{bmatrix} \quad (10)$$

Where  $[A]$  is the square matrix in equation (9).

The eigenvalues of  $[A]$  are directly the values of  $S$ . Eigenvalues that are complex occur in conjugate pairs. Eigenvalues that are real occur in pairs, but in general are not equal in magnitude. Writing  $S = \lambda + i\omega$ , we can define the log decrement  $\delta = -2\pi\lambda/\omega$ .



**D. L. Blausler**  
Market Manager,  
Traditional Products.

**U. Gulati**  
Senior Performance Engineer,  
Gas Turbines.

Dresser Clark Division,  
Dresser Industries,  
Olean, N.Y.

# Performance Considerations in Selection and Application of Gas Turbine Drivers for Centrifugal Compressors

## Introduction

The dramatic increase in fuel costs over the past several years has resulted in a restructuring of evaluation criteria in the selection of gas turbine drivers for all services, including that of compressor drive. Previously, mechanical considerations received primary emphasis. Today, considerable attention is being given to the basic parameters of gas turbine thermal efficiency and compressor efficiency. Proper integration and matching of the primary components and of ancillaries will result in optimum capital and operating costs for an installation meeting the application objective. In order to determine the most cost-effective solution, the engineer should have a clear understanding of the factors influencing these costs and should identify and examine alternative solutions.

Gas turbine power varies with ambient factors, output speed, inlet and exhaust losses, degradation, control method, and rating methods. Compressor required horsepower and throughput may vary due to changing process conditions and degradation of compressor internals and other process components. Adequate margin between required power and available site power must be considered in selection of the driver if plant throughput is to be maintained. However, excessive conservatism can be costly, both in initial investment and in cost of service.

Since two-shaft gas turbines are the most commonly used for compressor drive service, the discussion is based on two-shaft turbine characteristics. Compressors under discussion are those typified by custom-built industrial compressors and by pipeline booster compressors which are frequently designed for specific applications. Mechanical factors involved in selection such as rotor response, stress, and metallurgical limitations are not a topic of this paper.

## Types of Duty

There are several types of compression duty for which variable-speed drivers are well-suited and gas turbines are

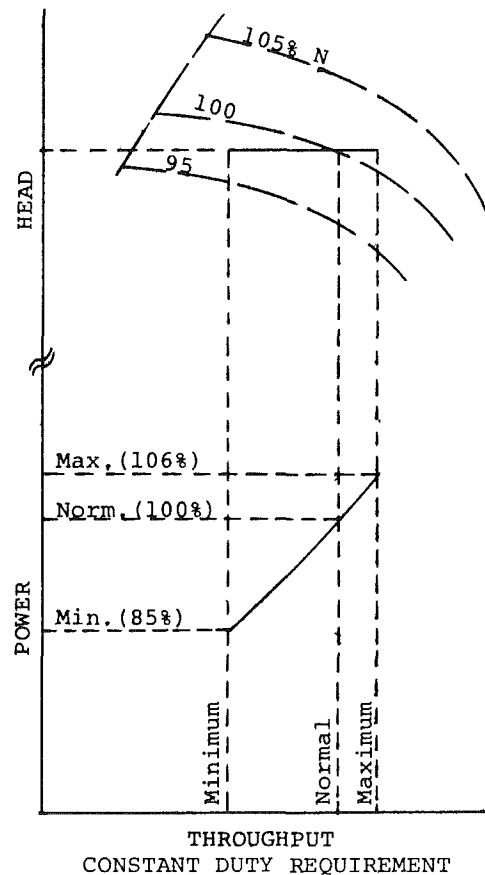


Fig. 1

being widely utilized. We will address three general types of applications which are relatively common.

**Constant Duty.** Constant-duty services include those for which the compressor horsepower and speed remain virtually constant within well-defined limits of service conditions. Such applications include petrochemical, LNG, and refining services: e.g., syn gas makeup and recirculation compressors, refrigeration compressors, hydrocracker recirculation and

Contributed by the Gas Turbine Division of THE AMERICAN SOCIETY OF MECHANICAL ENGINEERS and presented at the 29th International Gas Turbine Conference and Exhibit, Amsterdam, The Netherlands, June 4-7, 1984. Manuscript received at ASME Headquarters, December 27, 1983. Paper No. 84-GT-45.

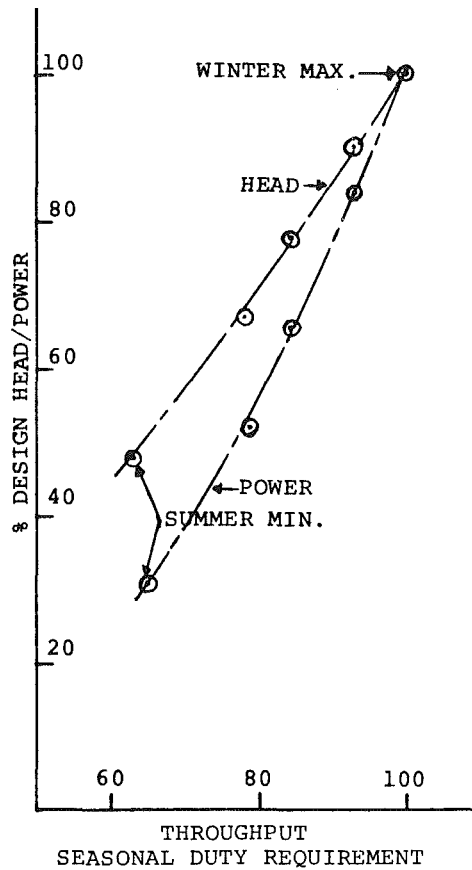


Fig. 2

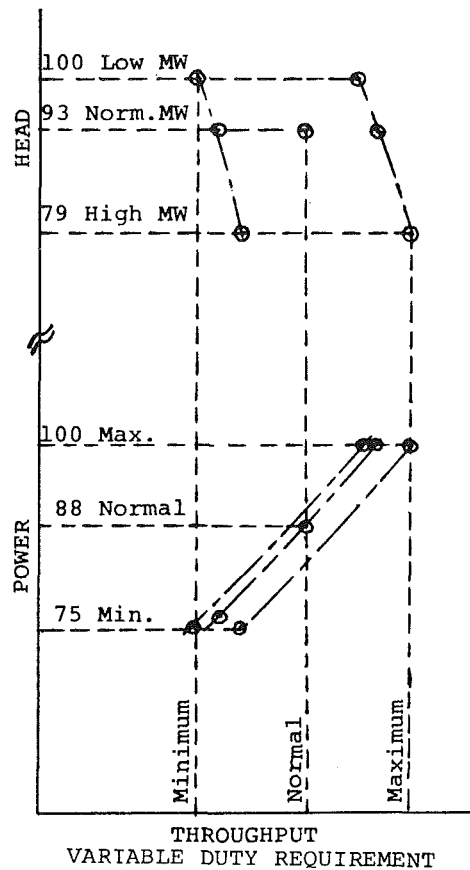


Fig. 3

makeup compressors, etc. For these applications, the composition of the gas being compressed, flow, and head are known, and plant operation is predictable within narrow margins. Demand is relatively constant, not significantly affected by environmental factors (Fig. 1).

**Seasonal Duty.** Seasonal duty services include those which are governed by climatic or annual demand cycles. An

example of seasonal duty may be found in some natural gas transmission services where demand is maximum in the winter and minimum in the summer. The process gas is virtually constant in composition and suction temperature varies within a narrow range. Operation of the compression unit can be well-defined in terms of required head and flow for seasonal demand conditions (Fig. 2).

For such applications, the gas turbine driver and com-

### Nomenclature

EGHP = gas generator exhaust gas power  
 EGT = gas generator exhaust gas temperature  
 $g$  = gravitational constant  
 GG = gas generator  
 $H$  = polytropic head  
 ISO = International Standards Organization  
 —operating conditions for gas turbine 59°F (15°C), 14.696 PSIA (101.3 kPa), no losses, 60 percent relative humidity  
 $k$  = ratio of specific heats  
 $M$  = mass flow  
 $N$  = rotational speed (rpm)  
 $N_s$  = specific speed parameter for turbo compressors, a correlation of kinematic and dynamic similarity of design (1)  
 $P$  = pressure-absolute  
 $Q$  = flow, normally at inlet  
 $R$  = universal gas constant  
 $R_c$  = pressure ratio ( $P_d/P_i$ )  
 $S$  = number of stages (impellers)  
 $T$  = temperature-absolute  
 $U$  = tangential velocity, at impeller tip for compressor, mean flowpath for turbine

$V_1$  or  $V_2$  = absolute velocity  
 $VR_1$  or  $VR_2$  = relative velocity  
 $V_{u1}$  or  $V_{u2}$  = tangential velocity  
 $Z$  = deviation or compressibility factor  
 $\delta$  = ambient pressure (abs.) divided by standard pressure  
 $\eta$  = efficiency  
 $\theta$  = ambient temperature divided by standard temperature (abs.)  
 $\mu$  = pressure coefficient for centrifugal compressor stage, determined by design

### Subscripts

av = average  
 $e$  = at compressor discharge  
 $f$  = first stage (impeller)  
 $i$  = at compressor inlet  
 $l$  = last stage (impeller)  
 $m$  = mean for compressor  
 pt = polytropic  
 stg = average per stage (impeller)

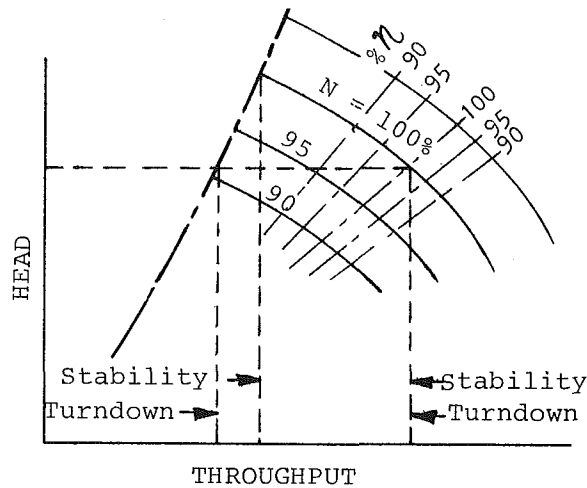


Fig. 4

pressor can be selected to operate at high efficiency over much of the annual duty cycle as the demand characteristic complements that of the gas turbine output characteristic relative to seasonal ambient temperatures.

**Variable Duty.** In variable-duty services, the compressor throughput is neither constant nor relatable to reasonable demand. Typical variable duty applications may be found in oil and gas production operations. In many oilfield applications, significant variation in production rates, varying gas/oil production ratios, and variation in gas composition, pressures, and temperatures create a broad range of operating conditions which must be accommodated. Such applications include associated gas gathering and processing, associated gas reinjection, and gas lift operations.

For such applications, a basic criterion is to provide adequate operating flexibility such that production is maintained for all operating points within defined limits (Fig. 3).

### Compressor Considerations

**Design Point Selection.** Optimum performance can usually be attained if the compressor design (peak efficiency) point selection is based on conditions at which the compressor will operate for the majority of its duty cycle. Higher flow/head conditions can usually be accommodated by the 5 percent over design speed capability traditionally provided for the turbine and compressor. However, for some services, it is necessary to design for higher than normal flow and/or head conditions. As this may result in significant performance loss under normal operating conditions, a careful assessment of real operating requirements is appropriate in establishing the design point.

After definition of the compression requirements, an allowance for compressor degradation may be made. The presence of abrasive, corrosive, or fouling agents in the process gas stream will cause deterioration of the process compressor components, which may decrease throughput and increase horsepower and/or speed requirements from the driver. This can best be evaluated by user experience and user/compressor manufacturer dialogue. Appropriate process design features such as filtration and scrubbing systems, together with compressor design features and material selection, will minimize in-service compressor deterioration. For example, in high-density process gas streams, suspended solids of small particle size may cause rapid erosion of sealing surfaces with resultant internal recirculation and loss of throughput and pressure ratio. Seal sleeves of high surface

hardness can be employed to reduce erosion. Dirty gas may result in deposition of contaminants in the compressor flowpath, reducing capacity. It should be noted that additional available driver horsepower may not overcome severe recirculation and fouling problems as these can result in surge/choke conditions within the compressor when additional speed is applied.

**Stability/Turndown.** Stability and turndown are terms referring to the capability of the centrifugal compressor to operate at less than design flow. Stability is determined in percent as:

$$\left( \frac{\text{suction flow at design} - \text{suction flow at expected surge}}{\text{suction flow at design}} \right) \times 100 \text{ over}$$

all at constant speed.

Turndown is determined in percent as:

$$\left( \frac{\text{suction flow at design} - \text{suction flow at expected surge}}{\text{suction flow at design}} \right) \times 100 \text{ over}$$

all at constant head (Fig. 4).

When operating at reduced flow, it may be necessary to recycle process gas through an appropriately designed system from discharge to suction to maintain stable operation. The tendency is to avoid operation in the recycle mode as this results in wasted work.

Stability is a function of compressor aerodynamic design. However, in multistage applications, stage-to-stage volume reduction with varying operating conditions make this parameter application sensitive. It is unwise to seek excessive stability to cover operating conditions that are applicable only for short-duty periods as the compressor supplier can achieve this only by undersizing the compressor, thereby penalizing design point efficiency of operation. The reduction in compressor efficiency at the design condition over the annual duty cycle is likely to be more significant than the short-term recycle losses.

**Specific Speed.** The basic indicator for compressor aerodynamic efficiency is the specific speed parameter  $N_s$ , where  $H_{stg}$  is head per stage in ft-lb/lb,  $N$  is rotative speed in rpm and  $Q$  is actual inlet volume flow in  $\text{ft}^3/\text{min}$ .

$$N_s = \frac{N(Q/60)^{1/2}}{H_{stg}^{3/4}} \quad (1)$$

For centrifugal compressors, specific speeds range from approximately 40 upward. The correlation between stage efficiency and specific speed is typical of that shown in Fig. 5 for centrifugal designs (1).

For compressors requiring low head, as is typical of pipeline booster compressors, heads up to 13,000 ft-lb/lb can be achieved in a single stage (single impeller). For other applications requiring higher head, multistage compressors are required. A typical impeller, with a pressure coefficient ( $\mu$ ) of 0.50 running at a tip speed ( $U$ ) of 800 ft/s will produce approximately 10,000 ft head. Therefore, the nominal number of impellers required can be approximated:

$$S = H/10,000 \quad (2)$$

In a multistage compressor, with significant volume reduction through the machine, specific speed varies stage to stage as a function of  $Q$  and  $H$  for each stage. For optimum efficiency, the engineer must examine the specific speed range throughout the compressor. Useful approximations can be made using ideal gas laws or actual gas properties if known. The following equations may be employed for approximating purposes (assuming equal pressure ratio per stage) on multistage compressors with no intercooling or compressor sections between intercoolers:

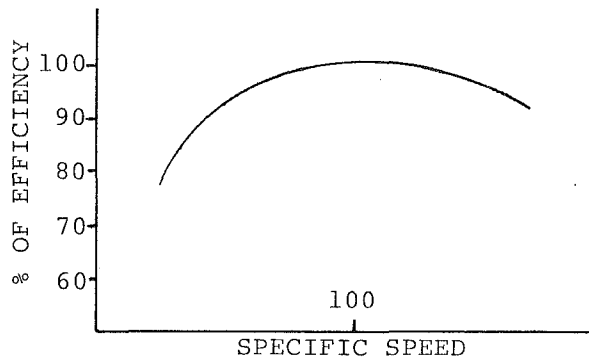


Fig. 5

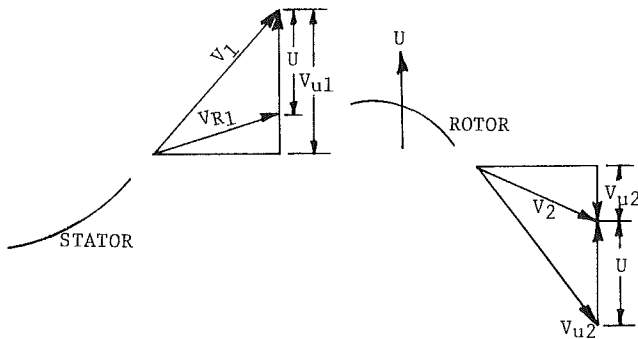


Fig. 6

$$N = \frac{200H_{stg}^{3/4}(Qi/60)^{-1/2}}{1 + R_c^{-x/n}} \quad (3)$$

where  $X = \frac{S-1}{2S}$  and  $\frac{n-1}{n} = \frac{k-1}{k\eta_{pt}}$

$$H = \frac{Z_{av}RTi \left( R_c^{\frac{n-1}{n}} - 1 \right)}{\left( \frac{n-1}{n} \right)} = \mu U^2 / g \quad (4)$$

$$Ns_m = \frac{N}{2H_{stg}^{3/4}} \left( \frac{Qi}{60} \right)^{1/2} (1 + R_c^{-x/n}) \quad (5)$$

$$Ns_f = \frac{N}{H_{stg}^{3/4}} \left( \frac{Qi}{60} \right)^{1/2} \quad (6)$$

$$Ns_l = \frac{N}{H_{stg}^{3/4}} \left( \frac{Qi}{60} \right)^{1/2} R_c^{-x/n} \quad (7)$$

For a conventional single-stage compressor,  $Ns$  should be above 80 for good efficiency. A target value of 110 to 120 should attain near optimum efficiency for conventional designs.

For conventional multistage centrifugal compressors, the maximum value for  $Ns$  should not exceed 130 for good efficiency and the mean value for  $Ns$  should be approximately 100.

$Ns$  of the first and last stage impellers should be within the acceptable range. If not, two or more compressor cases, possibly operating at different speeds, or double flowing the low stages, should be evaluated [1]. This is frequently required for high molecular weight gases in high-pressure ratio services. It is wise to consider the driver options before finalizing selections as the goal is to optimize the entire gas turbine/compressor train. A basic decision of whether to direct drive a gear is made at this stage. The selection is then

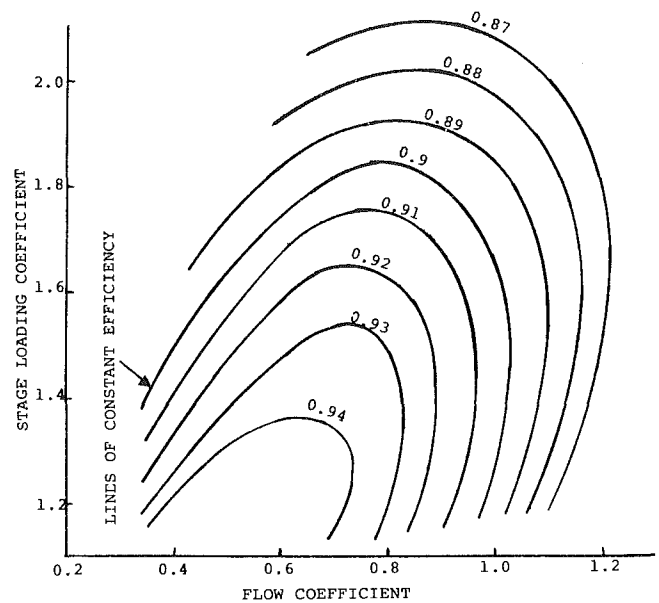


Fig. 7 (Smith's correlation)

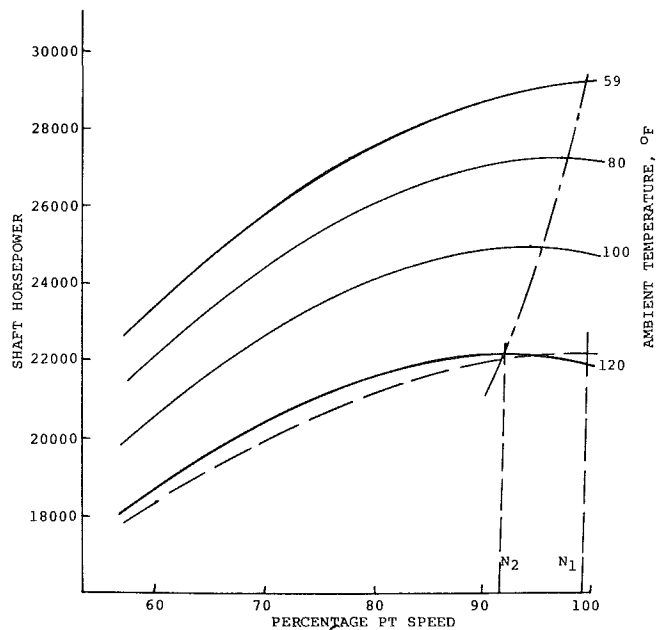


Fig. 8

refined by precise calculation and modified to fit mechanical constraints, cost, etc. Product constraints sometimes force the engineer out of the optimum specific speed range, resulting in compromised performance.

### Turbine Considerations

Having established the required head and flow and desired speed for the compressor at its normal operating point, with allowance for process variation and compressor deterioration, attention can now be transferred to the driver.

**Power Turbine Speed.** Power turbine design speed is established in the early stages of power turbine design based on aerodynamic and mechanical considerations. The velocity diagrams for a single stage turbine are shown in Fig. 6. The torque produced is proportional to the change of tangential

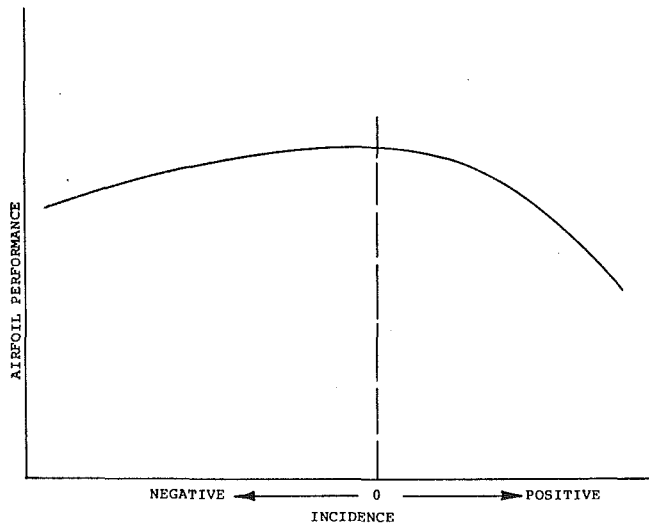


Fig. 9

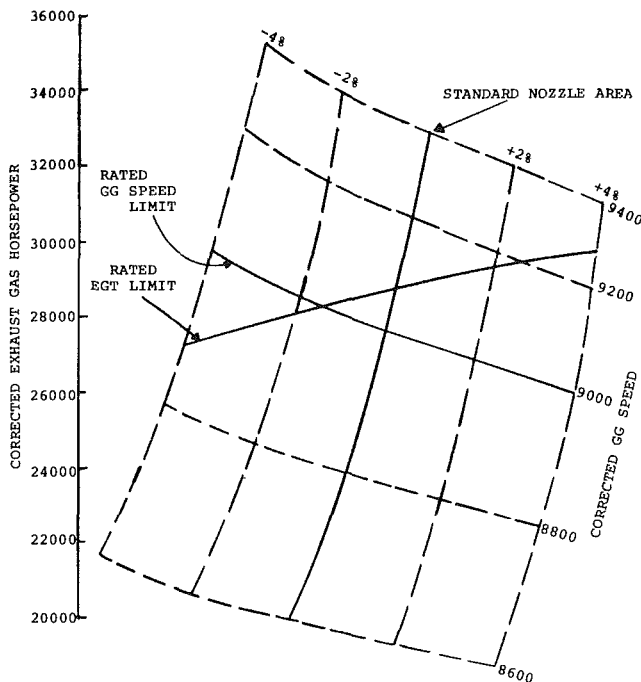


Fig. 10

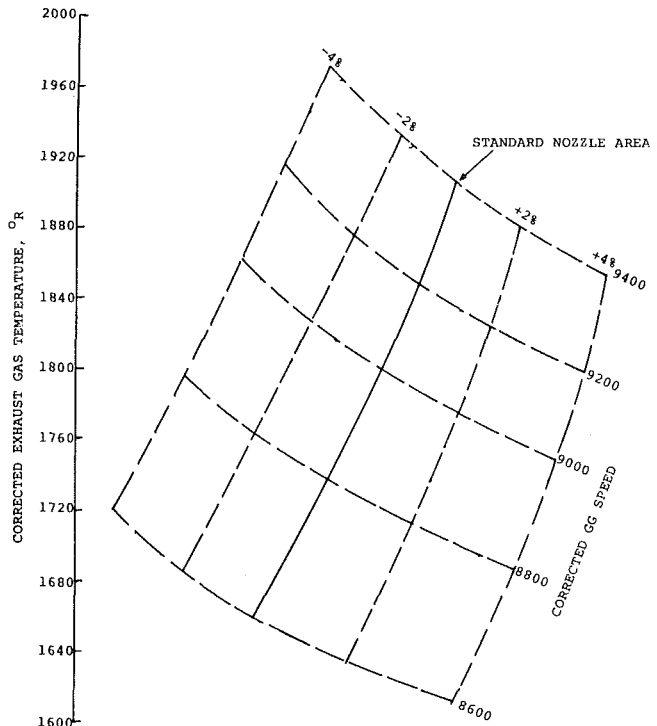


Fig. 11

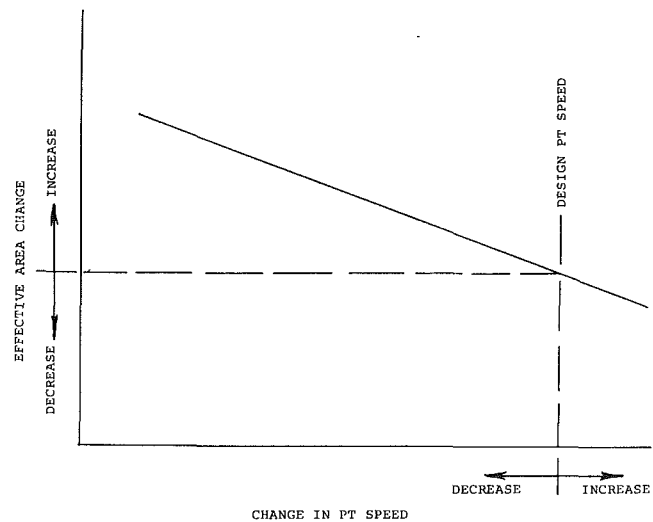


Fig. 12

velocity; i.e.,  $(V_{u1} + V_{u2})$ . The specific work, the work done per unit flow rate, is proportional to  $U(V_{u1} + V_{u2})/2g$ .

Similar parameters to the specific speed parameter for centrifugal compressors are applicable to turbines. Smith's correlation (Fig. 7) of blading efficiency is such a parameter [10]. However, since turbine designs are not custom to each application, as are those of centrifugal compressors, the application of stage loading versus efficiency correlations is of academic interest in application. This is not to imply that design point speed for a given gas turbine application is confined to a specific value as will be discussed later.

It is a standard practice to rate gas turbines at ISO conditions (2 and 3). A typical output speed versus shaft horsepower plot with constant ambient temperature lines is shown in Fig. 8. As the ambient temperature increases, the power turbine speed reduces for optimum performance. (The locus of these peak performance points is referred to as the "cube line." If adjustment or variation of turbine geometry is available, the cube line can be shifted as much as plus or minus 10 percent without significant impact on performance.

This is the approximate limit over which geometry changes will not result in poor incidence angles in the blading with consequent efficiency loss [4].

Typical effect of incidence on airfoil performance is shown in Fig. 9. Performance drops off as a function of the incidence angle to the second power for negative incidence and to the fourth power for positive incidence. The peak performance is usually around  $-8$  deg incidence angle. The efficiency of typical turbine blading (50 percent reaction) does not decrease significantly up to  $-35$  to  $-40$  deg incidence angle but drops sharply once the incidence angle becomes positive (usually above  $+10$  deg).

For a particular application, if the site ambient temperature is  $120^\circ\text{F}$  and the maximum output is required at  $N_1$  instead of  $N_2$  (Fig. 8), this can be achieved by readjusting the nozzle area. The output power line for this application at an ambient temperature of  $120^\circ\text{F}$  is shown as a dotted line.

To further understand how turbine speed may be op-

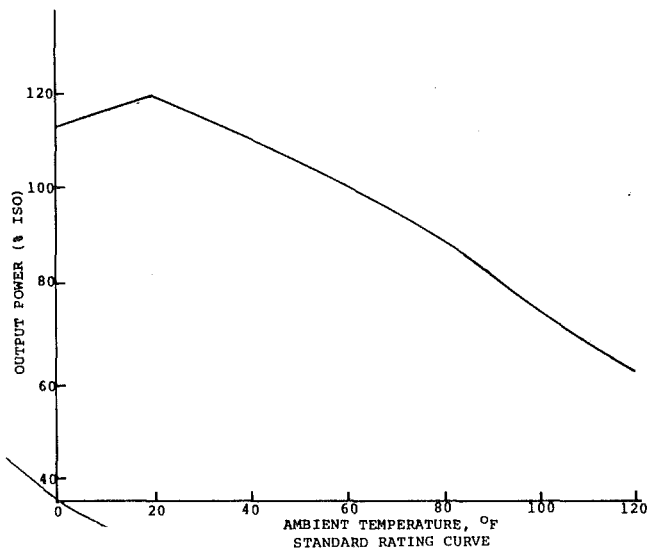


Fig. 13

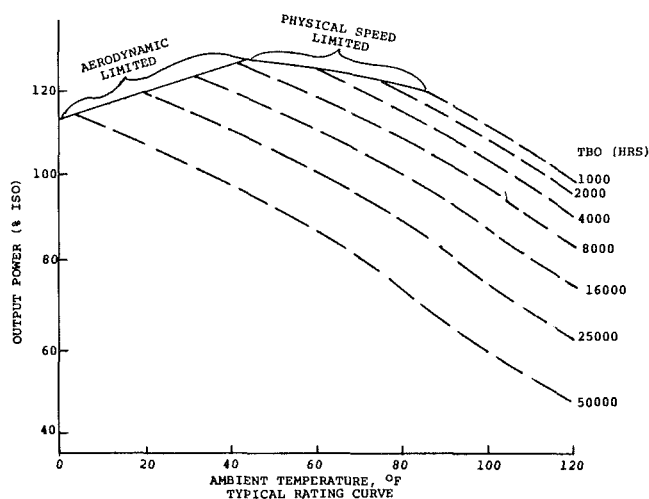


Fig. 14

timized, it is necessary to examine the relationship of power turbine effective area to gas generator performance.

**Gas Generator/Power Turbine Matching.** A specific gas generator will provide optimum operation, at design conditions, with a certain standard (hot effective) nozzle area. For a power turbine to properly accommodate a particular gas generator, the overall power turbine effective area (which consists of stators/nozzles, rotors, exhaust diffuser, and any other necessary ducting) has to be equivalent to the standard (hot effective) nozzle area. Figures 10 and 11 show typical gas generator characteristics: EGHP, EGT, and GG speed are the corrected parameters, the solid line represents "Standard Nozzle Area," and the dotted area lines are for nonstandard conditions.

Variation in effective area from standard will impact performance. If the effective area is oversize by 1 percent, the gas turbine cycle temperature is reduced, at constant GG speed, and a power reduction of 2 to 4 percent is typical. Should the effective area be undersize by 1 percent, the gas generator speed is reduced, at constant temperature, and a similar reduction in power occurs.

When optimizing an existing turbine for off-design speed, the nozzle area is adjusted to compensate for the resultant change in effective area (Fig. 12) subject to limitations to change in incidence angle (Fig. 9). This is required to achieve

EXAMPLE OF CONSTANT POWER RATING

ANNUAL RUNNING TIME (HRS)	AT AMBIENT TEMPERATURE (°C)	EXPECTED OVERHAUL LIFE (HRS)	LIFE USED ANNUALLY (%)
100	40	5000	2.0
500	34	15000	3.3
5400	29	25000	21.6
2200	23	35000	6.3
<u>200</u>	15	45000	<u>0.4</u>

8500 HRS/YR

33.6%

EXPECTED TBO =  $8500 / 0.336 = 25300$  HRS

Fig. 15

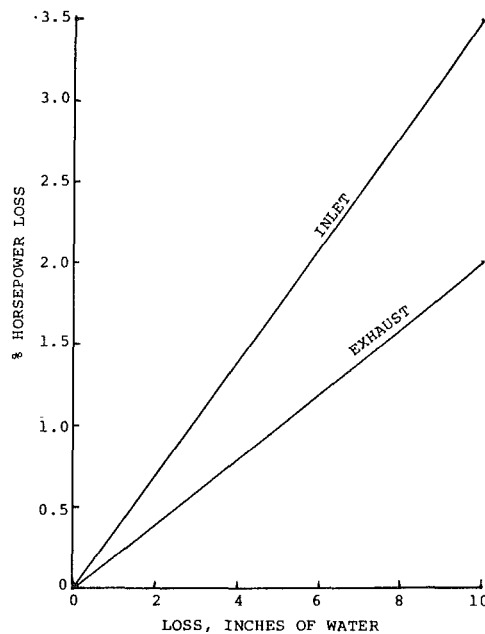


Fig. 16

the shift in the optimum performance point at constant speed as shown in Fig. 8.

**Rating Basis.** Gas turbine ratings are defined in terms of the operating limits for a specified operation mode and under defined operating and site conditions. Ratings will vary depending on the type of duty cycle over which the engine is to operate; i.e., by the number of starts per fired hour of operation. Thermal stresses are imposed on the hot gas parts during starting and stopping, thus the frequency of starting and stopping affects maintenance intervals. For industrial service, the following duty cycles are commonly used [2]:

**Continuous Load:** Operation requiring 24,000 hrs without planned shutdowns.

**Base Load:** Operation with at least 8000 hrs between major inspection intervals and generally not less than 100 fired hrs per start.

**Peak Load:** Operation of approximately 5 hrs per start with at least 5000 hrs between major inspections.

The standard turbine performance curve defines horsepower versus ambient temperature (Fig. 13). The turbine may be operated at any point on the curve and retain the expected TBO even though temperature and stress levels may not be constant over the range.

Alternative basis for ratings are available and are being widely applied. These may be referred to as constant power ratings, site ratings, electrical base, peak, etc. The basic difference between these ratings and the standard rating is

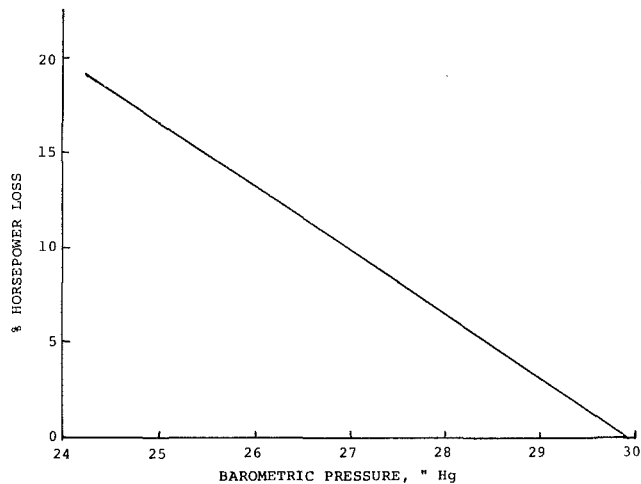


Fig. 17

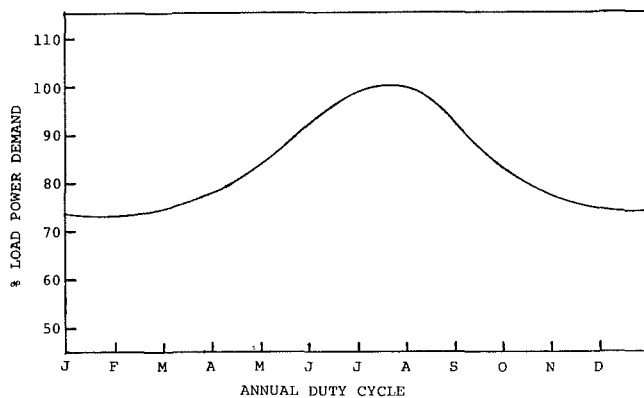


Fig. 18

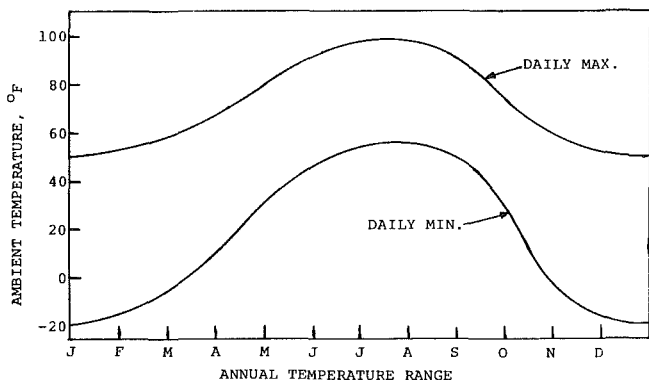


Fig. 19

that the expected operating duty cycle is evaluated and factored. Figure 14 shows a typical rating map with ratings to achieve various expected TBO values. Time between overhauls as noted is based on continuous operation at the various ratings. It is frequently advantageous, where power demands are nearly constant over the annual operating cycle or where peak demand may occur at any time during the annual cycle, to rate the gas turbine at constant power or to use a rating other than standard. Figure 15 (table) shows how constant power ratings may be derived. These techniques can provide substantial benefits in reduced capital expense and operating costs by utilizing smaller gas turbines operating at higher load factors with consequently better fuel consumption than underloaded solutions.

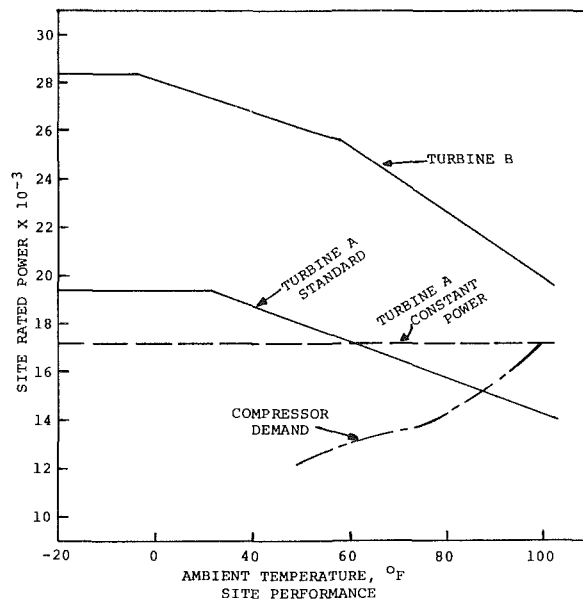
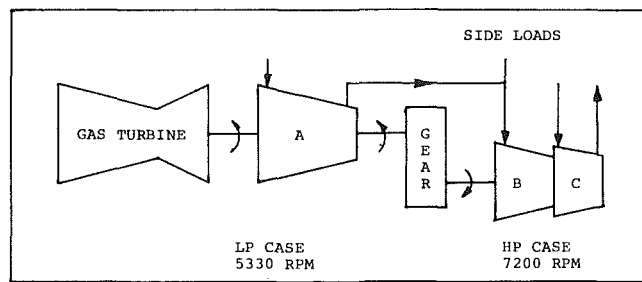


Fig. 20



COMPRESSOR TRAIN ARRANGEMENT

Fig. 21

### Turbine Performance at Site

The engineer must determine the range of service conditions over which the driver is to deliver the required power.

1. *Ambient Temperature.* Ambient temperature, to be effectively considered, must be quantified in range as well as time to make the most cost-effective selection. For example, a typical site temperature may have an ambient range of 20°F to 110°F when considering absolute historic data. However, when considering the temperature range corresponding to 95 percent of the actual operating time, this may reduce to a range of 30°F to 100°F. If a turbine is selected to meet the horsepower requirement at 100°F, and 2 1/2 percent of the time the temperature exceeds that, a potential maximum loss in throughput on an annual basis of approximately 0.07 percent will be incurred.

2. *Inlet Losses.* The inlet system provides:

- (a) Attenuation of intake noise to meet required sound levels. The design of the silencer determines the pressure loss.
- (b) Quality of intake air. The intake air filtration system is a function of environmental conditions at site. Fouling, erosion, and corrosion of gas turbine components are caused by dust particles, pollen, insects, salt, smoke, etc. Adequate air filtration at the intake to avoid severe degradation in turbine performance due to fouling, erosion and/or corrosion of compressor blades and turbine hot section components should be given due consideration [5, 6, 7]. It is

practical, in most cases, to adequately filter intake air such that, with acceptable compressor cleaning intervals, degradation due to fouling can be held to under 3 percent. The pressure loss in the intake filtration system is determined by the quantity and type of filtration provided.

**3. Exhaust Losses.** The exhaust system for a turbine consists of an exhaust silencer for the purpose of attenuating exhaust noise (8) and ducting to carry the exhaust gases away from the unit plus any waste heat recovery devices.

Figure 16 shows a typical plot of inlet and exhaust pressure drop versus percentage loss in output power. Intake loss penalizes performance by reducing air density at the compressor intake, thus reducing mass flow, as well by reducing the relative expansion ratio whereas exhaust pressure loss acts solely to reduce the turbine pressure ratio. Hence, inlet loss penalty is substantially greater in terms of power loss. Both intake and exhaust loss affect fuel consumption equally as this is due to the effect on expansion ratio only.

**4. Barometric Pressure.** Altitude is a fixed parameter at a site that can be readily quantified. However, barometric pressure will vary between high and low [up to  $\pm 1$  in. (2.5 mm)Hg] and is not solely dependent on altitude but also weather conditions. Therefore, the range of barometric pressure should be determined for a specific site. Figure 17 shows barometric pressure versus percentage loss in output power.

**5. Humidity.** The effect of humidity in the ambient air is of a minor nature. On an ISO day (59°F, 60 percent R.H.), the effects of changes in relative humidity are negligible. On a hot day (over 100°F), the effect may approach 1 percent under extreme conditions. Humidity is generally ignored in performance calculations (9).

### Degradation Allowance

The most common cause of gas turbine and load compressor performance degradation is fouling of the aerodynamic components. Other causes include erosion and corrosion of aerodynamic components as well as seals. Although some performance loss is inevitable, experience has shown that it can be minimized by proper attention to design and selection of intake filtration systems, fuel filtration/treatment, and process gas conditioning systems. In addition, remedial action systems (such as compressor washing) will substantially restore performance of the compressor sections by cleaning of the aerodynamic components.

Performance loss due to fouling of the gas turbine compressor can range from 3 to 10 percent of the output horsepower for axial designs, usually substantially less for centrifugal designs. The amount of power loss depends on the control parameters employed. If the gas generator primary control parameter is speed, a lower degradation, in terms of power, will be observed than that which occurs if exhaust temperature is the primary control. Proper cleaning of the compressor will normally restore performance to within 1 percent or so of new performance provided deterioration is due to fouling only and not erosion/corrosion. Erosion can be prevented by good intake filtration and avoiding use of erosive cleaning agents. Corrosion is avoided by use of corrosion resistant materials and, in certain cases, by the use of inhibitors, in addition to effective intake filtration.

Corrosion and erosion of hot section components is dependent on quality of combustion air, fuel and material selection. Most suppliers select materials having at least fair corrosion resistance and corrosion resistance coatings are frequently applied. With appropriate intake air filtration and

fuel treatment, performance deterioration in the hot section should not exceed 1 percent/year.

Load compressor performance degradation is difficult to quantify. It ranges from essentially zero for a compressor in clean service to as much as 10 percent where heavy fouling in a small capacity compressor takes place. Erosion and/or corrosion can be a problem where dirty or wet gas of high density is being compressed. The user should, whenever possible, assure that the process gas stream is free of contaminants. Where this is not practical, a realistic assessment of probable performance deterioration is required.

The following would be typical degradation allowances for well-designed installations using quality hardware and where good maintenance practices are employed:

Service	Clean	Moderate	Dirty
Gas Turb Comp Fouling	1%	2%	3%
Hot Section Deterioration	1%	3%	3%
Total GT Allowance*	2%	5%	6%
Load Comp Typical Service	1%	2%	4%
Total Degradation Margin	3%	7%	10%

\* Degradation allowance required depends on control method.

### Examples

#### Inverse Seasonal Duty

Application—Refrigeration of Ammonia (NH<sub>3</sub>) Storage  
Process Gas—NH<sub>3</sub> (MW 17.03)

Section	A	B	C
$P_i$ (PSIA)	14.6	54.5	106
$T_i$ (°F)	5	77	106
$P_d$ (PSIA)	64.5	119.0	275
$R_c$	4.418	2.183	2.594
$Q_i$ (ACFM)	35450	17920	10640
$H$ (ft-lb/lb)	77760	41460	53530
$S = \frac{H}{10000}$	7	4	5
$N$ (ref equation (3))	5490	6480	8880
BHP	17770		

Load Profile - The refrigeration load is ambient-sensitive due to heat input from ambient and process cooler performance (Fig. 18). Ambient profiles at site were established per Fig. 19.

Two turbines were evaluated for this service. On the basis of the standard rating, the smaller unit did not meet the required power during the peak load period. A constant power rating was investigated for this unit. The three ratings investigated are plotted on Fig. 20.

Two alternatives were pursued; the first using Turbine A at constant power rating, the second using Turbine B at standard rating.

Turbine	A	B
Site Power @ 100°F	17200	19900
$N$ Mechanical Design (100%)	5330	5000
$N$ Optimum at 100°F	5220	4900
Thermal Efficiency at 100°F	0.27	0.32

In either case, optimum performance could be shifted to the mechanical design speed by nozzle adjustment.

Compressor selections were completed on the basis of two compressor bodies; one direct-coupled to the gas turbine and the second driven through a speed increaser gearbox as shown in Fig. 21. The two high-pressure sections were compromised to operate at the same speed. However, the final selection with careful tuning had a better efficiency than assumed for the original study and a total required horsepower of 17,160



was achieved. The final selection power demand is shown in Fig. 20.

Although the fuel consumption of Turbine B was sixteen percent less than Turbine A at site rated power, the differential diminished at required power to eleven percent at 100°F, the margin decreasing with temperature below 100°F at required power. The differential in turbine prices exceeded the fuel cost of service penalty (this particular site has a very low fuel cost) and Turbine A was favored as the most cost-effective solution. Final speeds and mean specific speeds worked out as follows:

Section	A	B	C
N Final	5200	7050	7050
Ns Final			
(m)	95	86	66
(f)	116	97	74
(l)	75	76	58

**Design Speed Adjustment.** For an application involving a high flow low head compressor, the compressor design speed was determined to be 89 percent of the gas turbine design speed. The turbine nozzle area was adjusted by opening it approximately one percent, shifting the turbine optimum efficiency to the compressor design speed resulting in a three percent saving in fuel consumption. On an annual basis, this resulted in a savings of approximately \$100,000.

### Summary

The subject of performance in regard to selection and application of gas turbine and centrifugal compressors has been addressed with the intent of stimulating the recipient to explore the options available. The subject of degradation should be carefully considered, particularly in selection of intake filtration, fuel treatment, control mode, and maintenance planning in order to minimize overall cost of service. Tradeoffs of increased maintenance costs versus decreased fuel costs should be carefully weighed in determining the load factor for a specific driver application. Thoughtful analysis of project requirements can minimize capital and service costs while meeting the true project needs.

### Conversions

Pressure		
psi	$\times 6.895$	= kPa
in. Hg	$\times 25.4$	= mm Hg
in. Hg	$\times 3.387$	= kPa
Mass		
lb	$\times 0.4536$	= Kg
Volume		
CFM	$\times 4.719 \times 10^{-4}$	= m <sup>3</sup> /s
Head		
ft-lb/lb	$\times 2.989 \times 10^{-3}$	= Kj/Kg
Temperature		
(°F - 32)	$\times 0.556$	= °C
°R	$\times 0.556$	= °K
Power		
HP	$\times 0.7457$	= KW

### References

- 1 Shemeld, D. E., *Turbocompressors—Applications, Selections, Limitations*, Dresser Clark, Oct. 1981.
- 2 Fejer, A. A., and Hendrickson, R. L., "Proposed Gas Turbine Procurement Standard Rating and Performance," ASME Paper No. 71-WA/GT-1.
- 3 Jenkins, D. R., and Harmon, R. A., "Proposed Gas Turbine Procurement Standard," ASME Paper No. 71-WA/GT-2.
- 4 Ainley, D. G., "Performance of Axial Flow Turbine," *Proceedings of Institute of Mechanical Engineers*, Vol. 159, 1948-1949, p. 230.
- 5 Labadie, P., and Boutzale, W., "Gas Turbine Air Filtration—A Means of Sulfidation Control," ASME Paper No. 76-GT-59.
- 6 Yoshimoto, K., Hirata, Y., and Chiba, M., "Salt in Sea Atmosphere and Its Removal for Gas Turbines," ASME Paper No. 76-GT-58.
- 7 Lages, F. P., III, "Air Filtration and Sound Control Systems for Gas Turbines—The State of the Art," *Proceedings of the Eighth Turbomachinery Symposium*, Texas A&M University, Nov. 1979.
- 8 Cumpsty, N. A., "Excess Noise from Gas Turbine Exhausts," ASME Paper No. 75-GT-61.
- 9 Samuels, J. C., and Gale, B. M., "Effect of Humidity on Performance of Turbojet Engines," NASA TN 2119, 1950.
- 10 Horlock, J. H., *Axial Flow Turbines*, Krieger Publishing Co., 1973, p. 127.

## A Horseshoe Vortex in a Duct<sup>1</sup>

**Dr. C. J. Baker.**<sup>2</sup> This writer has recently completed a reappraisal of his Ph.D. work and the work of other investigators on the flow around the bases of wall-mounted circular cylinders [1]. He derived empirical formulae for the distance of the primary separation upstream of the cylinder leading edge(s) and for the distance of the primary vortex from that point  $v$ . For tall cylinders of diameter  $D$  with displacement thickness Reynolds number  $U_\infty \delta_1 / \nu > 10,000$  mounted on a wall with a turbulent boundary layer of shape factor  $H$ , these formulae are

$$s/D = 15.6(U_\infty \delta_1 / \nu)^{-0.35} (H/H_0)^{1.8} \quad (1)$$

$$v/D = 0.10(U_\infty \delta_1 / \nu)^{-0.1} \quad (2)$$

$H_0$  is the form parameter for a corresponding zero pressure gradient boundary layer with displacement thickness Reynolds number  $U_\beta \delta_1 / \nu$ . Equations (1) and (2) can thus be used to calculate  $s/D$  and  $v/D$  for the conditions of the experiments reported in the paper (Tables 1 and 2). These formulae give

$$s/D = 0.63 \quad v/D = 0.26 \quad (3)$$

The results shown in Fig. 6 of the paper give

$$s = 0.058 \text{ m} \quad v = 0.026 \text{ m} \quad (4)$$

The vortex position is taken to be at the point of minimum pressure. If an "effective cylinder diameter" of 0.095 m is assumed for the experimental model, this gives

$$s/D = 0.61 \quad v/D = 0.27 \quad (5)$$

Now the model has a width of 0.13 m far downstream of the leading edge, so an effective diameter of 0.095 m in the leading edge region seems very reasonable. Thus it can be concluded that the present results are not inconsistent with the results of previous investigators.

## Reference

- 1 Baker, C. J., "The Position of Points of Maximum and Minimum Shear Stress Upstream of Cylinders Mounted Normal to Flat Plates," submitted to the *Aeronautical Journal*.

<sup>1</sup>By J. Moore and T. J. Forlini, published in the July 1984 issue of the *JOURNAL OF ENGINEERING FOR GAS TURBINES AND POWER*, Vol. 106, No. 3, pp. 668-676.

<sup>2</sup>University of Nottingham, Department of Civil Engineering, Nottingham, England

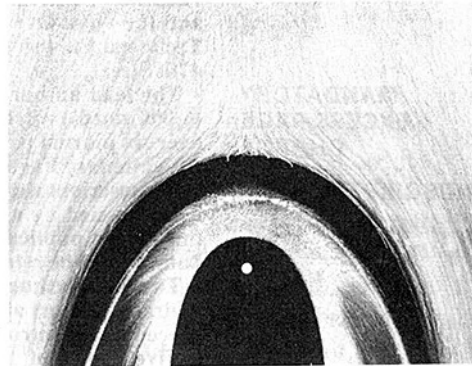


Fig. 1 Flow visualization of the limiting streamlines on the endwall around the Rankine half-body. The white dot on the body, near the leading edge, is the location of the line source.

## Authors' Closure

The authors thank Dr. Baker for his thoughtful and complementary discussion. The locations of the minimum in pressure and the saddle point of primary separation upstream of the body on the duct endwall do appear in good agreement with the locations given by Dr. Baker's formulae. However, we just happened to have a static pressure tapping at the location where Dr. Baker's formula predicts a minimum. Our static pressures did indeed show a minimum there, but this is only slender support for the equation.

In further discussion of our paper, both in Amsterdam and at the von Karman Institute in Brussels, Dr. Sieverding described an alternative method for locating the primary and secondary separation lines. He uses a similar endwall oil-flow visualization technique but applies the mixture in two regions, one upstream of the body and the other near the body. The upstream fluid is moved downstream by the primary flow while the other fluid is moved away from the body by the secondary flow. Using this technique for the present Rankine half-body flow gave the result shown in Fig. 1. It can be seen that the primary separation line is now sharply defined as the limit of the upstream titanium dioxide flow. The secondary separation line is seen as an accumulation of white titanium dioxide near the outer limit of surface flow away from the body. The interesting feature of this flow visualization is the dark area between the two separation lines where the titanium dioxide did not reach.

The authors believe this modification of the surface oil-flow visualization technique by Dr. Sieverding and the formulae presented by Dr. Baker will be of lasting interest in the study of endwall flow and heat transfer in turbomachines.